Mémoire en vue d'obtenir le diplôme d'

Habilitation à Diriger des Recherches

Spécialité : Terre, Univers, Environnement
Université Grenoble Alpes

Présenté par Erwan Pathier

Earthquake cycle, aseismic deformation and tectonics: some contributions from satellite geodesy

Soutenance prévue le 02 novembre 2020

Composition du comité d'HDR

Jian-Cheng Lee (Prof. Academia Sinica, Taiwan), rapporteur
Lucilla Benedetti (Dir. Rech. CNRS, Univ. Aix-Marseille), rapporteure
Juliet Biggs (Prof. Univ. of Bristol), rapporteure
Stéphane Mazzotti (Prof. Univ. Montpellier), examinateur
Michel Campillo (Prof. Univ. Grenoble Alpes), examinateur

Abstract

This document presents my research activities since 2004, which have been centered on the broad topics of the earthquake cycle, aseismic deformation and tectonics. I have favored an observational approach using satellite geodesy (InSAR and GPS) to address various issues presented in the following order: (1) Coseismic deformations from geodetic measurements (InSAR, SAR image correlation, GPS), illustrated with case studies in Pakistan, Mexico, and Indonesia ; (2) the role of aseismic deformations occurring in the seismogenic zone during the seismic cycle, including interseismic deformation at regional scale (Northeast Iran, Taiwan Island), slow earthquakes in subduction zone (Mexico) and aseismic creep of active faults in Taiwan and Venezuela ; (3) the role of aseismic deformation in long-term deformation over many seismic cycles, including comparison of current deformation rates with geological rates and preliminary on-going work on numerical modelling of the aseismic deformation by the Discrete Element Method. Those studies have also implies methodological work about InSAR, including atmospheric corrections in InSAR, data fusion, source separation and massive processing of InSAR data. I also investigate other techniques like image correlation or Lidar and study other phenomena like landsides and subsidence with a methodological perspective. This work has resulted into 24 papers published in peer-reviewed international journals and more than 80 communications in international meetings and workshops. I closely worked with seven PhD students including five co-supervision, four post-docs and supervised fifteen master students. Since 2007, in parallel to my teaching activities, I participated in three European projects, five ANR projects, six national and bilateral projects, about twenty projects with space agencies and about ten projects in response to local calls for tenders. I have also been involved in the development of research infrastructures related to massive data processing and on-demand InSAR processing services in DataTerra/ForM@Ter at national level and EPOS at European level.

Remerciements

Je souhaite tout d'abord remercier Juliet Biggs, Lucilla Benedetti et Jian-Cheng Lee d'avoir accepté d'être rapporteurs de ce travail, ainsi que Stéphane Mazzotti et Michel Campillo qui par leur complémentarité m'ont permis d'avoir un jury d'une grande richesse. Merci pour le temps que vous avez consacré à la lecture de ce document et à vos questions et remarques stimulantes lors de la soutenance. Un remerciement supplémentaire à Michel Campillo qui a accepté de présider ce jury et de me tenir compagnie dans l'amphithéâtre vide d'ISTerre face à des écrans de visioconférences. Je remercie au passage le Coronavirus de ne pas s'être invité parmi nous.

Ils n'étaient pas là en présence, mais beaucoup m'ont exprimé leur soutien, un grand merci à tous les membres d'ISTerre qui permettent d'avoir un environnement de travail agréable et varié au quotidien et très enrichissant sur le long terme. J'aurais aimé pouvoir partager un moment de convivialité avec vous après la soutenance (heureusement, j'ai pu discuter un peu avec la machine à café du rez-de-chaussée, fidèle au poste…), j'espère que ce n'est que partie remise ! Merci également à tous mes collègues avec qui j'ai pu collaborer, en France, à Taiwan, au Royaume-Uni, au Mexique, en Iran et ailleurs, avec une mention spéciale pour Bénédicte Fruneau qui m'a initié à l'interférométrie radar et avec qui j'ai toujours plaisir à collaborer depuis.

Merci encore à L'équipe « Cycle sismique et déformations Transitoires » et ses « secondaires », une équipe où je me sens bien. Une équipe qui a beaucoup évoluée depuis 2007 et qui continuera surement d'évoluer en préservant, je l'espère, sa parité et sa convivialité. Merci particulièrement à Marie-Pierre Doin et Mathilde Radiguet qui étaient en pratique les premières directement concernées par cette HDR, et qui m'ont fait confiance et ont toujours abordée la question avec tact et parcimonie (contrairement à d'autres qui se reconnaitront… mais que je pardonne car ils ont su y mettre de l'humour).

Merci aussi à tous les étudiants, doctorants et post-doctorants avec qui j'ai eu l'occasion de travailler, c'est toujours un réel plaisir pour moi d'apprendre à vous connaitre, vous voir évoluer, vous transmettre autant que je peux, et en retour être questionné, stimulé, surpris...

Pour finir, mes remerciements vont à Anne, Manon, Eline et Romain, désolé pour cet été 2020 plus studieux que prévu, merci pour votre soutien indéfectible et vos marques d'attention au quotidien.

Contents

I – General Introduction

Through a synthesis of my research activities since 2004, this document aims to show the main scientific issues that have guided my research work during these years and to present my research prospective for the coming years. It also seeks to highlight the specificity of my research at the crossroads of several disciplines, and the choices and strategies adopted to address the scientific questions raised. It also aims to highlight the role of supervision of students and early stage researchers that accompanies my own research.

My scientific interests originally stem from a strong curiosity for understanding the phenomena that shape the Earth's relief and my attraction for observing the Earth from space. During my PhD, I focused more specifically on active tectonics and its link with the seismic cycle and I was introduced to the world of satellite radar interferometry (InSAR). During my post-doc from 2004 to 2006, I clearly made the choice to tackle scientific issues directly related to the seismic cycle. My research project when I was recruited in 2006 as an assistant professor at the University Joseph Fourier (now Université Grenoble Alpes) was a concrete expression to my interest in this theme and in particular, on the modalities that deformation can take during the cycle: transient or permanent, seismic or seismic, localized or distributed.

Since then, I have kept my focus on this subject, emphasizing the question of inter-seismic aseismic deformations, and always keeping in mind the need to make the link with the longer-term deformation observable in the relief. "Earthquake cycle, aseismic deformation and tectonics" are therefore three major facets of my research. Taken together, these three themes form a vast field at the interface of several disciplines such as seismology, geodesy, paleoseismology, tectonics, geology, physics, mechanics, numerical modelling, etc., which go far beyond the field of competence of one person. Taking advantage of my affinities and skills, I adopted the "parti pris" of observation to tackle these subjects, and more particularly observations from satellite geodesy and more particularly observations from satellite geodesy that allow to cover large areas of study in a homogeneous and systematic way. Years later I'm still convinced that new observations significantly contributes to the scientific advancement by bringing important constraint to the kind of physics needed and helping to discriminate between theoretical models and thus usefully guide the geophysical modeling, especially in the domain of aseismic slip, where the physics of the phenomena is still largely unknown and debated.

This strategy involved looking for new observations where it was most relevant and on different sites and objects of study. Apart from some "opportunistic" studies, the choices of my study areas were guided with on the one hand, by the availability to access in-situ data in places where surface deformation rate is strong enough for InSAR and, on the other hand, the possibility to establish long-term scientific collaborations favorable to long observation times essential for interseismic study. I was able to benefit in my laboratory (called LGIT at the time before becoming ISTerre a few years later) from a very favorable environment, especially in my early years concerning the emerging issue of transient deformations such as slow earthquakes. With many skills around me in seismology, GPS and tectonics, I was able to focus on satellite imagery, and more particularly InSAR. Indeed, from the point of view of the methods used in my research, I have mainly used observations from modern techniques of satellite geodesy (GPS, image correlation, InSAR), a field which has seen a strong development of these capabilities over the last 20 years. Geodetic techniques are indeed fundamental for the observation of aseismic

deformations, even if in fact this term covers phenomena also observable by "subtle" seismology, which makes the geodetic and seismological approaches very complementary.

This observational approach was inseparable from work on methodology and to understand the limits of the observation methods I used. Observations from space involve understanding the signal related to the atmosphere being passed through or to the vegetation or snow cover. It is also necessary to be able to separate the tectonic signal from other geophysical signals related to hydrology, compaction subsidence, landslides, or human activities for examples. This led me to explore other methods of ground deformation measurements and other data analysis techniques, sometimes applied on objects quite different from my initial research (subsidence, landslide, urban environment). Those "thematic detours" were often ultimately beneficial to my central research themes. Another consequence of the satellite observation approach on my activities has been the need to invest time in computational aspects and their associated infrastructures. Indeed, one of the most striking evolutions in InSAR over the last 20 years has been the explosion of the volume of data with the emergence of the “Big Data” issue. Getting the capacity to process those data is a problem in itself and we have tried to find solutions to it.

Most of my activities have been carried out through collaborations and through research training. In the course of my career, I have had the opportunity to supervise several PhD students and about fifteen Master's or engineering school students. Most of this work has taken place in the framework of scientific projects at international, national or local level either as a participant or as Principal Investigator. Since 2007, I have participated in three European projects, five ANR projects, six national and bilateral projects, about twenty projects with space agencies and about ten projects in response to local research calls. At the same time, I have also been involved in the animation of research at national and local level, and teaching activities related to my position as “Maître de conférences” (eq. to Assistant Professor) whose missions in France are half teaching and half research.

In this document, I have tried to synthesize and make links between all these elements, which should help to evaluate my research and supervision activities in the context of my teaching and research position. The following section describes the choice I made in the organization of this document to bring all these elements together and, I hope, to allow the reader to navigate between the different parts without too much difficulty.

Document organization

The main body of the document is dedicated to a synthesis of my research activities since 2004, my research prospective for the coming years, ending by a brief conclusion:

- Part II – Synthesis of Research Activities
- Part III – Research Prospective
- Conclusion

Then is a list of the bibliographical references cited in the document, from which the references to my own pieces of work has been moved to the following section « Publications and communication as author or coauthor » that gather my scientific production:

- Bibliography
- Publications and communication as author or coauthor

In the objective to help the reader to assess my contributions, the citations of others works followed the convention (author date), while citations of work I contributed to are cited with a letter followed by a number as a clickable link (e.g. A18), that follows this classification:

- A## : Peer-reviewed Journal Article published in international journals
- P## : Peer-reviewed Conference Proceedings
- C## : Communications (Oral or Poster presentation) in international meetings
- O## : Other communications (e.g. in French, not peer-reviewed article, unpublished reports, …)

In this list of publication, Author* indicates when the first author is a student or a post-doctoral researcher I have supervised.

For convenience, six of my journal articles that are the most significant with respect to this memoir are provided in Appendix 1 and referred in the text as pdf-# that is a clickable link to the article (e.g. pdf-1)

The document finished by appendix 2 to 7 aiming to give a synthetic view of different aspect done in my career:

- Appendix 2: CV
- Appendix 3: List of the different study-areas I have work on.
- Appendix 4: List of the different research projects I have been involved in.
- Appendix 5: List of PhD, Master students and post-doc young researchers I have work with
- Appendix 6: List of responsibilities and other activities related to research.
- Appendix 7: summary of my teaching activities.

Bonne lecture …

II – Synthesis of Research Activities

1 – Introduction

Scientific context

The question of the importance of aseismic deformation in the seismic cycle arose very early in the theoretical framework of plate tectonics. At plate boundaries, the question of aseismic deformation is rather seen at that time as a possible « negative » of seismicity where there are long duration seismic gaps (e.g. Kelleher et al., 1973). This view is then very much influenced by the numerous works dating back to the 1960s on the aseismic slip observed in central California and notably on the San Andrea fault system (e.g. Steinbrugge et al., 1960; Schulz et al., 1982). Those observations made by ground-based geodesy already laid the foundations for the notions of afterslip, transient aseismic slip ("creep events"), propagating slip events, slip heterogeneity, slip events triggered by remote earthquakes and possible aseismic slip as precursors of earthquakes (for a review see Wesson, 1988). Those observations are also already prompting research into the physics of fault slip, to understand what determines the seismic or aseismic character of fault slip (Scholz, 1990).

Knowing where and when the aseismic deformations take place during the earthquake cycle and to what extent it releases the tectonic stress is also fundamental for the seismic hazard estimation, as it determines the amount of energy still to be released during earthquakes. However, until the 1990s, outside of California, observations of aseismic slip on continental faults were limited to a few sites (e.g. on the North Anatolian Fault, Turkey, Ambraseys, 1970; Aytun, 1982; on the Longitudinal Valley Fault, Taiwan, S.-B. Yu & Liu, 1989).

In the early 1990s, the first results of satellite geodesy observations gradually changed the situation. Here again the impulse will come from studies in California, where GPS observations of interseismic deformations, started around 1986, gave their first results after a few years of measurements (e.g. Feigl et al., 1990, 1993). They complement on a regional scale near-fault ground-based studies, which continue to be carried out and confirm the transient nature of slip events (Gladwin et al., 1994; Linde et al., 1996). On the InSAR side, it is the Landers earthquake that really gives the start of the technique as a tool to measure tectonic deformations with the study of the coseismic displacements by Massonnet et al. (1993) using data from the ERS-1 satellite launched in 1991 (Figure 1)

Since then, GPS and InSAR will become very complementary companions for the study of surface displacements. However, GPS will become operational much more quickly because of its origins (a military system with strong operational constraints), whereas InSAR, despite its "sensational" beginnings, will take much longer to express its potential. This is certainly because InSAR was based on satellite missions not specifically dedicated to the measurement of surface displacements, not compatible with each other and lacking acquisition continuity (Figure 1).

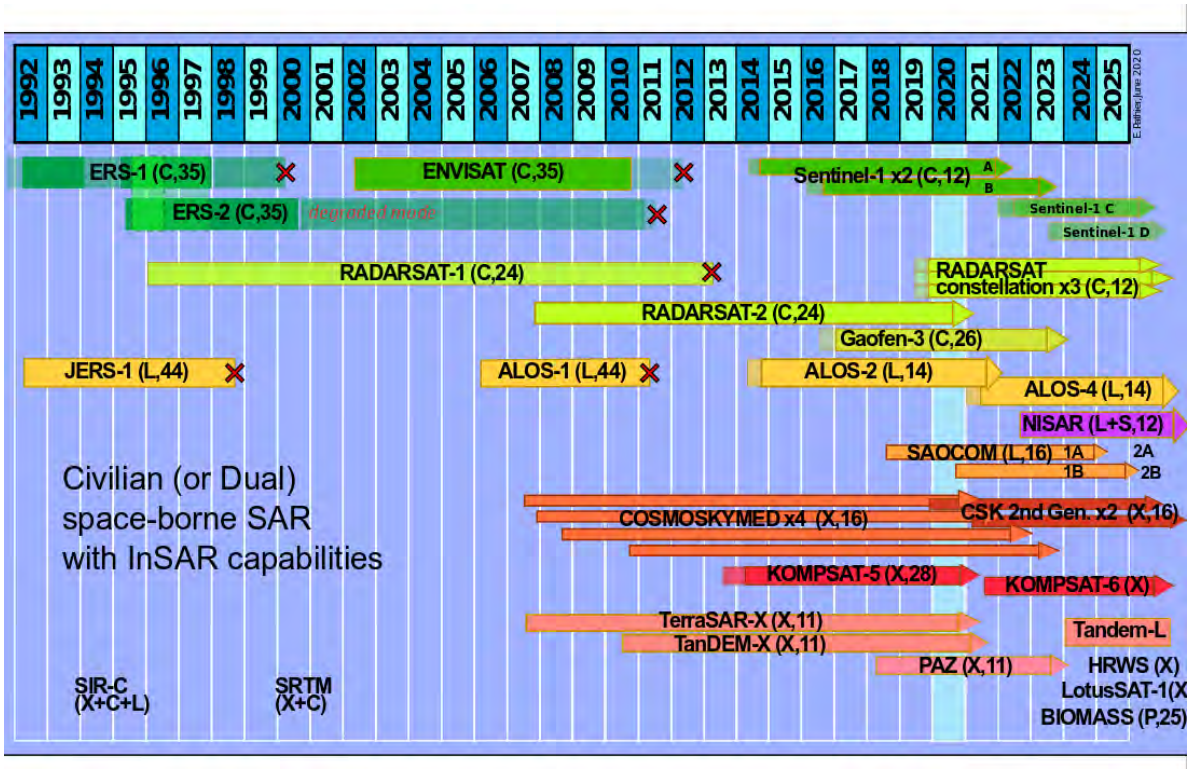

Figure 1 : Time-line of civilian or dual civil-military space-borne SAR imaging systems with InSAR capabilities. In brackets, letters indicate the microwave domain of the radar (L-band 15–30 cm, C-band 3.75–7.5 cm and X-band 2.4–3.75 cm) and numbers the repeat cycle.

The first observations of aseismic deformation by InSAR will be on the post-seismic deformation of the Landers earthquake (Massonnet et al., 1994; Massonnet, Thatcher, et al., 1996; Peltzer et al., 1996, 1998). The ERS-1 and ERS-2 satellites will also allow the first shallow creep observations on the San Andreas fault (Werner et al., 1997; Rosen et al., 1998) and on the Hayward fault (Bürgmann et al., 1998; Bürgmann, Schmidt, et al., 2000). The review papers of Massonnet and Feigl (1998) and Bürgmann et al. (2000) are good syntheses of the InSAR advances of the 1990s. The first analyses of interseismic deformation that are more distributed than the much localized deformation caused by superficial creep, will only arrive at the turn of the century. Indeed, they require a longer observation time to get the tectonic signal out of the other sources like atmospheric perturbations or noise (Bawden et al., 2001; Borgia et al., 2000; Peltzer, Crampé, Hensley, et al., 2001; Wright, Parsons, et al., 2001; A02).

However, this momentum will be partly slowed down with the ERS-2 gyroscope problems in the 2000s turning it into a degraded mode for InSAR (Figure 1), before accelerating again with the launch of Envisat in 2002 and ALOS-1 in 2006. It should be noted that JERS-1 satellite (due to a too loose orbital control) and Radarsat-1 satellite (due to a restricted data acquisition and distribution policy), did not allow such a wide use for the measurement of tectonic deformations, despite some successes (e.g. Massonnet, Feigl, et al., 1996; Murakami et al., 1996; Tobita et al., 1998; Fujiwara et al., 1998; Nishimura et al., 2001; Feigl et al., 2002; Doubre & Peltzer, 2007).

The early 2000s also marked a turning point in the analysis of InSAR data, with the start of time series analysis, making it possible to reconstruct a chronology of displacement from a network of pairs of images. Until then, to bring out the tectonic signal the stacking method (assuming steady state deformations) had been used to analyze interseismic deformations. Two main time-series approaches have emerged: the so-called « small baselines » approach (Usai et

al., 1999; Usai, 2003; Berardino et al., 2002; Lanari et al., 2004), and methods grouped under the term PSI (Persistent Scatterers Interferometry), including the Permanent Scatterers (PS) method (Ferretti et al., 1999, 2000, 2001; Colesanti et al., 2003) which was the first to be developed followed by many other variants (e.g. Bovenga et al., 2003; Hooper et al., 2004; Kampes & Adam, 2003; Mora et al., 2003; Wegmüller et al., 2004).

From the 2000s, alternative methods to InSAR for the measurement of coseismic displacement by remote sensing also emerged: SAR images correlation (Fialko et al., 2001; Jonsson et al., 2002; Michel et al., 1999; Peltzer, Crampé, & Rosen, 2001) and optical images correlation (Dominguez et al., 2003; Feigl et al., 2002; Michel & Avouac, 2002; Van Puymbroeck et al., 2000). At the same time, with the development of permanent GPS networks aided by the decreasing cost of GPS stations, observations of aseismic deformations are increasing worldwide, especially in subduction zones where the first periodic slow earthquakes were discovered in the early 2000s. Most of the progress is concentrated on two subduction zones: in the Cascades and in Japan (Dragert, 2001; Obara et al., 2004; Rogers & Dragert, 2003). On this occasion the very definition of aseismic deformation has evolved somewhat, in the sense that advances in seismology have made it possible to show that there were weak seismic signals associated with this deformation such as non-volcanic tremors and low frequency earthquakes (e.g. Obara, 2002; Peng & Gomberg, 2010). This illustrates a long-term trend of a rapprochement of the two disciplines of geodesy and seismology that began in the previous decade with the joint inversions of coseismic slip (e.g. Delouis et al., 2000; Hernandez et al., 1997; Ruegg et al., 1996; Wald et al., 1996).

Since their beginnings, the geodetic observations of aseismic deformation described above have been accompanied by an in-depth debate on the representativeness of these measurements made over a few years, compared to the longer-term deformation seen for instance in paleoseismology or in the relief by geomorphology (e.g. Schulz et al., 1982; Bilham et al., 1997; Bendick et al., 2000; Friedrich et al., 2003; Mériaux et al., 2004; K. Wallace et al., 2004; England & Molnar, 2005). This question, which is still topical, touches both the question of the present-day position of a fault within the seismic cycle (e.g. Brendan J. Meade et al., 2013; Dolan & Meade, 2017), but also raises the potential role of aseismic deformation in relief formation with respect to the role of seismic increments.

Research studies choices along with evolutions of data and methods

It is in this scientific context described above that my post-thesis work, which began in 2004 and is described in this dissertation, takes place. To address the issues related to the seismic cycle, I have favored the observational approach using satellite geodesy (mainly InSAR and GPS), well adapted to the study of the earthquake cycle (Elliott, Walters, et al., 2016). It allows both to cover large area of active fault systems (typically 100 km x 100 km and more), and at the same time having a good spatial and temporal resolution. There has clearly been a strong link between the evolution of satellite geodetic observation methods over the last 16 years and the research topics I have studied. The evolution of sensors but also of data analysis methods have given me the opportunity to progress into my scientific problems through new observations on sites already studied or to tackle new study cases not accessible before.

Regarding coseismic studies, in the case of the 2006 Pakistan earthquake, InSAR was very limited by strong decorrelation problem in near-field. We were able to take advantage of the radar (SAR) images correlation technique, the feasibility of which had recently been demonstrated by Michel et al. (1999) to overcome the InSAR limitation (A06). It was, to my knowledge, the first study to allow the reconstruction of a continuous 3D coseismic displacement

field just from SAR images correlation. I then extended this topic by working on data fusion and uncertainty estimation during the Yajin Yan's PhD thesis (A10 ; A12), issues related to the increasing use of different datasets acquired by different techniques (GPS, INSAR, images correlation) and in different acquisition modes. For instance, the combination of InSAR with optical images correlation provided a more precise vision of the deformation on the 2018 Palu earthquake (A23).

From a methodological point of view, I also studied, in the framework of Ulrich Kniess' PhD thesis, the Lidar technique applied to landslides (A09, A17). During the PhD, we developed a correlation method for multi-dates DEM Lidar acquisitions, which allows to measure multi-decimetric displacements, which was a useful complement to correlation of optical satellite images Sentinel-2 in a later study on landslide reactivation (A22), but could also be applied to earthquake studies

With regard to aseismic deformation, I chose to give priority to studies on interseismic deformation over post-seismic deformation, because it seemed to me to be a less explored field. Between 2002 and 2010, the Envisat satellite acquired a large dataset suitable for InSAR, significantly improving the spatial and temporal coverage on a global scale compared to its predecessor ERS-1 and ERS-2. This made it possible to investigate new study sites, poorly covered by ERS, such as the Mexican subduction (A13), or Iran (A16). When I arrived at Grenoble, the Guerrero region in the Mexican subduction was indeed a target of choice because of the discovery by the analysis of the permanent GPS network of slow earthquakes in the seismic gap of Guerrero a few years earlier (Lowry et al., 2001; Kostoglodov et al., 2003; Larson et al., 2004; Franco et al., 2005), and the willingness of several lab teams of the lab to set up a stimulating project (called GGAP) on this subject in collaboration with colleagues from Mexico at UNAM. This work involved Olivier Cavalié's post-doc and Guillaume Bacques' PhD thesis. On N-E Iran, it is during Zahra Mousavi's PhD thesis that Envisat data covering several years of interseismic deformation have allowed us to better quantify the slip rate of the Doruneh and Sharoud fault systems.

In 2006, the long-awaited launch of the ALOS-1 satellite also opened up new prospects with respect to Envisat. This radar satellite, operating in L-band, made it possible to have a better InSAR signal-to-noise ratio than in C-band (ERS, ENVISAT) in areas with a high vegetation cover. Moreover, ALOS-1 also benefited from better orbital control and better spatial and temporal coverage than its predecessor JERS-1 did. After a few years of ALOS-1 observation, sufficiently long time series for interseismic studies was available so that we were able to revisit the Taiwan area on which I worked during my PhD thesis (A11 ; A19) and to investigate active faults deformation in Venezuela (A18). They were two very relevant zones due to their high rate of aseismic deformation (S.-B. Yu et al., 1997; Angelier et al., 2000; J. C. Weber et al., 2001; François Jouanne et al., 2011) but whose study by InSAR was limited by the strong temporal decorrelation of previous C-band SAR data. In Taiwan, the study of the creep of the Longitudinal Valley Fault and the aseismic deformation of the SW fold-and-Thrust belt were done in the PhD thesis of Johann Champenois, and in Venezuela the study of the creep of the El Pillar fault was done in the PhD thesis of Léa Pousse. Improvement in the NSBAS processing chain developed in Grenoble (P04) also allowed us to go beyond the results of J. Champenois' thesis on Taiwan. It led to the identification of the geological structures causing the strongest aseismic deformation in southwestern Taiwan and the first spatially continuous deformation map at the scale of Taiwan Island demonstrating the continuous nature of the deformation across the central chain compatible with the global uplift of the chain (C59 ; C66 ; A20).

It was not until the start of the Sentinel-1 (C-band) and ALOS-2 (L-band) missions at the end of 2014 that a new era for the study of tectonic deformation was launched, following a « data gap » between 2011 and 2014 that could not really be filled by a new generation of X-band satellites (CosmoSkymed and TerraSAR-X) launched in 2007 (Figure 1). For several reasons, these X-band satellites have been relatively little used to study large-scale tectonic deformations, mainly due to the lack of a systematic global acquisition strategy for InSAR, a restricted data access policy, and the fact that they operate in X-band (3 cm wavelength), which is less favorable for natural environment observation than C- or L-band. The Sentinel-1 and ALOS-2 satellites have overcome these three difficulties and in turn opened up new prospects. Thanks to these satellites, the study of large earthquakes (M>6) on-land becomes more systematic, and is facilitated even in areas with high vegetation such as the case of the Palu earthquake in 2018 (A23). Above all, they make it possible to carry out studies on interseismic deformations on a larger scale than before. For example, in the framework of Louise Maubant's PhD thesis, we have been able to extend the study area of slow slip event and interseismic coupling in the Mexican subduction zone (A24).

Each of these evolutions in satellite data has been accompanied by new needs in terms of processing and analysis. From this point of view, the opportunities for processing of large study areas made possible by the arrival of Sentinel-1 and ALOS-2 data require me to be involved in other topics, quite far from my central research thematic, those related to massive data computing. This challenge, which goes beyond the framework of laboratory facilities, has required me for several years now to be involved in national and European projects (C74 ; C78).

In this part II about the synthesis of my research activities, the various research issues mentioned in this introduction are more detailed and are grouped thematically in the following six sections:

- Coseismic deformations
- Interseismic deformation with assumption of steady-state slip at depth
- Slow slip events in subduction zone: transients slip at depth
- Creeping faults at shallow depth: an InSAR favorite
- Aseismic deformations in upper crust: what can we learn from SW Taiwan
- InSAR evolutions: data, method and processing

2 – Coseismic deformations

Even if my main subject of study has been aseismic deformation, I have occasionally taken part in earthquake studies, as coseismic deformation remains a key element at the heart of the earthquake cycle. Indeed, it is important to properly quantify the spatial and temporal distribution of the coseismic slip, part of which may be aseismic and thus not be seem by seismology. Some of these works are part of a research strategy as in Mexico or Taiwan; others have been more opportunistic as is sometimes the case for large earthquakes. Here are first presented three examples of my work that are representative studies of the evolution of the estimation of the coseismic slip distribution over the last 15 years, followed by another representative example of earthquake-related aseismic deformations on secondary geological structures.

Coseismic slip distributions

Satellite imagery (InSAR, radar or optical image correlations) has now become a standard tool in the study of large earthquakes (typically Mw > 6), responsible for on-shore surface deformation. After a very promising start with the 1992 Landers earthquake InSAR study by Massonnet *et al* (1993), 20 years later, Wright *et al* (2013) report about 80 continental earthquakes (Mw > 5.5) studied by InSAR. This is actually only a part of the cases reaching the surface displacements requirement to be studied by satellite geodesy, mainly due to the limitations of satellite acquisition capabilities during this period dominated by Envisat data. It is really only from 2015 onwards, that the promise of being able to study large earthquakes with significant (at least centimetric) on-shore deformation in an almost systematic way begins to be realized thanks to the radar Sentinel-1 and ALOS-2 missions completed by optical imagery in case of large (>20 cm) near-fault displacements.

EnviSAT era: the Kashmir earthquake case study and the generalization of multi-methods and multi-datasets coseismic studies.

On 8 October 2005, when the deadly Kashmir Mw 7.6 earthquake occurred, there were no GPS stations close to the event. As the preliminary seismological results had significant uncertainties about the location of the fault and field work was not possible because communication routes were cut, the question arose as to which geological structure the earthquake occurred on and what was its significance in the long series of large historical earthquakes on the south-Himalayan front (Bilham, 2004). This case study is a very representative situation of Envisat capabilities to study an earthquake using remote sensing technique only.

Launched in 2002, Envisat was then the only operational satellite for InSAR with Radarsat1, but with the advantage over the latter of having a more global and systematic acquisition strategy and a more open data access policy. Thus in October 2005, there is an EnviSAT archive of data acquired over the Kashmir area in the months preceding the earthquake, this short time is fundamental for optimal comparison of images before and after the earthquake (Meng Wei & Sandwell, 2010). The images cover the study area in different viewing directions (ascending orbit

and descending with eastward and westward radar-looking respectively), making it possible to constrain the 3-D surface displacement. The European Space Agency (ESA) was able at that time to quickly plan new acquisitions, InSAR-compatible with previous acquisitions. The orbital control of EnviSAT is good enough to get baselines (distance between two orbital trajectories) small enough (<300m) to perform good quality SAR images comparison. Moreover, the provision by ESA of SAR data just after their acquisition is now fast (24 hours) and centralized without depending on local reception stations. Data processing times are then of the order of 2 days. All these conditions represent significant improvements over the use of the ERS-1, ERS-2 or JERS-1 satellites in the previous decade.

This supports a more systematic study of large earthquakes on a global scale, although the 35-day EnviSAT orbital cycle remained a strong limitation. Indeed, such a revisit time is an obstacle to the use of the results from the first days after an earthquake in the context of disaster management, especially since in practice data are not systematically acquired every cycle, which often results in a time gap of several months between pre- and post-event images. This situation is also degrading the quality of InSAR observations. Moreover, in the case of the Kashmir earthquake, due to the strong gradient of displacement on the surface and the presence of steep slopes in this mountainous region, the interferograms are very noisy near-fault where they are not exploitable. On the other hand, this dataset favors the use of another less accurate but more robust technique for measuring displacement: sub-pixel correlation of SAR images. By combining the different measurements, it is then possible to reconstruct the surface displacement field in 3-D with sub-metric accuracy (Figure 2). Those measurements will be complemented by the visual analysis of Quick-Bird optical images (60cm resolution) to precisely map the fault trace, and will be used to perform an inversion of the slip distribution. This study, carried out during my post-doc, resulted in a publication (A06) provided in the appendix (pdf-1).

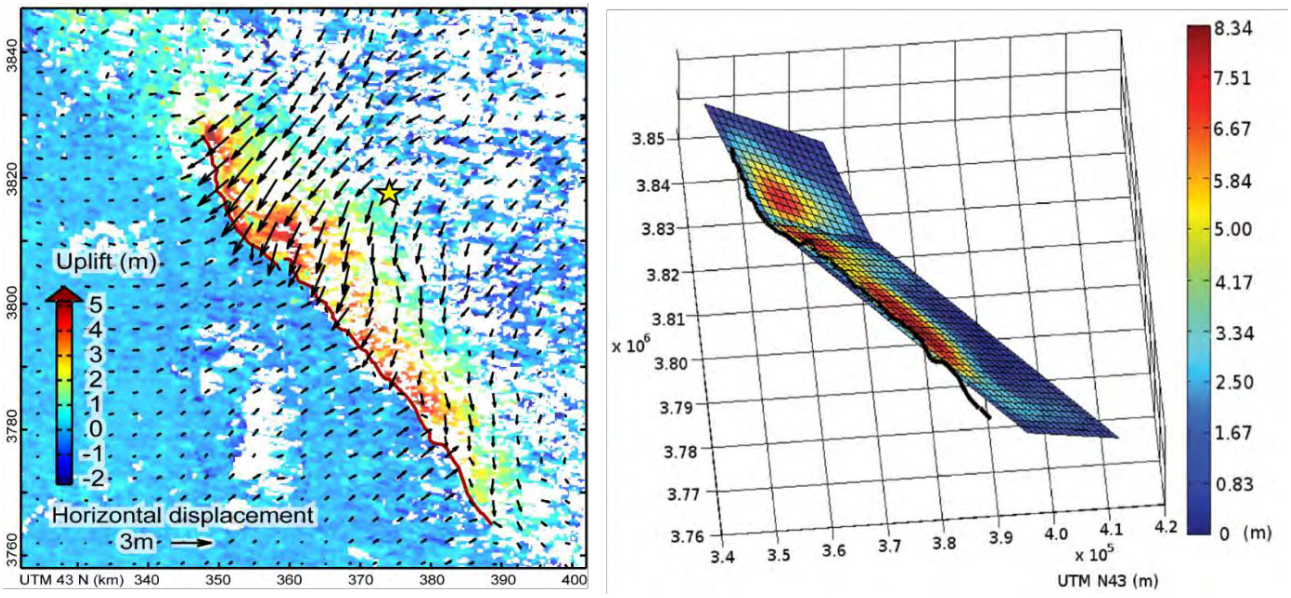

Figure 2 : Coseismic study of the 8 October 2005 Kashmir Earthquake. Left: 3D surface displacement field of the retrieved from EnviSAT SAR images correlation (A06). Right: coseismic slip distribution from InSAR and SAR data (A12).

Precise mapping of the rupture trace and coseismic slip distribution showed that the fault had ruptured two thrust-fault segments along an ancient major geological boundary known as the

Main Boundary Thrust (MBT) and that the segments are in line with the Indus-Kohistan seismic zone (IKSZ). The coseismic displacement field also suggests a structural control on the slip distribution, with the Jhelum Fault marking the discontinuity between the two fault segments, and to the north the end of the rupture corresponding to a dramatic bend of the MBT. Such structural control seems to be a quite common feature (e.g. Manighetti et al., 2005; Lasserre et al., 2005; Y. Klinger et al., 2006; Z. Wang et al., 2009; Elliott et al., 2011). In the northern extension of the Kashmir earthquake rupture, a more diffuse zone of deformation is observed where aftershock activity is concentrated, suggesting some slip at depth on the IKSZ ramp, but without being able to say whether the slip took place at the time of the earthquake or in early afterslip.

Later, when I arrived in Grenoble, I extended this study by working on the fusion of different data sources within the framework of Yajing Yan's PhD thesis in the ANR project EFIDIR ("Extraction and Fusion of Information for Displacement Measurement in Radar Imagery"). This work was in the context of the increasing use of different geodetic data sources for the estimation of the coseismic slip distribution that emerged strongly in the early 2000s, especially with three other satellite imaging methods complementing InSAR. The first, is the SAR image correlation used in the Kashmir study mentioned above (A06), which was following previous studies, the first of which were on the 1992 Landers earthquake (Michel et al., 1999), 1999 Hector Mine earthquake (Fialko et al., 2001; Peltzer, Crampé, & Rosen, 2001; Jonsson et al., 2002), and 1999 Chichi earthquake (O03). The second, following a first attempt by Crippen (1992), is the optical images correlation technique (Van Puymbroeck et al., 2000) first applied to the 1999 Izmit earthquake (Michel & Avouac, 2002; Feigl et al., 2002) and to the 1999 Chichi earthquake (Dominguez et al., 2003). The third method is a derivative of InSAR allowing the measurement of horizontal displacements along the satellite track which appears a few years later under the name of Multiple Aperture Interferometry (MAI, Bechor & Zebker, 2006) with an application on the 1999 Hector Mine earthquake, followed by others like the 2003 Altai event (Barbot et al., 2008). Those three methods are complementary with InSAR (Simons & Rosen, 2007), notably because they are more robust in near-fault for image correlation techniques, and provide measurements along different view directions allowing the reconstruction of the first 3-D coseismic surface displacements field (Fialko et al., 2001, 2005; Wright, Parsons, & Lu, 2004; Wright et al., 2006, A06). Several of the earthquake studies will then combine several datasets, acquired by different sensors in different acquisition modes and geometry and by different methods (e.g. Feigl et al., 2002; Fialko et al., 2001).

Yajing Yan's PhD thesis, which was between a signal processing lab (LISTIC) and an earth sciences lab (ISTerre), dealt with the question of how to combine different displacement measurement data sets taking into account their respective uncertainties. Yajing compared different approaches: is it better to invert all datasets together (joint inversion) or to adopt a pre-fusion scheme before inversion to keep only the best data in the inversion with a fuzzy approach? Based on the example of the Kashmir earthquake (SAR correlation and InSAR datasets), this study showed that the second approach had the advantage of estimating more realistic uncertainty by avoiding over-simplified assumptions about the properties of sources of error (A10).

Then during Jonathan Perrin's Master's project, following the results of Avouac *et al* (2006) we applied the optical images correlation to ASTER data using the Cosicorr method (Leprince et al., 2007) to estimate the coseismic offsets along the fault trace of the Kashmir earthquake. These results were integrated into the study by Yan *et al* (A12), which better constrained the slip distribution (Figure 2, right) and its uncertainty. We also discussed in this paper the question of the possible influence of post-seismic displacements in the measurements made by satellite

imagery, which is a recurrent problem since post-event images can be acquire several days or several months after the earthquake and thus may contain a non-negligible proportion of post-seismic displacement. Based on measurements made over several years by GPS stations installed one month after the earthquake, Jouanne *et al* (2011) suggested that post-seismic is dominated by afterslip along a flat north of the ramp affected by the main shock. By integrating this flat into the fault model geometry and taking into account the uncertainties in the measurements, the Yan's study showed that the amount of post-seismic had little influence on the coseismic distribution model. Subsequently, Wang and Fialko (2014) will confirm that the post-seismic deformation over a few years is dominated by afterslip mainly down-dip of the coseismic displacement.

Sentinel1-ALOS-2 Era: systematization of coseismic studies and wider use of combination of InSAR and Optical correlation.

At the end of 2010, ENVISAT's orbit is modified to extend its lifetime, but this led to the end of its interferometric mission. A few months later, in April 2011, the ALOS-1 satellite stopped working. These two shutdowns were a serious brake on the use of radar imagery for the study of earthquakes. The L-band ALOS-1 has been a significant step forward, especially for the study of large earthquakes, such as the 2007 Mw 6.6 Noto Hanto earthquake (Fukushima et al., 2008; Ozawa et al., 2008), the 2008 Mw 7.9 Wenchuan earthquake (Chini et al., 2010; A08 ; de Michele et al., 2010; Fielding et al., 2013), the 2009 Mw 7.8 Dusky Sound earthquake (Beavan et al., 2010), the 2010 Mw 7.0 Haiti earthquake (Calais et al., 2010; Jung & Hong, 2017), the 2010 Mw 8.8 Maule earthquake (Xiaopeng Tong et al., 2010; Delouis et al., 2010), the 2011 Mw 6.8 Burma earthquake (W. Feng et al., 2013) or the 2011 Mw 9.0 Tohoku-Oki earthquake (Kobayashi et al., 2011; G. Feng & Jónsson, 2012). Between April 2011 and the end of 2014, despite few successes often in combination with other datasets (e.g. Stramondo et al., 2011; Salvi et al., 2012; Jolivet et al., 2014), the presence of two X-band satellite constellations (CosmoSkymed and Terra-SAR X, Figure 1), which are less suitable for studying major earthquakes, will not compensate for this loss.

For instance, for the study of the Mexican subduction, in which I was involved when I arrived in Grenoble within the framework of the ANR GGAP project, the 20 March 2012 Mw 7.5 Ometepec earthquake could not be analyzed by InSAR, the geodetic measurement relying only on few GPS stations (Graham et al., 2014). For the Petalan Mw 7.2 earthquake of April 18, 2014, we tried to use data from the commercial RADARSAT-2 satellite via an ESA project. However, despite a fast tasking of post-event acquisitions, the time interval with the closest pre-event images was more than 6 months and the orbital baseline was too long (> 150m) so that the interferograms were too noisy and the test was unsuccessful. Although Radarsat-2 has been successfully used many times to study earthquakes (Samsonov et al., 2014), this case is representative of the difficulties of using a satellite like Radarsat-2, running multi-purposes commercial operations, and which does not have a frequent and systematic global acquisition strategy in an background default acquisition mode dedicated to INSAR.

It is this lack that the Sentinel-1a and ALOS-2 satellites launched in 2014, to be completed by the twin satellite Sentinel1-b in 2016, will fill with a great start with the 25 April 2015, Mw 7.8 Nepal Gorkha earthquake (Avouac et al., 2015; Lindsey et al., 2015; Raphaël Grandin et al., 2015; Elliott, Jolivet, et al., 2016). These missions with shorter revisit time, more systematic acquisitions on a global scale and with two complementary wavelengths (C-band at 5.6 cm for Sentinel 1 and L-band at 23 cm for ALOS2) are finally bringing satellite imagery very close to an operational coseismic observation mode. They can now cover most of the continental crustal earthquake M

> 6 with depth < 50 km, except in area with abundant snow cover but also a significant number of subduction earthquake, close enough to the coast to produce centimetric on-shore surface displacement (Elliott, Walters, et al., 2016).

Coming back to the Mexican subduction case, during the Louise Maubant's PhD Thesis, we have been able to process interferograms for all the major earthquake related to the subduction since 2015 (O16 and Figure 3) :

- The 08/09/2017 Chiapas Earthquake (Mw 8.1)
- The 19/09/2017 Puebla Earthquake (Mw 7.1)
- The 16/02/2018 Oaxaca Earthquake (Mw 7.2)
- The 23/06/2020 Oaxaca Earthquake (Mw 7.4)

The first two were intraslab earthquakes, and the last two occurred on the subduction interface. This is a typical example of a « routine » monitoring of earthquake allowed by Sentinel-1 and ALOS-2 mission. This measurement can be used to invert slip distribution (Atzori et al., 2019), or to give constraint in time series analysis when looking for slow slip events.

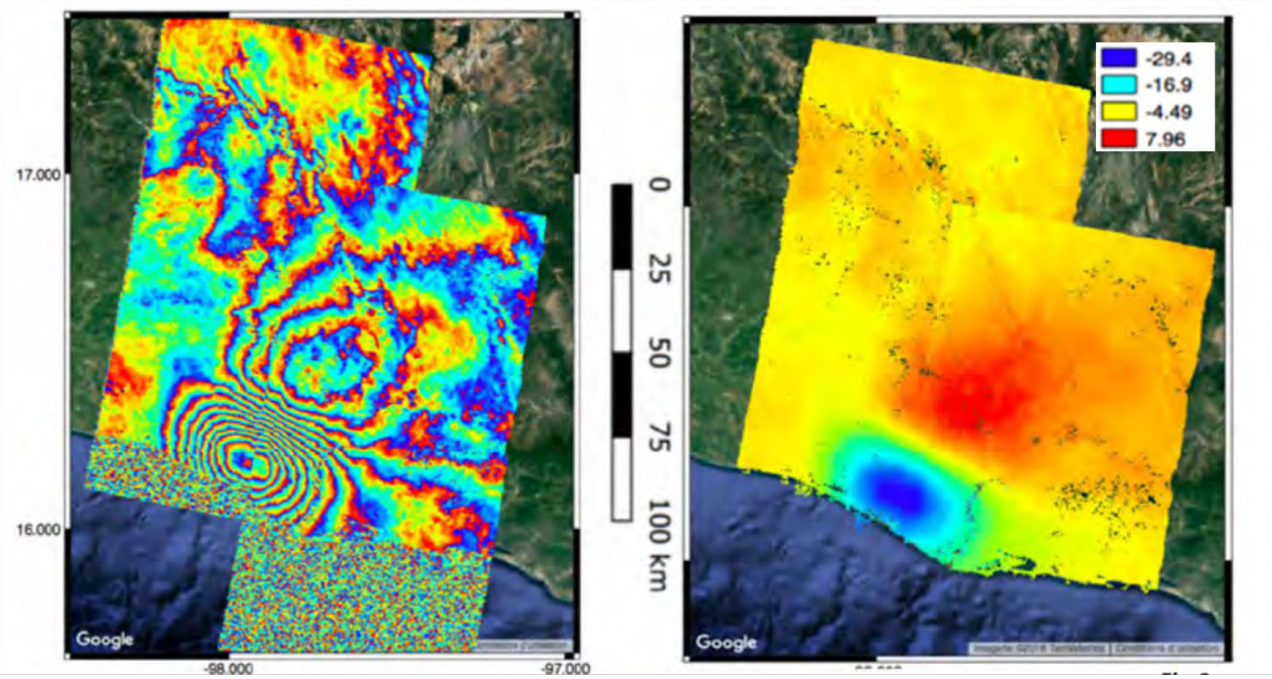

Figure 3 : InSAR measurement of the surface displacements due to the 16 February 2018 (Mw 7.1) earthquake in the Oaxaca region of Mexico captured by two tracks of SENTINEL-1. Left: interferogram. Right: unwrapped interferogram showing the coseismic surface displacement (blue color: toward the satellite, red: away from satellite). Processed by L. Maubant (O17).

The study of the 28 September 2018 Mw 7.5 Palu earthquake in Sulawesi, Indonesia (A23, Figure 4) is a representative example of another heavy trend in remote-sensing analysis of large earthquake with surface rupture: the more and more systematic combination of optical images correlation with InSAR. In the past 10 years, the number of optical satellites suitable for surface displacement measurement has significantly increased, ranging from constellations of high

resolution (<1 m) satellites like QuickBird, Pleiades, WorldView or Geoeye, to satellites with medium-resolution (10 m) and global coverage archives like Landsat-8 and twin Sentinel-2 satellites.

This wide range of data makes it possible to use these satellites to measure localized (<1km) decimetric or more surface displacements. This capacity is very complementary to that of InSAR, which tends to have decorrelation for such gradient of displacement and to be more sensitive to vertical displacement. In the competition between optical and SAR images, optical images have a small lead over radar images in terms of spatial resolution. This results in more accurate correlation results, which is one of the reasons that tends to favor optical images correlation over SAR images even in cloudy environment like Indonesia, as the coexistence of many optical satellites allows post-event cloud free images to be acquired in a reasonable amount of time (a few weeks). All this explains the nowadays wide use of the duo InSAR/optical correlation (Elliott, Walters, et al., 2016).

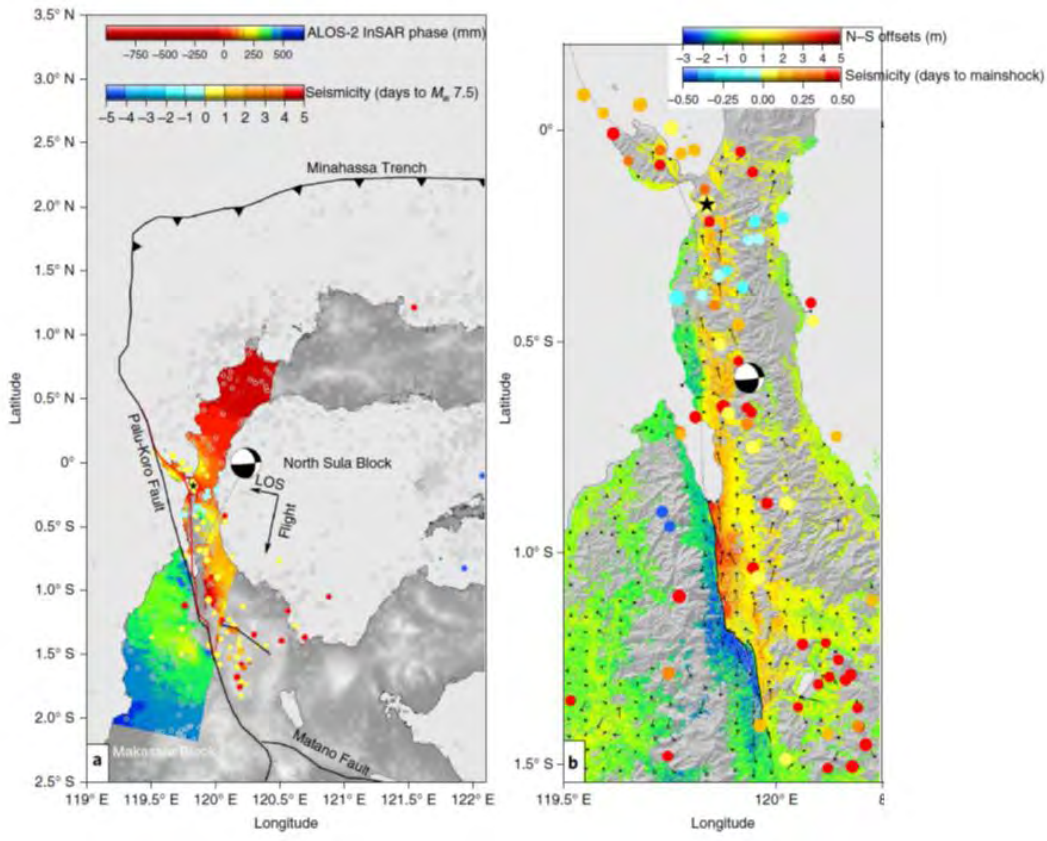

Figure 4 : Surface displacements associated with Mw 7.5 Palu earthquake from InSAR (left) and optical image correlation (right). The colored dots represent one month of foreshock (blue) and aftershock (yellow and red) seismicity (different temporal color scales are provided on each panel to show the detailed evolution of the seismic sequence). A), Unwrapped ALOS-2 interferogram. The surface trace of the ruptured fault is shown as a red line. Grey circles represent the background seismicity. b) Map of the horizontal surface displacement computed by the correlation of Sentinel-2 images. The arrows show the horizontal displacement, whereas the colors correspond to the N–S component of the displacements (from A23).

In the case of the Palu earthquake, the combination of the two techniques gives a detailed images of the fault trace and secondary structures and at the same time far field measurement that constraints inversion of slip distribution at depth. Results show that the slip initiated on a structurally complex and previously unknown fault to the north, extended southwards over 180

km and passed through two major releasing bends. Our study was somehow a bit provocative because it does not involved seismological data but concludes that the Palu earthquake probably ruptured a 30 km fault section south of Palu city at supershear velocities. This conclusion was mainly based on observation from satellite geodesy showing that this section of the rupture is very linear and slightly offset from the mapped geological fault at the surface and shows large and smooth surface slip of 4–7 m with almost no aftershock seismicity, which are characteristics similar to those from known supershear segments.

This has been confirmed by other studies including seismic data, teleseismic array and regional broadband stations (Bao et al., 2019; Fang et al., 2019; Y. Zhang et al., 2019). Fang et al. propose a supershear model quite similar to Bao et al. with a persistent supershear rupture from early on. On the other hand, Zhang et al. obtains a model with a slow start of the rupture and a supershear acceleration only around 20 seconds.

In addition to these examples, I had opportunities to investigate other earthquakes (see Appendix 3) ranging from the Mw 7.8 2008 Wenchuan earthquake to the shallow Mw 5, 2019 Le Teil earthquake. Even if such studies are opportunistic, they contribute to build a growing catalogue of coseismic slip distribution like SRCMOD (Mai & Thingbaijam, 2014) which is needed for several research problematics. However, despite significant efforts from teams like ARIA at NASA (https://aria.jpl.nasa.gov/) or COMET at NERC (https://comet.nerc.ac.uk) to be very responsive to event, we are not yet in a situation of a quick, automated response. Indeed, some technical steps for surface deformation measurement from satellite are still requiring human intervention, for instance InSAR still face unwrapping error problem in automatic computation, and more generally free and near-real data access is now only available from a few satellites like Sentinel-1 and Sentinel-2. In addition, joint inversion of slip distribution from joint inversion for a given earthquake can be quite different from one author to another because of variability in inversion process (fault geometry, smoothing, velocity model, etc.). This leads to relativize the interpretation beyond the first order of slip inversions.

Nonetheless, all the studies carried out now make it possible to tackle several fundamental scientific questions about earthquake, for instance, the question of representativeness of the complexity of the rupture in surface on slip at depth. Is this complexity, often not reproduced in slip distribution models, only a near-surface effect? If this question often comes up against the uncertainty on the geometry of the fault at depth and the myopia of geodetic measurements with depth, examples such as the 13 November 2016 Mw 7.8 Kaikoura (New-Zealand) earthquake show that a great complexity of geometry and slip in the crust can exist (Cesca et al., 2017; Duputel & Rivera, 2017; Zinke et al., 2019; H. Zhang et al., 2017).

Another issue that has emerged from the analysis of different distributions is the "shallow slip deficit » problem (Fialko et al., 2005). For strike-slip faults, inverted slip distributions tend to show a maximum slip at its maximum between 3 and 6 km that decreases towards the surface, raising the question of how and when the deformation in the first 3 km of the crust accommodates the missing displacement on the long-term displacement. Is it due to a deformation taking place in the interseismic period and/or distributed over a wider area (off-fault deformations) (e.g. Fialko et al., 2005; Dolan & Haravitch, 2014) or alternatively caused by a measurement sampling problem (Xu et al., 2016) or an artifact linked to the simplifications made when we model the fault and the medium (Kaneko & Fialko, 2011; Marchandon et al., 2020 in review)? This is related to an issue of aseismic deformations triggered by earthquakes on nearby geological structures that motivated me to study earthquake and which is the subject of the following section.

Aseismic deformation triggered to earthquake

Aseismic deformation observed in surface related to earthquake can take different forms that has been first observed from fieldwork or ground-based geodesy since the 1960 mainly in California:

- Afterslip slip along a fault ruptured by a large earthquake starting after that event as observed after the 1966 Parkfield Earthquake (e.g. Smith & Wyss, 1968) or the 1968 Borrego mountain earthquake (e.g. R. O. Burford, 1972).
- Creep rate change after an event, like acceleration recorded in January 1960 on the San Andrea fault due to a local earthquake (Steinbrugge et al., 1960).
- Off-fault deformation: inelastic deformation around the main fault that can be expressed by folding, warping, granular flow, rigid-block rotation, minor secondary faulting, and/or microcracking, and that are mainly within the 100-200m from the fault, but can be distributed at kilometer scale (Milliner et al., 2015; see also ref. in Kaneko & Fialko, 2011) as observed after the 1987 superstition Hills earthquake sequence (e.g. R. E. Klinger & Rockwell, 1989; Hudnut et al., 1989).
- Triggered aseismic fault slip or folding: deformation observed just after a nearby earthquake (up to 100 km), but on geological structures not necessarily connected to the seismic fault, like displacements on the San Andreas fault triggered by the Borrego Mountain earthquake (Allen et al., 1972), the 1979 Imperial Valley earthquake (Sieh, 1982; Fuis, 1982), the 1986 North Palm Springs earthquake (P. L. Williams et al., 1988), or the 1992 Landers earthquake sequence (Bodin et al., 1994).

From the start, these observations raised the problem of estimating seismic hazard from field measurement of fault offsets (Allen et al., 1972) or paleoseismology. From the 1990s, satellite geodesy allowed more extensive measurements of these deformations (Bürgmann, Rosen, et al., 2000) with also the same difficulties to know what is the proportion of aseismic slip and seismic slip in the measured deformation. As we have already seen in the case of the 2005 Kashmir earthquake (A06), this question arises in particular for the early afterslip which can be important in the first days after an earthquake (e.g. Lienkaemper et al., 2016). High frequency GPS is presently the best technique to address this issue (e.g. Twardzik et al., 2019). I have not investigate this issue as satellite imagery remains poorly suited for this purpose because of its poor temporal sampling, even if it can help to estimate the spatial extent of such processes. Creep rate changes are discussed in section II-5.

Regarding off-fault deformation, optical imagery turns out to be the most performant tool as this deformation area often located in near-field of large earthquake were InSAR may decorrelate. Our study of the Palu Earthquake (A23) was a typical example of that. Numerous other studies have extensively investigated this kind of deformation using optical image correlation, like for the unavoidable 1992 Landers earthquake (Milliner et al., 2015, 2016), the 2001 Mw 7.8 Kokoxili earthquake in Tibet (Y. Klinger et al., 2006), the 2013 Mw 7.7 Balochistan earthquake (Zinke et al., 2014; Vallage et al., 2015; Gold et al., 2015), the 2016 Mw 7.8 Kaikoura earthquake (Zinke et al., 2019). Those studies confirm that field measurements are under-estimating the total deformation caused by earthquake. Dolan and Haravitch (2014) proposed that the amount of off-fault deformation increases according to the degree of structural maturity of the fault, but the high variability of the off-fault deformation along a same rupture suggests that other parameters are controlling the process (Milliner et al., 2015).

I have been more interested by triggered slip on nearby faults. Especially in SW Taiwan where shallow (< 6 km) geological structures, showing interseismic aseismic deformation for some of them, are activated by earthquake on deeper faults (> 15 km) like the 2010 mw 6.2 Jiashian and the 2016 Mw 6.4 Meinong earthquakes (C66, A20, A26 in prep, Figure 5). Interestingly earthquakes here play a role of natural perturbation in an already deforming thrust-and-fold system.

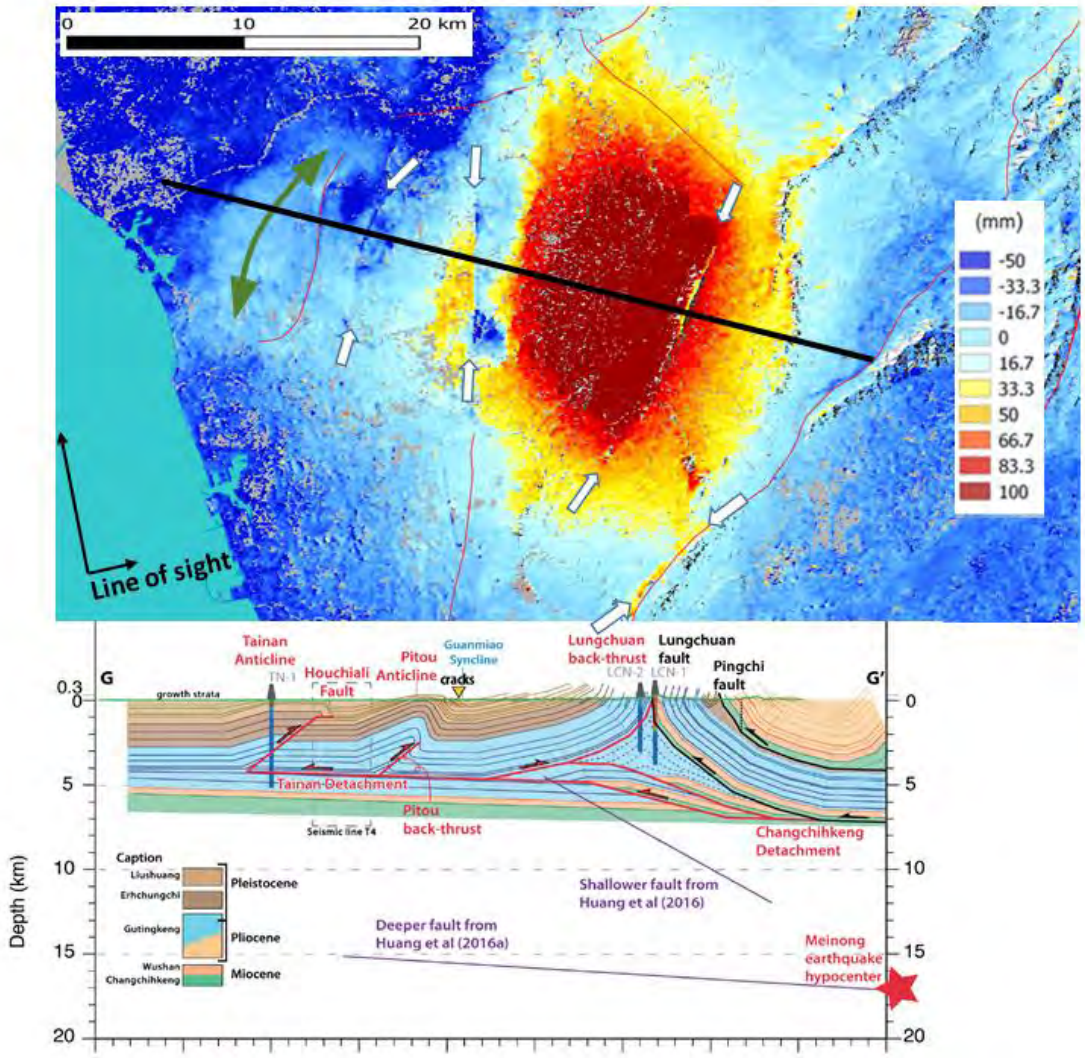

Figure 5 : Coseismic of 6 Feb 2016, Mw 6.4 Meinong earthquake (SW Taiwan) and triggered deformations on shallow geological structures. Top : surface displacement (along the radar line of sight) from ALOS-2 interferogram (26 Nov. 2015 - 18 Feb. 2016) capturing the Meinong earthquake 6 Feb. 2016 that rupture a deeper fault at 15km (M.-H. Huang, Tung, et al., 2016), but also triggered deformation on faults, some of them pointed by the white arrows, and active anticline (green arrowed line). Bottom: Cross section (from A20, location shown by black line on the map), showing the shallow geological structure of the thrust-and-fold belt of SW Taiwan

Such triggered aseismic slips on nearby fault, can be efficiently mapped by InSAR if they reach the surface, leading to numerous observations done related to earthquake of different magnitude and in various tectonic contexts, e.g.:

- 1992 Mw 7.3 Landers, California, Strike-slip (Massonnet et al., 1994; Price & Sandwell, 1998; Fialko, 2004)

- 1994 Mw 5.9 Double Spring Flat, Nevada, Strike-slip (Amelung & Bell, 2003).
- 1998 Mw 6.6 Fandoqa, Iran, strike-slip triggering thrust (Berberian et al., 2001; Fielding et al., 2004; Copley & Jolivet, 2016)
- 1999 Mw 7.5 Izmit, Turkey, strike-slip (Wright, Fielding, et al., 2001)
- 1999 Mw 7.6 Chichi, Taiwan, thrust (A03)
- 1999 Mw 7.1 Hector Mine, California (Sandwell et al., 2000; Fialko et al., 2002)
- 2000 Mw 6.6 South Iceland Seismic Zone, (Pedersen et al., 2001; Pagli et al., 2003)
- 2010 Mw 7.2 El Mayor-Cucapah, Baja California, strike-slip (Donnellan et al., 2014; Wei et al., 2011)
- 2014 Mw 6.0 South Napa, California, strike-slip (DeLong et al., 2016; Ponti et al., 2019)
- 2015 Mw 7.9 Gorkha, Nepal, thrust (Elliott, Jolivet, et al., 2016)
- 2018 Mw 7.5 Palu, Indonesia, strike-slip (A23 Suppl. Fig. S1)
- 2019 Mw 7.1 Ridgecrest, California, strike-slip (Xu et al., 2020)

Indeed, when good quality InSAR observation are available, such triggered slip seems quite common and may have a non-negligible effect in the earthquake cycle. Other observations also suggest triggered aseismic folding (Kaneko et al., 2015; Simon Daout et al., 2019; C66).

The question of the aseismic nature of such triggered deformation can be tricky as they can occur almost at the same time than the triggering earthquake. As triggered slip are usually of small amplitude with respect to the main earthquake, it may be difficult to identify them in the seismicity if the triggered slip is also seismic and close to the main fault. For instance, the triggered slip on the Chenghua and Tuntzuchio faults by the 1999 Chichi earthquake (A03) were not associated with aftershocks, but we cannot exclude that it occurs seismically during the main shock rupture. For the 2012 Jiashian earthquake and the 2016 Meinong earthquake, in SW Taiwan, the joint inversions of geodetic and seismic data (K.-C. Lin et al., 2016; M.-H. Huang, Tung, et al., 2016) result in the need for a secondary shallower patch of slip (see Figure 5 for the Meinong earthquake), mainly driven by geodetic data. However, they were no aftershock at that depth. Lin et al (2016) suggest that the 2012 Jiashian event is a continuous seismic event, but admit that they cannot exclude a primarily aseismic slip on the shallower fault plane from seismological waveform analysis. Furthermore, the geometry of their secondary fault plane is not consistent with geological observation. Hollingsworth et al. (2017) report about a rare case of slip on a secondary splay fault triggered by the 2016 Kaikoura, New Zealand, earthquake, for which seismic signal can be seen in the seismological waveforms. However the seismic moment of triggered slip can be significantly lower than the geodetic moment suggesting if it is the case that the slip is mostly aseismic (e.g. Amelung & Bell, 2003).

Regarding the mechanism of triggered slip, static stress change or dynamic effect has been invoked. The static stress change alone cannot explain all the observations assuming classical coulomb stress change criteria (e.g. Allen et al., 1972; Du et al., 2003; Kaneko et al., 2015), and alternative processes of dynamic triggering have been proposed (Bodin et al., 1994; Bodin & Gomberg, 1994; Gomberg & Bodin, 1994). However to explain anomalous displacement of nearby-fault with respect to coulomb stress change that is a retrograde displacement opposite to long-term geologic slip, elastic response of compliant fault zones has been also invoked (Fialko et al., 2002). Compliant fault zones are zones of reduced effective shear modulus around the fault. In the case-study investigated by Fialko et al. (2002; 2004), a reduction in the effective shear modulus by about a factor of two within 2-km-wide fault zones is needed. Such a reduction may be due to damage zones around the faults. Inelastic response of compliant fault zone can also be caused by dynamic stress perturbations (Duan, 2010). The recent observations by InSAR of

retrograde motion by Xu and Sandwell (2020) on unknown faults, highlight the need of combining field work, geophysical survey and satellite geodesy in order to test the compliant fault hypothesis and more generally to better understand the mechanics of aseismic triggered slip.

3 – Interseismic deformation with assumption of steady state slip at depth

Interseismic deformation is the part of the earthquake cycle where tectonic stress built up and is reloading the seismogenic part of the fault. First geodetic observations of interseismic deformation come back to the beginning of the 20th century with observations done by Reid H.F. after the 1906 San Francisco earthquake. He then laid the foundation of the elastic rebound theory (Reid, 1910, 1911). One very popular mathematical formulation of this theory was set up in the 1970's by Savage and Burford (Savage & Burford, 1973) in which interseismic deformation of strike-slip fault is modelled by steady-state interseismic slip on a dislocation buried in an homogeneous elastic half-space. See also Segall (2010) for an historical view of the progresses in observation and modelling since Reid's observations and a comprehensive description of the Savage and Burford model and other alternative models).

Knowing the loading rate of a fault is a fundamental parameter in seismic hazard assessment and geodetic measurement is useful to get measurement of the present-day slip rate to complement usually sparse geological or paleosismological estimates. Up to the end of the 1990's, ground-based geodetic surveys and GPS were the main tools to measure interseismic deformations. Regarding GPS, when only a few campaign measurement are available along a line of stations crossing the fault, the elastic dislocation model is a reasonably simple model to be used to infer the geodetic slip rate. It is usually done with the assumption of a steady-state creep on the fault below a certain depth called locking depth, above which the fault is locked (no slip) during the interseismic period. This corresponds to a transition from stable regime to unstable regime in the formalism of rate-and-state friction law (Scholz, 1998).

The first InSAR analysis of the distributed interseismic deformation of locked faults were done on the East California Shear Zone (Peltzer, Crampé, Hensley, et al., 2001) and on the North Anatolian Fault (Wright, Parsons, et al., 2001). A decade later, Wright et al (2013) made a review of interseismic studies providing fault locking depth and report about one hundred GPS and InSAR interseismic studies, most of them using the half-space elastic model approach. Even if at that time they were already studies proposing alternative models with no steady-state creep assumption (e.g. Hetland & Hager, 2005, see also discussion hereafter), those more complex models required additional information (like about past seismic events or rock viscosities) often not available. That is why at the end of 2010, when started the PhD of Zahra Mousavi that I co-supervised with A. Walpersdorf, we decided to adopt the classical elastic approach to infer slip rate of some major continental faults in North Eastern Iran.

The study area covers NE Iran as shown in Figure 6. The first study of the PhD (A14) was using permanent and campaign GPS stations to investigate the first-order present-day deformation field in an area where the pattern of faulting accommodating the Arabia–Eurasia collision deformation is complex involving thrust and strike-slip faults with slip rates largely unknown. Results showed that the rigid-body rotation of the South Caspian about an Euler pole is located further away than previously thought and suggested that the fault zones along the eastern Alborz and western Kopeh-Dagh may accommodate slip at much faster rates than previously thought. First geodetic slip rate were estimated on the Ashkhabad fault, the Sharoud fault system and the Doruneh fault.

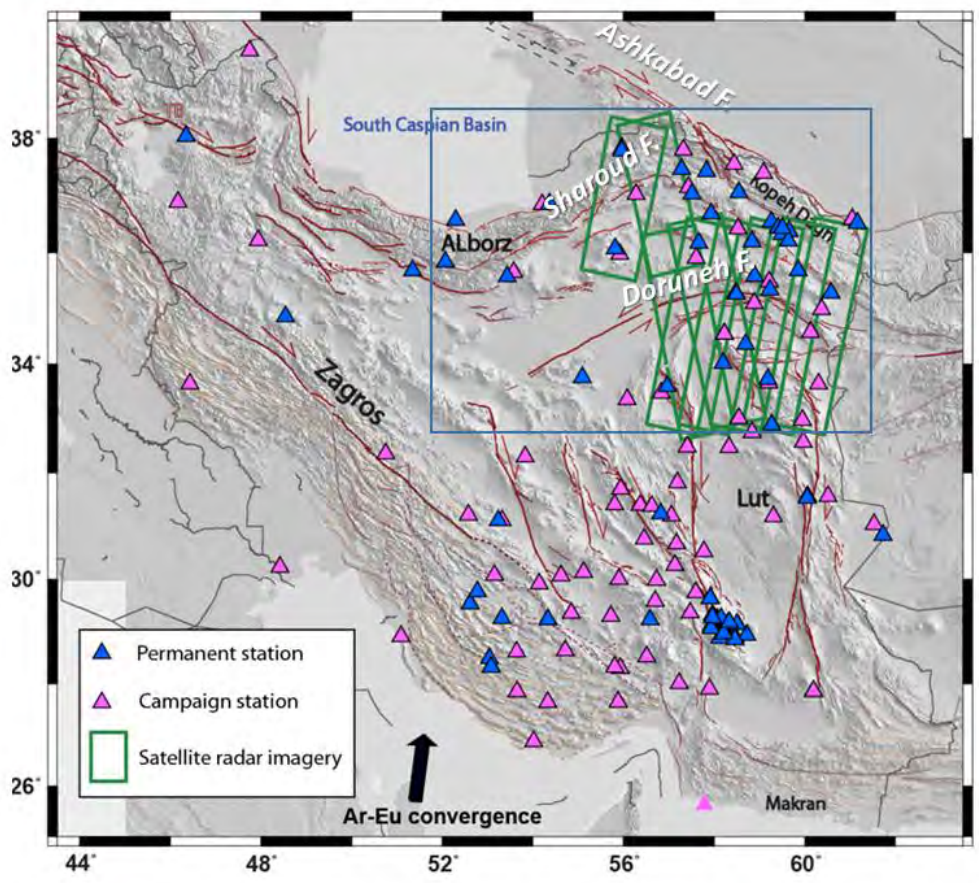

Figure 6 : Shaded DEM of Iran showing the study areas investigated during the PhD of Z. Mousavi: blue rectangle for GPS study (A14), green rectangles show Envisat footprints used for the InSAR study of the Sharoud Fault system (A16) and the Doruneh Fault (A25). Red lines show active faults and triangles show GPS stations (adapted from Mousavi PhD defense presentation Nov. 2013)

However because the fault slip rates of those 100's km long major faults were only relying on few GPS stations unevenly distributed, we decided to also use InSAR to better constrain the slip rate of the eastern Sharoud fault zone (A16, pdf-4) and of the Doruneh fault (C42, A25). The Ashkhabad fault have been studied by InSAR at the same time by Walters et al (2013). Even if interseismic slip rate can be relatively well estimated by GPS in case of a spatially smooth interseismic deformation signal, InSAR is an efficient tool to verify this assumption over a whole fault system by looking for possible spatial discontinuities (see also section II-5), and to investigate possible along-strike variations of slip rate or locking depth.

The Sharoud Fault system is a major active structure of the eastern Alborz. With no large instrumental earthquake in the last 50 years, this fault system have ruptured in 1890 near Sharoud city (Ambraseys & Melville, 1982), however there is no historical record on its eastern part near the Jajarm and Cheshmeh-Nik faults on which geological slip rates were unknown. To cover this area by InSAR we used Envisat data acquired during 2003–2010 on two tracks (ascending and descending see Figure 6 and Figure 7). Inversion results are consistent with a left-lateral slip rate of 4.75 ± 0.8mm/yr. on the Abr and Jajarm, strands of the Sharoud fault, with a 10 ± 4 km locking depth.

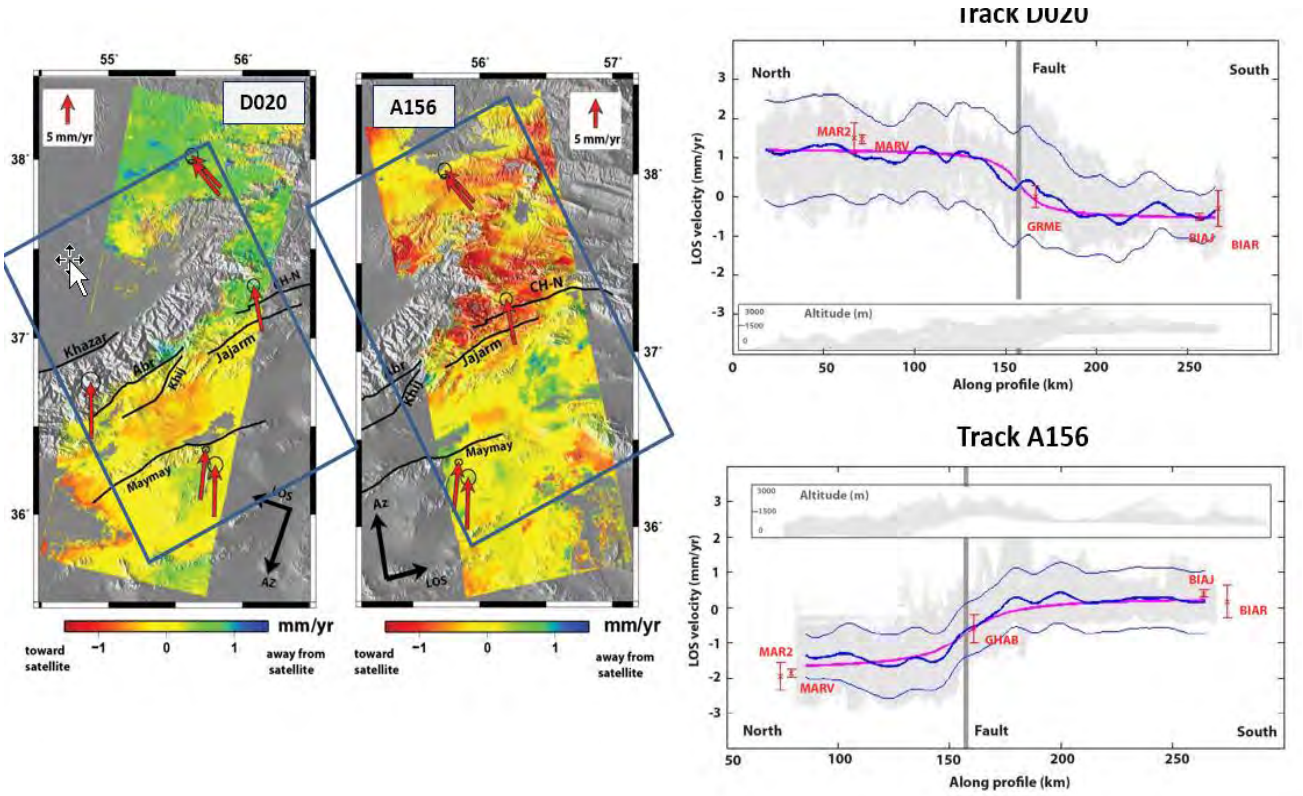

Figure 7 : Slip rate of Sharoud Fault System from INSAR and GPS analysis. RIGHT: Ground surface mean velocity maps (along Line of Sight) from InSAR time series analysis for two Envisat track (see location in Figure 6). Red arrows present the GPS velocity field of this area with respect to Eurasia. Black lines are fault traces (CH-N is Cheshmeh-Nik fault). Blue boxes, oriented perpendicular to the SFS, show location of profiles shown on the left. LEFT: Mean LOS velocity profiles (gray dots) and the weighed averaged profile (thick blue line) with 2-sigma deviation (blue lines). All the points within the blue rectangle shown on the right are projected onto the profile as gray dots. The gray boxes show the elevation profile for the same area. The dark gray line shows the location of modeled Sharoud Fault. The red stars with error bars are the LOS velocity derived from five continuous GPS stations, assuming only horizontal displacements. The pink line is the best fitting model with slip rate 4.75 ± 0.8 mm/yr. and 10 ± 4 km locking depth. (Adapted from A16)

The Doruneh is another major fault in NE Iran. The fault trace is well marked in the geology and geomorphology, but geodetic slip rate inferred from interseismic strain accumulation across the Doruneh fault are contradictory: Pezzo et al. (2012) measure ~5 mm/y of left-lateral strain accumulation from InSAR, whereas campaign and permanent GPS measurements (A14 ; Walpersdorf et al., 2014) show little discernible strain accumulation, with a maximum ~ 2 mm/yr. The InSAR analysis gives upper bound of deformation and shows that less than 4 mm/y – and likely only 1-3 mm/y - of slip accumulates across the fault. The InSAR analysis has been since completed by geomorphological analysis, field work and dating leading to a paper now in review (A25), which concludes that within the uncertainty of our measurements the slip-rate has remained constant over the last ~100 Kyr and is representative of the strain accumulation at the present-day. The slip-rate is consistent with the E-W left-lateral Doruneh fault accommodating N-S right lateral faulting by 'bookshelf' faulting, with clockwise rotation about a vertical axis.

It is interesting to note that in the Wright et al review of InSAR interseismic studies of continental fault (2013), there are almost only strike-slip faults, except for a thrust system in

Taiwan (A07) which is a particular case of a shallow (< 5 km) thrust-related fold (see also section II-6). Indeed, when excluding shallow creeping faults studies, steady-state slip rate of thrust or normal fault systems inferred from InSAR interseismic studies are relatively rare (e.g. Kang et al., 2015; Raphaël Grandin et al., 2012; Marshall et al., 2013; He et al., 2015; S. Daout et al., 2016; Simon Daout et al., 2018; Letizia Anderlini et al., 2020). In compressive context, it may be explained by a more distributed deformation style on several faults segment leading to smaller surface deformation rate and sometimes more difficult condition for InSAR related to high topographic gradient and snow cover (Raphaël Grandin et al., 2012). In extensive domain, the deformation can also be more distributed but it is rather the fact that tectonics is often related to transient magmatic events (e.g. Biggs et al., 2009; Doubre et al., 2017; Doubre & Peltzer, 2007)) that make steady-state slip rate analysis less appropriate.

For subduction zone, it is usually assumed that downdip of the seismogenic zone the subduction interface is creeping at a constant rate equivalent to the long-term plate velocity convergence, even if there is observation pointing for time-variation over the seismic cycle (Avouac, 2015). Assuming a fixed constant slip rate at depth, geodetic studies are rather investigating up-did coupling variability. As on-land observation can be relatively far from the subduction interface and from the trench, the corresponding interseismic deformation by satellite geodesy is usually quite smooth spatially and the inverted coupling can lack resolution near the trench (e.g. Chlieh et al., 2008). In this configuration, the InSAR impact is less significant when a dense GPS network is already present like in Japan. However it can still be useful when GPS station are sparse or to investigate deformation partitioning in the upper crust (e.g. Shirzaei et al., 2012; Tung et al., 2019; Fukushima et al., 2019). Other difficulties like the lack of enough large and continuous on-land surface (e.g. Aleoutian, Kourile and Tonga Kermadec subductions) and/or land-cover are not favorable to InSAR observation (e.g. Equator, Central America, Alaska, Cascadia, Indonesia subductions). This makes the use of InSAR for interseismic coupling studies limited to a few subduction zones so far, like in Chile ((e.g. Chlieh et al., 2004; Béjar-Pizarro et al., 2010, 2013; Jolivet et al., 2020), Makran (Y. N. Lin et al., 2015) and Mexico (Louise Maubant's PhD work in progress).

In the last decade, the major trends in InSAR interseismic studies are the ability to investigate more challenging environments for InSAR observation (e.g. Raphaël Grandin et al., 2012; Cavalié & Jónsson, 2014; Walters et al., 2014), smaller deformation rate, and wider area. Large coverage is useful to understand the spatial variability of interseismic deformation over entire long fault systems (e.g. X. Tong et al., 2013; E. Chaussard et al., 2016; Fattahi & Amelung, 2016). A good illustration of that trend is the study of interseismic deformation in Turkey. It started with a narrow 100km wide swath across the North Anatolian fault (Wright, Parsons, et al., 2001) extending to larger and larger parts of the NAF (Kaneko et al., 2013; Hussain, Hooper, et al., 2016; Hussain et al., 2018) and the Eastern Anatolian Fault (Cavalié et al., 2008; Walters et al., 2014), up to a now complete coverage of Anatolia thanks to Sentinel-1 data (Weiss et al., 2020). A similar spreading occurs in Tibet (Wright, Parsons, England, et al., 2004; Elliott et al., 2008; Cavalié et al., 2008; H. Wang & Wright, 2012; Garthwaite et al., 2013; Simon Daout et al., 2018; Hua Wang et al., 2019).

Another trend allowed by longer and denser InSAR time-series is the study of transient deformation signals like those discussed in the following sections II-4 (slow slip events in subduction) and II-5 (creeping faults).

To finish with this section about slip rate inferred assuming steady-state rate, it is noteworthy to mention the issue the representativeness of geodetic measurement made over a few years or decades within the earthquake cycle. Figure 8, from Meade et al (2013), illustrates this issue by taking into account the possibility of long-term visco-elastic or afterslip effects (e.g. Marone, 1998; K. M. Johnson & Segall, 2004; Hetland & Hager, 2005; Trubienko et al., 2013) that do not fill the steady state assumptions. Other perturbations to the linearity in time of interseismic displacement can come from fault interaction (e.g. Perfettini & Avouac, 2004b) or long transient deformations (B. J. Meade & Loveless, 2009)..

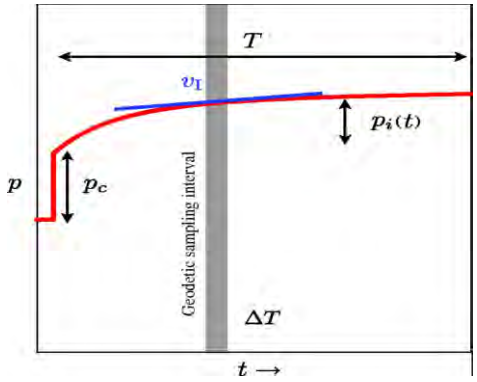

Figure 8 : Schematic diagram from Meade et al. (2013) showing a geodetic sampling interval in relation to the earthquake cycle. « Earthquake recurrence intervals (T) typically range from 100 to 10,000 years whereas the duration geodetic observations, ΔT (vertical gray shading), used to infer fault slip rates, is typically decadal in length, sampling only a small fraction of the earthquake cycle. A linear fit to the geodetic position time series p_i (t) (red line) throughout T gives the nominal interseismic velocity, v_I (blue line). Estimates of v_I may vary throughout the earthquake cycle because of the nonlinear variation in surface deformation throughout the interseismic period ».

All these effects can make the short-term geodetic deformation not representative of the full interseismic period. Off course, this has also implication about the related issue of the comparison of the geodetic and geologic slip rates (e.g. Friedrich et al., 2003; Allmendinger et al., 2009; Menant et al., 2020).

Some authors have reduced discrepancies between geodetic and geological slip rates by using an elastic plate over a viscoelastic half-space instead of an elastic half-space (Tong 2018). However, the simple conceptual model in Figure 8, which implies lower slip rate at the end the interseismic period, can be mathematically reproduced trough different mechanical models. Some of them, like rate-and-state frictional afterslip models or power law shear zone models, can lead to a relatively rapid return to an almost steady-state approximation (Wright et al., 2013; Ingleby & Wright, 2017) consistently with some observations (Hussain et al., 2018).

Furthermore, this conceptual model does not apply everywhere. Dolan and Meade (2017) report geodetic rates a few years before an earthquake that are faster than geological rates. The authors propose four possible mechanisms: « (1) earthquake-cycle effects related to previous clusters or lulls in earthquake occurrence and fault displacement; (2) temporal variability in fault strength; (3) regional kinematic fault interactions; and (4) temporal variability of relative plate motion rates. ». Transient slow slip events (B. J. Meade & Loveless, 2009; Loveless & Meade, 2016), may be part of the solution.

4 – Slow slip events in subduction zone

Slow slip events (SSE) are transient slip events that, like earthquakes, propagate over a fault but are much slower and last longer and therefore radiate little or no measurable seismic energy. In this sense, they are mainly aseismic; however, they can be associated with certain seismic signals such as tremors and interact with « classical » seismicity. There seems to be a continuum between tremors, low frequency earthquakes and very low-frequency earthquakes and SSE (Peng & Gomberg, 2010). The more generic term « slow earthquake » has been used to group these phenomena (Ide et al., 2007) and the term SSE is now increasingly taking precedence over « silent earthquake » proposed in the 1970s for slip events too slow to be measured by seismology.

If geodetic observations of transient creep aseismic events were made as early as the 1950s on the San Andreas fault (Steinbrugge et al., 1960), it is through seismology that the first indications of transient slip in subduction zones were made, making the simple vision of a steady-state aseismic creep loading seismic asperities on the subduction interface more complex. This started with observations based on long-period seismology, of relatively small magnitude earthquakes but generating large tsunami, called "tsunami earthquakes" (Kanamori, 1972; Kanamori & Kikuchi, 1993), of slow slip preceding main shock like for the 1960 Great Chilean earthquake (Kanamori & Cipar, 1974; Cifuentes & Silver, 1989) or of slow events triggered by earthquakes (Kanamori & Stewart, 1979). This was complemented by more systematic studies of seismological records (Beroza & Jordan, 1990; Ihmlé & Jordan, 1994) and the first observations from borehole strain meters (Sacks et al., 1978; Linde et al., 1988) or geodetic surveys (Shimazaki, 1974; Linde & Silver, 1989). At the same time, studies have been carried out to establish a link between laboratory friction experiments and slow slip observations (e.g. Dieterich, 1978, 1979; Ruina, 1983).

In those first observations, most of the slow slips take place just before or just after an earthquake and with a spatial connection to the seismic rupture zone. This has since been confirmed by several studies (e.g. for Tohoku Mw 9, Kato et al., 2012; Bouchon et al., 2016; for Iquique Mw 8.2 Meng et al., 2015; Socquet et al., 2017; and N. K. Voss et al., 2017 for afterslip and triggered SSE). In this part II-4, we will rather focus on SSEs in the subduction zone that do not have such a strong spatial and temporal proximity to an earthquake: they have their own "life" with their own periodicity, which does not prevent them from interacting with the seismicity. It is only at the end of the 1990's that this type of event began to be measured, notably thanks to the densification of permanent GPS networks compensating for the insufficient temporal sampling of campaign geodetic measurements. This has been done almost in parallel in three different subduction zones: (1) in Japan at several locations along the Nankai zone : Bongo Channel (Hirose et al., 1999; Ozawa et al., 2001, 2004; Miyazaki et al., 2003; Hirose & Obara, 2005), Tokai (Ozawa et al., 2002; Hirose & Obara, 2006) and Boso (Ozawa et al., 2003) ; (2) in the Cascade area, Canada/USA (Dragert, 2001; Rogers & Dragert, 2003) ; (3) in Mexico (Kostoglodov et al., 2003; Larson et al., 2004; Lowry et al., 2001; Yoshioka et al., 2004). It was also in the early 2000s that the first observations of periodic slow slip associated with non-volcanic tremors were made (Obara, 2002; Obara et al., 2004; Rogers & Dragert, 2003). Tremors are low amplitude signals observed by seismometers but with little or no impulsive radiation and with a low frequency content.

Depending on the location, SSEs cover a relatively wide range of amplitude, duration, and periodicity (Schwartz & Rokosky, 2007), for instance a few cm slip lasting several weeks with periodicity of 13-16 months in Cascadia, and about 20 cm slip lasting several months with periodicity of about 4 years in Guerrero (Mexico). However they seems to share a common scaling between their characteristic duration and their equivalent seismic moment magnitude but in a different way than regular earthquakes do (Ide et al., 2007).

It is in this context, full of new observations described in more detail in the review paper by Schwartz and Rokosky (2007), that when I arrived in Grenoble in 2006, I had the opportunity to start working on this subject. Thanks to the willingness of several members of different teams of the laboratory and to the already existing collaboration with Mexican colleagues, a project was set up focusing on the Mexican subduction and more particularly on the Guerrero seismic gap zone where the first SSE observations in Mexico had been made (Figure 9). It was the ANR GGAP project, the name of which evokes one of the major issues of the project. The slow earthquakes observed until then were located close to the Guerrero seismic gap which had not broken at least since 1911, whereas the seismic cycle in the Mexican subduction zone have an average recurrence time of 30-60 years for large subduction earthquakes (Nishenko & Singh, 1987). In its broadest definition, if the seismic gap were to rupture, it could give rise to a Mw 8 earthquake (Suárez et al., 1990; Singh & Mortera, 1991). The question of whether slow earthquakes release a significant part of the stress in the seismogenic zone or, on the contrary, are downdip the seismogenic zone (deeper than 20-25 km) and load it on each event is therefore crucial (Mazzotti & Adams, 2004; Kostoglodov et al., 2003). This question is related to the more general issue of interaction between SSE and larges earthquakes. To address this question for this a good spatial resolution of the slip distribution is necessary.

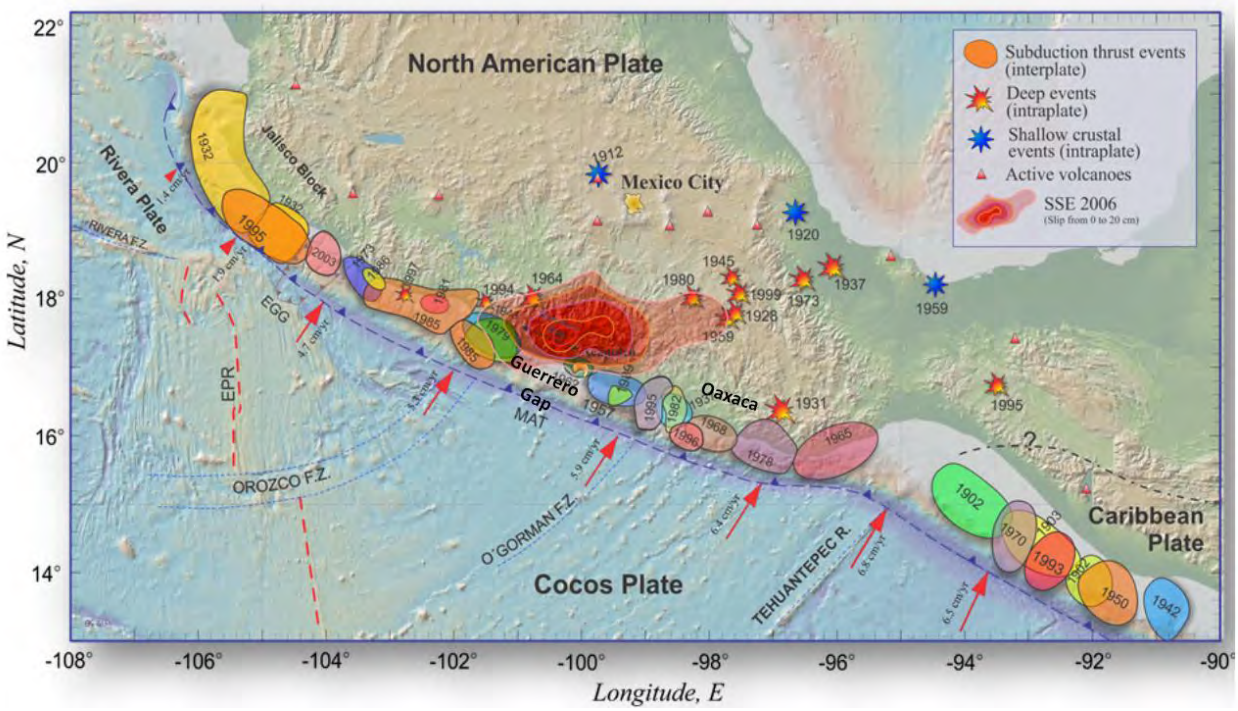

Figure 9 : Subduction earthquakes along the Mexican subduction and the 2006 Slow Slip Event. Colored patches are the approximate rupture area of large instrumental earthquakes. The reddish patch correspond to the slip distribution of the 2006 Slow Slip Event on the subduction interface inverted from InSAR and GPS (A13). The SSE is located at the Guerrero Seismic Gap. Red arrows give the Coco-North America plates convergence. (From Kostoglodov et al., 2015).

In this project, my challenge was to apply radar interferometry to measure deformations of a slow earthquake, which had not been done until then. In spite of the obstacles represented by the strong variations of topography and vegetation cover of the area, the characteristics of Guerrero's SSEs made them an interesting target because they are large SSEs, on a relatively flat subduction, allowing on-land deformation observations far from the trench. This work started with Olivier Cavalié's post-doc targeting the 2006 SSE which was the best documented (Larson et al., 2007) and for which pre- and post-event archive images from the Envisat satellite were available.

Using a stacking approach, we were able to demonstrate for the first time the feasibility of InSAR measurement of an SSE (C18, A13 pdf-3, Figure 10). Similar results were obtained by another group using another approach called StaMPS (Hooper et al., 2012; Bekaert, Hooper, et al., 2015). InSAR allowed to measure with a high spatial density the surface displacements related to the 2006 SSE and to show its lateral variability, with shallower slip in the Guerrero seismic gap where the slow slip seems to penetrate into the seismogenic zone (Figure 9, Figure 10), as suggested by Radiguet et al. (2011, 2012) based only on GPS data.

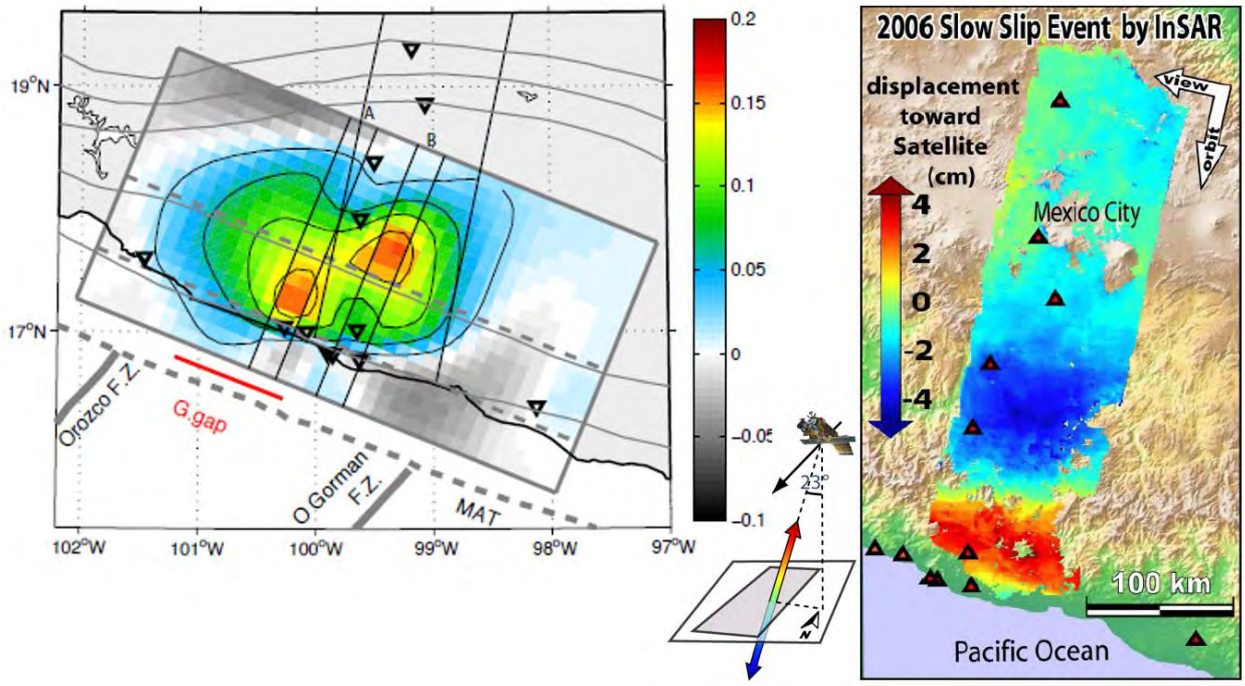

Figure 10 : Slip distribution and surface deformation of the 2006 SSE in Guerrero. LEFT: slip distribution of the 2006 event inverted from InSAR and GPS measurements showing a lateral variation in the depth of the slip at the east side of the Guerrero seismic gap. At profile A, the slip is shallower and penetrates into the seismogenic zone (dashed grey line represents from south to north the depth of the interface at 0 km, 15 km and 42 km. RIGHT: SSE mean velocity map obtained from a stack of interferograms from the Envisat satellite. (From A13 pdf-3)

Then I have also investigated the following large SSE in Guerrero which lasted about one year from June 2009 to June 2010 in two steps (Walpersdorf et al., 2011), the second steps being likely triggered by the remote 2010 Mw 8.8 Maule, Chile, earthquake (Zigone et al., 2012). It was one of target of Guillaume Bacques' PhD Thesis. For this event, despite Envisat acquisitions request done in 2010, the quality of the interferogram network was not optimal with respect to the timing of the event, in addition to challenging atmospheric perturbations. We were able to get

results comparable to the 2006 SSE on a wider area (C40 ; Bacques, 2013), but we did not succeed to catch the kinematics of the event.

The following 2014 large SSE in Guerrero was associated with a triggered Mw 7.2 earthquake (Radiguet et al., 2016; Gualandi et al., 2017). At that time, the Envisat satellite was over and Sentinel-1 and ALOS-2 satellites not yet launched. In cooperation with Sergey Samsonov and David Bekaert, we tried ordering Radarsat-2 data to investigate this event, but it was unsuccessful due to the too large decorrelation of interferograms formed with the pre-event images.

The last large SSE to occur in Guerrero lasted from May 2017 to June 2018. We investigate it by Sentinel-1 InSAR and GPS in the framework of the CNES funded PhD thesis of Louise Maubant. With the aims to get the full benefit of the wide coverage and dense time-series of Sentinel-1, the first part of the PhD project was to setup methods to separate the different sources of signal present in InSAR time-series. With a strategy taking into account the context of the Mexican subduction zone, that is large topographic gradients and atmospheric perturbations, mixing of coseismic, postseismic and SSE tectonic signal, and low spatial density of permanent GPS stations with uneven distribution. We used parametric decomposition of InSAR time series with constraint from GPS zenithal tropospheric delay and Independent Component Analysis to extract the SSE signal. A first-order slip distribution is inverted giving consistent results with respect to previous SSEs (A24 pdf-6).

InSAR results allow to give a better view of the spatial distribution of the large SSEs of Guerrero and to highlight lateral variations along the subduction. Why large SSE occur in Guerrero and not further West in the Michaocan area? The reason for such lateral variations is still debated and hypothetical. Several authors rather favors the hypothesis that such variations are permanent over many seismic cycles, based on the spatial correlation with seismological observations such as the presence of an ultra-slow velocity layer (Song et al., 2009), seismic anisotropy (Song & Kim, 2012), or magnetotelluric and geological observations (Husker et al., 2018). Husker et al. propose that past magmatic activity may have "produced an impermeable gabbroic layer in the lower crust within the Guerrero gap" and that "this body acted as a seal to trap fluids and over-pressurize the plate interface". Rousset et al. (2016) based on the observation of inter-SSE coupling and the coast-to-trench distance, which represents a long-term feature, propose that persistent frictional asperities partly control the inter-SSE coupling. However all those explanations remain debatable and it cannot be excluded that geodetically observed lateral variations are not stable on the time-scale of a few seismic cycles. They may be representative of very large transient slow slip at longer time scales (decade to centuries), as proposed by Meade 2009, based on the scaling law of Ide et al (2007; see also discussion in Bürgmann, 2018).

In parallel to this work on large SSE, it is worth noting the discovery of other smaller SSEs in the Mexican subduction, and related studies about the strong correlation between seismicity and SSE. Following studies on the link between SSE and non-volcanic tremors in Japan and Cascadia, Kostoglodov et al (2010) showed that in Guerrero there is an increase in tremor activity during large SSEs but that the two phenomena are spatially distinct and that there are also tremor bursts outside large SSE periods. Vergnolle et al. (2010) showed that several of these bursts are correlated with small displacement anomalies in GPS time-series and interpreted them as smaller and shorter SSEs. This small SSEs would be rather located downdip to large SSEs (Kostoglodov et al., 2015). This was confirmed by a further analysis of the GPS data by Rousset et al (2017) who detected about 30 of these short-term SSEs (equivalent Mw 6.3 to 7.2) lasting between 3 and 39 days over the period 2005-2014. It should be noted that short-term SSEs have also been located up-dip of large SSE in New-Zealand (L. M. Wallace et al., 2012).

This search for smaller events has been accompanied for some years now by a return of the pendulum from geodesy to seismology for the study of slow slip. Indeed, because of the noise of GPS measurements, it is difficult to detect event smaller than Mw 6 in the Guerrero area only based on GPS data (Rousset et al., 2017). However, seismic signatures of SSE has been demonstrated using burst of tremors or bursts of low frequency earthquakes (LFE), repeating earthquakes, earthquake swarms, changes in background seismicity or in seismic velocity (e.g. Igarashi et al., 2003; Matsumura, 2006; Ozawa et al., 2007; Holtkamp & Brudzinski, 2011; Marsan et al., 2013, 2017; Vallée et al., 2013; Mavrommatis et al., 2015; Reverso et al., 2016; Khoshmanesh et al., 2020). Several of these studies have been done based on the Guerrero case (Y. Liu et al., 2007; Frank et al., 2014, 2015; Rivet et al., 2014; Colella et al., 2017). The reverse way then can be done: using seismology as an indicator of slow slip not detected by geodesy. A nice example is the case of Boso in Japan, where seismicity is used to infer past SSEs back to 1982 (e.g. Hirose et al., 2012; Gardonio et al., 2018). In Guerrero, Frank et al (2016; 2018) use a catalogue of LFEs to extract the GPS time series sequences associated with burst of LFEs and show that slip outside large SSEs but also during SSEs correspond to clusters of short-duration slow transients rather than continuous slip. Husker et al (2019) show from a catalogue of tremors that short-term SSEs are widely present and extent beyond the Guerrero zone, notably in the Oaxaca zone.

The SSEs in the Mexican subduction are indeed not restricted to Guerrero. In Oaxaca region (see location in Figure 9), periodic SSE with duration of about 3-6 months and slip of about 10 cm (Mw 7-7.3), repeat every 1-2 years, more frequently than in Guerrero (Brudzinski et al., 2007; Correa-Mora et al., 2009; Graham et al., 2016). The relationship and spatial connection between this two zones of slow slip are still in discussion, but several studies suggest that there is no gap between these two regions (Graham et al., 2016; Maury et al., 2018) and that there are interactions between them (Graham et al., 2016; Radiguet et al., 2020). More systematic searches for tremor activities all along the Mexican subduction zone show that tremors occur up to the Jalisco area (Brudzinski et al., 2016; Husker et al., 2019). Maury et al. (2018) and suggest a continuity of a tremor band all along the subduction but with changes in terms of slow slip behavior West of Guerrero, where only short-term SSEs would occur, which could be linked to change in the subduction geometry.

Even if, because of noise threshold, InSAR cannot contribute to measure short-term SSE, this highlight the interest to investigate the seismic cycle at the scale of a whole subduction zone, like the Mexican one, where different portions of the subduction are at different stages of their seismic cycle. There are mixing of SSE, post-seismic and co-seismic signal and the ability to establish a budget of seismic and aseismic slip at that spatial scale is fundamental in term of seismic hazard assessment. For instance, Avouac (2015) propose to use interseismic coupling to constrain the return period of the maximum magnitude earthquake based on this budget. With this aim in mind, a work in progress of the PhD of Louise Maubant is to establish an interseismic coupling map covering the Mexican subduction zone from Guerrero up to Jalisco, based on Sentinel-1 and GPS data.

Since 20 years, observations of transient slow slip have increased world-wide, like in New-Zealand (e.g. Douglas, 2005; L. M. Wallace et al., 2012), in Ryukiu (Kano et al., 2018), in Northeastern Japan (e.g. Uchida et al., 2016; Khoshmanesh et al., 2020), in Alaska (e.g. Ohta et al., 2006; Fu & Freymueller, 2013), in Costa Rica (Outerbridge et al., 2010; Y. Jiang et al., 2012), in Equator (Vallée et al., 2013; Rolandone et al., 2018), or in Chile (Socquet et al., 2017; Klein et al., 2018). These observations have shown that transient slow slip is a relatively common feature

in subduction zones with a broad range of behaviors. For a more comprehensive view, there are good review papers dealing with the subject. Schwartz & Rokosky (2007) give an overview of the beginning of the discovery of Slow slip Events, see also Beroza & Ide (2011) for a comprehensive historical view of the slow slip studies in Cascadia. Peng & Gomberg (2010), Rubinstein et al. (2009) and Beroza & Ide (2011) give a more seismological perspective about slow earthquakes. Obara & Kato (2016) focus on the relationship of transient slow slip to large earthquakes, see also Voss et al. (2018) that give several examples of slow slip preceding large earthquakes.

To make the transition with the following section that focusses on creep at shallow depth (< 5km), it should be noted that Slow Slip Events can occur at depth < 15km in subduction zone, like in New-Zealand (McCaffrey et al., 2008; L. M. Wallace et al., 2016; Barnes et al., 2020), in Nankai (Yamashita et al., 2015; Araki et al., 2017), in Costa Rica (E. E. Davis & Villinger, 2006; Dixon et al., 2014; LaBonte et al., 2009) or in Equator (Vallée et al., 2013). Furthermore, slow slip on crustal faults in the upper-plate can occur associated to subduction, like reported in New-Zealand (Hamling & Wallace, 2015) or in Chile (Shirzaei et al., 2012). In Mexico, there are geological and geodetic evidences that a 650-km long left-lateral strike-slip fault system called « La Venta-Chacalapa » (LVC) is active (Gaidzik et al., 2016; Kazachkina et al., 2020). The LVC accommodates most of the oblique component of the convergence between the Cocos and North America at 3-6 mm/y as illustrated in Figure 11. Such a partitioning tectonic process has been already well documented in several subduction zone (Fitch, 1972; Jarrard, 1986; McCaffrey, 1992, 1994). Kostoglodov et al (Kostoglodov et al., 2015) also suggested that some slow slip events may be associated to the LVC activity. In 2016, with Graciela Rojo-Limon a Master student, we investigate using INSAR if any shallow deformation may be associated to LVC and how slip on the LVC may affect results from interseismic or slow slip event studies. Using SAR data over one Envisat track crossing the LVC, we were not able to detect clear surface deformation signal of left-lateral displacement on the LVC. This suggests that slip-rate is lower than a few mm/y and/or the locking depth is greater than 4-5 km. Simple elastic models show that the GPS signal could be explained either by model without LVC but with significant variation of the slip rake on the subduction interface or by model with slip rake fixed and with slip on the LVC. However, geodetic observations does not allow us to discriminate between the two models (C67). This subject deserves further InSAR investigation using Sentinel-1 and ALOS-2 data.

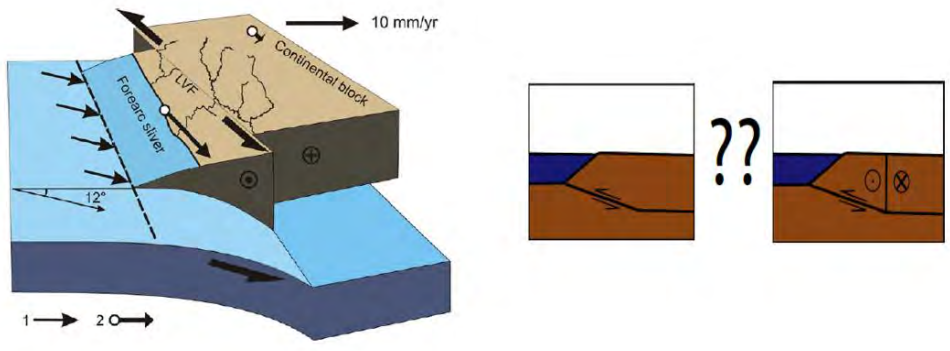

Figure 11 : Left (From Gaidzik et al. 2016). Diagram presenting the hypothesis of a plate-boundary sub-parallel left-lateral strike-slip La Venta-Chacalapa Fault System (LVC) and a forearc sliver produced by the oblique Mexican subduction. Bottom: This hypothesis raise the question whether or not shall we take into account upper crust deformation when modelling interseismic and slow slip events in the Guerrero area (from C67).

5 – Creeping faults at shallow depth: an InSAR favorite

This section presents two studies of shallow creeping faults to which I contributed. After a reminder of the historical scientific context preceding these works, the study on the Longitudinal Valley Fault in Taiwan done in the framework of Johann Champenois' PhD thesis is presented. It showed the spatial continuity, variations and local complexities of the creep phenomenon along the fault and clarified the trace of this major active fault. Then the study on the major El-Pilar fault in Venezuela done in the framework of Léa Pousse's PhD thesis is presented. Carried out on a zone that had never been studied by InSAR, it clearly demonstrated the location of the creep on the fault as well as transient creep variations over several years. Finally, the capacity of InSAR to systematically search for shallow creep will be shown on the example of the Taiwan Island.

Historical scientific context

When progressive damages at the Taylor Winery building near Hollister, California, in 1956 were reliably linked to fault creep process on the San Andreas Fault, periodic measurements were made there to monitor creep, and three continuously recording creepmeters were installed starting in 1957, with a seismometer. Results show that the creep is « concentrated in spasms of duration on the order of a week. These periods of creep are separated by intervals of weeks or months during which little or no creep accumulates » (Steinbrugge et al., 1960). The US Coast and Geodetic Survey established there a local triangulation network (aperture of a few hundred meters) measured in September 1957 and April 1959, giving a creep rate of about 2cm/y consistent with in-situ measurements. This prompted to review earlier triangulation surveys crossing the San Andreas Fault and to investigate more systematically creep along the San Andreas Fault. This was the start of geodetic measurement of shallow creeping faults.

In the following decades, ground-based geodesy developed dramatically in California using several methods covering different spatial scales:

- Triangulation and trilateration networks, with campaign measurements (theodolite, geodolite or short-range distance-meter) across fault zones with typical aperture from km to tens of km (e.g. Thatcher, 1979; Lisowski & Prescott, 1981)
- Alignment arrays, typically a few hundred meters across the fault (e.g. R. O. Burford & Harsh, 1980; Galehouse & Lienkaemper, 2003).
- Creepmeters, with periodic or continuous infra-millimetric measurement, at rates of up to 5 mm/minute, and 5-20m length (Bilham et al., 2004; Schulz et al., 1982; Schulz, 1989)
- Wells measurement : Tiltmeters (Johnston et al., 1976), strainmeters that can reach 1 nanostrain sensitivity, and water level change (e.g. Johnston et al., 1977; Gladwin et al., 1994; Linde et al., 1996).
- Levelling, the only method giving vertical displacement across faults (Sylvester, 1995)

Usually, long aperture measurements are less accurate but catch more deformation if there is some distributed deformation in subsurface. They also allow better constraining the depth of the creep. More references about instrumentation are given by Wesson (1988) who also review the main results of about 30 years of measurements, which can be summarized as follow:

Depending on the location, creep can be relatively steady state or show transient irregular fault creep events. Both can be superimposed suggesting slip at different depths. Creep events have duration from hours to days and can be made of several sub-events. There are evidences of propagation of creep event along fault (tens of meter per hour to km per hour, Evans et al., 1981).

There is a clear slip heterogeneity along fault. Earthquakes on nearby faults can trigger creep events. Earthquakes can also affect long-term creep rate, for instance by slip following an earthquake (afterslip) usually with a logarithmic decay. Creep occur mainly in the first km of the crust, but can extend deeper on certain fault sections. Locked asperities can be surrounded by creeping area, causing their progressive loading that leads to their seismic rupture. Creep can be associated with microseismicity or repeating earthquakes. There are also indication of creep retardation in the years to months preceding some earthquakes. In addition, Bilham (2004) mentions potential precursory signals reported by Thurber and Session (1998). Detecting precursory signal, like in creep records, was one objective of the ambitious Parkfield Experiment for which a dense instrumentation network was deployed on the San Andreas fault near Parkfield at the end of the 1980's (Bakun et al., 2005). It was motivated by a long-term prediction that an earthquake would occur here before 1993, based on past seismic activity of the fault. Eventually the earthquake occurred only in 2004, but none of the instrumental networks (seismographs, strainmeters, creepmeters, magnetometers, and continuous GPS stations) detected precursory signal...

Until the 1990s, outside of California, observations of shallow creep were limited to a few sites like on the North Anatolian Fault, Turkey (Ambraseys, 1970; Aytun, 1982), the Dasht-e-Bayaz fault, Iran (G. C. P. King et al., 1975), the Motagua Fault, Guatemala (afterslip, Bucknam et al., 1978), or on the Longitudinal Valley Fault, Taiwan (Bonilla, 1975; S.-B. Yu & Liu, 1989). The scientific issues, the conceptual and theoretical developments about fault creep processes were then at that time mainly inspired by the numerous and detailed Californian observations and by experimental rock friction studies.

The use of the mechanics of friction instead of just fracturation of intact rocks for earthquake really developed in the 60' (Brace & Byerlee, 1966) based on laboratory experiments, which turned out to be well adapted to explain the new observations of creep phenomena (e.g. Dieterich, 1972, 1979; Marone et al., 1990). All these works lead to established constitutive friction laws (Dieterich, 1979; Ruina, 1983) providing a theoretical framework that has been very successful up to now. Two synthesis papers from Marone (1998) and from Scholz (1998) give the state-of-the-art of friction concepts related to the earthquake cycle at the end of the 1990's. The rate- and state-dependent friction laws generate two key concepts: the velocity strengthening or weakening behavior and the related stability regimes: stable, conditionally stable and unstable. Velocity strengthening means that frictional resistance increases with slip-rate, preventing earthquake rupture initiation or propagation. This occurs in the stable regime where slip is aseismic. In opposite, velocity weakening favor unstable behavior. This occurs in the unstable regime where earthquakes can nucleate and develop, leading to infrequent large earthquakes separated by interseismic periods (stick-slip behavior). In between, there is the conditionally stable regime where the slip is stable under quasistatic loading but can become unstable under dynamic loading. That corresponds to a primarily aseismic slip associated with steady rates of small-event activity which can never develop into large seismic event as observed in the shallow creep observations in California.

Fault models that obeys rate- and state-variable friction law are able to reproduce a rich variety of complex behaviors, like periodic creep events, seismic coupling, earthquakes with a large spectrum of event sizes, afterslip, etc. in agreement with laboratory and in-situ observations (e.g. Tse & Rice, 1986; Rice, 1993). They also predict precursory signal to large events (Dieterich, 1978) more difficult to observe, as shown by the Parkfield Experiment mentioned here before. However, those laws were derived empirically from laboratory

experiments and required further work to get a physical interpretation. For instance, to explain why creep seems to be often restricted to the first km of the crust and why it does not occur for all faults, Marone (1990) made experiments on simulated fault gouge showing that velocity strengthening within granular gouge is the result of dilatancy. This was supporting the hypothesis that stable shallow creep (< 3-5 km) is favored by the presence of unconsolidated fault gouge and/or unconsolidated sediments. Shallow creep should then be found on well-developed fault that is fault enough mature to have developed thick zone of unconsolidated granular material (Marone, 1998), like the San Andreas Fault, but may be absent on less mature faults on which little or no gouge had developed (Marone & Scholz, 1988). The role of minerals like serpentinite or talc (e.g. Reinen et al., 1991) has also been invoked based on laboratory experiments.

However, such interpretation had to be verified more systematically in the field and on other faults in other tectonic contexts. Furthermore, even if they are powerful to reproduce a wealth of observations, those laws rely on several parameters poorly constrained in natural environment: μ_0 the steady-state friction, *a* and *b* related to material properties, *L* the critical slip and σ the effective normal stress. This allowed a lot of hypothesis about physical interpretation to be done without being able to test them in-situ. The effective normal stress (applied normal stress minus pore pressure) is often invoked in various hypothesis. For instance, Scholz (1998) proposed that the most likely mechanism for the anomalous behavior of the creeping section of the San Andreas fault, where creep is not restricted to the first kilometers and seems to extend deeper, is the presence of unusually high pore pressures in the fault zone (decreasing the effective normal stress). He also invoked the effective normal stress, to explain the possible effect of geometric asperities.

The shallow creep phenomenon, which can be studied directly when it reaches the surface, has allowed an enriching round trip between laboratory experiments limited by scale-up problems, and the Californian "natural laboratory". Nevertheless, it was necessary to better control the conditions of this natural laboratory and to check its reproducibility in other natural laboratories elsewhere in the world. This will be one of the contributions of InSAR and GPS measurements that arrived in the early 1990s.

Indeed, several key questions were needed new observations. What is controlling the spatial variation of slip behaviors along fault is one of them. Hypothesis of control by the fault zone geology like the presence of unconsolidated gouge or specific mineralogy as mentioned above or by the thickness sediment with overpressurized pore fluids (Sieh & Williams, 1990) or by structural/geometrical control (e.g. Bakun et al., 1980), has been proposed. Testing those hypotheses can be done based on spatial correlation between those parameters and deformation measurements. But despite an ambitious program to deploy about 40 creepmeters from 1968 to the 1980's, mainly on the San Andreas fault system (Schulz et al., 1982; Bilham et al., 2004), ground-based geodetic methods were still limited to investigate in detail the spatial continuity and variability of the creep. The temporal variability of slip behavior is another important question. As shallow creep is quite sensitive to local and regional effects like earthquakes and fault interactions, a more comprehensive monitoring of creep to test hypothesis related to seismicity is needed (e.g. Schulz et al., 1982). This requires being able to monitor the interseismic and coseismic deformation of the whole faults system. Having far-field observation also allows the depth of the creep to be better constrained.

We have seen in sections II-2 and II-3 how InSAR since the 1990's have contributed to the study of coseismic and interseismic deformation at regional scale and about triggered slip.

Here we focused on the interseismic shallow creep observation. Starting from 1986, GPS despite its great contribution to earthquake analysis and to the regional tectonics (Bock et al., 1997; Feigl et al., 1993; Brendan J. Meade & Hager, 2005), and because of the typical km to tens of km distance between stations was not a game changer regarding the study of localized shallow creep. For such study, InSAR is more appropriate. It is at its best level of detection when displacement of a fraction of its radar wavelength (decimetric to centimetric) are localized within a few tens of meter across a fault trace reaching the surface without major topographic change. At such short distance atmospheric noise is very low and the displacement signal appears like a knife-cut in the images (e.g. like in Figure 13). The Californian creeping strike-slip faults with their relatively low vegetal landcover are then good targets for InSAR, which usefully complement the ground measurements by providing the spatial continuity of the measurement.

The ERS-1 and ERS-2 satellites provided the first shallow creep observations on the San Andreas fault Northwest of Parkfield (Werner et al., 1997; Rosen et al., 1998) and on the Hayward fault (Bürgmann et al., 1998; Bürgmann, Schmidt, et al., 2000). Several others studies will follow on the Southern San Andreas Fault (Lyons & Sandwell, 2003), on the San Juan Bautista segment (Johanson & Bürgmann, 2005) and on the Rodger Creek Fault (Funning et al., 2007).

Outside California, the first InSAR observations were done on the Izmetpasa segment of the North Anatolian Fault (Çakir et al., 2005), on the Longitudinal Valley Fault (L. Hsu & Bürgmann, 2006), on the Haiyuan fault, China (Cavalié et al., 2008), the Chaman Fault, Afghanistan (Furuya & Satyabala, 2008). In this list, the Longitudinal Valley Fault (LVF) is the only case of creep on a thrust fault and not on strike-slip fault. Indication for shallow creep have been observed or inferred by other techniques on other tectonic contexts like on normal faults, e.g. in Gran Sasso massif, Italy (Amoruso et al., 2002) and may be on the Alto Tiberina Fault (Chiaraluce et al., 2007) but with no evidence that the creep reaches the surface. The other interest of the LVF is that the fault is also the place of large earthquakes, and of microseismicity with repeating earthquake (K. H.-H. Chen et al., 2008).

It is in this context that I started working with Johann Champenois on the LVF. Johann started his PhD Thesis about the interseismic deformation in Taiwan using InSAR in Oct. 2008, during which he also confirmed the presence of creep on the Fengchung fault that I detected during my PhD and found evidence of creep on the Hengchung fault (Johann Champenois, 2011; C52 ; Deffontaines et al., 2018).

Creep on the Longitudinal Valley Fault in Taiwan

The Longitudinal Valley Fault located in Eastern Taiwan is a major tectonic boundary of the Taiwan collision zone, separating the coastal Range that is geologically made of the Luzon volcanic arc of the Philippines Sea Plate, from the Central Range that belongs to the Eurasian Plate (Figure 12). This primarily reverse fault accommodates about 3cm/year of the 8 cm/year convergence between the two tectonic plates (S.-B. Yu & Kuo, 2001).

First geodetic evidence of aseismic creep on the central segment of the LVF are given by Yu and Liu (1989) from levelling and trilateration network. In Chihshang, were evidence of progressive deformation of concrete human structures have been reported since the 1980's, those geodetic measurements were completed from 1990 by in-situ measurement (Lee, 1994; Angelier et al., 1997, 2000), and local leveling lines and trilateration networks (Lee & Angelier, 1993), in parallel to the setup of an Island-wide network of GPS (S.-B. Yu et al., 1997). Creepmeters were installed in Chihshang in 1998 (Lee, Angelier, et al., 2001; Lee et al., 2000) and creep rate variation were identified (Lee et al., 2003, 2005), some of them being related to

ground water change (Chang et al., 2009). At the southern termination of the LVF in the Peinanshan, which shows a more complex partitioning (Barrier et al., 1982; Shyu et al., 2008), denser trilateration, levelling and GPS measurement have also been performed (Lee et al., 1998; H.-Y. Chen et al., 2012, 2013).

However, those measurements remained quite punctual with respect to the fault size making difficult to address key issues, like possible lithological controls on the creep requiring knowing the precise spatial extent of the creep, its continuity and its variation along the fault. Furthermore, it was not excluded that other surrounding faults (see Figure 12), like the Central Range Fault located on the western side of the Valley (Shyu et al., 2006) or the Chimei Fault in the Coastal Range (W. Chen et al., 1991), show also creep behavior.

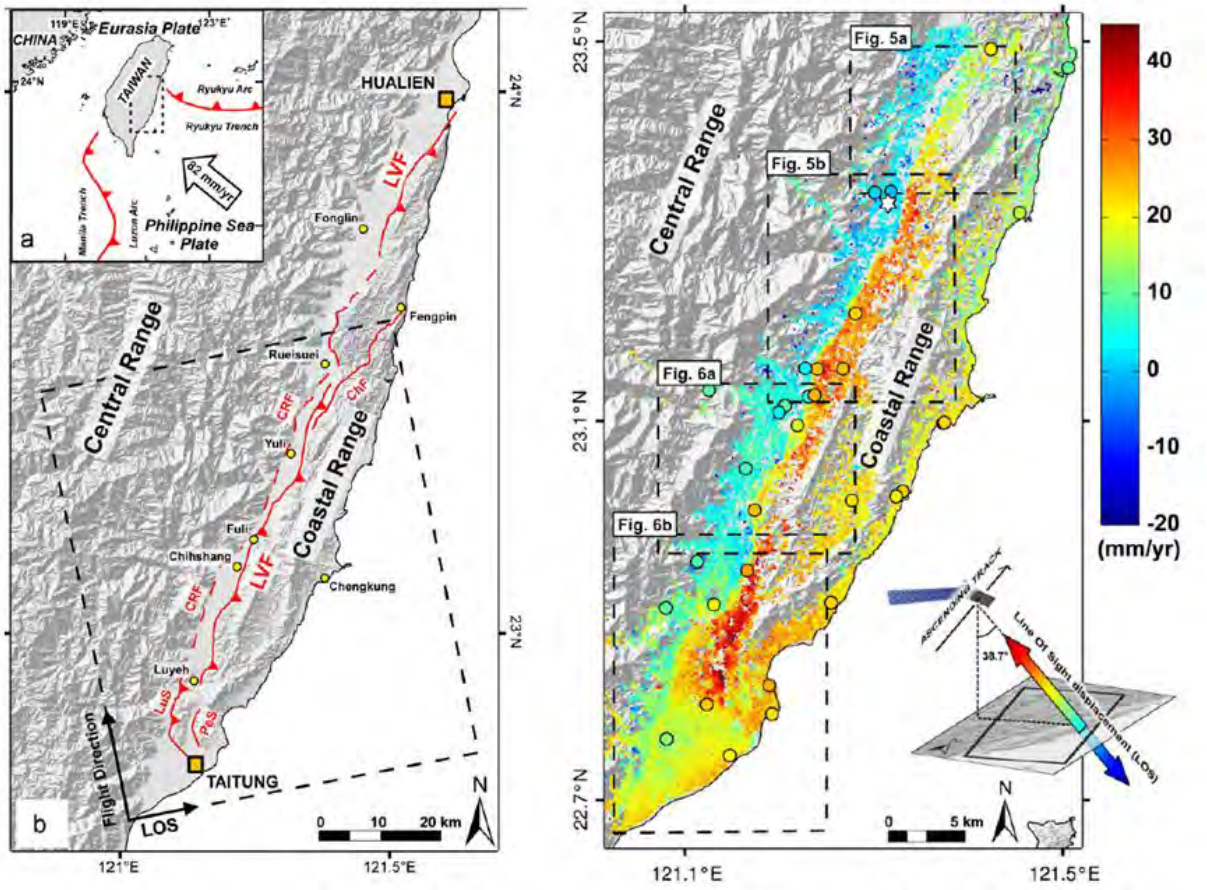

Figure 12 : Location of the Longitudinal Valley Fault and mean velocity surface displacement map from INSAR and GPS. LEFT: Shaded DEM of Eastern Taiwan with active faults in red: Longitudinal Valley Fault (LVF), the Peinan Strand (PeS), the Luyeh Strand (LuS), the Chimei Fault (ChF) and the Coastal Range Fault (CRF).The dashed frame represents the area covered by ALOS-1 images. RIGHT: Map of mean velocities along the satellite line-of-sight (LOS) for the period Jan. 2007 to Feb. 2010. The colored circle are GPS measurements reprojected in LOS. See pdf-2 for the detailed view shown by the dashed rectangle. (Adapted From A11)

Two INSAR studies were previously done on the LVF using C-Band ERS-1/2 data, one spanning the 1997-2000 period (L. Hsu & Bürgmann, 2006) and the other using a larger dataset form 1993 to 1999 (Peyret et al., 2011). However, those studies were strongly limited by the rapid temporal decorrelation of C-Band data in the vegetated landcover of Eastern Taiwan.

In the Champenois' study (A11 pdf-2) a Persistent Scatterers SAR interferometry approach (StaMPS) is applied using L-band SAR images from ALOS satellite acquired over the period 2007–2010. Interferograms from L-Band data show a dramatic improvement of coherence in comparison to previous studies using C-Band ERS data. The density of measurement give a continuous view of the deformation along the Valley and giving information on its borders (Figure 12). The most striking feature of the resulting mean velocity map is a clear velocity discontinuity localized in a narrow band (0.1–1 km) along the LVF and responsible for up to 3 cm/y velocity offset along the radar line of sight, which is attributed to shallow interseismic creep. InSAR results are in good agreement with continuous GPS measurements over the same period (0.3 cm/y rms). The density of measurement allows us to improve fault trace map along the creeping section of the LVF (with accuracy of about 100 m) and to find new field evidences of the fault activity. In some places, our trace differs significantly (hundreds of meters) from previous published traces. The creep rate shows significant variations along the fault. At the southern end of the valley, the deformation is distributed on several structures, and drops significantly south of the Peinanshan. A local study of the interseismic deformation of the Pingtung terraces based on this dataset has also been published (A19).

Johann completed this dataset further north, resulting into a complete InSAR coverage of the LVF. This dataset has been useful in the study of Thomas et al (2014 b) that investigate the lithological control on the creep behavior on the LVF. This work was motivated by previous observations of spatial correlation between creep behavior and the presence of thick unconsolidated alluvial deposits on the footwall of the LVF and the Lichi Mélange on the hanging wall (e.g. Lee et al., 2006), in line with InSAR based observations in California (Wei et al., 2009). Thomas et al show that there is a strong lithological control by the presence of the Lichi Mélange that promotes aseismic creep. However, they also show that this control is rather dominated by internal microstructure of the fault gouge than its mineralogy it-self. Similar investigation of lithological control have been done on the North Anatolian Fault (Kaduri et al., 2017, 2019) where several InSAR studies have provided spatially detailed creep observation (Kaneko et al., 2013; E. Cetin et al., 2014; Hussain, Wright, et al., 2016; Rousset, Jolivet, et al., 2016) that can be confronted to geological field observations. Kaduri et al. (2017) show a clear correlation between shallow creep and near-surface fault gouge composition.

The InSAR results on the LVF were also critical in the study of Thomas et al (2014 a), addressing the spatiotemporal evolution of seismic and aseismic slip on the LVF. Indeed the LVF shows an evolution from aseismic creep at shallow depth to stick-slip behavior at 10-25km, where locked asperities are able to produce up to Mw 6.8 earthquake, like the 2003 Mw 6.5 Chengkung earthquake. Such asperities seem to coexist with creeping areas as revealed by observations of repeating earthquakes sequences (K. H.-H. Chen et al., 2008, 2009). Thomas et al used geodetic observation (levelling, GPS and InSAR) to get the spatial and temporal slip distribution on the LVF. It shows that the earthquake was located on an asperity surrounded by creep, and that its rupture propagated into the shallow creeping zone but stopped before reaching the surface. This slip distribution is in spatial agreement with repeating earthquakes observation, but repeating earthquakes where not used to constrain the inversion. I am currently working with a post-doc Wei Peng and Mathilde Radiguet to incorporate information from repeating earthquakes into slip distribution inversion of the LVF in addition to GPS and InSAR data.

In the study of Thomas et al. (2014 a), it is mainly the GPS data that are giving the time dependence information, dominated by the first year of post-seismic signal following the 2003 Chengkun earthquake. Our InSAR time series analysis, which are only based on ten ALOS-1

acquisitions, are not showing clear temporal variation for the period 2007-2010. However, preceding the postseismic transient creep signal (Lee et al., 2006), a decrease of the creep rate has been observed years before the earthquake (Lee et al., 2005), consistent with indication of creep retardation in the years to months preceding some earthquakes in California (Robert O. Burford, 1988). In addition, Murase et al (2013) report a local uplift rate increase in 2011-2012 based on levelling observation, that they interpret as an episodic acceleration event of shallow creep. All those observations call to further InSAR investigation using Sentinel-1 and ALOS-2 data.

The beginning of the 2010's is marked by the multiplication of InSAR studies based on the years-long ENVISAT and ALOS-1 time series reporting transient shallow creep events and giving spatially detailed coupling map, like on the North Anatolian Fault (Çakir et al., 2012; Kaneko et al., 2013; E. Cetin et al., 2014). Rousset et al (2016 a) using 1-year of temporally dense CosmoSkymed SAR images identify a major burst of shallow creep on the NAF spanning 31 days with a maximum slip of 2 cm, between the surface and 4 km depth. In California, Wei et al (2009) identify transient slip on the Superstition Hills Fault, Turner et al (2015) a pulse of deformation with a 2-year period on the creeping section of the San-Andreas fault, while on the same section Jolivet et al (2015) show creep spatial heterogeneities indicating several locked asperities consistent with evidence for past magnitude >6 earthquakes. Similar observations are done on the Hayward Fault (Shirzaei & Bürgmann, 2013; E. Chaussard et al., 2015) consistent with previous studies (Bürgmann, Schmidt, et al., 2000; Simpson et al., 2001). On the Haiyuan Fault in China, shallow creep is confirmed (Jolivet et al., 2012) with evidence of burst-like temporal variation of creep (Jolivet, Candela, et al., 2015; Jolivet et al., 2013).

In the following section, I present another contribution of InSAR to shallow creep study documenting transient creep acceleration on the major El Pilar fault (A18). I work on this study in the frame of the Léa Pousse's PhD thesis.

Creep on the El-Pilar Fault, Venezuela

The El-Pilar fault, is a major strike-slip fault in northeastern Venezuela that accommodates most of the 2cm/year relative displacement of the Caribbean-South America plate boundary (J. C. Weber et al., 2001; François Jouanne et al., 2011).

The fault have been the place of several large earthquakes in the past. The last one is M 6.8 1997, Cariaco earthquake, for which field observation of afterslip reaching the surface have been done (Audemard 2006). Jouanne et al. (2011) based on two campaign measurements made in 2003 and 2005 of a regional GPS network with about 25 points located on both side of the fault noticed high interseismic strain centered on the El-Pillar fault, suggesting aseismic creep in the first 10 km. New campaign observations in 2013 confirmed that result (Reinoza 2015) and suggest along-strike variation of the creep.

However, the sparsity of GPS measurements lets open several first-order questions, like what is the spatial continuity and extent of the creep and its potential segmentation? Is the creep the decaying continuation of the afterslip from 1997, or does the afterslip initiated sustained creep behavior like observed on the North Anatolia Fault after the 1999 Izmit earthquake (Çakir et al., 2012)? InSAR measurements had the potential to answer those questions.

François Jouanne who was at the initiation of this study that was part of the Léa Pousse PhD project. Despite the tropical context with dense vegetal cover unfavorable to InSAR measurement, my experience on the Longitudinal Valley Fault in Taiwan give us some confidence

to start this InSAR study using time series of 18 L-band ALOS-1 acquisition covering the 2007-2011 period. We get very clear evidence of shallow creep reaching the surface along about 70 km of the fault, with some segmentation and creep rate variation along strike up to 25 mm/year (Figure 13 top, A18 pdf-5). There is also temporal creep rate variation (Figure 13 bottom), showing transient creep acceleration in 2009-2010 not consistent with afterslip decay of the 1997 Cariaco earthquake. The creep is thus interpreted as sustained aseismic slip during, which has a pulse- or transient-like behavior. There is no clear temporal correlation with the available seismicity.

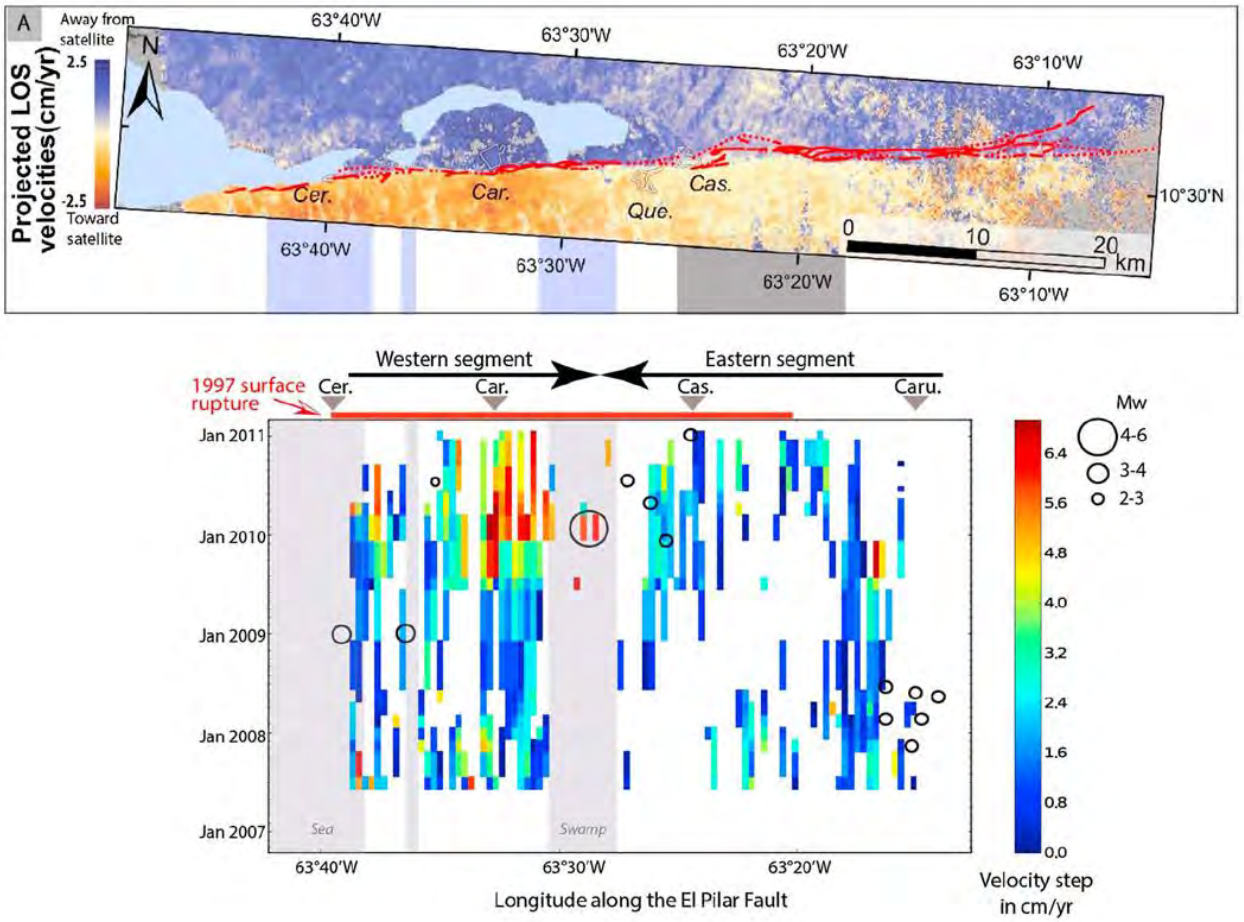

Figure 13 : InSAR mean velocity map and temporal creep variation of the El-Pillar Fault. TOP: InSAR mean velocity map (2007–2011 period) with fault trace in red (Car., city of Cariaco; Que., Quebrada del Tigre; Cas. Casanay; and Caru., Carupano). BOTTOM: Time evolution of velocity steps across the fault, in function of the longitude. White and grey area corresponds to areas where the step could not be estimated. Black dots correspond to the local seismicity (Mw>2).

The western part of the creeping section of the El-Pillar is faster than the eastern one, which seems to be correlated with the segmentation of the fault trace. As already suggested by several authors, the geometry of the fault trace and in particular its segmentation is a controlling factor of slip behavior (e.g. Bakun et al., 1980, 2005; Lindsey et al., 2014).

This study is an example of how InSAR can contribute to understand shallow creep. The main present-day research trend is focused on the temporal variations. For instance, recent InSAR paper show the importance of static stress changes in creep rate modulation even if dynamic

effects from remote earthquakes can trigger long-term creep changes (Xu et al., 2018; Tymofyeyeva et al., 2019). For a more generic review of other possible physical mechanisms controlling slip behavior, see Harris (2017) and Burgmann (2018). See also Jolivet & Frank (2020) about the transient and intermittent nature of slow slip. To finish this part about shallow creep, I illustrate in the following section the ability of INSAR to systematically search for surface displacement discontinuities even in a challenging environment like the Taiwan Island.

Looking for shallow creep at large scale, the sharp eyes of InSAR

In active tectonic area, the spatial density and availability of GPS data are growing and presently provide a good basis to constrain regional deformation in most of the active tectonic areas (see for instance data available from the Nevada Geodetic Laboratory GPS Networks Map (http://geodesy.unr.edu/NGLStationPages/gpsnetmap/GPSNetMap.html). However, even in well-instrumented places like Taiwan, the density of stations is often not enough to distinguish smooth surface deformation distributed over kilometric distance from shallow creep reaching the surface and localizing the deformation in a few tens of meter. InSAR, with typical spatial resolution ranging from meter to tens of meter is the perfect companion of GPS to achieve this goal.

I already mentioned examples of search for shallow creep using Envisat data at the la Venta-Chacalapa fault in the Mexican Subduction zone (II-4) and on the Doruneh fault in Iran (II-3) giving informative negative results. Indeed several InSAR coverages of entire large fault systems for interseismic studies have already been achieved using Envisat and/or ALOS-1 data in InSAR friendly environment like on the Chaman Fault system (Fattahi & Amelung, 2016; Barnhart, 2017) or on the San-Andreas fault system (X. Tong et al., 2013). Studies in more vegetated environment like Sumatra (X. Tong et al., 2018) and Venezuela (A18, A21) have also been done.

Here, I illustrate the potential of InSAR in the case of the Taiwan Island, which is an even more challenging environment because of the high topography gradients of the Central Range in addition to dense vegetal cover. For this case, the processing has been done with Bénédicte Fruneau with the help of Marie-Pierre Doin using L-band ALOS-1 data (C61, C66). It is noteworthy that despite the better temporal sampling of C-band Sentinel-1 data (about 12 days in Taiwan), our first test using time series of Sentinel-1 data on Taiwan show that crossing the Central range by spatially continuous InSAR measurement will be a challenging issue. L-band ALOS-2 data are more promising but required significant additional processing (taking into account azimuth frequency modulation rate error, ionospheric phase effect and azimuth shift caused by the ionosphere) especially when dealing with several years of times series analysis looking for interseismic deformation (Liang et al., 2018). The coming L-band mission NiSAR (Figure 1) should ease the processing.

For the processing, we used ALOS-1 images on four adjacent tracks (Figure 14). Our dataset consists of about 300 images that is all the ALOS-1 images available for those tracks covering the 2007-2011 period. SAR images are processed through a small baseline approach (Berardino et al., 2002) with the NSBAS processing chain, developed at ISTerre (P04)

A critical point in this processing is to apply several corrections before the unwrapping step, in particular correction of atmospheric delays predicted from the global atmospheric re-analysis ERA-Interim model (M.-P. Doin et al., 2009; Jolivet et al., 2011), and local DEM error correction (Ducret et al., 2014). These corrections are of particular importance as they reduce the variance

of the phase across regions with high topographic gradients, hence preventing unwrapping errors. GPS data are used to correct LOS velocity map from a residual large-scale quadratic ramp that could remain on InSAR results. This is performed by estimating and removing a polynomial of second degree.

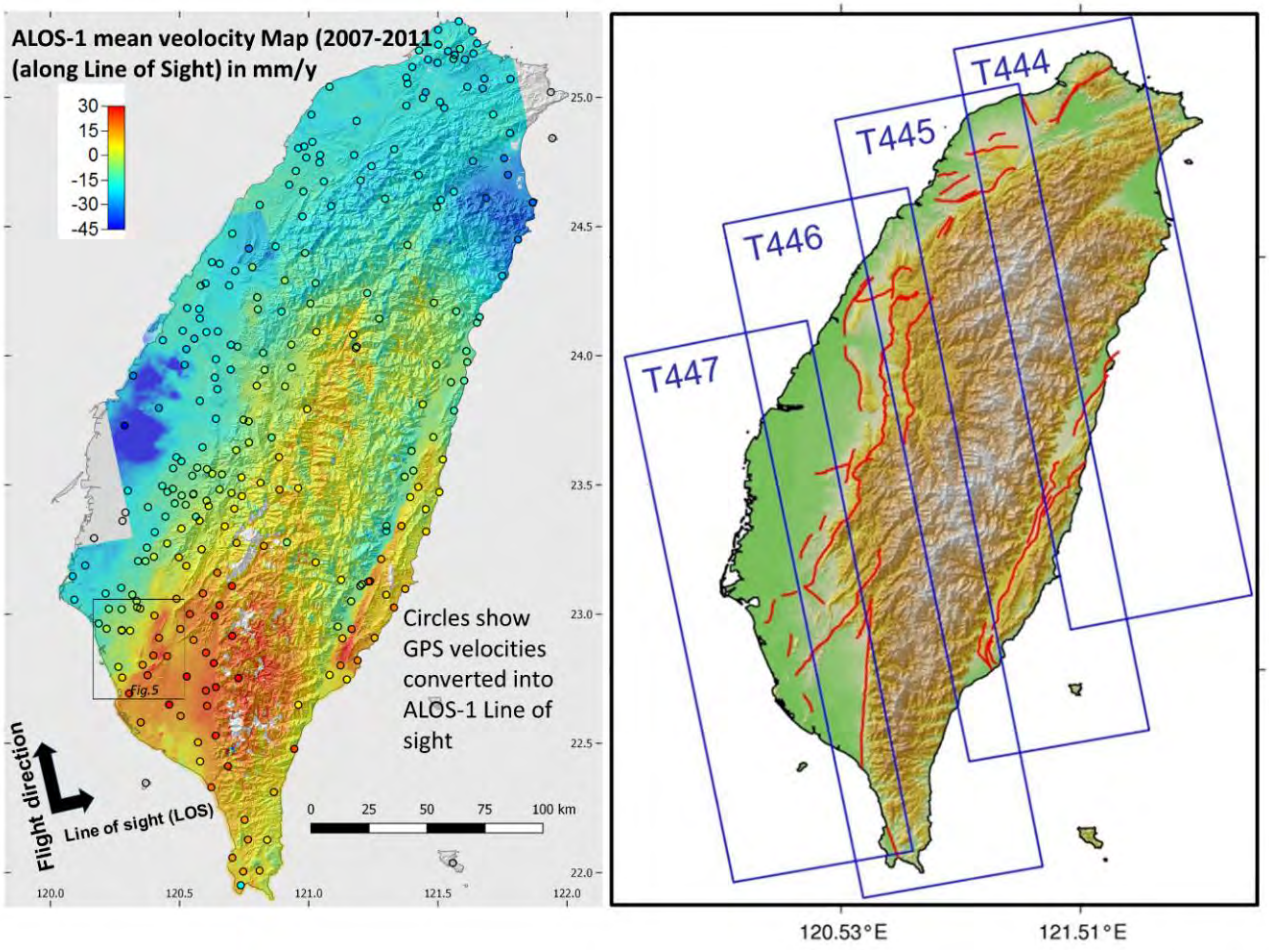

Figure 14 : ALOS-1 mean surface velocity map. Velocity correspond to displacement along the radar line-of-sight for the period 2007-2008. The left figure show the topography with the Central Range culminating at 4000m and the track coverage of the ALOS-1 data (from C70).

The results give an almost complete and continuous deformation map of all Taiwan over the period 2007-2011 (C66). Figure 14 shows that we can retrieve information across the Central Range offering an unprecedented continuous view of the deformation field of the entire Island. To the East, one can clearly see the Longitudinal Valley Fault discontinuity (A11). The Central Range shows a relatively smooth pattern of deformation, consistent with a rapid uplift (cm/y) of the Central Range South of the island. This uplift, already partially documented by GPS and leveling (e.g. Ching et al., 2011) seems to show an overall continuity and InSAR excludes major shallow creep discontinuities. To the West, significant anthropic subsidence of anthropic origin can be seen in dark blue on Figure 14 (Tung & Hu, 2012). In South-Western Taiwan large gradients of deformation are observed (inside the black square on Figure 14), that will be discussed in the next part.

6 – Aseismic deformation in a thrust-and-fold belt: what can we learn from SW Taiwan?

Thrust-and-fold belts are characterized by the presence of fault-related fold that can be at relatively shallow structural level (Suppe, 1981; Suppe & Medwedeff, 1990; McClay et al., 2011). The question of the aseismic or seismic growth of anticline has been strongly related to the capacity to measure geodetically such growth. Before the 1980's folding is mainly seen as a progressive slow aseismic process, but geodetic measurements of coseismic fold growth an several Californian anticlines like during the 1983 Coalinga earthquake has radically change this vision (Stein & King, 1984; Geoffrey C. P. King et al., 1988; Stein et al., 1988; Stein & Yeats, 1989). Coseismic growth was also supported by paleoseismological observations of incremental coseismic folding done after the 1980 El Asman, Algeria earthquake (e.g. G. C. P. King & Vita-Finzi, 1981; Meghraoui & Doumaz, 1996). In this vision, elastic interseismic deformation built up and is released by earthquakes on blind faults that are associated to fault-cored anticlines, resulting in incremental folding. Coseismic deformation can be absorbed in the bulk of the fold through flexural folding (R. E. Klinger & Rockwell, 1989) and secondary faulting. Post seismic deformation can also occur, as observed for the Coalinga case, which is interpreted by fault tip propagation into the core of the anticline releasing the high stress increase caused be the earthquake at the tip of the fault. This stress release can also be done through the aftershocks (Stein & Ekström, 1992).

Do all the fault-related folds follow the same coseismic growth mechanism is then a fundamental question, but has also great implication for earthquake hazard assessment, as the two opposite mechanisms have very different impact. In the model defended by Stein et al. (1988), the interseismic uplift shows a different spatial signature from the coseismic one and from the « long-term » uplift resulting after a few earthquake cycles. The peak of interseismic uplift is shifted toward the hangingwall with respect to the peak of coseismic uplift and with respect to the peak of long-term uplift, whereas in the case of a progressive aseismic growth, long-term and « interseismic » spatial pattern are similar because there is no more proper interseismic deformation. One can also have intermediate situation, where both progressive aseismic and anelastic deformations coexist with coseismic deformation. In this case, arises the problem of assessing the contribution of each processes and then using the spatial pattern discrimination becomes more difficult. One of the major problems to address this issue is indeed the capacity to measure interseismic fold deformation in thrust-and-fold belts.

At the beginning of the 1990's few measurements of interseismic deformation of fault-related fold were available. However, in the two following decades, GPS, INSAR and levelling have help to document such deformation, giving weight to the coseismic folding hypothesis. For the Himalayan Front, for Instance, Cattin & Avouac (2000) proposed a mechanical model where the Main Himalayan Thrust (MHT) is creeping at depth but is locked in the first 10 km, in good agreement with geological, erosion and geodetic data and thermal structure. Based on the Himalayan example, Avouac (2003) proposed a comprehensive and coherent picture of the mountain building and the seismic cycle, in which the Himalayan frontal folds are growing incrementally through earthquakes. However, at that time, no coseismic deformation measurements from large earthquake were available to test the model on the Himalayan case. Grandin et al (2012) based on InSAR measurement found that the interseismic uplift peak matches the long-term uplift peak, above the MHT ramp, but interpreted it as the result of the

long-term migration of the active ramp location. No interseismic uplift is seen on the folds located at the main frontal thrust in agreement with coseismic folding model.

In 1999, the Mw 7.6 Chi-Chi earthquake occurred on the Chelungpu fault, a major thrust of the western margin of the Taiwan orogen (another book-example of thrust-and-fold belt (D. Davis et al., 1983)), giving the opportunity to apply - with success - this conceptual model. With a relatively simple elastic model, Loevenbruck & Cattin (2001) were able to explain the geodetic observations with an interseismic signal due to aseismic slip on a 10 km deep décollement, causing strain accumulation on the Chelungpu fault. This model was refined by Cattin et al. (2004) taking into account post-seismic deformation, showing that part of the Chelungpu fault connecting to the décollement may be unlocked.

On the Zagros fold belt, the study from Barnhard & Lohman (2012) using InSAR was inconclusive. They do not found evidence for interseismic displacement along folds or faults certainly because signal was below the InSAR detection level (<2-3 mm/y). In parallel to interseismic studies, several other studies were giving growing evidences of incremental coseismic fold growth, either from geological arguments (Leon et al., 2007) or InSAR coseismic observations (e.g. Nissen et al., 2007; Belabbès et al., 2009; Pezzo et al., 2013; Tizzani et al., 2013). Triaxial shear experiments on rocks also favor earthquake related deformation over aseismic slow deformation for near surface folding (H. Cetin, 1998). The 1999 Chi-Chi earthquake also provided a lot of evidence of coseismic folding in sub-surface on pluri-metric fold scarp (Y.-G. Chen et al., 2007; Lee, Chen, et al., 2001; Streig et al., 2007; Lee et al., 2004) or at larger scale (Yue et al., 2005; Graveleau et al., 2014).

At the beginning of the 2010's, despite few divergent observations (e.g. Sylvester, 2000), the main stream view have shifted toward the view that most anticlines in thrust-and-fold belt are fault-cored fold deforming during seismic slip on underlying faults. Apart from the specific case of salt-related creep process, there were actually very few examples of blind fault creeping aseismically up to shallow depth below an anticline. In such case, the potential for coseismic slip may be reduced as shallower sediment are less prone to store elastic energy and locked fault area is reduced. Such configuration may allow fold to growth aseismically and showing a topographic long-term spatial signature similar to the geodetic one (assuming no major erosion). A possible case was the Tainan anticline located in South-Western Taiwan (Figure 15, see location in Figure 14) that I studied during my PhD (A02).

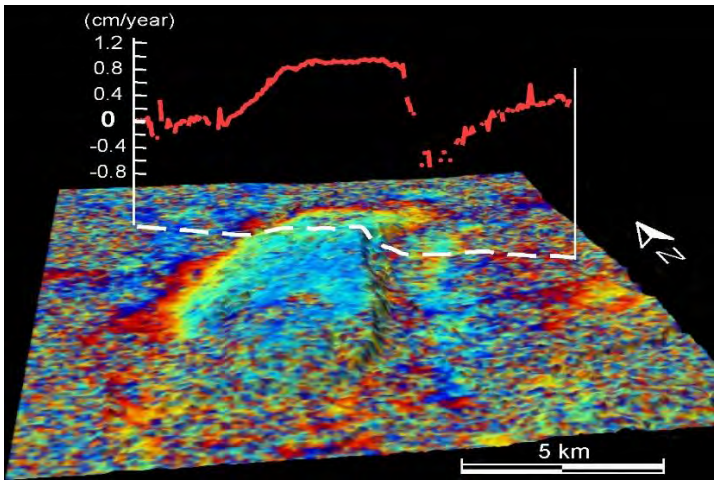

Figure 15 : ERS Interferogram draped on Digital Elevation Model, showing an interseismic deformation pattern (red curve) matching the topography (white curve) of the Tainan anticline.

The topographic expression of this anticline is the 12 km long and 4 km-wide Tainan tableland. ERS interferometry shows an uplift deformation rate of about 1 cm/year over the period 1996-2000 consistent with levelling and GPS data. The spatial pattern of deformation follow the topographic expression of the anticline. Simple Elastic models need very shallow creep on underlying faults to reproduce such a pattern (A7).

It is in this context that, in 2014, with Bénédicte Fruneau and Marie-Pierre Doin, we started to reprocess ALOS-1 data in SW Taiwan using the NSBAS processing chain. We were surprised to discover that in area located further inland east of the Tainan city (either not covered or too noisy in previous InSAR studies) even larger deformations occur on other tectonic structures like the Lungchuan ridge (Figure 16, C53, C59). The largest signal was on the Lungchuan anticline that has not been identified before because it was not well covered by the permanent GPS network. This illustrates the interest of InSAR to finely identify geological active features, even in a country having one of the highest density of permanent GPS stations in the world.

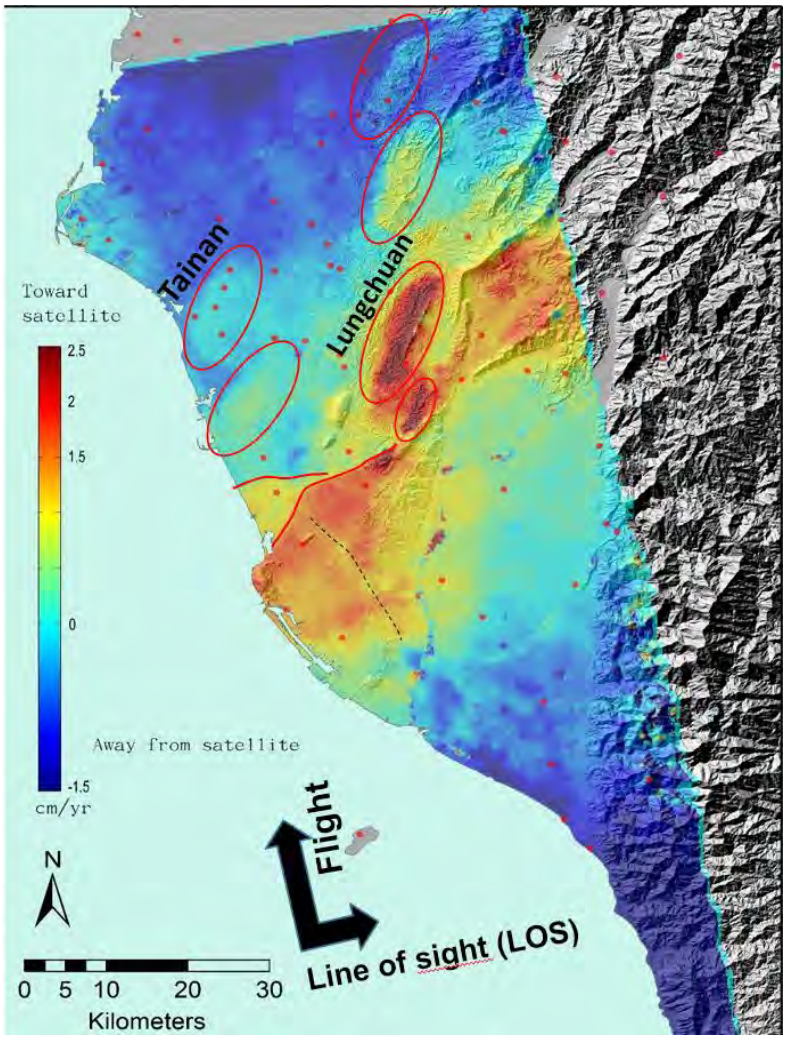

Figure 16 : Mean velocity map of South-Western Taiwan from NSBAS processing of ALOS-1 ascending data. Velocity correspond to surface displacement along the radar line-of-sight for the period 2007-2010. Red dot show the permanent GPS stations. The red ellipse show deformation related to fault-related fold including the Tainan and Lungchuan anticline. Red line and black dashed line correspond to shallow creeping faults. A shaded DEM is in background (from C59).

A compilation of the available geological cross sections available in the area, done during the Master internship of Liao Yu-Tzu, showed that deformation signal at the Lungchuan ridge is centered above an anticline axis west to the ridge rather than related to creep activity on the East dipping Lungchuan thrust fault. We also showed the spatial correlation between the Gutingkeng clayey mudstone formation and the area of high strain.

Comparison with terraces deformation analysis from Hsieh et al. (M.-L. Hsieh & Knuepfer, 2001) shows that the pattern of deformation seen by geodesy during interseismic period is consistent with Holocene tilting of fluvial terraces (C70). Terraces tilt gives a tilt of about 1.5 mm/km over 2Ky, levelling data gives about 4mm/km and InSAR 5mm/km with a good spatial correlation of the signal (Figure 17). This will deserve further fieldwork to better constraint the Holocene deformation.

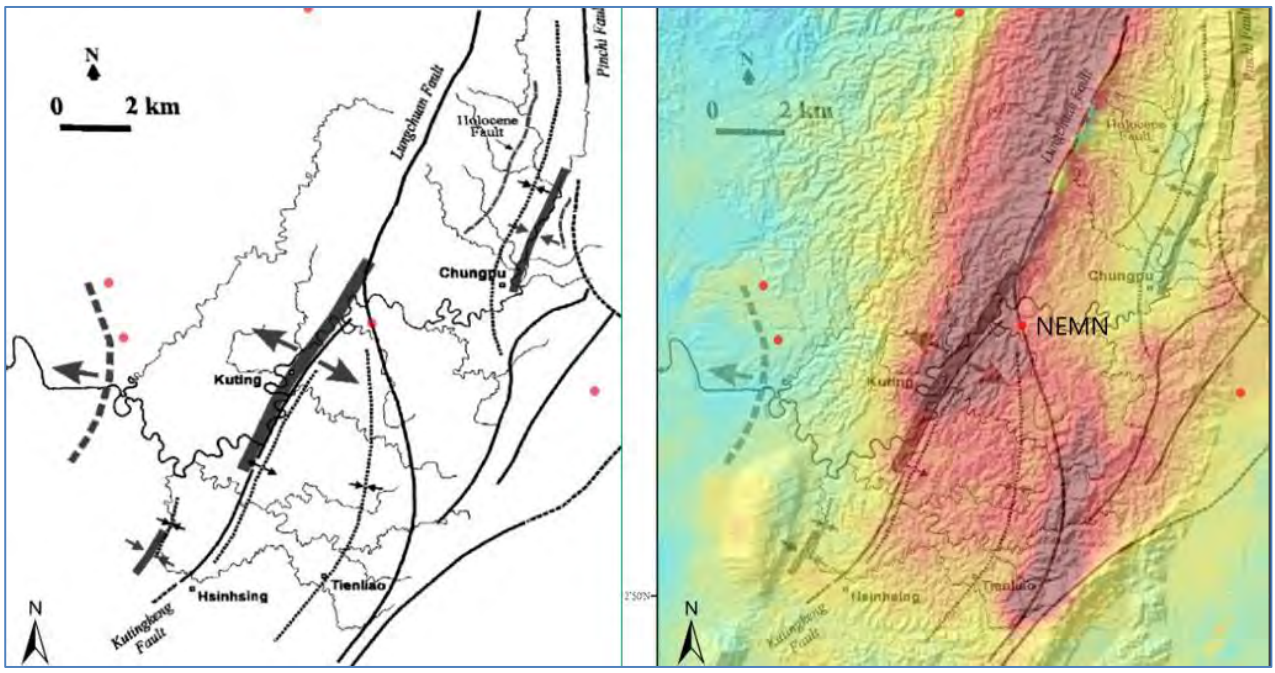

Figure 17 : Comparison between Holocene uplift located on anticline and syncline axis (Thick black lines) derived from fluvial terraces analysis along the Erhjen river (M.-L. Hsieh & Knuepfer, 2001) and interseismic deformation signal at the Lungchuan ridge (see Figure 16). Note the good spatial correspondence between the long-term deformation signal shown by the thick black lines and the geodetic signal (C70)

This work has been completed by an analysis of Sentinel-1 data from Nov. 2014 to 2018 made during the Master internship of Fekaouni Miloud. Sixty-three acquisition dates have been processed using NSBAS to get time series and LOS mean velocity map, corrected from the coseismic step of the Mw 6.4 2016 Meinong earthquake. Sentinel-1 LOS mean velocity map show new evidences about on-going deformation (several mm/year) on the Chungchou anticline (C77). Located in the coastal plain, south of the Tainan anticline, the Chungchou anticline is slightly marked in the landscape with elevation between 20-40m (Figure 18). Its morphologic signature was identified by several authors (Lacombe et al., 1999; Shyu, 2005) but its present-day activity was not quantified. The Chungchou anticline was also known since the 60's from gravity anomaly and seismic measurements (S. H. Hsieh, 1972; Pan, 1968).

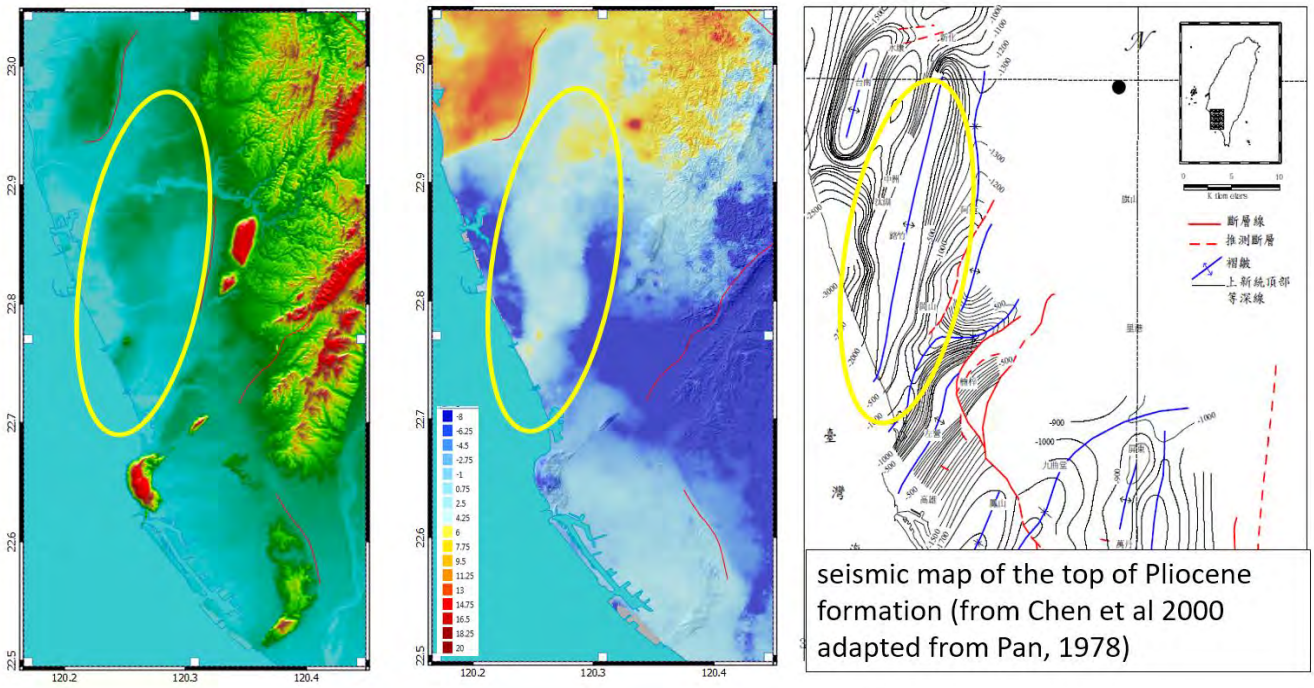

Figure 18 : Comparison of descending Sentinel-1 mean velocity map in mm/y (Center) with topographic map with dark green corresponding to 20-40 m elevation (Left) and with the isodepth map of the top of the folded Pliocene formation in meter (Right). Note the good spatial correspondence of the interseismic deformation with long-term geological expression of folding of the Chungchou anticline (adapted from C77).

InSAR time-series analysis reveals a surface deformation pattern spatially well correlated with the NNE-SSW anticline axis. These observations also clearly suggest an offshore prolongation of the anticline deformation toward the SSW, which is structurally consistent with offshore seismic profiles and derived seismic map of the top of Pliocene formation. The geology and the spatial wavelength of the observed deformation suggest a relatively shallow (> 6km) origin. Indeed, geological cross-sections proposed by Le Béon et al (A20) across the Tainan and Lungchuan anticline indicate that all the fault-related folds observed in the area are in connection with a relatively shallow décollement showing flat and ramp at 5-7 km depth.

This is an interesting point, because the investigated active folding are in a particular area in Taiwan where there is almost no seismicity (Magnitude >2) in the first 10 km of the crust, contrasting with the Western foothills where happens the 1999 Chi-Chi earthquake. This suggests that SW Taiwan exhibits a different deformation style from the Western Foothills and indicates that the spatial short wavelength (about 5 km) of the interseismic surface deformation seen by InSAR is primarily aseismic. The most direct interpretation is that shallow creep drives the deformation on fault-related anticlines as inferred on the Tainan anticline but we cannot exclude off-fault processes. The clayey rocks of the Gutingkeng formation with the presence of overpressurized fluids attested by the presence of mud volcanoes (Shih, 1967; Sun et al., 2010) may be favorable for aseismic slow slip (Bürgmann, 2018), suggesting a lithological control of the deformation mode along the Taiwan thrust-and-fold belt.

However, there is deeper seismicity perturbing this fault and fold system as seen in section II_2 (Figure 5). The 4 march 2010 M. 6.4 Jiashian earthquake and the 2016 Mw 6.4 Meinong earthquake were located on sources deeper that 15 km (Y.-J. Hsu et al., 2011; Rau et al., 2012; K.-C. Lin et al., 2016; M.-H. Huang, Tung, et al., 2016). ALOS-1, Sentinel-1 and ALOS-2 data show

that shallower geological structures react to that earthquakes (C66, A20, M.-H. Huang, Tung, et al., 2016; Tsukahara & Takada, 2018). The connection between the shallow décollement and this deeper source is still unclear. Nonetheless, ALOS-1 and Sentinel-1 time series show that the coseismic and post-seismic response of the Lungchuan anticline to both earthquakes show a similar spatial pattern with the interseismic signal suggesting an acceleration of the aseismic creeping process triggered by the earthquake (A26 in prep). Such transient accelerations have been reported in other places (e.g. Copley & Jolivet, 2016). In collaboration with Kate Chen, in the framework of the Dragon Gate project, we looked for repeating earthquakes sequence and tremor-like signal in the area that could be associated with aseismic creep, but we did not find clear signal. Transient deformation have also been reported from INSAR analysis on the Tainan anticline before those earthquakes, maybe in relation with the remote Chi-Chi earthquake (Johann Champenois, 2011; Wu et al., 2013). At a more regional scale, Huang et al. (2016) mention possible transients in relation to hydrological effect. GPS data also suggest transient deformations in the months preceding the Meinong earthquake (Tsai et al., 2017).

The earthquake potential of Southwestern Taiwan is then a big question. The coastal plain has a high population density with the city of Tainan having about 2 million inhabitants. Shyu et al. (2005) suggest a debatable potential M 7.7 assuming a continuous thrust structure extending southward off-shore. Our analysis tends to favor far lower magnitude as shallow creep is reducing the surface of up-dip locked fault and strain caused by the creep is located in the first kilometers of a sedimentary layer more prone to off-fault distributed strain (for instance by flexural slip at layer contacts). However, we have not yet investigated the coupling on the different faults and the décollement. Aseismic creep can coexist with higher coupled asperities prone to earthquake as seen in the previous section II-5. For instance, Marinière et al (2020) show that for the 20-km long Quito Fault (Equator), where there are geodetic evidence for shallow creep with a 1-km locking depth, the moment slip deficit may cause a magnitude 6.5 earthquake.

Furthermore, even at shallow depth (< 3 km), earthquakes can nucleate in the strongest rocks like for instance limestone, whereas more clayey formation can accommodate at least part of the tectonic loading by aseismic creep (Gratier, Thouvenot, et al., 2013). Such contrasted mechanical behavior is not expected in South-Western Taiwan where fault-related folds are within young sedimentary detritic deposits or within the thick clayey Gutingkeng mudstone formation (see cross section in Figure 5). The Gutingkeng thick sedimentary layer is continuing offshore, where evidence of mud-diapirism and mud-volcanoes have been found (S.-C. Chen et al., 2014; C.-S. Liu et al., 1997). Our observations clearly suggest an offshore prolongation of the Chungchou anticline deformation toward the SSW, which is structurally consistent with offshore seismic profiles and derived seismic map of the top of Pliocene formation. The possible connection between off-shore diapirism and on-land folding is still a subject of debate (e.g. A02 ; Lacombe et al., 2004; Ching et al., 2016).

As also suggested by the spatial match between interseismic deformation, long-term topographic features and Holocene deformation, one cannot exclude that part of the interseismic deformation in surface is not elastic and may contribute significantly to the deformation over several seismic cycles. Johnson K. (2018) following a work of Huang & Johnson (2016) investigates the growth of Fault-Cored Anticlines by coupled processes of fault slip and flexural slip folding by Boundary Element Modeling. He concludes that *"fault-cored anticlines may not grow strictly by the mechanism of fault slip, but that folds in a mechanically layered medium can be significantly amplified by buckling under horizontal compression with a significant portion of shortening being distributed through the fold»* and that despite *« there is a large body*

of research centered on estimating fault slip and or earthquake recurrence using kinematic models of folding and associated growth strata (e.g., Dolan & Avouac, 2007, and references therein) […] the buckling mechanism discussed in this paper is a significantly active mechanism in active fault-related folding, a potentially large component of fold growth might be attributed to buckling, in addition to slip on the underlying fault."

This clearly highlight the limitation of elastic model and purely kinematic model. I experimented the use of kinematic model during the Master internship of Corentin Abraham in 2019 using the trishear approach (Hardy & Allmendinger, 2011) using the Move software. The goal of the study was to compare incremental surface deformation of the kinematic model with deformation from elastic model using the same geometry inspired from the SW Taiwan (Figure 19). However, this was somehow quite frustrating as kinematic model required to set up several parameters in addition to the geometrical parameter, like the trishear angle and the propagation to slip ratio, which are not well constrained.

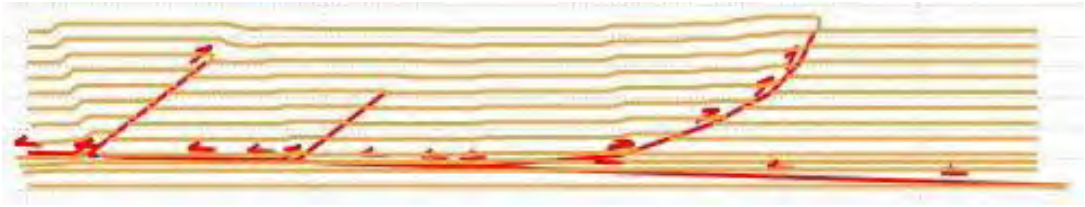

Figure 19 : one example of kinematics model done with the Move software during the master internship of Corentin Abraham in 2019.

I'm presently working in collaboration with Frédéric Donzé and a post-doc Yang Zhou on Discrete Element Method (using the open source code Yade (Šmilauer, 2015). The research project aims to answer, through numerical modelling, whether bulk visco-plastic deformation is a key ingredient or not to reproduce the spatial and temporal patterns of deformation observed by geodesy.

Regarding anelastic process of folding in a similar context of interseismic creep punctuated by transient creep event on a thrust fault, Copley & Jolivet (Copley & Jolivet, 2016) did an interesting study about the case of a triggered thrust by the 1998 Mw 6.6 Fandoqa, Iran, earthquake (Berberian et al., 2001; Fielding et al., 2004). They observe steady-state creep on the thrust, assumed to be driven by topographic gradient, accelerating following the nearby 1968 Fandoqa earthquake. They interpret it as slip governed by rate- and state-dependent friction law allowing non-linear relationship between shear stress and slip rate. The shallow creep, which in some place reaches the surface, and the lack of aftershocks suggest a mainly aseismic thrust with no stick-slip behavior. They investigate how and when in the earthquake cycle, folded beds observed in the field on top of the thrust are formed. They observed compatible deformation gradient only in interferograms covering the earthquake and the afterslip period. They cannot distinguish between elastic or permanent deformation and they cannot rule out continuous deformation at a rate slow enough to be below the InSAR detection threshold during interseismic period. However, they rather suggest that the folding happens during the relatively rapid deformation following nearby earthquakes that impose stress on the fold belt.

If such interpretation is invoked in other recent studies (Simon Daout et al., 2018, 2019), the larger interseismic deformation signal seen in SW Taiwan at the Lungchuan fault suggests that the contribution of the interseismic creep is certainly significant. In both case-studies the mechanism leading to permanent fold deformation, like by pressure solution, diffusion or other

processes (e.g. Gratier, Dysthe, et al., 2013; Bürgmann, 2018) remains uncertain and deserves further investigation.

To conclude this section, I am convinced the SW Taiwan is a pertinent place to study several aspects of aseismic deformation related to the earthquake cycle and long-term deformation. The high strain rate occurring on-land is favorable to good quality geodetic observation supported by a quite dense campaign and permanent GPS network, and regular levelling. The particular geological setting of SW Taiwan favors aseismic creep in the sedimentary cover. In addition, the frequent significant M>6 earthquakes at 15-20 km depth represent a quite unique opportunity to understand how aseismic creep process reacts the stress changes. The richness of observed transient deformations caused by different sources of perturbation makes SW Taiwan a natural laboratory, from which we can learn about this wide range of behavior. This has interests that go beyond the context of a thrust-and-fold belt.

7 – InSAR evolutions: data, method and processing

I did my first interferogram in 1999, about 20 years ago, using data from ERS-1 satellite that was primarily designed to observe ocean. Data were available on compact exabyte tapes, which were taking months to be obtained from ESA and were given in limited amount (typically a few tens of dates). The processing of a 100 km by 100 km interferogram using the relatively robust but not open-source CNES Diapason software on a desktop workstation were taking about one day. However sometimes it may require specific adjustment depending of the local station of reception receiving data from satellite. According to Didier Massonnet, this was already a significant improvement from his pioneering processing from the beginning of the 1990's which was requiring old-fashion magnetic tapes, days of processing on very expensive processing facilities at the CNES using code developed from scratch. Surprisingly, despite his successes, he also reports to me he was struggling to get very limited amount of data from ESA at that time.

Now a day we are dealing with time series of few hundreds of Sentinel-1 SAR images which requires a thousand of interferograms to be processed. The Sentinel-1 mission has dedicated instrument and strategy to monitor surface displacements and benefits from a long-term commitment of EU. Data are freely available in a standardized format and can be downloaded on-line within hours after acquisitions. Processing is typically done on high-performance computing facilities using distributed processing and partially automatized codes. Sentinel-1 acquisitions have shorter revisit times thanks to wide swath acquisition mode, which allow 250 km width by several hundreds of km long strip to be processed at a global scale.

The time-lines of SAR missions in Figure 1 discussed in introduction, show the non-linear evolution of SAR mission operating at different wavelengths. During my career I have favored data and methods that allow me to cover large tectonic areas and that can be applied everywhere in natural environment (e.g. see section II-5). That explained why I did not used the high resolution X-band missions, as reflected by Appendix 3 that gives a list of my studied area and which Satellite data I used (ERS, ENVISAT, RADARSAT, ALOS-1, ALOS-2, SENTINEL-1).

I had experience with various processing codes:

- DIAPASON from CNES, not open source, but initially freely available to French scientist, before a fixed yearly cost was introduced after the code was maintained by a private company Altamira.
- Commercial software: GAMMA and its PS processing module IPTA, and ENVI SARSCAPE (used to processed ScanSAR Envisat data),
- Open source software: ROIPAC and ISCE from NASA-JPL, DORIS from Delft University as preprocessing for StaMPS from A. Hooper, NSBAS, GMTSAR for processing ALOS-2 ScanSAR, and SNAP from ESA.

I mainly used ROIPAC that had the big advantage to be open-source and on which the NSBAS processing chain was developed by several French scientists leaded by Marie-Pierre Doin. The fact that in the 2000 is the CNES kept its DIAPASON code closed and delegates its development to a private company ALTAMIRA was retrospectively a bad move, as almost all the French scientists move toward alternative solutions. Ironically, about 30 years after the code start to be developed, and after that the ALTAMIRA company has fused with another Italian company TRE (both being bought by CLS, a subsidiary company of CNES!), CNES recently decided to put some part of the code open-source in the Orpheo Tool Box (OTB).

Since the initial « 3-pass » approach to get differential interferogram (Gabriel et al., 1989), a lot of progress have been made in term of InSAR processing. The introduction of the 2-pass approach using an external DEM was a main move in the 1990's. As mentioned in introduction, the early 2000's was marked by the new era of time series analysis with Permanent Scatterers approach and small baseline approach and hybrid methods (e.g. Hooper, 2008), continuing in the 2010's (e.g. Ferretti et al., 2011; Iglesias et al., 2015). The NSBAS method, based on ROI_pac modules (Rosen et al., 2004), is a constrained SBAS version in which time series can be reconstructed from disconnected subsets of interferograms using some constraints as described in Doin et al (P04). Note that there variants of the NSBAS time-series algorithm to get time-series from the network of interferograms (Cavalié et al., 2007; López-Quiroz et al., 2009; Jolivet et al., 2012, 2013), depending on the method used to temporally connect the data (linear or quadratic function, Laplacian smoothing or Gaussian filtering) and also depending of the use of additional constrain in the inversion (for instance estimation of DEM error depending on the perpendicular baseline). NSBAS has since incorporated other developments. Major ones are the capacity to process Sentinel-1 data in TOPS mode (Raphael Grandin, 2015), additional corrections before unwrapping with closure through the interferometric network and improvement of atmospheric corrections (M.-P. Doin et al., 2015).

The importance of atmospheric correction has increased with time along with the increase of interferogram surface coverage, which revealed the complexity of atmospheric patterns in INSAR signal. This led to various atmospheric correction methods (e.g. Bekaert, Walters, et al., 2015). More systematic integration of GPS tropospheric delay in those correction are underway (C. Yu et al., 2018). A focus is now on ionospheric corrections critical in L-Band data but also sometimes in C-Band (Gomba et al., 2016, 2017; Gomba, 2018). The in-built ionospheric correction design of the future NiSAR mission seems promising with that respect (Kellogg et al., 2020). In addition, ocean tides (DiCaprio & Simons, 2008; C. Yu et al., 2020) and solid tides (Xu & Sandwell, 2020) corrections, which has been used for a long-time in GPS processing, start to be integrated in INSAR processing.

Two other trends in INSAR processing that appear in the recent years are the development of generic toolboxes and the development of services to save the user the burden of the heavily demanding computation of large amount of data especially for Sentinel-1.

Generic toolboxes target specific tasks, like atmospheric correction, time-series analysis or other post-processing tools, that could be interfaced with existing processing chains, in line with the very successful Matlab StaMPS package to do Permanent Scatterers analysis (https://github.com/dbekaert/stamps, Hooper 2012). Some examples of such toolboxes are:

- GIAnT, Generic InSAR Analysis Toolbox (http://earthdef.caltech.edu/projects/giant/wiki ; Agram et al., 2013)¶
- TRAIN, Toolbox for Reducing Atmospheric InSAR Noise (https://github.com/dbekaert/TRAIN ; Bekaert, Walters, et al., 2015)
- GACOS, Generic Atmospheric Correction Online Service for InSAR, http://ceg-research.ncl.ac.uk/v2/gacos/ (C. Yu et al., 2018)
- LICSBAS (Morishita et al., 2020)
- OTB, Orpheo Tool Boxes (https://www.orfeo-toolbox.org) and SNAP S1TBX toolboxes (https://step.esa.int/main/toolboxes/snap).

Examples of on-line and/or on-demand services are:

- LICS from COMET: a freely available on-line catalogue of systematically and automatically processed interferograms on tectonic and volcanic areas around the world (https://comet.nerc.ac.uk/comet-lics-portal/) which also provide a soft package LICSBAS to post-process the data (Morishita 2020) and is interfaced with GACOS.
- The Geohazard Platform of ESA (https://geohazards-tep.eu), which provides INSAR commercial services like TRE-Altamira, but also the P-SBAS Sentinel-1 processing on-demand by CNR-IREA (Casu 2014, De Luca 2015, Manunta 2019).
- FLATSIM (ForM@Ter LArge-scale multi-Temporal Sentinel-1 Interferometry processing chain in Muscate) a starting on-demand service provided by CNES for large-scale processing of InSAR, but for the moment limited to French Scientists in response to a call-for-idea (https://www.poleterresolide.fr/projets/en-cours/flatsim ; C78)

However, so far there is not widely accepted common international standard for data format exchange in INSAR, which would be useful to benefit fully from all those tools and services.

A last important issue that arise recently is the problem of systematic bias in estimating velocity in vegetated area when using algorithm based on spatial averaging and short-time interferograms, like most of the SBAS algorithms when using 6 or 12 days interval Sentinel-1 interferograms. This affect algorithm dealing with distributed scatterers but not method based on single scatterers like pure PS approach. We noticed that effect when using NSBAS on several case-studies for instance when processing data about Mexico-city subsidence for the MDIS 2017 workshop. It was also the case during the Master study of Thomas Gaubert in 2018 using Sentinel-1 to study the Southern Apennines, or during the Master study of Pedro Espin working on Equator (C75): In some vegetated area, the derived velocity where unexpectedly very large when using only short-time interferograms in the network.

De Zan et al (2015, 2018, 2019), show that this effect in coming phase-closure inconsistency introduced by spatial averaging (multi-looking) when several independent scattering mechanisms are present. They show that velocity bias can come for instance from soil moisture or vegetation water content variations when using short-time interferograms. This can be avoided using specific algorithms (Ansari et al., 2017, 2019), but this effect can be mitigated in SBAS approach by introducing long-term interferograms in the network (M. Doin, 2019). However, such a strategy has to be done carefully to avoid decorrelation of the signal. That is why this bias was not affecting significantly previous studies exploiting time-series based on 35-days or more interferograms of ENVISAT data, in which vegetated area were often not exploitable because completely decorrelated. This illustrates that an expert view on the processing is still needed, despite the increasing availability of free tools and more and more user friendly automatic InSAR processing.

Regarding my contribution to methodological evolutions in INSAR processing, it was most of the time motivated by scientific need. I did participate to the development of NSBAS through several projects (ANR EFIDIR, CNRS-AO Mastodons) and more recently in the framework of the national Solid-Earth pole (ForM@Ter) of the currently in development French research infrastructure DataTerra (https://www.data-terra.org/). Indeed, in most of the studies I worked on, there were necessity to develop new strategies or processing schemes. In the following, I describe some of those contributions about coregistration and atmospheric perturbation. I also describe methodological works I have done implying other techniques that are complementary to INSAR. To finish, I detail my involvement into national and European project to deal with massive processing and related research infrastructures.

SAR images coregistration enhancement for InSAR

Following the work I done on the coseismic deformation of the 2005 Pakistan earthquake using SAR images correlation (see section II-2, A06); I investigated the aliasing effect interferograms caused by the too high coseismic displacement gradient in near field. We find out that it is not the main reason of decorrelation in near field, suggesting that misregistration problem dominates. To mitigate the image coregistration problem in ROI_PAC, we proposed a method to improve interferogram (C15), which make use of a known displacements field (in this case the 3D displacements field from SAR images correlation). It is a 2 steps method (see Figure 20):

- Step 1: improving the coregistration model with respect to the standard polynomial approach (e.g. ROI_pac [Rosen et al. 2004] use a second order polynomial to coregister images). Here, coregistration is based on the sum of (1) geometrical offsets (modelled using a DEM and orbital data), (2) deformation offset (inferred from the known displacement field) and (3) translational offset.
- Step 2: following Yun et al. [2007], the displacement model is also used to facilitate the unwrapping process.

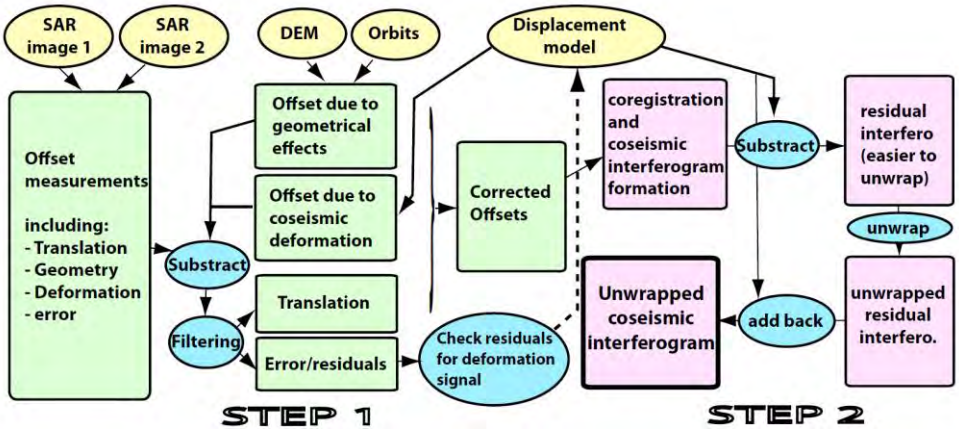

Figure 20 : workflow to improve SAR image coregistration for INSAR using a known displacement field model (From C15)

Marie-Pierre Doin has implemented the step 1 into NSBAS when we were working on the 2008 Wenchuan earthquake.

Spatially variable empirical atmospheric corrections

Using meteorological models to perform atmospheric correction can be seen as an equivalent effort than introducing deterministic correction from Digital Elevation Model to remove topographic effect (2-pass interferometry). First attempts (Wadge et al., 2002; Foster et al., 2006; Puysségur et al., 2007) relying on local assimilation scheme of metrological model were not applicable everywhere, pushing for the use of regional or global meteorological models (M.-P. Doin et al., 2009; Jolivet et al., 2011). However, when I started working on the 2006 Slow Slip Event in Guerrero (see section II_4), I noticed that corrections based on the North American Regional Reanalysis (NARR) meteorological model sometimes degrade interferograms instead of improving them. On the other hand, at that time, empirical correction methods based on phase-topography correlation were assuming spatially homogeneous relationship between phase and

topography (e.g. Cavalié et al., 2008). However, in interferograms covering the Guerrero area (100 x 400 km), we observe that the phase-topography trend can be spatially highly variable with changing sign and sometime over distance less than 60 km. Comparison with the phase-topography relationship estimated from NARR confirm this variability. To take into account this effect, I proposed a spatially variable correction of each interferogram based on empirical computation of the phase-topography correlation over 32km x 32km window (C20). An improved method has been implemented by Marie-Pierre Doin in NSBAS (P04).

Using GPS data for tropospheric and ionospheric corrections

I also participate to some work to implement existing methods using GPS measurements to estimate tropospheric ionospheric delay in INSAR measurements. In 2010, Gregory Clouvel during his Master internship, used GPS Zenithal Tropospheric Delay to estimate InSAR tropospheric delay on North Eastern Iran, based on previous published method (S. Williams et al., 1998; Li et al., 2006; Onn & Zebker, 2006). The same year Haythem Balti, also a Master student I supervised, did comparison of global meteorological model (NARR, ERA40) with GPS ZTD on the Guerrero area (Mexico). In 2011, Rana Charara (post-doc), implemented existing method to estimate ionospheric delay in interferogram from GPS measurement, and applied it to the case of Longitudinal Valley of Taiwan (C37).

Source Separations

In InSAR Time series, the surface deformation signal can be largely dominated by atmospheric signal, and the surface deformation signal itself can be composed of different source (inter-, co-, or post-seismic deformation, transient slow slip event, subsidence, landslide, etc.). During the PhD of Louise Maubant (2017-2020), we investigated two sources separation methods to extract slow slip event signal in the Guerrero area (A24). The first method is based on a functional parametrization of InSAR time-series as done in previous studies (e.g. Hetland et al., 2012; Simon Daout et al., 2019), such approach being directly inspired from GPS time-series analysis (Dong et al., 2002; Bevis & Brown, 2014). The second method is the Independent Component Analysis (ICA) (Comon, 1994; Hyvärinen & Oja, 1997), which has the advantage with respect to the previous one to be a blind source separation approach that do not require strong a priori knowledge of the sources. ICA had been already applied to analyze InSAR time series but on other contexts (Estelle Chaussard et al., 2017; Cohen-Waeber et al., 2018; Ebmeier, 2016).

Other methodological works

I mainly used InSAR to address my research interests. However, in many cases, InSAR alone is not enough and it has to be combined with other methods. I have not restricted myself to INSAR imagery and I have worked on other data and techniques. I already mentioned other kind of data or methods I used in combination with INSAR, like GPS, levelling, SAR images correlation, slip distribution inversion. I also describe in section II-2 the methodological work done on data fusion. Here I develop on other data and approaches I have been working with, in the framework of projects that were not directly related on my main research interest but that had useful feedbacks on it. Those projects are related to surface processes, subsidence, geomorphology, and change detection and classification methods. For instance, Landslides and subsidence are two examples of surface deformation signal that should be taken into account when investigating tectonics signal, either by masking those signals or by using them to get information on structural tectonics control (e.g. Bawden 2001).

Lidar and Digital Elevation Model

In 2007, shortly after my arrival in Grenoble, I was given the opportunity to participate to a Marie-Curie Research Training Network European Project « Mountain Risks ». The aims was to apply multi-techniques approach to active clayey landslides, with a case study in the Trièves area close to Grenoble, at 45 min drive from our lab. Another objective was to make the link between long-term deformation imprinted in the landscape and the present-day landslide activity showing a wide range of deformation rate from mm-cm slow moving landslide (Avignonet Landslide), to several meters (Harmalière Landslide). Such an approach combining photogrammetry, Lidar, GPS and InSAR seemed to me also relevant and transposable into some studies of the earthquake cycle. Furthermore, I found it interesting to have in the framework of methodological developments on measurement methods, a local site allowing easier ground-truth acquisition, field / image comparison and validation. This work was mainly done through Ulrich Kniess' PhD thesis, which I co-supervised.

A first part of this work was using morphological analysis of Lidar 1-m DEM, combined with GPS and historical aerial photos analysis of denudation. In combination with geophysical measurements (seismic ambient noise measurements, electrical prospecting) we were able to show paleo-topographical and lithological controls on the landslides activity (P02 ; A09 ; A17 ; Kniess, 2011). A second part was dedicated to multi-temporal LiDAR DEM analysis using image correlation techniques. Ulrich Kniess developed a correlation method to get 3D displacements from 1-m resolution DEMs acquired at different dates (Figure 21).

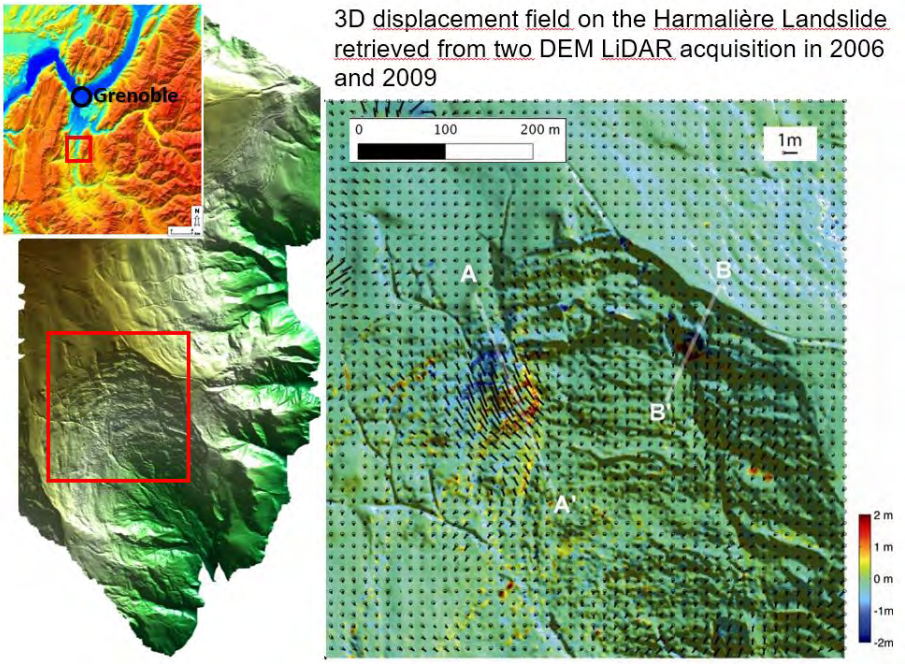

Figure 21 : Lidar-derived displacement field of the Harmalière landslide, located in the Trièves area, south of Grenoble (France). Color show vertical displacement, and Black lines horizontal displacements (from Kniess 2011)

Those measurements have been used subsequently in a study using image correlation of Sentinel-2 images for the detection of precursory motions before landslide failures (A22)

After this project, I had also opportunities to work on DEM analysis. In the last 20 years, High precision topography from Lidar has become a standard for geomorphological studies. During

the master internship of Johanne Ngouegne-Okouma in 2015, we perform a morphometric analysis of the drainage network along the Belledonne area using a 1-m Lidar DEM looking for possible indices of fault activity, without success.

I also did some work on the TanDEM-X 12-m resolution DEM, which is so far the best global DEM available to scientists. Unfortunately, the version available to scientists is not fully corrected and requires some post-processing to be exploitable. During the Master internship of Aicha Diomandé, we did an evaluation of the quality of the TanDEM-X DEM in Mexico in comparison with other DEM (INEGI, PRISM, SRTM, ASTER) and we developed a method for improving the TanDEM-X DEM for application to satellite radar interferometry. I also helped in handling the TanDEM-X DEM used by Léa Pousse for a paleoseismological study on the Bocono Fault in Venezuela, on which we did InSAR ALOS-1 interseismic measurement showing no shallow creep signal (A21).

Change detection using radar Amplitude.

In 2009, I had a try of applying change detection technique to detect rock falls in the surrounding mountains of Grenoble using times-series of ERS SAR amplitude images (Master internship of Jérémy Barnavol) but without success.

Relating basin subsidence rate and thickness of sediments

InSAR has been used for a long time to monitor subsidence phenomena (e.g. Carnec et al., 1996; Carnec & Fabriol, 1999; Galloway et al., 1998; Amelung et al., 1999; Fruneau & Sarti, 2000; Raucoules et al., 2003). The Mexico City case is one of the most striking case of rapid basin subsidence related to compaction of young sediment. Through time it has become a benchmark case for InSAR studies (e.g. Strozzi & Wegmüller, 1999; Strozzi et al., 2003; Cabral-Cano et al., 2008; López-Quiroz et al., 2009; Osmanoğlu et al., 2011; Yan et al., 2012; Estelle Chaussard et al., 2014).

In such cases, one can expect some correlation between the subsidence rate and the thickness of bassin sediment, which is a critical parameter for seismic amplification effect in bassin. That was the purpose of Sylvain Michel Master internship in 2009, who investigate whether subsidence rate may serve as proxy for seismic site effects, based on the Grenoble basin case.

By comparing subsidence rate inferred from INSAR and levelling with bedrock thickness (constrain by borehole and gravity measured) and resonance period inferred from H/V seismic ambient, we were showing that InSAR can be a useful proxy applicable at city scale to give a first-order approximation of resonance period and site-effect. This can help to guided geophysical survey in the field (Figure 22, C23, C24). We also applied a similar approach on the Beirut city (Lebanon) during the Master Internship of Clement Roussel in 2014.

Grenoble and Beirut basin subsidence are about a few mm/year, compared to rate up to 30 cm/year in Mexico City. Such a rapid rate seems to be associated to temporal changes in the seismic response of the basin (Avilés & Pérez-Rocha, 2010), leading some authors to propose to use InSAR to monitor such changes (Albano et al., 2016).

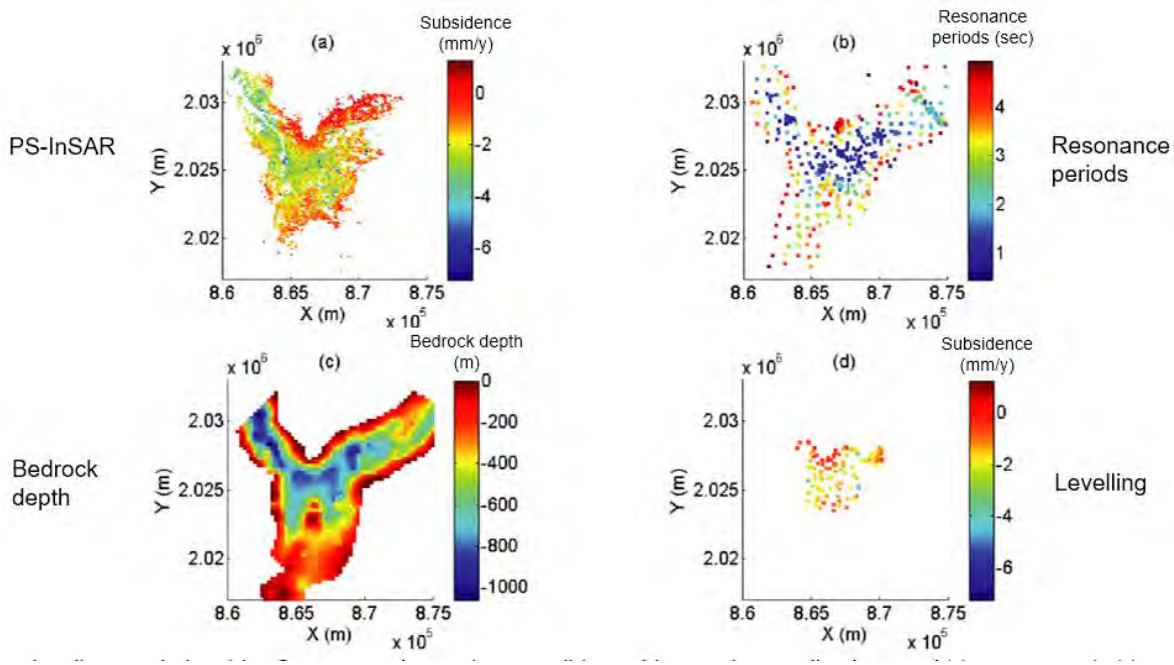

Figure 22 : Comparison of subsidence rate derived from InSAR (Top Left) and levelling (Bottom Right) over the Grenoble area, with thickness of sediment (Bedrock depth Bottom Left) and Resonance periods from H/V ambient noise seismic measurement (from C24).

Supervised learning techniques

I discovered supervised learning techniques in 2011 during Panagiota Matsuka's PhD Thesis. This PhD project was in the framework of the ANR project URBASIS led by Philippe Gueguen. One of the goals of the PhD was to investigate the possibility to use high-resolution remote sensing imagery in combination to in-situ data to have a first-order assessment of the building seismic vulnerability at the scale of a city like Grenoble or Nice. The idea was to derive different metrics of building (like elevation, roof shape) using High resolution DEM and satellite or aerial optical imagery and to related them to seismic vulnerability using in-situ information about building (like number of storage, material of construction, date of construction etc.) that are first-order indicator of seismic vulnerability. The relationship was established using supervised estimation scheme based on support vector machine (SVM). SVM are a generalization of linear classifiers that can be used as classification method for multi-variate data. The preliminary results were promising (P05), but Panagiota left prematurely his PhD. Nonetheless, this approach has been then developed in the thesis of Ismaël Riedel resulting in a journal article (A15). It was an interesting experience for me that introduces me to the domain of Machine Learning and Data mining, which nowadays, are usually included in the broad field of artificial intelligence.

Massive InSAR processing and research Infrastructures.

The beginning of the 2010's has been a transition period for InSAR marked by the end of ENVISAT and ALOS-1 time-series acquisitions for InSAR and the prospect for the ambitious Sentinel program from the UE, that will really start in 2014 with the launch of the Sentinel-1A radar satellite. The Italian Space Agency had encountering problem to deal with the large amount of data generated by the CosmoSkymed satellite constellation started in 2017. The experience of

processing the 10-years long ENVISAT time-series over increasingly larger areas and the perspective of a massive data volume increase from Sentinel-1 data due to more systematic and more frequent acquisitions (35 days to 6 days), rise the need to develop new ways to handle and process InSAR data. The new usual unit of data volume will be the Terabyte. This was concomitant with the broad diffusion of the « Big Data » issue across scientific disciplines. The finding was that the multi-temporal INSAR processing could no longer be done by an individual researcher on his own computer nor even at the level of a lab for ambitious projects. Due to larger data stream when dealing with large geographical areas area, even solutions on the scale of a meso-computing center at University level could have failed. Thus, actions had to be done at national and European level to ensure sustainable access to equipment that meets the scientific challenges of the future.

With other members of my research team and in particular Marie-Pierre Doin and Cecile Lasserre, we have therefore dedicated part of our time in this direction to establish and strengthen our contacts at the national and European levels, with a view to federating the national community and being present in computing infrastructure projects for the massive processing of satellite data.

Actions done at national Level

At national level, we got a project in 2013 at the CNRS call « Défi Mastodons - Les Big Data en recherche » with the aim to optimize and adapt our ground deformation measurement tools to the processing of large volumes of data. This consist in making processing chains more automatic, in implementing of calculation to distributed environment on meso-center and in responding to the challenge of storing and distribute the data (C50). At the same time, the CNES was pushing for the creation of a national Pole in Solid Earth (ForM@Ter, Formes et Mouvements de la Terre) to federate effort dealing with satellite data for scientific use, which was supported by CNRS INSU. This was then a straightforward direction for us, and we get fully involved in it from 2012. Since ForM@Ter is part of the French Research Infrastructure DataTerra (https://www.data-terra.org).

To federate the national community we also initiated in 2013 in Autrans near Grenoble, the biannual meeting MDIS (Mesure de la Déformation par Imagerie Satellite / Deformation measurement by space imagery), whose last edition was held in 2019 in Strasbourg.

In addition to ForM@Ter, the CNES' PEPS initiative to provide a computing center backed by a data center on the Sentinel-1 satellite offered complementary perspectives to possible solutions at European level. In practice, the participation of the different members of the team in the ForM@Ter and PEPS meetings made it possible for the NSBAS processing chain developed in the team to be selected as a prototype in the framework of a project piloted by ForM@Ter and funded by the French « Programme d'Investissement d'Avenir » (PIA/Etalab). The Project started in 2015 and resulted in a prototype of an on-demand service to compute interferogram. In its design, the service is implemented in a distributed way: a web graphical interface operated by IPGP (Paris) manages users and product selection from PEPS (Toulouse). It then requests web services operated in Grenoble. These web services drive the calculations on the computing centers (at Grenoble in the framework of this proof of concept).

We have been also involved in another project to develop another kind of service for French scientist called FLATSIM for « ForM@Ter LArge-scale multi-Temporal Sentinel-1 Interferometry

processing chain in MUSCATE » (C78). The project is also led by ForM@Ter Solid Earth cluster in collaboration with CNES. It proposes to French researchers a systematic processing of Sentinel-1 data. INSAR Processing are performed on pre-defined zones determined by the scientific community. The processing is carried out by the NSBAS processing chain, which has been implemented on the CNES HPC facilities and result available through a data portal.

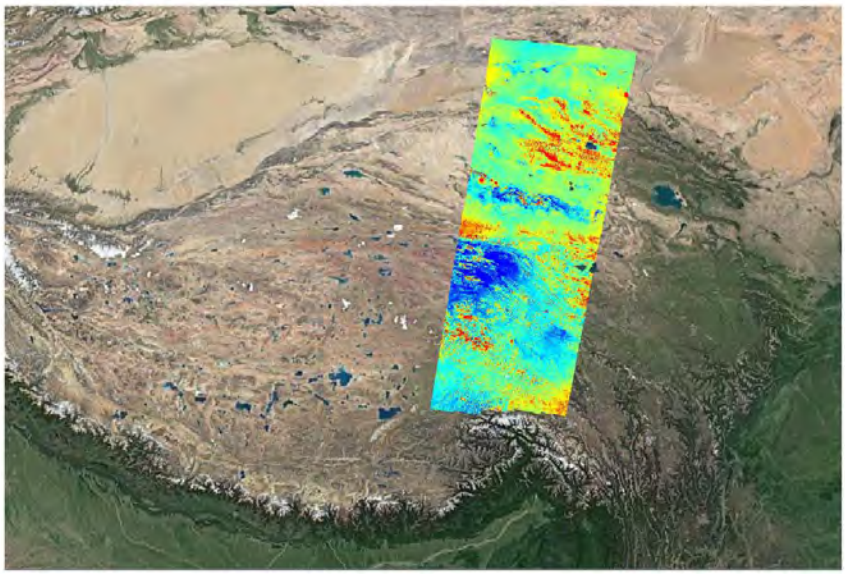

Figure 23 : First results from automatic processing of INSAR at large scale for FLATSIM project processed on CNES HPC. The area cover the Western part of Tibet (China).

After preliminary tests validated on Tibet (Figure 23), this project was concretized in 2020 by the first FLATSIM call for tenders (https://www.poleterresolide.fr/appel-a-idees-de-formter-pour-un-service-dedie-a-linterferometrie-radar/).

Actions done at international Level

At European level, we have been involved in EPOS (European Plate Observatory System, www.epos-eu.org) that is a large European project aiming to federate and integrate Solid Earth research infrastructures and to provide access both to data and to services and equipment. It was therefore important that our needs could be expressed in this project.

After a 4-year preparatory phase that started in November 2010, EPOS responded in January 2015 to the European call for tender infradev-3-2015 aimed at developing new excellent research infrastructures. The French seismological and GPS community was very involved in this response, especially at ISTerre, as it was present from the very beginning of EPOS and already well federated at the national level thanks to the RESIF project. On the other hand, from the point of view of users of optical or radar satellite imagery for the study of the Solid Earth, the community grouped in the young ForM@Ter structure was much less mature. Nevertheless, it was decided to propose a French response on this aspect. I participated in autumn 2014 in the elaboration of this response which was coordinated by Mioara Mandea on behalf of CNRS in workpackage 12 (Satellite Data). This workpackage is dedicated to the implementation of Earth Observation satellite services, transversal to the large community covered by EPOS for the study of physical processes controlling earthquakes, volcanic eruptions and tectonic forcing. Among other

contributions like LICSAR from UK, or P-SBAS from Italy, the French contribution is made through the proposal of the GDM (Ground Deformation Monitoring) service, which aims to provide the European community with an integrated Optical and Radar service for the measurement of ground displacements. The GDM-SAR part is largely based on the prototype developed by ForM@Ter at national level (see above, C73, C74). The implementation phase of the EPOS project run from October 2015 to October 2019 and Since October 2018, the European Commission granted the legal status of European Research Infrastructure Consortium (ERIC) to EPOS. In 2021 the first Thematic Core Services, including GDM-SAR should start to operate.

At the international level, I have also been involved in the European Space Agency (ESA) Geohazard Exploitation Platform (GEP, https://geohazards-tep.eu) project, as well as in the Seismic hazards Pilot of the Committee on Earth Observation Satellites (CEOS, http://ceos.org/ourwork/workinggroups/disasters/earthquakes), which is an international grouping of about fifty space agencies whose objective is to coordinate the various Earth observation programs and facilitate data sharing.

GEP comes originally from the Supersites Exploitation Platform, which was specialized for the exploitation of Satellite data resources in the context of the Geohazard Supersites & Natural Laboratories. It has expended into a storage and computing platform developed by ESA to support a wide use of satellite data for natural hazards related to earthquakes, volcanoes and landslides. It is an ESA contribution to a broader Seismic and Volcano Pilots initiative led by CEOS to improve hazard and risk management of these natural phenomena. GEP and the Seismic Hazards Pilot are two feasibility demonstration projects that could be extended to other themes if successful. In practice, our InSAR group have been involved in GEP since 2015 to try to implement a version of our NSBAS processing chain. However, the design of the platform turns out to be less adapted to NSBAS than implementation on HPC center like in CNES. Consequently, in 2019 we decided to stop our effort to implement NSBAS on GEP in order to focus our working force on other priorities. Nonetheless, GEP will be used to store the metadata catalogue of validated results generated by GDM SAR in the framework of the EPOS project, and to provide the EPOS user interface toward satellite data.

To conclude this section II-7, I would said that those problematics might look very far from my research interest. Indeed my involvement in those projects was the result of the feeling of being at the foot of the wall. It was a necessary move to maintain academic competence at the national level in a field where there are large international players like DLR in Germany, COMET in UK, CNR-IREA in Italy or JPL-NASA in US.

The example of the discovery of possible bias problem in velocity maps from the SBAS approach using Sentinel-1 data mentioned above, illustrates the importance of being able to maintain a strong processing expertise but also to have the associated processing infrastructure in order to be able to react quickly to modify processing strategies without depending on others. Having several independent academic analysis centers based on open-source software at the international level also allows verifying the reliability and reproducibility of the results, which is a fundamental corner of open-science.

III – Research Prospective

In this last part, I present what will be the main directions of my research activities in the following years and how these research topics stand in relation to my past activities and the current research stream.

In part II, aseismic processes have been somehow artificially divided in different sections (afterslip, deep creep during interseismic deformation, slow slip events in subduction zone, creeping fault at shallow depth …). Nonetheless, they are clearly common processes and share common remaining broad scientific questions: what are the physical parameters that control the space and time variability of aseismic slip on fault, and how can we get reliable values of those parameters from geological, geochemical, geophysical or geodetic observations?

We have seen in section II-5 that rate- and state-dependent friction laws achieved at the end of the 1990's provided an elegant and powerful framework to study aseismic slip on fault (e.g. Scholz, 1998). Fault models based on such laws are capable of producing a great wealth of behaviors, supported by various observations. However, we saw that some of the parameters were lacking physical interpretation and other, like the effective normal stress, were open to a lot of interpretations as it depends on several variables (temperature, fluid pore pressure, state of stress, fault geometry, etc.).

Since, numerical models of earthquake cycle have evolved toward more physically-based models, including radiation of seismic waves (e.g. Rice et al., 2001; Lapusta & Liu, 2009; Barbot et al., 2012; Barbot, 2019b). For instance, thermal pressurization of pore fluid due to shear heating has been proposed to explain both shallow creep and coseismic slip near the trench of subduction zone (Noda & Lapusta, 2013; Cubas et al., 2015). Recently, micromechanical models of rate and state friction have also been proposed investigating the physics of contacts (Perfettini & Molinari, 2017; Molinari & Perfettini, 2017, 2019; Barbot, 2019a). See Barbot (2019a) for additional references.

Based on work showing that afterslip can be the driving factor in aftershock sequences (Perfettini & Avouac, 2004a; Perfettini et al., 2005) and can explain aftershock migration (Perfettini et al., 2018, 2019), Frank et al. (2017) use aftershocks seismicity to derive constraints about the frictional properties and loading conditions of active faults. However, it is still difficult to find direct observable that can constrain rate and state model parameters. Repeating earthquakes or locked asperities coexist with aseismic creep or slow slip event at similar depth, but it is difficult to know whether it is due to local geometrical or lithological complexity. Based on off-shore drilling and seismic reflection images of the Hikurangi subduction zone (New Zealand), Barnes et al. (2020) show that the plate interface can be quite heterogeneous in terms of lithology and associated with geometrical complexity like subducted seamounts.

We have seen in section II-5 that on-land fault geology can give more detailed investigations on deformation processes (e.g. M. Y. Thomas, Avouac, Gratier, et al., 2014; Kaduri et al., 2017; Bürgmann, 2018). However, such studies are still limited to a few places, and it is difficult to decipher what are the present-day slip processes from observation of gouges deformation and mineralogical changes that cumulated over geological time. For instance knowing from fault samples whether a fault had seismic event or only slow creep is not an obvious task in earthquake geology (e.g. Rowe and Griffith 2015). In his recipe for fault creep, Bürgmann (2018) highlights

the role of fluids to promote slow slip, but it is again a parameter difficult to observe in-situ. Research have focused on area were aseismic slip occurs, but if it is a universal process, we also have to understand where it does not occur at similar depth and temperature and lithological conditions. Is it due to limitation of our observation capabilities? In any case, we still have to understand what is controlling the intensity of aseismic slip phenomena

The question of the persistence through time of aseismic creep behavior is another big issue. At the scale of the earthquake cycle, fault models based on rate and state friction do not preclude seismic rupture penetrating into velocity-strengthening area in the stable domain (Scholz, 1998). Cubas et al. (2015) propose that thermal pressurization favor this phenomena at shallow depth. This can allow the rupture to jump from one asperities to another to form large earthquake sequences. However, if the velocity-strengthening area is large enough, it tends to stop the rupture. There are evidences that areas in conditionally stable domain prone to slow slip events impede earthquake and promote afterslip (e.g. Rolandone et al., 2018). So at the time-scale of several earthquake cycles, if friction is mainly controlled by structural and lithological factors, one may expect in large places dominated by one slip mode, a long-term influence of this slip behavior.

Considering the case of large area with interseismic creep in subduction zone, such long-term influence have been suggested by several studies proposing that a small part of the interseismic deformation is not restored during megathrust earthquakes and can be converted into plastic deformation. For instance, Mazzotti et al (2000, 2001) suggested such a process for Nankai and Central Japan. However, they did not exclude that short-term transients, like slow slip events discovered after their study, might change their conclusion. More recent studies also favor a long-term effect of persistent slip behavior on subduction (e.g. Rousset, Lasserre, et al., 2016; Saillard et al., 2017; Jolivet et al., 2020). Along the South American active margin, Saillard et al. (2017) show a correlation between interseismic coupling and fore-arc long-term features (100 Kyr) that are interpreted as resulting from anelastic deformation. Jolivet et al. (2020) also report such correlation in Northern Chile and propose that about 4-8% of the vertical interseismic uplift convert over multiple earthquake cycles into permanent anelastic deformation of the fore-arc. However, as shown by Menant et al. (2020) such a relation may be perturbed by other long term processes. They show that lateral variation of uplift and subsidence pattern at 100 Kyr along the subduction may be reflecting different stages of longer-term (Myr) cycles of underplating process. In addition post-seismic visco-elastic processes at lithospheric scale are also changing the interpretation of geodetic measurement as only due to slip on faults (e.g. Trubienko et al., 2013).

To address those questions, a big trend of the last 15 years has been the increasing cooperation between geodesy and seismology. I already present in section II-4 how recent studies are using seismology as an indicator of slow slip not detected by geodesy in subduction zone and show intermittence of slow slip events (e.g. Frank et al., 2018; Gardonio et al., 2018). One can also mention works from Shelly et al. (Shelly, 2009; Shelly et al., 2009; 2011) inferring deep aseismic slip on the San Andreas Fault from tremor analysis, or studies using repeating earthquakes on the Longitudinal Valley Fault (K. H.-H. Chen et al., 2009; Y. Chen et al., 2020) following Nadeau et al (1999). It has also been suggested that passive ambient noise correlation technique can be used to monitor fluids (e.g. Chaves & Schwartz, 2016; Voisin et al., 2017), which is often invoked as a major parameters for fault creep behaviors (Bürgmann, 2018). Combining geodesy with seismology is clearly a direction to follow to progress an aseismic slip issues.

Another underlying trend is the increasing convergence toward aseismic off-fault deformation issues between communities that were quite distinct in the 2000's: scientist working on structural geology using kinematic approach and scientists using numerical modelling and geodesy applied to the earthquake cycle. This happens through the development of (1) mechanical models complementary to purely kinematical approach of fault-related folding (e.g. Kaj M. Johnson & Johnson, 2002; Hardy & Allmendinger, 2011), (2) modelling off-fault damage around fault zones (e.g. Manighetti et al., 2004; Kaneko & Fialko, 2011), (3) using satellite imagery and geodetic observation of off-fault deformations (Zinke et al., 2014; Milliner et al., 2016), and (4) explicit numerical modelling studies trying to describe volumic anelastic deformation in fault-related folds (Kaj M. Johnson, 2018; Barbot, 2018; Sathiakumar et al., 2020).

As I am neither a seismologist nor a modeler, nor a specialist in fault geology, what can be my contributions in the following years to answer the current scientific questions about the role of aseismic deformation in earthquake cycle and active tectonics? In recent years, I have tried to turn more into those disciplines so that I can better discuss with specialists in these fields. For example, I have an ongoing post-doc project on numerical modelling using the Discrete Element Method to study fault-related folding, and I am working with a seismologist Kate Chen on the joint use of seismology and geodesy to study aseismic deformation in Taiwan. Thus, my bottom line is still to continue to favor an observational approach to help answer these questions, but to combine it closely with other disciplines.

The projects detailed below respond to the need for observations in different geological contexts. There are starting projects but also more prospective ones which may be not all fully achieved but give my current view in my field of research. I favor case studies where geodetic observations can be combined with other methods such as seismology and/or long-term deformation measurements. This, as always, will require new ways of using spatial geodesy and pushing these methods to the limit of their capacity, requiring suitable tools and processing resources to match.

Interseismic deformation in an extensive tectonics settings: the Apennines case

This topic is part of the ANR-funded project EQTIME starting end of August 2020 aiming at « quantifying the temporal and spatial slip variability in the earthquake cycle spanning months to million years timescales ». The Apennines belt has been chosen as target because it meet several conditions needed for this ambitious objective

The 400 km long and 100 km wide Apennines belt shows an extension rate of 3-4 mm/yr (D'Agostino, 2014) accommodated by 10-30 km long normal faults. Those normal faults developing in carbonate landscape are favorable for paleoseismological studies going back up to 20 Kyr (Benedetti et al., 2013; Tesson & Benedetti, 2019) and for morphological studies up to 100 Kyr (Godard et al., 2016; F. Thomas et al., 2018). Furthermore, the historical and instrumental seismicity is well recorded and active enough to provide several recent examples of coseismic and postseismic displacements like during the 2016 Mw 5 to 6.5 earthquake sequence. Italy have on the densest seismic and geodetic monitoring network in Europe, and a lot of geological work regarding the Apennines fault system has already been published.

All of those points are needed to make the link between the present-day deformation and the long-term morphological build-up from successive earthquake cycles. In this project, I will be

involved in the study of interseismic deformation to better understand how the regional tectonic loading is accommodated by the network of segmented faults. GPS already gives the first order of the strain accumulation and vertical velocities from a continuous GPS network with baselines on the order of 10 km. As the normal fault system is much segmented, we want to use Sentinel-1 InSAR to improve the spatial resolution looking for localized deformation and possible transient deformations. However, this is challenging because of the low strain rates, and the presence of vegetation and snow. This is also challenging in term of source separation as GPS show that there is strong hydrological effect some of them related to Karstic charge and discharge cycle. Furthermore, it is sometime needed to discriminate between tectonic and gravity processes (e.g. Delorme et al., 2020).

Nonetheless, Apennines are interesting because it is an extensive tectonic regime that has been little studied for interseismic by InSAR outside magmatic/volcanic zones. Regarding aseismic deformation, there is few evidences of shallow creep except in Gran Sasso massif (Amoruso et al., 2002) and on the Alto Tiberina Fault (Chiaraluce et al., 2007; Hreinsdottir & Bennett, 2009; L. Anderlini et al., 2016; Vadacca et al., 2016). The carbonate environment is also interesting as it is prone to specific processes like pressure-dissolution for anelastic off-fault deformation (e.g. Croizé et al., 2013; Gratier, Dysthe, et al., 2013).

An additional interesting point of the project is to address the question of what we can learn from geodetic strain estimates in seismic hazard models. It is a rising topic, since the increasing availability of strain maps estimated from GPS and InSAR (e.g. Mazzotti et al., 2011, 2020; Mazzotti & Gueydan, 2018; Elliott, Walters, et al., 2016)

Lateral variation of coupling and slip budget on subduction zone

This project is in the continuity of the Louise Maubant's PhD thesis who performed Sentinel-1 InSAR time-series analysis combined with GPS data to study the 2017-2018 Slow slip events on the Mexican subduction zone (see also section II-4), and estimated an interseismic coupling map covering the Mexican subduction zone from Guerrero up to Jalisco.

From her results, that could be completed by ALOS-2 InSAR analysis, I would like with Mathilde Radiguet and Mohammed Chlieh to follow the way proposed by Avouac (2015) to address seismic hazard assessment issue. This approach consists in estimating the seismic and aseismic slip budget from geodetic measurement and earthquake catalogue. For that, the spatial distribution of interseismic coupling is used to constrain the return period of the maximum magnitude earthquake assuming that seismic and aseismic slip sum to the long-term slip given by plate convergence rate.

In parallel, I will start by the end of 2020 a project on the Makran subduction zone with Zahra Mousavi and an Iranian PhD student Meysam Amari with similar goals. The Makran subduction zone is very interesting as it shows a clear segmentation between western and eastern Makran, where large and shallow earthquake occurred like the 1945 Mw 8 earthquake. In contrast, the western Makran exhibits an almost absence of megathrust earthquake in both instrumental and historical periods. There, earthquakes rather occur within the down going plate at intermediate depths (Byrne et al., 1992). This raises the question whether the megathrust in the western Makran is capable of producing a very large earthquakes or alternatively is the place of aseismic creep and/or slow slip events.

Lin et al. (2015) from Envisat InSAR time series analysis have shown that eastern Makran subduction zone has high interseismic coupling. In the project, we would like to investigate using Sentinel-1 data the interseismic loading of the Western Makran subduction zone.

During those two projects, we will also look in geodetic data for potential regional transients, which may be present to explain possible earthquake interaction at long distance, not easily explained by coseismic static stress changes. Those interactions suggested from observation in other subduction zones (e.g. Bouchon et al., 2016) may explain the recent earthquake sequence observed in the Mexican subduction zones (Atzori et al., 2019), including also the June 2020 Mw 7.4 earthquake.

From a methodological point of view, InSAR processing of data from the L-band ALOS-2 satellite (2015-2020) is relevant and complementary to Sentinel-1 for the measurement of coseismic deformations. However, for the study of interseismic and SSE, it proved to be more difficult due to ionospheric disturbances (much larger than in C-band). The ionospheric phase delay can indeed be very important in L-band interferograms, up to several decimeters, whereas the tectonic signal is of the order of the centimeter. In order to exploit ALOS-2 data to its full potential, it will requires the implementation of ionospheric correction algorithms for ALOS-2 ScanSAR data (Gomba et al., 2017). Other kind of observations like gravimetric changes, or bottom-sea geodetic measurements would be interesting to complement our analysis, but are more difficult to obtain and to interpret.

Monitoring mud volcanoes as a window on aseismic creep in SW Taiwan

In section II-6, I explained why SW Taiwan is a pertinent place to studies several aspects of aseismic deformation related to the earthquake cycle and long-term deformation. However, we have seen that despite some efforts to find tremors or repeating earthquakes, the first 10-km of that area remain a « seismic desert » while having very high strain rate (up to 10^{-6} per year). In SW Taiwan, the coverage of the national broadband seismic network BATS (Broadband Array in Taiwan for Seismology) is not so good (http://bats.earth.sinica.edu.tw/Station). Temporary improvement of it may help to find seismic signal related to aseismic creep and transient slip events in the shallow sedimentary cover, where décollement and fault-related fold are developing.

In complement to that, I would like to set up a more original monitoring network of mud-volcanoes. There are tens of active mud volcanoes in SW Taiwan (Shih, 1967) (see pictures of two examples in Figure 24). Most of the studies about those mud volcanoes have focused on their geochemistry (Yang et al., 2004; You et al., 2004; Sun et al., 2010; Chao et al., 2011; C.-C. Liu et al., 2012; Chao et al., 2013). Those studies found that mud volcano fluids originate at depth where clay dehydration occurred. The up-to-5-km thick Pleistocene Gutingkeng mudstone formation is a good candidate for their source. It is also where is the décollement, on which thrust faults root (e.g. A20). Most of the time, the SW mud volcanoes are located on or near fault traces or anticline axis. Some authors have proposed that the spatial distribution of the mud volcanoes are related to extensional tectonic in releasing bend (Sung et al., 2010), however such releasing bend are not well documented and mud volcanoes are more pervasive than the area investigated by the authors. There is also report of coseismic eruption of mud volcanoes in the Coastal range of Taiwan (G.-J. Jiang et al., 2011). It has been interpreted as the result of local stress permutation. Yassir (2003) notes the worldwide close association of mud volcanoes and compressional tectonics setting, and shows that « shear stress applied to low permeability

sediments can produce a dramatic increase in pore pressure and cause sediment flow. Interestingly, his two field examples are Taiwan and Trinidad in Venezuela. In Trinidad, the central Range fault, which is one fault strand of the eastern continuation of the creeping El-pillar fault (A18), seems also to be creeping at shallow depth (J. Weber et al., 2020; J. C. Weber et al., 2001). I am actually currently helping François Jouanne to process ALOS-2 InSAR data on the Trinidad Island.

Figure 24 : Two example of mud volcanoes in SW Taiwan. Left: a dead mud Volcanoes, Right: an active one.

In any case, mud volcanoes in SW Taiwan show variable activity, with pulses of eruptions, and are typically associated with bubbling at the surface. The idea behind this project, which is at a very preparatory stage, is that activity of mud volcanoes may show some pulses signal that are not random and are related to fluid circulation on fault at depth. Those faults probably root on the décollement and mud volcanoes activity could then be correlated to aseismic creep on it. By simultaneously monitoring a network of mud volcanoes distant from several km to tens of km, one can search for possible correlation in activities that would indicates common sources at depth. Off course, possible rain and shallow hydrological effects should be also investigated and must be set apart. If mud-volcanoes signals are correlated to tremor or LFE activities at depth or to geodetic transients (Tsai et al., 2017), the network could provide a unique window on deep aseismic processes and related fluids circulation. The monitoring system would consist in continuously recording acoustic or seismic sensors located very close to mud volcanoes, complemented by more distant seismic stations. Separation of surface bubbling signal from other deeper families signal may be an interesting signal processing challenge that could be addressed unsupervised machine learning approach (e.g. Seydoux et al., 2020).

Note that there is also evidence of off-shore mud volcanoes in South-Western Taiwan (e.g. S.-C. Chen et al., 2010, 2014). As mentioned in section II-6, there is a structural continuity between offshore and on-shore geological features in SW Taiwan. From South to North those structure are at different stages of evolution of an accretionary prism being incorporated into a collision belt. Indeed on-shore observation of aseismic processes in SW Taiwan like proposed in this project, may give some clues on processes occurring at below-sea level subduction accretionary prisms.

Discriminating between volumic permanent deformation and elastic deformation

In section II-6, I introduced through the case of fault-related folds the issue of when and how the permanent deformation represented in geological structures formed in the shallow crust is acquired. Is it mainly during coseismic events or rather during interseismic or post-seismic period? I argued that SW Taiwan is a pertinent place to investigate if part of the interseismic deformation can be transformed from elastic recoverable deformation into permanent penetrative deformation. For instance, Jolivet et al. (2020) quantify that 4-8% of the interseismic deformation observed in the Northern Chile subduction zone is transferred into permanent deformation.

I see several ways to address this issue in SW Taiwan. The first one is through comparison of interseismic and coseismic deformation with respect to Holocene (10ky) deposits deformations that recorded several earthquake cycles. A preliminary work (C70, Figure 17) based on fluvial terraces analysis (M.-L. Hsieh & Knuepfer, 2001) has been done but should be extended to the other anticlines seen in Figure 16, with more dating. This could be done through collaboration with Maryline Le Béon or Martine Simoes who have recently worked there on dating deformed Holocene deposits.

Other approaches are related to the Pleistocene Gutingkeng formation made of mudstone and that seems to be correlated to the presence of high interseismic strain rate. For instance, there is a 500 m wide zone of Gutingkeng formation located in between the southern prolongation of the Lungchuan Fault (also called Chekualin Fault there) and the Chishan fault where up to 8cm/y of vertical displacement occurs within about 500 m. This area has been monitored by GPS because it is crossed by the highway number 3 with a bridge followed by a tunnel, both of them suffering progressive damages due to the aseismic high strain. InSAR analysis show that this phenomenon occurs along a several-km-long strip. The clayey and very easily erodable Gutingkeng formation may have a velocity strengthening behavior and at the same time accommodates penetrative deformation through inter-bed shearing. To test this hypotheses several aspects could be investigated:

- **Mineralogical and microstructural analysis**. Such analysis (M. Y. Thomas, Avouac, Gratier, et al., 2014; Kaduri et al., 2017) could be done on fault zone where outcrop are available, investigating what are the deformation processes and look for evidence of coseismic slip (Rowe & Griffith, 2015).
- **Comparison with long-term uplift.** The several cm/year of uplift do not produce significant topography in this area, but at the same time the Gutingkeng formation is having high erosion rate, catchment area including this formation record up to 3 cm/year of erosion rate (Dadson et al., 2003). Denudation rate derived from cosmogenic data (Siame et al., 2011) may help to compare long-term uplift to the present-day geodetic rate. Quantitative geomorphological approach as proposed by Godart et al (Godard et al., 2016) may be also of interest
- **Microseismicity related to volumic deformation.** The Gutingkeng formation is mainly made of clayey mudstone. However, there is also some brittle intercalated sandstone beds that can reach metric thickness. At the surface those beds are often heavily fractured and for the thinnest ones dislocated. If significant penetrative deformation occurs during the interseismic period, one may expect that the brittle failure of those beds produced a widespread off-fault microseismicity that could be recorded by local network if noise level is low enough.

Another angle of attack would be involving numerical modeling to test if we can discriminate from surface geodetic measurements between volumic permanent deformation and elastic deformation. For the case of flexural slip folding, Johnson (2018) investigates off-fault deformation based on a boundary element model consisting of viscoelastic layers in which inelasticity occurs at contacts (as frictional slip). He shows that if sedimentary layers act as a stack of mechanical layers with contact slip, off-fault deformation in the bulk of the fold can dramatically amplify the folding process and should produce a different spatial signature than when slip is only located on the fault. It also show that the characteristic relaxation time of the medium is an important parameter: fast relaxation time inhibits bulk flexural slip folding. Other modelling approaches have been proposed (Choi et al., 2013; Ta et al., 2015; e.g. Barbot, 2018; Sathiakumar et al., 2020) and may be worth to be tested.

Regional uplift in active orogens

This part is not a ready-to-go project and remains quite prospective. I just would like to emphasize that InSAR is now close to give valuable information of the regional uplift of active orogens. I showed at the end of section II-5 an InSAR velocity map from ALOS-1 data covering the whole Taiwan orogen. Although this map give the displacement only along one radar line-of-sight, which is not enough to separate the vertical and horizontal contributions, this limitation should be overcome by using data acquired by ascending and descending passes of ALOS-2 and Sentinel-1 satellites. At ISTerre, Marie-Pierre Doin with her student Pauline André are doing a similar work using Sentinel-1 to get a vertical uplift rate map covering the Western Alps. We can also expect to get some results on the Apennines during the EQTIME project. The order of magnitude of uplift and horizontal rates for those three case are the following:

- Taiwan : 1-2 cm/year regional uplift and 4-5 cm/year of shortening (K.-H. Chen et al., 2011; Ching et al., 2011)
- Western Alps : 2-3 mm/year of uplift with <0.3mm/year significant shortening across the whole range (Nocquet et al., 2016; Masson et al., 2019), but with some local extension in the center of the range (Walpersdorf et al., 2018)
- Apennines : 1-2mm /year regional uplift and 3-4 mm/year of extension (D'Agostino, 2014; Hammond & D'Agostino, 2019).

In those three cases, InSAR has the potential to increase considerably the spatial resolution of GPS measurements, which in return will be used to fix the long wavelength of InSAR signal. Such results should contribute to the debate about the physical processes driving the orogenic uplift. In the Western Alps for instance several candidates have been proposed like mantellic process, slab tear, gravitational energy, isostasy response to erosion or glacial isostatic adjustment (e.g. Vernant et al., 2013; Nocquet et al., 2016; Chéry et al., 2016; Mazzotti et al., 2020). Constraints about the <20-km spatial wavelength of the uplift signal may help to discriminate between some of those hypotheses.

Methodological developments in InSAR and associated processing issues

While InSAR best performances to measure relative displacement of the ground are achieved at short distances, data from recent sensors has the potential to achieve a precision of mm/year over distance up to 100 km for steady state displacement. However, turbulent tropospheric

signal and ionospheric perturbations remain major limitations for InSAR techniques especially when looking for transient tectonic signal covered by only a few dates of acquisitions. Unwrapping errors are another big issue in automatic processing.

Reaching the millimetric level is also meeting new problems that other methods like creepmeters or GPS have already faced. Bilham (2004) mentions problems related to rain and soil moisture for creepmeters installed in clayey sediments generating noise at the level of mm/year even with anchoring design. Thermal effects can also be important at this level of precision. With other sources of noise, monument stability problems also affect GPS measurement. Nonetheless, by combining carefully selected set of GPS stations, it is possible to go up to 0.2 mm/year precision on spatial scale of 100-200 km (Masson et al., 2019). Fiber-optic technologies (e.g. Zumberge & Wyatt, 1998; Coutant et al., 2015; Zhan, 2020) have also the potential to measure strain with high precision over such long distance.

InSAR measurement can rarely relies on well monumented reflectors and, in natural environment, phase measurement is sensible to snow, soil moisture and vegetation water-content (e.g. De Zan & Gomba, 2018; Gomba & De Zan, 2019). However, InSAR can benefit of its huge number of measurement points to improve its accuracy and to separate different sources of deformation, like discriminating near-surface processes (landslide, soil creep, permafrost, hydrological effects) from deeper tectonics processes.

To respond to the challenges posed by a study such as the one proposed on the Apennines in the ANR EQTIME (see above), several avenues are possible to get better estimate of interseismic velocity:

- Correction before unwrapping: in addition to the correction already implemented in NSBAS, correction of oceanic tide and earth tide already mentioned in section II-7 could also be taken into account as well as some ionospheric error correction.
- Unwrapping error: automatic detection and correction methods are already implemented in NSBAS, but we could also test new algorithm like CorPhU (Benoit et al., 2020). Upstream effort can also be done to reduce the number of fringes before unwrapping. An iterative method using corrections made after unwrapping may also be applied.
- Data flow processing: there is some work remaining in the NSBAS processing chain to process continuously on the fly the Sentinel-1 data flow (one date every 6 days).
- Multi-sensor analysis : the availability of several SAR satellites observing the same area offer great opportunities (e.g. Pepe & Calò, 2017) that are currently underexploited. Integration of multi-sensor data could be done during the processing chain and not just only as a post-processing step.
- Composite time-series: there is the possibility to reconstruct long-time series from several dataset overlapping in time or even with data gaps. This need to be able to revisit old dataset with new processing methods, which can improve past results (e.g. Pepe et al., 2011 for Radarsat-1 data) but implies to keep expertise on old data processing.

In a broader perspective, we could consider going further using other kinds of data. Using external data in InSAR processing has proven to be useful with DEM or meteorological weather model, especially when those data are globally available. New products from remote-sensing are now routinely processed at national or global scale and could be useful during InSAR processing. For instance, products from Theia (French data center for land surface https://www.theia-land.fr/en) are available like snow cover, land-cover classification or water body that could be

used. Their simplest usage could be to create mask on interferograms during the processing. One may also ambition more sophisticated usage with machine learning methods.

Automatic detection of phenomena is also a new problematic that emerged from systematic and massive data processing. Nice examples are coming from the volcano community who is investigating automatic detection of volcanic events from Sentinel-1 InSAR database (Anantrasirichai et al., 2019; Albino et al., 2020).

Similar approach could be applied to improve automatic earthquake analysis. In this case, seismology is usually used to detect events and provides a quick estimation of the earthquake location and focal mechanism or CMT (Centroid Moment Tensor). For the largest events, finite source models are computed and requests for coseismic interferogram processing can be done. Preliminary finite source models are often suffering from uncertainties about fault geometry or even from ambiguity about the focal plane. One can envision a machine learning approach allowing automatic feedback from coseismic interferogram (or optical or SAR correlation techniques) on the fault geometry and surface displacement to improve finite source modelling. This could be generalized to propagative or diffusive phenomena like afterslip and aftershock sequence.

However, all those methodological ideas are coming with a profusion of published algorithms and methods that are impossible to digest for a single Earth sciences oriented team like the one we have in ISTerre. Testing and implementing those methods and to make them working on large dataset require a higher level of organization. Just to be able to process our InSAR data at larger scale with existing processing chain requires us to be involved in national or European structures as already mentioned in section II-7. With the EPOS research infrastructure, the European Copernicus Ground Motion Service (https://land.copernicus.eu/user-corner/technical-library/european-ground-motion-service) and other actors including commercial ones, the year 2021 will be marked by the beginning of a new era of operational services for InSAR. Shall we use them as a black box or alternatively make significant efforts to keep some expertise and independence on our processing capability? It is a big issue. So far, our team have made the choice to do this effort at the national level with the support of the CNES. Despite limited human resources and fragile sources of funding, we hope that our involvement will be transformed into a sustainable and efficient organization.

IV – Conclusions

In 1999, I was running my first interferogram and 20 years later I am always happy to discover colorful new interferograms created from ugly raw complex radar images. Seeing Earth from space and measuring millimetric surface deformation from images captured at a distance of one thousand kilometers is still fascinating for me. My curiosity and interest in linking relief to active tectonic through satellite Earth observation remain intact. This was a primary motivation for me to enter the field of Earth sciences.

From a scientific point of view, my common thread has been the question of the role of aseismic deformation in the earthquake cycle and in the long-term deformation that accumulates in many cycles. My contributions to those topics have focused on various aspects, from which one can highlight slow slip events in subduction zone and aseismic slip of active faults. For instance, in the Mexican subduction we have been able to bring significant constraints on the spatial distribution of slow slip event on the subduction interface and thus better understand the interaction between earthquakes and slow earthquakes in the Guerrero seismic gap. Concerning the aseismic slip on active faults, work centered on sites in Taiwan and Venezuela, has shown the spatial variability of this phenomenon related to geometric and geological complexities, but also that creep transient, seismic and post-seismic slip can occurs in the same place. In the SW Taiwan case, localized high strain rate and low level of seismicity are motivating research on aseismic off-fault deformation.

Without changing its main course, several evolutions of my research have taken place during these years at ISTerre. A progressive evolution towards analyses of tectonic deformation over larger areas at a regional scale and with much denser time series has been related to the evolution of computing means and sensors. These last years have also been marked by my will to make more links between geodesy and seismology and by the initiation of numerical modelling work to tackle the problem of the relationship between short-term deformation as seen by geodesy and long-term geological deformation.

To address my research topics the InSAR/GPS couple was fundamental. Those very complementary methods should never be opposed to each other. Year after year, we have been discovering the wealth of microwave signals travelling from space to Earth, confronting us to troposphere, ionosphere, vegetation and soil humidity issue (and certainly other surprises to come). To be able to extract the tiny tectonics signal at the cm-mm level, one need to separate it from others sources of deformation like near-surface effects, landslide or hydrological signals.

Thus, in parallel to my topics related to the seismic cycle, I also conducted research on landslides and basin subsidence. This research was mainly motivated by methodological reasons. Most of the scientific questions I have tackled in my career have indeed been accompanied by the need for methodological developments, the resolution of which has occupied a significant part of my time: adaptation of InSAR processing to large study areas including adequate atmospheric corrections, merging data from different origins, change detection, source separation, etc. One of the main changes in my activity over the last six years has come from the mass of data produced by new satellite missions, which for Sentinel-1 is freely accessible as a continuous data flow. This has changed the way we work in Earth observation and led to the

need for the development of new automated processing and associated computing and storage facilities beyond those available to the individual researcher in most French research laboratories. I have therefore become involved in the issue of massive processing of InSAR data in the framework of the development of new research infrastructures (EPOS, DataTerra). This has undeniably broadened my horizon as considerations related to national and European research policies and strategies are added to technical or scientific constraints and must be taken into account.

All these activities were interesting but they cover a wide range of topics. The balance is difficult not to disperse too much while remaining open-mind because often innovation and advances come from where we do not expect them. In the third part of this document, I have drawn some research directions, but the paths leading to them are not all traced. Human encounters are fundamental there. For me, science must remain a human adventure with colleagues and students (all of them, even those who start from far away, but whom we have the satisfaction of helping and seeing progress) and it must not be done at any price.

Bibliography

Agram, P. S., Jolivet, R., Riel, B., Lin, Y. N., Simons, M., Hetland, E., Doin, M.-P., & Lasserre, C. (2013). New Radar Interferometric Time Series Analysis Toolbox Released. *Eos, Transactions American Geophysical Union*, *94*(7), 69–70. https://doi.org/10.1002/2013EO070001

Albano, M., Polcari, M., Bignami, C., Moro, M., Saroli, M., & Stramondo, S. (2016). An innovative procedure for monitoring the change in soil seismic response by InSAR data: application to the Mexico City subsidence. *International Journal of Applied Earth Observation and Geoinformation*, *53*, 146–158. https://doi.org/10.1016/j.jag.2016.08.011

Albino, F., Biggs, J., Yu, C., & Li, Z. (2020). Automated Methods for Detecting Volcanic Deformation Using Sentinel-1 InSAR Time Series Illustrated by the 2017–2018 Unrest at Agung, Indonesia. *Journal of Geophysical Research: Solid Earth*, *125*(2), e2019JB017908. https://doi.org/10.1029/2019JB017908

Allen, C. R., Wyss, M., Brune, J. N., Grantz, A., & Wallace, R. E. (1972). Displacements on the Imperial, Superstition Hills, and San Andreas faults triggered by the Borrego Mountain earthquake. In *The Borrego Mountain Earthquake of April 9, 1968* (Vol. 787, pp. 87–104). U.S. Geol. Survey. Prof. Papers. Retrieved from https://pubs.er.usgs.gov/publication/pp787

Allmendinger, R. W., Loveless, J. P., Pritchard, M. E., & Meade, B. (2009). From decades to epochs: Spanning the gap between geodesy and structural geology of active mountain belts. *Journal of Structural Geology*, *31*(11), 1409–1422. https://doi.org/10.1016/j.jsg.2009.08.008

Ambraseys, N. N. (1970). Some characteristic features of the Anatolian fault zone. *Tectonophysics*, *9*(2), 143–165. https://doi.org/10.1016/0040-1951(70)90014-4

Ambraseys, N. N., & Melville, C. P. (1982). *A History of Persian Earthquakes*. Cambridge Univ. Press, New York.

Amelung, F., & Bell, J. W. (2003). Interferometric synthetic aperture radar observations of the 1994 Double Spring Flat, Nevada, earthquake (M5.9): Main shock accompanied by triggered slip on a conjugate fault. *Journal of Geophysical Research: Solid Earth*, *108*(B9), ETG10-1–11. https://doi.org/10.1029/2002JB001953

Amelung, F., Galloway, D. L., Bell, J. W., Zebker, H. A., & Laczniak, R. J. (1999). Sensing the ups and downs of Las Vegas; InSAR reveals structural control of land subsidence and aquifer-system deformation. *Geology*, *27*(6), 483–486.

Amoruso, A., Crescentini, L., Morelli, A., & Scarpa, R. (2002). Slow rupture of an aseismic fault in a seismogenic region of Central Italy. *Geophysical Research Letters*, *29*(24), 72-1-72–4. https://doi.org/10.1029/2002GL016027

Anantrasirichai, N., Biggs, J., Albino, F., & Bull, D. (2019). A deep learning approach to detecting volcano deformation from satellite imagery using synthetic datasets. *Remote Sensing of Environment*, *230*, 111179. https://doi.org/10.1016/j.rse.2019.04.032

Anderlini, L., Serpelloni, E., & Belardinelli, M. E. (2016). Creep and locking of a low-angle normal fault: Insights from the Altotiberina fault in the Northern Apennines (Italy). *Geophysical Research Letters*, *43*(9), 4321–4329. https://doi.org/10.1002/2016GL068604

Anderlini, Letizia, Serpelloni, E., Tolomei, C., Martini, P. M. D., Pezzo, G., Gualandi, A., & Spada, G. (2020). New insights into active tectonics and seismogenic potential of the Italian Southern Alps from vertical geodetic velocities. *Solid Earth Discussions*, 1–27. https://doi.org/10.5194/se-2020-10

Angelier, J., Chu, H.-T., & Lee, J.-C. (1997). Shear concentration in a collision zone; kinematics of the Chihshang Fault as revealed by outcrop-scale quantification of active faulting, Longitudinal Valley, eastern Taiwan. *Tectonophysics*, *274*(1–3), 117–143.

Angelier, J., Chu, H.-T., Lee, J.-C., & Hu, J.-C. (2000). Active faulting and earthquake hazard: the case study of the Chihshang Fault, Taiwan. *Journal of Geodynamics*, *29*(3–5), 151–85.

Ansari, H., De Zan, F., & Bamler, R. (2017). Sequential Estimator: Toward Efficient InSAR Time Series Analysis. *IEEE Transactions on Geoscience and Remote Sensing*, *55*(10), 5637–5652. https://doi.org/10.1109/TGRS.2017.2711037

Ansari, H., De Zan, F., Gomba, G., & Bamler, R. (2019). EMI: Efficient Temporal Phase Estimation and its Impact on High-Precision InSAR Time Series Analysis. In *IGARSS 2019 - 2019 IEEE International Geoscience and Remote Sensing Symposium* (pp. 270–273). https://doi.org/10.1109/IGARSS.2019.8900409

Araki, E., Saffer, D. M., Kopf, A. J., Wallace, L. M., Kimura, T., Machida, Y., Ide, S., Davis, E., & Scientists, I. E. 365 shipboard. (2017). Recurring and triggered slow-slip events near the trench at the Nankai Trough subduction megathrust. *Science*, *356*(6343), 1157–1160. https://doi.org/10.1126/science.aan3120

Atzori, S., Antonioli, A., Tolomei, C., De Novellis, V., De Luca, C., & Monterroso, F. (2019). InSAR full-resolution analysis of the 2017–2018 M>6 earthquakes in Mexico. *Remote Sensing of Environment*, *234*, 111461. https://doi.org/10.1016/j.rse.2019.111461

Avilés, J., & Pérez-Rocha, L. E. (2010). Regional subsidence of Mexico City and its effects on seismic response. *Soil Dynamics and Earthquake Engineering*, *30*(10), 981–989. https://doi.org/10.1016/j.soildyn.2010.04.009

Avouac, J.-P. (2003). MOUNTAIN BUILDING, EROSION, AND THE SEISMIC CYCLE IN THE NEPAL HIMALAYA. In *Advances in Geophysics* (Vol. 46, pp. 1–80). Elsevier. https://doi.org/10.1016/S0065-2687(03)46001-9

Avouac, J.-P. (2015). From Geodetic Imaging of Seismic and Aseismic Fault Slip to Dynamic Modeling of the Seismic Cycle. *Annual Review of Earth and Planetary Sciences*, *43*(1), 233–271. https://doi.org/10.1146/annurev-earth-060614-105302

Avouac, J.-P., Ayoub, F., Leprince, S., Konca, O., & Helmberger, D. V. (2006). The 2005, Mw 7.6 Kashmir earthquake: sub-pixel correlation of ASTER images and seismic waveforms analysis. *Earth and Planetary Science Letters*, *249*(3–4), 514–528. https://doi.org/10.1016/j.epsl.2006.06.025

Avouac, J.-P., Meng, L., Wei, S., Wang, T., & Ampuero, J.-P. (2015). Lower edge of locked Main Himalayan Thrust unzipped by the 2015 Gorkha earthquake. *Nature Geoscience*, *8*(9), 708–711. https://doi.org/10.1038/ngeo2518

Aytun, A. (1982). Creep measurements in the Ismetpasa region of the North Anatolian fault zone. In *Progress in Earthquake Prediction Research, Multidisciplinary Approach to Earthquake Prediction edited by A.M. Isikara and A. Vogel* (pp. 279–292). Braunschweigl Wiesbaden, Federal Republic of Germany: Friedrich Vieweg,.

Bacques, G. (2013, November 19). *Étude de variations spatio-temporelles de glissements asismiques le long de failles majeures par Interférométrie RADAR Différentielle satellitaire : Cas du séisme lent de 2009-2010 de Guerrero (Mexique) : Cas de la déformation postsismique suite au séisme de Parkfield (2004, Mw6, Californie)* (PhD thesis). Université de Grenoble, Grenoble, France. Retrieved from https://tel.archives-ouvertes.fr/tel-01124228

Bacques, G., de Michele, M., Raucoules, D., Aochi, H., & Rolandone, F. (2018). Shallow deformation of the San Andreas fault 5 years following the 2004 Parkfield earthquake (Mw6) combining ERS2 and Envisat InSAR. *Scientific Reports*, *8*(1), 6032. https://doi.org/10.1038/s41598-018-24447-3

Bakun, W. H., Stewart, R. M., Bufe, C. G., & Marks, S. M. (1980). Implication of seismicity for failure of a section of the San Andreas Fault. *Bulletin of the Seismological Society of America*, *70*(1), 185–201.

Bakun, W. H., Aagaard, B., Dost, B., Ellsworth, W. L., Hardebeck, J. L., Harris, R. A., Ji, C., Johnston, M. J. S., Langbein, J., Lienkaemper, J. J., Michael, A. J., Murray, J. R., Nadeau, R. M., Reasenberg, P. A., Reichle, M. S., Roeloffs, E. A., Shakal, A., Simpson, R. W., & Waldhauser, F. (2005). Implications for prediction and hazard assessment from the 2004 Parkfield earthquake. *Nature*, *437*(7061), 969–974. https://doi.org/10.1038/nature04067

Bao, H., Ampuero, J.-P., Meng, L., Fielding, E. J., Liang, C., Milliner, C. W. D., Feng, T., & Huang, H. (2019). Early and persistent supershear rupture of the 2018 magnitude 7.5 Palu earthquake. *Nature Geoscience*, *12*(3), 200–205. https://doi.org/10.1038/s41561-018-0297-z

Barbot, S. (2018). Deformation of a Half-Space from Anelastic Strain Confined in a Tetrahedral VolumeDeformation of a Half-Space from Anelastic Strain Confined in a Tetrahedral Volume. *Bulletin of the Seismological Society of America*, *108*(5A), 2687–2712. https://doi.org/10.1785/0120180058

Barbot, S. (2019a). Modulation of fault strength during the seismic cycle by grain-size evolution around contact junctions. *Tectonophysics*, *765*, 129–145. https://doi.org/10.1016/j.tecto.2019.05.004

Barbot, S. (2019b). Slow-slip, slow earthquakes, period-two cycles, full and partial ruptures, and deterministic chaos in a single asperity fault. *Tectonophysics*, *768*, 228171. https://doi.org/10.1016/j.tecto.2019.228171

Barbot, S., Hamiel, Y., & Fialko, Y. (2008). Space geodetic investigation of the coseismic and postseismic deformation due to the 2003 Mw7.2 Altai earthquake: Implications for the local lithospheric rheology. *Journal of Geophysical Research: Solid Earth*, *113*(B3). https://doi.org/10.1029/2007JB005063

Barbot, S., Lapusta, N., & Avouac, J.-P. (2012). Under the Hood of the Earthquake Machine: Toward Predictive Modeling of the Seismic Cycle. *Science*, *336*(6082), 707–710. https://doi.org/10.1126/science.1218796

Barnes, P. M., Wallace, L. M., Saffer, D. M., Bell, R. E., Underwood, M. B., Fagereng, A., Meneghini, F., Savage, H. M., Rabinowitz, H. S., Morgan, J. K., Kitajima, H., Kutterolf, S., Hashimoto, Y., Oliveira, C. H. E. de, Noda, A., Crundwell, M. P., Shepherd, C. L., Woodhouse, A. D., Harris, R. N., Wang, M., Henrys, S., Barker, D. H. N., Petronotis, K. E., Bourlange, S. M., Clennell, M. B., Cook, A. E., Dugan, B. E., Elger, J., Fulton, P. M., Gamboa, D., Greve, A., Han, S., Hüpers, A., Ikari, M. J., Ito, Y., Kim, G. Y., Koge, H., Lee, H., Li, X., Luo, M., Malie, P. R., Moore, G. F., Mountjoy, J. J., McNamara, D. D., Paganoni, M., Screaton, E. J., Shankar, U., Shreedharan, S., Solomon, E. A., Wang, X., Wu, H.-Y., Pecher, I. A., LeVay, L. J., & Scientists, I. E. 372. (2020). Slow slip source characterized by lithological and geometric heterogeneity. *Science Advances*, *6*(13), eaay3314. https://doi.org/10.1126/sciadv.aay3314

Barnhart, W. D. (2017). Fault creep rates of the Chaman fault (Afghanistan and Pakistan) inferred from InSAR: Chaman Fault Creep Rates. *Journal of Geophysical Research: Solid Earth*, *122*(1), 372–386. https://doi.org/10.1002/2016JB013656

Barnhart, W. D., & Lohman, R. B. (2012). Regional trends in active diapirism revealed by mountain range-scale InSAR time series. *Geophysical Research Letters*, *39*(8). https://doi.org/10.1029/2012GL051255

Barrier, E., Angelier, J., Chu, H.-T., & Teng, L. S. (1982). Tectonic analysis of compressional structure in an active collision zone: the deformation of the Pinanshan conglomerates, eastern Taiwan. *Volume 25, 1982, Pages 123-138*, *25*, 123–138.

Bawden, G. W., Thatcher, W., Stein, R. S., Hudnut, K. W., & Peltzer, G. (2001). Tectonic contraction across Los Angeles after removal of groundwater pumping effects. *Nature*, *412*(6849), 812–815.

Beavan, J., Samsonov, S., Denys, P., Sutherland, R., Palmer, N., & Denham, M. (2010). Oblique slip on the Puysegur subduction interface in the 2009 July MW 7.8 Dusky Sound earthquake from GPS and InSAR observations: implications for the tectonics of southwestern New Zealand. *Geophysical Journal International*, *183*(3), 1265–1286. https://doi.org/10.1111/j.1365-246X.2010.04798.x

Bechor, N. B. D., & Zebker, H. A. (2006). Measuring two-dimensional movements using a single InSAR pair. *Geophysical Research Letters*, *33*(16). https://doi.org/10.1029/2006GL026883

Béjar-Pizarro, M., Carrizo, D., Socquet, A., Armijo, R., Barrientos, S., Bondoux, F., Bonvalot, S., Campos, J., Comte, D., de Chabalier, J. B., Charade, O., Delorme, A., Gabalda, G., Galetzka, J., Genrich, J., Nercessian, A., Olcay, M., Ortega, F., Ortega, I., Remy, D., Ruegg, J. C., Simons, M., Valderas, C., & Vigny, C. (2010). Asperities and barriers on the seismogenic zone in North Chile: state-of-the-art after the 2007 Mw 7.7 Tocopilla earthquake inferred by GPS and InSAR data: Seismogenic zone in North Chile. *Geophysical Journal International*, *183*(1), 390–406. https://doi.org/10.1111/j.1365-246X.2010.04748.x

Béjar-Pizarro, M., Socquet, A., Armijo, R., Carrizo, D., Genrich, J., & Simons, M. (2013). Andean structural control on interseismic coupling in the North Chile subduction zone. *Nature Geoscience*, *6*(6), 462–467. https://doi.org/10.1038/ngeo1802

Bekaert, D. P. S., Hooper, A., & Wright, T. J. (2015). Reassessing the 2006 Guerrero slow-slip event, Mexico: Implications for large earthquakes in the Guerrero Gap. *Journal of Geophysical Research: Solid Earth*, *120*(2), 1357–1375. https://doi.org/10.1002/2014JB011557

Bekaert, D. P. S., Walters, R. J., Wright, T. J., Hooper, A. J., & Parker, D. J. (2015). Statistical comparison of InSAR tropospheric correction techniques. *Remote Sensing of Environment*, *170*, 40–47. https://doi.org/10.1016/j.rse.2015.08.035

Belabbès, S., Meghraoui, M., Çakir, Z., & Bouhadad, Y. (2009). InSAR analysis of a blind thrust rupture and related active folding: the 1999 Ain Temouchent earthquake (Mw 5.7, Algeria) case study. *Journal of Seismology*, *13*(4), 421–432. https://doi.org/10.1007/s10950-008-9135-x

Bendick, R., Bilham, R., Freymueller, J. T., Larson, K. M., & Guanghua, Y. (2000). Geodetic evidence for a low slip rate in the Altyn Tagh fault system. *Nature*, *403*(6773), 69–72.

Benedetti, L., Manighetti, I., Gaudemer, Y., Finkel, R., Malavieille, J., Pou, K., Arnold, M., Aumaître, G., Bourlès, D., & Keddadouche, K. (2013). Earthquake synchrony and clustering on Fucino faults (Central Italy) as revealed from in situ 36Cl exposure dating. *Journal of Geophysical Research: Solid Earth*, *118*(9), 4948–4974. https://doi.org/10.1002/jgrb.50299

Benoit, A., Pinel-Puysségur, B., Jolivet, R., & Lasserre, C. (2020). CorPhU: an algorithm based on phase closure for the correction of unwrapping errors in SAR interferometry. *Geophysical Journal International*, *221*(3), 1959–1970. https://doi.org/10.1093/gji/ggaa120

Berardino, P., Fornaro, G., Lanari, R., & Sansosti, E. (2002). A new algorithm for surface deformation monitoring based on small baseline differential SAR interferograms. *IEEE Transactions on Geoscience and Remote Sensing*, *40*(11), 2375–83. https://doi.org/10.1109/TGRS.2002.803792

Berberian, M., Jackson, J. A., Fielding, E. J., Parsons, B. E., Priestley, K., Qorashi, M., Talebian, M., Walker, R., Wright, T. J., & Baker, C. (2001). The 1998 March 14 Fandoqa earthquake (Mw 6.6) in Kerman province, southeast Iran: re-rupture of the 1981 Sirch earthquake fault, triggering of slip on adjacent thrusts and the active tectonics of the Gowk fault zone. *Geophysical Journal International*, *146*, 371–398.

Beroza, G. C., & Ide, S. (2011). Slow Earthquakes and Nonvolcanic Tremor. *Annual Review of Earth and Planetary Sciences*, *39*(1), 271–296. https://doi.org/10.1146/annurev-earth-040809-152531

Beroza, G. C., & Jordan, T. H. (1990). Searching for slow and silent earthquakes using free oscillations. *Journal of Geophysical Research: Solid Earth*, *95*(B3), 2485–2510. https://doi.org/10.1029/JB095iB03p02485

Bevis, M., & Brown, A. (2014). Trajectory models and reference frames for crustal motion geodesy. *Journal of Geodesy*, *88*(3), 283–311. https://doi.org/10.1007/s00190-013-0685-5

Biggs, J., Amelung, F., Gourmelen, N., Dixon, T. H., & Kim, S.-W. (2009). InSAR observations of 2007 Tanzania rifting episode reveal mixed fault and dyke extension in an immature continental rift. *Geophysical Journal International*, *179*(1), 549–558. https://doi.org/10.1111/j.1365-246X.2009.04262.x

Bilham, R. (2004). Earthquakes in India and the Himalaya: tectonics, geodesy and history. *Annals of Geophysics*, *47*(2–3), 839– 858. https://doi.org/10.4401/ag-3338

Bilham, R., Larson, K. M., Freymueller, J. T., & Project Idylhim members. (1997). GPS measurements of present-day convergence across the Nepal Himalaya. *Nature*, *386*(6620), 61–64.

Bilham, R., Suszek, N., & Pinkney, S. (2004). California Creepmeters. *Seismological Research Letters*, *75*(4), 481–492. https://doi.org/10.1785/gssrl.75.4.481

Bock, Y., Wdowinski, S., Fang, P., Zhang, J., Williams, S. D. P., Johnson, H., Behr, J., Genrich, J. F., Dean, J., van Domselaar, M., Agnew, D. C., Wyatt, F. K., Stark, K., Oral, B., Hudnut, K. W., King, R. W., Herring, T. A., Dinardo, S., Young, W., Jackson, D. D., & Gurtner, W. (1997). Southern California Permanent GPS Geodetic Array: continuous measurements of regional crustal deformation between the 1992 Landers and 1994 Northridge earthquakes. *Journal of Geophysical Research*, *102*(B8), 18013–33.

Bodin, P., & Gomberg, J. (1994). Triggered seismicity and deformation between the Landers, California, and Little Skull Mountain, Nevada, earthquakes. *Bulletin of the Seismological Society of America*, *84*(3), 835–43.

Bodin, P., Bilham, R., Behr, J., Gomberg, J., & Hudnut, K. W. (1994). Slip triggered on southern California faults by the 1992 Joshua Tree, Landers, and big bear earthquakes. *Bulletin of the Seismological Society of America*, *84*(3), 806–816.

Bonilla, M. G. (1975). *A review of recently active faults in Taiwan* (Vol. 75–41). Reston, VA, United States United-States: U.S. Geological Survey. Retrieved from http://geopubs.wr.usgs.gov/open-file/of75-41

Borgia, A., Lanari, R., Sansosti, E., Tesauro, M., Berardino, P., Fornaro, G., Neri, M., & Murray, J. B. (2000). Actively growing anticlines beneath catania from the distal motion of Mount Etna's Decollement measured by SAR interferometry and GPS. *Geophysical Research Letters*, *27*(20), 3409–3412. https://doi.org/10.1029/1999GL008475

Bouchon, M., Marsan, D., Durand, V., Campillo, M., Perfettini, H., Madariaga, R., & Gardonio, B. (2016). Potential slab deformation and plunge prior to the Tohoku, Iquique and Maule earthquakes. *Nature Geoscience*, *9*(5), 380–383. https://doi.org/10.1038/ngeo2701

Bovenga, F., Stramaglia, S., Nutricato, R., & Refice, A. (2003). Discrimination of different sources of signals in Permanent Scatterers technique by means of Independent Component Analysis. Presented at the IGARSS 2003. IEEE 2003 International Geoscience and Remote Sensing Symposium, Toulouse, France: IEEE, Piscataway, NJ, USA.

Brace, W. F., & Byerlee, J. D. (1966). Stick-Slip as a Mechanism for Earthquakes. *Science*, *153*(3739), 990–992. https://doi.org/10.1126/science.153.3739.990

Brudzinski, M. R., Cabral-Cano, E., Correa-Mora, F., DeMets, C., & Márquez-Azúa, B. (2007). Slow slip transients along the Oaxaca subduction segment from 1993 to 2007. *Geophysical Journal International*, *171*(2), 523–538. https://doi.org/10.1111/j.1365-246X.2007.03542.x

Brudzinski, M. R., Schlanser, K. M., Kelly, N. J., DeMets, C., Grand, S. P., Márquez-Azúa, B., & Cabral-Cano, E. (2016). Tectonic tremor and slow slip along the northwestern section of the Mexico subduction zone. *Earth and Planetary Science Letters*, *454*, 259–271. https://doi.org/10.1016/j.epsl.2016.08.004

Bucknam, R. C., Plafker, G., & Sharp, R. V. (1978). Fault movement (afterslip) following the Guatemala earthquake of February 4, 1976. *Geology*, *6*(3), 170–173. https://doi.org/10.1130/0091-7613(1978)6<170:FMAFTG>2.0.CO;2

Burford, R. O. (1972). Continued slip on the Coyote Creek fault after the Borrego Mountain earthquake. In *The Borrego Mountain Earthquake of April 9, 1968* (Vol. 787, pp. 105–111). U.S. Geol. Survey. Prof. Papers. Retrieved from https://pubs.er.usgs.gov/publication/pp787

Burford, R. O., & Harsh, P. W. (1980). Slip on the San Andreas fault in central California from alinement array surveys. *Bulletin of the Seismological Society of America*, *70*(4), 1233–1261.

Burford, Robert O. (1988). Retardations in fault creep rates before local moderate earthquakes along the San Andreas fault system, central California. *Pure and Applied Geophysics*, *126*(2), 499–529. https://doi.org/10.1007/BF00879008

Bürgmann, R. (2018). The geophysics, geology and mechanics of slow fault slip. *Earth and Planetary Science Letters*, *495*, 112–134. https://doi.org/10.1016/j.epsl.2018.04.062

Bürgmann, R., Fielding, E., & Sukhatme, J. (1998). Slip along the Hayward fault, California, estimated from space-based synthetic aperture radar interferometry. *Geology*, *26*(6), 559–562. https://doi.org/10.1130/0091-7613(1998)026<0559:SATHFC>2.3.CO;2

Bürgmann, R., Schmidt, D. A., Nadeau, R. M., d'Alessio, M. A., Fielding, E. J., Manaker, D. M., McEvilly, T. V., & Murray, M. H. (2000). Earthquake potential along the Northern Hayward fault, California. *Science*, *289*(5482), 1178–1182.

Bürgmann, R., Rosen, P. A., & Fielding, E. J. (2000). Synthetic Aperture Radar Interferometry to Measure Earth's Surface Topography and Its Deformation. *Annual Review of Earth and Planetary Sciences*, *28*(1), 169–209. https://doi.org/10.1146/annurev.earth.28.1.169

Byrne, D. E., Sykes, L. R., & Davis, D. M. (1992). Great thrust earthquakes and aseismic slip along the plate boundary of the Makran Subduction Zone. *Journal of Geophysical Research: Solid Earth*, *97*(B1), 449–478. https://doi.org/10.1029/91JB02165

Cabral-Cano, E., Dixon, T. H., Miralles-Wilhelm, F., Díaz-Molina, O., Sánchez-Zamora, O., & Carande, R. E. (2008). Space geodetic imaging of rapid ground subsidence in Mexico CitySpace geodetic imaging of rapid ground subsidence in Mexico City. *GSA Bulletin*, *120*(11–12), 1556–1566. https://doi.org/10.1130/B26001.1

Çakir, Z., Akoglu, A., Belabbes, S., Ergintav, S., & Meghraoui, M. (2005). Creeping along the Ismetpasa section of the North Anatolian fault (Western Turkey): Rate and extent from InSAR. *Earth and Planetary Science Letters*, *238*(1–2), 225–234. https://doi.org/10.1016/j.epsl.2005.06.044

Çakir, Z., Ergintav, S., Ozener, H., Dogan, U., Akoglu, A. M., Meghraoui, M., & Reilinger, R. (2012). Onset of aseismic creep on major strike-slip faults. *Geology*, *40*(12), 1115–1118. https://doi.org/10.1130/G33522.1

Calais, E., Freed, A., Mattioli, G., Amelung, F., Jónsson, S., Jansma, P., Hong, S.-H., Dixon, T., Prépetit, C., & Momplaisir, R. (2010). Transpressional rupture of an unmapped fault during the 2010 Haiti earthquake. *Nature Geoscience*, *3*(11), 794–799. https://doi.org/10.1038/ngeo992

Carnec, C., & Fabriol, H. (1999). Monitoring and modeling land subsidence at the Cerro Prieto geothermal field, Baja California, Mexico, using SAR interferometry. *Geophysical Research Letters*, *26*(9), 1211–1214.

Carnec, C., Massonnet, D., & King, C. (1996). Two examples of the use of SAR interferometry on displacement fields of small spatial extent. *Geophysical Research Letters*, *23*(24), 3579–3582.

Cattin, R., & Avouac, J.-P. (2000). Modeling mountain building and the seismic cycle in the Himalaya of Nepal. *Journal of Geophysical Research*, *105*(B6), 13389–13407.

Cattin, R., Loevenbruck, A., & Le Pichon, X. (2004). Why does the co-seismic slip of the 1999 Chi-Chi (Taiwan) earthquake increase progressively northwestward on the plane of rupture? *Tectonophysics*, *386*(1–2), 67–80. https://doi.org/10.1016/j.tecto.2004.05.002

Cavalié, O., & Jónsson, S. (2014). Block-like plate movements in eastern Anatolia observed by InSAR. *Geophysical Research Letters*, *41*(1), 26–31. https://doi.org/10.1002/2013GL058170

Cavalié, O., Doin, M.-P., Lasserre, C., & Briole, P. (2007). Ground motion measurement in the Lake Mead area, Nevada, by differential synthetic aperture radar interferometry time series analysis: Probing the lithosphere rheological structure. *Journal of Geophysical Research*, *112*(B3), B03403. https://doi.org/10.1029/2006JB004344

Cavalié, O., Lasserre, C., Doin, M.-P., Peltzer, G., Sun, J., Xu, X., & Shen, Z.-K. (2008). Measurement of interseismic strain across the Haiyuan fault (Gansu, China), by InSAR. *Earth and Planetary Science Letters*, *275*(3–4), 246–257. https://doi.org/10.1016/j.epsl.2008.07.057

Cavalié, O., Pathier, E., Radiguet, M., Vergnolle, M., Cotte, N., Walpersdorf, A., Kostoglodov, V., & Cotton, F. (2013). Slow slip event in the Mexican subduction zone: Evidence of shallower slip in the Guerrero seismic gap for the 2006 event revealed by the joint inversion of InSAR and GPS data. *Earth and Planetary Science Letters*, *367*(0), 52–60. https://doi.org/10.1016/j.epsl.2013.02.020

Cesca, S., Zhang, Y., Mouslopoulou, V., Wang, R., Saul, J., Savage, M., Heimann, S., Kufner, S.-K., Oncken, O., & Dahm, T. (2017). Complex rupture process of the Mw 7.8, 2016, Kaikoura earthquake, New Zealand, and its aftershock sequence. *Earth and Planetary Science Letters*, *478*, 110–120. https://doi.org/10.1016/j.epsl.2017.08.024

Cetin, E., Çakir, Z., Meghraoui, M., Ergintav, S., & Akoglu, A. M. (2014). Extent and distribution of aseismic slip on the Ismetpaşa segment of the North Anatolian Fault (Turkey) from Persistent Scatterer InSAR. *Geochemistry, Geophysics, Geosystems*, *15*(7), 2883–2894. https://doi.org/10.1002/2014GC005307

Cetin, H. (1998). Near-surface folding along an active fault: seismic or aseismic? *Tectonophysics*, *292*(3–4), 279–291. https://doi.org/10.1016/S0040-1951(98)00074-2

Champenois, J., Fruneau, B., Pathier, E., Deffontaines, B., Lin, K.-C., & Hu, J.-C. (2012). Monitoring of active tectonic deformations in the Longitudinal Valley (Eastern Taiwan) using Persistent Scatterer InSAR method with ALOS PALSAR data. *Earth and Planetary Science Letters*, *337–338*, 144–155. https://doi.org/10.1016/j.epsl.2012.05.025

Champenois, Johann. (2011, December 12). *Caractérisation des déformations tectoniques inter-sismiques de l'île de Taiwan par interférométrie radar* (thesis). Paris Est Marne-la-Vallée, Marne-le-Vallée. Retrieved from http://www.theses.fr/2011PEST1008

Chang, S.-H., Wang, W.-H., & Lee, J.-C. (2009). Modelling temporal variation of surface creep on the Chihshang fault in eastern Taiwan with velocity-strengthening friction. *Geophysical Journal International*, *176*(2), 601–613. https://doi.org/10.1111/j.1365-246X.2008.03995.x

Chao, H.-C., You, C.-F., Wang, B.-S., Chung, C.-H., & Huang, K.-F. (2011). Boron isotopic composition of mud volcano fluids: Implications for fluid migration in shallow subduction zones. *Earth and Planetary Science Letters*, *305*(1), 32–44. https://doi.org/10.1016/j.epsl.2011.02.033

Chao, H.-C., You, C.-F., Liu, H.-C., & Chung, C.-H. (2013). The origin and migration of mud volcano fluids in Taiwan: Evidence from hydrogen, oxygen, and strontium isotopic compositions. *Geochimica et Cosmochimica Acta*, *114*, 29–51. https://doi.org/10.1016/j.gca.2013.03.035

Chaussard, E., Bürgmann, R., Fattahi, H., Johnson, C. W., Nadeau, R., Taira, T., & Johanson, I. (2015). Interseismic coupling and refined earthquake potential on the Hayward-Calaveras fault zone. *Journal of Geophysical Research: Solid Earth*, *120*(12), 8570–8590. https://doi.org/10.1002/2015JB012230

Chaussard, E., Johnson, C. W., Fattahi, H., & Bürgmann, R. (2016). Potential and limits of InSAR to characterize interseismic deformation independently of GPS data: Application to the southern San Andreas Fault system. *Geochemistry, Geophysics, Geosystems*, *17*(3), 1214–1229. https://doi.org/10.1002/2015GC006246

Chaussard, Estelle, Wdowinski, S., Cabral-Cano, E., & Amelung, F. (2014). Land subsidence in central Mexico detected by ALOS InSAR time-series. *Remote Sensing of Environment*, *140*, 94–106. https://doi.org/10.1016/j.rse.2013.08.038

Chaussard, Estelle, Milillo, P., Bürgmann, R., Perissin, D., Fielding, E. J., & Baker, B. (2017). Remote Sensing of Ground Deformation for Monitoring Groundwater Management Practices: Application to the Santa Clara Valley During the 2012–2015 California Drought. *Journal of Geophysical Research: Solid Earth*, *122*(10), 8566–8582. https://doi.org/10.1002/2017JB014676

Chaves, E. J., & Schwartz, S. Y. (2016). Monitoring transient changes within overpressured regions of subduction zones using ambient seismic noise. *Science Advances*, *2*(1), e1501289. https://doi.org/10.1126/sciadv.1501289

Chen, H.-Y., Lee, J.-C., Tung, H., Yu, S.-B., Hsu, Y.-J., & Lee, H. (2012). Determination of Vertical Velocity Field of Southernmost Longitudinal Valley in Eastern Taiwan: A Joint Analysis of Leveling and GPS Measurements. *Terrestrial, Atmospheric and Oceanic Sciences*, *23*(4), 355. https://doi.org/10.3319/TAO.2012.02.29.01(TT)

Chen, H.-Y., Lee, J.-C., Tung, H., Yu, S.-B., Hsu, Y.-J., & Lee, H. (2013). A New Velocity Field from a Dense GPS Array in the Southernmost Longitudinal Valley, Southeastern Taiwan. *Terrestrial, Atmospheric and Oceanic Sciences*, *24*(5), 837. https://doi.org/10.3319/TAO.2013.06.18.01(T)

Chen, K. H.-H., Nadeau, R. M., & Rau, R.-J. (2008). Characteristic repeating earthquakes in an arc-continent collision boundary zone: The Chihshang fault of eastern Taiwan. *Earth and Planetary Science Letters*, *276*(3–4), 262–272. https://doi.org/10.1016/j.epsl.2008.09.021

Chen, K. H.-H., Rau, R.-J., & Hu, J.-C. (2009). Variability of repeating earthquake behavior along the Longitudinal Valley fault zone of eastern Taiwan. *Journal of Geophysical Research*, *114*(B5), B05306. https://doi.org/10.1029/2007JB005518

Chen, K.-H., Yang, M., Huang, Y.-T., Ching, K.-E., & Rau, R.-J. (2011). Vertical Displacement Rate Field of Taiwan From Geodetic Levelling Data 2000-2008. *Survey Review*, *43*(321), 296–302. https://doi.org/10.1179/003962611X13055561708380

Chen, S.-C., Hsu, S.-K., Tsai, C.-H., Ku, C.-Y., Yeh, Y.-C., & Wang, Y. (2010). Gas seepage, pockmarks and mud volcanoes in the near shore of SW Taiwan. *Marine Geophysical Researches*, *31*(1–2), 133–147. https://doi.org/10.1007/s11001-010-9097-6

Chen, S.-C., Hsu, S.-K., Wang, Y., Chung, S.-H., Chen, P.-C., Tsai, C.-H., Liu, C.-S., Lin, H.-S., & Lee, Y.-W. (2014). Distribution and characters of the mud diapirs and mud volcanoes off southwest Taiwan. *Journal of Asian Earth Sciences*, *92*, 201–214. https://doi.org/10.1016/j.jseaes.2013.10.009

Chen, W., Huang, M., & Liu, T. (1991). Neotectonic significance of the Chimei Fault in the Coastal Range, Eastern Taiwan. Chen, W.,. *Proc. Geol. Soc. China*, *34*, 43–56.

Chen, Y., Chen, K. H., Hu, J.-C., & Lee, J.-C. (2020). Probing the Variation in Aseismic Slip Behavior Around an Active Suture Zone: Observations of Repeating Earthquakes in Eastern Taiwan. *Journal of Geophysical Research: Solid Earth*, *125*(5), e2019JB018561. https://doi.org/10.1029/2019JB018561

Chen, Y.-G., Lai, K.-Y., Lee, Y.-H., Suppe, J., Chen, W.-S., Lin, Y.-N. N., Wang, Y., Hung, J.-H., & Kuo, Y.-T. (2007). Coseismic fold scarps and their kinematic behavior in the 1999 Chi-Chi earthquake Taiwan. *Journal of Geophysical Research: Solid Earth*, *112*(B3). https://doi.org/10.1029/2006JB004388

Chéry, J., Genti, M., & Vernant, P. (2016). Ice cap melting and low-viscosity crustal root explain the narrow geodetic uplift of the Western Alps. *Geophysical Research Letters*, *43*(7), 3193–3200. https://doi.org/10.1002/2016GL067821

Chiaraluce, L., Chiarabba, C., Collettini, C., Piccinini, D., & Cocco, M. (2007). Architecture and mechanics of an active low-angle normal fault: Alto Tiberina Fault, northern Apennines, Italy. *Journal of Geophysical Research: Solid Earth*, *112*(B10). https://doi.org/10.1029/2007JB005015

Ching, K.-E., Hsieh, M.-L., Johnson, K. M., Chen, K.-H., Rau, R.-J., & Yang, M. (2011). Modern vertical deformation rates and mountain building in Taiwan from precise leveling and continuous GPS observations, 2000–2008. *Journal of Geophysical Research*, *116*(B8), B08406. https://doi.org/10.1029/2011JB008242

Ching, K.-E., Gourley, J. R., Lee, Y.-H., Hsu, S.-C., Chen, K.-H., & Chen, C.-L. (2016). Rapid deformation rates due to development of diapiric anticline in southwestern Taiwan from geodetic observations. *Tectonophysics*, *692*, 241–251. https://doi.org/10.1016/j.tecto.2015.07.020

Chini, M., Atzori, S., Trasatti, E., Bignami, C., Kyriakopoulos, C., Tolomei, C., & Stramondo, S. (2010). The May 12, 2008, (Mw 7.9) Sichuan Earthquake (China): Multiframe ALOS-PALSAR DInSAR Analysis of Coseismic Deformation. *IEEE Geoscience and Remote Sensing Letters*, *7*(2), 266–270. https://doi.org/10.1109/LGRS.2009.2032564

Chlieh, M., de Chabalier, J.-B., Ruegg, J.-C., Armijo, R., Dmowska, J., Campos, J., & Feigl, K. L. (2004). Crustal deformation and fault slip during the seismic cycle in the North Chile subduction zone, from GPS and InSAR observations. *Geophysical Journal International*, *158*(2), 695–711. https://doi.org/10.1111/j.1365-246X.2004.02326.x

Chlieh, M., Avouac, J.-P., Sieh, K., Natawidjaja, D. H., & Galetzka, J. (2008). Heterogeneous coupling of the Sumatran megathrust constrained by geodetic and paleogeodetic measurements. *Journal of Geophysical Research: Solid Earth*, *113*(B5). https://doi.org/10.1029/2007JB004981

Choi, E., Tan, E., Lavier, L. L., & Calo, V. M. (2013). DynEarthSol2D: An efficient unstructured finite element method to study long-term tectonic deformation. *Journal of Geophysical Research: Solid Earth*, *118*(5), 2429–2444. https://doi.org/10.1002/jgrb.50148

Cifuentes, I. L., & Silver, P. G. (1989). Low-frequency source characteristics of the great 1960 Chilean earthquake. *Journal of Geophysical Research: Solid Earth*, *94*(B1), 643–663. https://doi.org/10.1029/JB094iB01p00643

Cohen-Waeber, J., Bürgmann, R., Chaussard, E., Giannico, C., & Ferretti, A. (2018). Spatiotemporal Patterns of Precipitation-Modulated Landslide Deformation From Independent Component Analysis of InSAR Time Series. *Geophysical Research Letters*, *45*(4), 1878–1887. https://doi.org/10.1002/2017GL075950

Colella, H. V., Sit, S. M., Brudzinski, M. R., Graham, S. E., DeMets, C., Holtkamp, S. G., Skoumal, R. J., Ghouse, N., Cabral-Cano, E., Kostoglodov, V., & Arciniega-Ceballos, A. (2017). Seismicity rate increases associated with slow slip episodes prior to the 2012 Mw 7.4 Ometepec earthquake. *Earth and Planetary Science Letters*, *464*, 35–45. https://doi.org/10.1016/j.epsl.2016.12.032

Colesanti, C., Ferretti, A., Locatelli, R., Novali, F., & Savio, G. (2003). Permanent Scatterers : Precision Assessment and Multi-platform Analysis. Presented at the IGARSS 2003. IEEE 2003 International Geoscience and Remote Sensing Symposium, Toulouse, France: IEEE, Piscataway, NJ, USA.

Comon, P. (1994). Independent component analysis, A new concept? *Signal Processing*, *36*(3), 287–314. https://doi.org/10.1016/0165-1684(94)90029-9

Copley, A., & Jolivet, R. (2016). Fault rheology in an aseismic fold-thrust belt (Shahdad, eastern Iran). *Journal of Geophysical Research: Solid Earth*, *121*(1), 412–431. https://doi.org/10.1002/2015JB012431

Correa-Mora, F., DeMets, C., Cabral-Cano, E., Diaz-Molina, O., & Marquez-Azua, B. (2009). Transient deformation in southern Mexico in 2006 and 2007: Evidence for distinct deep-slip patches beneath Guerrero and Oaxaca. *Geochemistry, Geophysics, Geosystems*, *10*(2), n/a-n/a. https://doi.org/10.1029/2008GC002211

Coutant, O., Mengin, M. D., & Coarer, E. L. (2015). Fabry-Perot optical fiber strainmeter with an embeddable, low-power interrogation system. *Optica*, *2*(5), 400–404. https://doi.org/10.1364/OPTICA.2.000400

Croizé, D., Renard, F., & Gratier, J.-P. (2013). Chapter 3 - Compaction and Porosity Reduction in Carbonates: A Review of Observations, Theory, and Experiments. In R. Dmowska (Ed.), *Advances in Geophysics* (Vol. 54, pp. 181–238). Elsevier. https://doi.org/10.1016/B978-0-12-380940-7.00003-2

Cubas, N., Lapusta, N., Avouac, J.-P., & Perfettini, H. (2015). Numerical modeling of long-term earthquake sequences on the NE Japan megathrust: Comparison with observations and implications for fault friction. *Earth and Planetary Science Letters*, *419*, 187–198. https://doi.org/10.1016/j.epsl.2015.03.002

Dadson, S. J., Hovius, N., Chen, H., Dade, B. W., Hsieh, M.-L., Willett, S. D., Hu, J.-C., Horng, M.-J., Chen, M.-C., Stark, C. P., Lague, D., & Lin, J.-C. (2003). Links between erosion, runoff variability and seismicity in the Taiwan orogen. *Nature*, *426*(6967), 648–51. https://doi.org/10.1038/nature02150

D'Agostino, N. (2014). Complete seismic release of tectonic strain and earthquake recurrence in the Apennines (Italy). *Geophysical Research Letters*, *41*(4), 1155–1162. https://doi.org/10.1002/2014GL059230

Daout, S., Barbot, S., Peltzer, G., Doin, M.-P., Liu, Z., & Jolivet, R. (2016). Constraining the kinematics of metropolitan Los Angeles faults with a slip-partitioning model. *Geophysical Research Letters*, *43*(21), 11,192-11,201. https://doi.org/10.1002/2016GL071061

Daout, Simon, Doin, M.-P., Peltzer, G., Lasserre, C., Socquet, A., Volat, M., & Sudhaus, H. (2018). Strain Partitioning and Present-Day Fault Kinematics in NW Tibet From Envisat SAR Interferometry. *Journal of Geophysical Research: Solid Earth*, *123*(3), 2462–2483. https://doi.org/10.1002/2017JB015020

Daout, Simon, Sudhaus, H., Kausch, T., Steinberg, A., & Dini, B. (2019). Interseismic and Postseismic Shallow Creep of the North Qaidam Thrust Faults Detected with a Multitemporal InSAR Analysis. *Journal of Geophysical Research: Solid Earth*, *124*(7), 7259–7279. https://doi.org/10.1029/2019JB017692

Davis, D., Suppe, J., & Dahlen, F. A. (1983). Mechanics of fold-and-thrust belts and accretionary wedges. *Journal of Geophysical Research*, *88*(B2), 1153. https://doi.org/10.1029/JB088iB02p01153

Davis, E. E., & Villinger, H. W. (2006). Transient formation fluid pressures and temperatures in the Costa Rica forearc prism and subducting oceanic basement: CORK monitoring at ODP Sites 1253 and 1255. *Earth and Planetary Science Letters*, *245*(1), 232–244. https://doi.org/10.1016/j.epsl.2006.02.042

De Zan, F., & Gomba, G. (2018). Vegetation and soil moisture inversion from SAR closure phases: First experiments and results. *Remote Sensing of Environment*, *217*, 562–572. https://doi.org/10.1016/j.rse.2018.08.034

De Zan, F., Zonno, M., & López-Dekker, P. (2015). Phase Inconsistencies and Multiple Scattering in SAR Interferometry. *IEEE Transactions on Geoscience and Remote Sensing*, *53*(12), 6608–6616. https://doi.org/10.1109/TGRS.2015.2444431

De Zan, F., Gomba, G., & Yokoya, N. (2018). The ambiguities related to Closure-Phase Model Inversion. In *EUSAR 2018; 12th European Conference on Synthetic Aperture Radar* (pp. 1–4).

De Zan, F., Parizzi, A., Gonzalez, F. R., Ansari, H., Gomba, G., Brcic, R., & Eineder, M. (2019). Insar Error Budget for Large Scale Deformation. In *IGARSS 2019 - 2019 IEEE International Geoscience and Remote Sensing Symposium* (pp. 2042–2045). https://doi.org/10.1109/IGARSS.2019.8900404

Deffontaines, B., Chang, K.-J., Champenois, J., Lin, K.-C., Lee, C.-T., Chen, R.-F., Hu, J.-C., & Magalhaes, S. (2018). Active tectonics of the onshore Hengchun Fault using UAS DSM combined with ALOS PS-InSAR time series (Southern Taiwan). *Natural Hazards and Earth System Sciences*, *18*(3), 829–845. https://doi.org/10.5194/nhess-18-829-2018

DeLong, S. B., Donnellan, A., Ponti, D. J., Rubin, R. S., Lienkaemper, J. J., Prentice, C. S., Dawson, T. E., Seitz, G., Schwartz, D. P., Hudnut, K. W., Rosa, C., Pickering, A., & Parker, J. W. (2016). Tearing the terroir: Details and implications of surface rupture and deformation from the 24 August 2014 M6.0 South Napa earthquake, California. *Earth and Space Science*, *3*(10), 416–430. https://doi.org/10.1002/2016EA000176

Delorme, A., Grandin, R., Klinger, Y., Pierrot-Deseilligny, M., Feuillet, N., Jacques, E., Rupnik, E., & Morishita, Y. (2020). Complex Deformation at Shallow Depth During the 30 October 2016 Mw6.5 Norcia Earthquake: Interference Between Tectonic and Gravity Processes? *Tectonics*, *39*(2), e2019TC005596. https://doi.org/10.1029/2019TC005596

Delouis, B., Lundgren, P. R., Salichon, J., & Giardini, D. (2000). Joint inversion of InSAR and teleseismic data for the slip history of the 1999 Izmit (Turkey) earthquake. *Geophysical Research Letters*, *27*(20), 3389–3392.

Delouis, B., Nocquet, J.-M., & Vallée, M. (2010). Slip distribution of the February 27, 2010 Mw = 8.8 Maule Earthquake, central Chile, from static and high-rate GPS, InSAR, and broadband teleseismic data. *Geophysical Research Letters*, *37*(17). https://doi.org/10.1029/2010GL043899

DiCaprio, C. J., & Simons, M. (2008). Importance of ocean tidal load corrections for differential InSAR. *Geophysical Research Letters*, *35*(22). https://doi.org/10.1029/2008GL035806

Dieterich, J. H. (1972). Time-dependent friction in rocks. *Journal of Geophysical Research (1896-1977)*, *77*(20), 3690–3697. https://doi.org/10.1029/JB077i020p03690

Dieterich, J. H. (1978). Preseismic fault slip and earthquake prediction. *Journal of Geophysical Research: Solid Earth*, *83*(B8), 3940–3948. https://doi.org/10.1029/JB083iB08p03940

Dieterich, J. H. (1979). Modeling of rock friction: 1. Experimental results and constitutive equations. *Journal of Geophysical Research*, *84*(B5), 2161. https://doi.org/10.1029/JB084iB05p02161

Dixon, T. H., Jiang, Y., Malservisi, R., McCaffrey, R., Voss, N., Protti, M., & Gonzalez, V. (2014). Earthquake and tsunami forecasts: Relation of slow slip events to subsequent earthquake rupture. *Proceedings of the National Academy of Sciences*, *111*(48), 17039–17044. https://doi.org/10.1073/pnas.1412299111

Doin, M. (2019, October). *Random walk and bias in INSAR time series of Sentinel-1 data associated with decorrelation: impact on ground deformation measurements and mitigation.* Presented at the

MDIS 2019, 5eme colloque MDIS-ForM@Ter (Mesure de la Déformation par Imagerie Spatiale), Strasbourg. Retrieved from https://mdis-2019.sciencesconf.org

Doin, M.-P., Lasserre, C., Peltzer, G., Cavalié, O., & Doubre, C. (2009). Corrections of stratified tropospheric delays in SAR interferometry: Validation with global atmospheric models. *Journal of Applied Geophysics*, *69*(1), 35–50. https://doi.org/10.1016/j.jappgeo.2009.03.010

Doin, M.-P., Twardzik, C., Ducret, G., Lasserre, C., Guillaso, S., & Jianbao, S. (2015). InSAR measurement of the deformation around Siling Co Lake: Inferences on the lower crust viscosity in central Tibet. *Journal of Geophysical Research: Solid Earth*, *120*(7), 5290–5310. https://doi.org/10.1002/2014JB011768

Dolan, J. F., & Haravitch, B. D. (2014). How well do surface slip measurements track slip at depth in large strike-slip earthquakes? The importance of fault structural maturity in controlling on-fault slip versus off-fault surface deformation. *Earth and Planetary Science Letters*, *388*, 38–47. https://doi.org/10.1016/j.epsl.2013.11.043

Dolan, J. F., & Meade, B. J. (2017). A Comparison of Geodetic and Geologic Rates Prior to Large Strike-Slip Earthquakes: A Diversity of Earthquake-Cycle Behaviors? *Geochemistry, Geophysics, Geosystems*, *18*(12), 4426–4436. https://doi.org/10.1002/2017GC007014

Dominguez, S., Avouac, J.-P., & Michel, R. (2003). Horizontal coseismic deformation of the 1999 Chi-Chi earthquake measured from SPOT satellite images: implications for the seismic cycle along the western foothills of Central Taiwan. *Journal of Geophysical Research*, *108*(B2), Ese8.1-Ese8.19.

Dong, D., Fang, P., Bock, Y., Cheng, M. K., & Miyazaki, S. (2002). Anatomy of apparent seasonal variations from GPS-derived site position time series. *Journal of Geophysical Research: Solid Earth*, *107*(B4), ETG 9-1-ETG 9-16. https://doi.org/10.1029/2001JB000573

Donnellan, A., Parker, J., Hensley, S., Pierce, M., Wang, J., & Rundle, J. (2014). UAVSAR observations of triggered slip on the Imperial, Superstition Hills, and East Elmore Ranch Faults associated with the 2010 M 7.2 El Mayor-Cucapah earthquake. *Geochemistry, Geophysics, Geosystems*, *15*(3), 815–829. https://doi.org/10.1002/2013GC005120

Doubre, C., & Peltzer, G. (2007). Fluid-controlled faulting process in the Asal Rift, Djibouti, from 8 yr of radar interferometry observations. *Geology*, *35*(1), 69. https://doi.org/10.1130/G23022A.1

Doubre, C., Déprez, A., Masson, F., Socquet, A., Lewi, E., Grandin, R., Nercessian, A., Ulrich, P., De Chabalier, J.-B., Saad, I., Abayazid, A., Peltzer, G., Delorme, A., Calais, E., & Wright, T. (2017). Current deformation in Central Afar and triple junction kinematics deduced from GPS and InSAR measurements. *Geophysical Journal International*, *208*(2), 936–953. https://doi.org/10.1093/gji/ggw434

Douglas, A. (2005). Slow slip on the northern Hikurangi subduction interface, New Zealand. *Geophysical Research Letters*, *32*(16), L16305. https://doi.org/10.1029/2005GL023607

Dragert, H. (2001). A silent slip event on the deeper Cascadia subduction interface. *Science*, *292*(5521), 1525–1528. https://doi.org/10.1126/science.1060152

Du, W.-X., Sykes, L. R., Shaw, B. E., & Scholz, C. H. (2003). Triggered aseismic fault slip from nearby earthquakes, static or dynamic effect? *Journal of Geophysical Research (B: Solid Earth)*, *108*(2), Ese 24-1-24-21. https://doi.org/10.1029/2002JB002008

Duan, B. (2010). Inelastic response of compliant fault zones to nearby earthquakes: INELASTIC RESPONSE OF FAULT ZONES. *Geophysical Research Letters*, *37*(16), n/a-n/a. https://doi.org/10.1029/2010GL044150

Ducret, G., Doin, M.-P., Grandin, R., Lasserre, C., & Guillaso, S. (2014). DEM Corrections Before Unwrapping in a Small Baseline Strategy for InSAR Time Series Analysis. *IEEE Geoscience and Remote Sensing Letters*, *11*(3), 696–700. https://doi.org/10.1109/LGRS.2013.2276040

Duputel, Z., & Rivera, L. (2017). Long-period analysis of the 2016 Kaikoura earthquake. *Physics of the Earth and Planetary Interiors*, *265*, 62–66. https://doi.org/10.1016/j.pepi.2017.02.004

Ebmeier, S. K. (2016). Application of independent component analysis to multitemporal InSAR data with volcanic case studies: ICA Analysis of InSAR Data. *Journal of Geophysical Research: Solid Earth*, *121*(12), 8970–8986. https://doi.org/10.1002/2016JB013765

Elliott, J. R., Biggs, J., Parsons, B., & Wright, T. J. (2008). InSAR slip rate determination on the Altyn Tagh Fault, northern Tibet, in the presence of topographically correlated atmospheric delays: ALTYN TAGH FAULT SLIP RATE. *Geophysical Research Letters*, *35*(12), n/a-n/a. https://doi.org/10.1029/2008GL033659

Elliott, J. R., Parsons, B., Jackson, J. A., Shan, X., Sloan, R. A., & Walker, R. T. (2011). Depth segmentation of the seismogenic continental crust: The 2008 and 2009 Qaidam earthquakes. *Geophysical Research Letters*, *38*(6). https://doi.org/10.1029/2011GL046897

Elliott, J. R., Jolivet, R., González, P. J., Avouac, J.-P., Hollingsworth, J., Searle, M. P., & Stevens, V. L. (2016). Himalayan megathrust geometry and relation to topography revealed by the Gorkha earthquake. *Nature Geoscience*, *9*(2), 174–180. https://doi.org/10.1038/ngeo2623

Elliott, J. R., Walters, R. J., & Wright, T. J. (2016). The role of space-based observation in understanding and responding to active tectonics and earthquakes. *Nature Communications*, *7*(1), 13844. https://doi.org/10.1038/ncomms13844

England, P., & Molnar, P. (2005). Late Quaternary to decadal velocity fields in Asia. *Journal of Geophysical Research*, *110*(B12), B12401. https://doi.org/10.1029/2004JB003541

Evans, K. F., Burford, R. O., & King, G. C. P. (1981). Propagating episodic creep and the aseismic slip behavior of the Calaveras Fault north of Hollister, California. *Journal of Geophysical Research: Solid Earth*, *86*(B5), 3721–3735. https://doi.org/10.1029/JB086iB05p03721

Fang, J., Xu, C., Wen, Y., Wang, S., Xu, G., Zhao, Y., & Yi, L. (2019). The 2018 Mw 7.5 Palu Earthquake: A Supershear Rupture Event Constrained by InSAR and Broadband Regional Seismograms. *Remote Sensing*, *11*(11), 1330. https://doi.org/10.3390/rs11111330

Fattahi, H., & Amelung, F. (2016). InSAR observations of strain accumulation and fault creep along the Chaman Fault system, Pakistan and Afghanistan. *Geophysical Research Letters*, *43*(16), 8399–8406. https://doi.org/10.1002/2016GL070121

Feigl, K. L., King, R. W., & Jordan, T. H. (1990). Geodetic measurement of tectonic deformation in the Santa Maria fold and thrust belt, California. *Journal of Geophysical Research*, *95*(B3), 2679–2699.

Feigl, K. L., Agnew, D. C., Bock, Y., Dong, D., Donnellan, A., Hager, B. H., Herring, T. A., Jackson, D. D., Jordan, T. H., King, R. W., Larsen, S., Larson, K. M., Murray, M. H., Shen, Z., & Webb, F. H. (1993). Space geodetic measurement of crustal deformation in central and southern California, 1984–1992. *Journal of Geophysical Research: Solid Earth*, *98*(B12), 21677–21712. https://doi.org/10.1029/93JB02405

Feigl, K. L., Sarti, F., Vadon, H., McClusky, S., Ergintav, S., Durand, P., Bürgmann, R., Rigo, A., Massonnet, D., & Reilinger, R. E. (2002). Estimating slip distribution for the Izmit mainshock from coseismic GPS, ERS-1, RADARSAT, and SPOT measurements. *Bulletin of the Seismological Society of America*, *92*(1), 138–160. https://doi.org/10.1785/0120000830

Feng, G., & Jónsson, S. (2012). Shortcomings of InSAR for studying megathrust earthquakes: The case of the Mw9.0 Tohoku-Oki earthquake. *Geophysical Research Letters*, *39*(10). https://doi.org/10.1029/2012GL051628

Feng, W., Li, Z., Elliott, J. R., Fukushima, Y., Hoey, T., Singleton, A., Cook, R., & Xu, Z. (2013). The 2011 MW 6.8 Burma earthquake: fault constraints provided by multiple SAR techniques. *Geophysical Journal International*, *195*(1), 650–660. https://doi.org/10.1093/gji/ggt254

Ferretti, A., Prati, C., & Rocca, F. (1999). Non-uniform Motion Monitoring Using the Permanent Scatterers Technique. In *Fringe 99 workshop* (Liège, Belgium, Vol. 478). European Space Agency. Retrieved from http://www.elet.polimi.it/upload/monti/sar/publicationtext.htm

Ferretti, A., Prati, C., & Rocca, F. (2000). Nonlinear subsidence rate estimation using permanent scatterers in differential SAR interferometry. *IEEE Transactions on Geoscience and Remote Sensing*, *38*(5), 2202–2212. https://doi.org/10.1109/36.868878

Ferretti, A., Prati, C., & Rocca, F. (2001). Permanent scatterers in SAR interferometry. *IEEE Transactions on Geoscience and Remote Sensing*, *39*(1), 8–20.

Ferretti, A., Fumagalli, A., Novali, F., Prati, C., Rocca, F., & Rucci, A. (2011). A New Algorithm for Processing Interferometric Data-Stacks: SqueeSAR. *IEEE Transactions on Geoscience and Remote Sensing*, *49*(9), 3460–3470. https://doi.org/10.1109/TGRS.2011.2124465

Fialko, Y. (2004). Probing the mechanical properties of seismically active crust with space geodesy: Study of the coseismic deformation due to the 1992 Mw 7.3 Landers (southern California) earthquake. *Journal of Geophysical Research*, *109*(B3), B03307.1-B03307.19. https://doi.org/10.1029/2003JB002756

Fialko, Y., Simons, M., & Agnew, D. (2001). The complete (3-D) surface displacement field in the epicentral area of the 1999 MW7.1 Hector Mine Earthquake, California, from space geodetic observations. *Geophysical Research Letters*, *28*(16), 3063–3066. https://doi.org/10.1029/2001GL013174

Fialko, Y., Sandwell, D. T., Agnew, D. C., Simons, M., Shearer, P., & Minster, J.-B. (2002). Deformation on nearby faults induced by the 1999 Hector Mine earthquake. *Science*, *297*(5588), 1858–62.

Fialko, Y., Sandwell, D., Simons, M., & Rosen, P. (2005). Three-dimensional deformation caused by the Bam, Iran, earthquake and the origin of shallow slip deficit. *Nature*, *435*(7040), 295–299. https://doi.org/10.1038/nature03425

Fielding, E. J., Wright, T. J., Muller, J. P., Parsons, B. E., & Walker, R. (2004). Aseismic deformation of a fold-and-thrust belt imaged by synthetic aperture radar interferometry near Shahdad, southeast Iran. *Geology*, *32*(7), 577–580. https://doi.org/10.1130/G20452.1

Fielding, E. J., Sladen, A., Li, Z., Avouac, J.-P., Bürgmann, R., & Ryder, I. (2013). Kinematic fault slip evolution source models of the 2008 M7.9 Wenchuan earthquake in China from SAR interferometry, GPS and teleseismic analysis and implications for Longmen Shan tectonics. *Geophysical Journal International*, *194*(2), 1138–1166. https://doi.org/10.1093/gji/ggt155

Fitch, T. J. (1972). Plate convergence, transcurrent faults, and internal deformation adjacent to Southeast Asia and the western Pacific. *Journal of Geophysical Research (1896-1977)*, *77*(23), 4432–4460. https://doi.org/10.1029/JB077i023p04432

Foster, J., Brooks, B., Cherubini, T., Shacat, C., Businger, S., & Werner, C. L. (2006). Mitigating atmospheric noise for InSAR using a high resolution weather model. *Geophysical Research Letters*, *33*(16). https://doi.org/10.1029/2006GL026781

Franco, S. I., Kostoglodov, V., Larson, K. M., Manea, V. C., Manea, M., & Santiago, J. A. (2005). Propagation of the 2001–2002 silent earthquake and interplate coupling in the Oaxaca subduction zone, Mexico. *Earth, Planets and Space*, *57*(10), 973–985. https://doi.org/10.1186/BF03351876

Frank, W. B. (2016). Slow slip hidden in the noise: The intermittence of tectonic release. *Geophysical Research Letters*, *43*(19), 10,125-10,133. https://doi.org/10.1002/2016GL069537

Frank, W. B., Shapiro, N. M., Husker, A. L., Kostoglodov, V., Romanenko, A., & Campillo, M. (2014). Using systematically characterized low-frequency earthquakes as a fault probe in Guerrero, Mexico: FRANK ET AL. *Journal of Geophysical Research: Solid Earth*, *119*(10), 7686–7700. https://doi.org/10.1002/2014JB011457

Frank, W. B., Radiguet, M., Rousset, B., Shapiro, N. M., Husker, A. L., Kostoglodov, V., Cotte, N., & Campillo, M. (2015). Uncovering the geodetic signature of silent slip through repeating earthquakes. *Geophysical Research Letters*, *42*(8), 2774–2779. https://doi.org/10.1002/2015GL063685

Frank, W. B., Poli, P., & Perfettini, H. (2017). Mapping the rheology of the Central Chile subduction zone with aftershocks. *Geophysical Research Letters*, *44*(11), 5374–5382. https://doi.org/10.1002/2016GL072288

Frank, W. B., Rousset, B., Lasserre, C., & Campillo, M. (2018). Revealing the cluster of slow transients behind a large slow slip event. *Science Advances*, *4*(5), eaat0661. https://doi.org/10.1126/sciadv.aat0661

Friedrich, A. M., Wernicke, B. P., Niemi, N. A., Bennett, R. A., & Davis, J. L. (2003). Comparison of geodetic and geologic data from the Wasatch region, Utah, and implications for the spectral character of Earth deformation at periods of 10 to 10 million years. *Journal of Geophysical Research*, *108*(B4), ETG7-1–23. https://doi.org/10.1029/2001JB000682

Fruneau, B., & Sarti, F. (2000). Detection of ground subsidence in the city of Paris using radar interferometry: isolation of deformation from atmospheric artifacts using correlation. *Geophysical Research Letters*, *27*(24), 3981–3984.

Fu, Y., & Freymueller, J. T. (2013). Repeated large Slow Slip Events at the southcentral Alaska subduction zone. *Earth and Planetary Science Letters*, *375*, 303–311. https://doi.org/10.1016/j.epsl.2013.05.049

Fuis, G. S. (1982). Displacement on the Superstition Hills fault triggered by the earthquake. In *The Imperial Valley, California, earthquake of October 15, 1979* (Vol. 1254, pp. 145–154). U.S. Geological Survey. https://doi.org/10.3133/pp1254

Fujiwara, S., Yarai, H., Ozawa, S., Tobita, M., Murakami, M., Nakagawa, H., Nitta, K., Rosen, P. A., & Werner, C. L. (1998). Surface displacement of the March 26, 1997 Kagoshima-Kenhokuseibu earthquake in Japan from synthetic aperture radar interferometry. *Geophysical Research Letters*, *25*(24), 4541–4.

Fukushima, Y., Ozawa, T., & Hashimoto, M. (2008). Fault model of the 2007 Noto Hanto earthquake estimated from PALSAR radar interferometry and GPS data. *Earth, Planets and Space*, *60*(2), 99–104. https://doi.org/10.1186/BF03352768

Fukushima, Y., Hashimoto, M., Miyazawa, M., Uchida, N., & Taira, T. (2019). Surface creep rate distribution along the Philippine fault, Leyte Island, and possible repeating of Mw ~ 6.5 earthquakes on an isolated locked patch. *Earth, Planets and Space*, *71*(1), 118. https://doi.org/10.1186/s40623-019-1096-5

Funning, G. J., Bürgmann, R., Ferretti, A., Novali, F., & Fumagalli, A. (2007). Creep on the Rodgers Creek fault, northern San Francisco Bay area from a 10 year PS-InSAR dataset. *Geophysical Research Letters*, *34*(19), L19306. https://doi.org/10.1029/2007GL030836

Furuya, M., & Satyabala, S. P. (2008). Slow earthquake in Afghanistan detected by InSAR. *Geophysical Research Letters*, *35*(6), L06309. https://doi.org/10.1029/2007GL033049

Gabriel, A. K., Goldstein, R. M., & Zebker, H. A. (1989). Mapping small elevation changes over large areas: Differential radar interferometry. *Journal of Geophysical Research: Solid Earth*, *94*(B7), 9183–9191. https://doi.org/10.1029/JB094iB07p09183

Gaidzik, K., Ramírez-Herrera, M. T., & Kostoglodov, V. (2016). Active Crustal Faults in the Forearc Region, Guerrero Sector of the Mexican Subduction Zone. *Pure and Applied Geophysics*, *173*(10–11), 3419–3443. https://doi.org/10.1007/s00024-015-1213-8

Galehouse, J. S., & Lienkaemper, J. J. (2003). Inferences Drawn from Two Decades of Alinement Array Measurements of Creep on Faults in the San Francisco Bay Region. *Bulletin of the Seismological Society of America*, *93*(6), 2415–2433. https://doi.org/10.1785/0120020226

Galloway, D. L., Hudnut, K. W., Ingebritsen, S. E., Phillips, S. P., Peltzer, G., Rogez, F., & Rosen, P. A. (1998). Detection of aquifer system compaction and land subsidence using interferometric synthetic aperture radar, Antelope Valley, Mojave Desert, California. *Water Resources Research*, *34*(10), 2573–2585.

Gardonio, B., Marsan, D., Socquet, A., Bouchon, M., Jara, J., Sun, Q., Cotte, N., & Campillo, M. (2018). Revisiting Slow Slip Events Occurrence in Boso Peninsula, Japan, Combining GPS Data and Repeating Earthquakes Analysis. *Journal of Geophysical Research: Solid Earth*, *123*(2), 1502–1515. https://doi.org/10.1002/2017JB014469

Garthwaite, M. C., Wang, H., & Wright, T. J. (2013). Broadscale interseismic deformation and fault slip rates in the central Tibetan Plateau observed using InSAR. *Journal of Geophysical Research: Solid Earth*, *118*(9), 5071–5083. https://doi.org/10.1002/jgrb.50348

Gladwin, M. T., Gwyther, R. L., Hart, R. H. G., & Breckenridge, K. S. (1994). Measurements of the strain field associated with episodic creep events on the San Andreas Fault at San Juan Bautista, California. *Journal of Geophysical Research: Solid Earth*, *99*(B3), 4559–4565. https://doi.org/10.1029/93JB02877

Godard, V., Ollivier, V., Bellier, O., Miramont, C., Shabanian, E., Fleury, J., Benedetti, L., & Guillou, V. (2016). Weathering-limited hillslope evolution in carbonate landscapes. *Earth and Planetary Science Letters*, *446*, 10–20. https://doi.org/10.1016/j.epsl.2016.04.017

Gold, R. D., Reitman, N. G., Briggs, R. W., Barnhart, W. D., Hayes, G. P., & Wilson, E. (2015). On- and off-fault deformation associated with the September 2013 Mw 7.7 Balochistan earthquake: Implications for geologic slip rate measurements. *Tectonophysics*, *660*, 65–78. https://doi.org/10.1016/j.tecto.2015.08.019

Gomba, G. (2018). Estimation of Ionosphere-Compensated Azimuth Ground Motion with Sentinel-1. In *EUSAR 2018; 12th European Conference on Synthetic Aperture Radar* (pp. 1–4).

Gomba, G., & De Zan, F. (2019). Estimating Soil Moisture from SAR Interferometry with Closure Phases. In *IGARSS 2019 - 2019 IEEE International Geoscience and Remote Sensing Symposium* (pp. 6983–6985). https://doi.org/10.1109/IGARSS.2019.8898546

Gomba, G., Parizzi, A., De Zan, F., Eineder, M., & Bamler, R. (2016). Toward Operational Compensation of Ionospheric Effects in SAR Interferograms: The Split-Spectrum Method. *IEEE Transactions on Geoscience and Remote Sensing*, *54*(3), 1446–1461. https://doi.org/10.1109/TGRS.2015.2481079

Gomba, G., Rodríguez González, F., & De Zan, F. (2017). Ionospheric Phase Screen Compensation for the Sentinel-1 TOPS and ALOS-2 ScanSAR Modes. *IEEE Transactions on Geoscience and Remote Sensing*, *55*(1), 223–235. https://doi.org/10.1109/TGRS.2016.2604461

Gomberg, J., & Bodin, P. (1994). Triggering of the Ms =5.4 Little Skull Mountain, Nevada, earthquake with dynamic strains. *Bulletin of the Seismological Society of America*, *84*(3), 844–53.

Graham, S. E., DeMets, C., Cabral-Cano, E., Kostoglodov, V., Walpersdorf, A., Cotte, N., Brudzinski, M. R., McCaffrey, R., & Salazar-Tlaczani, L. (2014). GPS constraints on the Mw = 7.5 Ometepec earthquake sequence, southern Mexico: coseismic and post-seismic deformation. *Geophysical Journal International*, *199*(1), 200–218. https://doi.org/10.1093/gji/ggu167

Graham, S. E., DeMets, C., Cabral-Cano, E., Kostoglodov, V., Rousset, B., Walpersdorf, A., Cotte, N., Lasserre, C., McCaffrey, R., & Salazar-Tlaczani, L. (2016). Slow Slip History for the Mexico Subduction Zone: 2005 Through 2011. *Pure and Applied Geophysics*, *173*(10–11), 3445–3465. https://doi.org/10.1007/s00024-015-1211-x

Grandin, Raphael. (2015). Interferometric Processing of SLC Sentinel-1 TOPS Data. In *Proceedings of FRINGE'15: Advances in the Science and Applications of SAR Interferometry and Sentinel-1 InSAR Workshop* (Vol. ESA SP-731). Frascati, Italy: ESA. https://doi.org/doi:10.5270/Fringe2015.116

Grandin, Raphaël, Doin, M.-P., Bollinger, L., Pinel-Puyssegur, B., Ducret, G., Jolivet, R., & Sapkota, S. N. (2012). Long-term growth of the Himalaya inferred from interseismic InSAR measurement. *Geology*, *40*(12), 1059–1062. https://doi.org/10.1130/G33154.1

Grandin, Raphaël, Vallée, M., Satriano, C., Lacassin, R., Klinger, Y., Simoes, M., & Bollinger, L. (2015). Rupture process of the Mw= 7.9 2015 Gorkha earthquake (Nepal): Insights into Himalayan megathrust segmentation. *Geophysical Research Letters*, *42*(20), 8373–8382. https://doi.org/10.1002/2015GL066044

Gratier, J.-P., Dysthe, D. K., & Renard, F. (2013). Chapter 2 - The Role of Pressure Solution Creep in the Ductility of the Earth's Upper Crust. In R. Dmowska (Ed.), *Advances in Geophysics* (Vol. 54, pp. 47–179). Elsevier. https://doi.org/10.1016/B978-0-12-380940-7.00002-0

Gratier, J.-P., Thouvenot, F., Jenatton, L., Tourette, A., Doan, M.-L., & Renard, F. (2013). Geological control of the partitioning between seismic and aseismic sliding behaviours in active faults: Evidence from the Western Alps, France. *Tectonophysics*, *600*, 226–242. https://doi.org/10.1016/j.tecto.2013.02.013

Graveleau, F., Suppe, J., Chang, K.-J., Dominguez, S., Ustazewski, M., & Huang, M.-H. (2014). Incremental vs. geological growth of folds: Examples of Tungshih anticline and Neiwan syncline during Taiwan Mw7.6 1999 ChiChi earthquake, *16*, 6910. Presented at the EGU General Assembly Conference Abstracts.

Gualandi, A., Perfettini, H., Radiguet, M., Cotte, N., & Kostoglodov, V. (2017). GPS deformation related to the Mw 7.3, 2014, Papanoa earthquake (Mexico) reveals the aseismic behavior of the Guerrero seismic gap. *Geophysical Research Letters*, *44*(12), 6039–6047. https://doi.org/10.1002/2017GL072913

Hamling, I. J., & Wallace, L. M. (2015). Silent triggering: Aseismic crustal faulting induced by a subduction slow slip event. *Earth and Planetary Science Letters*, *421*, 13–19. https://doi.org/10.1016/j.epsl.2015.03.046

Hammond, W. C., & D'Agostino, N. (2019). GPS Imaging of Uplift and Extension in the Apennines, Italy. *AGU Fall Meeting Abstracts*, *33*. Retrieved from http://adsabs.harvard.edu/abs/2019AGUFM.G33A..01H

Hardy, S., & Allmendinger, R. W. (2011). Trishear: A Review of Kinematics, Mechanics, and Applications. In K. R. McClay, J. H. Shaw, & J. Suppe (Eds.), *Thrust fold related folding*. American Association of Petroleum Geologists. Retrieved from DOI:10.1306/13251334M943429

Harris, R. A. (2017). Large earthquakes and creeping faults. *Reviews of Geophysics*, *55*(1), 169–198. https://doi.org/10.1002/2016RG000539

He, P., Wen, Y., Xu, C., Liu, Y., & Fok, H. S. (2015). New evidence for active tectonics at the boundary of the Kashi Depression, China, from time series InSAR observations. *Tectonophysics*, *653*, 140–148. https://doi.org/10.1016/j.tecto.2015.04.011

Hernandez, B., Cotton, F., Campillo, M., & Massonnet, D. (1997). A comparison between short-term (coseismic) and long-term (1 year) slip for the Landers earthquake; measurements from strong motion and SAR interferometry. *Geophysical Research Letters*, *24*(13), 1579–1582.

Hetland, E. A., & Hager, B. H. (2005). Postseismic and interseismic displacements near a strike-slip fault: A two-dimensional theory for general linear viscoelastic rheologies. *Journal of Geophysical Research: Solid Earth*, *110*(B10), B10401. https://doi.org/10.1029/2005JB003689

Hetland, E. A., Musé, P., Simons, M., Lin, Y. N., Agram, P. S., & DiCaprio, C. J. (2012). Multiscale InSAR Time Series (MInTS) analysis of surface deformation. *Journal of Geophysical Research: Solid Earth*, *117*(B2), n/a-n/a. https://doi.org/10.1029/2011JB008731

Hirose, H., & Obara, K. (2005). Repeating short- and long-term slow slip events with deep tremor activity around the Bungo channel region, southwest Japan. *Earth Planets and Space*, *57*(10;), 961–972.

Hirose, H., & Obara, K. (2006). Short-term slow slip and correlated tremor episodes in the Tokai region, central Japan. *Geophysical Research Letters*, *33*(17), L17311. https://doi.org/10.1029/2006GL026579

Hirose, H., Hirahara, K., Kimata, F., Fujii, N., & Miyazaki, S. (1999). A slow thrust slip event following the two 1996 Hyuganada Earthquakes beneath the Bungo Channel, southwest Japan. *Geophysical Research Letters*, *26*(21), 3237–3240. https://doi.org/10.1029/1999GL010999

Hirose, H., Kimura, H., Enescu, B., & Aoi, S. (2012). Recurrent slow slip event likely hastened by the 2011 Tohoku earthquake. *Proceedings of the National Academy of Sciences*, *109*(38), 15157–15161. https://doi.org/10.1073/pnas.1202709109

Hollingsworth, J., Ye, L., & Avouac, J.-P. (2017). Dynamically triggered slip on a splay fault in the Mw 7.8, 2016 Kaikoura (New Zealand) earthquake. *Geophysical Research Letters*, *44*(8), 3517–3525. https://doi.org/10.1002/2016GL072228

Holtkamp, S. G., & Brudzinski, M. R. (2011). Earthquake swarms in circum-Pacific subduction zones. *Earth and Planetary Science Letters*, *305*(1), 215–225. https://doi.org/10.1016/j.epsl.2011.03.004

Hooper, A. (2008). A multi-temporal InSAR method incorporating both persistent scatterer and small baseline approaches. *Geophysical Research Letters*, *35*(16), L16302. https://doi.org/10.1029/2008GL034654

Hooper, A., Zebker, H., Segall, P., & Kampes, B. (2004). A new method for measuring deformation on volcanoes and other natural terrains using InSAR persistent scatterers: A NEW PERSISTENT SCATTERERS METHOD. *Geophysical Research Letters*, *31*(23). https://doi.org/10.1029/2004GL021737

Hooper, A., Bekaert, D., Spaans, K., & Arıkan, M. (2012). Recent advances in SAR interferometry time series analysis for measuring crustal deformation. *Tectonophysics*, *514–517*, 1–13. https://doi.org/10.1016/j.tecto.2011.10.013

Hreinsdottir, S., & Bennett, R. A. (2009). Active aseismic creep on the Alto Tiberina low-angle normal fault, Italy. *Geology*, *37*(8), 683–686. https://doi.org/10.1130/G30194A.1

Hsieh, M.-L., & Knuepfer, P. L. K. (2001). Middle-late Holocene river terraces in the Erhjen River Basin, southwestern Taiwan : implications of river response to climate change and active tectonic uplift. *Geomorphology*, *38*(3–4), 337–372.

Hsieh, S. H. (1972). Subsurface Geology and Gravity Anomalies of the Tainan and Chungchou Structures of the Coastal Plain of Southwestern Taiwan. *Petroleum Geology of Taiwan*, *10*, 323–338.

Hsu, L., & Bürgmann, R. (2006). Surface creep along the Longitudinal Valley fault, Taiwan from InSAR measurements. *Geophysical Research Letters*, *33*(6), L06312. https://doi.org/10.1029/2005GL024624

Hsu, Y.-J., Yu, S.-B., Kuo, L.-C., Tsai, Y.-C., & Chen, H.-Y. (2011). Coseismic deformation of the 2010 Jiashian, Taiwan earthquake and implications for fault activities in southwestern Taiwan. *Tectonophysics*, *502*(3–4), 328–335. https://doi.org/10.1016/j.tecto.2011.02.005

Huang, M.-H., Bürgmann, R., & Hu, J.-C. (2016). Fifteen years of surface deformation in Western Taiwan: Insight from SAR interferometry. *Tectonophysics*, *692*, 252–264. https://doi.org/10.1016/j.tecto.2016.02.021

Huang, M.-H., Tung, H., Fielding, E. J., Huang, H.-H., Liang, C., Huang, C., & Hu, J.-C. (2016). Multiple fault slip triggered above the 2016 Mw 6.4 Meinong earthquake in Taiwan: Coseismic Slip Model of MeiNong Earthquake. *Geophysical Research Letters*, *43*(14), 7459–7467. https://doi.org/10.1002/2016GL069351

Huang, W.-J., & Johnson, K. M. (2016). A Fault-Cored Anticline Boundary Element Model Incorporating the Combined Fault Slip and Buckling Mechanisms. *Terrestrial, Atmospheric and Oceanic Sciences*, *27*(1), 073. https://doi.org/10.3319/TAO.2015.06.18.01(TT)

Hudnut, K., Seeber, L., Rockwell, T., Goodmacher, J., Klinger, R., Lindvall, S., & McElwain, R. (1989). Surface ruptures on cross-faults in the 24 November 1987 Superstition Hills, California, earthquake sequence. *Bulletin of the Seismological Society of America*, *79*(2), 282–296.

Husker, A., Ferrari, L., Arango-Galván, C., Corbo-Camargo, F., & Arzate-Flores, J. A. (2018). A geologic recipe for transient slip within the seismogenic zone: Insight from the Guerrero seismic gap, Mexico. *Geology*, *46*(1), 35–38. https://doi.org/10.1130/G39202.1

Husker, A., Frank, W. B., Gonzalez, G., Avila, L., Kostoglodov, V., & Kazachkina, E. (2019). Characteristic Tectonic Tremor Activity Observed Over Multiple Slow Slip Cycles in the Mexican Subduction Zone. *Journal of Geophysical Research: Solid Earth*, *124*(1), 599–608. https://doi.org/10.1029/2018JB016517

Hussain, E., Wright, T. J., Walters, R. J., Bekaert, D., Hooper, A., & Houseman, G. A. (2016). Geodetic observations of postseismic creep in the decade after the 1999 Izmit earthquake, Turkey: Implications for a shallow slip deficit. *Journal of Geophysical Research: Solid Earth*, *121*(4), 2980–3001. https://doi.org/10.1002/2015JB012737

Hussain, E., Hooper, A., Wright, T. J., Walters, R. J., & Bekaert, D. P. S. (2016). Interseismic strain accumulation across the central North Anatolian Fault from iteratively unwrapped InSAR measurements. *Journal of Geophysical Research: Solid Earth*, *121*(12), 9000–9019. https://doi.org/10.1002/2016JB013108

Hussain, E., Wright, T. J., Walters, R. J., Bekaert, D. P. S., Lloyd, R., & Hooper, A. (2018). Constant strain accumulation rate between major earthquakes on the North Anatolian Fault. *Nature Communications*, *9*(1), 1392. https://doi.org/10.1038/s41467-018-03739-2

Hyvärinen, A., & Oja, E. (1997). A Fast Fixed-Point Algorithm for Independent Component Analysis. *Neural Computation*, *9*(7), 1483–1492. https://doi.org/10.1162/neco.1997.9.7.1483

Ide, S., Beroza, G. C., Shelly, D. R., & Uchide, T. (2007). A scaling law for slow earthquakes. *Nature*, *447*(7140), 76–79. https://doi.org/10.1038/nature05780

Igarashi, T., Matsuzawa, T., & Hasegawa, A. (2003). Repeating earthquakes and interplate aseismic slip in the northeastern Japan subduction zone. *Journal of Geophysical Research: Solid Earth*, *108*(B5), Ese 8-1-8-9. https://doi.org/10.1029/2002JB001920

Iglesias, R., Mallorqui, J. J., Monells, D., López-Martínez, C., Fabregas, X., Aguasca, A., Gili, J. A., & Corominas, J. (2015). PSI Deformation Map Retrieval by Means of Temporal Sublook Coherence on Reduced Sets of SAR Images. *Remote Sensing*, *7*(1), 530–563. https://doi.org/10.3390/rs70100530

Ihmlé, P. F., & Jordan, T. H. (1994). Teleseismic Search for Slow Precursors to Large Earthquakes. *Science*, *266*(5190), 1547–1551. https://doi.org/10.1126/science.266.5190.1547

Ingleby, T., & Wright, T. J. (2017). Omori-like decay of postseismic velocities following continental earthquakes. *Geophysical Research Letters*, *44*(7), 3119–3130. https://doi.org/10.1002/2017GL072865

Jarrard, R. D. (1986). Relations among subduction parameters. *Reviews of Geophysics*, *24*(2), 217–284. https://doi.org/10.1029/RG024i002p00217

Jiang, G.-J., Angelier, J., Lee, J.-C., Chu, H., Hu, J.-C., & Mu, C.-H. (2011). Faulting and Mud Volcano Eruptions Inside of the Coastal Range During the 2003 M-w=6.8 Chengkung Earthquake in Eastern Taiwan. *Terrestrial, Atmospheric and Oceanic Sciences*, *22*, 463–473. https://doi.org/10.3319/TAO.2011.04.22.01(TT)

Jiang, Y., Wdowinski, S., Dixon, T. H., Hackl, M., Protti, M., & Gonzalez, V. (2012). Slow slip events in Costa Rica detected by continuous GPS observations, 2002-2011. *Geochemistry, Geophysics, Geosystems*, *13*(4), n/a-n/a. https://doi.org/10.1029/2012GC004058

Johanson, I. A., & Bürgmann, R. (2005). Creep and quakes on the northern transition zone of the San Andreas fault from GPS and InSAR data: SAN JUAN BAUTISTA CREEP AND QUAKES. *Geophysical Research Letters*, *32*(14), n/a-n/a. https://doi.org/10.1029/2005GL023150

Johnson, K. M., & Segall, P. (2004). Viscoelastic earthquake cycle models with deep stress-driven creep along the San Andreas fault system. *Journal of Geophysical Research: Solid Earth*, *109*(B10). https://doi.org/10.1029/2004JB003096

Johnson, Kaj M. (2018). Growth of Fault-Cored Anticlines by Flexural Slip Folding: Analysis by Boundary Element Modeling. *Journal of Geophysical Research: Solid Earth*, *123*(3), 2426–2447. https://doi.org/10.1002/2017JB014867

Johnson, Kaj M., & Johnson, A. M. (2002). Mechanical models of trishear-like folds. *Journal of Structural Geology*, *24*(2), 277–287. https://doi.org/10.1016/S0191-8141(01)00062-1

Johnston, M. J. S., Mchugh, S., & Burford, R. O. (1976). On simultaneous tilt and creep observations on the San Andreas Fault. *Nature*, *260*(5553), 691–693. https://doi.org/10.1038/260691b0

Johnston, M. J. S., Jones, A. C., & Daul, W. (1977). Continuous strain measurements during and preceding episodic creep on the San Andreas Fault. *Journal of Geophysical Research (1896-1977)*, *82*(36), 5683–5691. https://doi.org/10.1029/JB082i036p05683

Jolivet, R., & Frank, W. B. (2020). The Transient and Intermittent Nature of Slow Slip. *AGU Advances*, *1*(1), e2019AV000126. https://doi.org/10.1029/2019AV000126

Jolivet, R., Grandin, R., Lasserre, C., Doin, M.-P., & Peltzer, G. (2011). Systematic InSAR tropospheric phase delay corrections from global meteorological reanalysis data. *Geophysical Research Letters*, *38*(17). https://doi.org/10.1029/2011GL048757

Jolivet, R., Lasserre, C., Doin, M.-P., Guillaso, S., Peltzer, G., Dailu, R., Sun, J., Shen, Z.-K., & Xu, X. (2012). Shallow creep on the Haiyuan Fault (Gansu, China) revealed by SAR Interferometry. *Journal of Geophysical Research: Solid Earth*, *117*(B6). https://doi.org/10.1029/2011JB008732

Jolivet, R., Lasserre, C., Doin, M.-P., Peltzer, G., Avouac, J.-P., Sun, J., & Dailu, R. (2013). Spatio-temporal evolution of aseismic slip along the Haiyuan fault, China: Implications for fault frictional properties. *Earth and Planetary Science Letters*, *377–378*, 23–33. https://doi.org/10.1016/j.epsl.2013.07.020

Jolivet, R., Duputel, Z., Riel, B., Simons, M., Rivera, L., Minson, S. E., Zhang, H., Aivazis, M. A. G., Ayoub, F., Leprince, S., Samsonov, S., Motagh, M., & Fielding, E. J. (2014). The 2013 Mw 7.7 Balochistan Earthquake: Seismic Potential of an Accretionary Wedge. *Bulletin of the Seismological Society of America*, *104*(2), 1020–1030. https://doi.org/10.1785/0120130313

Jolivet, R., Simons, M., Agram, P. S., Duputel, Z., & Shen, Z.-K. (2015). Aseismic slip and seismogenic coupling along the central San Andreas Fault. *Geophysical Research Letters*, *42*(2), 297–306. https://doi.org/10.1002/2014GL062222

Jolivet, R., Candela, T., Lasserre, C., Renard, F., Klinger, Y., & Doin, M.-P. (2015). The Burst-Like Behavior of Aseismic Slip on a Rough Fault: The Creeping Section of the Haiyuan Fault, ChinaShort Note. *Bulletin of the Seismological Society of America*, *105*(1), 480–488. https://doi.org/10.1785/0120140237

Jolivet, R., Simons, M., Duputel, Z., Olive, J.-A., Bhat, H. S., & Bletery, Q. (2020). Interseismic Loading of Subduction Megathrust Drives Long-Term Uplift in Northern Chile. *Geophysical Research Letters*, *47*(8), e2019GL085377. https://doi.org/10.1029/2019GL085377

Jonsson, S., Zebker, H. A., Segall, P., & Amelung, F. (2002). Fault slip distribution of the 1999 Mw 7.1 Hector Mine, California, earthquake, estimated from satellite radar and GPS measurements. *Bulletin of the Seismological Society of America*, *92*(4), 1377–1389.

Jouanne, F., Awan, A., Madji, A., Pêcher, A., Latif, M., Kausar, A., Mugnier, J. L., Khan, I., & Khan, N. A. (2011). Postseismic deformation in Pakistan after the 8 October 2005 earthquake: Evidence of afterslip along a flat north of the Balakot-Bagh thrust. *Journal of Geophysical Research*, *116*(B7), B07401. https://doi.org/10.1029/2010JB007903

Jouanne, François, Audemard, F. A., Beck, C., Van Welden, A., Ollarves, R., & Reinoza, C. (2011). Present-day deformation along the El Pilar Fault in eastern Venezuela: Evidence of creep along a major transform boundary. *Journal of Geodynamics*, *51*(5), 398–410. https://doi.org/10.1016/j.jog.2010.11.003

Jung, H.-S., & Hong, S.-M. (2017). Mapping three-dimensional surface deformation caused by the 2010 Haiti earthquake using advanced satellite radar interferometry. *PLOS ONE*, *12*(11), e0188286. https://doi.org/10.1371/journal.pone.0188286

Kaduri, M., Gratier, J.-P., Renard, F., Çakir, Z., & Lasserre, C. (2017). The implications of fault zone transformation on aseismic creep: Example of the North Anatolian Fault, Turkey. *Journal of Geophysical Research: Solid Earth*, *122*(6), 4208–4236. https://doi.org/10.1002/2016JB013803

Kaduri, M., Gratier, J.-P., Lasserre, C., Çakir, Z., & Renard, F. (2019). Quantifying the Partition Between Seismic and Aseismic Deformation Along Creeping and Locked Sections of the North Anatolian Fault, Turkey. *Pure and Applied Geophysics*, *176*(3), 1293–1321. https://doi.org/10.1007/s00024-018-2027-2

Kampes, B. M., & Adam, N. (2003). Velocity Field Retrieval from Long Term Coherent Points in Radar Interferometric Stacks. Presented at the IGARSS 2003. IEEE 2003 International Geoscience and Remote Sensing Symposium, Toulouse, France: IEEE, Piscataway, NJ, USA.

Kanamori, H. (1972). Mechanism of tsunami earthquakes. *Physics of the Earth and Planetary Interiors*, *6*(5), 346–359. https://doi.org/10.1016/0031-9201(72)90058-1

Kanamori, H., & Cipar, J. J. (1974). Focal process of the great Chilean earthquake May 22, 1960. *Physics of the Earth and Planetary Interiors*, *9*(2), 128–136. https://doi.org/10.1016/0031-9201(74)90029-6

Kanamori, H., & Kikuchi, M. (1993). The 1992 Nicaragua earthquake: a slow tsunami earthquake associated with subducted sediments. *Nature*, *361*(6414), 714–716. https://doi.org/10.1038/361714a0

Kanamori, H., & Stewart, G. S. (1979). A slow earthquake. *Physics of the Earth and Planetary Interiors*, *18*(3), 167–175. https://doi.org/10.1016/0031-9201(79)90112-2

Kaneko, Y., & Fialko, Y. (2011). Shallow slip deficit due to large strike-slip earthquakes in dynamic rupture simulations with elasto-plastic off-fault response. *Geophysical Journal International*, *186*(3), 1389–1403. https://doi.org/10.1111/j.1365-246X.2011.05117.x

Kaneko, Y., Fialko, Y., Sandwell, D. T., Tong, X., & Furuya, M. (2013). Interseismic deformation and creep along the central section of the North Anatolian Fault (Turkey): InSAR observations and implications for rate-and-state friction properties. *Journal of Geophysical Research: Solid Earth*, *118*(1), 316–331. https://doi.org/10.1029/2012JB009661

Kaneko, Y., Hamling, I. J., Van Dissen, R. J., Motagh, M., & Samsonov, S. V. (2015). InSAR imaging of displacement on flexural-slip faults triggered by the 2013 Mw 6.6 Lake Grassmere earthquake, central New Zealand. *Geophysical Research Letters*, *42*(3), 2014GL062767. https://doi.org/10.1002/2014GL062767

Kang, C.-C., Chang, C.-P., Siame, L., & Lee, J.-C. (2015). Present-day surface deformation and tectonic insights of the extensional Ilan Plain, NE Taiwan. *Journal of Asian Earth Sciences*, *105*, 408–417. https://doi.org/10.1016/j.jseaes.2015.02.013

Kano, M., Fukuda, J., Miyazaki, S., & Nakamura, M. (2018). Spatiotemporal Evolution of Recurrent Slow Slip Events Along the Southern Ryukyu Subduction Zone, Japan, From 2010 to 2013. *Journal of Geophysical Research: Solid Earth*. https://doi.org/10.1029/2018JB016072

Kato, A., Obara, K., Igarashi, T., Tsuruoka, H., Nakagawa, S., & Hirata, N. (2012). Propagation of Slow Slip Leading Up to the 2011 Mw 9.0 Tohoku-Oki Earthquake. *Science*, *335*(6069), 705–708. https://doi.org/10.1126/science.1215141

Kazachkina, E., Kostoglodov, V., Cotte, N., Walpersdorf, A., Ramirez-Herrera, M. T., Gaidzik, K., Husker, A., & Santiago, J. A. (2020). Active 650-km Long Fault System and Xolapa Sliver in Southern Mexico. *Frontiers in Earth Science*, *8*, 155. https://doi.org/10.3389/feart.2020.00155

Kelleher, J., Sykes, L., & Oliver, J. (1973). Possible criteria for predicting earthquake locations and their application to major plate boundaries of the Pacific and the Caribbean. *Journal of Geophysical Research*, *78*(14), 2547–2585. https://doi.org/10.1029/JB078i014p02547

Kellogg, K., Hoffman, P., Standley, S., Shaffer, S., Rosen, P., Edelstein, W., Dunn, C., Baker, C., Barela, P., Shen, Y., Guerrero, A. M., Xaypraseuth, P., Sagi, V. R., Sreekantha, C. V., Harinath, N., Kumar, R., Bhan, R., & Sarma, C. V. H. S. (2020). NASA-ISRO Synthetic Aperture Radar (NISAR) Mission. In *2020 IEEE Aerospace Conference* (pp. 1–21). https://doi.org/10.1109/AERO47225.2020.9172638

Khoshmanesh, M., Shirzaei, M., & Uchida, N. (2020). Deep slow-slip events promote seismicity in northeastern Japan megathrust. *Earth and Planetary Science Letters*, *540*, 116261. https://doi.org/10.1016/j.epsl.2020.116261

King, G. C. P., & Vita-Finzi, C. (1981). Active folding in the Algerian earthquake of 10 October 1980. *Nature*, *292*(5818), 22–26. https://doi.org/10.1038/292022a0

King, G. C. P., Bilham, R. G., Campbell, J. W., Mckenzie, D. P., & Niazi, M. (1975). Detection of elastic strainfields caused by fault creep events in Iran. *Nature*, *253*(5491), 420–423. https://doi.org/10.1038/253420a0

King, Geoffrey C. P., Stein, R. S., & Rundle, J. B. (1988). The Growth of Geological Structures by Repeated Earthquakes 1. Conceptual Framework. *Journal of Geophysical Research: Solid Earth*, *93*(B11), 13307–13318. https://doi.org/10.1029/JB093iB11p13307

Klein, E., Duputel, Z., Zigone, D., Vigny, C., Boy, J. -P., Doubre, C., & Meneses, G. (2018). Deep Transient Slow Slip Detected by Survey GPS in the Region of Atacama, Chile. *Geophysical Research Letters*, *45*(22), 12,263-12,273. https://doi.org/10.1029/2018GL080613

Klinger, R. E., & Rockwell, T. K. (1989). Flexural-slip folding along the Eastern Elmore Ranch fault in the Superstition Hills earthquake sequence of November 1987. *Bulletin of the Seismological Society of America*, *79*(2), 297–303.

Klinger, Y., Michel, R., & King, G. (2006). Evidence for an earthquake barrier model from Mw∼7.8 Kokoxili (Tibet) earthquake slip-distribution. *Earth and Planetary Science Letters*, *242*(3–4), 354–364. https://doi.org/10.1016/j.epsl.2005.12.003

Kniess, U. (2011, October 24). *Quantification de l'évolution de glissement de terrain argileux par des techniques de télédétection. Application à la région du Tirèves (Alpes Françaises)* (PhD). *ISTerre*. Université de Grenoble, Grenoble. Retrieved from https://tel.archives-ouvertes.fr/tel-00728238/document

Kobayashi, T., Tobita, M., Nishimura, T., Suzuki, A., Noguchi, Y., & Yamanaka, M. (2011). Crustal deformation map for the 2011 off the Pacific coast of Tohoku Earthquake, detected by InSAR analysis combined with GEONET data. *Earth, Planets and Space*, *63*(7), 20. https://doi.org/10.5047/eps.2011.06.043

Kostoglodov, V., Singh, S. K., Santiago, J. A., Franco, S. I., Larson, K. M., Lowry, A. R., & Bilham, R. (2003). A large silent earthquake in the Guerrero seismic gap, Mexico. *Geophysical Research Letters*, *30*(15), Sde9.1-Sde9.4. https://doi.org/10.1029/2003GL017219

Kostoglodov, V., Husker, A., Shapiro, N. M., Payero, J. S., Campillo, M., Cotte, N., & Clayton, R. (2010). The 2006 slow slip event and nonvolcanic tremor in the Mexican subduction zone. *Geophysical Research Letters*, *37*(24), n/a-n/a. https://doi.org/10.1029/2010GL045424

Kostoglodov, V., Husker, A. L., Santiago, J. A., Cruz-Atienza, V. M., Cotte, N., & Walpersdorf, A. (2015). *Three types of Slow Slip Events in Guerrero, Mexico*. Presented at the Tectonic Tremor and Silent Seismicity, 25-27 February 2015 International Workshop, Instituto de Geofisica, UNAM, Mexico.

LaBonte, A. L., Brown, K. M., & Fialko, Y. (2009). Hydrologic detection and finite element modeling of a slow slip event in the Costa Rica prism toe. *Journal of Geophysical Research: Solid Earth*, *114*(B4). https://doi.org/10.1029/2008JB005806

Lacombe, O., Mouthereau, F., Deffontaines, B., Angelier, J., Chu, H.-T., & Lee, C.-T. (1999). Geometry and Quaternary kinematics of fold-and-thrust units of southwestern Taiwan. *Tectonics*, *18*(6), 1198–223.

Lacombe, O., Angelier, J., Mouthereau, F., Chu, H.-T., Lee, J.-C., Deffontaines, B., Rocher, M., Chen, R.-F., & Siame, L. (2004). The Liuchiu Hsu island offshore SW Taiwan : tectonic vs diapiric anticline development and comparisons with onshore structures. *Comptes Rendus Geosciences*, *336*(9), 815–825. https://doi.org/10.1016/j.crte.2004.02.007

Lanari, R., Mora, O., Manunta, M., Mallorqui, J. J., Berardino, P., & Sansosti, E. (2004). A small-baseline approach for investigating deformations on full-resolution differential SAR interferograms. *IEEE Transactions on Geoscience and Remote Sensing*, *42*(7), 1377–1386.

Lapusta, N., & Liu, Y. (2009). Three-dimensional boundary integral modeling of spontaneous earthquake sequences and aseismic slip. *Journal of Geophysical Research: Solid Earth*, *114*(B9). https://doi.org/10.1029/2008JB005934

Larson, K. M., Lowry, A. R., Kostoglodov, V., Hutton, W., Sánchez, O., Hudnut, K., & Suárez, G. (2004). Crustal deformation measurements in Guerrero, Mexico. *Journal of Geophysical Research: Solid Earth*, *109*(B4). https://doi.org/10.1029/2003JB002843

Larson, K. M., Kostoglodov, V., Miyazaki, S., & Santiago, J. A. S. (2007). The 2006 aseismic slow slip event in Guerrero, Mexico: New results from GPS. *Geophysical Research Letters*, *34*(13), n/a-n/a. https://doi.org/10.1029/2007GL029912

Lasserre, C., Peltzer, G., Crampé, F., Klinger, Y., Van der Woerd, J., & Tapponnier, P. (2005). Coseismic deformation of the 2001 Mw = 7.8 Kokoxili earthquake in Tibet, measured by synthetic aperture radar interferometry. *Journal of Geophysical Research*, *110*(B12), B12408. https://doi.org/10.1029/2004JB003500

Lee, J.-C. (1994). *Structure et déformation active d'un orogène: Taiwan* (Ph.D. Thesis;). *Laboratoire de Tectonique*. Université Pierre et Marie Curie, Paris, France.

Lee, J.-C., & Angelier, J. (1993). Localisation des déformations actives et traitement des données géodsiques : L'exemple de la faille de la Vallée Longitudinale, Taïwan. *Bulletin de La Societe Geologique de France*, *164*(4), 533–540.

Lee, J.-C., Angelier, J., Chu, H.-T., Yu, S.-B., & Hu, J.-C. (1998). Plate-boundary strain partitioning along the sinistral collision suture of the Philippine and Eurasian plates: analysis of geodetic data and geological observation in southeastern Taiwan. *Tectonics*, *17*(6), 859–71.

Lee, J.-C., Jeng, F.-S., Chu, H.-T., Angelier, J., & Hu, J.-C. (2000). A rod-type creepmeter for measurement of displacement in active fault zone. *Earth, Planets and Space*, *52*(5), 321–8.

Lee, J.-C., Chen, Y.-G., Sieh, K., Mueller, K., Chen, W.-S., Chu, H.-T., Chan, Y.-C., Rubin, C., & Yeats, R. S. (2001). A vertical exposure of the 1999 surface rupture of the Chelungpu Fault at Wufeng, western Taiwan; structural and paleoseismic implications for an active thrust fault. *Bulletin of the Seismological Society of America*, *91*(5), 914–929. https://doi.org/10.1785/0120000742

Lee, J.-C., Angelier, J., Chu, H.-T., Hu, J.-C., & Jeng, F.-S. (2001). Continuous monitoring of an active fault in a plate suture zone: a creepmeter study of the Chihshang Fault, eastern Taiwan. *Tectonophysics*, *333*(1–2), 219–240.

Lee, J.-C., Angelier, J., Chu, H.-T., Hu, J.-C., Jeng, F.-S., & Rau, R.-J. (2003). Active fault creep variations at Chihshang, Taiwan, revealed by creep meter monitoring, 1998-2001. *Journal of Geophysical Research*, *108*(B11), Etg4.1-Etg4.21. https://doi.org/10.1029/2003JB002394

Lee, J.-C., Rubin, C., Mueller, K., Chen, Y.-G., Chan, Y.-C., Sieh, K., Chu, H.-T., & Chen, W.-S. (2004). Quantitative analysis of movement along an earthquake thrust scarp: a case study of a vertical exposure of the 1999 surface rupture of the Chelungpu fault at Wufeng, Western Taiwan. *Journal of Asian Earth Sciences*, *23*(2), 263–273. https://doi.org/10.1016/S1367-9120(03)00122-6

Lee, J.-C., Angelier, J., Chu, H.-T., Hu, J.-C., & Jeng, F. S. (2005). Monitoring active fault creep as a tool in seismic hazard mitigation. Insights from creepmeter study at Chihshang, Taiwan. *Comptes Rendus Geoscience*, *337*(13), 1200–1207.

Lee, J.-C., Chu, H.-T., Angelier, J., Hu, J.-C., Chen, H.-Y., & Yu, S.-B. (2006). Quantitative analysis of surface coseismic faulting and postseismic creep accompanying the 2003, Mw = 6.5, Chengkung earthquake in eastern Taiwan. *Journal of Geophysical Research: Solid Earth*, *111*(B2). https://doi.org/10.1029/2005JB003612

Leon, L. A., Christofferson, S. A., Dolan, J. F., Shaw, J. H., & Pratt, T. L. (2007). Earthquake-by-earthquake fold growth above the Puente Hills blind thrust fault, Los Angeles, California: Implications for fold kinematics and seismic hazard. *Journal of Geophysical Research: Solid Earth*, *112*(B3), B03S03. https://doi.org/10.1029/2006JB004461

Leprince, S., Barbot, S., Ayoub, F., & Avouac, J.-P. (2007). Automatic and Precise Orthorectification, Coregistration, and Subpixel Correlation of Satellite Images, Application to Ground Deformation Measurements. *IEEE Transactions on Geoscience and Remote Sensing*, *45*(6), 1529–1558. https://doi.org/10.1109/TGRS.2006.888937

Li, Z., Fielding, E. J., Cross, P., & Muller, J.-P. (2006). Interferometric synthetic aperture radar atmospheric correction: GPS topography-dependent turbulence model. *Journal of Geophysical Research: Solid Earth*, *111*(B2), n/a-n/a. https://doi.org/10.1029/2005JB003711

Liang, C., Liu, Z., Fielding, E. J., & Burgmann, R. (2018). InSAR Time Series Analysis of L-Band Wide-Swath SAR Data Acquired by ALOS-2. *IEEE Transactions on Geoscience and Remote Sensing*, *56*(8), 4492–4506. https://doi.org/10.1109/TGRS.2018.2821150

Lienkaemper, J. J., DeLong, S. B., Domrose, C. J., & Rosa, C. M. (2016). Afterslip Behavior following the 2014 M 6.0 South Napa Earthquake with Implications for Afterslip Forecasting on Other Seismogenic Faults. *Seismological Research Letters*, *87*(3), 609–619. https://doi.org/10.1785/0220150262

Lin, K.-C., Delouis, B., Hu, J.-C., Nocquet, J.-M., & Mozziconacci, L. (2016). Reassessing the complexity of the rupture of the 2010 Jia-Shian earthquake (Mw 6.2) in Southwestern Taiwan by inverting jointly teleseismic, strong-motion and CGPS data. *Tectonophysics*, *692*, 278–294. https://doi.org/10.1016/j.tecto.2015.09.015

Lin, Y. N., Jolivet, R., Simons, M., Agram, P. S., Martens, H. R., Li, Z., & Lodi, S. H. (2015). High interseismic coupling in the Eastern Makran (Pakistan) subduction zone. *Earth and Planetary Science Letters*, *420*, 116–126. https://doi.org/10.1016/j.epsl.2015.03.037

Linde, A. T., & Silver, P. G. (1989). Elevation changes and the Great 1960 Chilean Earthquake: Support for aseismic slip. *Geophysical Research Letters*, *16*(11), 1305–1308. https://doi.org/10.1029/GL016i011p01305

Linde, A. T., Suyehiro, K., Miura, S., Sacks, I. S., & Takagi, A. (1988). Episodic aseismic earthquake precursors. *Nature*, *334*(6182), 513–515. https://doi.org/10.1038/334513a0

Linde, A. T., Gladwin, M. T., Johnston, M. J. S., Gwyther, R. L., & Bilham, R. (1996). A slow earthquake sequence on the San Andreas fault. *Nature*, *383*(6595), 65–68. https://doi.org/10.1038/383065a0

Lindsey, E. O., Fialko, Y., Bock, Y., Sandwell, D. T., & Bilham, R. (2014). Localized and distributed creep along the southern San Andreas Fault. *Journal of Geophysical Research: Solid Earth*, *119*(10), 7909–7922. https://doi.org/10.1002/2014JB011275

Lindsey, E. O., Natsuaki, R., Xu, X., Shimada, M., Hashimoto, M., Melgar, D., & Sandwell, D. T. (2015). Line-of-sight displacement from ALOS-2 interferometry: Mw 7.8 Gorkha Earthquake and Mw 7.3 aftershock. *Geophysical Research Letters*, *42*(16), 6655–6661. https://doi.org/10.1002/2015GL065385

Lisowski, M., & Prescott, W. H. (1981). Short-range distance measurements along the San Andreas fault system in central California, 1975 to 1979. *Bulletin of the Seismological Society of America*, *71*(5), 1607–1624.

Liu, C.-C., Maity, J. P., Jean, J.-S., Reza, A. H. M. S., Li, Z., Nath, B., Lee, M.-K., Lin, K.-H., & Bhattacharya, P. (2012). Geochemical characteristics of the mud volcano fluids in southwestern Taiwan and their possible linkage to elevated arsenic concentration in Chianan plain groundwater. *Environmental Earth Sciences*, *66*(5), 1513–1523. https://doi.org/10.1007/s12665-011-1391-3

Liu, C.-S., Huang, I. L., & Teng, L. S. (1997). Structural features off southwestern Taiwan. *Marine Geology*, *137*(3–4), 305–319. https://doi.org/10.1016/S0025-3227(96)00093-X

Liu, Y., Rice, J. R., & Larson, K. M. (2007). Seismicity variations associated with aseismic transients in Guerrero, Mexico, 1995–2006. *Earth and Planetary Science Letters*, *262*(3–4), 493–504. https://doi.org/10.1016/j.epsl.2007.08.018

Loevenbruck, A., & Cattin, R. (2001). Slip distribution of the 21 September earthquake in Taiwan from inversion of GPS and SPOT images. *EOS Transactions of the American Geophysical Union*, *87*(47), F1177, abstract T32A-0871.

López-Quiroz, P., Doin, M.-P., Tupin, F., Briole, P., & Nicolas, J.-M. (2009). Time series analysis of Mexico City subsidence constrained by radar interferometry. *Journal of Applied Geophysics*, *69*(1), 1–15. https://doi.org/10.1016/j.jappgeo.2009.02.006

Loveless, J. P., & Meade, B. J. (2016). Two decades of spatiotemporal variations in subduction zone coupling offshore Japan. *Earth and Planetary Science Letters*, *436*, 19–30. https://doi.org/10.1016/j.epsl.2015.12.033

Lowry, A. R., Larson, K. M., Kostoglodov, V., & Bilham, R. (2001). Transient fault slip in Guerrero, southern Mexico. *Geophysical Research Letters*, *28*(19), 3753–3756. https://doi.org/10.1029/2001GL013238

Lyons, S. N., & Sandwell, D. T. (2003). Fault creep along the southern San Andreas from interferometric synthetic aperture radar, permanent scatterers, and stacking. *Journal of Geophysical Research*, *108*(B1), Etg11.1-Etg11.24. https://doi.org/10.1029/2002JB001831

Mai, P. M., & Thingbaijam, K. K. S. (2014). SRCMOD: An Online Database of Finite-Fault Rupture Models. *Seismological Research Letters*, *85*(6), 1348–1357. https://doi.org/10.1785/0220140077

Manighetti, I., King, G., & Sammis, C. G. (2004). The role of off-fault damage in the evolution of normal faults. *Earth and Planetary Science Letters*, *217*(3–4), 399–408. https://doi.org/10.1016/S0012-821X(03)00601-0

Manighetti, I., Campillo, M., Sammis, C., Mai, P. M., & King, G. C. P. (2005). Evidence for self-similar, triangular slip distributions on earthquakes : Implications for earthquake and fault mechanics. *Journal of Geophysical Research*, *110*(B5), B05302.1-B05302.25. https://doi.org/10.1029/2004JB003174

Marchandon, M., Hollingsworth, J., & Radiguet, M. (2020). Origin of the Shallow Slip Deficit on a strike slip fault: influence of elastic structure, topography, and data coverage. *EPSL*, *in review*.

Marinière, J., Nocquet, J.-M., Beauval, C., Champenois, J., Audin, L., Alvarado, J. A., Baize, S., & Socquet, A. (2020). Geodetic evidence for shallow creep along the Quito fault, Ecuador. *Geophysical Journal International*, *220*(3), 2039–2055. https://doi.org/10.1093/gji/ggz564

Marone, C. (1998). Laboratory-derived friction laws and their application to seismic faulting. *Annual Review of Earth and Planetary Sciences*, *26*(1), 643–696. https://doi.org/10.1146/annurev.earth.26.1.643

Marone, C., & Scholz, C. H. (1988). The depth of seismic faulting and the upper transition from stable to unstable slip regimes. *Geophysical Research Letters*, *15*(6), 621–624. https://doi.org/10.1029/GL015i006p00621

Marone, C., Raleigh, C. B., & Scholz, C. H. (1990). Frictional behavior and constitutive modeling of simulated fault gouge. *Journal of Geophysical Research: Solid Earth*, *95*(B5), 7007–7025. https://doi.org/10.1029/JB095iB05p07007

Marsan, D., Prono, E., & Helmstetter, A. (2013). Monitoring Aseismic Forcing in Fault Zones Using Earthquake Time Series. *Bulletin of the Seismological Society of America*, *103*(1), 169–179. https://doi.org/10.1785/0120110304

Marsan, D., Bouchon, M., Gardonio, B., Perfettini, H., Socquet, A., & Enescu, B. (2017). Change in seismicity along the Japan trench, 1990–2011, and its relationship with seismic coupling. *Journal of Geophysical Research: Solid Earth*, *122*(6), 4645–4659. https://doi.org/10.1002/2016JB013715

Marshall, S. T., Funning, G. J., & Owen, S. E. (2013). Fault slip rates and interseismic deformation in the western Transverse Ranges, California. *Journal of Geophysical Research: Solid Earth*, *118*(8), 4511–4534. https://doi.org/10.1002/jgrb.50312

Masson, C., Mazzotti, S., Vernant, P., & Doerflinger, E. (2019). Extracting small deformation beyond individual station precision from dense Global Navigation Satellite System (GNSS) networks in France and western Europe. *Solid Earth*, *10*(6), 1905–1920. https://doi.org/10.5194/se-10-1905-2019

Massonnet, D., & Feigl, K. L. (1998). Radar interferometry and its application to changes in the Earth's surface. *Reviews of Geophysics*, *36*(4), 441–500. https://doi.org/10.1029/97RG03139

Massonnet, D., Rossi, M., Carmona, C., Adragna, F., Peltzer, G., Feigl, K. L., & Rabaute, T. (1993). The displacement field of the Landers earthquake mapped by radar interferometry. *Nature*, *364*(6433), 138–142.

Massonnet, D., Feigl, K., Rossi, M., & Adragna, F. (1994). Radar interferometric mapping of deformation in the year after the Landers earthquake. *Nature*, *369*(6477), 227–230. https://doi.org/10.1038/369227a0

Massonnet, D., Feigl, K. L., Vadon, H., & Rossi, M. (1996). Coseismic deformation field of the M = 6.7 Northridge, California earthquake of January 17, 1994 recorded by two radar satellites using interferometry. *Geophysical Research Letters*, *23*(9), 969–972.

Massonnet, D., Thatcher, W., & Vadon, H. (1996). Detection of postseismic fault-zone collapse following the Landers earthquake. *Nature*, *382*(6592), 612–616.

Matsumura, S. (2006). Seismic activity changes progressing simultaneously with slow-slip in the Tokai area. *Tectonophysics*, *417*(1–2), 5–15. https://doi.org/10.1016/j.tecto.2005.08.026

Maubant, L., Pathier, E., Daout, S., Radiguet, M., Doin, M.-P., Kazachkina, E., Kostoglodov, V., Cotte, N., & Walpersdorf, A. (2020). Independent Component Analysis and Parametric Approach for Source Separation in InSAR Time Series at Regional Scale: Application to the 2017–2018 Slow Slip Event in Guerrero (Mexico). *Journal of Geophysical Research: Solid Earth*, *125*(3). https://doi.org/10.1029/2019JB018187

Maury, J., Ide, S., Cruz-Atienza, V. M., & Kostoglodov, V. (2018). Spatiotemporal Variations in Slow Earthquakes Along the Mexican Subduction Zone. *Journal of Geophysical Research: Solid Earth*, *123*(2), 1559–1575. https://doi.org/10.1002/2017JB014690

Mavrommatis, A. P., Segall, P., Uchida, N., & Johnson, K. M. (2015). Long-term acceleration of aseismic slip preceding the Mw 9 Tohoku-oki earthquake: Constraints from repeating earthquakes. *Geophysical Research Letters*, *42*(22), 9717–9725. https://doi.org/10.1002/2015GL066069

Mazzotti, S., & Adams, J. (2004). Variability of Near-Term Probability for the Next Great Earthquake on the Cascadia Subduction Zone. *Bulletin of the Seismological Society of America*, *94*(5), 1954–1959. https://doi.org/10.1785/012004032

Mazzotti, S., & Gueydan, F. (2018). Control of tectonic inheritance on continental intraplate strain rate and seismicity. *Tectonophysics*, *746*, 602–610. https://doi.org/10.1016/j.tecto.2017.12.014

Mazzotti, S., Leonard, L. J., Cassidy, J. F., Rogers, G. C., & Halchuk, S. (2011). Seismic hazard in western Canada from GPS strain rates versus earthquake catalog. *Journal of Geophysical Research: Solid Earth*, *116*(B12). https://doi.org/10.1029/2011JB008213

Mazzotti, S., Jomard, H., & Masson, F. (2020). Processes and deformation rates generating seismicity in metropolitan France and conterminous Western EuropeProcessus et taux de déformation générant la sismicité en France métropolitaine et en Europe occidentale proche. *Bulletin de La Société Géologique de France*, *191*(1). https://doi.org/10.1051/bsgf/2020019

McCaffrey, R. (1992). Oblique plate convergence, slip vectors, and forearc deformation. *Journal of Geophysical Research*, *97*(B6), 8905. https://doi.org/10.1029/92JB00483

McCaffrey, R. (1994). Global variability in subduction thrust zone-forearc systems. *Pure and Applied Geophysics*, *142*(1), 173–224. https://doi.org/10.1007/BF00875971

McCaffrey, R., Wallace, L. M., & Beavan, J. (2008). Slow slip and frictional transition at low temperature at the Hikurangi subduction zone. *Nature Geoscience*, *1*(5), 316–320. https://doi.org/10.1038/ngeo178

McClay, K. R., Shaw, J. H., & Suppe, J. (Eds.). (2011). *Thrust fault-related folding*.

Meade, B. J., & Loveless, J. P. (2009). Predicting the geodetic signature of MW ≥ 8 slow slip events. *Geophysical Research Letters*, *36*(1). https://doi.org/10.1029/2008GL036364

Meade, Brendan J., & Hager, B. H. (2005). Block models of crustal motion in southern California constrained by GPS measurements. *Journal of Geophysical Research: Solid Earth*, *110*(B3). https://doi.org/10.1029/2004JB003209

Meade, Brendan J., Klinger, Y., & Hetland, E. A. (2013). Inference of Multiple Earthquake-Cycle Relaxation Timescales from Irregular Geodetic Sampling of Interseismic Deformation. *Bulletin of the Seismological Society of America*, *103*(5), 2824–2835. https://doi.org/10.1785/0120130006

Meghraoui, M., & Doumaz, F. (1996). Earthquake-induced flooding and paleoseismicity of the El Asnam, Algeria, fault-related fold. *Journal of Geophysical Research: Solid Earth*, *101*(B8), 17617–17644. https://doi.org/10.1029/96JB00650

Menant, A., Angiboust, S., Gerya, T., Lacassin, R., Simoes, M., & Grandin, R. (2020). Transient stripping of subducting slabs controls periodic forearc uplift. *Nature Communications*, *11*(1), 1–10. https://doi.org/10.1038/s41467-020-15580-7

Meng, L., Huang, H., Bürgmann, R., Ampuero, J. P., & Strader, A. (2015). Dual megathrust slip behaviors of the 2014 Iquique earthquake sequence. *Earth and Planetary Science Letters*, *411*, 177–187. https://doi.org/10.1016/j.epsl.2014.11.041

Mériaux, A.-S., Ryerson, F. J., Tapponnier, P., Van der Woerd, J., Finkel, R. C., Xiwei, X., Zhiqin, X., & Caffee, M. W. (2004). Rapid slip along the central Altyn Tagh fault: Morphochronologic evidence from Cherchen He and Sulamu Tagh. *Journal of Geophysical Research: Solid Earth*, *109*(B6), B06401.1-B06401.23. https://doi.org/10.1029/2003JB002558

Michel, R., & Avouac, J.-P. (2002). Deformation due to the 17 August 1999 Izmit, Turkey, earthquake measured from SPOT images. *Journal of Geophysical Research*, *107*(B4), Etg 2-1-Etg 2-7.

Michel, R., Avouac, J.-P., & Taboury, J. (1999). Measuring ground displacements from SAR amplitude images : application to the Landers earthquake. *Geophysical Research Letters*, *26*(7), 875–878.

de Michele, M., Raucoules, D., de Sigoyer, J., Pubellier, M., & Chamot-Rooke, N. (2010). Three-dimensional surface displacement of the 2008 May 12 Sichuan earthquake (China) derived from Synthetic Aperture Radar: evidence for rupture on a blind thrust: 3D surface displacement of Sichuan earthquake. *Geophysical Journal International*, *183*(3), 1097–1103. https://doi.org/10.1111/j.1365-246X.2010.04807.x

Milliner, C. W. D., Dolan, J. F., Hollingsworth, J., Leprince, S., Ayoub, F., & Sammis, C. G. (2015). Quantifying near-field and off-fault deformation patterns of the 1992 M_w 7.3 Landers earthquake: Deformation of the Landers earthquake. *Geochemistry, Geophysics, Geosystems*, *16*(5), 1577–1598. https://doi.org/10.1002/2014GC005693

Milliner, C. W. D., Dolan, J. F., Hollingsworth, J., Leprince, S., & Ayoub, F. (2016). Comparison of coseismic near-field and off-fault surface deformation patterns of the 1992 Mw 7.3 Landers and 1999 Mw

7.1 Hector Mine earthquakes: Implications for controls on the distribution of surface strain. *Geophysical Research Letters*, *43*(19), 10,115-10,124. https://doi.org/10.1002/2016GL069841

Miyazaki, S., McGuire, J. J., & Segall, P. (2003). A transient subduction zone slip episode in southwest Japan observed by the nationwide GPS array. *Journal of Geophysical Research (B: Solid Earth)*, *108*(2), Etg 7-1-7-15. https://doi.org/10.1029/2001JB000456

Molinari, A., & Perfettini, H. (2017). A micromechanical model of rate and state friction: 2. Effect of shear and normal stress changes. *Journal of Geophysical Research: Solid Earth*, *122*(4), 2638–2652. https://doi.org/10.1002/2016JB013307

Molinari, A., & Perfettini, H. (2019). Fundamental aspects of a new micromechanical model of rate and state friction. *Journal of the Mechanics and Physics of Solids*, *124*, 63–82. https://doi.org/10.1016/j.jmps.2018.10.002

Mora, O., Mallorqui, J. J., & Broquetas, A. (2003). Linear and nonlinear terrain deformation maps from a reduced set of interferometric SAR images. *IEEE Transactions on Geoscience and Remote Sensing*, *41*(10), 2243–2253.

Morishita, Y., Lazecky, M., Wright, T. J., Weiss, J. R., Elliott, J. R., & Hooper, A. (2020). LiCSBAS: An Open-Source InSAR Time Series Analysis Package Integrated with the LiCSAR Automated Sentinel-1 InSAR Processor. *Remote Sensing*, *12*(3), 424. https://doi.org/10.3390/rs12030424

Mousavi, Z., Pathier, E., Walker, R. T., Walpersdorf, A., Tavakoli, F., Nankali, H., Sedighi, M., & Doin, M.-P. (2015). Interseismic deformation of the Shahroud fault system (NE Iran) from space-borne radar interferometry measurements. *Geophysical Research Letters*, *42*(14), 5753–5761. https://doi.org/10.1002/2015GL064440

Murakami, M., Tobita, M., Fujiwara, S., Saito, T., & Masaharu, H. (1996). Coseismic crustal deformations of 1994 Northridge, California, earthquake detected by interferometric JERS 1 synthetic aperture radar. *Journal of Geophysical Research: Solid Earth*, *101*(B4), 8605–8614. https://doi.org/10.1029/95JB02912

Murase, M., Matta, N., Lin, C.-H., Chen, W.-S., & Koizumi, N. (2013). An episodic creep-slip event detected by precise levelling surveys in the central part of the Longitudinal Valley Fault, eastern Taiwan, in 2011–2012. *Tectonophysics*, *608*, 904–913. https://doi.org/10.1016/j.tecto.2013.07.027

Nadeau, R. M., & McEvilly, T. V. (1999). Fault Slip Rates at Depth from Recurrence Intervals of Repeating Microearthquakes. *Science*, *285*(5428), 718–721. https://doi.org/10.1126/science.285.5428.718

Nishenko, S. P., & Singh, S. K. (1987). Conditional probabilities for the recurrence of large and great interplate earthquakes along the Mexican subduction zone. *Bulletin of the Seismological Society of America*, *77*(6), 2095–2114.

Nishimura, T., Fujiwara, S., Murakami, M., Tobita, M., Nakagawa, H., Sagiya, T., & Tada, T. (2001). The M6.1 earthquake triggered by volcanic inflation of Iwate volcano, northern Japan, observed by satellite radar interferometry. *Geophysical Research Letters*, *28*(4), 635–8.

Nissen, E., Ghorashi, M., Jackson, J., Parsons, B., & Talebian, M. (2007). The 2005 Qeshm Island earthquake (Iran)—a link between buried reverse faulting and surface folding in the Zagros Simply Folded Belt? *Geophysical Journal International*, *171*(1), 326–338. https://doi.org/10.1111/j.1365-246X.2007.03514.x

Nocquet, J.-M., Sue, C., Walpersdorf, A., Tran, T., Lenôtre, N., Vernant, P., Cushing, M., Jouanne, F., Masson, F., Baize, S., Chéry, J., & van der Beek, P. (2016). Present-day uplift of the western Alps. *Scientific Reports*, *6*(1), 28404. https://doi.org/10.1038/srep28404

Noda, H., & Lapusta, N. (2013). Stable creeping fault segments can become destructive as a result of dynamic weakening. *Nature*, *493*(7433), 518–521. https://doi.org/10.1038/nature11703

Obara, K. (2002). Nonvolcanic deep tremor associated with subduction in Southwest Japan. *Science*, *296*(5573), 1679–1681. https://doi.org/10.1126/science.1070378

Obara, K., & Kato, A. (2016). Connecting slow earthquakes to huge earthquakes. *Science*, *353*(6296), 253–257. https://doi.org/10.1126/science.aaf1512

Obara, K., Hirose, H., Yamamizu, F., & Kasahara, K. (2004). Episodic slow slip events accompanied by non-volcanic tremors in southwest Japan subduction zone. *Geophysical Research Letters*, *31*(23). https://doi.org/10.1029/2004GL020848

Ohta, Y., Freymueller, J., Hreinsdottir, S., & Suito, H. (2006). A large slow slip event and the depth of the seismogenic zone in the south central Alaska subduction zone. *Earth and Planetary Science Letters*, *247*(1–2), 108–116. https://doi.org/10.1016/j.epsl.2006.05.013

Onn, F., & Zebker, H. A. (2006). Correction for interferometric synthetic aperture radar atmospheric phase artifacts using time series of zenith wet delay observations from a GPS network. *Journal of Geophysical Research: Solid Earth*, *111*(B9). https://doi.org/10.1029/2005JB004012

Osmanoğlu, B., Dixon, T. H., Wdowinski, S., Cabral-Cano, E., & Jiang, Y. (2011). Mexico City subsidence observed with persistent scatterer InSAR. *International Journal of Applied Earth Observation and Geoinformation*, *13*(1), 1–12. https://doi.org/10.1016/j.jag.2010.05.009

Outerbridge, K. C., Dixon, T. H., Schwartz, S. Y., Walter, J. I., Protti, M., Gonzalez, V., Biggs, J., Thorwart, M., & Rabbel, W. (2010). A tremor and slip event on the Cocos-Caribbean subduction zone as measured by a global positioning system (GPS) and seismic network on the Nicoya Peninsula, Costa Rica. *Journal of Geophysical Research: Solid Earth*, *115*(B10). https://doi.org/10.1029/2009JB006845

Ozawa, S., Murakami, M., & Tada, T. (2001). Time-dependent inversion study of the slow thrust event in the Nankai trough subduction zone, southwestern Japan. *Journal of Geophysical Research: Solid Earth*, *106*(B1), 787–802. https://doi.org/10.1029/2000JB900317

Ozawa, S., Murakami, M., Kaidzu, M., Tada, T., Sagiya, T., Hatanaka, Y., Yarai, H., & Nishimura, T. (2002). Detection and monitoring of ongoing aseismic slip in the Tokai region, central Japan. *Science*, *298*(5595), 1009–1012. https://doi.org/10.1126/science.1076780

Ozawa, S., Miyazaki, S., Hatanaka, Y., Imakiire, T., Kaidzu, M., & Murakami, M. (2003). Characteristic silent earthquakes in the eastern part of the Boso peninsula, Central Japan. *Geophysical Research Letters*, *30*(6), 1283. https://doi.org/10.1029/2002GL016665

Ozawa, S., Hatanaka, Y., Kaidzu, M., Murakami, M., Imakiire, T., & Ishigaki, Y. (2004). Aseismic slip and low-frequency earthquakes in the Bungo channel, southwestern Japan. *Geophysical Research Letters*, *31*(7), L07609.1-L07609.5. https://doi.org/10.1029/2003GL019381

Ozawa, S., Suito, H., & Tobita, M. (2007). Occurrence of quasi-periodic slow-slip off the east coast of the Boso peninsula, Central Japan. *Earth, Planets and Space*, *59*(12), 1241–1245. https://doi.org/10.1186/BF03352072

Ozawa, S., Yarai, H., Tobita, M., Une, H., & Nishimura, T. (2008). Crustal deformation associated with the Noto Hanto Earthquake in 2007 in Japan. *Earth, Planets and Space*, *60*(2), 95–98. https://doi.org/10.1186/BF03352767

Pagli, C., Pedersen, R., Sigmundsson, F., & Feigl, K. L. (2003). Triggered fault slip on June 17, 2000 on the Reykjanes Peninsula, SW-Iceland captured by radar interferometry. *Geophysical Research Letters*, *30*(6), 6-1-6–4.

Pan, Y. S. (1968). Interpretation and seismic coordination of the Bouger gravity anomaly obtained in southwestern Taiwan. *Petrol. Geol. Taiwan*, *6*, 197–208.

Pathier, E., Fielding, E. J., Wright, T. J., Walker, R., Parsons, B. E., & Hensley, S. (2006). Displacement field and slip distribution of the 2005 Kashmir earthquake from SAR imagery. *Geophysical Research Letters*, *33*(20), L20310. https://doi.org/10.1029/2006GL027193

Pedersen, R., Sigmundsson, F., Feigl, K. L., & Árnadóttir, T. (2001). Coseismic interferograms of two Ms = 6.6 earthquakes in the South Iceland Seismic Zone, June 2000. *Geophysical Research Letters*, *28*(17), 3341–3344. https://doi.org/10.1029/2001GL013235

Peltzer, G., Rosen, P. A., Rogez, F., & Hudnut, K. W. (1996). Postseismic rebound in fault step-overs caused by pore fluid flow. *Science*, *273*(5279), 1202–1204.

Peltzer, G., Rosen, P. A., Rogez, F., & Hudnut, K. W. (1998). Poroelastic rebound along the Landers 1992 earthquake surface rupture. *Journal of Geophysical Research*, *103*(B12), 30131–30145.

Peltzer, G., Crampé, F., & Rosen, P. (2001). The Mw 7.1, Hector Mine, California earthquake: surface rupture, surface displacement field, and fault slip solution from ERS SAR data. *Comptes Rendus de l'Académie Des Sciences - Series IIA - Earth and Planetary Science*, *333*(9), 545–555. https://doi.org/10.1016/S1251-8050(01)01658-5

Peltzer, G., Crampé, F., Hensley, S., & Rosen, P. (2001). Transient strain accumulation and fault interaction in the Eastern California shear zone. *Geology*, *29*(11), 975–978. https://doi.org/10.1130/0091-7613(2001)029<0975:TSAAFI>2.0.CO;2

Peng, Z., & Gomberg, J. (2010). An integrated perspective of the continuum between earthquakes and slow-slip phenomena. *Nature Geoscience*, *3*(9), 599–607. https://doi.org/10.1038/ngeo940

Pepe, A., & Calò, F. (2017). A Review of Interferometric Synthetic Aperture RADAR (InSAR) Multi-Track Approaches for the Retrieval of Earth's Surface Displacements. *Applied Sciences*, *7*(12), 1264. https://doi.org/10.3390/app7121264

Pepe, A., Berardino, P., Bonano, M., Euillades, L. D., Lanari, R., & Sansosti, E. (2011). SBAS-Based Satellite Orbit Correction for the Generation of DInSAR Time-Series: Application to RADARSAT-1 Data. *IEEE Transactions on Geoscience and Remote Sensing*, *49*(12), 5150–5165. https://doi.org/10.1109/TGRS.2011.2155069

Perfettini, H., & Avouac, J.-P. (2004a). Postseismic relaxation driven by brittle creep: A possible mechanism to reconcile geodetic measurements and the decay rate of aftershocks, application to the Chi-Chi earthquake, Taiwan. *Journal of Geophysical Research: Solid Earth*, *109*(B2). https://doi.org/10.1029/2003JB002488

Perfettini, H., & Avouac, J.-P. (2004b). Stress transfer and strain rate variations during the seismic cycle. *Journal of Geophysical Research*, *109*(B6), B06402.1-B06402.8. https://doi.org/10.1029/2003JB002917

Perfettini, H., & Molinari, A. (2017). A micromechanical model of rate and state friction: 1. Static and dynamic sliding. *Journal of Geophysical Research: Solid Earth*, *122*(4), 2590–2637. https://doi.org/10.1002/2016JB013302

Perfettini, H., Avouac, J.-P., & Ruegg, J.-C. (2005). Geodetic displacements and aftershocks following the 2001 Mw= 8.4 Peru earthquake: Implications for the mechanics of the earthquake cycle along subduction zones. *Journal of Geophysical Research: Solid Earth*, *110*(B9). https://doi.org/10.1029/2004JB003522

Perfettini, H., Frank, W. B., Marsan, D., & Bouchon, M. (2018). A Model of Aftershock Migration Driven by Afterslip. *Geophysical Research Letters*, *45*(5), 2283–2293. https://doi.org/10.1002/2017GL076287

Perfettini, H., Frank, W. B., Marsan, D., & Bouchon, M. (2019). Updip and Along-Strike Aftershock Migration Model Driven by Afterslip: Application to the 2011 Tohoku-Oki Aftershock Sequence.

Journal of Geophysical Research: Solid Earth, *124*(3), 2653–2669. https://doi.org/10.1029/2018JB016490

Peyret, M., Dominguez, S., Cattin, R., Champenois, J., Leroy, M., & Zajac, A. (2011). Present-day interseismic surface deformation along the Longitudinal Valley, eastern Taiwan, from a PS-InSAR analysis of the ERS satellite archives. *Journal of Geophysical Research*, *116*(B3), B03402. https://doi.org/10.1029/2010JB007898

Pezzo, G., Tolomei, C., Atzori, S., Salvi, S., Shabanian, E., Bellier, O., & Farbod, Y. (2012). New kinematic constraints of the western Doruneh fault, northeastern Iran, from interseismic deformation analysis: Doruneh fault (Iran) interseismic deformation. *Geophysical Journal International*, *190*(1), 622–628. https://doi.org/10.1111/j.1365-246X.2012.05509.x

Pezzo, G., Boncori, J. P. M., Tolomei, C., Salvi, S., Atzori, S., Antonioli, A., Trasatti, E., Novali, F., Serpelloni, E., Candela, L., & Giuliani, R. (2013). Coseismic Deformation and Source Modeling of the May 2012 Emilia (Northern Italy) Earthquakes. *Seismological Research Letters*, *84*(4), 645–655. https://doi.org/10.1785/0220120171

Ponti, D. J., Rosa, C. M., & Blair, J. L. (2019). *The Mw 6.0 South Napa earthquake of August 24, 2014—Observations of surface faulting and ground deformation, with recommendations for improving post-earthquake field investigations* (USGS Numbered Series No. 2019–1018). *The Mw 6.0 South Napa earthquake of August 24, 2014—Observations of surface faulting and ground deformation, with recommendations for improving post-earthquake field investigations* (Vol. 2019–1018, p. 64). Reston, VA: U.S. Geological Survey. https://doi.org/10.3133/ofr20191018

Pousse Beltran, L., Pathier, E., Jouanne, F., Vassallo, R., Reinoza, C., Audemard, F., Doin, M. P., & Volat, M. (2016). Spatial and temporal variations in creep rate along the El Pilar fault at the Caribbean-South American plate boundary (Venezuela), from InSAR. *Journal of Geophysical Research: Solid Earth*, *121*(11), 8276–8296. https://doi.org/10.1002/2016JB013121

Price, E. J., & Sandwell, D. T. (1998). Small-scale deformations associated with the 1992 Landers, California, earthquake mapped by synthetic aperture radar interferometry phase gradients. *Journal of Geophysical Research*, *103*(B11), 27001–27016.

Puysségur, B., Michel, R., & Avouac, J.-P. (2007). Tropospheric phase delay in interferometric synthetic aperture radar estimated from meteorological model and multispectral imagery. *Journal of Geophysical Research: Solid Earth*, *112*(B5), B05419. https://doi.org/10.1029/2006JB004352

Radiguet, M., Cotton, F., Vergnolle, M., Campillo, M., Valette, B., Kostoglodov, V., & Cotte, N. (2011). Spatial and temporal evolution of a long term slow slip event: the 2006 Guerrero Slow Slip Event. *Geophysical Journal International*, *184*(2), 816–828. https://doi.org/10.1111/j.1365-246X.2010.04866.x

Radiguet, M., Cotton, F., Vergnolle, M., Campillo, M., Walpersdorf, A., Cotte, N., & Kostoglodov, V. (2012). Slow slip events and strain accumulation in the Guerrero gap, Mexico. *Journal of Geophysical Research: Solid Earth*, *117*(B4), n/a-n/a. https://doi.org/10.1029/2011JB008801

Radiguet, M., Perfettini, H., Cotte, N., Gualandi, A., Valette, B., Kostoglodov, V., Lhomme, T., Walpersdorf, A., Cabral-Cano, E., & Campillo, M. (2016). Triggering of the 2014 Mw7.3 Papanoa earthquake by a slow slip event in Guerrero, Mexico. *Nature Geoscience*, *9*(11), 829–833. https://doi.org/10.1038/ngeo2817

Radiguet, M., Kazachkina, E., Maubant, L., Cotte, N., Kostoglodov, V., Gualandi, A., & Chanard, K. (2020, March). *Systematic characterization of slow slip events along the Mexican subduction zone from 2000 to 2019*. Presented at the EGU2020 annual meeting, Vienna. https://doi.org/10.5194/egusphere-egu2020-17441

Rau, R.-J., Lee, J.-C., Ching, K.-E., Lee, Y.-H., Byrne, T. B., & Chen, R.-Y. (2012). Subduction-continent collision in southwestern Taiwan and the 2010 Jiashian earthquake sequence. *Tectonophysics*, *578*, 107–116. https://doi.org/10.1016/j.tecto.2011.09.013

Raucoules, D., Maisons, C., Carnec, C., Le Mouélic, S., King, C., & Hosford, S. (2003). Monitoring of slow ground deformation by ERS radar interferometry on the Vauvert salt mine (France): Comparison with ground-based measurement. *Remote Sensing of Environment*, *88*(4), 468–478. https://doi.org/10.1016/j.rse.2003.09.005

Reid, H. F. (1910). The mechanics of the earthquake. In *A. C. Lawson (Ed.), The California earthquake of April 18, 1906, Report of the State Earthquake Investigation Commission* (Washington, DC: Carnegie Institute ofWashington, Vol. II, pp. 3–55).

Reid, H. F. (1911). The elastic rebound theory of earthquakes. *Bulletin of the Department of Geology, University of California Publications*, *6*(19), 413–444.

Reinen, L. A., Weeks, J. D., & Tullis, T. E. (1991). The frictional behavior of serpentinite: Implications for aseismic creep on shallow crustal faults. *Geophysical Research Letters*, *18*(10), 1921–1924. https://doi.org/10.1029/91GL02367

Reverso, T., Marsan, D., Helmstetter, A., & Enescu, B. (2016). Background seismicity in Boso Peninsula, Japan: Long-term acceleration, and relationship with slow slip events. *Geophysical Research Letters*, *43*(11), 5671–5679. https://doi.org/10.1002/2016GL068524

Rice, J. R. (1993). Spatio-temporal complexity of slip on a fault. *Journal of Geophysical Research: Solid Earth*, *98*(B6), 9885–9907. https://doi.org/10.1029/93JB00191

Rice, J. R., Lapusta, N., & Ranjith, K. (2001). Rate and state dependent friction and the stability of sliding between elastically deformable solids. *Journal of the Mechanics and Physics of Solids*, *49*(9), 1865–1898. https://doi.org/10.1016/S0022-5096(01)00042-4

Rivet, D., Campillo, M., Radiguet, M., Zigone, D., Cruz-Atienza, V., Shapiro, N. M., Kostoglodov, V., Cotte, N., Cougoulat, G., Walpersdorf, A., & Daub, E. (2014). Seismic velocity changes, strain rate and non-volcanic tremors during the 2009–2010 slow slip event in Guerrero, Mexico. *Geophysical Journal International*, *196*(1), 447–460. https://doi.org/10.1093/gji/ggt374

Rogers, G., & Dragert, H. (2003). Episodic tremor and slip on the Cascadia subduction zone: The chatter of silent slip. *Science*, *300*(5627), 1942–1943. https://doi.org/10.1126/science.1084783

Rolandone, F., Nocquet, J.-M., Mothes, P. A., Jarrin, P., Vallée, M., Cubas, N., Hernandez, S., Plain, M., Vaca, S., & Font, Y. (2018). Areas prone to slow slip events impede earthquake rupture propagation and promote afterslip. *Science Advances*, *4*(1), eaao6596. https://doi.org/10.1126/sciadv.aao6596

Rosen, P. A., Werner, C. L., Fielding, E. J., Hensley, S., Buckley, S. M., & Vincent, P. (1998). Aseismic creep along the San Andreas Fault northwest of Parkfield, CA measured by radar interferometry. *Geophysical Research Letters*, *25*(6), 825–828. https://doi.org/10.1029/98GL50495

Rosen, P. A., Hensley, S., Peltzer, G., & Simons, M. (2004). Updated Repeat Orbit Interferometry Package Released. *EOS Transactions of the American Geophysical Union*, *85*(5).

Rousset, B., Jolivet, R., Simons, M., Lasserre, C., Riel, B., Milillo, P., Çakir, Z., & Renard, F. (2016). An aseismic slip transient on the North Anatolian Fault. *Geophysical Research Letters*, *43*(7), 3254–3262. https://doi.org/10.1002/2016GL068250

Rousset, B., Lasserre, C., Cubas, N., Graham, S. E., Radiguet, M., DeMets, C., Socquet, A., Campillo, M., Kostoglodov, V., Cabral-Cano, E., Cotte, N., & Walpersdorf, A. (2016). Lateral Variations of Interplate Coupling along the Mexican Subduction Interface: Relationships with Long-Term Morphology and Fault Zone Mechanical Properties. *Pure and Applied Geophysics*, *173*(10), 3467–3486. https://doi.org/10.1007/s00024-015-1215-6

Rousset, B., Campillo, M., Lasserre, C., Frank, W. B., Cotte, N., Walpersdorf, A., Socquet, A., & Kostoglodov, V. (2017). A geodetic matched filter search for slow slip with application to the Mexico subduction zone. *Journal of Geophysical Research: Solid Earth*, *122*(12), 10,498-10,514. https://doi.org/10.1002/2017JB014448

Rowe, C. D., & Griffith, W. A. (2015). Do faults preserve a record of seismic slip: A second opinion. *Journal of Structural Geology*, *78*, 1–26. https://doi.org/10.1016/j.jsg.2015.06.006

Rubinstein, J. L., Shelly, D. R., & Ellsworth, W. L. (2009). Non-volcanic Tremor: A Window into the Roots of Fault Zones. In S. Cloetingh & J. Negendank (Eds.), *New Frontiers in Integrated Solid Earth Sciences* (pp. 287–314). Dordrecht: Springer Netherlands. https://doi.org/10.1007/978-90-481-2737-5_8

Ruegg, J.-C., Campos, J., Armijo, R., Barrientos, S. E., Briole, P., Thiele, R., Arancibia, M., Canuta, J., Duquesnoy, T., Chang, M., Lazo, D., Lyon-Caen, H., Ortlieb, L., Rossignol, J. C., & Serrurier, L. (1996). The Mw=8.1 Antofagasta (North Chile) Earthquake of July 30, 1995 : First results from teleseismic and geodetic data. *Geophysical Research Letters*, *23*(9), 917–920.

Ruina, A. (1983). Slip instability and state variable friction laws. *Journal of Geophysical Research: Solid Earth*, *88*(B12), 10359–10370. https://doi.org/10.1029/JB088iB12p10359

Sacks, I. S., Linde, A. T., Suyehiro, S., & Snoke, J. A. (1978). Slow earthquakes and stress redistribution. *Nature*, *275*(5681), 599–602. https://doi.org/10.1038/275599a0

Saillard, M., Audin, L., Rousset, B., Avouac, J.-P., Chlieh, M., Hall, S. R., Husson, L., & Farber, D. L. (2017). From the seismic cycle to long-term deformation: linking seismic coupling and Quaternary coastal geomorphology along the Andean megathrust. *Tectonics*, *36*(2), 241–256. https://doi.org/10.1002/2016TC004156

Salvi, S., Atzori, S., Tolomei, C., Antonioli, A., Trasatti, E., Merryman Boncori, J. P., Pezzo, G., Coletta, A., & Zoffoli, S. (2012). Results from INSAR monitoring of the 2010–2011 New Zealand seismic sequence: EA detection and earthquake triggering. In *2012 IEEE International Geoscience and Remote Sensing Symposium* (pp. 3544–3547). https://doi.org/10.1109/IGARSS.2012.6350654

Samsonov, S. V., Gonzalez, P. J., Tiampo, K. F., & Czarnogorska, M. (2014). *RADARSAT-2 for mapping natural hazard events: case studies from around the world*. Scientific Presentation no. 3 presented at the Geomatics Canada, Natural Resources Canada. Retrieved from https://doi.org/10.4095/295562

Sandwell, D. T., Sichoix, L., Agnew, D. C., Bock, Y., & Minster, J.-B. (2000). Near real-time radar interferometry of the Mw 7.1 Hector Mine Earthquake. *Geophysical Research Letters*, *27*(19), 3101–3104.

Sathiakumar, S., Barbot, S., & Hubbard, J. (2020). Earthquake Cycles in Fault-Bend Folds. *Journal of Geophysical Research: Solid Earth*, *125*(8), e2019JB018557. https://doi.org/10.1029/2019JB018557

Savage, J. C., & Burford, R. O. (1973). Geodetic determination of relative plate motion in central California. *Journal of Geophysical Research (1896-1977)*, *78*(5), 832–845. https://doi.org/10.1029/JB078i005p00832

Scholz, C. H. (1990). *The mechanics of earthquakes and faulting*. Cambridge, United-Kingdom: Cambridge University Press.

Scholz, C. H. (1998). Earthquakes and friction laws. *Nature*, *391*(6662), 37–42. https://doi.org/10.1038/34097

Schulz, S. S. (1989). *Catalog of creepmeter measurements in California from 1966 through 1988*. *Open-File Report*. Dept. of the Interior, U.S. Geological Survey,. https://doi.org/10.3133/ofr89650

Schulz, S. S., Mavko, G. M., Burford, R. O., & Stuart, W. D. (1982). Long-term fault creep observations in central California. *Journal of Geophysical Research: Solid Earth*, *87*(B8), 6977–6982. https://doi.org/10.1029/JB087iB08p06977

Schwartz, S. Y., & Rokosky, J. M. (2007). Slow slip events and seismic tremor at circum-Pacific subduction zones: SLOW SLIP AND SEISMIC TREMOR. *Reviews of Geophysics*, *45*(3), n/a-n/a. https://doi.org/10.1029/2006RG000208

Segall, P. (2010). *Earthquake and Volcano Deformation*. Princeton University Press. Retrieved from https://press.princeton.edu/books/hardcover/9780691133027/earthquake-and-volcano-deformation

Seydoux, L., Balestriero, R., Poli, P., Hoop, M. de, Campillo, M., & Baraniuk, R. (2020). Clustering earthquake signals and background noises in continuous seismic data with unsupervised deep learning. *Nature Communications*, *11*(1), 3972. https://doi.org/10.1038/s41467-020-17841-x

Shelly, D. R. (2009). Possible deep fault slip preceding the 2004 Parkfield earthquake, inferred from detailed observations of tectonic tremor. *Geophysical Research Letters*, *36*(17). https://doi.org/10.1029/2009GL039589

Shelly, D. R., & Johnson, K. M. (2011). Tremor reveals stress shadowing, deep postseismic creep, and depth-dependent slip recurrence on the lower-crustal San Andreas fault near Parkfield: TREMOR, STRESS, AND LOWER-CRUSTAL CREEP. *Geophysical Research Letters*, *38*(13), n/a-n/a. https://doi.org/10.1029/2011GL047863

Shelly, D. R., Ellsworth, W. L., Ryberg, T., Haberland, C., Fuis, G. S., Murphy, J., Nadeau, R. M., & Bürgmann, R. (2009). Precise location of San Andreas Fault tremors near Cholame, California using seismometer clusters: Slip on the deep extension of the fault? *Geophysical Research Letters*, *36*(1), L01303. https://doi.org/10.1029/2008GL036367

Shih, T. T. (1967). A survey of active mud volcanoes in Taiwan and a study of their types and the character of the mud. *Petrol. Geol. Taiwan*, *5*, 259–293.

Shimazaki, K. (1974). Pre-seismic crustal deformation caused by an underthrusting oceanic plate, in eastern Hokkaido, Japan. *Physics of the Earth and Planetary Interiors*, *8*(2), 148–157. https://doi.org/10.1016/0031-9201(74)90127-7

Shirzaei, M., & Bürgmann, R. (2013). Time-dependent model of creep on the Hayward fault from joint inversion of 18 years of InSAR and surface creep data. *Journal of Geophysical Research: Solid Earth*, *118*(4), 1733–1746. https://doi.org/10.1002/jgrb.50149

Shirzaei, M., Bürgmann, R., Oncken, O., Walter, T. R., Victor, P., & Ewiak, O. (2012). Response of forearc crustal faults to the megathrust earthquake cycle: InSAR evidence from Mejillones Peninsula, Northern Chile. *Earth and Planetary Science Letters*, *333–334*, 157–164. https://doi.org/10.1016/j.epsl.2012.04.001

Shyu, J. B. H. (2005). Neotectonic architecture of Taiwan and its implications for future large earthquakes. *Journal of Geophysical Research*, *110*(B8), B08402. https://doi.org/10.1029/2004JB003251

Shyu, J. B. H., Sieh, K. E., Chen, Y.-G., & Chung, L.-H. (2006). Geomorphic analysis of the Central Range fault, the second major active structure of the Longitudinal Valley suture, eastern Taiwan. *Geological Society of America Bulletin*, *118*(11–12), 1447–1462. https://doi.org/10.1130/B25905.1

Shyu, J. B. H., Sieh, K., Chen, Y.-G., Chuang, R. Y., Wang, Y., & Chung, L.-H. (2008). Geomorphology of the southernmost Longitudinal Valley fault: Implications for evolution of the active suture of eastern Taiwan. *Tectonics*, *27*(1), n/a-n/a. https://doi.org/10.1029/2006TC002060

Siame, L. L., Angelier, J., Chen, R.-F., Godard, V., Derrieux, F., Bourlès, D. L., Braucher, R., Chang, K.-J., Chu, H.-T., & Lee, J.-C. (2011). Erosion rates in an active orogen (NE-Taiwan): A confrontation of

cosmogenic measurements with river suspended loads. *Quaternary Geochronology*, *6*(2), 246–260. https://doi.org/10.1016/j.quageo.2010.11.003

Sieh, K. E. (1982). Slip along the San Andreas fault associated with the earthquake. In *The Imperial Valley, California, earthquake of October 15, 1979* (Vol. 1254, pp. 155–160). U.S. Geological Survey. https://doi.org/10.3133/pp1254

Sieh, K. E., & Williams, P. L. (1990). Behavior of the southernmost San Andreas Fault during the past 300 years. *Journal of Geophysical Research: Solid Earth*, *95*(B5), 6629–6645. https://doi.org/10.1029/JB095iB05p06629

Simons, M., & Rosen, P. A. (2007). 3.12 - Interferometric Synthetic Aperture Radar Geodesy. In G. Schubert (Ed.), *Treatise on Geophysics* (pp. 391–446). Amsterdam: Elsevier. https://doi.org/10.1016/B978-044452748-6.00059-6

Simpson, R. W., Lienkaemper, J. J., & Galehouse, J. S. (2001). Variations in creep rate along the Hayward Fault, California, interpreted as changes in depth of creep. *Geophysical Research Letters*, *28*(11), 2269–2272. https://doi.org/10.1029/2001GL012979

Singh, S. K., & Mortera, F. (1991). Source time functions of large Mexican subduction earthquakes, morphology of the Benioff Zone, age of the plate, and their tectonic implications. *Journal of Geophysical Research: Solid Earth*, *96*(B13), 21487–21502. https://doi.org/10.1029/91JB02047

Šmilauer, V. (2015). *Yade Documentation 2nd ed. The Yade Project (http://yade-dem.org/doc/)*. Retrieved from Doi 10.5281/zenodo.34073

Smith, S. W., & Wyss, M. (1968). Displacement on the San Andreas fault subsequent to the 1966 Parkfield earthquake. *Bulletin of the Seismological Society of America*, *58*(6), 1955–1973.

Socquet, A., Valdes, J. P., Jara, J., Cotton, F., Walpersdorf, A., Cotte, N., Specht, S., Ortega-Culaciati, F., Carrizo, D., & Norabuena, E. (2017). An 8 month slow slip event triggers progressive nucleation of the 2014 Chile megathrust. *Geophysical Research Letters*, *44*(9), 4046–4053. https://doi.org/10.1002/2017GL073023

Song, T.-R. A., & Kim, Y. (2012). Localized seismic anisotropy associated with long-term slow-slip events beneath southern Mexico: ANISOTROPY, FOLIATION AND SLOW-SLIP. *Geophysical Research Letters*, *39*(9), n/a-n/a. https://doi.org/10.1029/2012GL051324

Song, T.-R. A., Helmberger, Donald. V., Brudzinski, M. R., Clayton, R. W., Davis, P., Pérez-Campos, X., & Singh, S. K. (2009). Subducting Slab Ultra-Slow Velocity Layer Coincident with Silent Earthquakes in Southern Mexico. *Science*, *324*(5926), 502–506. https://doi.org/10.1126/science.1167595

Stein, R. S., & Ekström, G. (1992). Seismicity and geometry of a 110-km-long blind thrust fault 2. Synthesis of the 1982–1985 California Earthquake Sequence. *Journal of Geophysical Research: Solid Earth*, *97*(B4), 4865–4883. https://doi.org/10.1029/91JB02847

Stein, R. S., & King, G. C. P. (1984). Seismic potential revealed by surface folding; 1983 Coalinga, California, earthquake. *Science*, *224*(4651), 869–872.

Stein, R. S., & Yeats, R. S. (1989). Hidden earthquakes. *Scientific American*, *260*(6), 48–57.

Stein, R. S., King, G. C. P., & Rundle, J. B. (1988). The growth of geological structures by repeated earthquakes. 2. Field examples of continental dip-slip faults. *Journal of Geophysical Research: Solid Earth*, *93*(B11), 13319–13331. https://doi.org/10.1029/JB093iB11p13319

Steinbrugge, K. V., Zacher, E. G., Tocher, D., Whitten, C. A., & Claire, C. N. (1960). Creep on the San Andreas fault. *Bulletin of the Seismological Society of America*, *50*(3), 389–415.

Stramondo, S., Chini, M., Bignami, C., Salvi, S., & Atzori, S. (2011). X-, C-, and L-Band DInSAR Investigation of the April 6, 2009, Abruzzi Earthquake. *IEEE Geoscience and Remote Sensing Letters*, *8*(1), 49–53. https://doi.org/10.1109/LGRS.2010.2051015

Streig, A. R., Rubin, C. M., Chen, W.-S., Chen, Y.-G., Lee, L.-S., Thompson, S. C., Madden, C., & Lu, S.-T. (2007). Evidence for prehistoric coseismic folding along the Tsaotun segment of the Chelungpu fault near Nan-Tou, Taiwan. *Journal of Geophysical Research: Solid Earth*, *112*(B3). https://doi.org/10.1029/2006JB004493

Strozzi, T., & Wegmüller, U. (1999). Land subsidence in Mexico City mapped by ERS differential SAR interferometry. In T. I. Stein (Ed.) (Vol. 4, pp. 1940–1942). Presented at the IGARSS'99. IEEE 1999 International Geoscience and Remote Sensing Symposium, Hamburg, Germany: IEEE, Piscataway, NJ, USA.

Strozzi, T., Wegmüller, U., Werner, C. L., Wiesmann, A., & Spreckeis, V. (2003). JERS SAR interferometry for land subsidence monitoring. *IEEE Transactions on Geoscience and Remote Sensing*, *41*(7), 1702–1708.

Suárez, G., Monfret, T., Wittlinger, G., & David, C. (1990). Geometry of subduction and depth of the seismogenic zone in the Guerrero gap, Mexico. *Nature*, *345*(6273), 336–338. https://doi.org/10.1038/345336a0

Sun, C.-H., Chang, S.-C., Kuo, C.-L., Wu, J.-C., Shao, P.-H., & Oung, J.-N. (2010). Origins of Taiwan's mud volcanoes: Evidence from geochemistry. *Journal of Asian Earth Sciences*, *37*(2), 105–116. https://doi.org/10.1016/j.jseaes.2009.02.007

Sung, Q.-C., Chang, H.-C., Liu, H.-C., & Chen, Y.-C. (2010). Mud volcanoes along the Chishan fault in Southwestern Taiwan: A release bend model. *Geomorphology*, *118*(1–2), 188–198. https://doi.org/10.1016/j.geomorph.2009.12.018

Suppe, J. (1981). Mechanics of mountain-building and metamorphism in Taiwan. *Memoirs of the Geological Society of China*, *4*, 67–89.

Suppe, J., & Medwedeff, D. A. (1990). Geometry and kinematics of faultpropagation folding. *Ecoglae Geologicae Helvetiae*, *83*, 409–454.

Sylvester, A. G. (1995). Nearfield vertical displacement in the creeping segment of the San Andreas fault, central California, 1975 to 1994. *Tectonophysics*, *247*(1–4), 25–47. https://doi.org/10.1016/0040-1951(94)00244-4

Sylvester, A. G. (2000). Aseismic Growth of Ventura Avenue Anticline, Southern California, 197 8-1997: Evidence from Precise Leveling. *Surveying and Land Information Systems, 60*(2), 95–108.

Ta, T., Choo, K., Tan, E., Jang, B., & Choi, E. (2015). Accelerating DynEarthSol3D on tightly coupled CPU–GPU heterogeneous processors. *Computers & Geosciences*, *79*, 27–37. https://doi.org/10.1016/j.cageo.2015.03.003

Tesson, J., & Benedetti, L. (2019). Seismic history from in situ 36Cl cosmogenic nuclide data on limestone fault scarps using Bayesian reversible jump Markov chain Monte Carlo. *Quaternary Geochronology*, *52*, 1–20. https://doi.org/10.1016/j.quageo.2019.02.004

Thatcher, W. (1979). Systematic inversion of geodetic data in central California. *Journal of Geophysical Research: Solid Earth*, *84*(B5), 2283–2295. https://doi.org/10.1029/JB084iB05p02283

Thomas, F., Godard, V., Bellier, O., Benedetti, L., Ollivier, V., Rizza, M., Guillou, V., Hollender, F., Aumaître, G., Bourlès, D. L., & Keddadouche, K. (2018). Limited influence of climatic gradients on the denudation of a Mediterranean carbonate landscape. *Geomorphology*, *316*, 44–58. https://doi.org/10.1016/j.geomorph.2018.04.014

Thomas, M. Y., Avouac, J.-P., Gratier, J.-P., & Lee, J.-C. (2014). Lithological control on the deformation mechanism and the mode of fault slip on the Longitudinal Valley Fault, Taiwan. *Tectonophysics*, *632*, 48–63. https://doi.org/10.1016/j.tecto.2014.05.038

Thomas, M. Y., Avouac, J.-P., Champenois, J., Lee, J.-C., & Kuo, L.-C. (2014). Spatiotemporal evolution of seismic and aseismic slip on the Longitudinal Valley Fault, Taiwan. *Journal of Geophysical Research: Solid Earth*, *119*(6), 5114–5139. https://doi.org/10.1002/2013JB010603

Thurber, C., & Sessions, R. (1998). Assessment of Creep Events as Potential Earthquake Precursors: Application to the Creeping Section of the San Andreas Fault, California. *Pure and Applied Geophysics*, *152*(4), 685–705. https://doi.org/10.1007/s000240050172

Tizzani, P., Castaldo, R., Solaro, G., Pepe, S., Bonano, M., Casu, F., Manunta, M., Manzo, M., Pepe, A., Samsonov, S., Lanari, R., & Sansosti, E. (2013). New insights into the 2012 Emilia (Italy) seismic sequence through advanced numerical modeling of ground deformation InSAR measurements. *Geophysical Research Letters*, *40*(10), 1971–1977. https://doi.org/10.1002/grl.50290

Tobita, M., Fujiwara, S., Ozawa, S., Rosen, P. A., Fielding, E. J., Werner, C. L., Murakami, M., Nakagawa, H., & Nitta, K. (1998). Deformation of the 1995 North Sakhalin earthquake detected by JERS-1/SAR interferometry. *Earth, Planets and Space*, *50*(4), 313–25.

Tong, X., Sandwell, D. T., & Smith-Konter, B. (2013). High-resolution interseismic velocity data along the San Andreas Fault from GPS and InSAR: INTERSEISMIC VELOCITY DATA ON SAN ANDREAS FAULT. *Journal of Geophysical Research: Solid Earth*, *118*(1), 369–389. https://doi.org/10.1029/2012JB009442

Tong, X., Sandwell, D. T., & Schmidt, D. A. (2018). Surface Creep Rate and Moment Accumulation Rate Along the Aceh Segment of the Sumatran Fault From L-band ALOS-1/PALSAR-1 Observations. *Geophysical Research Letters*, *45*(8), 3404–3412. https://doi.org/10.1002/2017GL076723

Tong, Xiaopeng, Sandwell, D., Luttrell, K., Brooks, B., Bevis, M., Shimada, M., Foster, J., Smalley, R., Parra, H., Soto, J. C. B., Blanco, M., Kendrick, E., Genrich, J., & Caccamise, D. J. (2010). The 2010 Maule, Chile earthquake: Downdip rupture limit revealed by space geodesy. *Geophysical Research Letters*, *37*(24). https://doi.org/10.1029/2010GL045805

Trubienko, O., Fleitout, L., Garaud, J.-D., & Vigny, C. (2013). Interpretation of interseismic deformations and the seismic cycle associated with large subduction earthquakes. *Tectonophysics*, *589*, 126–141. https://doi.org/10.1016/j.tecto.2012.12.027

Tsai, M.-C., Shin, T.-C., & Kuo, K.-W. (2017). Pre-seismic strain anomalies and coseismic deformation of Meinong earthquake from continuous GPS. *Terrestrial, Atmospheric and Oceanic Sciences*, *28*(5), 763–785. https://doi.org/10.3319/TAO.2017.04.19.01

Tse, S. T., & Rice, J. R. (1986). Crustal earthquake instability in relation to the depth variation of frictional slip properties. *Journal of Geophysical Research: Solid Earth*, *91*(B9), 9452–9472. https://doi.org/10.1029/JB091iB09p09452

Tsukahara, K., & Takada, Y. (2018). Aseismic fold growth in southwestern Taiwan detected by InSAR and GNSS. *Earth, Planets and Space*, *70*(1), 52. https://doi.org/10.1186/s40623-018-0816-6

Tung, H., & Hu, J.-C. (2012). Assessments of serious anthropogenic land subsidence in Yunlin County of central Taiwan from 1996 to 1999 by Persistent Scatterers InSAR. *Tectonophysics*, *578*, 126–135. https://doi.org/10.1016/j.tecto.2012.08.009

Tung, H., Horng-yue, C., Hsu, Y.-J., Hu, J.-C., Chang, Y.-H., & Kuo, Y.-T. (2019). Triggered slip on multifaults after the 2018 Mw 6.4 Hualien earthquake by continuous GPS and InSAR measurements. *Terrestrial, Atmospheric and Oceanic Sciences*, *30*, 285–300. https://doi.org/10.3319/TAO.2019.04.03.01

Turner, R. C., Shirzaei, M., Nadeau, R. M., & Bürgmann, R. (2015). Slow and Go: Pulsing slip rates on the creeping section of the San Andreas Fault. *Journal of Geophysical Research: Solid Earth*, *120*(8), 5940–5951. https://doi.org/10.1002/2015JB011998

Twardzik, C., Vergnolle, M., Sladen, A., & Avallone, A. (2019). Unravelling the contribution of early postseismic deformation using sub-daily GNSS positioning. *Scientific Reports*, *9*(1), 1775. https://doi.org/10.1038/s41598-019-39038-z

Tymofyeyeva, E., Fialko, Y., Jiang, J., Xu, X., Sandwell, D., Bilham, R., Rockwell, T. K., Blanton, C., Burkett, F., Gontz, A., & Moafipoor, S. (2019). Slow Slip Event On the Southern San Andreas Fault Triggered by the 2017 Mw8.2 Chiapas (Mexico) Earthquake. *Journal of Geophysical Research: Solid Earth*, *124*(9), 9956–9975. https://doi.org/10.1029/2018JB016765

Uchida, N., Iinuma, T., Nadeau, R. M., Bürgmann, R., & Hino, R. (2016). Periodic slow slip triggers megathrust zone earthquakes in northeastern Japan. *Science*, *351*(6272), 488–492. https://doi.org/10.1126/science.aad3108

Usai, S. (2003). A least squares database approach for SAR interferometric data. *IEEE Transactions on Geoscience and Remote Sensing*, *41*(4), 753–760. https://doi.org/10.1109/TGRS.2003.810675

Usai, S., Del Gaudio, C., Borgstrom, S., & Achilli, V. (1999). Monitoring Terrain Deformations at Phlegrean Fields with SAR interferometry. In *Fringe 99 workshop* (Liège, Belgium, Vol. 478). European Space Agency.

Vadacca, L., Casarotti, E., Chiaraluce, L., & Cocco, M. (2016). On the mechanical behaviour of a low-angle normal fault: the Alto Tiberina fault (Northern Apennines, Italy) system case study. *Solid Earth*, *7*(6), 1537–1549. https://doi.org/10.5194/se-7-1537-2016

Vallage, A., Klinger, Y., Grandin, R., Bhat, H. S., & Pierrot-Deseilligny, M. (2015). Inelastic surface deformation during the 2013 Mw 7.7 Balochistan, Pakistan, earthquake. *Geology*, G37290.1. https://doi.org/10.1130/G37290.1

Vallée, M., Nocquet, J.-M., Battaglia, J., Font, Y., Segovia, M., Régnier, M., Mothes, P., Jarrin, P., Cisneros, D., Vaca, S., Yepes, H., Martin, X., Béthoux, N., & Chlieh, M. (2013). Intense interface seismicity triggered by a shallow slow slip event in the Central Ecuador subduction zone. *Journal of Geophysical Research: Solid Earth*, *118*(6), 2965–2981. https://doi.org/10.1002/jgrb.50216

Van Puymbroeck, N., Michel, R., Binet, R., Avouac, J.-P., & Taboury, J. (2000). Measuring earthquakes from optical satellite images. *Applied Optics*, *39*(20), 3486–3494. https://doi.org/10.1364/AO.39.003486

Vergnolle, M., Walpersdorf, A., Kostoglodov, V., Tregoning, P., Santiago, J. A., Cotte, N., & Franco, S. I. (2010). Slow slip events in Mexico revised from the processing of 11 year GPS observations. *Journal of Geophysical Research*, *115*(B8), B08403. https://doi.org/10.1029/2009JB006852

Vernant, P., Hivert, F., Chéry, J., Steer, P., Cattin, R., & Rigo, A. (2013). Erosion-induced isostatic rebound triggers extension in low convergent mountain ranges. *Geology*, *41*(4), 467–470. https://doi.org/10.1130/G33942.1

Voisin, C., Guzmán, M. A. R., Réfloch, A., Taruselli, M., & Garambois, S. (2017). Groundwater Monitoring with Passive Seismic Interferometry. *Journal of Water Resource and Protection*, *9*(12), 1414–1427. https://doi.org/10.4236/jwarp.2017.912091

Voss, N., Dixon, T. H., Liu, Z., Malservisi, R., Protti, M., & Schwartz, S. (2018). Do slow slip events trigger large and great megathrust earthquakes? *Science Advances*, *4*(10), eaat8472. https://doi.org/10.1126/sciadv.aat8472

Voss, N. K., Malservisi, R., Dixon, T. H., & Protti, M. (2017). Slow slip events in the early part of the earthquake cycle: Early Earthquake Cycle SSEs. *Journal of Geophysical Research: Solid Earth*, *122*(8), 6773–6786. https://doi.org/10.1002/2016JB013741

Wadge, G., Webley, P. W., James, I. N., Bingley, R., Dodson, A., Waugh, S., Veneboer, T., Puglisi, G., Mattia, M., Baker, D., Edwards, S. C., Edwards, S. J., & Clarke, P. J. (2002). Atmospheric models, GPS and InSAR measurements of the tropospheric water vapour field over Mount Etna. *Geophysical Research Letters*, *29*(19), 11-1-11–4. https://doi.org/10.1029/2002GL015159

Wald, D. J., Heaton, T. H., & Hudnut, K. W. (1996). The slip history of the 1994 Northridge, California, earthquake determined from strong-motion, teleseismic, GPS, and leveling data. *Bulletin of the Seismological Society of America*, *86*(1; Part B Suppl.), 49–70.

Wallace, K., Guanghua, Y., & Bilham, R. (2004). Inescapable slow slip on the Altyn Tagh fault. *Geophysical Research Letters*, *31*(9), L09613.1-L09613.4. https://doi.org/10.1029/2004GL019724

Wallace, L. M., Beavan, J., Bannister, S., & Williams, C. (2012). Simultaneous long-term and short-term slow slip events at the Hikurangi subduction margin, New Zealand: Implications for processes that control slow slip event occurrence, duration, and migration. *Journal of Geophysical Research: Solid Earth*, *117*(B11). https://doi.org/10.1029/2012JB009489

Wallace, L. M., Webb, S. C., Ito, Y., Mochizuki, K., Hino, R., Henrys, S., Schwartz, S. Y., & Sheehan, A. F. (2016). Slow slip near the trench at the Hikurangi subduction zone, New Zealand. *Science*, *352*(6286), 701–704. https://doi.org/10.1126/science.aaf2349

Walpersdorf, A., Cotte, N., Kostoglodov, V., Vergnolle, M., Radiguet, M., Santiago, J. A., & Campillo, M. (2011). Two successive slow slip events evidenced in 2009-2010 by a dense GPS network in Guerrero, Mexico. *Geophysical Research Letters*, *38*(15). https://doi.org/10.1029/2011GL048124

Walpersdorf, A., Manighetti, I., Mousavi, Z., Tavakoli, F., Vergnolle, M., Jadidi, A., Hatzfeld, D., Aghamohammadi, A., Bigot, A., Djamour, Y., Nankali, H., & Sedighi, M. (2014). Present-day kinematics and fault slip rates in eastern Iran, derived from 11 years of GPS data. *Journal of Geophysical Research: Solid Earth*, *119*(2), 1359–1383. https://doi.org/10.1002/2013JB010620

Walpersdorf, A., Pinget, L., Vernant, P., Sue, C., Déprez, A., & the RENAG team. (2018). Does Long-Term GPS in the Western Alps Finally Confirm Earthquake Mechanisms? *Tectonics*, *37*(10), 3721–3737. https://doi.org/10.1029/2018TC005054

Walters, R. J., Elliott, J. R., Li, Z., & Parsons, B. (2013). Rapid strain accumulation on the Ashkabad fault (Turkmenistan) from atmosphere-corrected InSAR. *Journal of Geophysical Research: Solid Earth*, *118*(7), 3674–3690. https://doi.org/10.1002/jgrb.50236

Walters, R. J., Parsons, B., & Wright, T. J. (2014). Constraining crustal velocity fields with InSAR for Eastern Turkey: Limits to the block-like behavior of Eastern Anatolia: WALTERS ET AL. *Journal of Geophysical Research: Solid Earth*, *119*(6), 5215–5234. https://doi.org/10.1002/2013JB010909

Wang, H., & Wright, T. J. (2012). Satellite geodetic imaging reveals internal deformation of western Tibet. *Geophysical Research Letters*, *39*(7). https://doi.org/10.1029/2012GL051222

Wang, Hua, Wright, T. J., Liu-Zeng, J., & Peng, L. (2019). Strain Rate Distribution in South-Central Tibet From Two Decades of InSAR and GPS. *Geophysical Research Letters*, *46*(10), 5170–5179. https://doi.org/10.1029/2019GL081916

Wang, K., & Fialko, Y. (2014). Space geodetic observations and models of postseismic deformation due to the 2005 *M* 7.6 Kashmir (Pakistan) earthquake: Relaxation due to Kashmir Earthquake. *Journal of Geophysical Research: Solid Earth*, *119*(9), 7306–7318. https://doi.org/10.1002/2014JB011122

Wang, Z., Fukao, Y., & Pei, S. (2009). Structural control of rupturing of the Mw7.9 2008 Wenchuan Earthquake, China. *Earth and Planetary Science Letters*, *279*(1), 131–138. https://doi.org/10.1016/j.epsl.2008.12.038

Weber, J., Geirsson, H., Femina, P. L., Robertson, R., Churches, C., Shaw, K., Latchman, J., Higgins, M., & Miller, K. (2020). Fault Creep and Strain Partitioning in Trinidad-Tobago: Geodetic Measurements, Models, and Origin of Creep. *Tectonics*, *39*(1), e2019TC005530. https://doi.org/10.1029/2019TC005530

Weber, J. C., Dixon, T. H., DeMets, C., Ambeh, W. B., Jansma, P., Mattioli, G., Saleh, J., Sella, G., Bilham, R., & Pérez, O. (2001). GPS estimate of relative motion between the Caribbean and South American plates, and geologic implications for Trinidad and Venezuela. *Geology*, *29*(1), 75–78. https://doi.org/10.1130/0091-7613(2001)029<0075:GEORMB>2.0.CO;2

Wegmüller, U., Werner, C., Strozzi, T., & Wiesmann, A. (2004). Multi-temporal interferometric point target analysis. In *Analysis of Multi-Temporal Remote Sensing Images* (Vol. Volume 3, pp. 136–144). WORLD SCIENTIFIC. https://doi.org/10.1142/9789812702630_0015

Wei, M., Sandwell, D., & Fialko, Y. (2009). A silent Mw 4.7 slip event of October 2006 on the Superstition Hills fault, southern California. *Journal of Geophysical Research: Solid Earth*, *114*(B7). https://doi.org/10.1029/2008JB006135

Wei, M., Sandwell, D., Fialko, Y., & Bilham, R. (2011). Slip on faults in the Imperial Valley triggered by the 4 April 2010 Mw 7.2 El Mayor-Cucapah earthquake revealed by InSAR. *Geophysical Research Letters*, *38*(1). https://doi.org/10.1029/2010GL045235

Weiss, J. R., Walters, R. J., Morishita, Y., Wright, T. J., Lazecky, M., Wang, H., Hussain, E., Hooper, A. J., Elliott, J. R., Rollins, C., Yu, C., González, P. J., Spaans, K., Li, Z., & Parsons, B. (2020). High-resolution surface velocities and strain for Anatolia from Sentinel-1 InSAR and GNSS data. *Geophysical Research Letters*, *n/a*(n/a), e2020GL087376. https://doi.org/10.1029/2020GL087376

Werner, C. L., Rosen, P. A., Hensley, S., Fielding, E. J., & Buckley, S. M. (1997). Detection of aseismic creep along the San Andreas fault near parkfield, California with ERS-1 radar interferometry. In *ERS symposium on space at the service of our environment* (Florence, Italy, Vol. 414, pp. 521–524). Netherlands: European Space Agency.

Wesson, R. L. (1988). Dynamics of fault creep. *Journal of Geophysical Research: Solid Earth*, *93*(B8), 8929–8951. https://doi.org/10.1029/JB093iB08p08929

Williams, P. L., McGill, S. F., Sieh, K. E., Allen, C. R., & Louie, J. N. (1988). Triggered slip along the San Andreas fault after the 8 July 1986 North Palm Springs earthquake. *Bulletin of the Seismological Society of America*, *78*(3), 1112–1122.

Williams, S., Bock, Y., & Fang, P. (1998). Integrated satellite interferometry: Tropospheric noise, GPS estimates and implications for interferometric synthetic aperture radar products. *Journal of Geophysical Research: Solid Earth*, *103*(B11), 27051–27067. https://doi.org/10.1029/98JB02794

Wright, T. J., Parsons, B., & Fielding, E. (2001). Measurement of interseismic strain accumulation across the North Anatolian Fault by satellite radar interferometry. *Geophysical Research Letters*, *28*(10), 2117–2120. https://doi.org/10.1029/2000GL012850

Wright, T. J., Fielding, E., & Parsons, B. (2001). Triggered slip : observations of the 17 August 1999 Izmit (Turkey) earthquake using radar interferometry. *Geophysical Research Letters*, *28*(6), 1079–1082. https://doi.org/10.1029/2000GL011776

Wright, T. J., Parsons, B. E., England, P. C., & Fielding, E. J. (2004). InSAR observations of low slip rates on the major faults of western Tibet. *Science*, *305*(5681), 236–239. https://doi.org/10.1126/science.1096388

Wright, T. J., Parsons, B. E., & Lu, Z. (2004). Toward mapping surface deformation in three dimensions using InSAR. *Geophysical Research Letters*, *31*(1), L01607.1-L01607.5. https://doi.org/10.1029/2003GL018827

Wright, T. J., Ebinger, C., Biggs, J., Ayele, A., Yirgu, G., Keir, D., & Stork, A. (2006). Magma-maintained rift segmentation at continental rupture in the 2005 Afar dyking episode. *Nature*, *442*(7100), 291–294. https://doi.org/10.1038/nature04978

Wright, T. J., Elliott, J. R., Wang, H., & Ryder, I. (2013). Earthquake cycle deformation and the Moho: Implications for the rheology of continental lithosphere. *Tectonophysics*, *609*, 504–523. https://doi.org/10.1016/j.tecto.2013.07.029

Wu, Y.-Y., Hu, J.-C., Lin, G.-P., Chang, C.-P., Tung, H., & Lu, C.-H. (2013). Transient active deformation in Tainan tableland using persistent scatterers SAR interferometry. *Bulletin de La Société Géologique de France*, *184*(4–5), 441–450. https://doi.org/10.2113/gssgfbull.184.4-5.441

Xu, X., & Sandwell, D. T. (2020). Toward Absolute Phase Change Recovery With InSAR: Correcting for Earth Tides and Phase Unwrapping Ambiguities. *IEEE Transactions on Geoscience and Remote Sensing*, *58*(1), 726–733. https://doi.org/10.1109/TGRS.2019.2940207

Xu, X., Tong, X., Sandwell, D. T., Milliner, C. W. D., Dolan, J. F., Hollingsworth, J., Leprince, S., & Ayoub, F. (2016). Refining the shallow slip deficit. *Geophysical Journal International*, *204*(3), 1867–1886. https://doi.org/10.1093/gji/ggv563

Xu, X., Ward, L. A., Jiang, J., Smith-Konter, B., Tymofyeyeva, E., Lindsey, E. O., Sylvester, A. G., & Sandwell, D. T. (2018). Surface Creep Rate of the Southern San Andreas Fault Modulated by Stress Perturbations From Nearby Large Events. *Geophysical Research Letters*, *45*(19), 10,259-10,268. https://doi.org/10.1029/2018GL080137

Xu, X., Sandwell, D. T., & Smith-Konter, B. (2020). Coseismic Displacements and Surface Fractures from Sentinel-1 InSAR: 2019 Ridgecrest Earthquakes. *Seismological Research Letters*, *91*(4), 1979–1985. https://doi.org/10.1785/0220190275

Yamashita, Y., Yakiwara, H., Asano, Y., Shimizu, H., Uchida, K., Hirano, S., Umakoshi, K., Miyamachi, H., Nakamoto, M., Fukui, M., Kamizono, M., Kanehara, H., Yamada, T., Shinohara, M., & Obara, K. (2015). Migrating tremor off southern Kyushu as evidence for slow slip of a shallow subduction interface. *Science*, *348*(6235), 676–679. https://doi.org/10.1126/science.aaa4242

Yan, Y., Doin, M.-P., Lopez-Quiroz, P., Tupin, F., Fruneau, B., Pinel, V., & Trouve, E. (2012). Mexico City Subsidence Measured by InSAR Time Series: Joint Analysis Using PS and SBAS Approaches. *IEEE Journal of Selected Topics in Applied Earth Observations and Remote Sensing*, *5*(4), 1312–1326. https://doi.org/10.1109/JSTARS.2012.2191146

Yang, T. F., Yeh, G.-H., Fu, C.-C., Wang, C.-C., Lan, T.-F., Lee, H.-F., Chen, C.-H., Walia, V., & Sung, Q.-C. (2004). Composition and exhalation flux of gases from mud volcanoes in Taiwan. *Environmental Geology*, *46*(8), 1003–1011. https://doi.org/10.1007/s00254-004-1086-0

Yoshioka, S., Mikumo, T., Kostoglodov, V., Larson, K. M., Lowry, A. R., & Singh, S. K. (2004). Interplate coupling and a recent aseismic slow slip event in the Guerrero seismic gap of the Mexican subduction zone, as deduced from GPS data inversion using a Bayesian information criterion. *Physics of the Earth and Planetary Interiors*, *146*(3–4), 513–530. https://doi.org/10.1016/j.pepi.2004.05.006

You, C.-F., Gieskes, Joris. M., Lee, T., Yui, T.-F., & Chen, H.-W. (2004). Geochemistry of mud volcano fluids in the Taiwan accretionary prism. *Applied Geochemistry*, *19*(5), 695–707. https://doi.org/10.1016/j.apgeochem.2003.10.004

Yu, C., Li, Z., Penna, N. T., & Crippa, P. (2018). Generic Atmospheric Correction Model for Interferometric Synthetic Aperture Radar Observations. *Journal of Geophysical Research: Solid Earth*, *123*(10), 9202–9222. https://doi.org/10.1029/2017JB015305

Yu, C., Penna, N. T., & Li, Z. (2020). Ocean Tide Loading Effects on InSAR Observations Over Wide Regions. *Geophysical Research Letters*, *47*(15), e2020GL088184. https://doi.org/10.1029/2020GL088184

Yu, S.-B., & Kuo, L.-C. (2001). Present-day crustal motion along the Longitudinal Valley Fault, eastern Taiwan. *Tectonophysics*, *333*(1–2), 199–217.

Yu, S.-B., & Liu, C.-C. (1989). Fault creep on the central segment of the longitudinal valley fault, eastern Taiwan. *Proceedings of the Geological Society of China*, *32*(3), 209–231.

Yu, S.-B., Chen, H.-Y., & Kuo, L.-C. (1997). Velocity field of GPS stations in the Taiwan area. *Tectonophysics*, *274*(1–3), 41–59.

Yue, L.-F., Suppe, J., & Hung, J.-H. (2005). Structural geology of a classic thrust belt earthquake: the 1999 Chi-Chi earthquake Taiwan (Mw=7.6). *Journal of Structural Geology*, *27*(11), 2058–2083. https://doi.org/10.1016/j.jsg.2005.05.020

Zhan, Z. (2020). Distributed Acoustic Sensing Turns Fiber-Optic Cables into Sensitive Seismic Antennas. *Seismological Research Letters*, *91*(1), 1–15. https://doi.org/10.1785/0220190112

Zhang, H., Koper, K. D., Pankow, K., & Ge, Z. (2017). Imaging the 2016 Mw 7.8 Kaikoura, New Zealand, earthquake with teleseismic P waves: A cascading rupture across multiple faults. *Geophysical Research Letters*, *44*(10), 4790–4798. https://doi.org/10.1002/2017GL073461

Zhang, Y., Chen, Y.-T., & Feng, W. (2019). Complex multiple-segment ruptures of the 28 September 2018, Sulawesi, Indonesia, earthquake. *Science Bulletin*, *64*(10), 650–652. https://doi.org/10.1016/j.scib.2019.04.018

Zigone, D., Rivet, D., Radiguet, M., Campillo, M., Voisin, C., Cotte, N., Walpersdorf, A., Shapiro, N. M., Cougoulat, G., Roux, P., Kostoglodov, V., Husker, A., & Payero, J. S. (2012). Triggering of tremors and slow slip event in Guerrero, Mexico, by the 2010 Mw 8.8 Maule, Chile, earthquake. *Journal of Geophysical Research: Solid Earth*, *117*(B9). https://doi.org/10.1029/2012JB009160

Zinke, R., Hollingsworth, J., & Dolan, J. F. (2014). Surface slip and off-fault deformation patterns in the 2013 MW 7.7 Balochistan, Pakistan earthquake: Implications for controls on the distribution of near-surface coseismic slip. *Geochemistry, Geophysics, Geosystems*, *15*(12), 5034–5050. https://doi.org/10.1002/2014GC005538

Zinke, R., Hollingsworth, J., Dolan, J. F., & Dissen, R. V. (2019). Three-Dimensional Surface Deformation in the 2016 MW 7.8 Kaikōura, New Zealand, Earthquake From Optical Image Correlation: Implications for Strain Localization and Long-Term Evolution of the Pacific-Australian Plate Boundary. *Geochemistry, Geophysics, Geosystems*, *20*(3), 1609–1628. https://doi.org/10.1029/2018GC007951

Zumberge, M. A., & Wyatt, F. K. (1998). Optical Fiber Interferometers for Referencing Surface Benchmarks to Depth. *Pure and Applied Geophysics*, *152*(2), 221–246. https://doi.org/10.1007/s000240050152

Publications and communications as author or coauthor

Summary of publications record: 24 per-reviewed Journal Article in international journal. More than 80 presentations in international congress or workshop.

H-Index: 15 (source Web of Science and Scopus, May 2020).

Citation of those items in this memoir is using a letter followed by a number as a clickable link (e.g. A18) following this classification:

- A##: Peer-reviewed Journal Article published in international journals.
- P##: Peer-reviewed Conference Proceedings.
- C##: Communications (Oral or Poster presentation) in international meetings.
- O##: Other communications (in French, not peer-reviewed article, unpublished reports…)

Author* indicates when the first author is a student or a post-doctoral researcher I have supervised.

Journal Article (A#)

[A26 In prep.] : Pathier, E. Fruneau B., Hu Jyr-Ching, Lebeon Maryline, Doin M.-P. Champenois, J., Fekaouni M., Deffontaines B., Tung H. et al. (In preparation) Structural Geodesy in the South-Western Taiwan fold-and-thrust belt. To be submitted to Frontiers in Sciences issue "Active Fold-and-Thrust Belts: From Present-Day Deformation to Structural Architecture and Modelling"

[A25] Mousavi, Z., Fattahi, M., Khatib, M., Talebian, M., Pathier, E., Walpersdorf, A., Sloan, A., Thomas, A., Rhodes, E., Clive, F., Dodds, N., Walker, R.. Constant slip-rate on the Doruneh strike-slip fault, Iran, averaged over Late Pleistocene, Holocene, and decadal timescales. Submitted to Tectonics 2020, in review.

[A24] Maubant*, L., Pathier, E., Daout, S., Radiguet, M., Doin, M. -P., Kazachkina, E., Kostoglodov, V., Cotte, N., & Walpersdorf, A. (2020). Independent Component Analysis and Parametric Approach for Source Separation in InSAR Time Series at Regional Scale: Application to the 2017–2018 Slow Slip Event in Guerrero (Mexico). Journal of Geophysical Research: Solid Earth, 125(3). https://doi.org/10.1029/2019JB018187

[A23] Socquet, A., Hollingsworth, J., Pathier, E., & Bouchon, M. (2019). Evidence of supershear during the 2018 magnitude 7.5 Palu earthquake from space geodesy. Nature Geoscience, 12(3), 192–199. https://doi.org/10.1038/s41561-018-0296-0

[A22] Lacroix, P., Bièvre, G., Pathier, E., Kniess, U., & Jongmans, D. (2018). Use of Sentinel-2 images for the detection of precursory motions before landslide failures. Remote Sensing of Environment, 215, 507–516. https://doi.org/10.1016/j.rse.2018.03.042

[A21] Pousse-Beltran*, L., Vassallo, R., Audemard, F., Jouanne, F., Carcaillet, J., Pathier, E., & Volat, M. (2017). Pleistocene slip rates on the Boconó fault along the North Andean Block plate boundary, Venezuela. Tectonics, 36(7), 1207–1231. https://doi.org/10.1002/2016TC004305

[A20] Béon, M. L., Huang, M.-H., Suppe, J., Huang, S.-T., Pathier, E., Huang, W.-J., Chen, C.-L., Fruneau, B., Baize, S., Ching, K.-E., & Hu, J.-C. (2017). Shallow geological structures triggered during the Mw 6.4 Meinong earthquake, southwestern Taiwan. Terrestrial, Atmospheric and Oceanic Sciences, 28(5), 663–681. https://doi.org/10.3319/TAO.2017.03.20.02

[A19] Deffontaines, B., Chang, K.-J., Champenois, J., Fruneau, B., Pathier, E., Hu, J.-C., Lu, S.-T., & Liu, Y.-C. (2017). Active interseismic shallow deformation of the Pingting terraces (Longitudinal Valley – Eastern Taiwan) from UAV high-resolution topographic data combined with InSAR time series. Geomatics, Natural Hazards and Risk, 8(1), 120–136. https://doi.org/10.1080/19475705.2016.1181678

[A18] Pousse Beltran*, L., Pathier, E., Jouanne, F., Vassallo, R., Reinoza, C., Audemard, F., Doin, M. P., & Volat, M. (2016). Spatial and temporal variations in creep rate along the El Pilar fault at the Caribbean-South American plate boundary (Venezuela), from InSAR. Journal of Geophysical Research: Solid Earth, 121(11), 8276–8296. https://doi.org/10.1002/2016JB013121

[A17] Bièvre, G., Jongmans, D., Goutaland, D., Pathier, E., & Zumbo, V. (2016). Geophysical characterization of the lithological control on the kinematic pattern in a large clayey landslide (Avignonet, French Alps). Landslides, 13(3), 423–436. https://doi.org/10.1007/s10346-015-0579-0

[A16] Mousavi*, Z., Pathier, E., Walker, R. T., Walpersdorf, A., Tavakoli, F., Nankali, H., Sedighi, M., & Doin, M.-P. (2015). Interseismic deformation of the Shahroud fault system (NE Iran) from space-borne radar interferometry measurements. Geophysical Research Letters, 42(14), 5753–5761. https://doi.org/10.1002/2015GL064440

[A15] Riedel, I., Guéguen, P., Dalla Mura, M., Pathier, E., Leduc, T., & Chanussot, J. (2015). Seismic vulnerability assessment of urban environments in moderate-to-low seismic hazard regions using association rule learning and support vector machine methods. Natural Hazards, 76(2),1111–1141. https://doi.org/10.1007/s11069-014-1538-0

[A14] Mousavi*, Z., Walpersdorf, A., Walker, R. T., Tavakoli, F., Pathier, E., Nankali, H., Nilfouroushan, F., & Djamour, Y. (2013). Global Positioning System constraints on the active tectonics of NE Iran and the South Caspian region. Earth and Planetary Science Letters, 377–378, 287–298. https://doi.org/10.1016/j.epsl.2013.07.007

[A13] Cavalié*, O., Pathier, E., Radiguet, M., Vergnolle, M., Cotte, N., Walpersdorf, A., Kostoglodov, V., & Cotton, F. (2013). Slow slip event in the Mexican subduction zone: Evidence of shallower slip in the Guerrero seismic gap for the 2006 event revealed by the joint inversion of InSAR and GPS data. Earth and Planetary Science Letters, 367, 52–60. https://doi.org/10.1016/j.epsl.2013.02.020

[A12] Yan*, Y., Pinel, V., Trouvé, E., Pathier, E., Perrin, J., Bascou, P., & Jouanne, F. (2013). Coseismic displacement field and slip distribution of the 2005 Kashmir earthquake from SAR amplitude image correlation and differential interferometry. Geophysical Journal International, 193(1), 29–46. https://doi.org/10.1093/gji/ggs102

[A11] Champenois*, J., Fruneau, B., Pathier, E., Deffontaines, B., Lin, K.-C., & Hu, J.-C. (2012). Monitoring of active tectonic deformations in the Longitudinal Valley (Eastern Taiwan) using Persistent Scatterer InSAR method with ALOS PALSAR data. Earth and Planetary Science Letters, 337–338, 144–155. https://doi.org/10.1016/j.epsl.2012.05.025

[A10] Yan*, Yajing, Trouvé, E., Pinel, V., Mauris, G., Pathier, E., & Galichet, S. (2012). Fusion of D-InSAR and sub-pixel image correlation measurements for coseismic displacement field estimation: Application to the Kashmir earthquake (2005). International Journal of Image and Data Fusion, 3(1), 71–92. https://doi.org/10.1080/19479832.2011.577563

[A09] Bièvre, G., Kniess, U., Jongmans, D., Pathier, E., Schwartz, S., van Westen, C. J., Villemin, T., & Zumbo, V. (2011). Paleotopographic control of landslides in lacustrine deposits (Trièves plateau, French western Alps). Geomorphology, 125(1), 214–224. https://doi.org/10.1016/j.geomorph.2010.09.018

[A08] de Michele, M., Raucoules, D., Lasserre, C., Pathier, E., Klinger, Y., Van Der Woerd, J., de Sigoyer, J., & Xu, X. (2010). The M w 7.9, 12 May 2008 Sichuan earthquake rupture measured by sub-pixel correlation of ALOS PALSAR amplitude images. Earth, Planets and Space, 62(11), 875–879. https://doi.org/10.5047/eps.2009.05.002

[A07] Huang, M.-H., Hu, J.-C., Ching, K.-E., Rau, R.-J., Hsieh, C.-S., Pathier, E., Fruneau, B., & Deffontaines, B. (2008). Active deformation of Tainan tableland of southwestern Taiwan based on geodetic measurements and SAR interferometry. Tectonophysics, 466(3–4), 322–334. https://doi.org/10.1016/j.tecto.2007.11.020

[A06] Pathier, E., Fielding, E. J., Wright, T. J., Walker, R., Parsons, B. E., & Hensley, S. (2006). Displacement field and slip distribution of the 2005 Kashmir earthquake from SAR imagery. Geophysical Research Letters, 33(20). https://doi.org/10.1029/2006GL027193

[A05] Huang, M.-H., Hu, J.-C., Hsieh, C.-S., Ching, K.-E., Rau, R.-J., Pathier, E., Fruneau, B., & Deffontaines, B. (2006). A growing structure near the deformation front in SW Taiwan as deduced from SAR interferometry and geodetic observation. Geophysical Research Letters, 33(12), L12305. https://doi.org/10.1029/2005GL025613

[A04] Chang, C. P., Wang, C. T., Chang, T. Y., Chen, K. S., Liang, L. S., Pathier, E., & Angelier, J. (2004). Application of SAR interferometry to a large thrust deformation: the 1999 Mw= 7.6 Chichi earthquake in central Taiwan. Geophysical Journal International, 159(1), 9–16. https://doi.org/10.1111/j.1365-246X.2004.02385.x

[A03] Pathier, E., Fruneau, B., Deffontaines, B., Angelier, J., Chang, C.-P., Yu, S.-B., & Lee, C.-T. (2003). Coseismic displacements of the footwall of the Chelungpu fault caused by the 1999, Taiwan, Chi-Chi earthquake from InSAR and GPS data. Earth and Planetary Science Letters, 212(1), 73–88. https://doi.org/10.1016/S0012-821X(03)00244-9

[A02] Fruneau, B., Pathier, E., Raymond, D., Deffontaines, B., Lee, C. T., Wang, H. T., Angelier, J., Rudant, J. P., & Chang, C. P. (2001). Uplift of Tainan Tableland (SW Taiwan) revealed by SAR Interferometry. Geophysical Research Letters, 28(16), 3071–3074. https://doi.org/10.1029/2000GL012437

[A01] Deffontaines, B., Liu, C.-S., Angelier, J., Lee, C.-T., Sibuet, J.-C., Tsai, Y.-B., Lallemand, S., Lu, C.-Y., Lee, C.-S., Hsu, S.-K., Chu, H.-T., Lee, J.-C., Pathier, E., Chen, R.-F., Cheng, C.-T., Cheng, C.-W., & L, C.-W. (2001). Preliminary Neotectonic Map of Onshore-offshore Taiwan. Terrestrial, Atmospheric and Oceanic Sciences, 12(2–1), 339. https://doi.org/10.3319/TAO.2001.12.S.339(T)

Conference Proceedings (P#)

[P05] Matsuka*, P., Chanussot, J., Pathier, E., & Gueguen, P. (2012). A support vector regression approach for building seismic vulnerability assessment and evaluation from remote sensing and in-situ data. In IGARS 2012 IEEE International Geoscience and Remote Sensing Symposium (pp. 7533–7536). Munich, Germany. https://doi.org/10.1109/IGARSS.2012.6351888

[P04] Doin, M.-P., Lodge, F., Guillaso, S., Jolivet, R., Lasserre, C., Ducret, G., Grandin, R., Pathier, E., & Pinel, V. (2011). Presentation of the small baseline NSBAS processing chain on a case example: The Etna deformation monitoring from 2003 to 2010 using Envisat data. In Proc. of the Fringe 2011 Workshop “Advances in the Science and Applications of SAR Interferometry” (Vol. ESA SP-697). Frascati, Italy: ESA. Retrieved from

https://earth.esa.int/documents/10174/1573056/Presentation_small_baseline_NSBAS_Etna_deformation_Envisat.pdf

[P03] Yan*, Y., Trouvé, E., Bisserier, A., Mauris, G., Galichet, S., Pinel, V., & Pathier, E. (2010). Assimilation of D-InSAR and sub-pixel image correlation displacement measurements for coseismic fault parameter estimation. In IGARS 2010 IEEE International Geoscience and Remote Sensing Symposium (pp. 3664–3667). Honolulu, HI, USA. https://doi.org/10.1109/IGARSS.2010.5654408

[P02] Jongmans, D., Renalier, F., Kniess, U., Schwartz, S., Pathier, E., Orengo, Y., Bièvre, G., Villemin, T., & Delacourt, C. (2008). Characterization of the Avignonet landslide (French Alps) with seismic techniques. In Z. Chen, J. Zhang, Z. Li, F. Wu, & K. Ho (Eds.), Landslides and Engineered Slopes. From the Past to the Future (pp. 395–401). Xian, China: CRC Press. https://doi.org/10.1201/9780203885284-c39

[P01] Pathier, E., Angelier, J., Fruneau, B., & Deffontaines, B. (2003). Contributions of InSAR to study active tectonics of Taiwan. In IGARSS 2003. 2003 IEEE International Geoscience and Remote Sensing Symposium. Proceedings (IEEE Cat. No.03CH37477) (Vol. 1, pp. 221–223). Toulouse, France: IEEE. https://doi.org/10.1109/IGARSS.2003.1293730

Communications (C#)

[C82] Hollingsworth, J., Maubant, L., Pathier, E., & Socquet, A. (2019, December). Shallow slip deficit and off-fault deformation in the 2016 Norcia earthquake derived from 3D optical image correlation. American Geophysical Union, Fall Meeting 2019, abstract #S21E-0551. http://adsabs.harvard.edu/abs/2019AGUFM.S21E0551H

[C81] Maubant*, L., Pathier, E., Daout, S., Radiguet, M., Doin, M. P., Kazachkina, E., Kostoglodov, V., Cotte, N., & Walpersdorf, A. (2019, December). Independent Component Analysis and parametric approach for source separation in InSAR time-series at regional scale: application to 2017 - 2018 Slow Slip Event in Guerrero (Mexico). American Geophysical Union, AGU Fall Meeting 2019, abstract #T13D-0306. http://adsabs.harvard.edu/abs/2019AGUFM.T13D0306M

[C80] Pathier, E., Fruneau, B., Fekaouni, M., Doin, M.-P., & Hu, J.-C. (2019, October). New evidences for active folding in the coastal plain of SW Taiwan from Sentinel-1 InSAR. Presented at the 8th France-Taiwan Symposium in Earth Sciences, Pau, France.

[C79] Maubant*, L., Pathier, E., Daout, S., Radiguet, M., Doin, M.-P., Kazachkina, E., Kostoglodov, V., Cotte, N., & Walpersdorf, A. (2019). Separating transient tectonic signal from atmospheric signal in InSAR time-series, the case of the 2017-2018 Slow Slip Event in Guerrero (Mexico). Presented at the Reunion Anual Union Geofisica Mexicana, Puerto Vallarta, Mexico.

[C78] Durand, P., Proy, C., Clesse, D., Donadieu, J., Doin, M.-P., Thollard, F., Pathier, E., Laurent, C., Lasserre, C., Grandin, R., & Deschamps-Ostanciaux, E. (2019). Large-scale spatial and temporal interferometry processing results and products. Status of PEPS processing services. Presented at the MDIS 2019, 5eme colloque MDIS-ForM@Ter (Mesure de la Déformation par Imagerie Spatiale), Strasbourg, France.

[C77] Pathier, E., Fruneau, B., Fekaouni, M., Doin, M.-P., & Hu, J.-C. (2019, October). New evidences for active folding in SW Taiwan from Sentinel-1 InSAR. Presented at the MDIS 2019, 5eme colloque MDIS-ForM@Ter (Mesure de la Déformation par Imagerie Spatiale), Strasbourg, France.

[C76] Maubant*, L., Pathier, E., Daout, S., Radiguet, M., Doin, M.-P., Kazachkina, E., Kostoglodov, V., Cotte, N., & Walpersdorf, A. (2019, October). Separating transient tectonic signal from atmospheric signal in InSAR time-series, the case of the 2017-2018 Slow slip event in Guerrero (Mexico). Presented at

the MDIS 2019, 5eme colloque MDIS-ForM@Ter (Mesure de la Déformation par Imagerie Spatiale), Strasbourg.

[C75] Espín Bedón*, Audin, L., Doin, M.-P., Pathier, E., Alvarado, A., Thollard, F., C.Laurent, Jm., Mothes, P., Segovia, M., Vaca, S., & Beauval, C. (2019, September). Deformation monitoring from Synthetic Aperture RadarInterferometry (INSAR) Sentinel data in Quito, Ecuador. Presented at the 8th International Symposium on Andean Geodynamics (ISAG), Quito, Ecuador.

[C74] Deschamps-Ostanciaux, E., Thollard, F., Monasson, S., Pointal, E., Laurent, C., Doin, M.-P., Pathier, E., Pinel, V., Lasserre, C., Grandin, R., & DIament, M. (2019, April). A new service for computing Sentinel-1 InSAR interferograms using NSBAS. Abstract Id.16898 presented at the 21st EGU General Assembly, EGU2019, Vienna, Austria.

[C73] Thollard, F., Monasson, S., Pointal, E., Laurent, C., Deschamps-Ostanciaux, E., Doin, M.-P., Pathier, E., Pinel, V., Lasserre, C., Grandin, R., & DIament, M. (2019, May). On demand service for Sentinel-1 InSAR processing using NSBAS. Presented at the ESA Living Planet Symposium, Milan, Italy.

[C72] Maubant*, L., Pathier, E., Daout, S., Radiguet, M., Doin, M. P., Kazachkina, E., Kostoglodov, V., & Cotte, N. (2018, December). The 2017 Slow slip event in Guerrero (Mexico), seen by spatial geodesy. Abstract T43E-0437 presented at the AGU Fall Meeting 2018, Washington, USA.

[C71] Pathier, E., Mousavi, Z., Walpersdorf, A., & Doin, M.-P. (2018, November). Potential of Sentinel-1 InSAR to study for active tectonics of Eastern Iran. Presented at the 2nd TRIGGER international Conference, University of Tehran, Iran.

[C70] Pathier, E., Fruneau, B., Doin, M.-P., & Hu, J.-C. (2018, September). Comparison between present-day and Holocene deformation in SW Taiwan based on a full coverage of the Taiwan Island by InSAR. Presented at the 19th general assembly of Wegener on earth deformation and the study of earthquakes using geodesy and geodynamics, Grenoble, France.

[C69] Maubant*, L., Pathier, E., Daout, S., Radiguet, M., Doin, M.-P., Kazachkina, E., Kostoglodov, V., & Cotte, N. (2018, September). The 2017 Slow Slip Event in Guerrero Area (Mexico), seen by spatial geodesy. Presented at the 19th general assembly of Wegener on earth deformation and the study of earthquakes using geodesy and geodynamics, Grenoble, France.

[C68] Pathier, E., Doin, M.-P., Lasserre, C., Kostoglodov, V., Thollard, F., & Volat, M. (2017, October). Potential of Sentinel-1 InSAR to study slow earthquakes in the Mexican subduction zone. Presented at the MDIS 2017, 4eme colloque MDIS-Form@Ter (Mesure de la Déformation par Imagerie Spatiale), Besse en Chandesse, France.

[C67] Pathier, E., Rojo-Limon, G., Radiguet, M., Kostoglodov, V., Cotte, N., Doin, M. P., Walpersdorf, A., & Volat, M. (2017, June). Interseismic deformation in the Mexican subduction zone, investigating for crustal deformation in the upper plate. Presented at the ESA Fringe 2017, Helsinki, Finland.

[C66] Fruneau, B., Pathier, E., Doin, M., Hu, J.-C., Tung, H., Doin, M. P., Walpersdorf, A., & Volat, M. (2017, June). Present-day Deformation in Taiwan Mountain Belt as Monitored by InSAR. Presented at the ESA Fringe 2017, Helsinki, Finland.

[C65] Pousse* Beltran, L., Jouanne, F., Pathier, E., Reinoza, C., Audemard, F., & Doin, M. P. (2017, June). Creeping behavior of El Pilar Fault is persistent over time? Presented at the ESA Fringe 2017, Helsinki, Finland.

[C64] Lasserre, C., Pinel-Puyssegur, B., Champenois, J., Vergnolle, M., Voisin, C., Klinger, Y., Doin, M.-P., Pathier, E., Brax, M., & Abdel-Massih, D. (2017, June). Present-day Deformation in Lebanon Measured by Synthetic Aperture Radar Interferometry (InSAR). Presented at the ESA Fringe 2017, Helsinki, Finland.

[C63] Le Béon Maryline, Mong-Han Huang, Erwan Pathier, John Suppe, Shiuh-Tsann Huang, Bénédicte Fruneau , Patterns and Mechanisms of Interseismic, Coseismic, Late Quaternary and Pliocene

Deformation in the Foothills of Southwestern Taiwan Mountain Belt, Abstract T21E-04, AGU 2016 Fall meeting.

[C62] Pathier Erwan, Marie-Pierre Doin, Matthieu Volat, Bekaert David, Mathilde Radiguet, Kostoglodov Vladimir, Cécile Lasserre, Nathalie Cotte, Andrea Walpersdorf. Exploring ALOS-2/SENTINEL-1 InSAR capability to study the earthquake cycle of the Mexican subduction zone. ESA Living Planet symposium, Prague, Czech Republic, 9-13 May 2016

[C61] Fruneau Bénédicte, Pathier Erwan, Doin Marie-Pierre, Hu Jyr-Ching, Volat Matthieu, Champenois Johann; Complete and Consistent Mapping of Taiwan Island with InSAR, ESA Living Planet symposium, Prague, Czech Republic, 9-13 May 2016

[C60] Pathier Erwan, Doin Marie-Pierre, Radiguet Mathilde, Bekaert David, Kostoglodov Vladimir, Walpersdorf Andrea, Lasserre Cécile, INSAR Contribution to the Study of Slow-Slip Events along the Mexican Subduction Zone. 2nd PI workshop for ALOS-2 Nov 2015, Tokyo.

[C59] Pathier Erwan, J-C Hu, B. Fruneau, M-P. Doin, Y-T. Liao, Champenois (2015), Present-day deformation of anticlines in an active foreland fold-and-thrust belt measured from ALOS-1 InSAR and GPS: the Southwestern Taiwan case. ESA Fringe 2015, Advances in the Science and Applications of SAR interferometry and Sentinel-1 InSAR workshop, http://seom.esa.int/fringe2015/files/presentation175.pdf 23-27 march 2015, ESA-ESRIN, Frascati, Italy.

[C58] Fruneau Bénédicte, Pathier Erwan, Doin Marie-Pierre, Volat Matthieu, Champenois Johann, Hu Jyr-Ching. (2015) Complete and Consistent Coverage of Taiwan Island by InSAR. ESA Fringe 2015, Advances in the Science and Applications of SAR interferometry and Sentinel-1 InSAR workshop, 23-27 march 2015, ESA-ESRIN, Frascati, Italy.

[C57] Pousse* Lea, F. Jouanne, E. Pathier, C. Reinoza, F. Audemard, R. Vassallo, M. Volat: Insight into a creeping plate boundary in Northeastern Venezuela from ALOS1 InSAR data. 2nd MDIS ForM@Ter workshop (Deformation measurement by space imagery), Autrans, 7-9 oct. 2015

[C56] Pathier Erwan, Fruneau B., Doin M.P., Hu J.-C., Liao Y.-T., Champenois Y., Present-day deformation in Taiwan measured from ALOS-1 InSAR and GPS, 2nd MDIS ForM@Ter workshop (Deformation measurement by space imagery), Autrans, 7-9 oct. 2015.

[C55] Pathier Erwan, Marie-Pierre Doin, Cécile Lasserre (2015). Observation of subduction slow slip events by Space-borne SAR interferometry: achievement, limits and potential. International Workshop on Tectonic Tremors and Silent Seismicity, February 25–27, 2015, Institute of Geophysics, UNAM, Mexico.

[C54] Pousse* Lea, Vassallo Ricardo, Jouanne François, Audemard Franck, Pathier Erwan, Carcaillet Julien, Garambois Stéphane, Oropeza J., Aray J. (2015). Geomorphological slip rate and preliminary paleoseismological study along the Bocono Fault, Venezuela.6th International INQUA Meeting on Paleoseismology, Active Tectonics and Archaeoseismology, 19-24 April 2015, Pescina, Fucino Basin, Italy.

[C53] Pathier E., B. Fruneau, M-P. Doin, Y-T. Liao, J-C Hu, Champenois (2014), What are the tectonic structures accommodating the present-day tectonic deformation in South-Western Taiwan? A new interpretation from ALOS-1 InSAR and GPS interseismic measurements. Geodynamics and Environment in East Asia: 7th France-Taiwan Earth Sciences Symposium. 12-15 novembre 2014, Hualien, Taiwan.

[C52] Champenois* J., B. Fruneau, B. Deffontaines, E. Pathier & J-C. Hu (2014) From Collision to subduction, monitoring of ground displacements of the Hengchun Peninsula using Persistent Scatterer Interferometry. Geodynamics and Environment in East Asia: 7th France-Taiwan Earth Sciences Symposium. 12-15 novembre 2014, Hualien, Taiwan.

[C51] Champenois* J., Benoit Deffontaines, Bénédicte Fruneau, Erwan Pathier, Jyr-Ching Hu (2014. Active interseismic shallow deformation from combined time-series SAR Interferometry: study case of the Pingting Terraces (Eastern Taiwan). Geodynamics and Environment in East Asia: 7th France-Taiwan Earth Sciences Symposium. 12-15 novembre 2014, Hualien, Taiwan.

[C50] Volat, M., Vernier, F., Doin, M.-P., Lasserre, C., Trouvé, E., & Pathier, E. (2014). Improving the execution of workflows for SAR image analysis. Presented at the Conference on Big Data from Space, Nov. 2014, Frascati, Italy.

[C50] Pathier Erwan, Bénédicte Fruneau, Marie-Pierre Doin, Jyr-Ching Hu, Johann Champenois, and Yu-Tzu Liao (2014), New Insight Into Southwestern Taiwan Active Tectonic Deformation From ALOS-InSAR and GPS Observations. GENAH, International Symposium on Geodesy for Earthquake and Natural Hazards (GENAH), Matsushima, Japan, 22 - 26 July 2014.

[C49] Deffontaines B., J. Champenois, B. Fruneau, E. Pathier, K.C. Lin, R.-F. Chen and J.-C.Hu, Active tectonics from PSI , Small baseline and DINSAR interferometry: case studies fromTaiwan, IAEG Torino 2014, session6.2.

[C48] Pathier Erwan, Guillaume Bacques; Marie-Pierre Doin, Olivier Cavalié, Mathilde Radiguet, Cécile Lasserre, Cotte Nathalie, Walpersdorf Andrea (2013), Extent of slow slip events in the Guerrero seismic gap (Mexico): observations from space-borne SAR interferometry. Abstract G23B-0783, AGU 2013 Fall meeting.

[C47] Liao* Yu-Tzu Liao, Jyr-Ching Hu, Johann Champenois, and Erwan Pathier, Assessment of the fault segmentation and strain accumulation in the northern Longitudinal Valley fault of eastern Taiwan by PS-InSAR with ALOS images, Geophysical Research Abstracts, Vol. 15, EGU2013-3825-1, 2013, EGU General Assembly 2013

[C46] Lasserre C., B. Pinel-Puysségur, M. Vergnolle, Y. Klinger, E. Pathier (2012). Active faults in Lebanon: kinematics and interseismic behavior measured from radar interferometry (InSAR). Abstract G51B-1103, AGU 2012 Fall meeting.

[C45] Mousavi* Z., A. Walpersdorf, R. T. Walker, F. Tavakoli, E. Pathier, H. Nankali, F. Nilfouroushan, A. Aghamohammadi, Y. Djamour (2012). Present-day deformation in NE Iran and the South Caspian constraint by Global Positioning System measurements. Abstract G52A-08, AGU 2012 Fall meeting.

[C44] Radiguet M., F. Cotton, O. Cavalié, E. Pathier, V. Kostoglodov, M. Vergnolle, M. Campillo, A. Walpersdorf, N. Cotte, J. Santiago, S. Franco (2012). Slow slip events in Guerrero, Mexico, and consequences on strain accumulation over the past 15 years. Abstract T12C-06, AGU 2012 Fall Meeting.

[C43] Matsuka*, P., J. Chanussot, E. Pathier and P. Gueguen. 2012. A new framework for assessing building seismic vulnerability using non-linear regression for remote sensing and in-situ data. A study case for Grenoble, France, 15th World Conf. Earhquake Engineering, 24-28 September 2012, Lisboa, Portugal.

[C42] Mousavi* Z., E. Pathier, A. Walpersdorf, C. Lassere, F. Tavakli, and H. Nankali (2012). InSAR Time Series Analysis of Interseismic Deformation in Eastern Iran. Ref: EGU2012-9846, EGU General Assembly 2012 meeting.

[C41] Hu J-C., J. Champenois, K.-C. Lin, B. Fruneau, E. Pathier. Monitoring of active faults along the collisional plate Boundary in Taiwan by PS-InSAR and continuous GPS measurements (2012), Modern and ancient Orogenic Belts. GSA Northeastern Section 47th Annual Meeting, 18-20 March 2012, Hartford Connecticut.

[C40] Bacques* G., E. Pathier, C. Lasserre, F. Cotton, M. Radiguet (2011). The 2009-2010 Guerrero Slow Slip Event Monitored by InSAR, Using Time Series Approach. Abstract G23A-0841, AGU 2011 fall meeting.

[C39] Hu J-C., J. Champenois, K-C. Lin, B. Fruneau, E. Pathier, Segmentation along the Longitudinal Valley Fault in a Collision Plate Boundary in Taiwan by PS-InSAR and Continuous GPS Measurements, G23A-0831, AGU 2011 Fall meeting.

[C38] Doin M.-P., F. Lodge, S. Guillaso, R. Jolivet, C. Lasserre, G. Ducret, R. Grandin, E. Pathier, and V. Pinel (2011), Presentation of the small baseline NSBAS processing chain on a case example: the Etna deformation monitoring from 2003 to 2010 using ENVISAT data. European Space Agency Fringe 2011 Workshop, Frascati, Italy.

[C37] Charara* R., M.-P. Doin, B. Fruneau, E. Pathier, J. Champenois, J.-C. Hu, K.-C. Lin (2011), Correcting DInSAR ALOS data using atmospheric delay estimated by GPS signals to constrain the surface deformation in the Longitudinal Valley (Taiwan Island). European Space Agency Fringe 2011 Workshop, Frascati, Italy.

[C36] Champenois* J., B. Fruneau, E. Pathier, B. Deffontaines, K.-C. Lin, J.-C. Hu (2011) , Monitoring of interseismic creep of the Longitudinal Valley Fault (Eastern Taiwan) using Persistent Scatterer InSAR with ALOS PALSAR data. European Space Agency Fringe 2011 Workshop, Frascati, Italy.

[C35] Champenois* J., B. Deffontaines, B. Fruneau, E. Pathier, J-C. Hu, K.-C. Lin. (2011) Persistent Scatterer InSAR applied to the South West of Taiwan: neotectonic implications. European Space Agency Fringe 2011 Workshop, Frascati, Italy.

[C34] Mousavi* Z., E. Pathier, A. Walpesrdorf, C. Lasserre, I. Manighetti, M. Vergnolle, F. Tavakoli, H. Nankali. (2011), InSAR Time series Analysis of Interseismic deformation of Eastern part of Iran. European Space Agency Fringe 2011 Workshop, Frascati, Italy.

[C33] Bacques* G, E. Pathier, C. Lasserre, M.-P. Doin, R. Jolivet, M. Radiguet, A. Walpersdorf, N. Cotte, D. Raucoules, F. Cotton. (2011), Estimation of the surface deformation due to the 2009-2010 slow slip event at Guerrero seismic gap (Mexico) by satellite SAR Interferometry. European Space Agency Fringe 2011 Workshop, Frascati, Italy.

[C32] Yan* Y., V. Pinel, E. Trouvé, E. Pathier (2011), Investigation of different strategies for fault parameters and slip distribution retrieval of the 2005 Kashmir earthquake using SAR imagery. European Space Agency Fringe 2011 Workshop, Frascati, Italy.

[C31] Radiguet, M., E. Pathier, G. Bacques, M. Campillo, N. Cotte, F. Cotton, V. Kostoglodov, M. Vergnolle, and A. Walpersdorf, Coupling and kinematic properties of slow slip events in the Guerrero Gap, Mexico, EGU General Assembly 2011, Vienna, Geophysical Research Abstracts, Vol. 13, EGU2011-9070, 2011.

[C30] Champenois* Johann, Bénédicte Fruneau, Erwan Pathier, Kuan-Chuan Lin, and Jyr-Ching Hu, Monitoring of the Longitudinal Valley Fault (Eastern Taiwan) using PS-InSAR method with ALOS data; EGU General Assembly 2011, Vienna, Geophysical Research Abstracts, Vol. 13, EGU2011-9070, 2011.

[C29] Mousavi* Zahra, Erwan Pathier, Andrea Walpersdorf, Isabelle Manighetti, Mathilde Vergnolle, Farokh Tavakoli, and Hamidreza Nankali, Investigation of interseismic deformation of active faults in eastern Iran: contribution of Spaceborne radar Interferometry, EGU General Assembly 2011, Vienna, Geophysical Research Abstracts, Vol. 13, EGU2011-9070 , 2011.

[C28] Bekaert D., Andrew Hooper, Erwan Pathier, Sang-Ho Yun (2010). InSAR time series analysis of the 2006 slow slip event on the Guerrero Subduction Zone, Mexico, AGU Fall meeting dec 2010

[C27] Pathier E., J. Champenois, B.Fruneau , B. Deffontaines, K.-C. Lin, J.-C. Hu, New observations of the Longitudinal Valley Fault creep (Taiwan) from PS-INSAR using ALOS data. 4th Joint PI Symposium of ALOS Data Nodes for ALOS Science Program, Tokyo, Nov 2010.

[C26] Yan* Y., E. Trouvé, V. Pinel, E. Pathier, A. Bisserier, G. Mauris, S. Galichet, Assimilation of D-InSAR and sub-pixel image correlation displacement measurements for coseismic fault parameter

estimation, Proceedings of the 2010 IEEE International Geoscience and Remote Sensing Symposium, Honolulu Hawaii, July 25, 2010, pp. 3664-3667, ISBN IEEE Xplore: 978-1-4244-9566-5, 2010

[C25]Champenois* J, B. Fruneau, E. Pathier, B. Deffontaines, K.-C. Lin, J.-C. Hu, Persistent Scatterer InSAR with ALOS data applied to the monitoring of the Longitudinal Valley fault (Taiwan), Geodynamics and Environment in East Asia International Conference & 6th Taiwan-France Earth Sciences Symposium, Aix-en-Provence, 5-9 Juillet 2010

[C24] Fruneau B, S. Michel, U. Kniess, E. Pathier, C. Cornou, G. Ménard, N. Casagli, P-Y. Bard, Subsidence of the Grenoble urban area (French Alps) from INSAR and its relationship to basin sedimentary deposits. ESA Living Planet Symposium June 2010.

[C23] Michel* Sylvain, C. Cornou, E. Pathier, G. Ménard, M. Collombet, U. Kniess, P.-Y. Bard, May subsidence rate serve as proxy for site effects? Seismological Society of America annual meeting 21–23 April 2010.

[C22] Cotte N., M. Campillo, V. Kostoglodov, A. Walpersdorf, M. Vergnolle, I. Manighetti, J.-A. Santiago, E. Pathier, M. Radiguet, F. Cotton, N. Shapiro, G. Cougoulat, E. Boucher and D. Zigone and all participants of the G-GAP Working Group. Anticipating the Next Large Silent Earthquake in Mexico. Ref: NH51B-1061, AGU Fall meeting - San Francisco - dec. 2009

[C21] de Michele M., D. Raucoules, J. de Sigoyer, M. Pubellier, C. Lasserre, E. Pathier, Y. Klinger, J. van der Woerd. Three-dimensional surface slip partitioning of the Sichuan earthquake from Synthetic Aperture Radar. Ref: T11A-1765, AGU Fall meeting - San Francisco - dec. 2009

[C20] Pathier E., Cavalié O., Lasserre C, and Walpersdorf A., Improving InSAR detection of the 2006 slow slip event in the Guerrero zone (Mexico) using atmospheric corrections, Geophysical Research Abstracts,Vol. 11, EGU2009-0, 2009, EGU General Assembly 2009.

[C19] Knieß* U., G. Bièvre, D. Jongmans, E. Pathier, S. Schwartz, and T. Villemin. Combined geophysical and remote-sensing investigations to study the kinematics of two clayey landslides in the Trièves area (French Alps). Geophysical Research Abstracts, Vol. 11, EGU2009-9591, 2009, EGU General Assembly 2009.

[C18] Cavalié*, O., E. Pathier, F. Cotton, M.-P Doin, N. Cotte, M. Vergnolle, and A. Walpersdorf. Mapping of the 2006 silent slow event in the Guerrero (Mexico) seismic gap by InSAR, Geophysical Research Abstracts,Vol. 11, EGU2009-5133, 2009, EGU General Assembly 2009

[C17] Cavalié*, O, Pathier, E.; Doin, M-P., InSAR Analysis of the 2006 Slow Slip Event in the Guerrero-Oaxaca Zone using NARR, American Geophysical Union, Fall Meeting 2008, abstract #G51A-0602, 2008

[C16] Kniess*, U.; Van Westen, C. J.; Villemin, T.; Bievre, G.; Pathier, E.; Jongmans, D.; Schwartz, S., Analysis of a high resolution LIDAR DEM over two large landslides within glaciolacustrine clays (Trieves area, French Alps), EGU2008-A-09989, 5th EGU General Assembly, Geophysical Research Abstracts, vol. 10, 2008.

[C15] Pathier, E; Pinel, V; Bascou, P; Jouanne, F; Fielding, E; Wright, T; Parsons, B, Combination of space-borne radar imagery techniques to study the October 2005, Mw=7.6, Kashmir earthquake, EGU2008-A-10044, 5th EGU General Assembly, Geophysical Research Abstracts, vol. 10, 2008.

[C14] Fruneau, Benedicte, J. C. Hu, B. Deffontaines, E. Pathier, Chen R. F., A. Arnaud and C. T. Lee, C. P. Chang, H. T. Chu (2005) Interferometry (DINSAR and PSI) in Taiwan, the case example of Tainan, Geodynamics and Environment in East Asia International Conference & 5th Taiwan-France Earth Science Symposium, 177.

[C13] Pathier, F. van Leijen, R. Hanssen, G. Ketelaar, P. Marinkovic, B. Parsons, et T. J. Wright, Measuring Interseismic Deformation Across The North Anatolian Fault: Comparison of InSAR techniques. Eos Transactions. AGU Fall Meeting Supplement. Abstract 86(52): Abstract G51C-0839 , 2005

[C12] Deffontaines, B; Hu, J.C.; Fruneau, B.; Arnaud, A.; Liu, C.S.; Angelier, J.; Pathier, E.; Chen, R.F.; Lee, C.T.; Rudant, J.P. Interferometry (DINSAR and SPN) and active folds : the Tainan case example (SW Taiwan) Geophysical Research Abstracts, Vol. 7, 10198, 2005.

[C11] Pathier E, F. van Leijen, R. Hanssen, G. Ketelaar, P. Marinkovic, B. Parsons, et T. J. Wright, Comparison of DINSAR techniques for measuring interseismic deformation across the North Anatolian Fault, European Space Agency Fringe ATSR workshop, 2005

[C10] Pathier, E., J.-C. Hu, B. Deffontaines, B. Fruneau et J. Angelier. New insights on active deformation of southwestern Taiwan from INSAR and GPS data. Geophysical Research Abstracts 6, 1st EGU General Assembly (Nice, France, 25-30 Avril 2004), ref. EGU04-A-06629. 2004.

[C09] Deffontaines, B., J.-C. Hu, A. Arnaud, B. Fruneau, E. Pathier, C.-T. Lee, J. Angelier (2004) Interferometry (DINSAR and PS) and Neotectonics: Tainan area a case example, France-Taiwan scientific meeting - Geodynamics and Natural Hazards, 46.

[C08] Chang C-P., C. Wang, T. Chang, K. Chen, L. Liang, E. Pathier, J. Angelier, Application of SAR Interferometry to a large thrusting deformation: The 1999 Mw=7.6 Chichi earthquake (Central Taiwan). AGU 2002 fall meeting, Ref T61B-1267, 2002.

[C07] Pathier E., B. Fruneau, B. Deffontaines, J. Angelier, C.-T. Lee and D. Raymond, InSAR Coseismic displacements of the footwall of the Chelungpu fault caused by the 1999, Chi-Chi, earthquake and comparisons with fault slip models, EGS XXVII, Nice, avril 2002. (Présentation orale).

[C06] Pathier E., B. Fruneau, B. Deffontaines, C.-T. Lee, J. Angelier, D. Raymond and S.-B. Yu. Coseismic regional surface deformation of the footwall of the Chelungpu Fault after the 1999 Chi-Chi earthquake (Taiwan) from InSAR and GPS data., Program proceeding of International Symposium on Earthquake and Active Tectonics (in Joint Geosciences Assembly), Taipei, Taiwan, p.22-24, sept. 2001. (Présentation orale)

[C05] Pathier E., B. Fruneau, B. Deffontaines, D. Raymond and J. Angelier. The September 21, 1999 Chichi Earthquake (Taiwan) : Contribution of InSar Interferometry to Analyse Permanent Ground Deformations. EUG XI, Strasbourg, J. Conf. Abs. 6(1), p.298, avril 2001. (Présentation orale)

[C04] Deffontaines B., C.-T. Lee, E. Pathier, J.-Y. Yu, B. Fruneau, H.-H. Chen, L.-S. Liang, A.-J. Chen, S.-K. Chen, D. Raymond, C.-L. Tseng, J.-P. Rudant, Y.-B. Tsai, J. Angelier, C.-P. Chang, T.-Y. Chang, F.-C. Li, C.-T. Wang and H.-H. His. Preliminary interferometric results on 921 chichi earthquake (central Taiwan), Proc. Int. Workshop on annual commemoration of Chichi earthquake, Vol 1. Science aspect, p.105-110, sept. 2001.

[C03] Deffontaines B., E. Pathier, C.-T. Lee, B. Fruneau, D. Raymond, J. Angelier, and J.-P. Rudant, Neotectonics and SAR Interferogram in Taiwan : Uplift of Tainan Anticline (SW Taiwan) and 921 Chichi Earthquake, CEOS-SAR Cal/Val Workshop in Tokyo, april 2001.

[C02] Fruneau B., F. Sarti, E. Pathier, B. Deffontaines and D. Raymond, Study of surface displacements in urban context with SAR interferometry: Application to the cities of Paris (France) and Tainan (Taiwan), Proc .Coll. Int. ESA Gothenborg, nov. 2000.

[C01] Deffontaines B., B. Fruneau B., E. Pathier, D. Raymond, C.-T. Lee, J. Angelier, H.-T. Wang and J.-P. Rudant, Long time SAR Interferometry for detection active ground motions: The Tainan anticline (SW Taiwan), Proceeding of Taiwan-France Symposium on Natural Hazard Mitigation, Taipei, mai 2000.

Others (O#)

Communications in French, not-peer reviewed article, thesis, unpublished reports, …

[O20] Allemand, P., Berthier, E., Bonvalot, S., Briottet, X., Cattin, R., Charlot, P., Coulot, D., Delacourt, C., Fruneau, B., Greff, M., Mandea, M., Panet, I., Pathier, E., Rolland, L., Thébault, E., & Wöppelmann, G. (2019). Rapport du groupe de travail Thématique Terre Solide. In Rapport de prospective, Seminaire de Prospective Scientifique du CNES (p. 10). Le Havre. Retrieved from https://sps2019.com/wp-content/uploads/SPS2019_RapportGT_15-GTh_Terre_Solide_V3_20190711.pdf

[O19] Pathier, E., & Deschamps-Ostanciaux, E. (2019, March). Projet GDM EPOS, présentation des produits, formats et métadonnées. Presented at the Atelier ForM@Ter SAR, Paris, France. Retrieved from https://www.poleterresolide.fr/atelier-formter-sar/

[O18] Fruneau, B., Pathier, E., Doin, M.-P., Hu, J.-C., Tung, H., & Le Béon, M. (2018, October). Couverture globale de Taiwan par InSAR pour le suivi des déformations de surface. Presented at the Réunion des Sciences de la Terre, Lille, France.

[O17] Pathier, E., (2018) Slow earthquakes and seismicity in the mexican subduction: contribution from space geodesy, CNES Activity Report to COSPAR 2018, World Committee on Space Research (COSPAR).

[O16] Pathier, E. (2018). Monitoring Slow-Slip Events Along The Mexican Subduction Zone by SAR Interferometry (Final Report for JAXA project ALOS RA-4 No. PI No 1293002). JAXA.

[O15] Pathier, E. (2018, May). Perspectives of InSAR applications for the SSE and seismic cycle studies in Mexico. Presented at the Mexico-France workshop, UNAM Mexico City, Mexico.

[O14] Pathier, E. (2018, January). Les séismes lents vus par la géodésie spatiale, l'exemple de la subduction Mexicaine. Presented at the Conférence du Bureau des Longitudes, Paris, France.

[O13] Pathier, E., Doin, M.-P., Radiguet, M., Kostoglodov, V., Cotte, N., Walpersdorf, A., Rojo-Limon, G., & Lasserre, C. (2017, June). Potentiel des satellites ALOS-2 et Sentinel-1 pour l'étude des séismes lents dans la subduction mexicaine par interférométrie radar satellitaire. Presented at the Colloque Société Française de Photogrammétrie et Télédétection, «télédétection radar : applications continentales », ENSG, Marne-La-Vallée, France.

[O12] Fruneau, B., Pathier, E., Doin, M.-P., Hu, J.-C., Tung, H., & Champenois, J. (2017, June). Couverture globale et homogène de Taiwan par InSAR pour le suivi des déformations de surface. Presented at the Colloque Société Française de Photogrammétrie et Télédétection, «télédétection radar : applications continentales », ENSG, Marne-La-Vallée, France.

[O11] Pathier Erwan, Radiguet Mathilde, Cotte Nathalie, Walpersdorf Andrea, Perfetini Hugo, Campillo Michel, Kostoglodov Vladimir, Rousset Baptiste, Rojo-Limon Graciela, Doin Marie Pierre, Franck William, Lasserre Cécile, Lhomme Thiphaine, Séismes lents et sismicité : exploration dans la subduction mexicaine à l'aide de la géodésie spatiale, [2e colloque de restitution du TOSCA, Paris 21-22 mars 2017], 2017.

[O10] Pathier E., G. Bacques, M. Campillo, N. Cotte, F. Cotton, R. Jolivet, C. Lasserre, M. Radiguet, M. Vergnolle, A. Walpersdorf, D. Zigone, Déformations transitoires dans le cycle sismique: séismes lents et glissement asismique, Invited talk Colloque annuel du Comité National de Géodésie et Géophysique, , Le Mans, 22-24 novembre 2010.

[O9] Bacques* G, F. Cotton, C. Lasserre, E. Pathier, Etude du dernier séisme lent sur la zone de subduction de Guerrero (Mexique) par interférométrie radar satellitaire. Colloque annuel du Comité National de Géodésie et Géophysique, Le Mans, 22-24 novembre 2010

[O8] Champenois* J, B. Fruneau1, E. Pathier, B. Deffontaines, K.-C. Lin, J.-C. Hu, Etude de la tectonique active de Taiwan par Interférométrie Radar et Réflecteurs Permanents, Exemple de la Vallée Longitudinale. Colloque annuel du Comité National de Géodésie et Géophysique, Le Mans, 22-24 novembre 2010.

[O7] Ménard G., Cornou C., Michel S., Pathier E. Déformations actuelle et récente dans la cuvette Grenobloise de part et d'autre de l'éperon de la Bastille (Chartreuse Méridionale). 23ème Réunion des Sciences de la Terre (RST), Oct 2010, Bordeaux, France.

[O6] Pathier E., Cavalié O., Vergnolle M., Cotte N., Walsperdorf A. et Cotton F., Les séismes lents de la zone de Guerrero (Mexique) : l'apport de l'interférométrie radar Satellitaire, Colloque annuel G2, 18 novembre 2009, Strasbourg, 2009.

[O5] Fruneau, B., Pathier, E., Deffontaines, B., Arnaud, A., & Raymond, D. (2009). L'interférométrie radar différentielle et la technique des réflecteurs permanents pour la mesure des faibles déplacements. Géochronique, (110 « Néotectonique »), 42–45.

[O4] Pathier, E. Preliminary Report on the subsidence in the Tehran area (North Iran) from InSAR. COMET internal Report, Univ. Oxford, 20 p., 2005

[O3] Pathier, E. (2003) Contributions to active tectonics of Taiwan from differential SAR interferometry. PhD Thesis at University Paris-Est Marne-la-Vallée and at University Paris 6. https://tel.archives-ouvertes.fr/tel-00007464

[O2] Pathier, E., B. Fruneau, B. Deffontaines, J. Angelier, C.-T. Lee et D. Raymond, Deux exemples d'application de l'interférométrie radar satellitaire à l'étude des déplacements tectoniques à Taiwan: le séisme de Chi-Chi et la croissance d'un anticlinal de front de chaîne sous la ville de Tainan. RST, Nantes, 2002.

[O1] Pathier E., Fruneau B., B. Deffontaines, D. Raymond, J.-P. Rudant, H. Chakroun, C.-T. Lee, H.-T. Wang et J. Angelier, Néotectonique du SW de Taiwan, Apports de l'interférométrie et du GPS , Réunion des Sciences de la Terre, Paris, p.135, avril 2000.

Appendix 1:
full text pdf of selected publications

This appendix reproduced six of my journal articles that are the most significant with respect to my main research interests

* indicates students or post-doc I have work with.

[pdf-1] Pathier, E., Fielding, E. J., Wright, T. J., Walker, R., Parsons, B. E., & Hensley, S. (2006). Displacement field and slip distribution of the 2005 Kashmir earthquake from SAR imagery. *Geophysical Research Letters*, *33*(20). https://doi.org/10.1029/2006GL027193

[pdf-2] Champenois*, J., Fruneau, B., Pathier, E., Deffontaines, B., Lin, K.-C., & Hu, J.-C. (2012). Monitoring of active tectonic deformations in the Longitudinal Valley (Eastern Taiwan) using Persistent Scatterer InSAR method with ALOS PALSAR data. *Earth and Planetary Science Letters*, *337–338*, 144–155. https://doi.org/10.1016/j.epsl.2012.05.025

[pdf-3] Cavalié*, O., Pathier, E., Radiguet, M., Vergnolle, M., Cotte, N., Walpersdorf, A., Kostoglodov, V., & Cotton, F. (2013). Slow slip event in the Mexican subduction zone: Evidence of shallower slip in the Guerrero seismic gap for the 2006 event revealed by the joint inversion of InSAR and GPS data. *Earth and Planetary Science Letters*, *367*, 52–60. https://doi.org/10.1016/j.epsl.2013.02.020

[pdf-4] Mousavi*, Z., Pathier, E., Walker, R. T., Walpersdorf, A., Tavakoli, F., Nankali, H., Sedighi, M., & Doin, M.-P. (2015). Interseismic deformation of the Shahroud fault system (NE Iran) from space-borne radar interferometry measurements. *Geophysical Research Letters*, *42*(14), 5753–5761. https://doi.org/10.1002/2015GL064440

[pdf-5] Pousse Beltran*, L., Pathier, E., Jouanne, F., Vassallo, R., Reinoza, C., Audemard, F., Doin, M. P., & Volat, M. (2016). Spatial and temporal variations in creep rate along the El Pilar fault at the Caribbean-South American plate boundary (Venezuela), from InSAR. *Journal of Geophysical Research: Solid Earth*, *121*(11), 8276–8296. https://doi.org/10.1002/2016JB013121

[pdf-6] Maubant*, L., Pathier, E., Daout, S., Radiguet, M., Doin, M. -P., Kazachkina, E., Kostoglodov, V., Cotte, N., & Walpersdorf, A. (2020). Independent Component Analysis and Parametric Approach for Source Separation in InSAR Time Series at Regional Scale: Application to the 2017–2018 Slow Slip Event in Guerrero (Mexico). *Journal of Geophysical Research: Solid Earth*, *125*(3). https://doi.org/10.1029/2019JB018187

[pdf-1] Pathier et al. 2006

The following pages reproduce the paper from Pathier et al. (2006)

Displacement field and slip distribution of the 2005 Kashmir earthquake from SAR imagery.

Pathier, E., Fielding, E. J., Wright, T. J., Walker, R., Parsons, B. E., & Hensley, S.

Published in 2006 in Geophysical Research Letters, 33(20).

https://doi.org/10.1029/2006GL027193

I did this work when I was post-doc at University of Oxford, in the COMET group funded by NERC.

.

Displacement field and slip distribution of the 2005 Kashmir earthquake from SAR imagery

E. Pathier,[1] E. J. Fielding,[2] T. J. Wright,[1] R. Walker,[1] B. E. Parsons,[1] and S. Hensley[2]

Received 10 June 2006; revised 9 August 2006; accepted 14 September 2006; published 24 October 2006.

[1] The 8th October 2005 Kashmir Earthquake M_w 7.6 involved primarily thrust motion on a NE-dipping fault. Sub-pixel correlation of ENVISAT SAR images gives the location of the 80 km-long fault trace (within 300–800 m) and a 3D surface displacement field with a sub-metric accuracy covering the whole epicentral area. The slip distribution inverted using elastic dislocation models indicates that slip occurs mainly in the upper 10 km, between the cities of Muzaffarabad and Balakot. The rupture reached the surface in several places. In the hanging wall, horizontal motions show rotation from pure thrust to oblique right-lateral motion that are not observed in the footwall. A segmentation of the fault near Muzaffarabad is also suggested. North of the city of Balakot, slip decreases dramatically, but a diffuse zone of mainly vertical surface displacements, which could be post-seismic, exists further north, where most of the aftershocks occur, aligned along the NW-SE Indus-Kohistan Seismic Zone. **Citation:** Pathier, E., E. J. Fielding, T. J. Wright, R. Walker, B. E. Parsons, and S. Hensley (2006), Displacement field and slip distribution of the 2005 Kashmir earthquake from SAR imagery, *Geophys. Res. Lett.*, *33*, L20310, doi:10.1029/2006GL027193.

1. Introduction

[2] On 8th October 2005, a M_w 7.6 earthquake occurred in northern Pakistan in the mountainous Kashmir region (Figure 1) causing more than 80,000 deaths. The Kashmir earthquake (also called the Pakistan Earthquake) is the latest in a series of large historical earthquakes located along the southern front of the Himalaya [*Bilham*, 2004]. The moment tensor solutions from Harvard and the USGS National Earthquake Information Center (NEIC) were available on the web a few hours after the earthquake, rapidly followed by the first slip models from seismological data (e.g., Martin Vallée, http://www-geoazur.unice.fr/SEISME/PAKISTAN081005/note1.html; Yuji Yagi, http://www.geo.tsukuba.ac.jp/press_HP/yagi/EQ/2005Pakistan), indicating a NE-dipping fault with primarily thrust motion. On 2 November, we made available a more precise fault location established from sub-pixel correlation of Synthetic Aperture Radar (SAR) images (http://comet.nerc.ac.uk/news_kashmir.html). This preliminary analysis was done within a few days after the first suitable post-event ENVISAT SAR acquisition, thanks to efforts of the European Space Agency (ESA) who made these data available as soon as possible. Using a similar approach, *Fujiwara et al.* [2006] showed that location of the highest displacement gradient match pre-existing fault traces previously mapped by *Nakata et al.* [1991].

[3] First analyses from seismology and remote-sensing suggested a large amount of shallow slip, locally in excess of 6 m, explaining the intensity of damage and number of casualties, and revealed heterogeneity in the slip distribution and possibly segmentation of the fault. The fault is located at the western end of the Himalaya, at the Hazara Syntaxis, where an old major geologic boundary of the range, the Main Boundary Thrust (MBT), bends around by 180°. The fault trace runs from Bagh to Balakot via the Jhelum river valley and the city of Muzaffarabad (Figure 1). In its northern part, it follows the MBT trace along the southwestern boundary of the Hazara syntaxis. The fault is also aligned with a zone of seismicity recorded by the Tarbela Seismic Network in 1973–1976, called the Indus-Kohistan Seismic Zone (IKSZ) that extends some 100 km to the NW of Balakot and has been proposed to be a NE-dipping ramp [*Armbruster et al.*, 1978]. *Parsons et al.* [2006] point out that, due to static stress changes, there is an increased stress on the IKSZ portion close to the fault, where most of the aftershocks occur. Possible structural controls over the slip distribution remain to be investigated. In this paper, we present a more extensive analysis of the surface deformation including new SAR data acquired with different geometries. These data allow us to construct a three-dimensional surface displacement field caused by the earthquake and to invert for the slip distribution on the fault plane using a homogeneous linear elastic model.

2. SAR Offset Data

[4] Near global coverage and all-weather, day-night capability make SAR data suitable for remote-sensing analysis of natural hazards. In this study, we used ENVISAT ASAR data (Table 1) because they have extensive coverage, high spatial resolution and the existing archive of previous acquisitions allows selection of pairs of pre- and post-event images with suitable baselines (distance separating the two orbits of a pair of images) and time interval. These last two parameters should be as small as possible when measuring coseismic displacements caused by earthquakes with SAR imagery. As shown in Figure 2, the epicentral area is well covered by three selected tracks in ascending and descending modes (i.e., satellite flying from south to north or from north to south, respectively).

[5] To measure surface deformation using SAR imagery, two main techniques are available: interferometric SAR

[1]Centre for the Observation and Modelling of Earthquakes and Tectonics, Department of Earth Sciences, University of Oxford, Oxford, UK.
[2]Jet Propulsion Laboratory, California Institute of Technology, Pasadena, California, USA.

0094-8276/06/2006GL027193$05.00

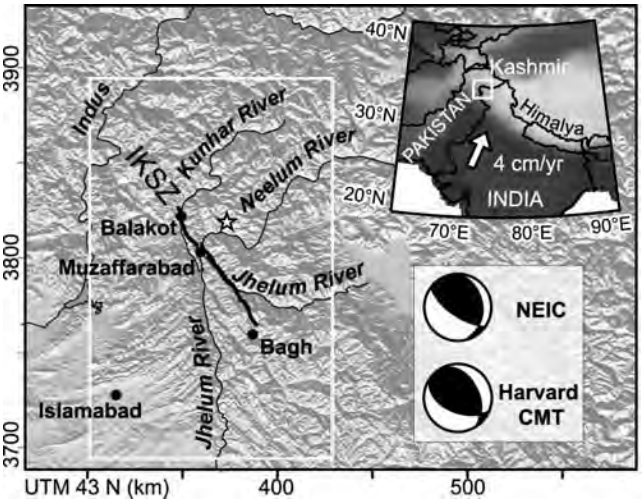

Figure 1. Inset: DEM showing the study area located in Kashmir at the Western Syntaxis of the Himalayan range. Main figure: shaded DEM of the Kashmir region. The star is the epicenter of the 8 October 2005 earthquake from NEIC. At about 100 km from Islamabad, the fault rupture (thick black line) runs from Balakot to Bagh via Muzaffarabad, and is aligned with the Indus-Kohistan Seismic Zone (IKSZ). Thin black lines are rivers and the white frame shows the extent of Figure 2.

(InSAR) [e.g., *Rosen et al.*, 2000] and sub-pixel image correlation [e.g., *Michel et al.*, 1999]. For the Kashmir earthquake, conventional InSAR, the most accurate technique (centimetric), can only give reliable measurement on a narrow band of the footwall in the Jhelum valley and in some far field areas where temporal and geometrical signal decorrelation (due to high topography and steep slopes) and decorrelation due to the large earthquake deformation itself are less severe. Although less accurate ($\sim$0.2–1.0 m), sub-pixel SAR image correlation is more robust for mountainous environments such as in Kashmir. This technique is based on measurement of line and column offset between two amplitude images. At the end of the process, two maps can be constructed for each track (Figure 2), giving two components of the displacements that occurs between the two acquisitions: one parallel to the satellite track (azimuth offset) and the other along its line of sight (range offset). Offsets have been computed using the Jet Propulsion Laboratory/California Institute of Technology ROI_pac software [*Rosen et al.*, 2004], using overlapping matching windows of 64 by 64 pixels (i.e., $\sim$300 m by $\sim$500 m in azimuth and range direction respectively) applied to full resolution images (4 m in azimuth, 8 m in slant range) with steps of 8 pixels in range and 16 in azimuth. Formal errors of the offset measurements are estimated from the width of the peak in the cross-correlation surface for each match. It is only a lower bound on the total error, but provides a criterion for discarding poor matches. Offsets with a formal error (1 σ) larger than 0.7 m and with a magnitude larger than 8 m are removed. These thresholds are based on a qualitative analysis, trying to reduce noise in the data while keeping a good data coverage. A weighted averaging procedure that uses the inverse of the variance of each match as a weighting is applied with a window of 5 samples in range by 11 samples in azimuth. We correct estimated offsets for image distortions due to the fact that images are not acquired exactly from the same point of view. For range offsets, distortions have been modeled using a DEM and precise orbital data, and we correct for a constant shift using far field data where we assumed no coseismic displacement. For azimuth offsets, we only apply long-wavelength flattening using a quadratic surface fit. Results are geocoded at 120 m resolution in UTM zone 43 using ROI_pac and a SRTM DEM.

[6] A clear deformation signal appears in the epicentral area (see Figure 2). The fault line oriented NW-SE is very straight in its southern portion. The largest displacements occur to the east of the fault on the hanging wall around the slightly curved north portion where the azimuth displacement shows a larger lobe than the range one. In the range offset data of ascending track 270 (data set with highest SNR), north of UTM northing 3830 km, a more diffuse zone of deformation is visible. Associated formal errors are about 0.35 m in average but vary with the geometry of acquisition, and with the topography and slopes (see auxiliary material Figure S1[1]). On average, due to its lower and smoother topography, footwall measurement are more accurate ($\sim$0.30 m) than the hanging wall ones ($\sim$0.39 m).

3. 3D Surface Displacements Map

[7] Each offset map is the projection of the full 3D displacement field in the range or azimuth direction. Where three or more such scalar components are available, it is possible to solve for the full 3D displacements field (i.e., the East, North and Up components). The resulting map (see Figure 3a) is easier to interpret than the offset maps. To construct the 3D displacement and associated formal error maps, we followed the method described by *Wright et al.* [2004]. We computed displacements only for points where azimuth and range offset data for both ascending and descending tracks are available (i.e., four to six scalar components of displacement are used for each point). Errors are propagated from formal errors in the measured offsets. The north-south component is the best constrained (σ = 0.07 m on average in the footwall and σ = 0.13 m in the hanging wall), while the east-west component is the least well constrained (σ = 0.19 m on average in the footwall and σ = 0.46 m in the hanging wall). For the vertical component, σ is about 0.09 m on average in the footwall and 0.20 m in the hanging wall; see auxiliary material Figure S2 for more details.

[8] Results show high gradient or discontinuity of displacement across an almost continuous 80 km-long NE-SW line that we interpret as the fault trace, the location of which can be mapped with an accuracy of $\sim$600 m. There is a left-step of about 1.5 km in the fault trace located just west of the area in Figure 3b, suggesting fault segmentation. This left step is located at the transition zone between the Muzaffarabad-Bagh 55 km-long straight southern portion of the fault, where the displacement across the fault is lower (with a maximum in the middle), and the curved

[1]Auxiliary materials are available in the HTML. doi:10.1029/2006GL027193.

Table 1. Details of the Six Offset Data Sets Used in This Study[a]

Direction	Track	Beam	Pre-Event	Start Date	End Date	⊥ Baseline, m	Azimuth (East North)	Range (East North Up)
Ascending	270	I6	5	25-06-2005	12-11-2005	60	[−0.18 −0.98]	[−0.67 −0.12 0.73]
Ascending	499	I6	4	19-09-2005	24-10-2005	270	[−0.18 −0.98]	[−0.63 −0.11 0.77]
Descending	463	I2	20	17-09-2005	26-11-2005	90	[0.21 −0.98]	[0.38 −0.08 0.92]

[a]Offsets are measured on pairs of ENVISAT ASAR images (in image mode) acquired before and after 8 October 2005. Each line corresponds to a pair. The number of images acquired during the two years preceding the event is given in column 4. For each pair, azimuth (component along track) and range (component along line of sight) offsets are measured. Exact orientation of these components depends on the geometry of acquisition and on the position of the measured point within the images. The last two columns give the unit vector of the measured components for a point near Muzaffarabad.

Muzaffarabad-Balakot 25 km-long portion where greater displacements occur. The largest displacements are concentrated on this part of the hanging wall and probably explains why Balakot and Muzaffarabad were the cities most affected by the earthquake. North of Balakot, displacements decrease abruptly, but there is still a diffuse zone of displacement (dominated by uplift) suggesting slip on a deeper fault. This zone coincides with the IKSZ and is also the area where most of the aftershocks occur.

[9] It is noteworthy that from north to south, there are changes in the direction of horizontal motion in the hanging wall. Approximately north of a line joining the epicenter to Muzaffarabad, displacements involve nearly pure thrust motion toward the SW. To the south, there is a progressive rotation of displacements toward the south implying a significant increase of the right-lateral slip and consequently some along-strike extension in the hanging wall. However, close to the fault trace, the right-lateral component tends to decrease. This observation is consistent with the Harvard and NEIC moment tensor solutions that indicate a right lateral component of the slip. In contrast, displacement in the footwall are more uniformly toward the north-east.

[10] Existence of surface rupture suggested by the presence of high gradients of displacement in Figures 2 and 3 is supported by high resolution Quick-Bird optical imagery analysis. Comparing pre- and post-event 60 cm resolution images, evidence of surface rupture can be found at several locations on the inferred fault trace. Figures 3b and 3c–3d illustrate two examples of surface ruptures. One is north of Muzzafarabad near the Neelum river and corresponds to a scarp, which is one of those recognized in the field and reported to be coseismic [see *Yeats et al.*, 2006, Figure 1].

4. Slip Distribution Model

[11] To model static deformation on the fault, we used a homogeneous linear elastic halfspace model assuming that the fault dislocation is a rectangular plane reaching the surface [*Okada*, 1985]. Slip distribution is estimated in two steps. First, the geometry of the fault plane is optimized assuming uniform slip and looking for a global minimum misfit with the offset data (that are downsampled using a quad-tree algorithm to about 2000 points per data set). The minimum misfit is found for the following parameters: strike 321.5°, dip 31.5°, depth 0–10 km, length 74 km. Second, this fault plane is then extended along strike and down dip to give a length of 100 km and a width of 30 km (corresponding bottom depth is 15.7 km, see Figure 3 and auxiliary material Figure S3 for location) and subdivided into 2 by 2 km patches. We then invert for the slip distribution with the same data, solving for the dip-slip and strike-slip motion of each patch and applying a Laplacian smoothing constraint to prevent unrealistic oscillations. This approach using a non-negative least-squares algorithm is described in more detail by *Funning et al.* [2005]. Note that due to the curved geometry of the real fault trace, some data points are on the wrong side of our simplified fault plane model. Such points are masked out in this second step. Among the solutions found for different smoothing factors we select the one shown in Figure 4,

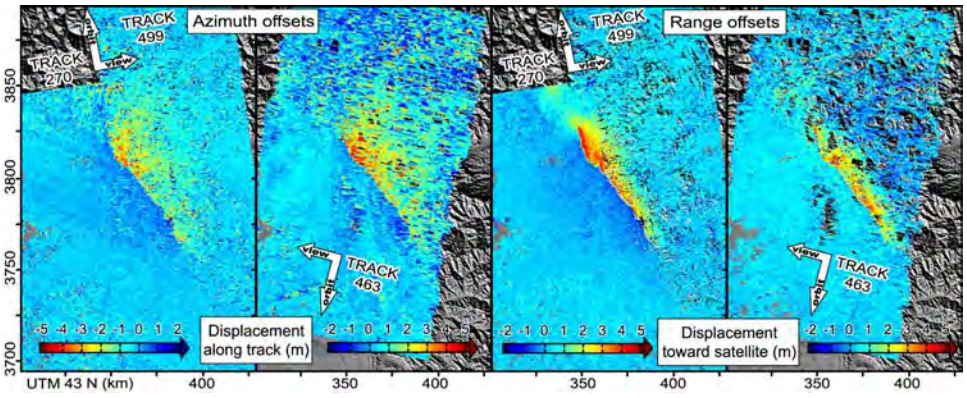

Figure 2. Azimuth and range offset measurements from ASAR ENVISAT images geocoded at 120 m resolution (range offsets are positive for a displacement toward the satellite). One descending and two ascending tracks are used to cover the epicentral area. Coseismic displacements of several meters, consistent with a NE-dipping thrust fault, are clearly visible at the center of the figure where the sharp color discontinuity delineates a highly deformed hanging wall to the east from a slightly deformed footwall to the west.

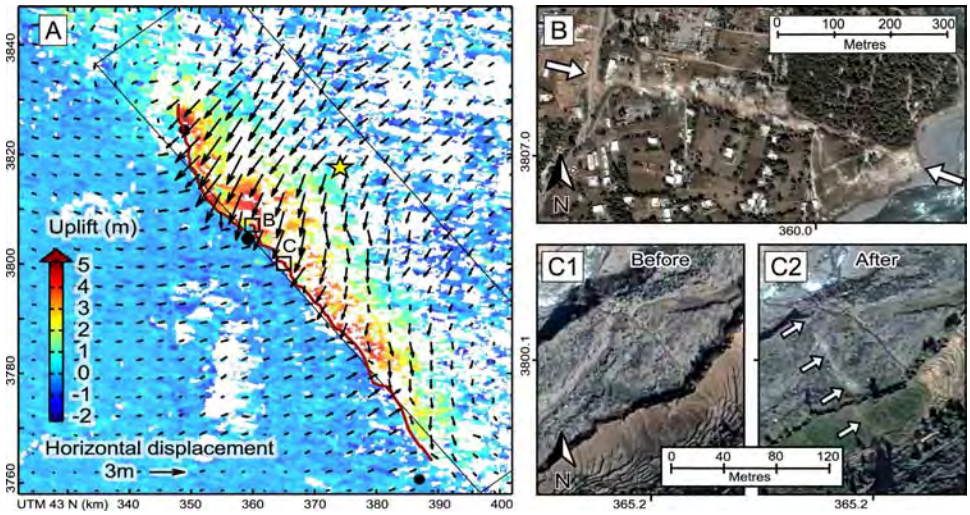

Figure 3. (A) 3D surface displacement field constructed from azimuth and range offset data sets. Arrows indicate horizontal displacements, and colors vertical displacements. Arrows are every 3.5 km and corresponds to the average displacements over a 4 km window (masking footwall data for hanging wall arrows and conversely for footwall arrows). From north to south, the black circles are the cities of Balakot, Muzaffarabad and Bagh. The squares indicate the location of the Quickbird imagery extracts (on the right side) showing evidences of surface rupture. The red line shows surface rupture trace inferred from satellite imagery (SAR, Quickbird and Landsat). The star is the NEIC epicenter and the thin black lines show the map projection of the plane used to model the fault. (B) Surface rupture located north of Muzaffarabad on the eastern bank of the Neelum river. Images (C1) before and (C2) after the earthquake showing the coseismic formation of a new fault scarp in the river bed of a tributary of the Jhelum river on the eastern flank of the valley.

based on a trade-off between high RMS misfit/low smoothness and low RMS misfit/high smoothness and on the minimization of the seismic moment (auxiliary material Figures S4a and S4b). The corresponding moment is 3.36×10^{20} N.m, which is larger than the moment of the Harvard CMT solution (2.94×10^{20} N.m). The global RMS misfit to the whole data set is ~58 cm and the 3D surface displacements constructed from the model show similar pattern to the one described in Figure 3 (see auxiliary material Figures S5, S6 and S7 for details). In order to estimate error on the model, the same inversion is applied to 100 data sets perturbated by introducing noise with characteristics similar to the noise found in the data. For each patch of the fault plane, the standard deviation of the 100 solutions gives an error estimation, which increase with depth up to 1.5 m (for details, see *Funning et al.* [2005] and auxiliary material Figure S8).

[12] The slip distribution pattern shows a main zone of slip larger than 6 m with a peak slip of 9.6 m (±1.1 m) at 4 km depth, located beneath the Muzaffarabad-Balakot segment. Beneath the southern segment, smaller slip occurs distributed on a second zone elongated along strike with a peak slip up to 7 m at 4 km depth. Slip larger than 3 m occurs down to depth of about 13 km (±1 km). The zone of maximum slip in our model is located further north than in the slip distribution derived by *Avouac et al.* [2006] from seismic waveforms and slip measurements at the fault trace (from correlation of optical satellite images). The difference is more pronounced when comparing with their slip distribution derived from the modeling of seismic waveforms alone. This suggests that geodetic measurements consistently indicate a zone of maximum slip within the Muzaffarabad-Balakot segment. In this part of the fault, our slip distribution shows more slip at depth than in their model, which could be explained by the different spatial coverage of the geodetic data used in the two studies, the surface measurements of *Avouac et al.* [2006] being limited to the fault trace. Alternatively, the geometry of the modeled fault plane could also account for the difference: *Avouac et al.* [2006] use a two segments geometry that follows more closely the fault trace in its northern part than in our study that used a single plane and consequently could require more slip at depth.

5. Discussion and Conclusion

[13] Using SAR offsets we have extracted a synoptic view of the surface displacements covering the whole epicentral area of the Kashmir earthquake. From simple

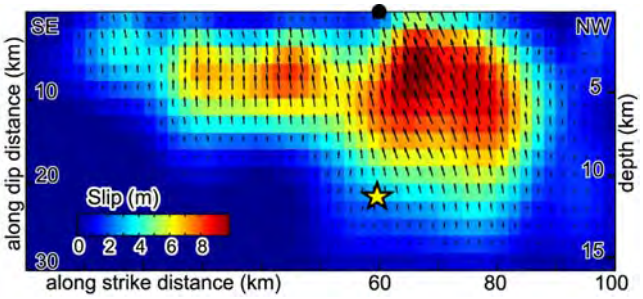

Figure 4. Slip distribution for a fault plane 100 km long, 30 km wide and dipping 31.5°NE (see location on Figure 3), inverted from the azimuth and range offset data sets. Magnitude of displacement is represented by color and slip vectors by the arrows. The star is the projection on the fault plane of the NEIC epicenter. The black dot represents the city of Muzaffarabad.

elastic modeling, we have estimated the slip distribution on the fault plane, which is able to reproduce the main features of the observed displacements. This spatially detailed analysis allows comparison with geological features that could have influenced the rupture process.

[14] The slip distribution shows that most of the slip corresponds to the rupture of the Balakot-Muzaffarabad northern segment. The left-step between the northern and southern fault segments is aligned with the North-South Jhelum valley southward of Muzaffarabad. *Tapponnier et al.* [2006], from geomorphic analysis, suggested that this left step could result from current left-lateral motion of the Jhelum fault, which runs along this valley. Another coincidence between slip distribution and geological features is that the fault trace follows more or less the MBT trace in its northern part and that displacements decrease abruptly north of Balakot where there is a dramatic bend of the MBT.

[15] All these observations are consistent with previous observations suggesting that the location of the rupture initiation or arrest tends to be at the location of intersecting faults or other features, implying a structural control on the slip distribution [e.g., *Manighetti et al.*, 2005]. In the case of the Kashmir earthquake, the hypocenter located at the down-dip edge of the zone of maximum slip is also at the transition zone between the two segments. However, such interpretation should be taken with caution as large errors can affect the hypocenter location (its depth $\sim$12 km is estimated from projection of the NEIC epicenter on the model fault plane).

[16] Regarding the zone of diffuse displacement observed north of Balakot that also coincide with the main concentration of aftershocks, triggered slip on a deeper part of the IKSZ ramp can be invoked. The data set used in this study does not allow us to discriminate between early post-seismic or coseismic deformation, as our first post-event image of that area was acquired on the 12th of November. This question deserves further investigations into the possible continuation of post-seismic displacements.

[17] Finally, we emphasize that for large (M > 6) shallow continental earthquakes, the robust, all-weather SAR correlation technique can be applied to produce precise fault locations and preliminary displacement maps, just days after post-event image acquisition using ESA crisis procedure for data distribution. The potential of remote sensing analysis, such as that described here, for operational use in the relief effort or rapid scientific investigation (such as postseimic study) should not be overlooked.

[18] **Acknowledgments.** This research has been supported by the UK Natural Environment Research Council through COMET. TJW is supported by a Royal Society University Research Fellowship. Part of this research was performed at the Jet Propulsion Laboratory, Caltech, under contract with NASA. We are grateful to the European Space Agency for providing the ENVISAT data used in this study (project AOE-621 and AOE-668). We thank Gareth Funning, who wrote parts of the code used for the slip inversion, and Nicola Capes of Nigel Press Associates for her help in obtaining the Quickbird imagery. We thank J. P. Avouac and two anonymous reviewers for helpful comments.

References

Armbruster, J., L. Seeber, and K. H. Jacob (1978), The northwestern termination of the Himalayan mountain front: Active tectonics from microearthquakes, *J. Geophys. Res.*, *83*(B1), 269–282.

Avouac, J.-P., F. Ayoub, S. Leprince, O. Konca, and D. V. Helmberger (2006), The 2005, Mw 7.6 Kashmir earthquake: Sub-pixel correlation of ASTER images and seismic waveforms analysis, *Earth Planet. Sci. Lett.*, *249*(3–4), 514–528, doi:10.1016/j.epsl.2006.06.025.

Bilham, R. (2004), Earthquakes in India and the Himalaya: Tectonics, geodesy and history, *Ann. Geophys.*, *47*, 839–858.

Fujiwara, S., et al. (2006), Satellite data give snapshot of the 2005 Pakistan earthquake, *Eos Trans. AGU*, *87*(7), 73–84.

Funning, G. J., B. E. Parsons, T. J. Wright, J. A. Jackson, and E. J. Fielding (2005), Surface displacements and source parameters of the 2003 Barn (Iran) earthquake from Envisat advanced synthetic aperture radar imagery, *J. Geophys. Res.*, *110*, B09406, doi:10.1029/2004JB003338.

Manighetti, I., M. Campillo, C. Sammis, P. M. Mai, and G. C. P. King (2005), Evidence for self-similar, triangular slip distributions on earthquakes: Implications for earthquake and fault mechanics, *J. Geophys. Res.*, *110*, B05302, doi:10.1029/2004JB003174.

Michel, R., J.-P. Avouac, and J. Taboury (1999), Measuring ground displacements from SAR amplitude images: Application to the Landers earthquake, *Geophys. Res. Lett.*, *26*(7), 875–878.

Nakata, T., H. Tsutsumi, S. H. Khan, and R. D. Lawrence (1991), *Active Faults of Pakistan*, 141 pp., Res. Cent. for Reg. Geogr., Hiroshima Univ., Hiroshima, Japan.

Okada, Y. (1985), Surface deformation due to shear and tensile faults in a half-space, *Bull. Seismol. Soc. Am.*, *75*(4), 1135–1154.

Parsons, T., R. S. Yeats, Y. Yagi, and A. Hussain (2006), Static stress change from the 8 October, 2005 M = 7.6 Kashmir earthquake, *Geophys. Res. Lett.*, *33*, L06304, doi:10.1029/2005GL025429.

Rosen, P. A., S. Hensley, I. R. Joughin, F. K. Li, S. N. Madsen, E. Rodriguez, and R. M. Goldstein (2000), Synthetic aperture radar interferometry, *Proc. IEEE*, *88*(3), 333–382, doi:10.1109/5.838084.

Rosen, P. A., S. Hensley, G. Peltzer, and M. Simons (2004), Updated repeat orbit interferometry package released, *Eos Trans. AGU*, *85*(5), 47.

Tapponnier, P., G. C. P. King, and L. Bollinger (2006), Active faulting and seismic hazard in the western Himalayan syntaxis, Pakistan, in *International Conference on 8 October 2005 Earthquake in Pakistan*, edited by A. B. Kausar, T. Karim, and T. Khan, pp. 2–3, Geol. Surv. of Pakistan, Quetta, Pakistan.

Wright, T. J., B. E. Parsons, and Z. Lu (2004), Toward mapping surface deformation in three dimensions using InSAR, *Geophys. Res. Lett.*, *31*, L01607, doi:10.1029/2003GL018827.

Yeats, R. S., A. B. Kausar, and T. Nakata (2006), Conferees examine deadly 2005 Kashmir earthquake, *Eos Trans. AGU*, *87*(11), 115.

B. E. Parsons, E. Pathier, R. Walker, and T. J. Wright, Centre for the Observation and Modelling of Earthquakes and Tectonics (COMET), Department of Earth Sciences, University of Oxford, Parks Road, Oxford OX1 3PR, UK. (erwan.pathier@earth.ox.ac.uk)

E. J. Fielding and S. Hensley, Jet Propulsion Laboratory, M.S. 300-233, California Institute of Technology, 4800 Oak Grove Drive, Pasadena, CA 91109, USA.

[pdf-2] Champenois*, Fruneau, Pathier et al. 2012

The following pages reproduce the paper from Champenois et al. (2012)

Monitoring of active tectonic deformations in the Longitudinal Valley (Eastern Taiwan) using Persistent Scatterer InSAR method with ALOS PALSAR data.

Champenois*, J., Fruneau, B., Pathier, E., Deffontaines, B., Lin, K.-C., & Hu, J.-C.

Published in 2012 in *Earth and Planetary Science Letters*, *337–338*, 144–155.

https://doi.org/10.1016/j.epsl.2012.05.025

* Johann Champenois did this work when he was a PhD student at Univ. Paris-Est Marne-La-Vallée, with Bénédicte Fruneau and Benoît Deffontaines as co-directors. I was not officially supervisor but I actively participated by supervising the InSAR part and some field work especially on the part of his thesis related to the Longitudinal Valley Fault.

Earth and Planetary Science Letters 337–338 (2012) 144–155

Contents lists available at SciVerse ScienceDirect

Earth and Planetary Science Letters

journal homepage: www.elsevier.com/locate/epsl

Letters

Monitoring of active tectonic deformations in the Longitudinal Valley (Eastern Taiwan) using Persistent Scatterer InSAR method with ALOS PALSAR data

J. Champenois [a,*], B. Fruneau [a], E. Pathier [b], B. Deffontaines [a], K.-C. Lin [c], J.-C. Hu [c]

[a] Université Paris-Est, GTMC, 5 Boulevard Descartes, 77454 Marne-la-Vallée Cedex 2, France
[b] Université Joseph Fourier, ISTerre, BP 53, 38041 Grenoble Cedex 9, France
[c] National Taiwan University, Department of Geosciences, Taipei, Taiwan

ARTICLE INFO

Article history:
Received 16 August 2011
Received in revised form
14 May 2012
Accepted 20 May 2012
Editor: P. Shearer

Keywords:
active tectonics
SAR interferometry
Persistent Scatterers
PSI
Longitudinal Valley Fault
Taiwan

ABSTRACT

This paper presents new observation of the interseismic deformation along the Longitudinal Valley (Eastern Taiwan) that represents a major tectonic boundary of the Taiwan collision zone. We investigate the southern part of the Valley from Rueisuei to Taitung (latitude 23.5°N–22.7°N), which is the part of the Valley where interseismic surface creep has already been observed at some points of the Longitudinal Valley Fault (LVF). A Persistent Scatterer SAR interferometry approach (StaMPS) is applied using ten L-band SAR images from ALOS satellite acquired over the period 2007–2010. Interferograms from L-Band data show a dramatic improvement of coherence in comparison to previous studies using C-Band ERS data. The density of measurement resulting from StaMPS processing is the highest achieved so far in the area (about 40–55 points per km^2 for a total of 77,000 points) allowing a continuous view of the deformation along the Valley and also giving information on its borders (Central Range and Coastal Range). The most striking feature of the resulting mean velocity map is a clear velocity discontinuity localized in a narrow band (0.1–1 km) along the LVF and responsible for up to 3 cm/yr velocity offset along the radar line of sight, which is attributed to shallow interseismic creep. InSAR results are in good agreement with continuous GPS measurements over the same period (0.3 cm/yr rms). The density of measurement allows us to improve fault trace map along the creeping section of the LVF (with accuracy of about 100 m) and to find new field evidences of the fault activity. In some places, our trace differs significantly (hundreds of meters) from previous published traces. The creep rate shows significant variations along the fault. At the southern end of the valley the deformation is distributed on several structures, including the Luyeh Strand, and drops significantly south of the Peinanshan. However there are discrepancies with previous studies made from ERS data over the period 1993–1999 that remain to be investigated. The mean velocity for each point of measure and the improved faults' trace are provided as Supplementary data.

1. Introduction

The Longitudinal Valley is a major geological and tectonically active boundary of the Taiwan orogen. According to GPS measurements, about 3 cm/yr of horizontal shortening are accommodated across this valley (Yu and Kuo, 2001). It is considered as a collision boundary zone between the Eurasian Plate and the Luzon volcanic arc of the Philippine Sea Plate (e.g., Angelier et al., 1997; Malavieille et al., 2002), which converge at a rate of 8.2 cm/yr in the direction N306°E (Seno et al., 1993; Yu et al., 1997) (Fig. 1a). On the eastern side of this narrow valley located between the Central Range to the west and the Coastal Range to the east (Fig. 1b), the 150-km-long Longitudinal Valley Fault (LVF) accommodates a significant part of the present-day convergence (Yu and Kuo, 2001) by earthquakes up to $M_L = 7.3$ but also by aseismic slip (interseismic creep or postseismic). Understanding the spatial and temporal variations of slip behavior, especially the part of aseismic slip, on this major fault is important for earthquake hazard assessment because it has direct implications on the seismogenic potential of the fault. Furthermore, the factors controlling the slip behavior, seismic or aseismic, are still not well understood. Such issues have already been addressed in other tectonic contexts, like strike-slip faults (e.g., Bürgmann et al., 2000b; Bakun et al., 2005) or subduction zones (e.g., Pritchard and Simons, 2006; Perfettini et al., 2010). However, the Longitudinal Valley is a rare and valuable case-study area showing a

* Corresponding author. Tel.: +33 1 49 32 90 63; fax: +33 1 49 32 91 37.
E-mail address: johann.champenois@univ-mlv.fr (J. Champenois).

0012-821X/$ - see front matter © 2012 Elsevier B.V. All rights reserved.
http://dx.doi.org/10.1016/j.epsl.2012.05.025

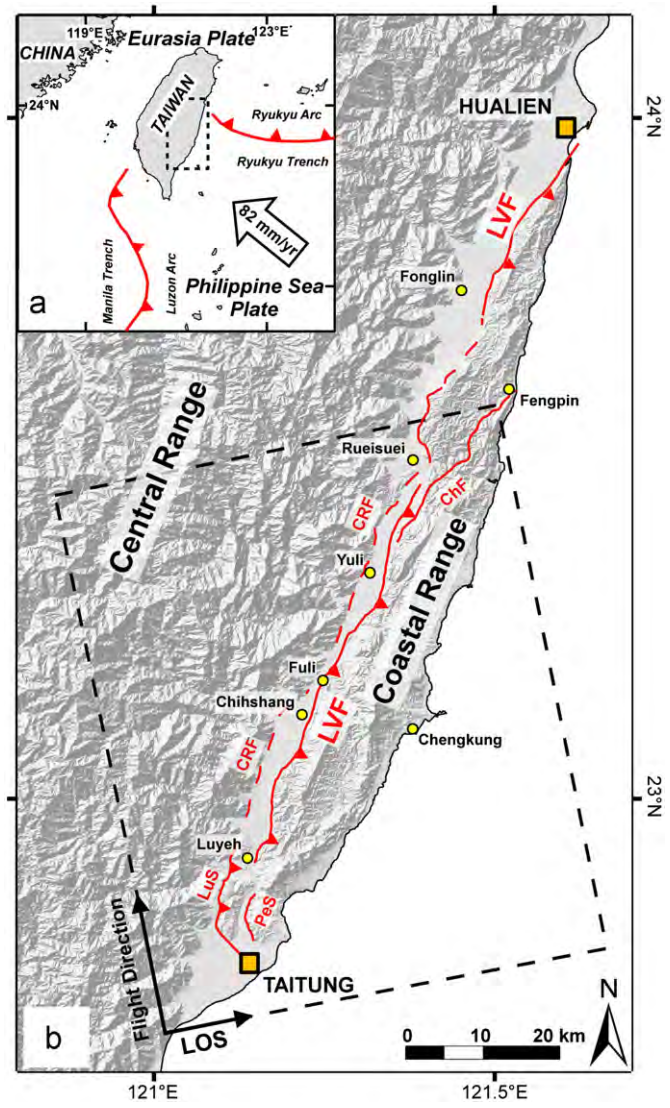

Fig. 1. (a) Tectonic framework of Taiwan. Taiwan is the result of the ongoing collision between the Eurasian Plate (EUP) and the Philippine Sea Plate (PSP). The collision occurs in a double inverse subduction context: in the south-west, the EUP subducts beneath the PHP, whereas in the north-east, the PHP subducts beneath the EUP. The black arrow indicates the direction of convergence between these two plates with an estimated rate of about 82 mm/yr (Seno et al., 1993; Yu et al., 1997) (black dashed frame: location of (b)). (b) Map of Eastern Taiwan. The Longitudinal Valley, located between the Central Range and the Coastal Range, is 150 km long and maximum 7 km width. This area is the plate suture boundary between the EUP and the PSP. Red lines show major fault traces located in the Longitudinal Valley from Central Geological Survey (2006): the Longitudinal Valley Fault (LVF) with triangles pointing in dip direction, the Peinan Strand (PeS), the Luyeh Strand (LuS), the Chimei Fault (ChF) and the blind Coastal Range Fault (CRF) in dashed line. The dashed frame represents the area covered by SAR images. In background, shaded relief is extracted from the 40 m digital elevation model. On the left bottom corner, two arrows indicate the flight direction of ALOS satellite associated with ascending track, and look direction of radar (line of sight). (For interpretation of the references to color in this figure caption, the reader is referred to the web version of this article.)

well-documented active fault with a significant reverse component and where steady-state shallow creep can be observed on land.

A first important issue before interpreting spatial variations of deformation, is to know whether other faults accommodate part of the deformation across the valley. This problem is critical in the Longitudinal Valley area because several active faults are present (Fig. 1b). The Central Range Fault (CRF) is located on the western side of the valley (Shyu et al., 2006). East of the LVF, in the Coastal Range, several faults have been mapped (Wang and Chen, 1993), amongst which the Chimei Fault seems to be a significant tectonic boundary (Chen et al., 1991); however, their present-day tectonic activity remains poorly known.

Some large instrumental earthquakes in the valley have shown that the LVF is not the only active fault. The M_L 7.3 1951 sequence of earthquakes (Chen et al., 2008b) produced surface ruptures along the LVF but also along a poorly documented primarily left-lateral strike-slip fault (Yuli Fault) (Shyu et al., 2007). A few kilometers west of the east-dipping Luyeh Strand (LuS), the M_W 6.1 2006 Peinan earthquake (also called Taitung earthquake) occurred at about 10-km-depth on a N–S high angle 80° west-dipping fault, which may be part of the Central Range Fault system (Wu et al., 2006; Chen et al., 2009a). Smaller earthquakes, even with precise relocation (Kuochen et al., 2004), cannot be easily attributed to known faults mapped in the valley, except for the east-dipping Chihshang segment of the LVF, especially well illuminated by the M_W 6.8 Chengkung earthquake aftershocks sequence in 2003 (Wu et al., 2006; Hu et al., 2007).

Analysis of GPS data over the period 1992–1999 indicates that in the Coastal Range, north of Chihshang and east of the central and northern segments of the LVF, other faults than the LVF may accommodate the deformation during interseismic period (Yu and Kuo, 2001). At the southern end of the LVF where it splits into the Luyeh Strand and the Peinan Strand (also called Lichi Fault), there are geodetic evidences of partitioning of the interseismic deformation (Lee et al., 1998). Nonetheless, the low spatial density of the geodetic measurements does not allow identifying precisely where these faults are located and how much of the deformation they accommodate, especially during the interseismic period.

The same problem of density of measurements arises when looking at interseismic variations of slip behavior along-dip and along-strike the LVF. Along-dip, the 2003 Chengkung earthquake gave evidences (Hu et al., 2007; Hsu et al., 2009) that, at least on the Chihshang segment, the LVF shows an evolution from aseismic creep at shallow depth to stick–slip behavior at 10–25 km, where locked asperities able to produce M_W 6.8 earthquake seem to coexist with creeping areas as revealed by observations of repeating earthquakes sequences (Chen et al., 2008a, 2009b). Along-strike, seismological and geodetic measurements have only been able to get the first-order variations of slip behavior along the LVF, showing a contrast between the southern Chihshang segment and the segments north of Rueisuei (Yu and Kuo, 2001; Kuochen et al., 2004; Huang et al., 2010). The shallow creep is only well-documented from the few sites instrumented by creepmeter, local geodetic network (Angelier et al., 1997, 2000; Lee et al., 2003, 2005) or repeated measurement along leveling lines (Chen et al., 2011; Ching et al., 2011). Those measurements are particularly focused on area where the deformation is localized within short distance around the fault trace (several cm/yr of shortening within a few hundreds of meters) causing damages to human made structures (e.g., at Chihshang (Mu et al., 2011) or at the Yuli Bridge (Yu and Kuo, 2001)). Away from these places, spatially continuous observations in the field are difficult due to absence of clear markers of deformation. The ground deformation can also be elastically distributed over several kilometers if the creep occurred at deeper level and if the shallower part of the fault plane is completely or partially looked. It is then necessary to have dense surface displacement measurements not only along-strike but also across-strike to catch the entire deformation signal.

Space-borne Interferometric Synthetic Aperture Radar (InSAR) techniques have the potential to dramatically improve the spatial density and continuity of surface displacement measurements, complementing GPS and ground-based measurements (e.g., Bürgmann et al., 2000a; Hooper et al., in press). Two InSAR studies

on the Longitudinal Valley have already been published. A first study applied conventional Differential SAR Interferometry (DInSAR) using a stacking approach based on ERS satellites C-band data spanning the 1997–2000 period (Hsu and Bürgmann, 2006). The authors were able to confirm the first-order spatial variability of the deformation along the LVF, but only based on eight local measurements of ground displacement offset across the fault. More recently, using a larger dataset of ERS data from 1993 to 1999 through the StaMPS Persistent Scatterer Interferometry (PSI) technique (Hooper et al., 2007), Peyret et al. (2011) were able to get a more comprehensive view of the deformation in the valley with about 20,000 points of measurement. However, their density of measurement dramatically decreases in hilly areas, like in the Coastal Range on the hanging-wall of the LVF fault. This makes precise mapping and interpretation of the creeping sections difficult on several parts of the fault, as well as the measurement of the ground velocity offset across the fault.

In this study, we present results from a new set of data acquired by the Advanced Land Observing Satellite (ALOS), which provide a larger density of measurement points even on hilly and vegetated area. These data, complemented by field work, allow us to address the main issues mentioned above by mapping with an unprecedented level of details the interseismic ground deformation in the Longitudinal Valley area, and by quantifying variation of creep rate along the LVF.

2. ALOS data and PSI method

2.1. Dataset

This study uses PALSAR (Phased Array type L-band Synthetic Aperture Radar) images provided by the ALOS satellite from the Japan Aerospace Exploration Agency (JAXA). A major characteristic of the PALSAR sensor is that it operates in L-band, with a wavelength ($\lambda = 23.6$ cm) which is five times longer than the wavelength of usual C-band sensors. The PALSAR choice is justified because the previous InSAR studies in Eastern Taiwan using C-band data (Hsu and Bürgmann, 2006; Peyret et al., 2011) were limited by temporal decorrelation notably due to a dense vegetation cover. It has been shown that ALOS L-band interferograms suffer less from temporal decorrelation even on vegetated areas than C-band ones because the longer wavelength penetrates deeper through the vegetation (Sandwell et al., 2008; Meng and Sandwell, 2010).

We considered all ALOS images available along the ascending path 445 that cover the part of the Longitudinal Valley between Rueisuei and Taitung (Fig. 1b), where the highest fault creep rates have been documented before. Images were acquired from January 2007 to February 2010 (Fig. 2) with a mean duration between each acquisition of about 3 months, with a 15 months gap in the dataset between May 2008 and August 2009 (this time gap can decrease the PS density and also the uncertainty associated to the measure of surface displacements). The chosen polarization mode for the SAR data is HH (horizontal–horizontal), which appears to provide higher performance than HV (horizontal–vertical) for InSAR studies using ALOS data (Cloude and Papathanassiou, 1998; Ge and, 2009).

2.2. PSI method: StaMPS processing

Using our ALOS dataset, conventional InSAR method is able to generate differential interferograms covering 3 yrs with a high coherence not only in the Longitudinal Valley but also in the Coastal Range and the Central Range (two examples are provided in Supplementary material S1). The quality of these interferograms makes possible a precise mapping of a clear phase discontinuity that separates the Coastal Range from the Longitudinal Valley, which corresponds to the LVF activity. Nevertheless, the quantification of the deformation from such interferograms can be highly affected by atmospheric perturbations. Furthermore, only some couples of dates give such a good quality, most of the other interferograms are more affected by decorrelation effects. In order to perform a proper time series analysis of the displacements and to mitigate decorrelation and atmospheric effects, recent techniques and in particular the ones based on identification and analysis of stable radar targets, also called Persistent Scatterers (PS), have

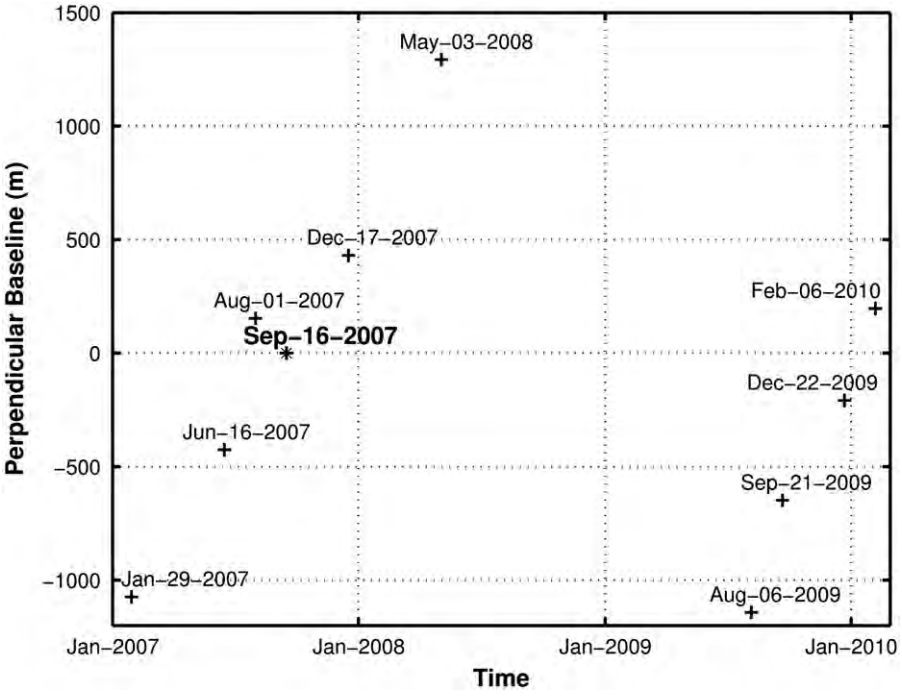

Fig. 2. Available ascending ALOS PALSAR acquisitions. Perpendicular baselines are plotted as a function of acquisition dates. Values are given with respect to the "Super Master" image (in bold) chosen for the StaMPS processing (September 16th 2007).

been developed (e.g., Ferretti et al., 2001; Hooper et al., 2007). Those techniques, relying on a set of interferograms built from SAR data acquired at different times, allow to measure displacements of specific points (presenting stable phase) at each date of SAR acquisition and over long periodof time. All interferograms are performed with a common master image with released limitations in temporal or spatial baselines, allowing in our case to use all the data even with high perpendicular baseline and large temporal difference. In PS approaches, different strategies can be used to estimate atmospheric signal and correct it, leading to higher precision of measure than with conventional InSAR. PS methods have proven to be very efficient to measure slow and small ground deformation, especially in urban environment, where density of PS is high because of the numerous man-made structures that constitute permanent and stable bright scatterers (e.g. Prati et al., 2010; Sousa et al., 2010).

In this study, the Stanford Method for Persistent Scatterers (StaMPS) developed by Hooper et al. (2007) is employed, which has proven to be reliable even in natural terrains. This method uses both information of amplitude dispersion and phase stability with time to determine which pixels can be considered as PS. Furthermore, it does not use any a priori model of deformation through time, as some PS approaches do, but it assumes that deformation and consequently the interferometric phase is spatially correlated. The StaMPS method is applied to the ALOS PALSAR dataset described previously. The main processing parameters are given in supplementary materials (S2). The image of September 16th 2007 has been chosen as the common master image of the interferograms. First, a set of nine differential interferograms was generated with this image as master reference, using ROI_PAC (Rosen et al., 2004) and a 40 m horizontal resolution DEM. At the end of the StaMPS processing chain, we obtain a map giving for each PS its mean velocity along the radar line of sight of the (LOS velocity) over the whole period. It is also possible to reconstruct the PS time series of displacements at each acquisition date.

3. Interseismic surface deformation analysis

3.1. PSI results

The PS mean LOS velocity map for the period 2007–2010 is shown in Fig. 3. Velocities are given with respect to the reference area which is located in the city of Yuli. A high density of measurements is obtained with more than 77,300 PS over the studied area. Two different areas can be distinguished: the southern end of the valley, near Taitung city and its surroundings, with a high PS density due to an important urbanization (more than $\sim$55 PS per km^2), and the rest of the valley where the PS density is lower ($\sim$40 PS per km^2) mainly due to the presence of vegetation and high topography on its borders. These density values are a real improvement compared to the Peyret et al. (2011) study using ERS data, especially in hilly areas like the Coastal Range and the Peinanshan. Regarding ground displacements, at first glance these results show clearly two blocks separated by an important discontinuity, consistent with thrusting of the Coastal Range over the Longitudinal Valley: one block with LOS velocities ranging between 10 mm/yr and 35 mm/yr toward the satellite, and a second block, with lower velocities, composed by the Longitudinal Valley and the Central Range with PS velocities between 0 mm/yr and 10 mm/yr. A more detailed analysis is given in Section 3.3.

3.2. Comparison with continuous GPS data

In order to complete and validate these PSI results, a comparison with the continuous GPS (cGPS) data has been done. The island of Taiwan is one of the most instrumented places in the world in term of cGPS monitoring. Nowadays, over its 150 km, the Longitudinal Valley is very well instrumented with 52 cGPS stations installed by different institutes (Central Weather Bureau, Academia Sinica, Ministry of Interior and National Taiwan University).

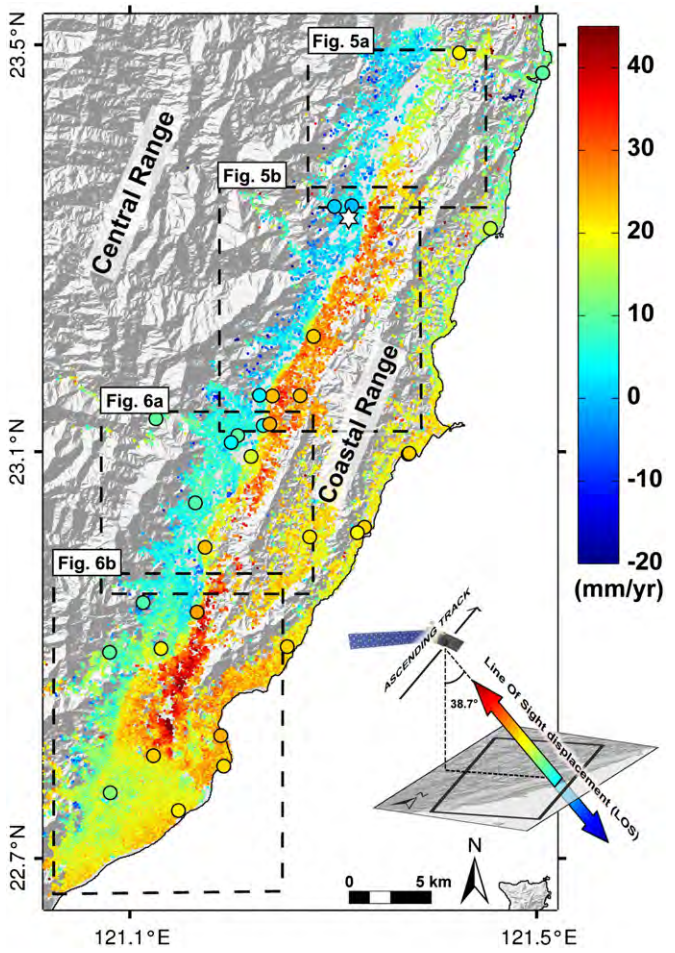

Fig. 3. Map of PS mean LOS velocities (in mm/yr) on the southern part of Longitudinal Valley between January 2007 and February 2010 derived from PALSAR dataset. The velocities are relative to the mean velocity of PS pixels of the reference area represented by the white star (Yuli city). The big dots with different colors represent the cGPS stations and their LOS velocities with the same color scale as PSI results. The figure on the bottom right corner illustrates the direction of the LOS vector of displacement. The four black dashed frames indicate the location of focus presented in Figs. 5 and 6. Near Fuli, the line of sight unit vector NEU is [−0.1339, −0.6092, 0.7816]. All PS measurements and unit vectors are given as Supplementary material S3.

We collected data from 32 cGPS located in our study area (Figs. 3 and 4a) and we chose the JULI station as the reference in order to have a similar reference between PS and cGPS. The velocities were estimated from daily solution from 29/01/2007 to 06/02/2010. The cGPS time series were defined for each component according to equation using the least-square method as modified from Nikolaidis (2002). Based on the catalog of the Central Weather Bureau, two medium events, the 13th May 2008, M_W=5.2 inland earthquake and the 29th July 2009, M_W=5.4 Pingtung offshore earthquake occurred during the period of study, but have a limited effect on the relative displacement between our selected stations (a few mm). In the secular time series, we corrected the coseismic part of those events and got the velocities field of the period 2007–2010. Smaller seismic events that have occurred at the same period in the study area do not introduce visible offsets in the cGPS time series.

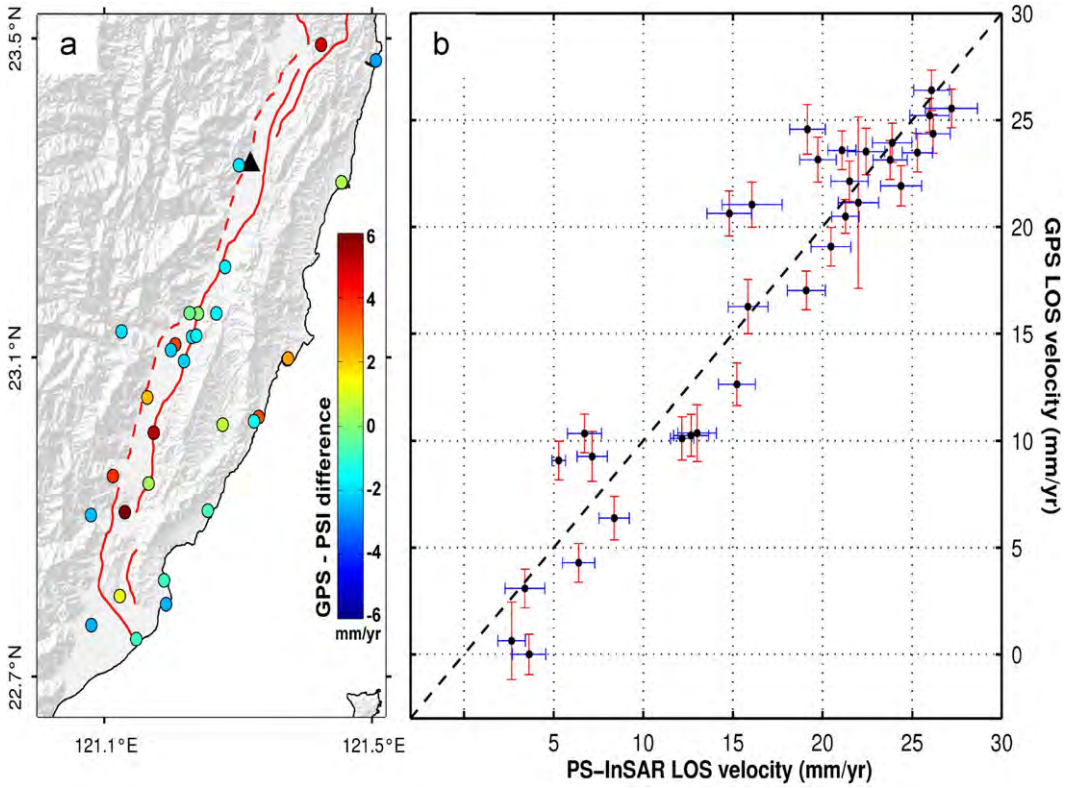

Fig. 4. Comparison between cGPS and PSI. (a) Map of location of the cGPS stations used in this study. Each station is represented by a colored circle representing the difference between cGPS and PSI velocities. Black triangle represents the reference cGPS station (located close to the PSI reference). Red lines show major fault traces presented in Fig. 1. (b) cGPS mean LOS velocities versus PS mean LOS velocities for the period January 2007–February 2010 period. The black dashed line represents the perfect correlation. (For interpretation of the references to color in this figure caption, the reader is referred to the web version of this article.)

To compare the displacements measured by PSI and cGPS, we first projected the 3D displacement vector provided by cGPS onto the line of sight (LOS) of the radar for each station. This is done using the components of the radar sensitivity vector, unit vector pointing from ground to satellite calculated by StaMPS (considering a mean azimuth angle of 12.4° and a variable incidence angle estimated at each station). As the PS density is higher than the density of cGPS stations, we estimate an average PS LOS velocity around each cGPS station by selecting all PS within a square area of 500 m by 500 m centered on each station (on average, more than 40 PS are selected around each station). Uncertainty of the average LOS velocity is estimated by the standard deviation of the individual PS LOS velocities inside this area. These uncertainties range from 1 mm/yr to 3 mm/yr (Fig. 4b).

The spatial analysis of the difference between cGPS LOS velocities and PS LOS velocities showed a linear trend that is certainly due to long wavelength residual orbital errors commonly found in InSAR. We estimated the corresponding spatial trend through a least square approach, and then corrected the PSI results from it (Figs. 3 and 4b show the corrected results). This correction improved the agreement between cGPS and PS measurements decreasing the RMS difference from 8.25 mm/yr to 2.58 mm/yr, which is more consistent with the estimated individual errors on cGPS and PS measurements. The corrected PS mean LOS velocity values and their corresponding LOS vectors are given in Supplementary materials (S3).

3.3. *Detailed analysis along the valley*

3.3.1. *From Rueisuei to Fuli*

At the latitude of Rueisuei, north of our study area (Fig. 5a), the LOS velocity change across the LVF is distributed over 2–4 km and do not show clear discontinuity. LOS values and the difference of cGPS velocities between the JSUI station, located on the hangingwall of the LVF, and the YULI and JULI stations located on the footwall are compatible with a thrust of the Coastal Range toward the valley and the Central Range. The smooth deformation pattern shown by the PS could be due to a distribution of slip on several small faults, branching at depth on the LVF (that could not be identified because of the too high uncertainty of the PS measurements and of the relative low density of PS west of Rueisuei). Alternatively, this could be explained by an elastic deformation related to deeper creep on the LVF occurring down-dip of a shallow locked zone of the fault. Concerning the Chimei Fault, which is mapped a few kilometers east of the LVF (Fig. 1) and is only partially covered in the PS velocity map, there is no evidence of interseismic surface deformation related to it.

Southward, the LOS velocity change across the LVF increases and becomes more and more localized on the fault (Profs. 1 and 2 in Fig. 5a). North of Yuli city, close to the JULI cGPS station, deformation occurs within 200–300 m with a difference of LOS velocity higher than 25 mm/yr between the footwall and the hangingwall (Prof. 3 in Fig. 5b). In the absence of any earthquake large enough to produce such a deformation signal, it is undoubtedly related to creep occurring at least at shallow depth.

There is no evidence of interseismic surface deformation associated to the Yuli Fault that ruptures during the 1951 series of earthquakes. Its fault trace, which is roughly parallel to the LVF but located in between the CRF and the LVF, is passing through the Yuli city where evidences for a left lateral coseismic rupture exists (Shyu et al., 2007).

Between Yuli and Fuli (Fig. 5b), the spatial continuity of the deformation along that 23 km long segment of the LVF can be established. The LOS velocity offset is relatively constant at

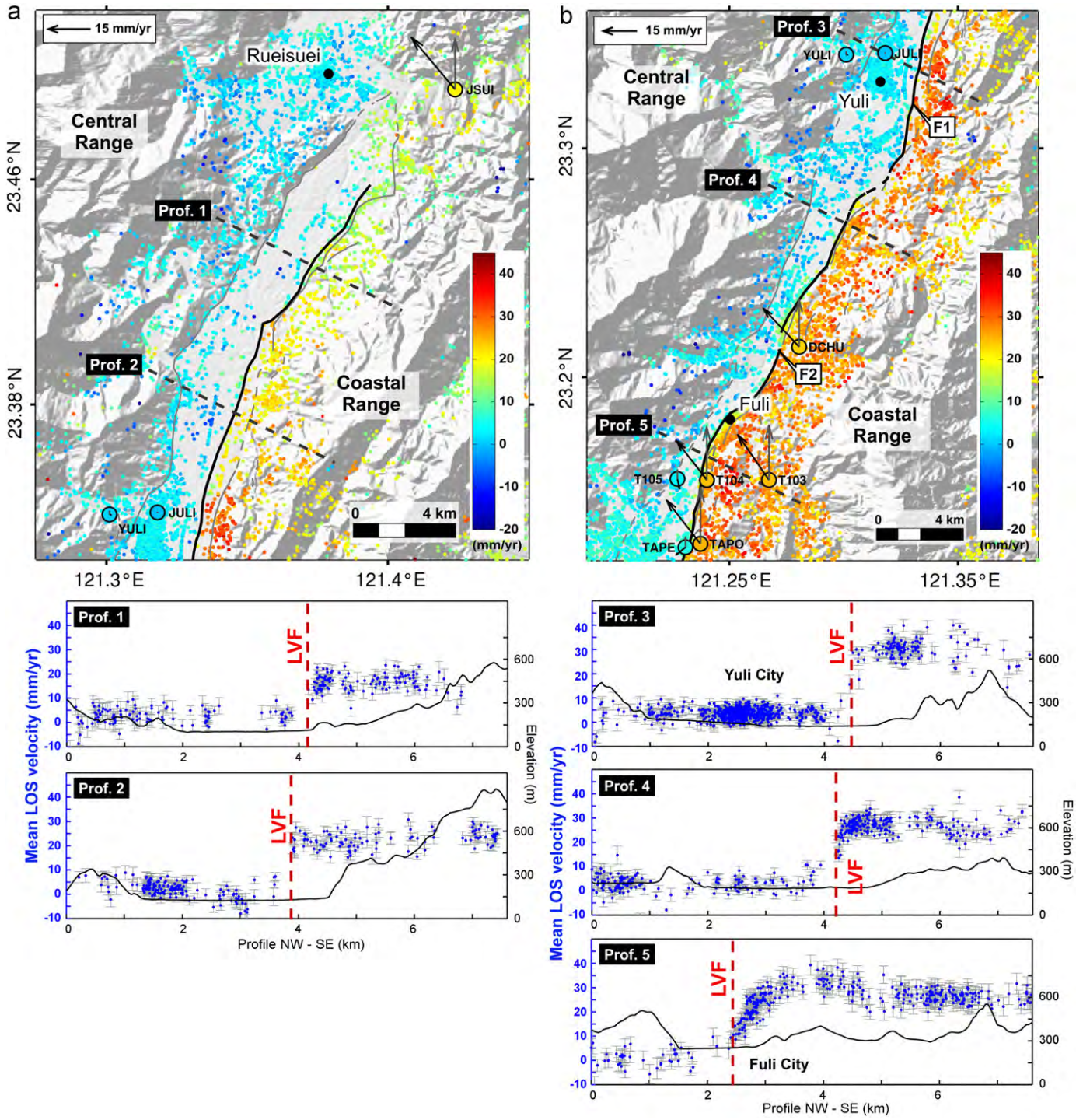

Fig. 5. PS mean LOS velocity maps between north Rueisuei and north Yuli with hill-shaded DEM as background (a) and between Yuli and south Fuli (b). Big dots with different colors represent the cGPS stations and their LOS velocities with the same color scale as PSI velocities. Black and grey arrows are, respectively, the horizontal and vertical components of each cGPS stations. Black lines show update fault traces obtained with the PSI results while grey lines show fault traces from Shyu et al. (2005) (dashed where inferred) and black dots indicate the major cities. Labels F1 and F2 indicate makers of deformation found on the field and shown in Fig. 7. The black dashed lines indicate the location of the PS profiles presented below (Profs. 1–5). These profiles are perpendicular to the major segment of the Longitudinal Valley Fault (LVF) and are superimposed on the topographic profiles from a 40 m digital elevation model. (For interpretation of the references to color in this figure caption, the reader is referred to the web version of this article.)

35–40 mm/yr (Profs. 4 and 5 in Fig. 5b). Regarding cGPS measurements, the stations installed on the Coastal Range present a significant uplift and a horizontal component consistent with the direction of convergence between the Eurasian Plate and the Philippine Sea Plate. The relative velocities with the four cGPS stations on the other side of the fault indicate mainly a thrust displacement with a left lateral component.

3.3.2. *From Fuli to Taitung*

South of Fuli (Fig. 6a), in the area of Chihshang (CHIH station), shallow creep is well documented and monitored by several creepmeters installed at Tapo and Chihshang since 1998 (Lee et al., 2003). PS results show a localized deformation (Prof. 6 in Fig. 6a) that is consistent with shallow creep reaching the surface. South of Chihshang, the gradient of LOS velocity is lower across

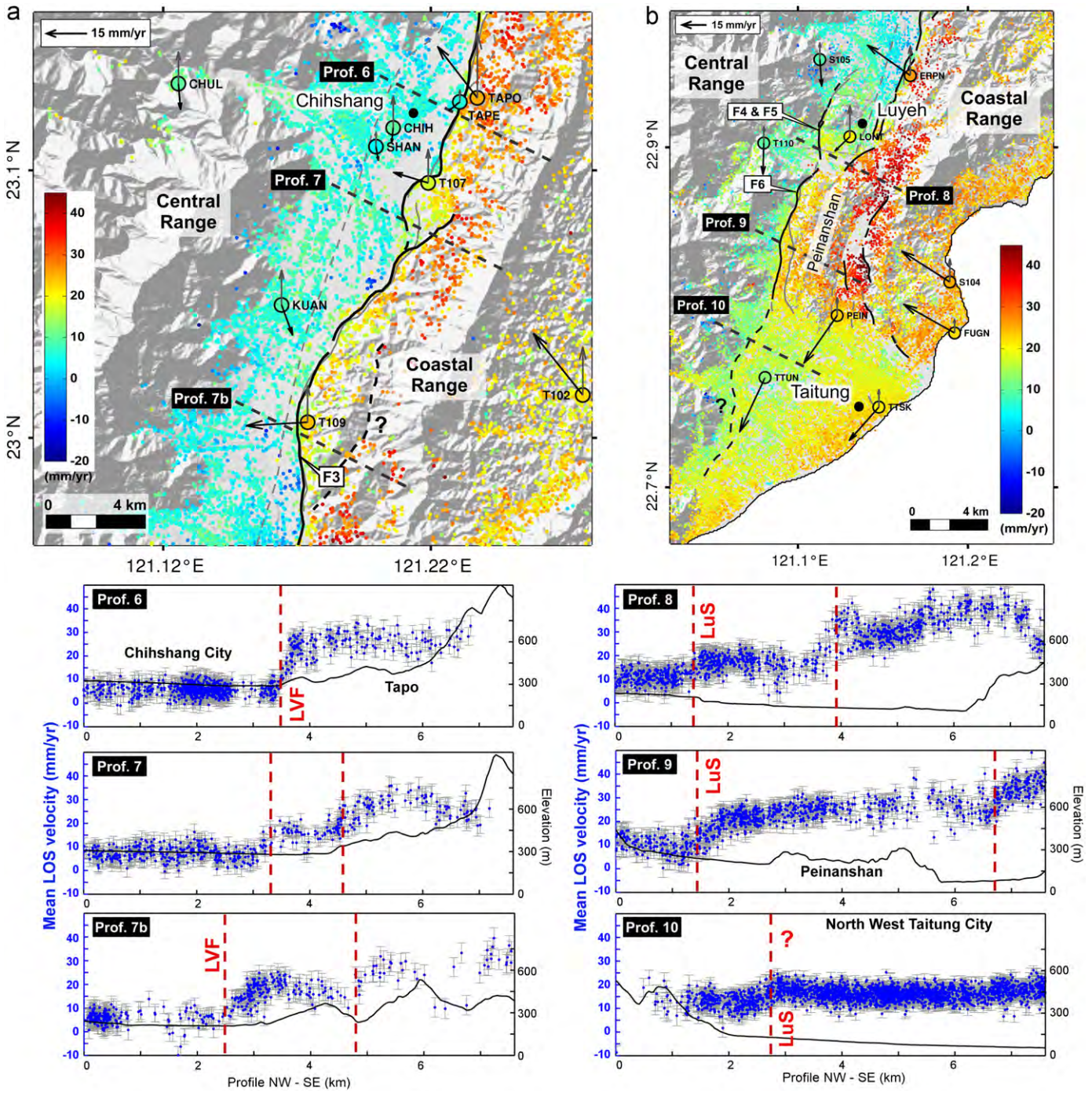

Fig. 6. PS mean LOS velocity maps between south Fuli and north Luyeh with hill-shaded DEM as background (a) and between north Luyeh and the south ending of the valley (b). Big dots with different colors represent the cGPS stations and their LOS velocities with the same color scale as PSI velocities. Black and grey arrows are, respectively, the horizontal and vertical components of each cGPS stations. Black lines show update fault traces obtained with the PSI results while grey lines show fault traces from Shyu et al. (2005) (dashed where inferred) and black dots indicate the major cities. Labels F4, F5 and F6 indicate makers of deformation found on the field and shown in Fig. 7. The black dashed lines indicate the location of the PS profiles perpendicular to the major that are presented below (Profs. 6–10). These profiles are perpendicular to the major segment of the Longitudinal Valley Fault (LVF) and the Luyeh Strand (LuS) and are superimposed on the topographic profiles from a 40 m digital elevation model. (For interpretation of the references to color in this figure caption, the reader is referred to the web version of this article.)

the LVF. In some places, the total deformation appears to be accommodated not only by the LVF, but also by other structures inside the Coastal Range like around the T107 cGPS station and the T109 cGPS station (Profs. 7 and 7b in Fig. 6a). East of the T109 station, a new active fault trace is proposed. This fault may branch on the LVF and could explain the decrease in LOS velocities across the LVF close to this station.

Regarding the activity of the Central Range Fault, separating the Central Range and the Longitudinal Valley, which is considered as an active but blind fault from Chihshang to the southern end of the valley (Shyu et al., 2006), there is no evidence of surface deformation in the PSI results.

In the southern end of the valley (Fig. 6b), between Luyeh and Taitung, the mean LOS velocity map reflects a more complex

tectonic setting. The deformation is accommodated on several active structures surrounding the Peinanshan Mountains (Profs. 8 and 9 in Fig. 6b). The density of measurements over the Peinanshan is enough to detect that no clear discontinuity of displacement occurs inside it. Near Luyeh, the LVF seems to split into several faults. South-East of the LONT station, a clear active NE-SW structure connects the Coastal Range to the Peinanshan, crossing the valley (Prof. 8 in Fig. 6b). Further west, a significant gradient of LOS velocity appears at the eastern boundary of the Central Range that corresponds to the LuS (Profs. 8 and 9 in Fig. 6b). It may be continuous over more than 25 km extending to the south into the Taitung basin (Prof. 10 in Fig. 6b). Deformation also occurs east of the Peinanshan, on the Peinan Strand. These observations are in agreement with a partitioning of the deformation on the Luyeh and Peinan Strands proposed by Lee et al. (1998). South of the Peinanshan a slight N–S gradient of LOS velocity seems to outline the south termination of a Coastal Range block with respect to the Taitung Basin (Fig. 6b). In this transition zone, two north-south profiles (see Supplementary material S4) show a progressive decrease of mean LOS velocities over more than 5 km with no clear discontinuity as observed across the Luyeh Strand. However, changes in the horizontal component of three cGPS stations (PEIN, TTUN and TTSK) indicate a rotation to the south west with respect to the stations in the Coastal Range. This implies some extension between the Coastal Range block and the Taitung basin and indicates a distinct behavior of the Taitung basin relative to the Coastal Range.

3.4. Fault mapping and field evidences

One aim of this study is the precise mapping of the active tectonic structures in the valley. Several previous studies have established structural maps of the Longitudinal Valley at different scales (Lee et al., 1998; Chang et al., 1998; Shyu et al., 2005). The Central Geological Survey Taiwan (CGS) published the first edition of active fault map of the island of Taiwan in 1998 with a 1/500,000 scale (Chang et al., 1998). Since this date, the map has been regularly updated while improving the scale. A recent version of the active faults map from the CGS dates 2006 (Fig. 1b). In 2005, Shyu et al. (2005), based on field work and geomorphological analysis of shaded relief maps, drew up a new map of active faults in Eastern Taiwan (Shyu et al., 2005) improving the scale of the CGS map.

Independently of these previous studies, we combined both information derived from single differential interferograms and PSI results to map the location of shallow creeping sections of the faults. We used two differential interferograms in complement to PSI because, in several places, these interferograms (with baselines lower than 70 m) including a large surface deformation signal (integrated over 3 yrs) highlight the location of the LOS velocity discontinuity with a greater spatial accuracy than the PSI results (see Supplementary material S1). The resulting fault traces (shown in Figs. 5 and 6 and provided in Supplementary material S5) can be compared to the map of Shyu et al. (2005). The traces look very similar at a regional scale where for its major part the LVF follows the basal relief of the western side of the Coastal Range. However, several portions of our LVF trace are located up to several hundred meters further west in the valley (comparisons between the PSI fault trace with the one of Shyu et al. (2005) are given as Supplementary material S6). Since the LVF trace runs along the Hualian, Hsiukuluan, and Peinandachi rivers, its morphological signature can be eroded or hidden beneath recent fluvial deposits (Chen et al., 2007). This can lead to positioning error when only geomorphological approach is used.

Two field trips have been conducted in our study area to find new evidences of deformation near the LVF and the Luyeh Strand in order to validate PSI fault traces. Near Yuli city (Fig. 5b), two adjacent bridges are affected by the activity of the LVF as documented by Yu and Kuo (2001) from geodetic measurements. However, the fault line from Shyu et al. (2005) is located about 1 km further east at the foot of the Coastal Range. Precise location of the bridges deformation in the field (between the second and the third pillars, F1 in Fig. 7) are actually in agreement with the location of a shallow creeping section revealed by the PS results, which show at that place a clear LOS velocity offset of about 2.5 cm/yr. PS results do not show surface deformation further east (Fig. 5b).

Southward, guided by the PSI map, we found an evidence of activity along a concrete dike situated north of Fuli city (Fig. 7, F2). The dike, perpendicular to the fault, shows clear marks of compression. At this place, the LOS velocity offset is about 2.5 cm/yr. Between Chihshang and Luyeh (Fig. 6), we found another nice field evidence of the active thrust fault affecting a dike (Fig. 7, F3), that is exactly located on the fault trace mapped from PSI.

South of the valley, near Luyeh and Taitung (Fig. 6b), the PSI fault trace map shows significant differences from the previous maps. One of the most interesting active structures visible on the PSI map connects the Coastal Range to the north of the Peinanshan. Actually, it exists in the PSI map an important discontinuity (about 1.8 cm/yr) but no interpretation on the nature of this structure can be made with these results. Previously this structure was identified with uncertainty as an anticline (Shyu et al., 2008). Regarding the Luyeh Strand located west of the Peinanshan, its activity is visible on the PSI results and also in the field. Along the fault, we found three markers of deformation in recent human-made constructions (Fig. 7, F4, F5 and F6), less important than those shown close to the LVF but indicating fault activity. Concerning the Peinan Strand, the PSI results show also differences with previous maps. Its traces seem more complicated with several possible active segments, certainly one at the eastern boundary of the Peinanshan and one at the western boundary of the Coastal Range. The southern termination of the Peinan Strand is often supposed to continue within the Taitung basin (e.g., Lee et al., 1998; Shyu et al., 2008), however the PSI map suggests that the E–W gradient of LOS velocity stops against the basin and turn into a more gentle N–S gradient along the south end of the Peinanshan and of the Coastal Range (Profs. 11 and 12 in Supplementary material S4). In contrast, the Luyeh Strand may continue southward, following the eastern side of the Central Range along the western side of the Taitung basin (Prof. 10 in Fig. 6b).

4. Shallow creep rate estimation

First order spatial variations of shallow creep activity have been shown by other geodetic studies (especially from GPS and InSAR), with creep rates changing according to the latitude (Hsu and Bürgmann, 2006; Peyret et al., 2011). The unprecedented spatial resolution of the map of mean LOS velocities and the new derived fault trace of this study allows us estimating more accurately the spatial variations of shallow creeping activity along the LVF and the Luyeh Strand. In order to examine the spatial variation along these faults, we created a set of 58 close profiles across the fault lines. We used an N20°E axis to create these series of orthogonal profiles every 2 km from Rueisuei to Taitung. All profiles include the PS located inside a 1 km by 8 km band and projected onto the profile. A subset of ten representative profiles is presented in Figs. 5 and 6.

We choose to quantify the LOS velocity offset (LOSVO) across the fault to give information on the creep activity of the fault. All profiles have a good quality, allowing us to separate the LVF and the LuS. But, regarding the Peinan Strand, the trace is not clear

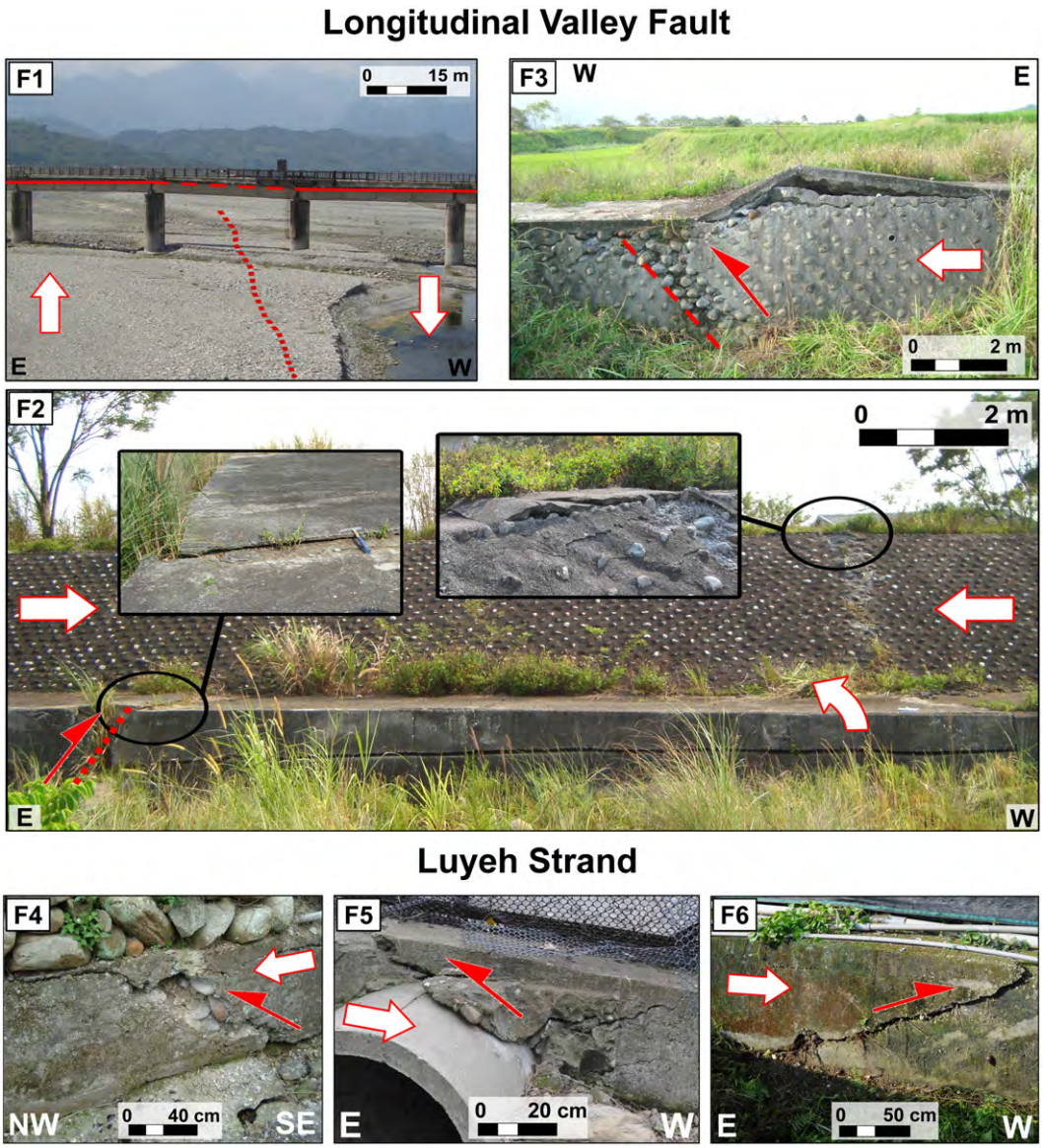

Fig. 7. Field evidences of tectonic activity over the Longitudinal Valley. F1, F2 and F3 are deformations connected to the Longitudinal Valley Fault (localized on Figs. 5b and 6a). F1 is the Yuli Bridge where the eastern part is uplifting contrary to the western part which is quite stable. F2 is localized north to Fuli, while F3 is localized north to Luyeh with a clear deformation affecting the dike. In this place, the deformation on the lower part of the dike shows clearly the thrust component of the fault displacement and the upper part is affected by a back thrust. F4, F5 and F6 are associated with the Luyeh Strand and present less important deformations (localized in Fig. 6b).

enough in the PSI results to lead to a proper measurement and interpretation.

To calculate the velocity offset between both sides of the fault, we separated the hangingwall and footwall according to the fault trace. A linear regression is first performed on each side. The LOS velocities for both sides are then computed at the fault trace and used to estimate the LOS velocity offset across the fault. We propagate the uncertainty by simply summing the two Root Mean Square values of LOS velocities estimated on the hangingwall and footwall sides.

The LOS velocity offsets are estimated on both LVF and Luyeh Strand with the use of 43 profiles and 17 profiles, respectively. These measurements are analyzed according to the latitude (Fig. 8). Concerning the LVF, LOSVO can be estimated between Rueisuei and north of Luyeh, ranging from 1 to 3.2 cm/yr. From north to south, the LOSVO increases rapidly between Rueisuei and Yuli with a quasi linear trend, followed by a stable segment until Fuli (LOSVO is about 2.6 cm/yr). The first maximum is localized south of Fuli. After this place, the LOSVO is decreasing until the south of Chihshang where we decided to estimate the total offset across both present structures (Prof. 7 in Fig. 6a). The LOSVO continues to decrease down to 1.3 cm/yr, corresponding to the place where we identify another potential active fault inside the Coastal Range (Prof. 7b in Fig. 6a). In this case, for the LOSVO estimation across the LVF, we exclude the part of the profile east of this fault. Part of the deformations is accommodated by this second fault system within the Coastal Range which is responsible for about 8–10 mm/yr of additional LOSVO. North of Luyeh, the LOSVO shows a second maximum up to 3 cm/yr. Another decrease can be observed just before the complex tectonic setting of the south end of the valley, where we decided to measure offsets on the Luyeh Strand only. The Luyeh Strand presents an increase of the LOSVO from North to South, reaching 1.4 cm/yr close to the Peinanshan over more than 5 km. The LOSVO slowly decreases along the Taitung basin and becomes stable with a rate of 0.5 cm/yr.

In addition, velocity offsets are estimated from cGPS data in five places where appropriate pairs of cGPS stations can be found,

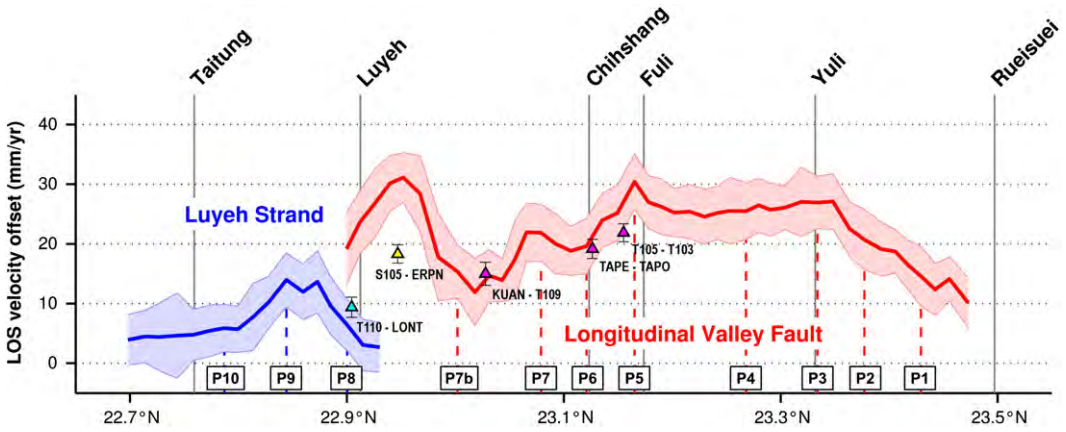

Fig. 8. Spatial evolution of LOS velocity offset (in mm/yr) across the Longitudinal Valley Fault (red line) and the Luyeh Strand (blue line). Triangles represent estimated LOS velocity offset from couple of nearby cGPS stations localized on both side of the faults. The magenta and yellow triangles are those associated with the LVF. The yellow one corresponds to a non-optimal cGPS configuration where one of the cGPS station is too close to the LVF and then do not measured the whole deformation of the hanging wall which is distributed over 2 km in that place. The blue triangle is associated with the Luyeh Strand. Profiles presented in Figs. 5 and 6 are represented by red and blue dashed lines. (For interpretation of the references to color in this figure caption, the reader is referred to the web version of this article.)

one across the Luyeh Strand and the four others across the LVF (triangles in Fig. 8). Estimation from the pair of cGPS stations T110 and LONT across the Luyeh Strand is in good agreement with PSI LOS velocity offset estimations. On the LVF, three estimations (corresponding from north to south to the pairs T105-T103, TAPE-TAPO and KUAN-T109) are also in agreement with the rates estimated from PS profiles. Offset estimated from the pair S105 and ERPN, is lower than the total velocity offset given by PSI. This can be explained by the location of the ERPN station which is too close to the fault on the hangingwall and do not encompass all the deformation.

This LOSVO profile in Fig. 8 should reflects spatial variation of fault creep rate: an increase of LOSVO can indicate a higher shallow slip rate. However, it can also mean a change of the fault slip orientation modifying the projection of the surface displacement along the radar line of sight. For example, given a fixed slip rate, an increase of the left-lateral component with a decrease of the reverse component will result in a smaller apparent LOS velocity offset (see geometry of the radar line of sight in Fig. 3). At least, the LOSVO gives a minimum shallow creep rate quantification.

5. Discussion

5.1. Spatial variation of creep

Changes of the along-dip distribution of shallow creep seem to occur along the LVF when considering the change of distance that is needed to reach the complete LOS velocity offset along our profiles. This parameter characterizes whether the deformation is diffused or localized near the fault trace. For instance, profiles 2 or 3 (Fig. 5) are showing deformation localized within a few hundreds of meters, contrasting with profile 5 where the deformation is distributed over 1–2 km, which suggests a deeper shallow creep not reaching the surface. Even in places where there are field evidences that the creep reaches the surface, splay faults branching on the LVF near the surface can cause distributed deformation, like at Chihshang where a three fault branches coupled with a 50–60-m-wide pop-up structure is observed in the hangingwall (Mu et al., 2011). This could occur at larger scale, like at the latitude of GPS station T109 (Prof. 7b in Fig. 6a) where a secondary fault located a few kilometers east of the LVF accommodates part of the deformation.

In any case, such narrow zones of deformation across the LVF (less than a few kilometers) indicate that creep occurs at least within the first kilometers of the crust and continuously from Rueisuei to the Peinanshan (Fig. 3). The velocity offsets across the LVF measured along the radar line of sight range from 1 to 3 cm/yr. They are relatively constant between Yuli and Fuli but more variable south of Fuli (Fig. 8). These variations can be explained (1) by the presence of secondary faults in the hangingwall, (2) by change of the slip rake depending of the left-lateral component of the slip, or (3) by a variation of the creep rates. It is difficult to discriminate between the last two possibilities because we only have measurement along one line of sight and because of the scarcity of the cGPS station in the area.

At its southern end, the LVF is divided into several active structures. The Luyeh Strand is passing west of the Peinanshan and have the same N20°E orientation as the LVF. Further south, the continuity of the Luyeh Strand along the eastern border of the Taitung basin may be questioned. Peyret et al. (2011) propose that the Luyeh Strand rather wraps around the south of the Peinanshan turning in E–W direction toward the sea. It is true that the Peinanshan is showing high LOS velocity values with respect to the footwall of the LVF and that the velocity decreases rapidly southward in the Taitung basin. However, this decrease is without clear discontinuity in contrast with the eastern border of the Taitung basin (see profiles 11 and 12 in S4 compared to profile 10 in Fig. 6). In any case, from a cinematic point of view, GPS and InSAR data show that the Taitung basin is a distinct unit from the Coastal Range and the Central Range. This supports the tectonic interpretation of Malavieille et al. (2002) who propose the existence of a geological major transfer zone of deformation at the latitude of Taitung delimitating the southern limit of a Coastal Range block overthrusting the Central Range to the west and backthrusting onto the Huatung Basin to the East.

At the northern end of the studied area, near Rueisuei, LOS velocity offset vanishes slowly and is more and more distributed suggesting a disappearance of the shallow creep. To explain such a change which seems to persist in the northern part of the Longitudinal Valley, some authors have proposed a correlation between shallow creep occurrence and presence of unconsolidated sediments of the Lichi mélange formation which is present along some creeping segments of the LVF (e.g., Angelier et al., 2000; Lee et al., 2006; Hsu et al., 2009). This explanation deserves further investigation, taking into account the improved fault map proposed in this study.

5.2. Comparison with previous InSAR studies

Comparison of ALOS interferograms with ERS ones published by Hsu and Bürgmann (2006) show the improvement of using L-band data in term of coherence. The density of measurement is also improved compared to the previous study of Peyret et al. (2011), which was also using the StaMPS software, but based on ERS data between 1993 and 1999. Density of PS is particularly increased over the Peinanshan and the Coastal Range.

Nonetheless the comparison of the spatial variation of velocity offset between our study and that of Peyret et al. (2011) shows significant differences. Comparing the LOS velocity offsets values along the LVF derived by the two studies, a major difference can be observed between Fuli and Yuli. For ascending ERS acquisition, offsets are between 0 and 1.0 cm/yr whereas the present study gives a mean offset of about 2.6 cm/yr. More generally, offsets are much lower with ERS results than with ALOS ones. The geometry of acquisition of ascending ERS data is slightly different from the ascending ALOS data used in this study, essentially by the incidence angle which is higher in ALOS data (about 38° versus 23°). However, this cannot explain more than a few millimeters of difference.

Another reason could be the different period of study. Indeed, we presented measures of deformation spanning January 2007–February 2010 period, whereas Peyret et al. used data covering the period between June 1993 and June 1996 for ascending data. No significant earthquakes occurred during both periods, but in between, important seismic events have occurred like the major M_W 7.6 Chi–Chi earthquake (21st of September 1999, in the western part of Taiwan), the Ms 6.5 Chengkung earthquake (10th of December 2003) and the M_W 6.1 Peinan earthquake (1st of May 2006) (Chen et al., 2009b). All these events may have affected faults activity and modified creep rates.

The 2003 Chengkung earthquake did not produce coseismic offset in creepmeters but induced a sudden increase of creep rate that decayed with time (Chang et al., 2009). This postseimic perturbation lasted up to 2006. In 2007–2009 creepmeters tend to be back to the interseismic rate (Mu et al., 2011). Noteworthy, the interseismic shortening rate of the creepmeters has also shown variation before the 2003 earthquake, slowing down from 2.7 cm/yr to about 2 cm/yr from 1993 to 2003 (Lee et al., 2005). However, the variation observed in the creepmeters between the periods 1993–1996 and 2007–2009 seems too small to explain the difference between the ERS and ALOS result, but possible temporal variations should deserve further investigations.

6. Conclusions

Our results show that Permanent Scatterer Interferometry using ALOS L-band data brings a significant improvement to interseismic ground displacement measurement in the Longitudinal Valley and the Coastal Range, especially in terms of point density, compared to previous studies using ERS C-band data or GPS networks.

The density of measurement allowed us to map with an unprecedented level of details the fault traces leading to the discovery of new field evidences of the LVF and Luyeh Strand present-day activities. These results should have direct implications for improving the ground-based monitoring of the creeping faults and to provide new relevant sites to augment the cGPS network.

Our results demonstrate the continuity of the shallow creep along the Longitudinal Valley Fault from Rueisuei to the Peinanshan. No evidence of shallow creep has been found on the Chimei Fault, on the Yuli Fault or on the western border of the Longitudinal Valley along the Central Range Fault. However, some secondary faults on the hangingwall of the LVF have been found to accommodates part of the interseismic deformation. PS results also show the present-day activity of a NE-SW segment connecting the Coastal Range to the Peinanshan.

The shallow creep along the LVF shows along-dip and along strike variations indicating that the mechanical behavior of the LVF is clearly not uniform. The new set of measurement provided by this study (available in Supplementary materials) should be determinant to perform a joint inversion of the slip distribution using all the available geodetic data, and useful for testing parameters controlling the slip behavior of the LVF. In this respect, the need of a temporal monitoring of the creep by InSAR overs tens of years with a better temporal sampling appears to be an important issue.

Acknowledgments

This research was supported by the Japan Aerospace Exploration Agency (JAXA) in the scope of PI 1120001 project, by INSU (project PNTS AO2006) and by the French Agence Nationale de la Recherche (EFIDIR project ANR-07-MDCO-004). We are grateful to A. Hooper for having developed and permitting use of the "StaMPS" freeware. We sincerely thank Jiang Guo-Chang for his help during our field investigations and M. Peyret for discussions and comments. The authors are grateful for the helpful comments and constructive reviews by two anonymous reviewers.

Appendix A. Supplementary data

Supplementary data associated with this article can be found in the online version at http://dx.doi.org.10.1016/j.epsl.2012.05.025.

References

Angelier, J., Chu, H.T., Lee, J.C., 1997. Shear concentration in a collision zone: kinematics of the chihshang fault as revealed by outcrop-scale quantification of active faulting, Longitudinal Valley, Eastern Taiwan. Tectonophysics 274 (1–3), 117–143.

Angelier, J., Chu, H.-T., Lee, J.-C., Hu, J.-C., 2000. Active faulting and earthquake hazard: the case study of the Chihshang Fault, Taiwan. J. Geodyn. 29 (3–5), 151–185.

Bakun, W.H., Aagaard, B., Dost, B., Ellsworth, W.L., Hardebeck, J.L., Harris, R.A., Ji, C., Johnston, M.J.S., Langbein, J., Lienkaemper, J.J., Michael, A.J., Murray, J.R., Nadeau, R.M., Reasenberg, P.A., Reichle, M.S., Roeloffs, E.A., Shakal, A., Simpson, R.W., Waldhauser, F., 2005. Implications for prediction and hazard assessment from the 2004 parkfield earthquake. Nature 437 (7061), 969–974, http://dx.doi.org/10.1038/nature04067.

Bürgmann, R., Rosen, P.A., Fielding, E.J., 2000a. Synthetic aperture radar interferometry to measure earths surface topography and its deformation. Annu. Rev. Earth Planet. Sci. 28 (1), 169–209.

Bürgmann, R., Schmidt, D., Nadeau, R.M., d'Alessio, M., Fielding, E., Manaker, D., McEvilly, T.V., Murray, M.H., 2000b. Earthquake potential along the northern hayward fault, california. Science 289 (5482), 1178–1182.

Chang, H.-C., Lin, C.-W., Chen, M.-M., Lu, S.-T., 1998. Active Fault Map of Taiwan, first ed.

Chang, S.-H., Wang, W.-H., Lee, J.-C., 2009. Modelling temporal variation of surface creep on the Chihshang Fault in Eastern Taiwan with velocity-strengthening friction. Geophys. J. Int. 176 (2), 601–613.

Chen, H.-Y., Hsu, Y.-J., Lee, J.-C., Yu, S.-B., Kuo, L.-C., Jiang, Y.-L., Liu, C.-C., Tsai, C.-S., 2009a. Coseismic displacements and slip distribution from gps and leveling observations for the 2006 Peinan earthquake (M_W 6.1) in Southeastern Taiwan. Earth Planets Space 61 (3), 20.

Chen, K.H., Nadeau, R.M., Rau, R.-J., 2008a. Characteristic repeating earthquakes in an arc-continent collision boundary zone: the Chihshang fault of Eastern Taiwan. Earth Planet. Sci. Lett. 276 (3–4), 262–272.

Chen, K.H., Rau, R.-J., Hu, J.-C., 2009b. Variability of repeating earthquake behavior along the Longitudinal Valley Fault zone of Eastern Taiwan. J. Geophys. Res. 114 (B5), B05306.

Chen, K.H., Toda, S., Rau, R.-J., 2008b. A leaping, triggered sequence along a segmented fault: the 1951 Ml 7.3 Hualien–Taitung earthquake sequence in Eastern Taiwan. J. Geophys. Res. 113 (B2), B02304.

Chen, K.-H., Yang, M., Huang, Y.-T., Ching, K.-E., Rau, R.-J., 2011. Vertical displacement rate field of Taiwan from geodetic levelling data 2000–2008. Surv. Rev. 43 (321), 296–302.
Chen, W., Huang, M., Liu, T., 1991. Neotectonic significance of the Chimei Fault in the Coastal Range, Eastern Taiwan. Proc. Geol. Soc. China 34, 43–56.
Chen, W.-S., Yen, I.C., Fengler, K.P., Rubin, C.M., Yang, C.-C., Yang, H.-C., Chang, H.-C., Lin, C.-W., Lin, W.-H., Liu, Y.-C., Lin, Y.-H., 2007. Late holocene paleoearthquake activity in the middle part of the Longitudinal Valley Fault, Eastern Taiwan. Earth Planet. Sci. Lett. 264 (3–4), 420–437.
Ching, K.-E., Hsieh, M.-L., Johnson, K.M., Chen, K.-H., Rau, R.-J., Yang, M., 2011. Modern vertical deformation rates and mountain building in Taiwan from precise leveling and continuous GPS observations, 2000–2008. J. Geophys. Res. 116 (B8), B08406.
Cloude, S.R., Papathanassiou, K.P., 1998. Polarimetric SAR interferometry. IEEE Trans. Geosci. Remote Sensing 36 (5), 1551–1565.
Ferretti, A., Prati, C., Rocca, F., 2001. Permanent scatterers in SAR interferometry. IEEE Trans. Geosci. Remote Sensing 39 (1), 8–20.
Ge, L., Ng, A.H.-M., Wang, H., Rizos, C., 2009. Crustal deformation in Australia measured by satellite radar interferometry using ALOS/PALSAR imagery. J. Appl. Geod. 3 (1), 47–53.
Hooper, A., Bekaert, D., Spaans, K., Arkan, M. Recent advances in SAR interferometry time series analysis for measuring crustal deformation. Tectonophysics, http://dx.doi.org/10.1016/j.tecto.2011.10.013, in press.
Hooper, A., Segall, P., Zebker, H., 2007. Persistent scatterer interferometric synthetic aperture radar for crustal deformation analysis, with application to Volcán Alcedo, Galapágos. J. Geophys. Res. 112 (B7), B07407.
Hsu, L., Bürgmann, R., 2006. Surface creep along the Longitudinal Valley Fault, Taiwan from InSAR measurements. Geophys. Res. Lett. 33 (6), L06312.
Hsu, Y.-J., Yu, S.-B., Chen, H.-Y., 2009. Coseismic and postseismic deformation associated with the 2003 Chengkung, Taiwan, earthquake. Geophys. J. Int. 176 (2), 420–430.
Hu, J.-C., Cheng, L.-W., Chen, H.-Y., Wu, Y.-M., Lee, J.-C., Chen, Y.-G., Lin, K.-C., Rau, R.-J., Kuochen, H., Chen, H.-H., Yu, S.-B., Angelier, J., 2007. Coseismic deformation revealed by inversion of strong motion and GPS data: the 2003 Chengkung earthquake in Eastern Taiwan. Geophys. J. Int. 169 (2), 667–674.
Huang, W.-J., Johnson, K.M., Fukuda, J., Yu, S.-B., 2010. Insights into active tectonics of Eastern Taiwan from analyses of geodetic and geologic data. J. Geophys. Res. 115 (B3), B03413.
Kuochen, H., Wu, Y.-M., Chang, C.-H., Hu, J.-C., Chen, W.-S., 2004. Relocation of Eastern Taiwan earthquakes and tectonic implications. Terr. Atmos. Oceanic Sci. 15 (4), 647–666.
Lee, J.-C., Angelier, J., Chu, H.-T., Hu, J.-C., Jeng, F.-S., 2005. Monitoring active fault creep as a tool in seismic hazard mitigation. Insights from creepmeter study at Chihshang, Taiwan. C. R. Geosci. 337 (13), 1200–1207.
Lee, J.-C., Angelier, J., Chu, H.-T., Hu, J.-C., Jeng, F.-S., Rau, R.-J., 2003. Active fault creep variations at Chihshang, Taiwan, revealed by creep meter monitoring, 1998–2001. J. Geophys. Res. 108 (B11), 2528.
Lee, J.-C., Angelier, J., Chu, H.-T., Yu, S.-B., Hu, J.-C., 1998. Plate-boundary strain partitioning along the sinistral collision suture of the Philippine and Eurasian Plates: analysis of geodetic data and geological observation in Southeastern Taiwan. Tectonics 17 (6), 859–871.
Lee, J.-C., Chu, H.-T., Angelier, J., Hu, J.-C., Chen, H.-Y., Yu, S.-B., 2006. Quantitative analysis of surface coseismic faulting and postseismic creep accompanying the 2003, M_W=6.5, Chengkung earthquake in Eastern Taiwan. J. Geophys. Res. 111 (B2), B02405.
Malavieille, J., Lallemand, S.E., Dominguez, S., Deschamps, A., Lu, C.-Y., Liu, C.-S., Schnuerle, P., Angelier, J., Collot, J.Y., Deffontaines, B., Fournier, M., Hsu, S.K., Le Formal, J.P., Liu, S.Y., Sibuet, J.C., Thareau, N., Wang, F., Crew, t.A.S., 2002. Arc-continent collision in Taiwan: new marine observations and tectonic evolution. Geol. Soc. Am. Spec. Pap. 358, 187–211. (Active Collision in Taiwan).
Meng, W., Sandwell, D.T., 2010. Decorrelation of L-band and C-band interferometry over vegetated areas in California. IEEE Trans. Geosci. Remote Sensing 48 (7), 2942–2952.
Mu, C.-H., Angelier, J., Lee, J.-C., Chu, H.-T., Dong, J.-J., 2011. Structure and holocene evolution of an active creeping thrust fault: the Chihshang fault at Chinyuan (Taiwan). J. Struct. Geol. 33 (4), 743–755.
Nikolaidis, R., 2002. Observation of Geodetic and Seismic Deformation with the Global Positioning System. University of California, San Diego.
Perfettini, H., Avouac, J.-P., Tavera, H., Kositsky, A., Nocquet, J.-M., Bondoux, F., Chlieh, M., Sladen, A., Audin, L., Farber, D.L., Soler, P., 2010. Seismic and aseismic slip on the central peru megathrust. Nature 465 (7294), 78–81 http://dx.doi.org/10.1038/nature09062.
Peyret, M., Dominguez, S., Cattin, R., Champenois, J., Leroy, M., Zajac, A., 2011. Present-day interseismic surface deformation along the Longitudinal Valley, Eastern Taiwan, from a PS-InSAR analysis of the ERS satellite archives. J. Geophys. Res. 116 (B3), B03402.
Prati, C., Ferretti, A., Perissin, D., 2010. Recent advances on surface ground deformation measurement by means of repeated space-borne SAR observations. J. Geodyn. 49 (3–4), 161–170.
Pritchard, M.E., Simons, M., 2006. An aseismic slip pulse in northern chile and along-strike variations in seismogenic behavior. J. Geophys. Res. 111 (B8), B08405.
Rosen, P.A., Henley, S., Peltzer, G., Simons, M., 2004. Updated repeat orbit interferometry package released. EOS Trans. Am. Geophys. Union, 85.
Sandwell, D.T., Myer, D., Mellors, R., Shimada, M., Brooks, B., Foster, J., 2008. Accuracy and resolution of ALOS interferometry: vector deformation maps of the father's day intrusion at Kilauea. IEEE Trans. Geosci. Remote Sensing 46 (11), 3524–3534.
Seno, T., Stein, S., Gripp, A.E., 1993. A model for the motion of the Philippine Sea Plate consistent with NUVEL-1 and geological data. J. Geophys. Res. 98 (B10), 17941–17948.
Shyu, J.B.H., Sieh, K., Chen, Y.-G., Liu, C.-S., 2005. Neotectonic architecture of Taiwan and its implications for future large earthquakes. J. Geophys. Res. 110 (B8), B08402.
Shyu, J.B.H., Chung, L.-H., Chen, Y.-G., Lee, J.-C., Sieh, K., 2007. Re-evaluation of the surface ruptures of the November 1951 earthquake series in Eastern Taiwan, and its neotectonic implications. J. Asian Earth Sci. 31 (3), 317–331.
Shyu, J.B.H., Sieh, K., Chen, Y.-G., Chuang, R.Y., Wang, Y., Chung, L.-H., 2008. Geomorphology of the southernmost Longitudinal Valley Fault: implications for evolution of the active suture of Eastern Taiwan. Tectonics 27 (1), TC1019.
Shyu, J.B.H., Sieh, K., Chen, Y.-G., Chung, L.-H., 2006. Geomorphic analysis of the Central Range Fault, the second major active structure of the Longitudinal Valley suture, Eastern Taiwan. Geol. Soc. Am. Bull. 118 (11–12), 1447–1462.
Sousa, J.J., Ruiz, A.M., Hanssen, R.F., Bastos, L., Gil, A.J., Galindo-Zaldvar, J., Sanz de Galdeano, C., 2010. PS-InSAR processing methodologies in the detection of field surface deformation—study of the Granada basin (Central Betic Cordilleras, Southern Spain). J. Geodyn. 49 (3–4), 181–189.
Wang, Y., Chen, W., 1993. Geological Map of Eastern Coastal Range 1:100,000.
Wu, Y.M., Chen, Y.G., Shin, T.C., Kuochen, H., Hou, C.S., Hu, J.C., Chang, C.H., Wu, C.F., Teng, T.L., 2006. Coseismic versus interseismic ground deformations, fault rupture inversion and segmentation revealed by 2003 M_W 6.8 Chengkung earthquake in Eastern Taiwan. Geophys. Res. Lett. 33 (2), L02312.
Yu, S.-B., Chen, H.-Y., Kuo, L.-C., 1997. Velocity field of GPS stations in the Taiwan area. Tectonophysics 274 (1–3), 41–59.
Yu, S.-B., Kuo, L.-C., 2001. Present-day crustal motion along the Longitudinal Valley Fault, Eastern Taiwan. Tectonophysics 333 (1–2), 199–217.

[pdf-3] Cavalié*, Pathier et al. 2013

The following pages reproduce the paper from Cavalié et al. (2013).

Slow slip event in the Mexican subduction zone: Evidence of shallower slip in the Guerrero seismic gap for the 2006 event revealed by the joint inversion of InSAR and GPS data.

Cavalié*, O., Pathier, E., Radiguet, M., Vergnolle, M., Cotte, N., Walpersdorf, A.,

Kostoglodov, V., & Cotton, F

Published in 2013 in Earth and Planetary Science Letters, 367, 52–60.

https://doi.org/10.1016/j.epsl.2013.02.020

* Olivier Cavalié started this work when he was Post-doc as ISTerre funded by CNRS to work with me in the framework of a project CNRS INSU 3F and the ANR projet GGAP

Earth and Planetary Science Letters 367 (2013) 52–60

Contents lists available at SciVerse ScienceDirect

Earth and Planetary Science Letters

journal homepage: www.elsevier.com/locate/epsl

Slow slip event in the Mexican subduction zone: Evidence of shallower slip in the Guerrero seismic gap for the 2006 event revealed by the joint inversion of InSAR and GPS data

O. Cavalié [a,b,*], E. Pathier [a], M. Radiguet [a,c], M. Vergnolle [a,b], N. Cotte [a], A. Walpersdorf [a], V. Kostoglodov [d], F. Cotton [a]

[a] Institut des Sciences de la Terre, Université de Grenoble 1, CNRS UMR 5265, F-38041 Grenoble, France
[b] Géoazur, Université de Nice Sophia-Antipolis, CNRS, IRD, Observatoire de la Côte d'Azur, 250 avenue Einstein, 06560 Valbonne, France
[c] Computational Solid Mechanics Laboratory, Ecole Polytechnique Fédérale de Lausanne, EPFL ENAC IIC LSMS, GC A2, Station 18, 1015 Lausanne, Switzerland
[d] Instituto de Geofísica, Universidad Nacional Autónoma de México, Mexico

ARTICLE INFO

Article history:
Received 19 June 2012
Received in revised form
16 February 2013
Accepted 17 February 2013
Editor: P. Shearer

Keywords:
InSAR
slow slip event
subduction zone processes
seismic cycle

ABSTRACT

Slow slip events (SSEs) in subduction zones have been observed in the last decade with continuous GPS stations. Some of them could be related to the lateral segmentation of subduction interface that seems to be a critical parameter for the propagation of large subduction earthquakes. In 2006, one of the largest SSEs recorded so far was captured by a dozen continuous GPS stations, in the Guerrero area (Mexico) along the Mexican subduction zone. Previous studies based on these data suggested a lateral variation of the updip depth of the SEE at the Guerrero seismic gap, but suffered from a lack of resolution east of the gap. Here, we show the ability of InSAR technique to capture a part of the 2006 SSE cumulative displacement east of the Guerrero gap by a stacking approach. We processed long strip Envisat interferograms corrected for orbital errors and interseismic signal using GPS data. We first use a forward modelling approach to test InSAR sensitivity to the amount of slip, depth and width of the slipping area on the subduction interface. Due to its high spatial resolution, InSAR allows one to comprehensively sample the North–South spatial wavelength of the SSE deformation, complementing the sparse GPS network. InSAR locates the maximum of uplift and subsidence caused by the SSE more precisely than the GPS data, giving better constraints on the updip slip limit of the SSE. We then inverted the InSAR and GPS data separately to understand how each inversion resolves the slip at depth. Finally, we performed a joint inversion of InSAR and GPS data, which constrained the SSE slip and its location on the plate interface over the entire Guerrero area. The joint inversion shows significant lateral variation of the SSE slip distribution along the trench with a shallower updip edge in the Guerrero seismic gap, west of Acapulco, and a deeper slip edge further east.

1. Introduction

Precise geodetic measurements, essentially GPS, allowed the discovery of slow transient dislocations in subduction zones such as slow slip events (SSEs) in Japan (e.g., Hirose and Obara, 2005), Cascadia (e.g., Dragert et al., 2004) and Mexico (e.g., Kostoglodov et al., 2003). The increasing number of observations in different regions has shown a variability in the duration, magnitude and recurrence of slow slip events (Ide et al., 2007). Moreover, some subduction areas present a clear correlation in time and space between non-volcanic tremor (NVT) and SSE, for example in Cascadia. Contrastingly in Mexico, these two phenomena are not directly associated: most of the NVT episodes occur downdip of the long-term SSE area and there is high NVT activity which is not correlated in time with large slow slip events (Payero et al., 2008; Kostoglodov et al., 2010). Precise determination of the slip distribution at depth and along the subduction trench is essential to reveal the physical processes involved in the slow slip events, and to understand their role in the seismic cycle of large subduction earthquakes. This study focuses on the Guerrero segment of the subduction zone in Mexico, where one of the best-recorded series of SSEs in the world exists. In this region, the subduction interface between the Cocos and North America plates is relatively flat, becoming steeper on both sides of this area

* Corresponding author at: Géoazur, Université de Nice Sophia-Antipolis, CNRS, IRD, Observatoire de la Côte d'Azur, 250 avenue Einstein, 06560 Valbonne, France. Tel.: +33 4 92 94 26 74.
E-mail addresses: ocavalie@geoazur.unice.fr (O. Cavalié), erwan.pathier@ujf-grenoble.fr (E. Pathier).

0012-821X/$ - see front matter © 2013 Elsevier B.V. All rights reserved.
http://dx.doi.org/10.1016/j.epsl.2013.02.020

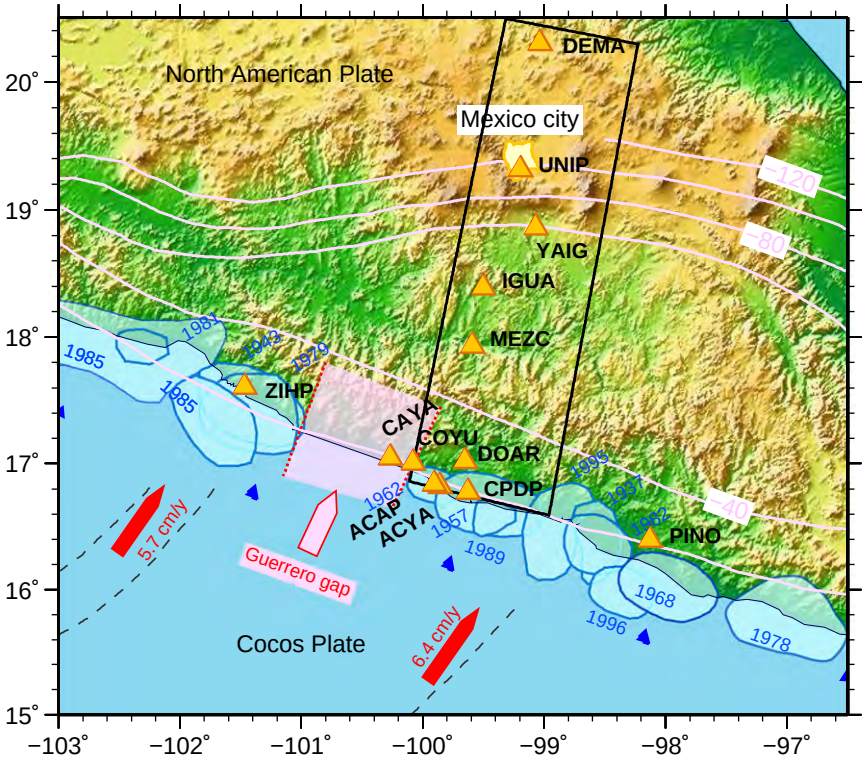

Fig. 1. Tectonic map of the Cocos-North America (NA) plates convergence zone in Central Mexico (from Kostoglodov et al., 2003). The dashed blue line represents the Middle America trench and the magnitude of the red arrows indicate the Cocos-NA convergence velocities (Demets et al., 2010). Pink lines denote the depth of the interface between the Cocos and NA plates. Blue patches represent the major earthquakes rupture zones. The locations of permanent GPS stations are indicated by orange triangles. The black rectangle indicates the coverage of the Envisat radar images used in this study (track 255, I2, stripmap mode). (For interpretation of the references to color in this figure legend, the reader is referred to the web version of this article.)

(Fig. 1). The largest crustal displacements during the SSEs have been observed in the Guerrero seismic gap area,[1] a ~120 km-long segment of the seismogenic zone where no major earthquake has occurred since the M_s 7.6 earthquake in 1911 (e.g., Nishenko and Singh, 1987; Kostoglodov and Ponce, 1994). If the recurrence period of large historical subduction thrust earthquakes in Mexico is of 30–60 yrs, then an earthquake in the Guerrero gap is overdue already. This raises the question of a possible relationship between the existence of a persisting seismic gap and the occurrence of large SSEs (Lowry et al., 2001; Kostoglodov et al., 2003; Yoshioka et al., 2004; Larson et al., 2007).

A related question is whether the SSEs are intruding into the seismogenic zone (e.g., Larson et al., 2004). This information is crucial to know how the subduction margin is segmented. A recurrent aseismic slip located in the seismogenic layer in the Guerrero seismic gap could act as a barrier and thus control the spatial extension of a potential mega-earthquake in the area. On the other hand, a deeper SSE location could increase the stress in the seismogenic zone and thus increase the probability of a mega-thrust event (Mazzotti and Adams, 2004). The 2011 Tohoku-Oki earthquake showed that understanding the lateral segmentation of a subduction zone has a huge impact on seismic hazard evaluation. Before the earthquake, Japanese hazard maps divided the offshore subduction interface located north of Tokyo into six segments, each roughly 150 km long (Kerr, 2011). This distribution, based on the past known seismicity, restricted drastically the probability of a mega-earthquake occurrence along this stretch of the Japan trench. However, based on GPS data, Loveless and Meade (2010) showed that the interseismic coupling did not respect this segmentation, and actually the Tohoku-Oki mega-earthquake broke the plane along a much bigger area than predicted by the hazard map. Knowing in details the lateral variations of the subduction dynamic along the trench is then a key point to properly assess its seismic hazard. The Mexican GPS network recorded the first large slow slip event in 1998 and since then SSEs occur on a cycle of about 4 yrs. However, individual events have different spatial and temporal characteristics (Radiguet et al., 2012). For instance, their durations range from 6 to 14 months; the longest duration was recorded for the SSE from July 2009 to September 2010 (Walpersdorf et al., 2011). The estimated values of fault slip are among the largest reported worldwide for periodic SSE (e.g., Ide et al., 2007), generating surface displacements up to 6 cm. The 2006 event occurred between April 2006 and February 2007 (Vergnolle et al., 2010) with an equivalent seismic moment estimated at 2.2×10^{20} Nm (Larson et al., 2007), corresponding to an equivalent M_W 7.5 earthquake. The GPS network designed to monitor the long-term interseismic deformation and SSE consists primarily of a North–South trench-perpendicular profile from the coast up to Mexico City, and a trench-parallel profile running along the coast. Despite efforts to increase the GPS network coverage since the discovery of the Guerrero SSEs in 1998 (Lowry et al., 2001), the spatial extent of the surface deformation remains poorly constrained, especially considering its inland East–West variation. For instance, the spatial extent of the 2006 SSE was monitored by only a dozen irregularly distributed permanent GPS stations (see Fig. 1). GPS data have been inverted to derive slip distribution on the subduction interface (Larson et al., 2007; Radiguet et al., 2011, 2012). Based on these results, Radiguet et al. (2012) have suggested lateral variations of SSE properties in the Guerrero seismic gap. However, their results suffer from a lack of resolution east of the

[1] Note that the Guerrero Gap is sometimes defined as extending up to longitude 99°W, but in this case two segments are distinguished: the NW Guerrero Gap (called Guerrero Gap in this paper) and the SE Guerrero Gap on which several earthquakes have occurred since 1911, e.g., 1957, 1962, 1989, 1995 (see Fig. 1, Suárez et al., 1990; Ortiz et al., 2000).

gap. Indeed, the reliability of the inverted distribution away from the two main GPS profiles remains an issue. And even along the profiles, the GPS network is not dense enough to properly sample the SSE crustal deformation. The lack of resolution of the past results only based on GPS data is a strong motivation for using space-borne Synthetic Aperture Radar Interferometry technique (InSAR). Due to its high spatial sampling, InSAR (e.g., Bürgmann et al., 2000) has the potential to provide far denser measurements of the surface displacement than sparse GPS network. In spite of vegetation cover and mountainous zones in the Guerrero area, which are usually limiting factors of C-band InSAR, preliminary results from Cavalié et al. (2009) showed, for the first time, that InSAR was able to capture the 2006 SSE surface displacement. Following this approach, our study uses InSAR to obtain dense surface displacement measurements with an extended coverage (Fig. 1), focusing on the 2006 SSE. The aim of this study is first to test the ability of InSAR to get new constraints for retrieving the SSE characteristics at depth. We then combine GPS and InSAR data sets to provide a better slip distribution model for the 2006 SSE. A further goal is to establish spatial relationships between the SSE and the Guerrero seismic gap.

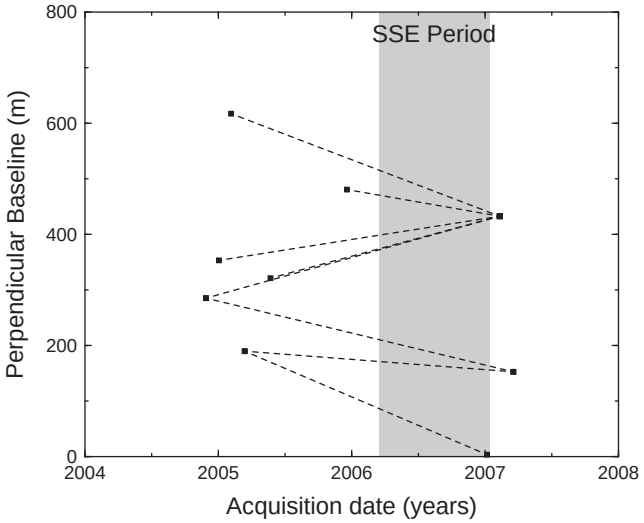

Fig. 2. Relative position of Envisat orbits on descending track 255 plotted as a function of image acquisition dates. Dashed lines show the eight interferograms selected for stacking. The gray area indicates the time span of the 2006 slow slip event.

2. Data and processing

The present study focuses on the 2006 event because a larger amount of suitable GPS and SAR data is available compared with the previously recorded events. Indeed, the 1998 event was not well documented by GPS (continuous record at only one station (Lowry et al., 2001) and the 2002 event was not well documented by SAR data (ERS-2 satellite had gyroscope problems at this time). InSAR analysis of the last SSE (2009–2010) is in progress but requires another processing strategy because of a different temporal distribution of SAR data. To map the surface displacement associated with the 2006 event, we use data from the Envisat SAR archive provided by the European Space Agency (ESA). Unfortunately, only data on descending tracks are exploitable, impeding the use of ascending data to constrain the SSW horizontal displacement. Among the possible descending tracks covering the Guerrero area, we focus on track 255, which provides the largest number of suitable images for our analysis. Track 255 also covers most of the permanent GPS stations, which are useful for correcting interferograms for orbital uncertainties and for validating InSAR measurements of ground deformation. Along the adjacent track (T26) less suitable images are available, and none of the five processed interferograms were coherent enough to be unwrapped (Chen and Zebker, 2000; Gens, 2003) in the coastal area, where most of the SSE signal is expected. Twelve images (see Table S1), acquired between November 2004 and March 2007 along track 255, were selected according to three criteria: (1) full coverage from the coast to north of Mexico City (around 500 km long) in order to include a far-field area not affected by the SSE, (2) acquisition date close to the SSE to limit temporal decorrelation, and (3) low perpendicular baseline dispersion (Fig. 2) to minimize geometrical decorrelation in interferograms. The ROI-PAC software (Rosen et al., 2004) was used to process the interferograms from raw data. In order to limit the geometrical phase decorrelation, we imposed perpendicular baselines to be smaller than 200 m. As no suitable images were acquired during the SSE with these constraints (Fig. 2), we cannot reconstruct the time evolution of the SSE deformation and therefore the analysis of the SSE finite displacements was only done. Consequently, a stacking approach has been adopted, based on the 12 interferograms that encompass the 2006 SSE. Those interferograms are corrected for orbital and topographic components using DEOS (Scharroo and Visser, 1998) and the 3-arc-second SRTM DEM (Farr and Kobrick, 2000), respectively. The main difficulties encountered during InSAR processing are related to phase decorrelation, which occurs between the coast and Mexico City. This is due to vegetation cover and to the steep slopes in the mountain ranges (Fig. 1). To help the phase unwrapping, interferograms are down-sampled using 32 looks in range and 5×32 looks in azimuth (Ferretti et al., 2007), resulting in a ~ 640 m pixel spacing. The loss of spatial resolution is acceptable, as the expected gradient for the ground displacement due to the SSE is low (a few centimeters distributed over tens of kilometers). This approach has been shown to efficiently recover phase coherence (Jónsson, 2008). Interferograms are then filtered using an adaptive filter (Goldstein and Werner, 1998) for further noise reduction. Some of the 12 interferograms have large areas of low coherence impeding the phase unwrapping. Consequently, eight interferograms (see Fig. 2) with acceptable unwrapped information are used to retrieve the tectonic signal. We correct the long wavelength orbital errors on each interferogram. As the SSE signal affects most of the interferograms, we cannot rely on stable areas to constrain the orbital error. We, thus, use GPS data to adjust a linear ramp in the North–South and East–West direction. A linear rather than a quadratic correction is applied due to the irregular spatial distribution and limited number of GPS stations available (from 5 to 6 depending on the interferogram) impeding a robust estimate of second order polynomial coefficients. The displacement of each GPS station (taken from Vergnolle et al., 2010) occurring between the two acquisition dates is computed along the radar line of sight (LOS). The parameters of the linear ramp are estimated by minimizing the misfit between LOS GPS displacements and InSAR displacements, which are averaged on a 10×10 pixel window centered on the location of GPS stations. Another correction is needed because the selected interferograms include both SSE deformation and interseismic signals. The amplitude of the latter depends mainly on the acquisition date of the first image (the second images of the interferograms have been acquired very shortly after the end of the SSE). The older the acquisition of the first image, the larger the recorded interseismic signal in the interferogram. Therefore, it is important to calibrate the interferograms containing different amounts of interseismic signal. To quantify the cumulated surface displacement of the SSE, we chose to measure the difference between the station position at a given date after the event (the second date of the SAR image that forms the interferogram) and a theoretical GPS position, based on pre-SSE interseismic displacement rates, supposing that the 2006 event had not occurred. In other words, the cumulated displacement of the SSE corresponds to the deviation from the interseismic trend induced by the SSE. GPS measurements show a relatively constant interseismic

velocity between two consecutive SSEs (Vergnolle et al., 2010; Radiguet et al., 2012). Continuous GPS data between 2002 and 2006 have been inverted to compute the inter-SSE coupling on the subducting interface using an inversion scheme similar to Radiguet et al. (2012). We used this model to derive the map of inter-SSE LOS surface displacement rates for each InSAR pixel. This rate is multiplied by the time span of each interferogram and subtracted from the interferogram to get the deviation from the interseismic trend caused by the SSE. After correcting for the interseismic deformation, the interferometric signal consists of the SSE displacement and of remaining perturbations, mainly atmospheric delays. To increase the signal-to-noise ratio and to mitigate the atmospheric perturbation, the eight corrected interferograms (see Fig. S1) are averaged (Zebker et al., 1997; Cavalié et al., 2008).

3. InSAR results

Fig. 3 shows the LOS ground displacement due to the 2006 SSE, obtained by averaging the interferogram stack. As the eight interferograms are not unwrapped over the same extent (see Fig. S1), only pixels of the stack where at least five interferograms were available are used (Fig. S2). The cumulated LOS surface displacements of the SSE, as defined in the previous section, range from 5.5 cm (toward the satellite) to −4.8 cm (away from the satellite). It is noteworthy that the LOS displacement is highly correlated to the vertical component because of the small angle (∼23°) between the LOS and the vertical axis, and because the LOS is nearly orthogonal to the horizontal component of the slow slip event motion. LOS displacement variations are mainly North–South. Thus, the map can be described as showing subsidence south of Mexico City from latitude 18.5°N to 17.6°N, with a maximum of subsidence around 18°N and an uplift from 17.4°N to the coast. The uplift is maximum around 17°N. The standard deviation of the LOS displacement is about 1.3 cm in average but can be up to 3.5 cm, with larger values near the coast where the number of available interferograms is smaller due to unwrapping problem (Figs. S2 and S3). Profiles perpendicular to the trench show no significant deformation north of Mexico City but a long wavelength signal south of it. The maximum LOS displacement is located at about 100–110 km from the trench, and the minimum at about 200–220 km (Fig. 3). Comparison with GPS measurements, projected along LOS, shows a good agreement with a root mean square (RMS) of 0.5 cm (computed at the six stations where InSAR values are available). This RMS is lower than the standard deviation of the LOS displacement. The spatially continuous InSAR measurement confirms that the spatial distribution of the GPS network was not optimal for sampling the displacement signal during the 2006 SSE. Particularly, due to the absence of stations between DOAR and MEZC, the GPS network was not able to determine the uplift peak of the 2006 event. The displacements of the GPS stations close to the coast (ACAP, ACYA, CPDP, and DOAR) are well explained by the decrease in the LOS displacement toward the coastline (Fig. 3). However, the COYU and CAYA stations, which are located about 10 km from the coast but tens of kilometers further west, present LOS displacements significantly higher than ACAP and ACYA, indicating a lateral variation of the surface displacement west of Acapulco (ACAP), an area which is unfortunately not covered by our InSAR measurements. Possible errors due to atmospheric delay have been investigated (Doin et al., 2009). By stacking interferograms, we expect to significantly decrease the random phase delays due to the atmospheric turbulence (Zebker et al., 1997; Hanssen, 2001). This decrease follows a square root function of the number of independent interferograms. On the contrary, the spatially correlated delays (tropostatic delay Cavalié et al., 2007, 2008) do not follow such a relation, and stacking methods are less efficient at removing this effect which is correlated (or anti-correlated) to the elevation. In our results on the 2006 SSE, some local correlations can be found at a kilometric scale (for instance at volcanoes), however, at larger scale there is no significant correlation between elevation and LOS displacements (see profiles

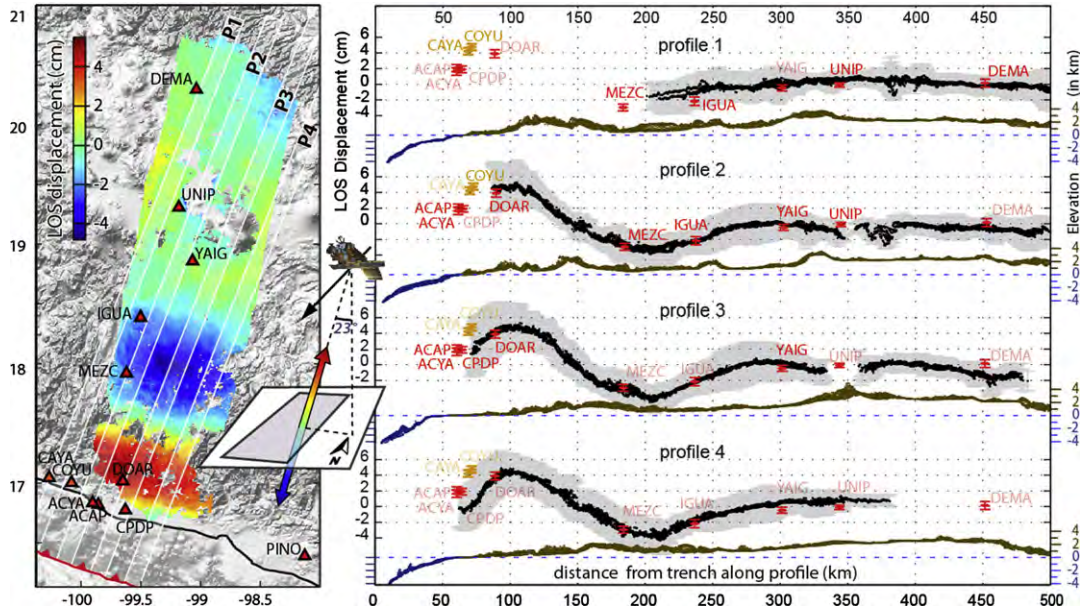

Fig. 3. Left panel: Map of surface displacement (in LOS, see drawing) caused by the 2006-SSE. After our processing, only few places stay incoherent: by the coast (north of Acapulco), on the steep slopes of two volcanoes (north-east of YAIG), and in Mexico City (east of UNIP). For this latest area, because of the spatial downsampling, the local high gradient of subsidence in Mexico City (López-Quiroz et al., 2009) causes aliasing, impeding the phase unwrapping. The white boxes (7 km wide) indicate the profile locations shown in the right panel. Right panel: Four profiles, perpendicular to the Middle America trench, showing the LOS displacement estimated from InSAR (black dots, the gray envelope represents the phase standard deviation of the individual interferograms before stacking) and the topography (blue dots offshore and brown dots overland). All InSAR and elevation points located in the white boxes are projected onto the corresponding profile. Red markers show LOS displacements inferred from GPS data. Orange markers are used for the two stations located within the Guerrero gap. Name of GPS stations located more than 10 km away from a profile are shown with a lighter color for this profile. The SSE surface signature is characterized by a smooth deformation with a 6 cm LOS displacement maximum at about 110 km from the trench and a minimum at about 220 km. (For interpretation of the references to color in this figure legend, the reader is referred to the web version of this article.)

in Figs. 3 and S4). Due to the limited number of interferograms used in the stack and its relatively high standard deviation (Figs. S2 and S3), it is possible that residual orbital errors or some effect of atmospheric perturbations not eliminated during the data processing still affect the LOS displacement signal. As we use GPS records to constrain the long wavelength of the signal and then average the interferograms, these errors are likely to propagate into smooth variations of the LOS displacement at a local-scale. The good agreement between InSAR and GPS results also suggests that they are limited to local-scale smooth perturbations of the signal within the error bars. In this case, the spatial position of the maximum and minimum of LOS displacements is a more robust feature than their absolute value. Similarly, the long-wavelength interseismic correction (ranging from −1 cm to 2 cm in LOS), which improves the agreement between InSAR and GPS data (RMS=5 mm with correction vs. 9 mm without correction), do not significantly change the position of the maximum and minimum of the LOS displacement (Fig. S5). Using an alternative InSAR processing approach (persistent scatterer technique Hooper et al., 2004), Hooper et al. (2012) found a similar position of the maximum and minimum of LOS displacements, as well as a similar range of the SSE displacements.

4. Modelling: forward approach

In order to better understand how surface displacement patterns projected along the LOS are controlled by the slip distribution, we performed a forward modelling exploration. This approach aims to see how InSAR is able to give more information about the slip location on the subduction interface. Our direct models are similar to the model of Radiguet et al. (2011), using the same interface geometry and assuming the slip on the interface to be pure thrust. Green's functions are evaluated in a layered elastic half-space using the 1D Earth's crustal model of Hernandez et al. (2001) (Table S2). Assuming a uniform slip distribution, we investigated the influence of three parameters: (1) depth of the updip slip limit from 12 km to 42 km, (2) width of the slipping area from 25 km to 150 km, and (3) slip amount from 6 cm to 20 cm. The results show that the position of the maximum LOS displacement with respect to the trench is essentially controlled by the depth of the updip slip limit (Fig. 4). As in our case InSAR measurements correspond mainly to the vertical motion, it is consistent with results from Savage (1983) showing that when the depth of the slip distribution decreases, the position of the uplift peak moves toward the trench. When the width of the slipping area increases, the position of the uplift peak remains stable, but the distance between positions of the maximum and minimum of the displacement increases (Fig. S6). Finally, increasing the amount of slip does not change the peak position as the model equations are linear. The forward model that best fits the InSAR data shows that east of the Guerrero gap, the distance between the trench and the uplift peak is greater than predicted by the slip distribution model (Radiguet et al., 2011) based only on the inversion of GPS data (Fig. 4). In agreement with our parameter analysis, the additional constraints obtained from InSAR data tend to locate the slip updip limit further downdip on the subduction interface, under the InSAR track location than the inversion entirely based on GPS data. The SSE

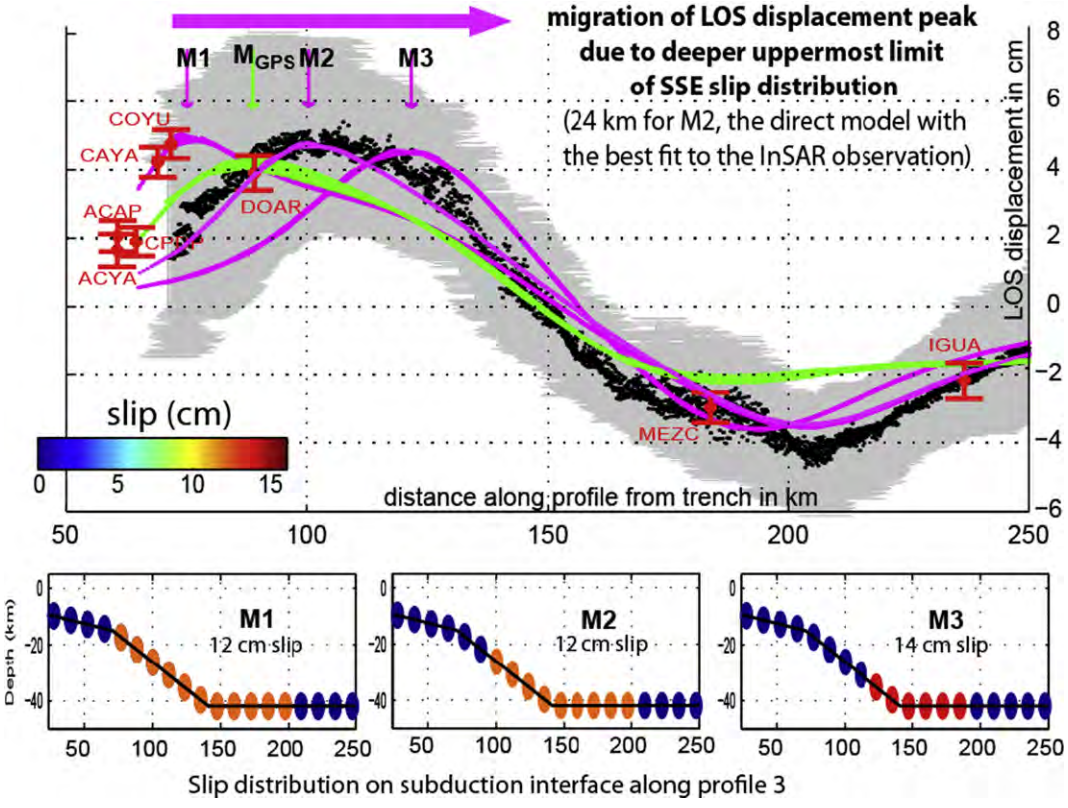

Fig. 4. SSE LOS displacements observed from InSAR (black dots) along the profile 3 (see location in Fig. 3) and predicted by three forward models (M1, M2 and M3). The slip distributions for the models are shown below (the color scale indicates the slip amplitude along the subfaults). The three models, with uniform slip, are the best models for an updip slip limit fixed at 15, 24, and 33 km, respectively. M2 is the best models among all the models explored (see details in text). These models have been chosen to illustrate how slip updip limit constrains the LOS displacements peak on the surface. For the best fitting model, M2, the updip limit is at 22 km depth. The comparison of InSAR displacement along profile 3 with the LOS displacement predicted by the Radiguet et al. (2011) model, green line, shows that models, constrained only by GPS data, estimate shallower updip limit of the SSE slip. This is due to the poor sampling of the displacement maximum by the sparse GPS network. The GPS inversion includes also CAYA and COYU GPS stations, located west of the profile 3, which fit better models with shallower slip (like M1). (For interpretation of the references to color in this figure legend, the reader is referred to the web version of this article.)

updip limit estimated from GPS data inversion (Radiguet et al., 2011) is between 15 and 22 km, which is shallower than the 24–28.5 km limit of the forward model that best fits the InSAR data. The difference in the estimated updip slip limits between the two models (GPS and InSAR) can be explained by the poor sampling of the uplift maximum by the GPS network due to the absence of stations between DOAR and MEZC. Moreover, in the Guerrero gap, the uniform forward models based on InSAR profiles cannot explain satisfactorily the displacements of CAYA and COYU stations at the coast. These two stations show a significantly larger horizontal and vertical SSE displacements compared to those at ACYA and ACAP (Vergnolle et al., 2010) in spite of the short distance (27 km) between COYU and ACYA. This suggests a sharp lateral variation of the slow slip distribution. To further investigate this lateral evolution of the slip distribution and its possible link with the seismic gap, we perform a joint inversion of InSAR and GPS data.

5. Joint inversion of InSAR and GPS data

To perform the static inversion of the GPS and InSAR cumulative displacements of the 2006 SSE, we used the method and parameterization described by Radiguet et al. (2011). It follows the formulation of Tarantola (2005) for linear problems. The cost function consist in two terms: the first term is the fit to the data, in which the data covariance matrix contains the uncertainties associated to each data, and the respective weight of InSAR and GPS data sets. The second term of the cost function is the proximity to the initial model (zero slip model). It contains the model covariance matrix used to introduce the correlation between nearby parameters. This corresponds to the addition of a smoothing operator on the slip distribution model. The correlation length (degree of smoothing) is 50 km. It was selected as the best compromise between the slip roughness and a low misfit to the data (Radiguet et al., 2012). To reduce the number of InSAR data while keeping high resolution at places where the deformation gradient is strong, we resampled the InSAR stack from $\sim 1.5 \times 10^6$ pixels to 257 pixels using a quadtree algorithm (Jónsson et al., 2002) (Fig. S7). The weight of each point is a function of the number of original pixels it contains and its standard deviation is the mean standard deviation of those pixels. One difficulty of joint inversion is to properly weight the different data sets. The relative importance between the GPS and InSAR data is introduced by a weighting factor in the data covariance matrix. Different weighting factors w have been tested, where $w = w_{InSAR}/w_{GPS}$ is the ratio of the InSAR weight over the GPS weight. We then evaluate what ratio is able to explain both data sets. The agreement between data and models is defined by RMS. Fig. 5 shows the RMS between the data and the model for GPS and InSAR separately, for w ranging from 10^{-3} to 10^3. We see that the values of w that keep a good agreement between the data and the model for both data sets lie between 1 and 5. We first inverted the data set separately to see the influence of each data type. We set $w=1000$ and then $w=0.001$, which almost correspond to the inversion of InSAR data or GPS data alone, respectively (Fig. 6). Then, according to the previous weighting tests (Fig. 5), we performed the joint inversion for three w ratios (2, 3, and 5). Fig. 7 shows the

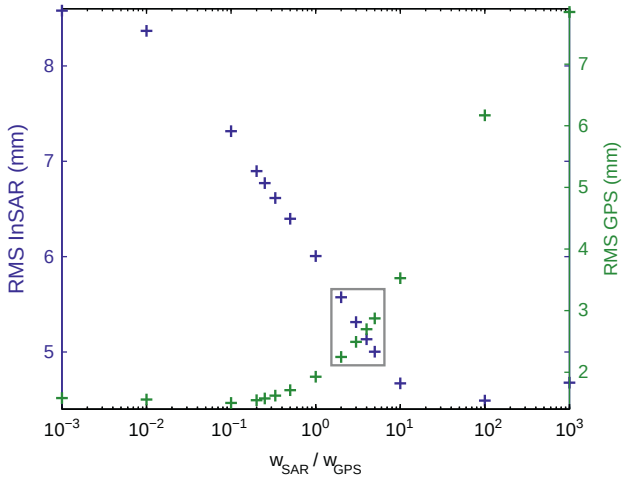

Fig. 5. Individual RMS values for InSAR data (blue) and GPS data (green) as a function of w. The gray area corresponds to the optimal w values used for the inversion results shown in Figs. 7 and S6. Note that the two vertical axis have different scalings. For $w=3$, InSAR RMS are larger than GPS RMS because the standard deviations of InSAR data are larger than the standard deviations of GPS data. (For interpretation of the references to color in this figure legend, the reader is referred to the web version of this article.)

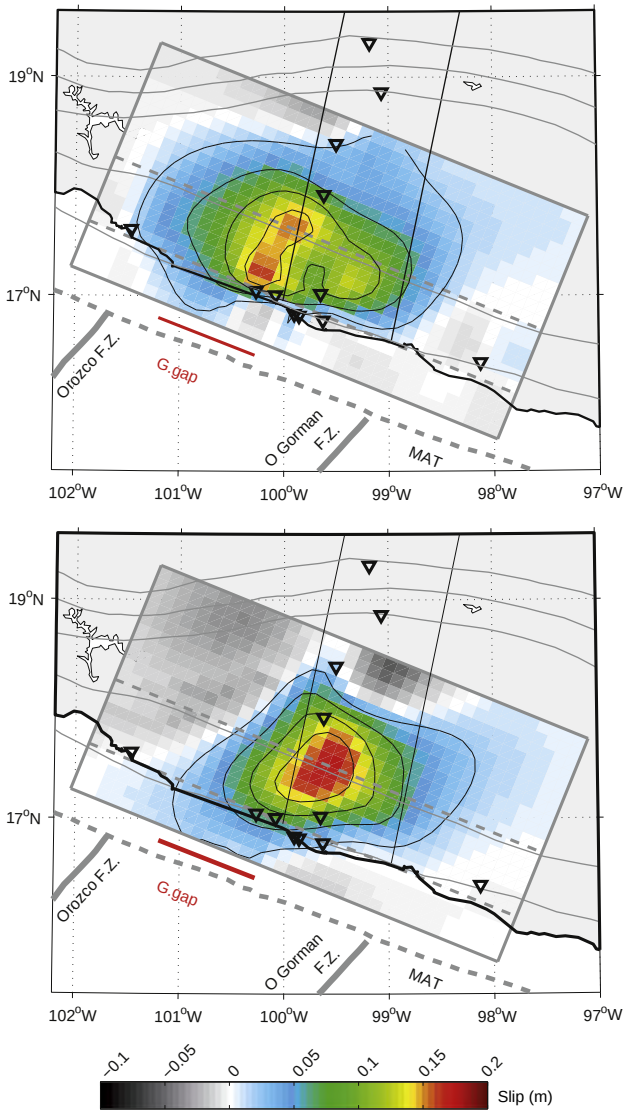

Fig. 6. Slip amplitude inferred by inversion with (a) $w=0.001$ (i.e. fit mainly the GPS data) or with (b) $w=1000$ (i.e. fit mainly InSAR data). GPS stations are represented by open black triangles and InSAR track by black box. Dashed thin gray lines indicate the changes in the dip of the model subduction plane (at 15 and 42 km). Dashed thick gray line represents the Middle American Trench (MAT) and thick continuous gray lines correspond to fracture zones. The location of the Guerrero gap (G.Gap) is shown in red. Negative slip values can appear because no positivity constraint is applied. They reflect uncertainties associated with the inversions. Low values of negative slip are an indication of the good quality of the model. (For interpretation of the references to color in this figure legend, the reader is referred to the web version of this article.)

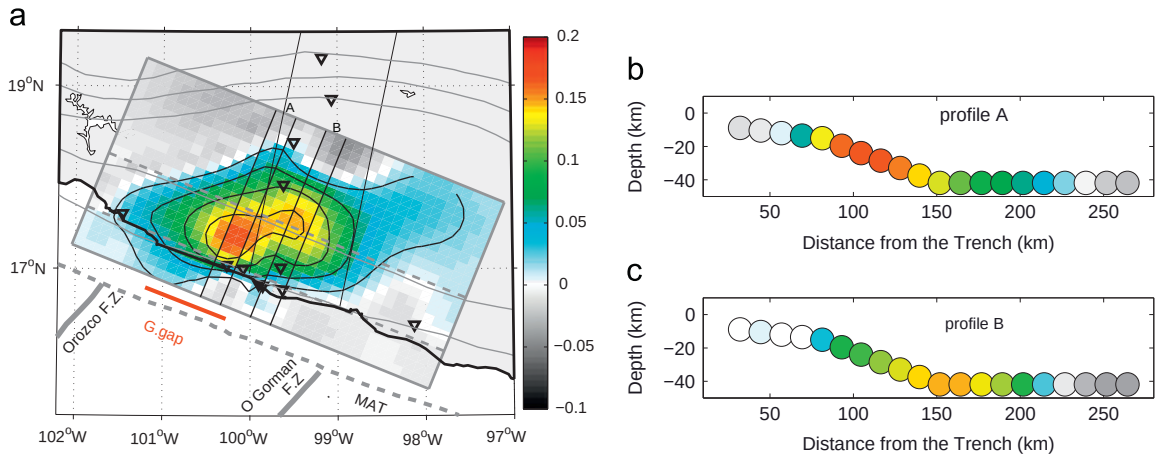

Fig. 7. Inversion results for $w=3$. (a) Slip distribution (in m, see the color bar) on the subduction plane. GPS stations are represented by open black triangles and InSAR track by black box. Dashed thin gray lines indicate the changes in the dip of the model subduction plane. Dashed thick gray line represents the Middle American Trench (MAT) and thick continuous gray lines correspond to fracture zones. The location of the Guerrero gap (G.Gap) is shown in red. (b) and (c) are the two profiles of this distribution across the subduction plane at locations indicated on (a). (For interpretation of the references to color in this figure legend, the reader is referred to the web version of this article.)

inversion for a ratio equal to 3. Results for a ratio of 2 and 5 give similar results (Fig. S8). Fig. 6 shows clearly that the inversion of one data type locates the slip where it can be resolved, i.e. by the observation spots. This is consistent with the resolution analysis of the inversion according to the type of data used (Radiguet et al., 2011 and Fig. S9). GPS inversion finds a shallow slip distribution with a maximum around CAYA and COYU stations while InSAR localizes most of the displacement under the track coverage with a maximum of slip at around 40 km depth. We see that the GPS inversion fits the GPS data very well, but does not reproduce precisely the LOS peak displacement observed by InSAR (Fig. 8a and d). The modelled displacement maximum is shifted toward the coast. This can be explained by the lack of GPS data needed to constrain the updip slip limit on the subduction plane as shown by the forward models analysis InSAR inversion reproduces the InSAR observations and fits relatively well the horizontal and vertical components of GPS data (Fig. 8b and d). For some stations, however, the amplitude and azimuth of modelled displacements are slightly off (e.g., COYU or CAYA stations). Note that, as previously observed with the forward approach, InSAR locates the slip deeper than the GPS along the InSAR track (i.e. east of the Guerrero gap). Inverting jointly both data sets allows one to increase the inversion resolution (Fig. S9) and thus to refine the results. Contrary to inversions with a single type of data, Fig. 7 shows a transition in the slip distribution, from a shallower patch in the seismic gap near CAYA and COYU stations ($\sim 100.2^{\circ}$W), to a deeper patch of slip further east ($\sim 99.5^{\circ}$W), in an area considered out of the Guerrero gap. According to the profiles, the maximum slip of the patch located in the gap occurs around 25 km depth (Fig. 7b), while the maximum slip on the second patch, occurs at the beginning of the flat section of the slab at 40 km depth (Fig. 7c). The continuity between the two patches is quite sensitive to the weighting parameter and the deeper slip patch is more pronounced when the relative weight of InSAR increases (Fig. S8). Fig. 8c and d shows that the joint inversion matches very well both InSAR and GPS data (global RMS=6.4 mm). As several subduction geometries have been proposed, we also checked that the results shown here do not change significantly using another subduction geometry for the inversion (e.g., Radiguet et al., 2012).

6. Discussion and conclusions

Combining GPS and InSAR data improves our knowledge of the slip distribution along the subduction plate interface during the 2006 SSE, especially in the eastern part of the Guerrero gap where the observation density is optimal (Fig. S9). At this location, the joint inversion reveals a lateral variation of the slip distribution along the trench that is, interestingly, spatially correlated to the eastern limit of the seismic gap delimited by the 1962 Acapulco earthquake rupture area (Ortiz et al., 2000). This observation suggests a link between the depth of the aseismic slip during the slow slip events, which repeat approximately every four years, and the recurrence interval of large earthquakes in the Guerrero subduction zone. In the seismic gap, a significant part of the aseismic slip takes place in the seismogenic zone, whereas further east, the inversion shows that the maximum of slow slip is located on the flat segment of the subduction interface (at about 40 km depth), deeper than the downdip limit of the seismogenic zone, which is expected to be at about 25 km in this section of the subduction zone (Suárez et al., 1990; Larson et al., 2004). This could explain why this area experiences more often large earthquakes like the $M_w=7.8$ event in 1957 (Ortiz et al., 2000) (Fig. 1). If the SSEs are definitively not strictly limited to the gap, the slip in it is located at a shallower depth, thus releasing in the gap part of the interseismic elastic stress that builds up in the seismogenic zone. As a consequence, it could explain the longer repeat time of large thrust earthquakes in the Guerrero Gap than in the rest of the Mexican subduction zone. Actually, no major earthquake occurred in the gap since the 1911 event, while the recurrence period out of the gap (including the segment where deeper slow slip occurs east of the gap) is estimated to be around 30–60 yrs. By improving the slip resolution, the joint inversion results support the analysis of Radiguet et al. (2012) where the slip deficit in Guerrero has been estimated over a 12 yr period (3 SSE cycles). They conclude that in the Guerrero seismic gap, the slip deficit is on average only one-quarter of what is observed on both sides of the gap. It is noteworthy that the location of this lateral transition observed at the eastern edge of the gap also corresponds to the limit of two distinct patches, in time and space, that slipped during the 2009–2010 event (Walpersdorf et al., 2011). Such a lateral variation could be controlled by heterogeneities of pore fluid pressure at the subduction interface as proposed by Song et al. (2009). For a better investigation of these phenomena, several GPS stations have been already installed after the 2006 event to increase the model resolution in the area of maximum slip in the Guerrero gap. However, as the region affected by SSEs is vast and in some places difficult to instrument, systematic InSAR coverage is still needed to complete the surface displacement observations. The Sentinel-1 C-band mission from the European Space Agency and ALOS-2 L-band mission from the Japanese Space Agency should fulfill

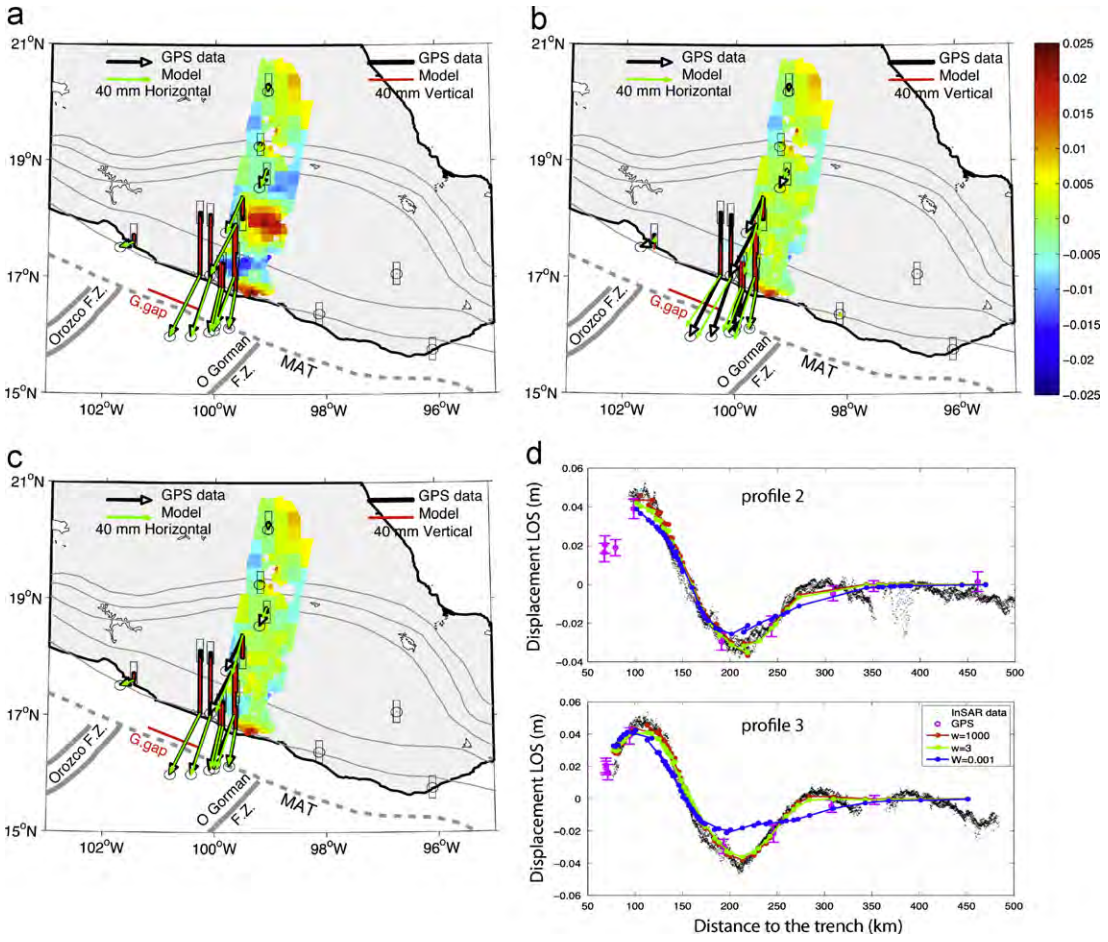

Fig. 8. Comparison between observed and modelled SSE displacements for inversions with w equal to 0.001 (a), 1000 (b), and 3 (c). Horizontal and vertical displacements measured by GPS are the black arrows and black bars, respectively, and the modelled displacement are represented by green arrows (horizontal) and red bars (vertical). Colors correspond to the residues (in meter, see the color scale) between LOS InSAR displacement and LOS modelled displacement. (d) Comparison between the observed and the modelled displacement along the profiles 2 and 3 shown in Fig. 3. GPS data are projected to the LOS (purple dots), InSAR measurements are the black dots. The blue, green, and red curves correspond to LOS modelled displacements with w equal to 0.001, 3, and 1000, respectively. (For interpretation of the references to color in this figure legend, the reader is referred to the web version of this article.)

this requirement (both satellites are planned to be launched in 2013). These new data sets will be decisive to observe in details the whole Guerrero gap, and in particular to establish possible similar behaviors in the western side of the Guerrero gap where currently very few geodetic data exists.

Acknowledgments

This work has been supported by the French national research agency through the project ANR-G-GAP RA0000C069 and by INSU project PNTS AO2006 and a CNRS postdoctoral fellowship. We would like to thank the European Space Agency (ESA) for providing Envisat images through category 1 project #5036. GPS network maintenance and data acquisition were funded by COANCYT 46064, 84544 and PAPIIT IN103808, and IN 114611 grants. We thank the two anonymous reviewers for their helpful comments.

Appendix A. Supplementary material

Supplementary data associated with this article can be found in the online version at http://dx.doi.org.10.1016/j.epsl.2013.02.020.

References

Bürgmann, R., Rosen, P.A., Fielding, E.J., 2000. Synthetic Aperture Radar interferometry to measure Earth's surface topography and its deformation. Annu. Rev. Earth. Planet. Sci. 28, 169–209.

Cavalié, O., Doin, M.-P., Lasserre, C., Briole, P., 2007. Ground motion measurement in the Lake Mead area, Nevada, by differential synthetic aperture radar interferometry time series analysis: probing the lithosphere rheological structure. J. Geophys. Res. 112 (B3).

Cavalié, O., Lasserre, C., Doin, M.-P., Peltzer, G., Sun, J., Xu, X., Shen, Z.-K., 2008. Measurement of interseismic strain across the Haiyuan fault (Gansu, China), by InSAR. Earth. Planet. Sci. Lett. 275, 246–257.

Cavalié, O., Pathier, E., Cotton, F., Doin, M.-P., Cotte, N., Vergnolle, M., Walpersdorf, A., 2009. Mapping of the 2006 silent slow event in the Guerrero (Mexico) seismic gap by InSAR. EGU General Assembly 11, EGU2009-5133.

Chen, C.W., Zebker, H.A., 2000. Network approaches to two-dimensional phase unwrapping: intractability and two algorithms. J. Opt. Soc. Am. A 17 (3).

Demets, C.R., Gordon, R., Argus, D., 2010. Geologically current plate motions. Geophys. J. Int. 181, 1–80.

Doin, M.-P., Lasserre, C., Peltzer, G., Cavalié, O., Doubre, C., 2009. Corrections of stratified tropospheric delays in SAR interferometry: validation with global atmospheric models. J. Appl. Geophys. 101 (B7), 16119–16135.

Dragert, H., Wang, K., Rogers, G., 2004. Geodetic and seismic signatures of episodic tremor and slip in the northern Cascadia subduction zone. Geology 56, 1143–1150.

Farr, T.G., Kobrick, M., 2000. Shuttle radar topography mission produces a wealth of data. Eos Trans. AGU 81 (48), 583–585.

Ferretti, A., Monti-Guarnieri, A., Prati, C., Rocca, C., Massonnet, D., 2007. InSAR Principles: Guidelines for SAR Interferometry Processing and Interpretation. ESA Publications.

Gens, R., 2003. Two-dimensional phase unwrapping for radar interferometry: developments and new challenges. Int. J. Remote Sensing 24 (4), 703–710.

Goldstein, R.M., Werner, C.L., 1998. Radar interferogram filtering for geophysical applications. Geophys. Res. Lett. 25 (21), 2517–2520.
Hanssen, R.F., 2001. Radar Interferometry, Data Interpretation and Error Analysis. Kluwer Academic Publishers.
Hernandez, B., Shapiro, N.M., Singh, S.K., Pacheco, J.F., Cotton, F., Campillo, M., Iglesias, A., Cruz, V., Gomez, J.M., Alcantara, L., 2001. Rupture history of September 30, 1999 intraplate earthquake of Oaxaca, Mexico (M_w=7.5) from inversion of strong-motion data. Geophys. Res. Lett. 385 (28), 363–366.
Hirose, H., Obara, K., 2005. Repeating short- and long-term slow slip events with deep tremor activity, around the Bungo channel region, southwest Japan. Earth Planets Space 57, 961–972.
Hooper, A., Bekaert, D., Spaans, K., Arikan, M., 2012. Recent advances in SAR interferometry time series analysis for measuring crustal deformation. Tectonophysics 513–517, 1–13.
Hooper, A., Zebker, H., Segall, P., Kampes, B., 2004. A new method for measuring deformation on volcanoes and other natural terrains using InSAR persistent scatterers. Geophys. Res. Lett. 31.
Ide, S., Beroza, G.C., Shelly, D.R., Uchide, T., 2007. A scaling law for slow earthquakes. Nature 447, 76–79.
Jónsson, S., 2008. Importance of post-seismic viscous relaxation in southern Iceland. Nat. Geosci. 1, 136–139.
Jónsson, S., Zebker, H., Segall, P., Amelung, F., 2002. Fault slip distribution of the 1999 M_W 7.1 Hector Mine, California, earthquake, estimated from satellite radar and GPS measurements. Bull. Seismol. Soc. Am. 92 (4), 1377–1389.
Kerr, R.A., 2011. New work reinforces megaquake's harsh lessons in geoscience. Science 332 (6032).
Kostoglodov, V., Husker, A., Shapiro, N.M., Payero, J.S., Campillo, M., Cotte, N., Clayton, R., 2010. The 2006 slow slip event and nonvolcanic tremor in the Mexican subduction zone. Geophys. Res. Lett. 37 (L24301).
Kostoglodov, V., Ponce, L., 1994. Relationship between subduction and seismicity in the Mexican part of the Middle America trench. J. Geophys. Res. 99, 729–742.
Kostoglodov, V., Singh, S.K., Santiago, J.A., Franco, S.I., Larson, K.M., Lowry, A.R., Bilham, R., 2003. A large silent earthquake in the Guerrero seismic gap, Mexico. Geophys. Res. Lett. 30.
Larson, K.M., Kostoglodov, V., Miyazaki, S., Santiago, J.-A., 2007. The 2006 aseismic slow slip event in Guerrero, Mexico: new results from GPS. Geophys. Res. Lett. 34 (L13309).
Larson, K.M., Lowry, A.R., Kostoglodov, V., Hutton, W., Sánchez, O., Hudnut, K., Suárez, G., 2004. Crustal deformation measurements in Guerrero, Mexico. J. Geophys. Res. 109 (B04409).
López-Quiroz, P., Doin, M.-P., Tupin, F., Briole, P., Nicolas, J.-M., 2009. Time series analysis of Mexico City subsidence constrained by radar interferometry J. Appl. Geophys. 69 (1).
Loveless, J., Meade, B.J., 2010. Geodetic imaging of plate motions, slip rates, and partitioning of deformation in Japan. J. Geophys. Res. 115 (B02410).
Lowry, A.R., Larson, K.M., Kostoglodov, V., Bilham, R., 2001. Transient fault slip in Guerrero, southern Mexico. Geophys. Res. Lett. 28 (19), 3753–3756.
Mazzotti, S., Adams, J., 2004. Variability of near-term probability for the next great earthquake on the Cascadia subduction zone. Bull. Seismol. Soc. Am. 94 (5), 1954–1959.
Nishenko, S.P., Singh, S.K., 1987. Conditional probabilities for the recurrence of large and great interplate earthquakes along the Mexican subduction zone. Bull. Seismol. Soc. Am. 77 (6).
Ortiz, M., Singh, S.K., Kostoglodov, V., Pacheco, J., 2000. Constraint on the rupture areas of the Acapulco San Marcos, Mexico earthquakes of the 1962 (M7.1, 7.0) and 1957 (M7.7), based on the analysis of tide records. Geofis. Int. 39, 337–348.
Payero, J.S., Kostoglodov, V., Shapiro, N., Mikumo, T., Iglesias, A., Perez-Campos, X., Clayton, R.W., 2008. Nonvolcanic tremor observed in the Mexican subduction zone. Geophys. Res. Lett. 35 (L07305).
Radiguet, M., Cotton, F., Vergnolle, M., Campillo, M., Valette, B., Kostoglodov, V., Cotte, N., 2011. Spatial and temporal evolution of a long term slow slip event: the 2006 Guerrero Slow Slip Event. Geophys. J. Int. 184 (2), 816–828.
Radiguet, M., Cotton, F., Vergnolle, M., Campillo, M., Walpersdorf, A., Cotte, N., Kostoglodov, V., 2012. Slow slip events and strain accumulation in the Guerrero gap, Mexico. J. Geophys. Res. 117 (B04305).
Rosen, P.A., Hensley, S., Peltzer, G., Simons, M., 2004. Updated repeat orbit interferometry package released. Eos Trans. AGU 85 (5), 47.
Savage, J.C., 1983. A dislocation model of strain accumulation and release at a subduction zone. J. Geophys. Res. 88, 4984–4996.
Scharroo, R., Visser, P.N.A.M., 1998. Precise orbit determination and gravity field improvement for the ERS satellites. J. Geophys. Res. 103 (C4), 8113–8127.
Song, T.-R.A., Helmberger, D.V., Brudzinski, M.R., Clayton, R.W., Davis, P., Perez-Campos, X., Singh, S.K., 2009. Subducting slab ultra-slow velocity layer coincident with silent earthquakes in southern Mexico. Science 324 (5926), 502–506.
Suárez, G., Monfret, T., Wittlinger, G., David, C., 1990. Geometry of subduction and depth of the seismogenic zone in the Guerero gap, Mexico. Nature 345, 336–338.
Tarantola, A., 2005. Inverse Problem Theory and Methods for Model Parameter Estimation. Society for Industrial and Applied Mathematics (SIAM), Philadelphia.
Vergnolle, M., Walpersdorf, A., Kostoglodov, V., Tregoning, P., Santiago, J.A., Cotte, N., Franco, S.I., 2010. Slow slip events in Mexico revised from the processing of 11 year GPS observations. J. Geophys. Res. 115 (B08403).
Walpersdorf, A., Cotte, N., Kostoglodov, V., Vergnolle, M., Radiguet, M., Santiago, J.S., Campillo, M., 2011. Two successive slow slip events evidenced in 2009–2010 by a dense GPS network in Guerrero, Mexico. Geophys. Res. Lett. 38 (L15307).
Yoshioka, S., Mikumo, T., V. Kostoglodov, K.M.L., Lowry, A.R., Singh, S.K., 2004. Interplate coupling and a recent aseismic slow slip event in the Guerrero seismic gap of the Mexican subduction zone, as deduced from GPS data inversion using a Bayesian information criterion. Phys. Earth Planet. Int. 146, 513–530.
Zebker, H.A., Rosen, P.A., Hensley, S., 1997. Atmospheric effects in interferometric synthetic aperture radar surface deformation and topographic maps. J. Geophys. Res. 102 (B4), 7547–7563.

[pdf-4] Mousavi* Pathier et al. 2015

The following pages reproduce the paper from Mousavi et al. (2015)

Interseismic deformation of the Shahroud fault system (NE Iran) from space-borne radar interferometry measurements.

Mousavi*, Z., Pathier, E., Walker, R. T., Walpersdorf, A., Tavakoli, F., Nankali, H.,

Sedighi, M., & Doin, M.-P.

Published in 2015 in Geophysical Research Letters, 42(14), 5753–5761.

https://doi.org/10.1002/2015GL064440

* Zahra Mousavi did this work when she was PhD student at ISTerre, I co-supervised her with Andrea Walpersdorf.

AGU PUBLICATIONS

Geophysical Research Letters

RESEARCH LETTER
10.1002/2015GL064440

Key Points:
- We find fast slip rate of 4–5 for Shahroud fault based on modeling of InSAR data
- The 5 mm of slip rate is absorbed on the Abr and Jajarm strands of Shahroud fault
- The new information provides useful data for hazard assessment estimation

Supporting Information:
- Text S1, Figures S1–S5, and Table S1

Correspondence to:
Z. Mousavi,
zahra.mousavi@ujf-grenoble.fr

Citation:
Mousavi, Z., E. Pathier, R. T. Walker, A. Walpersdorf, F. Tavakoli, H. Nankali, M. Sedighi, and M.-P. Doin (2015), Interseismic deformation of the Shahroud fault system (NE Iran) from space-borne radar interferometry measurements, *Geophys. Res. Lett.*, *42*, 5753–5761, doi:10.1002/2015GL064440.

Received 15 MAY 2015
Accepted 23 JUN 2015
Accepted article online 26 JUN 2015
Published online 20 JUL 2015

Interseismic deformation of the Shahroud fault system (NE Iran) from space-borne radar interferometry measurements

Z. Mousavi[1,2], E. Pathier[1], R. T. Walker[3], A. Walpersdorf[1], F. Tavakoli[4], H. Nankali[4], M. Sedighi[4], and M.-P. Doin[1]

[1]ISTerre, Joseph Fourier University, CNRS, Grenoble, France, [2]Department of Earth Sciences, Institute for Advanced Studies in Basic Sciences, Zanjan, Iran, [3]Department of Earth Sciences, University of Oxford, Oxford, UK, [4]Geodetic Department, National Cartographic Center, Tehran, Iran

Abstract The Shahroud fault system is a major active structure in the Alborz range of NE Iran whose slip rate is not well constrained despite its potential high seismic hazard. In order to constrain the slip rate of the eastern Shahroud fault zone, we use space-borne synthetic aperture radar interferometry with both ascending and descending Envisat data to determine the rate of interseismic strain accumulation across the system. We invert the slip rate from surface velocity measurements using a half-space elastic dislocation model. The modeling results are consistent with a left-lateral slip rate of 4.75 ± 0.8 mm/yr on the Abr and Jajarm, strands of the Shahroud fault, with a 10 ± 4 km locking depth. This is in good agreement with the 4–6 mm/yr of left-lateral displacement rate accumulated across the total Shahroud fault system obtained from GPS measurements.

1. Introduction

The Alborz range of northern Iran, along with the Zagros in the south, accommodates the major part of the northward motion of Arabia relative to Eurasia, which is at a rate of 22 mm/yr at longitude 57°E [*Vernant et al.,* 2004]. The Alborz is located between the plateau of central Iran and the South Caspian (SC) basin, with a NW-SE trend in the west, and a NE-SW trend in the east.

It is likely that in addition to taking up N-S regional shortening, the range also accommodates the relative motion between the Iranian plateau and the SC basin, which is an aseismic block that appears to be moving independently of its surroundings [*Jackson et al.,* 2002; *Djamour et al.,* 2010]. The SC motion relative to Iran is accommodated on the left-lateral Astaneh-Shahroud fault system [*Wellman*, 1966; *Tatar et al.,* 2007; *Hollingsworth et al.,* 2008], whereas shortening across the Alborz is likely to be accommodated on the range-parallel Khazar thrust. Along the Astaneh-Shahroud fault system, an eastward decrease of the height of the Alborz range suggests an eastward reduction in the component of shortening across the range (see Figure 1).

Although the kinematics of the eastern Alborz are broadly understood from studies of geomorphology, seismicity, and GPS geodesy [*Berberian,* 1983; *Allen et al.,* 2003; *Ritz et al.,* 2006; *Hollingsworth et al.,* 2010; *Djamour et al.,* 2010; *Javidfakhr et al.,* 2011], there are still several first-order unknowns. In particular, the slip rates of the major faults in the eastern Alborz are not known, which are critical constraints for seismic hazard estimations, as well as being highly relevant for describing the kinematics of Iran and the SC [*Jackson et al.,* 2002; *Djamour et al.,* 2010; *Mousavi et al.,* 2013].

The Shahroud left-lateral fault system, in the eastern Alborz between longitudes 55–57°E, has been mapped as several discontinuous northeast trending left-lateral fault segments (the Abr, Khij, Jajarm, and Cheshmeh-Nik faults) [*Wellman,* 1966; *Hollingsworth et al.,* 2008; *Javidfakhr et al.,* 2011]. There have been no large instrumental earthquakes on the Shahroud fault system (SFS)in the last 50 years, but destructive earthquakes are known from historical records, including an event directly north of Shahroud in 1890 [*Ambraseys and Melville*, 1982]. Strike-slip faults within more westerly parts of the Alborz range have also shown a potential for large, destructive earthquakes. The Astaneh fault is likely to have been responsible for the 856 A.D. Qumis earthquake, which killed over 200,000 people [*Ambraseys and Melville*, 1982; *Hollingsworth et al.,* 2010].

No historical earthquakes are recorded on the easternmost ~150 km of the SFS, which consists of the parallel Jajarm and Cheshmeh-Nik faults. The geological slip rates of these fault segments are unknown, and yet they

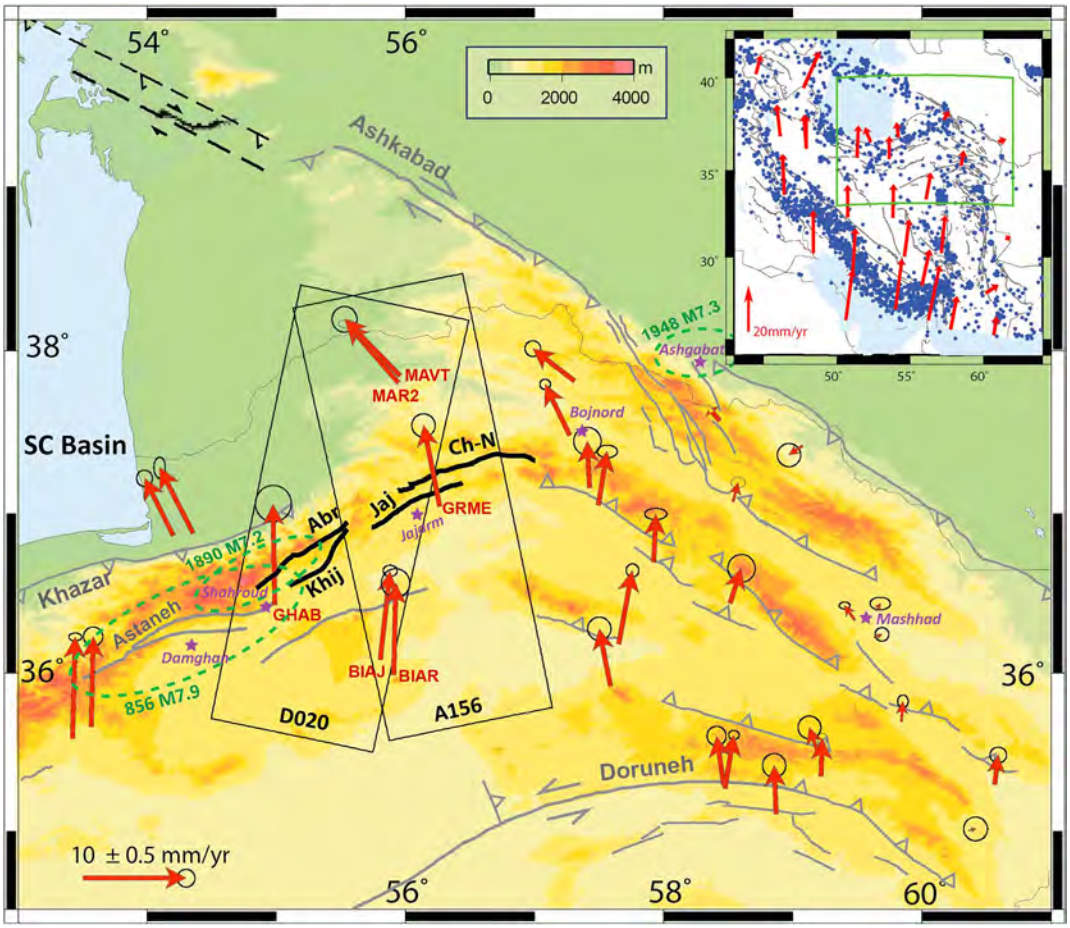

Figure 1. Location of the Shahroud fault system. Inset: Active fault map of Iran with GPS vectors in red (with respect to Eurasia fixed from *Vernant et al.* [2004]) showing that approximately N-S shortening between Arabia and Eurasia is accommodated throughout Iran. Blue dots are earthquake epicenters ($M_w \geq 5$) in Iran extracted from the Harvard catalog (http://www.globalcmt.org/CMTsearch.html) during the period 1976–2012. The green rectangle indicates the location of the map in the main figure. Main figure: tectonic map of the Eastern Alborz showing the location of the Shahroud fault system (in bold black) and other active faults (in gray). The Shahroud fault system (SFS) contains four segments, Abr, Jajarm, and Cheshmeh-Nik fault from 55° to 57° longitude. Abbreviations: SC Basin: South Caspian Basin, AS: Astaneh fault, Ch-N: Cheshmeh-Nik fault, Jaj: Jajarm fault, Kh: Khazar trust, and SFS: Shahroud fault system. Dashed green ellipses indicate the approximate location of the 1890 (*M*7.2) and 856 (*M*7.9) earthquakes close to the Damghan and Shahroud regions [*Ambraseys and Melville*, 1982]. The black rectangles show the coverage of the Envisat synthetic aperture radar (SAR) data analyzed in this study, with their track numbers (A for ascending, D for descending). The red vectors and their associated error ellipses present the GPS velocity field with respect to Eurasia from *Djamour et al.* [2010] and *Mousavi et al.* [2013]. The stars represent cities mentioned in the text. The thin black lines delineate the coastline and the political border between Iran and Turkmenistan.

pose a substantial hazard to local populations: the Jajarm fault is 20 km north of Jajarm city and strikes NE for more than 130 km [*Hollingsworth et al.,* 2008, 2010; *Javidfakhr et al.,* 2011], and the 120 km long Cheshmeh-Nik fault terminates in the east at the city of Bojnord.

Using GPS measurements, *Mousavi et al.* [2013] estimated between 2.5 ± 1 mm/yr and 4–6.5 mm/yr of summed left-lateral displacement rate across Jajarm and Cheshmeh-Nik faults. The lower value (2.5 ± 1 mm/yr) results from a block modeling approach, in which the SC rotates about an Euler pole located immediately NE of Iran, whereas the higher value (4–6.5 mm/yr) results from simply taking profiles of fault-parallel velocities across the eastern Alborz, from stations located in the Iranian plateau to those in the lowlands fringing the Caspian Sea. It is important to note that slip rates estimated from profiles of fault-parallel GPS velocity may be biased by clockwise rotation of the SC relative to its surroundings, whose Euler pole may be located nearby to the Caspian Basin itself [*Djamour et al.,* 2010]. It is thus important to determine independent measurements of the strain accumulation across the SFS.

In this study we provide the first direct measurement of interseismic deformation across the eastern SFS, where both slip rate and earthquake history are unknown using two tracks of Envisat-Advanced Synthetic Aperture Radar (ASAR) satellite images. First, we present the image data set, second the multitemporal differential SAR interferometry (InSAR) processing strategy to increase signal to noise ratio, and then the Small baseline Subset Algorithm (SBAS) technique of time series analysis resulting in a map of the ground mean velocity along the radar line of sight (LOS) for the period 2003–2010. Finally, a slip rate is inverted through a 2-D interseismic elastic model and discussed with respect to its tectonic context.

2. InSAR Data and Processing

Synthetic aperture radar (SAR) images from the ASAR instrument on board the Envisat have been used in this study to investigate interseismic deformation across the SFS. The data set was acquired during 2003–2010 with 22 and 23 images for descending (D020) and ascending (A159) tracks, respectively. The raw data were processed with ROI_PAC (Repeat Orbit Interferometry PACkage) [*Rosen et al.,* 2004]. Precise Doppler orbitography and radiopositioning integrated by satellite orbital data for Envisat provided by European Space Agency (ESA) has been used for interferometric processing. The topographic phase contribution was estimated from the 90 m SRTM DEM (Shuttle Radar Topography Mission Digital Elevation Model), which has been oversampled to 45 m, and referenced to the WGS84 ellipsoid. We processed interferograms with perpendicular baseline smaller than 700 m and temporal baseline larger than 2 months and less than 5 years (see Figure S1 in the supporting information). The resulting differential interferogram phase φ_{ij} between dates i and j is related to phase change contributions from the deformation signal, tropospheric delay, orbital error, DEM error, and noise (equation (1))

$$\varphi_{ij} = \varphi_{ij}^{\text{DEM\_res}} + \varphi_{ij}^{\text{orb\_res}} + \varphi_{ij}^{\text{atmo}} + \varphi_{ij}^{\text{disp}} + \varphi_{ij}^{\text{noise}} \tag{1}$$

where $\varphi_{ij}^{\text{DEM}_\text{r}\text{es}}$ is related to residual DEM errors, $\varphi_{ij}^{\text{orb}_\text{r}\text{es}}$ is the phase component related the residual orbital delay, $\varphi_{ij}^{\text{atmo}}$ is the difference of atmospheric delay (Atmospheric Phase Screen, APS) between the two dates, $\varphi_{ij}^{\text{disp}}$ is ground displacement, and $\varphi_{ij}^{\text{noise}}$ is the noise from coregistration and unwrapping. In order to estimate interseismic deformation from interferograms, it is useful to correct orbital DEM errors and tropospheric delay before unwrapping in order to improve the spatial phase coherency for the unwrapping step (see supporting information Text S1 for detail description of removing these errors).

3. Smoothed Constrained Time Series Analysis

Once all interferograms have been corrected from residual errors, unwrapped, and referenced by using a common phase reference, we perform a time series analysis for each track. The time series is applied based on the phase evolution through time in the small baseline interferograms network. To obtain the phase delay time series by least squares inversion, we invert the following linear system for each pixel in the interferograms [*Berardino et al.,* 2002; *Lanari et al.,* 2004]:

$$\varnothing_{ij} = \sum_{k=i}^{j-1} \delta\varphi_k \quad \text{and} \quad \varphi_1 = 0 \tag{2}$$

where $\varnothing_{ij}$ is the propagation delay for interferogram i and j and $\delta\varphi_k$ is the incremental delay between images k and $(k+1)$ for each pixel. To be able to solve this inversion using the least squares method, in spite of incoherency in some areas, and disconnections between some groups of pixels from the remainder of the points through time, we add a constraint component [*Lopez-Quiroz et al.,* 2009; *Doin et al.,* 2011; *Jolivet et al.,* 2012].

$$\sum_{k=1}^{n-1} \delta\varphi_k = V\Delta t_n - \alpha B_n^{\perp} - \varphi_n^{\text{smooth}} + c \tag{3}$$

where V is the mean LOS velocity for the considered pixel, Δt_n is the time interval between acquisition 1 and n, α is proportional to the DEM error, $B_n^{\perp}$ is the perpendicular baseline of acquisition n with respect to the first acquisition, and c is a constant. This component is affected by the turbulent tropospheric pattern of each image. We weight this component based on the amplitude of atmospheric patterns ($1/\text{APS}_n$). We add one

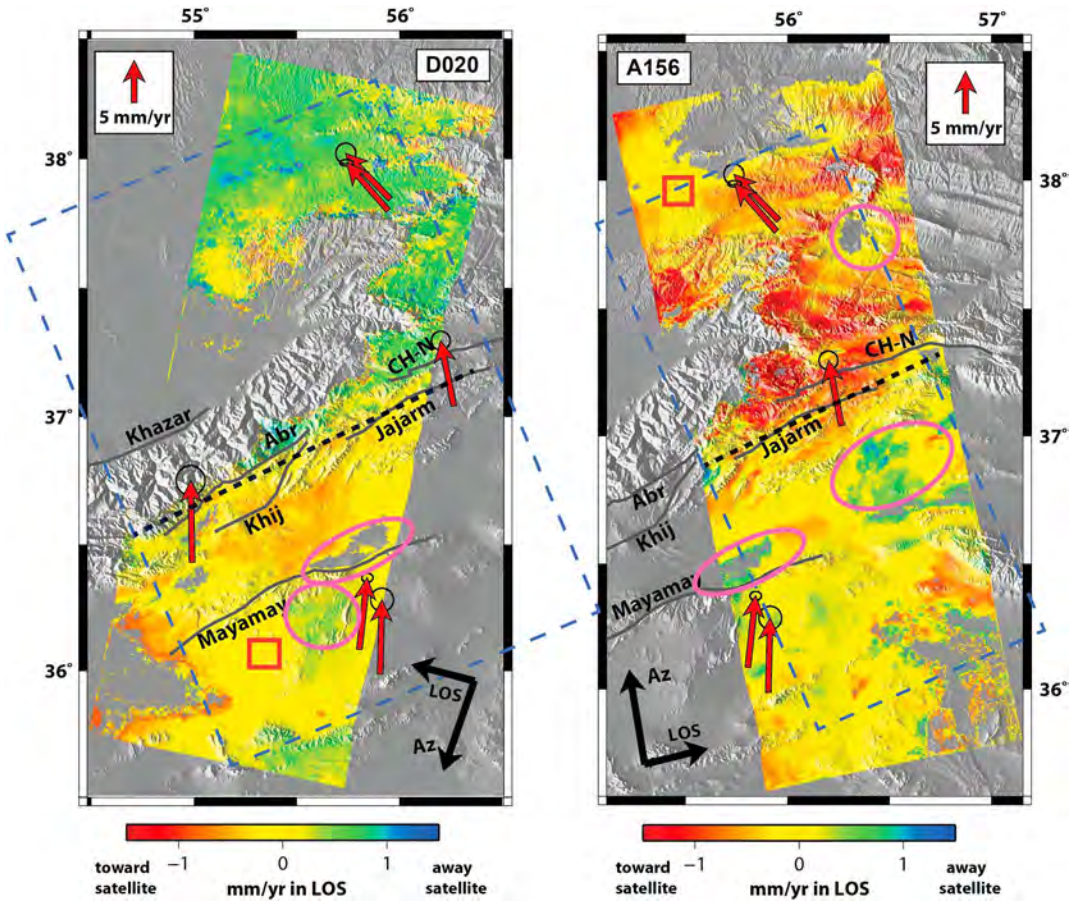

Figure 2. Ground surface mean LOS velocity maps from InSAR time series analysis for track (left) D020 and (right) A156. Background is a shaded-relief DEM (SRTM), and red arrows present the GPS velocity field of this area with respect to Eurasia. Black lines are fault traces along the SFS. Blue boxes, oriented perpendicular to the SFS, show location of profiles in Figure 2. CH-N is Cheshmeh-Nik fault. The large amount of groundwater extraction in arid parts of Iran results in a fast displacement in those areas in which extraction is occurring. The subsidence areas that we suspect are caused by groundwater extraction (pink ellipses) are masked in the inversion. The dashed rectangles present the profiles perpendicular to the fault which is plotted in Figure 3 for each track. The dashed lines indicate the fault location which is used for the 2-D modeling for each track.

more constraint which is a temporal smoothing, obtained by minimizing the curvature of the inverted phase temporal evolution [*Schmidt and Bürgmann*, 2003; *Cavalié et al.,* 2007; *Doin et al.,* 2011].

$$\frac{\partial^2 \varphi_n^{\text{smooth}}}{\partial t^2} = 0 \tag{4}$$

We choose the weighting of this component in the inversion system equal to Δt_i, the mean time interval across the five-point differential operator, to be able to smooth less in the densely spaced acquisitions and smooth more in scattered space acquisitions [*Cavalié et al.,* 2007; *Doin et al.,* 2011]. Now we can invert this system using the least squares inversion [*Lopez-Quiroz et al.,* 2009; *Jolivet et al.,* 2012] to investigate the long-wavelength tectonic signal due to interseismic strain accumulation.

Figure 2 shows the mean velocity map derived from the time series analysis of the descending and ascending tracks after georeferencing. The first noticeable point is the LOS velocity change across the SFS on the two tracks. This gradient has opposite signs on descending and ascending tracks, consistent with left-lateral motion of the SW-NE fault system, and the velocity difference across the faults reaches up to ~2 mm/yr in LOS direction. Local subsidence probably related to groundwater extraction can be detected (pink ellipses in Figure 2). The possible sources of error in the velocity map are the effect of unwrapping error, residual orbital errors, and residual stratified and turbulent atmospheric perturbations

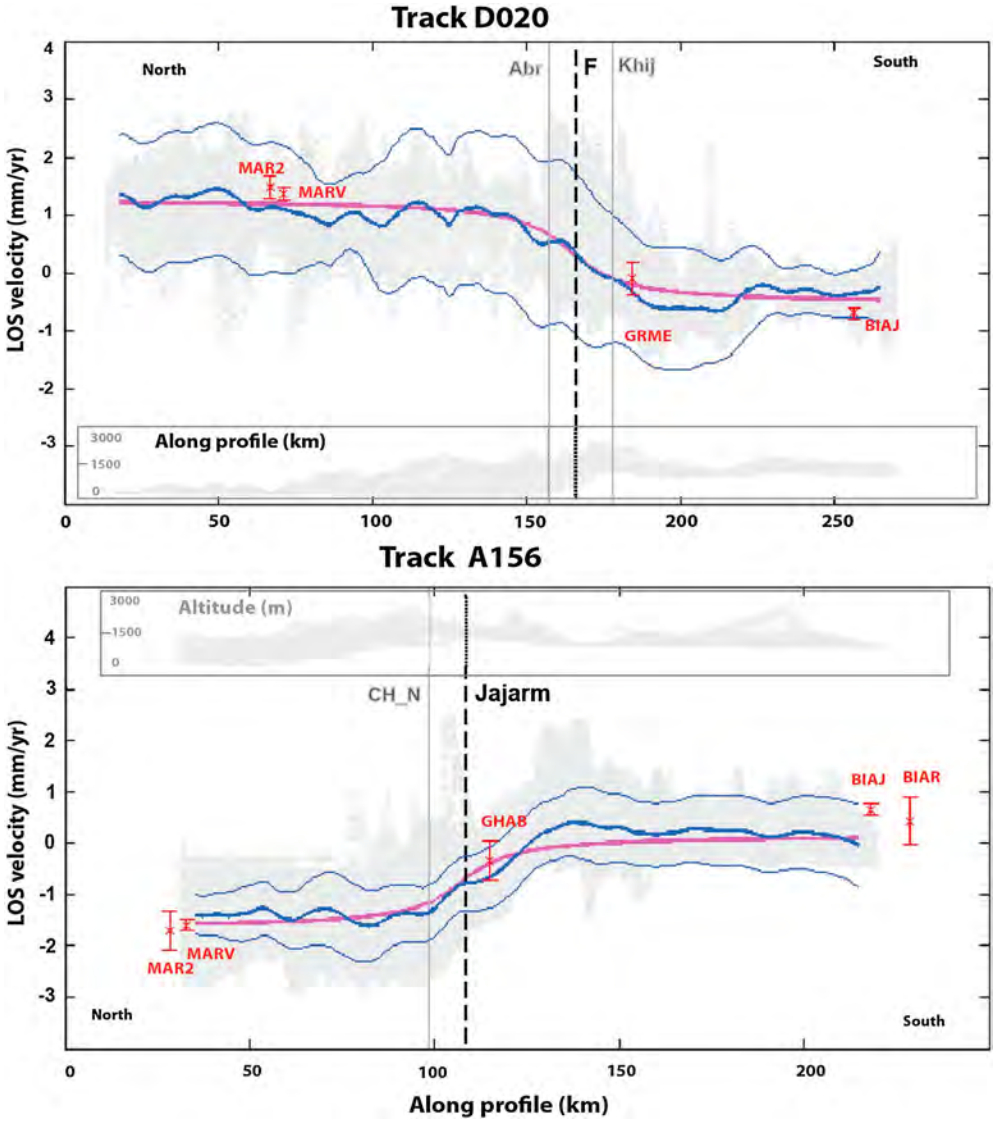

Figure 3. Mean LOS velocity profiles (gray dots) and the weighed averaged profile (thick blue line) with 2 sigma deviation (blue lines). All the points within the blue rectangle shown in Figure 1 are projected onto the profile as gray dots. The gray boxes show the elevation profile for the same area. The dark gray line shows the location of the SFS. The red stars with error bars are the LOS velocity derived from five continuous GPS stations, assuming only horizontal displacements. Note that the sign of the signal is inversed between ascending and descending track, which is consistent with surface displacement due to the left-lateral fault seen from the two different satellite points of view. The pink line is the best fitting model with slip rate 4.75 ± 0.8 mm/yr and 10 ± 4 km locking depth.

in the interferograms (not corrected by the atmospheric model and phase ramp corrections in wrapped interferograms). There is no clear correlation between the topography and the mean velocity map (supporting information Figure S2 and Table S1) indicating that the stratified atmospheric correction has been effective and that no significant residual atmospheric effect related to the topography is affecting the results.

Figure 3 presents profiles of LOS velocity perpendicular to the SFS for both tracks, which are consistent overall with a classic arctangent shape predicted by elastic models across a strike-slip fault [*Savage and Burford,* 1973]. Note that at a distance more than a few tens of kilometers from the fault zone, the profiles are satisfactorily flattened, meaning that the overall estimation of the linear ramp in azimuth done on 300 km long tracks has not been significantly affected by the localized gradient of velocity around the fault zone, preserving the investigated tectonic signal related to the SFS. Another argument to support

that conclusion is that the profiles across the SFS are in good agreement with the local velocity measurements at existing GPS stations (red error bars in Figure 3) [*Mousavi et al.,* 2013; *Djamour et al.,* 2010], indicating that the removed ramp signal was essentially related to orbital error or atmospheric effect.

4. Interseismic Deformation Modeling

To help the interpretation of the LOS mean velocity map, we used a simple elastic model with a single fault geometry. A north-south velocity change is clearly visible across the SFS. Figures 1 and 2 show that there is a high north-south mean velocity gradient close to the Jajarm fault location in track A156. For track D020, the high-velocity gradient is located near the Abr, Jajarm, and Cheshmeh-Nik faults, but it is hard to distinguish which fault could be the most related to the velocity change, and the large-scale deformation signal seems instead to be controlled by the fault system as a whole rather than by a single fault. We thus chose to model the whole fault system as a single vertical dislocation with the surface trace that approximately follows the SFS trace and is roughly coincident with the Jajarm fault in track A156 and the Abr fault in track D020 (see dashed line in Figure 2). We also assume a pure strike-slip fault with no vertical deformation.

The hypothesis of minimal vertical deformation is justified by the subdued topography in this eastern section of the Alborz, and by the fact that the independent horizontal GPS are in a good agreement with the InSAR measurement for both ascending and descending InSAR data: if significant vertical velocity signal was present, disagreement should be found when comparing horizontal GPS displacement only with both ascending and descending InSAR data. Furthermore, the GPS data from nearby stations do not show major interseismic shortening [see *Mousavi et al.,* 2013, Figure 5]. The existence of topography north of the Shahroud fault zone may be related to an earlier tectonic phase, such as that suggested by *Javidfakhr et al.* [2011], who suggested temporal changes in the stress state from compressional to transpressional tectonic regime during the Plio-Quaternary based on the inversions of fault kinematic data. The assumption of minimal vertical deformation can also be tested a posteriori looking at the consistency of model results from the independent ascending and descending tracks: the presence of a significant vertical gradient of displacement across the fault, which is not taking into account in our model, should introduce discrepancies in the modeled parameters.

Under this assumption, we convert displacement of each profile in LOS direction into horizontal displacements parallel to the fault. We determine the slip rate (s) and locking depth (d) of the fault based on the *Savage and Burford* [1973] analytical solution which provides the surface displacement (y) parallel to the fault at a given perpendicular distance (x) from the fault: $y = (s/p) \times \arctan(x/d)$. The parameter estimation is based on the minimization of the sum of the RMS misfit between the observed and modeled velocity profiles estimated for each track.

We used a systematic parameter search over the ranges 1–10 mm/yr for slip rate and 1–35 km for locking depth, at 0.5 mm/yr and 0.5 km intervals, respectively. We first perform this search for a fixed fault trace location (dashed line in Figure 2). Our best fit model for joint inversion is determined by the minimum of the sum of the RMS misfits of both ascending and descending data sets (red star in Figure 4). It gives a slip rate of 4.75 mm/yr and a locking depth of 10 km. This result corresponds to the modeled profiles (pink line) shown in Figure 3. Also, the individual solutions of RMS misfit for each track is in good agreement with the joint solution indicating that the two independent data sets are consistent (red stars in Figure 4 and supporting information Figure S3) and validate a posteriori our assumption of no significant large-scale vertical gradient across the fault zone.

Regarding the error associated to these parameters, as mentioned in section 2, the main source of remaining errors in the mean velocity map is related to the residual turbulent atmospheric perturbations and the residual orbital error in the interferograms. Therefore, we try to estimate the impact of such perturbations in our fault parameter estimation. To do that, 100 perturbed mean velocity maps were generated and used in the same inversion scheme as for the nonperturbed data set. The mean velocity map is the result of the SBAS time series analysis starting from the network of corrected interferograms. In order to introduce a realistic noise in the mean velocity map, we choose to attribute to each date of the network an Atmospheric Phase Screen (APS, which may also contain residual orbital error) and then to combine the APS of the dates to produce synthetic interferograms simulating atmospheric noise. The time series analysis is then applied to the network of synthetic interferograms the same way as to the original data,

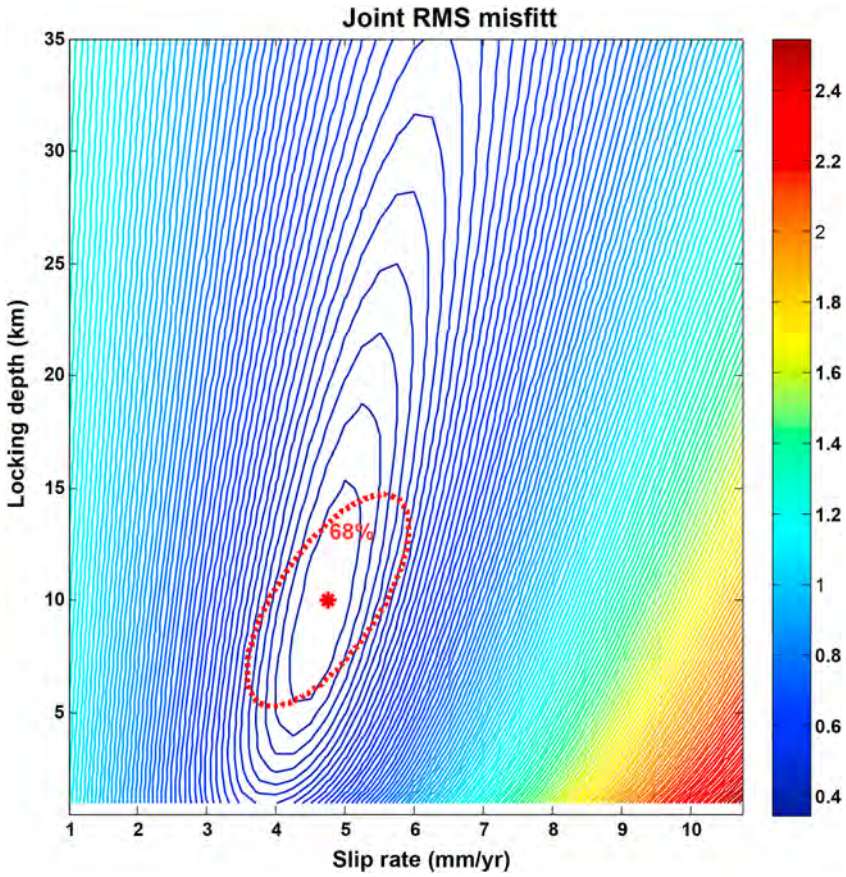

Figure 4. Solution space plot for our model showing results of the Monte Carlo error analysis for joint ascending track A156 and descending track D020. Contours show the joint RMS misfit in mm/yr for the unperturbed data set. The red star show the best fitting solution (locking depth: 10 ± 4 km and slip rate: 4.75 ± 0.8 mm/yr), the 68% and 95% confidence ellipse is estimated from the Monte Carlo error analysis using perturbed data set.

and the result, a mean velocity map including the simulated atmospheric noise, is added to the original mean velocity map (see supporting information Figure S4 as an example of applying this method).

To generate the simulated APS for each date, we used interferograms with 35 days or 70 days, in which we assume that phase variations are due to atmospheric delay changes or to residual orbital errors. Because the number of such short-time interferograms is less than the number of acquisition dates in the network, we complete the simulated APS data set by generating synthetic APS using an approach similar to *Parsons et al.* [2006] and *Biggs et al.* [2007]. In that approach, the statistical characteristics of the contribution of the turbulent atmosphere to a short-time interferogram are described using a 1-D covariance function [*Hanssen*, 2001], which is used along with a full variance-covariance matrix to simulate the correlated noise. To create 100 different perturbed velocity maps, simulated APS are randomly attributed to each date of the network. The parameter uncertainties were determined using the standard deviation of the slip and locking depth estimation of the 100 runs leading to the following values: 4.75 ± 0.8 for slip rate and 10 ± 4 km for locking depth.

5. Discussion

Our mean velocity map confirms the general left-lateral kinematics of the SFS and simple 2-D modeling gives some constraint on the slip rate and locking depth. Our model implies a left-lateral displacement rate across SFS of 4.75 ± 0.8 mm/yr and 10 ± 4 km of locking depth. This ~5 mm/yr of displacement rate is accommodated on the Abr and Jajarm strands of SFS. The new result of the InSAR study of the SFS with respect to other quantitative data available on the present-day deformation field is that the fault system is effectively locked with no shallow creep.

The choice of a single fault model was motivated by the fact that there is no clear individual fault signature in the geomorphology through the SFS and in the InSAR mean velocity map. To test our choice of the position of the fault in the model, which was fixed when inverting the slip and locking depth parameter, we perform another inversion in which we determined the location parameters of the fault trace for track D020 using a fixed 12 km locking depth as suggested by *Engdahl et al.* [2006] based on the average depth of the regional seismicity. Fixing the locking depth and rake, we found that the best fitting north-south location of the fault corresponds to the a priori location we used in our joint inversion (supporting information Figure S5). This a priori fault location is close to the Abr and Jajarm faults in Track D020, and it also confirms that the Jajarm fault accommodates the strain in track A156. It may be possible that the different strands visible at the surface (Jajarm and Cheshmeh-Nik) are merged in one single fault below 10 km depth. This could explain why our model is not sensitive to the geometric complexity of the shallower part of the faults, located in the locked zone of the model.

6. Conclusion

Previous geodetic results based on a regional GPS network [*Djamour et al.,* 2010; *Mousavi et al.,* 2013] present ~7 mm/yr of deformation accommodated between Central Iran and the SC basin along SFS and Khazar thrust at longitude 56°E. Rigid block modeling in those papers yielded 2.4 ± 1 and 3.3 ± 1 mm/yr of left-lateral motion absorbing across SFS and Khazar thrust, respectively, where as projection of GPS station velocities onto an across-fault profile appeared to yield a slip rate of 4–6 mm/yr of left-lateral motion on SFS and no significant strike-slip deformation on Khazar thrust [*Mousavi et al.,* 2013]. The InSAR result is in good agreement with the rates obtained from GPS profiles, rather than from those obtained by rigid block modeling, indicating that most of the left-lateral displacement is accommodated in the eastern Alborz, along the SFS. We also note that our results may help to constrain the slip rate of the Ashkabad fault at the NE limit of the SC basin, as the GPS stations MAR2 and MAVT in the eastern Caspian lowlands, which give good agreement with the InSAR-derived interseismic rate on the SFS, are also compatible with a fast interseismic strain accumulation on the Ashkabad fault at *Mousavi et al.* [2013] and *Walters et al.* [2013].

This new information provides precious insights into the seismogenic potential of the Shahroud fault system. The existence of a large historical earthquake (M_w 7.2) on the Abr segment of the SFS in 1890, and the large number of inhabitants (~1.5 million) in this region, shows the requirement for geomorphological and palaeoseismological investigations to fill the gaps in information required assessing the behavior of individual fault strands. Such studies will give a more complete assessment of slip rates and recurrence intervals in order to estimate the seismic hazard along these important active faults.

Acknowledgments

We would like to thank the European Space Agency (ESA) for providing Envisat SAR images through CAT-1 project 7023. We are grateful to JPL/Caltech for use of the ROI_PAC software. Richard Walker is grateful for a Visiting Fellowship from OSUG (Observatoire des Sciences de l'Univers de Grenoble) that allowed him to work at ISTerre (University Joseph Fourier). Maps were prepared using Generic Mapping Tools software [*Wessel and Smith*, 1995].

The Editor thanks Manoochehr Shirzaei and an anonymous reviewer for their assistance in evaluating this paper.

References

Allen, M. B., M. R. Ghassemi, M. Shahrabi, and M. Qorashi (2003), Accommodation of late Cenozoic oblique shortening in the Alborz range, northern Iran, *J. Struct. Geol.*, *25*, 659–672.

Ambraseys, N. N., and C. P. Melville (1982), *A History of Persian Earthquakes*, Cambridge Univ. Press, New York.

Berardino, P., G. Fornaro, R. Lanari, and E. Santosti (2002), A new algorithm for surface deformation monitoring based on small baseline differential SAR interferograms, *IEEE Trans. Geosci. Remote Sens.*, *40*(11), 2375–2383.

Berberian, M. (1983), The southern Caspian: A compressional depression floored by a trapped, modified oceanic crust, *Can. J. Earth Sci.*, *20*, 163–183.

Biggs, J., T. Wright, Z. Lu, and B. Parsons (2007), Multi-interferogram method for measuring interseismic deformation: Denali fault, Alaska, *Geophys. J. Int.*, *170*(3), 1165–1179.

Cavalié, O., M. P. Doin, C. Lasserre, and P. Briole (2007), Ground motion measurement in the Lake Mead area, Nevada, by differential synthetic aperture radar interferometry time series analysis: Probing the lithosphere rheological structure, *J. Geophys. Res.*, *112*, B03403, doi:10.1029/2006JB004344.

Djamour, Y., et al. (2010), GPS and gravity constraints on continental deformation in the Alborz mountain range, Iran, *Geophy. J. Int.*, *183*, 1287–1301.

Doin, M. P., S. Guillaso, R. Jolivet, C. Lasserre, F. Lodge, G. Ducret, and R. Grandin (2011), Presentation of the small baseline NSBAS processing chain on a case example: The Etna deformation monitoring from 2003 to 2010 using ENVISAT data, in *Proceedings of the Fringe Symposium*, ESA SP-697, Frascati, Italy.

Engdahl, E. R., J. A. Jackson, S. C. Myers, E. A. Bergman, and K. Priestley (2006), Relocation and assessment of seismicity in the Iran region, *Geophys. J. Int.*, *167*(2), 761–778.

Hanssen, R. F. (2001), *Radar Interferometry: Data Interpretation and Error Analysis*, vol. 2, Springer, Netherlands.

Hollingsworth, J., J. Jackson, R. Walker, and H. Nazari (2008), Extrusion tectonics and subduction in the eastern South Caspian region since 10 Ma, *Geology*, *36*(10), 763–766.

Hollingsworth, J., H. Nazari, J. F. Ritz, R. Salamati, M. Talebian, A. Bahroudi, R. Walker, M. Rizza, and J. Jackson (2010), Active tectonics of the east Alborz mountains, NE Iran: Rupture of the left-lateral Astaneh fault system during the great 856 A.D. Qumis earthquake, *J. Geophys. Res.*, *115*, B12313, doi:10.1029/2009JB007185.

Jackson, J., K. Priestley, M. Allen, and M. Berberian (2002), Active tectonics of the South Caspian Basin, *Geophys. J. Int.*, *148*, 214–245.
Javidfakhr, B., O. Bellier, E. Shabanian, L. Siame, L. Léanni, D. Bourlès, and S. Ahmadian (2011), Fault kinematics and active tectonics at the southeastern boundary of the eastern Alborz (Abr and Khij fault zones): Geodynamic implications for NNE Iran, *J. Geodyn.*, *52*, 290–303.
Jolivet, R., C. Lasserre, M.-P. Doin, S. Guillaso, G. Peltzer, R. Dailu, J. Sun, Z.-K. Shen, and X. Xu (2012), Shallow creep on the Haiyuan Fault (Gansu, China) revealed by SAR Interferometry, *J. Geophys. Res.*, *117*, B06401, doi:10.1029/2011JB008732.
Lanari, R., P. Berardino, S. Borgström, C. Del Gaudio, P. De Martino, G. Fornaro, S. Guarino, G. Ricciardi, E. Sansosti, and P. Lundgren (2004), The use of IFSAR and classical geodetic techniques for caldera unrest episodes: Application to the Campi Flegrei uplift event of 2000, *J. Volcanol. Geotherm. Res.*, *133*(1), 247–260.
Lopez-Quiroz, P., M.-P. Doin, F. Tupin, P. Briole, and J.-M. Nicolas (2009), Time series analysis of Mexico City subsidence constrained by radar interferometry, *J. Appl. Geophys.*, *69*, 1–15.
Mousavi, Z., A. Walpersdorf, R. T. Walker, F. Tavakoli, E. Pathier, H. Nankali, F. Nilfouroushan, and Y. Djamour (2013), Global Positioning System constraints on the active tectonics of NE Iran and the South Caspian region, *Earth Planet. Sci. Lett.*, *377–378*, 287–298.
Parsons, B., T. Wright, P. Rowe, J. Andrews, J. Jackson, R. Walker, M. Khatib, M. Talebian, E. Bergman, and E. Engdahl (2006), The 1994 Sefidabeh (eastern Iran) earthquakes revisited: New evidence from satellite radar interferometry and carbonate dating about the growth of an active fold above a blind thrust fault, *Geophys. J. Int.*, *164*(1), 202–217.
Ritz, J.-F., H. Nazari, A. Ghassemi, R. Salamati, A. Shafei, S. Solaymani, and P. Vernant (2006), Active transtension inside central Alborz: A new insight into northern Iran–southern Caspian geodynamics, *Geology*, *34*, 477–480.
Rosen, P., S. Hensley, G. Peltzer, and M. Simons (2004), Updated repeat orbit interferometry package released, *Eos Trans. AGU*, *85*(5), 47, doi:10.1029/2004EO050004.
Savage, J. C., and R. O. Burford (1973), Geodetic determination of relative plate motion in central California, *J. Geophys. Res.*, *78*, 832–845, doi:10.1029/JB078i005p00832.
Schmidt, D. A., and R. Bürgmann (2003), Time-dependent land uplift and subsidence in the Santa Clara valley, California, from a large interferometric synthetic aperture radar data set, *J. Geophys. Res.*, *108*(B9), 2416, doi:10.1029/2002JB002267.
Tatar, M., J. Jackson, D. Hatzfeld, and E. Bergman (2007), The 2004 May 28, Baladeh earthquake (M_w 6.2) in the Alborz, Iran: Overthrusting the South Caspian Basin margin, partitioning of oblique convergence and the seismic hazard of Tehran, *Geophys. J. Int.*, *170*, 249–261.
Vernant, P., et al. (2004), Present-day crustal deformation and plate kinematics in the middle east constrained by GPS measurements in Iran and northern Oman, *Geophys. J. Int.*, *157*(1), 381–398.
Walters, R., J. Elliott, B. Parsons, and Z. Li (2013), Rapid strain accumulation on the Ashkabad fault (Turkmenistan) from atmosphere-corrected InSAR, *J. Geophys. Res. Solid Earth*, *118*, 3674–3690, doi:10.1002/jgrb.50236.
Wellman, H. W. (1966), Active wrench faults of Iran, Afghanistan and Pakistan, *Int. J. Earth Sci.*, *55*, 716–735.
Wessel, P., and W. Smith (1995), New version of the Generic Mapping Tools released, *Eos Trans. AGU*, *76*, 329, doi:10.1029/95EO00198.

[pdf-5] Pousse*, Pathier et al. 2016

The following pages reproduce the paper from Pousse et al. (2016)

Spatial and temporal variations in creep rate along the El Pilar fault at the Caribbean-South American plate boundary (Venezuela), from InSAR

Pousse Beltran*, L., Pathier, E., Jouanne, F., Vassallo, R., Reinoza, C., Audemard, F.,

Doin, M. P., & Volat, M.

Published in 2016 in Journal of Geophysical Research: Solid Earth, 121(11), 8276–

8296. https://doi.org/10.1002/2016JB013121

* Léa Pousse did this work when she was PhD student at ISTerre, with François Jouanne and Riccardo Vassalo as co-directors. I was not officially supervisor but I actively participated to supervised her for the InSAR processing and analysis especially for her thesis part related to the El-Pillar Fault.

AGU PUBLICATIONS

JGR

Journal of Geophysical Research: Solid Earth

RESEARCH ARTICLE
10.1002/2016JB013121

Key Points:
- New observations of aseismic slip along a segment of a major plate boundary (El Pilar fault, Venezuela)
- Evidence of spatial and temporal variations in creep over the 2007–2011 period
- Creep occurs on the segment ruptured in 1997, it corresponds to an afterslip which evolved into interseimic creep showing transients

Supporting Information:
- Supporting Information S1

Correspondence to:
L. Pousse Beltran,
pousselea@gmail.com

Citation:
Pousse Beltran, L., E. Pathier, F. Jouanne, R. Vassallo, C. Reinoza, F. Audemard, M. P. Doin, and M. Volat (2016), Spatial and temporal variations in creep rate along the El Pilar fault at the Caribbean-South American plate boundary (Venezuela), from InSAR, *J. Geophys. Res. Solid Earth*, *121*, 8276–8296, doi:10.1002/2016JB013121.

Received 25 APR 2016
Accepted 18 OCT 2016
Accepted article online 20 OCT 2016
Published online 14 NOV 2016

Spatial and temporal variations in creep rate along the El Pilar fault at the Caribbean-South American plate boundary (Venezuela), from InSAR

Léa Pousse Beltran[1], Erwan Pathier[2], François Jouanne[1], Riccardo Vassallo[1], Carlos Reinoza[3], Franck Audemard[3], Marie Pierre Doin[4], and Matthieu Volat[4]

[1]ISTerre, Université de Savoie Mont Blanc, Le Bourget du Lac, France, [2]ISTerre, Université Grenoble Alpes, Grenoble, France, [3]Venezuelan Foundation for Seismological Research, Caracas, Venezuela, [4]ISTerre, CNRS, Grenoble, France

Abstract In eastern Venezuela, the Caribbean-South American plate boundary follows the El Pilar fault system. Previous studies based on three GPS campaigns (2003–2005–2013) demonstrated that the El Pilar fault accommodates the whole relative displacement between the two tectonic plates (20 mm/yr) and proposed that 50–60% of the slip is aseismic. In order to quantify the possible variations of the aseismic creep in time and space, we conducted an interferometric synthetic aperture radar (InSAR) time series analysis, using the (NSBAS) New Small BAseline Subset method, on 18 images from the Advanced Land Observing Satellite (ALOS-1) satellite spanning the 2007–2011 period. During this 3.5 year period, InSAR observations show that aseismic slip decreases eastward along the fault: the creep rate of the western segment reaches 25.3 ± 9.4 mm/yr on average, compared to 13.4 ± 6.9 mm/yr on average for the eastern segment. This is interpreted, through slip distribution models, as being related to coupled and uncoupled areas between the surface and ~ 20 km in depth. InSAR observations also show significant temporal creep rate variations (accelerations) during the considered time span along the western segment. The transient behavior of the creep is not consistent with typical postseismic afterslip following the 1997 M_s 6.8 earthquake. The creep is thus interpreted as persistent aseismic slip during an interseismic period, which has a pulse- or transient-like behavior.

1. Introduction

Shallow fault creep can be detected by measurement of localized aseismic displacement gradients crossing faults [e.g., *Thatcher*, 1979]. This shallow creep is common during a postseismic period, as localized afterslip phenomena, but it can also exist during the interseismic period, as observed on the San Andreas fault system, Haiyuan fault in China, North Anatolian fault, and the Longitudinal Valley fault of Taiwan among others [e.g., *Schmidt et al*., 2005; *Cavalié et al*., 2008; *Champenois et al*., 2012; *Kaneko et al*., 2013; *Lindsey et al*., 2014]. *Avouac* [2015] reviewed key factors controlling aseismic slip. This slip can depend on lithology [e.g., *Wei et al*., 2013; *Thomas et al*., 2014a] or can be related to the fault geometry [e.g., *Jolivet et al*., 2013; *Lindsey et al*., 2014]. The influence of thermal control and fluid pressure on slip-mode processes has also been proposed (e.g., respectively, *Blanpied et al*. [1991] and *Gratier et al*. [2011]. In addition, previous seismic ruptures have an influence on the subsequent slip-mode processes [e.g., *Zweck et al*., 2002; *Çakir et al*., 2003]. However, the relative contributions of these different factors in controlling aseismic slip remain poorly understood, especially since spatiotemporal variations of aseismic slip have been detected [e.g., *Wei et al*., 2009; *Barbot et al*., 2013; *Jolivet et al*., 2013; *Cetin et al*., 2014; *Thomas et al*., 2014b; *Khoshmanesh et al*., 2015; *Turner et al*., 2015]. More case studies of faults showing spatial and temporal variations in creep, from a range of different geodynamic and geological contexts, are thus needed to unravel the causes and implications of aseismic slip. Since both steady and unsteady aseismic slips affect stress accumulation on a fault, it is important these processes are taken into account the assessment of slip deficit and seismic hazard [*Ryder and Bürgmann*, 2008; *Shirzaei and Bürgmann*, 2013; *Shirzaei et al*., 2013]. In this study, we present new observations of temporal and spatial variations along the El Pilar fault system, which is part of the Caribbean-South American plate boundary.

The E-W dextral strike-slip El Pilar fault, which accommodates almost all of the 20 mm/yr relative displacement between the Caribbean and South American plates (Figure 1) [*Weber et al*., 2001; *Jouanne et al*., 2011], is an interesting case study for analyzing the relationship between aseismic and seismic slip modes.

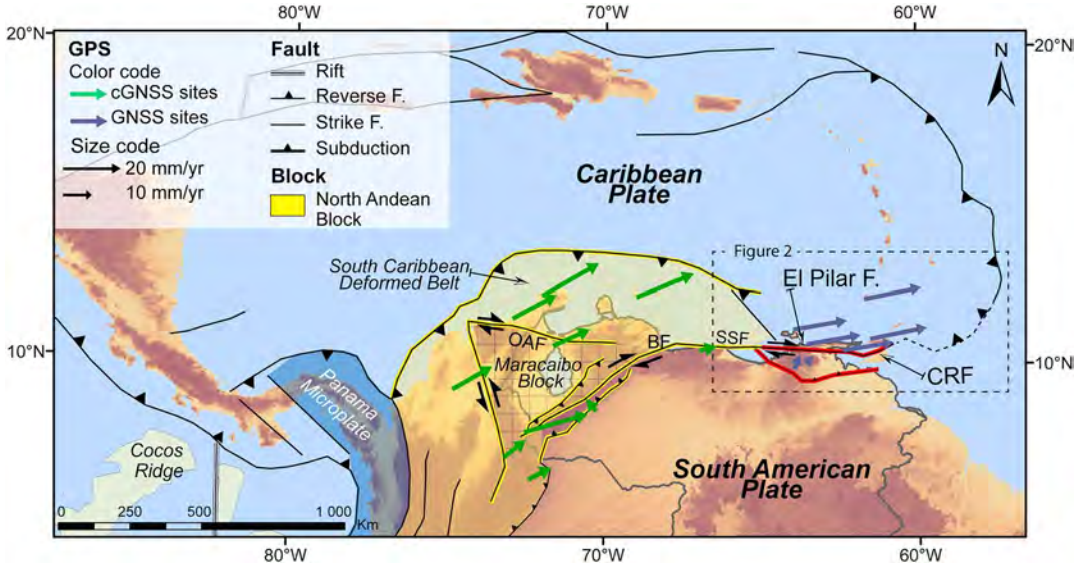

Figure 1. Geodynamic map of the Caribbean/South American plates. Arrows are GNSS (Global Navigation Satellite Systems) velocities in the Caribbean region with respect to a fixed South American plate, calculated by *Reinoza* [2014]. Green arrows represent velocities measured on permanent GNSS sites (cGNSS) from the FUNVISIS, REMOS-IGVSB, and GEORED networks. Blue arrows represent velocities derived from episodic GNSS data measured in 2003–2005 and 2013 [*Reinoza*, 2014]. Yellow and red lines are fault systems that represent, respectively, the western and eastern plate boundary systems in Venezuela. The GNSS velocity field shows that the El Pilar fault accommodates all the relative displacement between the Caribbean and South American plates. Plate boundary mapping is based on *Beltran* [1993], *Audemard et al.* [2000], *Pindell et al.* [2006], and *Audemard* [2009]. DEMs are from the USGS [*Rabus et al.*, 2003]. CRF, Central Range fault; SSF, San Sebastian fault; OAF, Ocá-Ancón fault; and BF, Boconó fault.

Seismicity, paleoseismology, and geodesy indicate that this fault exhibits seismic as well as aseismic behavior [*Audemard*, 2006, 2007; *Reinoza et al.*, 2015]. For example, the El Pilar fault produced seismic events in 1684, 1797, 1853, 1929, and 9 July 1997 [*Audemard*, 1999, 2006, 2007, 2011; *Altez and Audemard*, 2008; *Aguilar et al.*, 2016]. In addition, aseismic slip has been detected through field observations, episodic measurements performed in 2003, 2005, and 2013 on a sparse network of 32 GNSS (Global Navigation Satellite Systems) stations, and measurements of one continuous GNSS station [*Audemard*, 2006; *Jouanne et al.*, 2011; *Reinoza et al.*, 2015]. Despite the low resolution in space and time, *Reinoza et al.* [2015] showed that, in the seismogenic layer (0–12 km depth), between 40 and 50% of the fault area is locked, and that the aseismic slip is certainly not spatially uniform.

However, measurements with better spatial and temporal resolution are needed to answer a number of remaining questions. Near field data can improve the spatial resolution of aseismic slip mapping and help identify potential segmentation of creep, as proposed by *Jouanne et al.* [2011] and *Reinoza et al.* [2015]. Denser and longer geodetic time series would also improve our knowledge about the creeping process, for instance, by distinguishing the nature of the creep: e.g., afterslip induced by the latest seismic event in 1997 (M_s 6.8) which has transitioned into a persistent interseismic slip or an afterslip which is still occurring. We would like to understand the local observation of slip acceleration in 2002 [*Jouanne et al.*, 2011] and the inconsistency between the return periods evaluated in trenches at 400 years [*Audemard*, 2011] and the return period estimated at up to 200 years, assuming a geological slip rate of 20 mm/yr and a characteristic slip of 1 to 4 m slip (coseismic slip and afterslip) [*Pérez et al.*, 2001; *Jouanne et al.*, 2011]. Finally, higher spatial resolution can also help to detect asperities that may trigger events like the M_s 6.8 in 1997 [e.g., *Chaussard et al.*, 2015a, 2015b; *Jolivet et al.*, 2015a].

This paper presents an analysis of 18 SAR (synthetic aperture radar) images from the L band Advanced Land Observing Satellite (ALOS-1) satellite spanning the 2007–2011 period using the spaceborne SAR interferometry technique (interferometric synthetic aperture radar, InSAR). These images, processed with the NSBAS method [*Doin et al.*, 2011], provide a coverage at high spatial and temporal resolution for the onshore section of the El Pilar fault and allow us to identify spatio temporal slip variations along the fault. In the last part of the

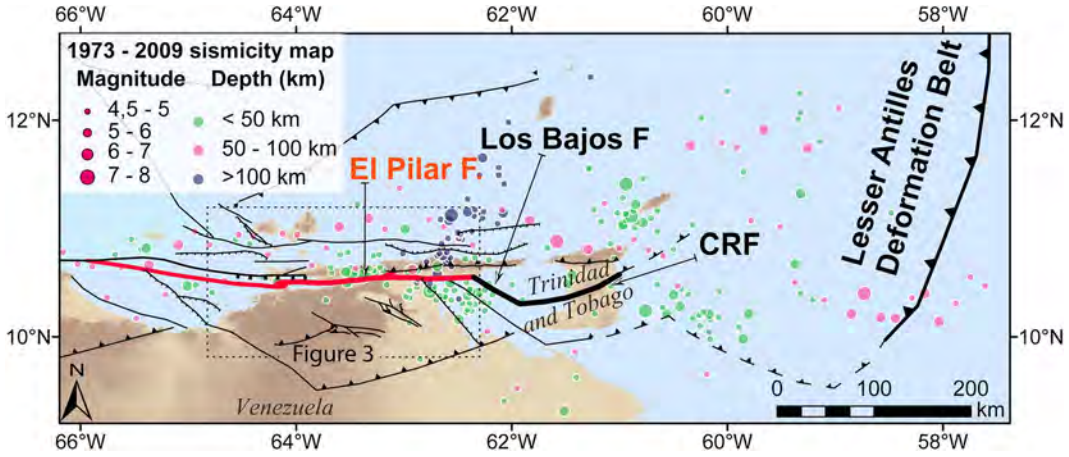

Figure 2. Seismotectonic map. In eastern Venezuela the major E-W relative displacement between the Caribbean and South American plates is accommodated along the El Pilar fault (in red). This fault is constituted by several segments onshore and offshore. Thrusts and reverse faults south of the El Pilar fault accommodate the minor N-S component of the relative displacement between the Caribbean and South American plates in Venezuela. Deep seismicity (in blue and purple) related to the Lesser Antilles subduction ends abruptly along dextral faults. Fault mapping is based on *FUNVISIS* [1994], *Audemard et al.* [2000], and on *Audemard* [2009]. The 1973–2009 seismicity data are provided by GeoMap App http://www.geomapapp.org/ [*Ryan et al.*, 2009]. CRF, Central Range fault.

paper we discuss the segmentation of the El Pilar fault and the relationship between aseismic slip and seismicity, and the implications for seismic hazard assessment.

2. The El Pilar Fault System: Seismotectonic and Geological Context

The Caribbean-South American plate boundary is a transpressional zone characterized by a complex system: distributed faults in the west (yellow thick lines in Figure 1) and a localized fault system in the east (red lines in Figure 1). GPS studies indicate ~2 cm/yr eastward motion of the Caribbean plate with respect to a fixed South American plate [*Pérez et al.*, 2001; *Weber et al.*, 2001; *DeMets et al.*, 2010]. In the eastern part of the plate boundary, neotectonic studies have shown the existence of strain partitioning: the major E-W component is accommodated by a tectonic boundary composed of several right-lateral faults (El Pilar, Los Bajos, and Central Range faults) [*Beltran et al.*, 1996; *Audemard and Audemard*, 2002], whereas the minor oblique or N-S component is accommodated by active thrusting to the south (Figures 1 and 2) with vertical deformation rates of 0.6 to 0.1 mm/yr [*Fajardo*, 2015]. Moreover, the seismicity related to the Lesser Antilles subduction ends abruptly along dextral faults, which suggests a tectonic relationship between both systems due to the tearing of the Lesser Antilles subducted oceanic lithosphere (Figure 2) [*Pérez and Aggarwal*, 1981; *Clark et al.*, 2008; *Audemard*, 2009].

The El Pilar fault, which belongs to the E-W dextral system, crosscuts a Mesozoic thrust system separating two contrasting Mesozoic terrains: a northern province consisting of low-grade metasediments associated with oceanic crustal remnants (schist, quartzite, and serpentine lenses) and a southern province made of non metamorphosed sediments (Figure 3) [*Metz*, 1965; *Vignali*, 1977; *Vierbuchen*, 1984; *Jacome et al.*, 1999]. Variations of elastic properties would also be expected across this tectonic boundary, as suggested by *Reinoza et al.* [2015]. The El Pilar fault is composed of several structural segments, defined by neotectonic analyses [*Beltran et al.*, 1996; *Audemard et al.*, 2000; *Van Daele et al.*, 2011]. Based on the joint interpretation of seismic, magnetic, and gravimetric data *Hernandez et al.* [1987] suggested a seismogenic depth of 15 to 20 km. Segmentation, 1997 rupture plane area, and dip changes (65° northward, to vertical, to 75° southward) of the upper part of the fault were investigated through the analysis of aftershocks following the 1997 M_s 6.8 event which were mainly located between the surface and 14 km depth [*Baumbach et al.*, 2004].

These geological and geometrical constraints were used by *Jouanne et al.* [2011] and *Reinoza et al.*, [2015] to explain, through modeling, the observed asymmetric velocity gradients on both sides of the fault and the high displacement gradient crossing the fault. They investigate different modeling approaches, and their results suggest the existence of spatial variations of interseismic coupling at seismogenic depths. However,

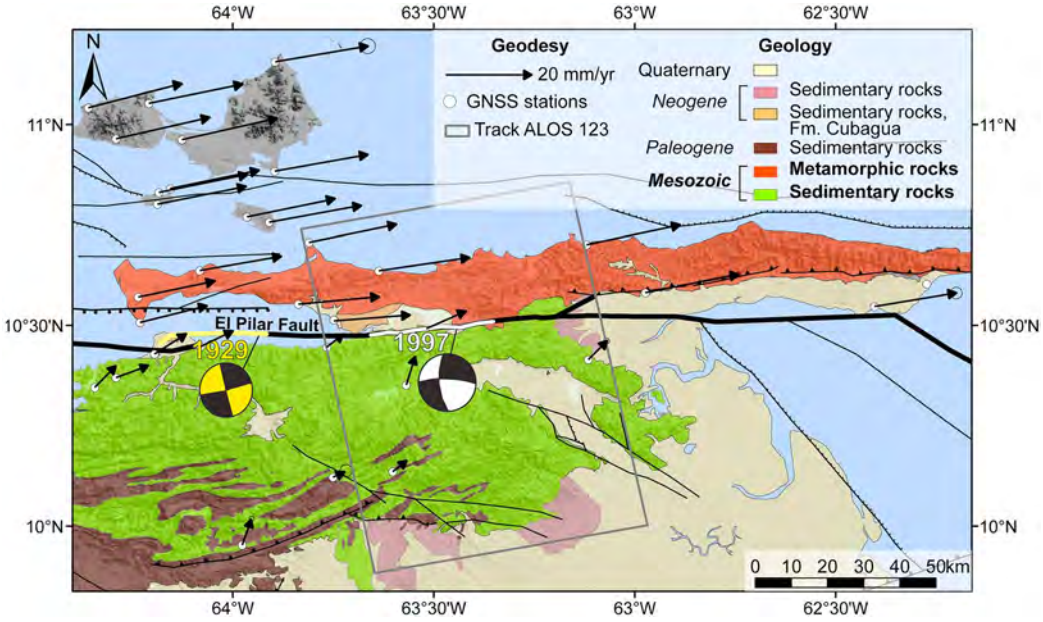

Figure 3. Schematic geological map and geodetic surveys of the El Pilar fault region. The block to the north of the fault is composed of Mesozoic metamorphosed sediments and oceanic remnants (schist, quartzite, and serpentines lenses), while to the south it is composed of Mesozoic non metamorphosed sediments [*Vignali*, 1977; *de Juana et al*., 1980; *Vierbuchen*, 1984; *Hackley et al*., 2005]. White dots are GNSS station. Black arrows are interseismic velocities estimated with GNSS data (considering a fixed South American plate) [*Reinoza et al*., 2015]. The rectangle is the shape of the InSAR ALOS-1 ascending track A123. Surface ruptures of the 1929 and 1997 events are, respectively, plotted as yellow and white lines, with their respective focal mechanisms [from *Baumbach et al*., 2004]. Faults mapping come from *Audemard et al*. [2000].

their results were limited by the sparsity of the geodetic network and the availability of only three GNSS campaign (2003, 2005, and 2013) and just one continuous GNSS station.

3. Interferometric Synthetic Aperture Radar (InSAR) Processing

To mitigate InSAR temporal decorrelation due to the dense Venezuelan equatorial vegetation cover, we used L band (23.6 cm wavelength) images from Advanced Land Observing Satellite (ALOS-1, JAXA), which gives better results than the C band or X band images in this type of environment [*Wei and Sandwell*, 2010] (several tests in this area performed with Sentinel-1A data yielded interferograms with less coherence than with ALOS data). ALOS SAR images were processed in Fine Beam Single polarization mode or in Fine Beam Dual polarization mode but using only the HH polarization, resampled at a spatial resolution of ~10 m. These images were acquired along the ALOS ascending track A123, frame 190. Eighteen SAR images spanning the 2007–2011 period (16 June 2007 to 2 September 2011) were used to form 73 differential interferograms with the NSBAS processing chain [*Doin et al*., 2011] based on the ROI-PAC software [*Rosen et al*., 2004]. The Shuttle Radar Topography Mission digital elevation model (DEM) at 3 arc sec resolution [*Rabus et al*., 2003], resampled at 45 m resolution, has been used to accurately coregister the focused SAR images and to correct interferograms from the topographic contribution to the interferometric phase. The interferogram network and examples of unfiltered and uncorrected interferograms are provided in the supporting information (Figures S1 and S2). European Centre for Median-Range Weather Forecast ERAI (ERAInterim) atmospheric reanalysis was used to correct atmospheric delay [*Doin et al*., 2009; *Jolivet et al*., 2011]. DEM errors were corrected on interferograms following the method of *Ducret et al*. [2014]. Before unwrapping, two kinds of filter were used with a spatial window of about 180 m: the adaptive filter of *Goldstein et al*. [1988] and the adaptive weighted filter of *Doin et al*. [2011].

In some unfiltered and unwrapped interferograms a clear phase jump is visible across the fault (see Figure S2); however, the time series analysis greatly improves the measurements. Another distinctive feature in the interferograms is the swamps where the interferometric phase maintains high coherence

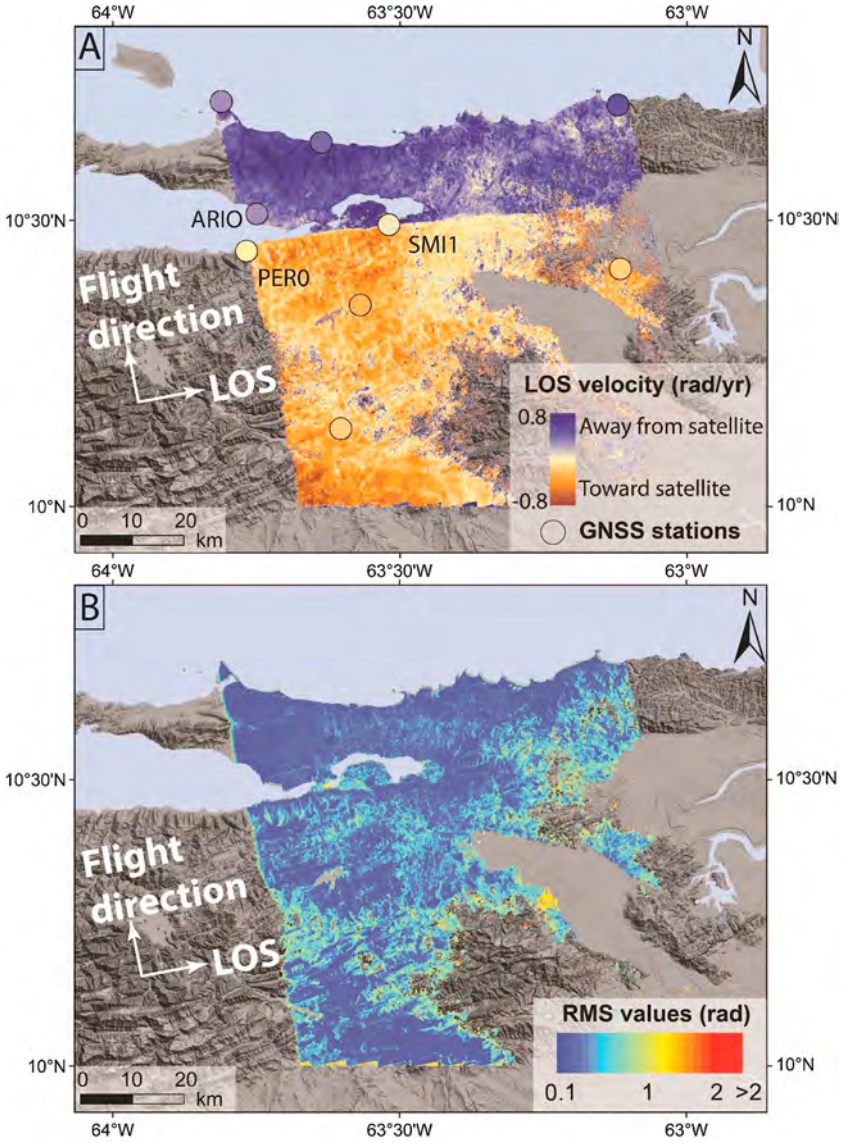

Figure 4. InSAR processing results for ascending track A123. (a) The 30 m resolution InSAR line-of-sight velocities estimated over 3.5 years (2007–2011). Dots are GNSS stations, the dot colors also represent GNSS horizontal projected in LOS (same color scale as InSAR). (b) RMS values map for each pixel, estimated over 3.5 years (2007–2011): close to swamps and in the east RMS values can exceed 0.5 rad. (ALOS-1 data distributed by Japan Space Systems © Ministry of Economy, Trade, and Industry and Japan Aerospace Exploration Agency).

and for which local fringes are detected. This is likely due to water level change (see Figure S3 in the supporting information). This pattern has been already observed in wetland areas and used to measure water level changes or subsidence [*Alsdorf et al*., 2000; *Kim et al*., 2009; *Chaussard et al*., 2013]. To avoid unwrapping issues due to these fringes, we chose to mask them. Unwrapping was performed in 2-D with the NSBAS chain using a method similar than in *Doin et al*. [2015]. The unwrapped interferograms were then systematically visually checked. When large unwrapping errors were detected, we used a manual bridge between coherent areas to correct them as explained in *Doin et al*. [2011] and *Grandin et al*. [2012] (Figure S4 in the supporting information).

To obtain a map of ground velocity along the line-of-sight (LOS) direction (Figure 4a) and a cumulative displacement map along the LOS for each date of acquisition, we applied a time series analysis using a model based on *López-Quiroz et al*., [2009], *Doin et al*. [2011], and *Jolivet et al*. [2012]. The final pixel size of our maps is approximately 30 m. The root-mean-square (RMS) on each pixel is given by the time series analysis model

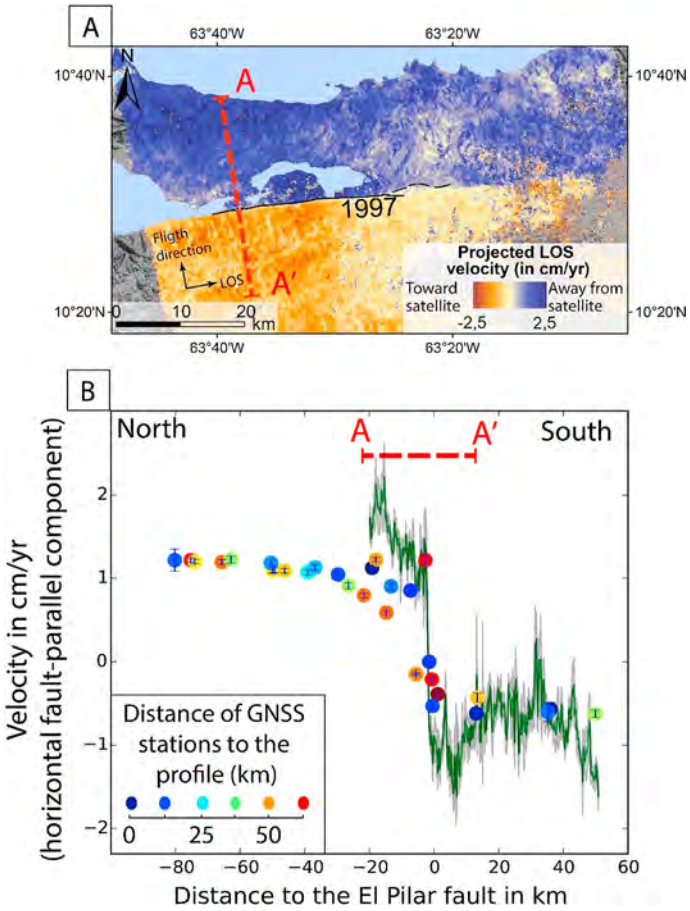

Figure 5. (a) The black line is the 1997 surface rupture [*Audemard*, 2006]. The red line (A–A') gives the location of the profile shown in Figure 5b. (b) GPS and INSAR velocity field profile across the El Pilar fault (A–A'). Dots correspond to GNSS velocities for the stations shown in Figure 3 [*Reinoza et al.*, 2015] projected along the A–A' profile (we keep GNSS stations situated up to 100 km of the A–A' profile). Dot color scale represents the distance between the GNSS stations and the profile. The green curve shows INSAR velocity (weighted average over 16 pixels (480 m) width across the profile) with 1 sigma deviation (gray zone). INSAR velocities have been converted to give an equivalent horizontal fault-parallel component velocities, and GNSS velocities are also given for the same component.

(Figure 4b) and is calculated "between the observed interferogram phase and the one reconstructed from inverted successive phase delays" [*López-Quiroz et al.*, 2009]. This RMS value is an estimation of the accuracy of the inversion scheme and gives a quality value for the LOS displacement or velocity for each pixel, which can be used to weight these data. For instance, in the following figures of this paper showing velocity profiles, plotted velocities are a weighted average of 16 pixels (that is 480 m) across the profile, with ± 1 sigma deviation shown in gray (see Figure 5 for example).

Due to the limited number of images available (18), a velocity map output from NSBAS may be affected by residual atmospheric, ionospheric, or orbital errors, producing a long wavelength signal. Indeed, our raw velocity map shows a residual ramp mainly in the range direction (Figure S5), which is almost parallel to the El Pilar fault. Such a signal is not seen in velocity fields derived from GNSS (Figure 4a). We remove this signal using a linear function in the radar range and azimuth direction. This deramping function ($ax + by + c$) is estimated in order to minimize the difference between the nine GNSS velocities measured within the boundaries of the InSAR track and InSAR velocities. The GNSS velocities are relative the SMI1 station. GNSS velocities are projected into the local satellite LOS (line of sight), and InSAR velocities are averaged in a circus of 2 km radius around every GNSS stations (Figure 4a). The choice of a simple deramping function was guided by the low number of GNSS stations covered by the track. It is important to note that this ramp correction does not affect the localized (<10 km) phase jump across the fault.

The lack of data acquired along descending tracks does not allow vertical velocity to be estimated. Assuming that the El Pilar fault is a pure strike-slip fault with no vertical component and that ground displacement is essentially in the fault-parallel direction, we project LOS InSAR data onto the horizontal surface for all the following figures of this paper in order to facilitate interpretations. Neglecting the vertical component is mainly justified by GNSS observations [*Jouanne et al*., 2011; *Reinoza et al*., 2015] and by field observations gathered along the surface rupture of the 1997 earthquake [*Audemard*, 2006]. We convert the LOS velocities in fault-parallel horizontal component velocities taking into account the variation of incidence and azimuth angles along the SAR data swath.

4. InSAR Inversion Results

4.1. Spatial Variation of Creep Rate

On the InSAR velocity map from 2007 and 2011, there is a sharp and linear velocity jump (E-W boundary between yellow and blue areas in Figures 4a and 5a corresponding, respectively, to relative displacements away from and toward the satellite). Visual comparison between the sharp boundary and the surface rupture of the 1997 earthquake mapped in detail by *Audemard* [2006] shows very good agreement (Figure 5a), within the limits of InSAR resolution and map uncertainties (<200 m). Furthermore, this sharp boundary continues away from the 1997 surface rupture and follows the El Pilar fault geological trace mapped by *Beltran et al*. [1996]. Those observations strongly suggest that the velocity boundary can be interpreted by the presence of creep along the El Pilar fault, at least in its shallowest part.

The InSAR velocity profile (A–A′) across the fault in Figure 5 shows clearly the velocity jump located at the fault trace. To compare GNSS and InSAR signals, all horizontal GNSS velocities (in fault-parallel component) from *Reinoza et al*. [2015] (plotted in Figure 3) were projected onto the profile. On this profile plotted in Figure 5, the jump across the fault is slightly higher in 2007–2011 InSAR velocities than in 2003–2005–2013 GNSS velocities. The slight differences between both kinds of data can be explained by (1) different acquisition periods: 2007–2011 period for average InSAR velocities and 2003–2005–2013 acquisition campaigns for GNSS velocities (see discussion in 6.3), (2) the vertical components which are not taken into account (not estimated in the InSAR velocity map), and (3) GPS velocity projections onto the profile, e.g., some GNSS stations are located 50 km away from the A–A′ profile where InSAR velocities are sampled in Figure 5.

Other InSAR velocity profiles across the fault show a large and abrupt step crossing the fault (Figure 6). As plotted on these profiles, the velocity step across the fault does not correlate with the topography. To quantify the step and the distance over which the step occurs, we fitted the InSAR velocity values to the following mathematical function, which is able to represent the main characteristics of our observed profiles (Figures 6 and S6 in the supporting information; the functions have been adapted from *Larson et al*. [2004] who use it for time series):

$$v(x) = v_0 + \frac{U}{2}\left(\tanh\left(\frac{x - X_0}{D}\right) - 1\right) + R * x \quad (1)$$

In this equation, x is the perpendicular distance to the fault (the x axis of the profile), $v(x)$ is the velocity at x, v_0 is the far field velocity, U is the velocity value corresponding to the step, X_0 is the median position of the large step, D is the distribution that describes the distance over which the step is measured, and R accounts for a possible velocity ramp along the section. In profiles crossing the fault, the velocity step between the northern and the southern blocks can be fitted by equation (1) (e.g., in Figure S6). Parameters and standard deviation errors are estimated from non linear least squares adjustment using the Levenberg-Marquardt algorithm [*Levenberg*, 1944; *Marquardt*, 1963]. To compare the fit quality of each profile, we performed a χ^2 statistical test which provides an estimation of the robustness of the fit. The advantage of this method is to provide an estimation for the step distribution (D in equation (1)), to evaluate the uncertainties on each unknown parameter, and to remove, through the R term in equation (1), the possible contribution of long wavelength residual orbital errors or atmospheric signals which have not been corrected in the azimuth direction (see section 3).

Using the mean velocity map over the 2007–2011 period, InSAR velocities were sampled across the fault along 94 profiles with 480 m spacing. Each profile is 3.4 km long and 480 m wide; they do not overlap.

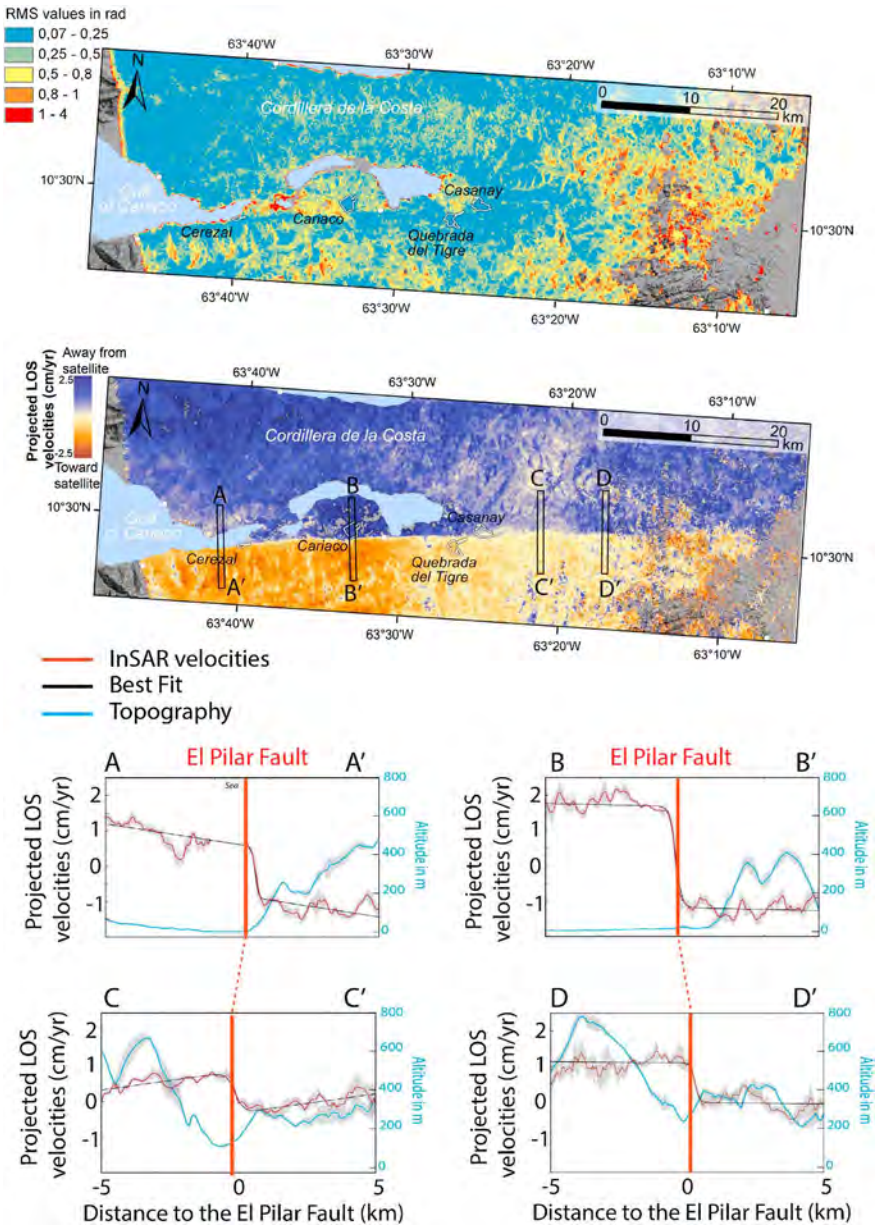

Figure 6. InSAR velocity map (2007–2011 period) and associated uncertainties. AA′, BB′, CC′, and DD′ are fault-perpendicular profiles, the red line indicates the position of the fault trace. Each plot displays the topography (blue line), the InSAR velocities projected onto the horizontal fault-parallel direction (weighted average over 16 pixels width (or 480 m)) (dark red line), 1 sigma deviation (gray zone), and the best fit of InSAR velocity values by the equation (1) (black line).

Profiles are then fitted by 1. Using this method, it appears that velocity steps vary along the El Pilar fault (Figure 7a). Between 63°42′W and 63°30′W along the fault the step regularly increases from ~13 mm/yr to ~40 mm/yr. In contrast, eastward of longitude 63°28′W, the step is lower, with a more constant value of about 13.4 ± 7.3 mm/yr. Unfortunately, the transition between these two portions of the fault is masked by the presence of swamps. Based on this geodetic contrast, hereafter in the paper, we propose to distinguish two "segments" (see Figure 7), separated at longitude 63°28′W. From a tectonic point of view this division point corresponds to a small fault step over [*Beltran et al*., 1996; *Baumbach et al*., 2004; *Audemard*, 2006]. *Baumbach et al*. [2004] do not recognize this step over as a major fault segment boundary (in their map of the fault trace our boundary corresponds to the middle of their segment 3). According to their map, one may argue that the limit could instead be defined at longitude 63°25′W,

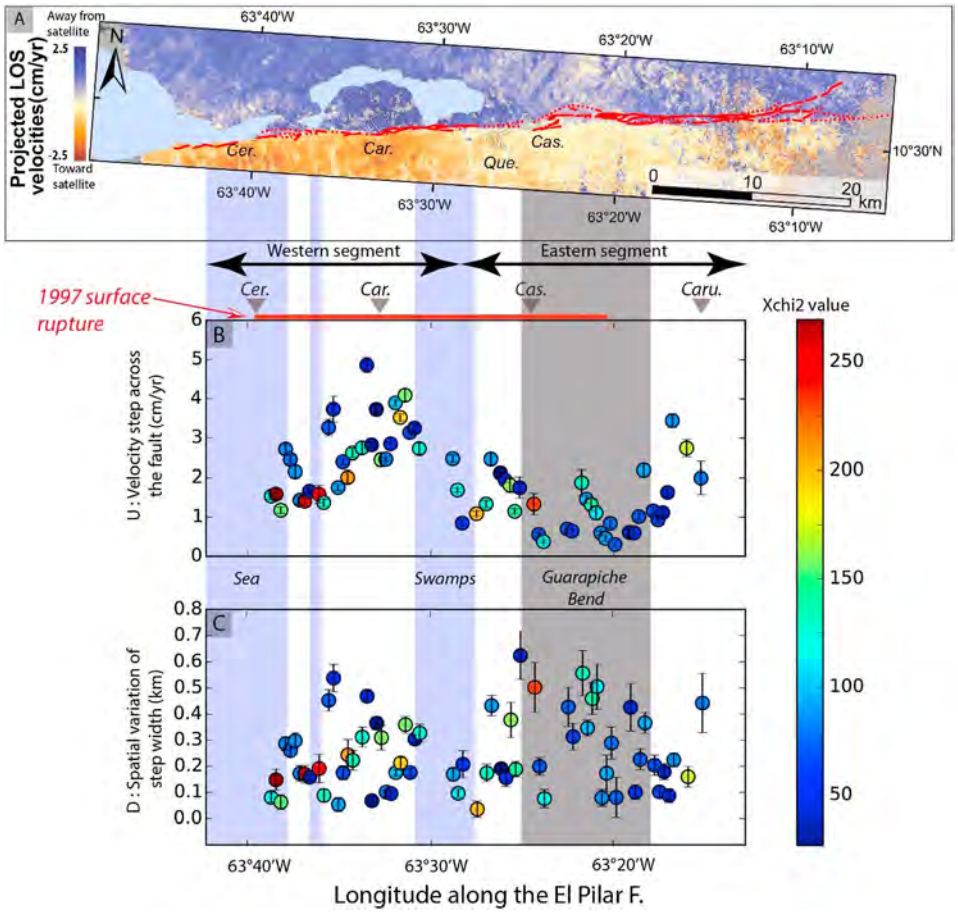

Figure 7. (a) InSAR mean velocity map (2007–2011 period), the El Pilar fault mapping of *Beltran et al*. [1996] is shown in red. Car., city of Cariaco; Que., Quebrada del Tigre; Cas., Casanay; and Caru., Carupano. (b) Spatial variation of velocity steps across the fault (U in equation (1)), as a function of longitude along the fault. (c) Spatial variation of step width (*D* in equation (1)), as a function of distance along the fault. For each estimation, the standard deviation (error bars) and the $\chi 2$ value (dot colors) are plotted.

corresponding to the Guarapiche fault bend. Nevertheless, our following analysis and conclusions remain valid for both definitions.

Regarding the distribution of the deformation across the fault, Figure 7b shows that most of the steps across the fault are distributed over less than 500 m. The velocity steps are thus essentially extremely localized, and this indicates that at least the shallow part of the fault is creeping, as suggested by *Reinoza et al*. [2015]. It should be noted that the step width estimation is limited at its lower boundary not only by the spatial resolution of the InSAR velocity map, which is 30 m, but also by the prior interferogram filtering done on the basis of 6 pixel size windows, which is 180 m (see section 3). Taking that limit into account, it is likely that in some places the creep could reach the surface, which is supported by field observations [*Audemard*, 2006; *Jouanne et al*., 2011].

4.2. Temporal Variation of Creep Rate

To estimate the temporal variations of the velocity steps across the fault, we follow the same method applied to the mean velocity map but applied to each time step of the smooth cumulative displacement time series. Using cumulative displacement profiles across the fault (same profile characteristics as in the section 4.1), displacement steps at the fault are estimated using equation (1) for each time increment (i.e., between two consecutive acquisition dates of SAR images) and are converted into incremental velocity steps (Figure 8). Some dates, for instance, 19 December 2008, contain profiles, which are too noisy to be fitted by equation (1), and explain the numerous gaps in velocity step estimations in Figure 8.

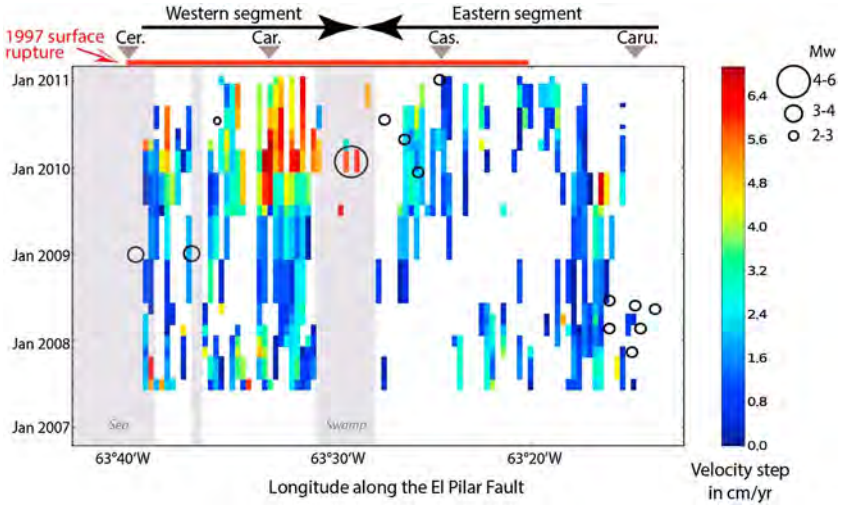

Figure 8. Velocity steps across the fault calculated between two consecutive dates; white area corresponds to areas where cumulative displacement could not be estimated. Black dots correspond to the seismicity provided by the *International Seismological Centre* [2013] ($M_w > 2$). There is no clear general correlation between seismicity and creep rate increases. One sigma deviation of the creep rate is shown in Figure S7 in the supporting information. Car., city of Cariaco; Que., Quebrada del Tigre; Cas., Casanay; and Caru., Carupano.

Comparing the velocity step variations along the fault and earthquakes ($M_w > 2$) recorded between 2007 and 2011 (Figure 8), we do not observe a clear spatial and temporal correlation between velocity step variations and the occurrence of these events, which means that the observed creep is mostly aseismic. The main seismic event is the January 2010 earthquake (M_w 5.5 at 2.4 km depth) with a dextral focal mechanism [*FUNVISIS*, 2010] which will be discussed below in section 6.2. Regarding the distribution of the deformation (parameter D in (1)), despite some noisy data, our results indicate that the deformation width remains stable through time, localized over less than 1 km (see Figure S8 in the supporting information).

Along the western segment, for each time interval, a spatial variation of the cumulative displacement steps across the fault is observed. In addition to these spatial variations, for each profile across the fault, we can see a temporal variation of the creep rate. It should be noted that short-term variations cannot be detected due to the low temporal sampling of ALOS-1 data (ranging from 1 to 6 months, see Figure S1 and Table S1 in the supporting information). According to our analyses, two phases can be distinguished (Figure 9a). Although the beginnings and endings of each phase are not well constrained due to the low temporal sampling, the two phases can be defined as Phase I between June 2007 and June 2009, with an average velocity of 15.2 ± 6.4 mm/yr, and Phase II from June 2009 to February 2011, during which time average velocity significantly increased and reached 30.2 ± 18.0 mm/yr. Such an acceleration has been already observed in the field based on measurements of local displacement markers during the 2002–2003 period following the 1997 earthquake [*Audemard*, 2006; *Jouanne et al*., 2011]. Velocities during the Phase II locally are higher than the relative plate motions [*Pérez et al*., 2001; *Weber et al*., 2001; *DeMets et al*., 2010]. This strongly suggests that it is a transient phenomenon.

No significant temporal variation in the velocity step is detected on the eastern segment (Figure 9b). We can notice that there is an exception for two profiles that cannot be included in the western segment which seem to be affected by similar temporal variations. However, these exceptions are isolated, and our conclusions remain valid. The step seems to be constant at 13.4 ± 6.9 mm/yr over the time period from 2007 to 2011 (which is consistent with the rate of 13.4 ± 7.3 mm/yr found in the mean velocity map over the 2007–2011 period).

5. Slip Distribution Model

Among the numerical models performed by *Reinoza et al*. [2015], their slip distribution inversion shows that the interseismic aseismic slip is not uniform in the seismogenic layer. However, the spatial resolution of their

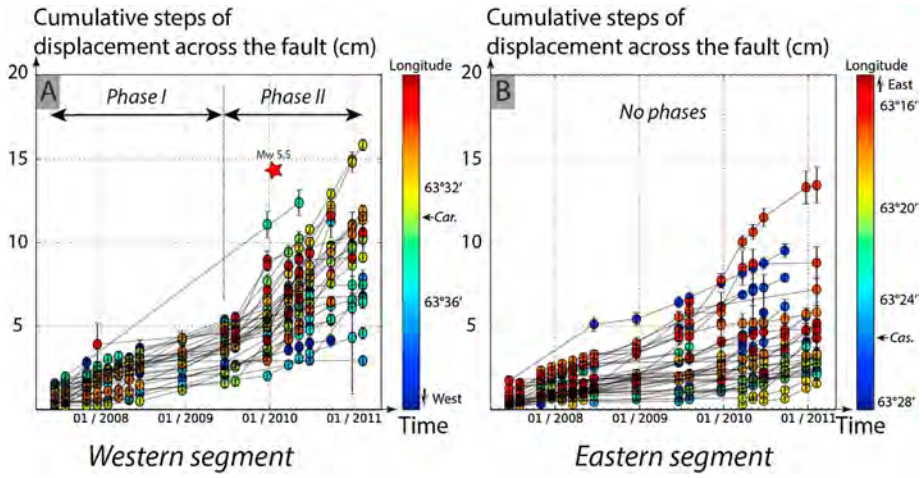

Figure 9. Cumulative displacement steps (in centimeters) across the El Pilar fault for each time step of the time series. Cumulative step estimation involves fitting the times series values weighted with RMS for each 480 m (or 16 pixels). For each estimation using 1, the standard deviation (error bars) is plotted. The dot color corresponds to the longitude along the fault. (a) Cumulative displacement steps (in centimeters) across the western segment. The average velocity of the two phases was defined using linear regression between cumulative displacement and the date at each longitude along the fault. Red star marks the M_w 5.5 earthquake in January 2010. (b) Cumulative displacement steps (in centimeters) across the eastern segment. X^2 value for each dot is plotted in Figure S9. Car., Cariaco and Cas., Casanay.

model was limited by the amount of available data. To improve the resolution, we carried out a similar inversion, but adding in our InSAR results. The GNSS velocity data used in the inversions result from three GNSS campaigns (2003–2005–2013) [*Reinoza et al*., 2015]. For InSAR, the LOS mean velocities (2007–2011 period) from this study are used. LOS values are projected onto horizontal fault-parallel components (assuming no vertical displacement and only fault-parallel displacements as discussed in part 3) and are downsampled (weighted by RMS pixel values) at 400 m spacing and restricted to data points located in near field within 5 km of the El Pilar fault. We chose to restrict InSAR data coverage to a 10 km wide band around the El Pilar fault to mitigate possible longer wavelength residual orbital error or atmospheric perturbation, and because our data analysis had shown that most of the creep velocity jump signal across the fault was distributed within less than a few kilometers from the fault trace.

The slip distribution model was performed using the SDM software [*Wang et al*., 2013a, 2013b], which has been successfully used to invert coseismic slip and afterslip [e.g., *Motagh et al*., 2008, 2010; *Wang et al*., 2009; *Diao et al*., 2010, 2011; *Xu et al*., 2010]. This inversion first performs a sensitivity-based iterative fitting approach; it calculates the portion of the data which can be explained per unit slip by a single patch. The slip distribution inversion uses an elastic half-space model [*Okada*, 1985] to calculate Green's function. To choose between the many possible slip models, the code chooses a slip model with an appropriate roughness in the slip distribution. Thus, the code solves a minimization problem applied to an objective function defined as

$$F(b) = ||Gb - y||^2 + \alpha^2 ||H\tau||^2 \quad (2)$$

where G is the Green's function, b is the slip of subfaults, y is the ground observation, α is a positive smoothing factor, H is the finite difference approximation of the Laplacian operator multiplied by a weighting factor proportional to the slip amplitude, and τ represents the shear stress drop related to the slip distribution on the whole fault plane [*Wang et al*., 2009].

We use a homogeneous Earth model with a Poisson ratio of 0.25 and a smoothing factor of 0.1 (see supporting information Figure S10). The fault is modeled by three vertical planes, with each plane segment separated into two parts: an upper part (0–20 km depth), which represents the seismogenic layer, and a lower part which represents the ductile layer. We considerably extended in depth and width the area of the model to avoid boundary effects. We considered only right-lateral slip (180° rake) on those planes. The upper part is discretized into square patches whose size is 1 km in length in the area covered by InSAR and 20 km elsewhere. The lower part is discretized into squares 10 km in length. The bend of Guarapiche (localized in Figure 7) is discretized separately. We fixed a threshold for the maximum of slip magnitude in the lower part

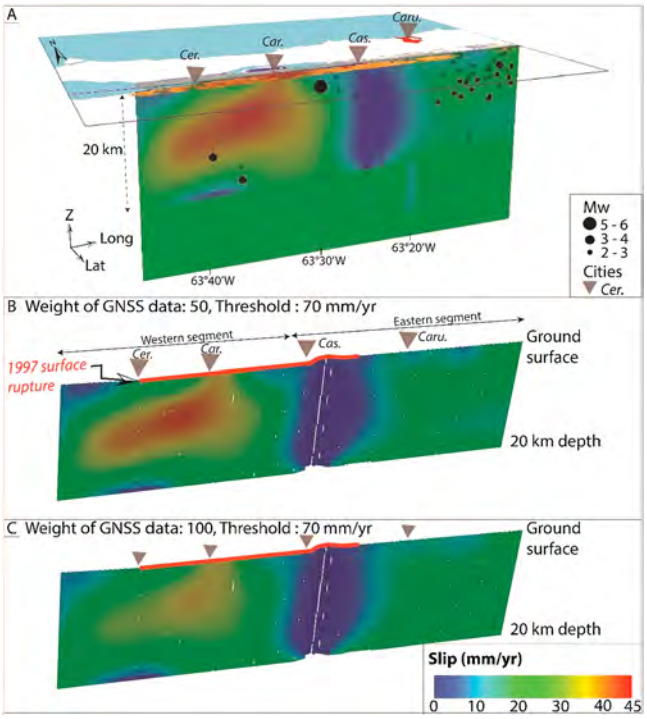

Figure 10. (a) Upper part 3-D view of western and eastern segments discretized for the slip distribution mode, with the seismicity recorded between 2007 and 2011 shown as black dots; the inversion displayed is the same than in Figure 10b. Slip distribution inversions performed with SDM. In these inversions, we used the LOS mean velocities measured during the 2007–2011 period (whole time span) and we remove the large wavelength from the InSAR data. (b) Slip distribution with a correlation of 95.20% for an inversion where GNSS data weight is 50 compared to InSAR data, and the slip magnitude cannot exceed 70 mm/yr. (c) Slip distribution with a correlation (or fit to the data) of 95.18% for an inversion where GNSS data have a weight of 100 compared to InSAR data, and the slip magnitude cannot exceed 70 mm/yr. Cer., Cerezal; Car., Cariaco; Cas., Casanay; and Caru., Carupano.

at 20 mm/yr in agreement with GPS far field velocities [*Pérez et al.*, 2001; *DeMets et al.*, 2010; *Jouanne et al.*, 2011; *Reinoza et al.*, 2015]. We also apply a threshold on the upper part of 70 mm/yr. We choose to use a relative weight for GNSS and InSAR data. The weight has been chosen in order to satisfy two criteria: allowing the model to reach long-term (geologic) slip rates below 20 km and to reduce residual errors for InSAR data. In order to invert velocities measured in 2007–2011 which is probably a transient event we give a low weight to the near field SMI1 station (0.01). Indeed, this station influence our inversion as the velocity estimated in 2003–2005–2013 represents an average fault behavior and not the transient behavior during the 2007–2011 period.

We tested several parameters in order to evaluate the robustness of coupled and uncoupled areas. For example, we tried several weightings for the GNSS and InSAR data, various slip magnitude thresholds (e.g., Figure 10), and change in dip for the upper dislocation (e.g., 65° northward, vertical, or 75° southward); we also tried using the InSAR data without first removing the large wavelength (the one shown in the supporting information Figure S6). The slip is not uniform in all our inversions, and the spatial distribution of slip is similar within ~5 km location uncertainty. For instance, in all inversions there is a zone between the western and eastern segments characterized by a slip rate lower than 3 mm/yr (Figure 10). Segmentation is also observed in all inversions: the western segment exhibits a widespread uncoupled area (characterized by a slip rate close to 30 mm/yr) reaching the surface, whereas the eastern segment slips at ~20 mm/yr. These patterns are in the same location in all the tests; thus, slip distribution inversions shown in Figure 10 are robust (see InSAR map of residuals in Figure 11 and simulated GNSS velocities in Figure S11). Our inversions show that during the ~3.5 year period, the aseismic slip (~17–18 mm/yr) released a moment of $\sim 8.5 \times 10^{17}$ N m which is equivalent to an earthquake of $M_w \sim 6.27$ (or M_w 6.25 for test C in Figure 10).

In addition, we inverted slip rates before and after the creep acceleration with the same method by keeping the same parameters and the same GNSS data (Figure 12). Slip distribution inversions show that the coupled zones are broadly at the same place during the two phases. These zones become smaller in Phase II (characterized by an increase of slip rate). These inversions are broadly consistent with cumulative displacement profiles across the fault (Figure 9), even if in the eastern segment profiles do not exactly match to the slip variation in the two inversions. Regarding residuals (shown in Figure S12), simulated GNSS velocities are similar to those of the first inversions (Figure S11); however, residuals for InSAR data are almost the double of the residuals in the slip distribution inversions of the velocities measured during the whole spanning interval (2007–2011). This difference is most important along the Guarapiche bend area in Phase II (Figure S11b).

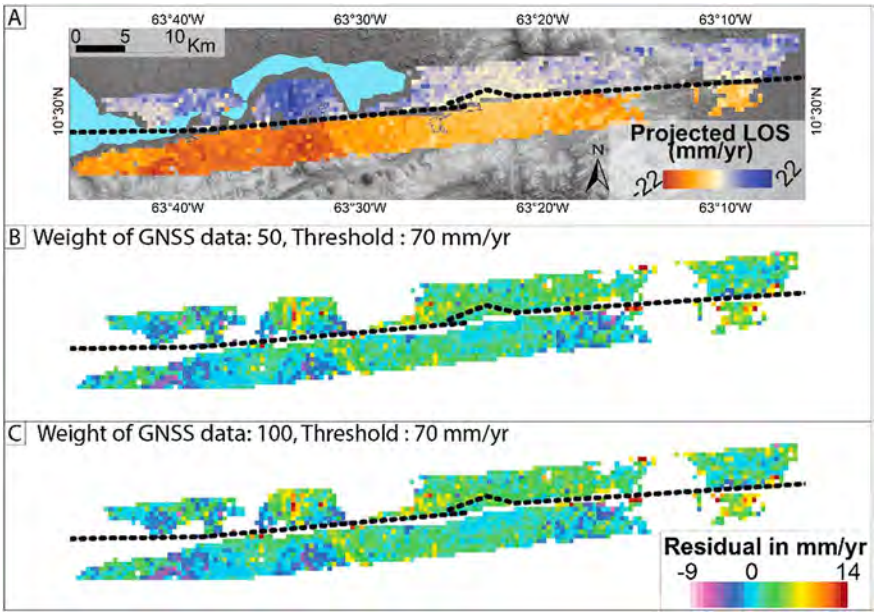

Figure 11. Map of residuals for three inversions. (a) InSAR velocity input. (b and c) Map of residuals for InSAR data for the two tests (displayed in Figures 10b and 10c). Simulated and observed GNSS velocities are displayed in Figure S11 in the supporting information.

6. Discussion

6.1. Short-Term Segmentation and Fault Properties

Detection of spatial variations in creep rate for the 2007–2011 period allows us to establish that two fault segments undergo different behavior. The shallow surface rate of the western segment reaches 25.3 ± 9.4 mm/yr on average (deduced from InSAR data) and has transient variations. On the contrary, slip in the eastern segment reaches 13.4 ± 6.9 mm/yr on average and does not present significant temporal variations. This segmentation observed in the short term (3.5 years) may not be persistent over longer timescales. For instance, it is possible that at other periods the western segment could return to a lower steady state value while the eastern segment could undergo acceleration. Nevertheless, GNSS campaigns (2003–2005–2013) show a consistent segmentation pattern (a western segment creeping faster than the eastern segment) [*Jouanne et al.*, 2011; *Reinoza et al.*, 2015].

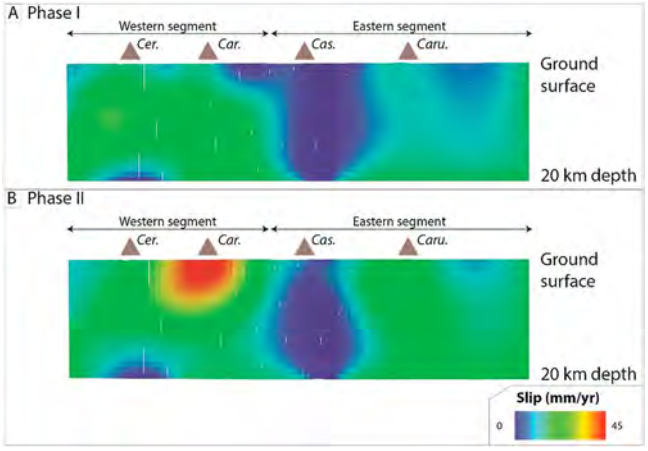

Figure 12. Slip distribution inversions before and after the acceleration (Phase I and Phase II in Figure 9). Inversions performed with SDM where GNSS data have a weight of 50 relative to InSAR data, and the slip magnitude cannot exceed 70 mm/yr. (a) Slip distribution inversions for InSAR velocities measured during the Phase I with a correlation of 91.50%. (b) Slip distribution inversions for InSAR velocities measured during the Phase II with a correlation of 90.82%. See residual map and simulated GNSS velocities in Figure S12. Cer., Cerezal; Car., Cariaco; Cas., Casanay; and Caru., Carupano.

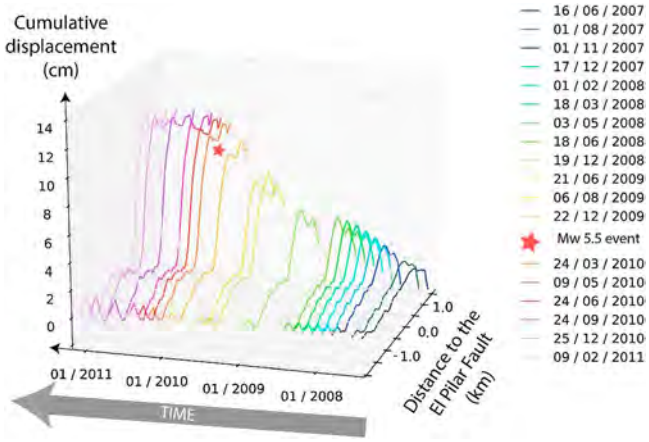

Figure 13. Profiles perpendicular to the fault showing smoothed cumulative displacement for each acquisition date (see Figure S13 in the supporting information for a version of this plot without smoothing). The profile crosses the fault at longitude 63°30′W, which is the location of the epicenter of the January 2010 M_w 5.5 earthquake (red star). Gray zones around curves correspond to the 1 sigma deviation.

Neotectonic analysis of geological markers shows evidence of fault geometry variations between the western and eastern creeping segments. As shown in Figure 7, the fault mapped in *Beltran et al*. [1996] is almost linear along the western segment, whereas the eastern segment is distributed along several parallel traces (e.g., bend of Guarapiche). Thus, the fault geometry could control the distribution of the creep as proposed by *Lindsey et al*. [2014] for the San Andreas fault.

Frictional properties could control the creep rate as predicted by the empirical law of the rate and state formalism [*Dieterich*, 1979; *Ruina*, 1983]. As the friction coefficient is related to the material characteristics surrounding the fault, there could be a lithological control on creep rate variations. Along the El Pilar fault, the presence of serpentine lenses, with quartzite and schist [*Vierbuchen*, 1984] along a fault plane characterized by an important creep (Figure 3), can be compared to experiments of shearing serpentinite ultramafic rocks juxtaposed against quartzite under hydrothermal conditions (200°–350°) carried out by *Moore and Lockner* [2013]. This experimental setup promotes aseismic slip at seismogenic depth more than serpentinite shearing experiments without quartzite rocks, and it also shows that long-term shearing of serpentinite against crustal rocks produces extremely weak minerals such as saponite and talc. Additionally, *Moore and Lockner* [2013] and *Scuderi et al*. [2015], among others suggest that faults can be characterized by strengthening and aseismic slip in the presence of high groundwater flow rates. This may be correlated to the existence of swamps near the western segment of the fault and also to the high number of hot springs and fumaroles [*Urbani*, 1989; *D'Amore et al*., 1994; *López*, 2013]. Lastly, we note the concentration of microseismicity ($M_w < 2$) in the area where there are no serpentinite lenses at the surface (Figures 3 and 10). This concentration in the eastern segment could be due to a concentration of small asperities which are loaded by adjacent creep and cause failure. Presence of numerous asperities can be thus correlated to the lack of serpentines. Another explanation could be the variation in pore fluid which would reduce the effective normal stress and therefore the apparent coefficient of friction [*Gratier*, 2011; *Richard et al*., 2014].

6.2. Link With Seismicity

Slip distribution models on the onshore segment of the El Pilar fault allow us to estimate that between 2007 and 2011 the slip released a moment of $8.0–8.5 \times 10^{17}$ N m, which corresponds to an earthquake of M_w ~6.26. Since moment released by the recorded seismicity during the same period of time is 1.55×10^{17} N m, the slip was mostly aseismic. This aseismic slip may control the distribution of microseismicity. Slip distribution models show that the microseismicity (M_w ~2) seems to occur in the transitional area between the uncoupled and coupled zones especially at the east (Figure 10a). In these areas, microseismicity could result from failure of asperities (coupled areas) loaded by adjacent creep in the surrounding uncoupled areas. The seismicity resulting from these failures is often linked to the creep rate [e.g., *Nadeau and McEvilly*, 2004] and can be defined as characteristically repeating earthquakes, although the waveforms and magnitudes of microseismic events would be needed to confirm this here.

Despite the low temporal resolution of InSAR analysis, it seems that there is no correlation between recorded seismicity and temporal slip rate variation (Figure 8). However, it should be noted that a M_w 5.5 event (January 2010), at the edge of the western segment, occurred after a period of creep rate acceleration. This may indicate that it was triggered by a rise in creep rate (Figure 13). A sequence of slow slip events followed by $M_w > 5$ earthquakes has been observed in subduction zones, where slow slip events probably induce abrupt stress changes and then earthquakes [e.g., *Radiguet et al*., 2016]. However, this sequence is unusual along strike-slip

faults, and in fact, the opposite is often observed; for instance, along the San Andreas fault and the Haiyuan, M_w 4–5.5 events promote aseismic slip in the adjacent areas [e.g., *Murray and Segall*, 2005; *Taira et al*., 2014].

At the regional scale, no significant seismic events were recorded in the vicinity of the El Pilar fault ($M_w > 4.5$) or in the neighboring countries ($M_w > 7$) [*International Seismological Centre*, 2013]. Therefore, local or remote earthquakes cannot explain the temporal creep variation that occurred in 2009. Slip distribution inversions from InSAR velocities measured before and after June 2009 show an increase of slip below Cariaco between the surface and 10 km depth (Figure 12). Changes in groundwater flow rates may explain this variation in the shallowest part (see section 6.1), especially as the western segment is close to swamp and hot springs. However, for the deepest part, the transient behavior could be explained by stress interactions with neighboring faults or by variation of friction properties [e.g., *Lienkaemper et al*., 1997; *Scholz*, 1998; *Wei et al*., 2013].

6.3. Aseismic Slip Types and Seismic Hazard

The 1997 event released a seismic moment of $M_o = 3.1 \times 10^{19}$ N m. The surface rupture was mapped in the field 2 days after the event over a distance of 30 km (Figures 14a and 14b). During this field investigation, the displacements measured yielded an average total slip ranging from ~20 cm to ~40 cm, assuming a crack-like rupture [*Pérez*, 1998; *Audemard*, 1999, 2006; *Baumbach et al*., 2004]. Considering earthquake fault scaling laws of *Leonard* [2010] a seismic moment of $M_o = 3.1 \times 10^{19}$ N m corresponds to an average fault displacement of ~1.1 m. Therefore, only 20–35% of the expected displacement was accounted by the total "coseismic" slip observed. This discrepancy could be explained in part by the occurrence of off-fault deformation [*Zinke et al*., 2014; *Milliner et al*., 2016] or by aseismic slip (after the earthquake) on the shallow part of the fault as proposed in *Hussain et al*. [2016].

Actually, localized aseismic slip was detected in the field during the 6 years following the 1997 event (Figures 14a–14b). The total measured slip triples the surface coseismic slip and ranges from 50 to 120 cm [*Audemard*, 2006; *Jouanne et al*., 2011], which is 50 to 100% of the expected average fault displacement corresponding to a M_w 6.9. This period of rapid slip after the earthquake is thus interpreted as an afterslip. Moreover, the logarithmic decay characterizing the afterslip phenomenon [*Marone et al*., 1991; *Chang et al*., 2013] has not been seen in the records from the 2003, 2005, and 2013 geodetic campaigns along the El Pilar fault segments (Figure 14a). This decay was also not detected by the temporal slip rate investigation between 2007 and 2011 carried out in this study; on the contrary, a rise in slip rate was observed. We can therefore hypothesize that short-term transient afterslip (during few years) may have been induced by the 1997 earthquake and it is over since 2002–2003.

In 2005 and 2013 two GNSS campaigns was carried out, considering stations ARI0-PER0 the El Pilar fault is creeping in average at 13 mm/yr. Between 2007 and 2011 the eastern segment showed a similar velocities (~13 mm/yr). However, in the western segment the creep is in average double (~26 mm/yr). This implies that the fault undergoes strong temporal variation to be in agreement with GNSS measurements. For example, along the western segment, between 2005 and 2007 and between 2012 and 2013 the creep rate had to decrease significantly (~0 mm/yr) to be in agreement with the 13 mm/yr deduced from GNSS measurements (Figure 14a). The El Pilar fault seems thus to be locked during several years and then undergoes transients of creep during several months. This transient behavior is also supported by the fact that the creep exceeds the plate relative velocity motion. This pattern was also observed in 2000–2003 in the western segment (markers b and d in Figure 14a). Several creeping fault around the world had a transient-like behavior: for example, the North Anatolian fault underwent a transient of 31 days [*Rousset et al*., 2016] or the Haiyuan fault [*Jolivet et al*., 2015b]. Moreover, along the 1999 Izmit surface rupture of the North Anatolian fault, *Hussain et al*. [2016] proposed that the steady state afterslip will probably undergo transient acceleration during the earthquake cycle. The installation of a creep meter will provide temporal coverage which could inform us about the duration creep events (i.e., several creep events during days or one creep event during several months).

Although it is not known if the El Pilar fault was creeping before 1997, 10 years after 1997 the aseismic slip is still high and undergoes accelerations. Thus, it is possible that the succession of locked and of large transients lasts during the interseismic period (before and after the 1997 events). To test this hypothesis, earthquake return periods can be evaluated for the cases with or without persistent creep and compared with available information about return period. For instance, considering a fully locked fault that is affected only by episodic

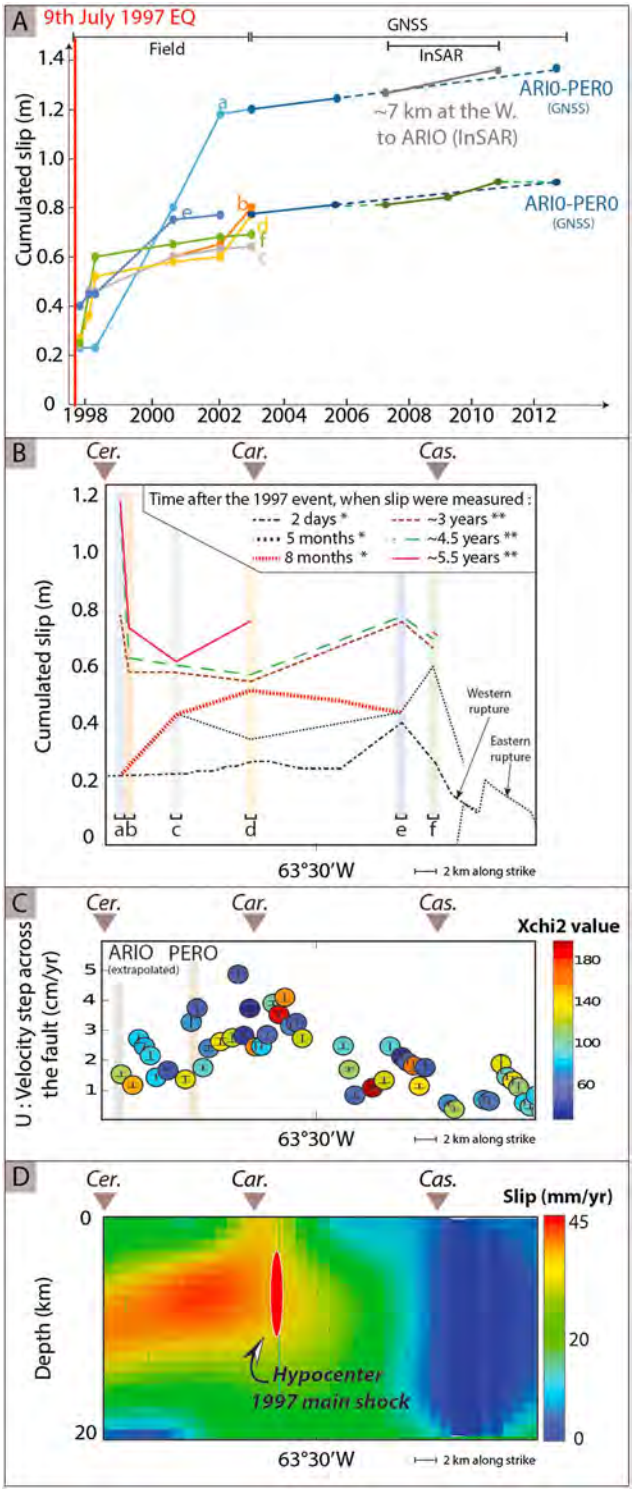

partial coupling due to transient aseismic afterslip during a short period of time (for example, less than 20 years) and a long-term slip rate of 20 mm/yr, the return period of a characteristic earthquake similar to the 1997 event (1 to 4 m of slip) would range from 50 to 200 years. However, assuming a stationary partial coupling of 12–13 mm/yr during the interseismic period, and a long-term slip rate of 20 mm/yr, the return period would increase from ~80 to 500 years. The latter case is more consistent with relevant paleoseismology studies which inferred return periods of ~ 400 years for large events [*Audemard*, 2006, 2011]. Thus, a short-term (several years) afterslip induced by an earthquake, succession of locked and of large transients during the interseismic period could better represent the seismic cycle of the El Pilar fault.

Considering that since 2003 the rapid afterslip decay has finished, we observe in Figures 14c and 14d the aseismic slip occurring during the earthquake cycle. We can thus propose that the coupled

Figure 14. Fault slip along the 1997 surface rupture. (a) Total slip measured after the 1997 event. Lines a, b, c, d, e, and f are localized in Figure 14b. These lines correspond to field measurements reported by *Audemard* [2006] and *Jouanne et al.* [2011]. Lines ARI0-PER0 display the total slip measured by GNSS between stations ARI0 and PER0 [*Reinoza et al.*, 2015]. (b) Field slip measurements along the 1997 surface rupture since 2–3 days after the 1997 event (Single asterisk and double asterisks signify that slip was measured in *Audemard* [2006] and *Jouanne et al.* [2011], respectively.) These measurements are the same than those plotted in Figure 14a. (c) InSAR velocity slip along the 1997 surface rupture (measured in this study from June 2007 to December 2011 in Figure 7). (d) Upper part of the slip distribution inversion performed in this study (see Figure 10). The figure displays the seismogenic layer until 20 km depth. The red area corresponds to the hypocenter of the 1997 event [*Baumbach et al.*, 2004, and references therein]. Figures 14b–14d are at the same scale (in longitude along the fault) and are located at the same localization (1997 surface rupture). Cer., City of Cerezal; Car., Cariaco; and Cas., Casanay.

area below Casanay corresponds to an asperity which may have been responsible for the 1997 earthquake (Figure 14d). At that time, the surrounding slipping areas could thus have been activated by the weakening dynamic triggered by the failure of this asperity. This could explain the existence of ground deformations (observed 2–3 days after the event) over a length exceeding the length of this asperity. Three months before the El Pilar 1997 event, a M_w 6.7 occurs in Tobago (~350 km from Casanay) [*Weber et al*., 2015]. Despite this earthquake had a normal cinematic, it could have induced stress variation along the El Pilar which triggers the event.

Considering a long-term slip rate of 20 mm/yr and a seismogenic depth below the 1997 surface rupture (of 20 km), the slip deficit estimated from our model corresponds to an earthquake of M_w 5.1–5.5 (accounting for the seismic moment release due to seismicity over the 3.5 year period of observation). This implies that the fault accumulates strain and can release it during an earthquake. Therefore, to accumulate a slip deficit equivalent to the seismic moment of $M_o = 3.1 \times 10^{19}$ N m released during the 1997 event requires more than 800 years. This period is higher than the return period which confirms that we observe a large transient episode along the western segment.

Regarding seismic hazard, along the western segment, as we inferred increases and decreases in the slip rate over the 3.5 year study period, it would probably be necessary to perform a time-dependent seismic hazard forecast, as it has been proposed for the San Andreas fault [e.g., *Khoshmanesh et al*., 2015] or for the Haiyuan fault [e.g., *Jolivet et al*., 2015b]. The bend in the eastern segment, which has a constant and lower creep rate, has been considered a seismic barrier by *Audemard* [2006]. However, it could be interesting to perform an accurate seismic hazard evaluation, because this kind of fault can generate large seismic slips, as explained by *Noda and Lapusta* [2013]. Particular attention should also be paid to the transition area between these segments. Indeed, this zone seems to be coupled and able to provoke failures due to loading by adjacent creep, as it certainly happened in the case of the M_w 5.5 event.

7. Conclusion

In this paper, we use InSAR analyses in order to characterize the spatial and temporal variation of creep rate along the El Pilar fault. InSAR velocity profiles across the fault show a large step (greater than 2 mm/yr when projected into horizontal fault-parallel velocity), and demonstrate the continuity of creep localized along the El Pilar fault trace at the surface. Slip distribution inversions using GNSS velocities from three campaigns (2003–2005–2013) and the LOS mean velocities (estimated here on the 2007–2011 period) show that the aseismic slip releases a moment of $\sim 8.0–8.5 \times 10^{17}$ N m between the surface and 20 km depth during the 3.5 year observation period. Considering a long-term slip rate of 2 cm/yr, this implies that the fault accumulates strain (equivalent to a M_w 5.4–5.6 over 3.5 years) which can be released during an earthquake.

Analysis of the spatial variability of the creep rate between 2007 and 2011 allows us to distinguish two fault segments of the El Pilar fault which showed different behavior. The creep rate of the western segment reached 25.3 ± 9.4 mm/yr on average and underwent transient behavior. On the contrary, slip on the eastern segment reached 13.4 ± 6.9 mm/yr on average and did not show significant temporal creep variation. Locally, creep rates are higher than the relative plate motions which strongly suggest that it is a transient phenomenon. We investigated the geometrical and lithological characteristics which could explain this difference, and it appears that the faster creeping segment corresponds to a linear and unique trace which crosscuts a province containing quartzite and serpentinite. Future geodetic monitoring (ALOS-2, Sentinel SAR data) and installation of a permanent creep meter will further constrain the link between the fault geometry and lithology [e.g., *Thomas et al*., 2014a].

Despite the relatively low temporal resolution (18 dates) of our study, the observation of transient behavior indicates that these segments were affected by episodic interseismic aseismic slip between 2007 and 2011. The rise in creep rate cannot be explained by a postseismic afterslip mechanism. The creep is thus interpreted as into interseimic creep showing transients.

Acknowledgments

We thank M.Y. Thomas, an anonymous reviewer, and Yosuke Aoki for their detailed and constructive reviews. We also thank James Hollingsworth for fruitful comments. Most of the computations presented in this paper were performed using the Froggy platform of the CIMENT infrastructure (https://ciment.ujf-grenoble.fr), which is supported by the Rhône-Alpes region (grant CPER07_13 CIRA), the OSUG@2020 labex (reference ANR10 LABX56), and the Equip@Meso project (reference ANR-10-EQPX-29-01) of the programme Investissements d'Avenir supervised by the Agence Nationale pour la Recherche. We are also grateful for DEM data provided by the U.S. Geological Survey. The original ALOS PALSAR data were distributed by Japan Space Systems (© METI and JAXA). We acknowledge JAXA for accepting ALOS sixth RA project PI 3223.

References

Aguilar, I., C. Beck, F. Audemard, A.-L. Develle, M. Boussafir, C. Campos, and C. Crouzet (2016), Last millennium sedimentation in the Gulf of Cariaco (NE Venezuela): Evidence for morphological changes of gulf entrance and possible relations with large earthquakes, *Comptes Rendus Geosci.*, *348*(1), 70–79, doi:10.1016/j.crte.2015.10.001.

Alsdorf, D. E., J. M. Melack, T. Dunne, L. A. K. Mertes, L. L. Hess, and L. C. Smith (2000), Interferometric radar measurements of water level changes on the Amazon flood plain, *Nature*, *404*(6774), 174–177, doi:10.1038/35004560.

Altez, R., and F. Audemard (2008), El sismo de 1629 en cumaná: Aportes para una nueva historia sísmica del oriente venezolano, *Bol. Téc. IMME*, *46*(2), 53–71.

Audemard, F. (2006), Surface rupture of the Cariaco July 09, 1997 earthquake on the El Pilar fault, northeastern Venezuela, *Tectonophysics*, *424*(1–2), 19–39, doi:10.1016/j.tecto.2006.04.018.

Audemard, F. (2007), Revised seismic history of the El Pilar fault, northeastern Venezuela, from the Cariaco 1997 earthquake and recent preliminary paleoseismic results, *J. Seismol.*, *11*(3), 311–326, doi:10.1007/s10950-007-9054-2.

Audemard, F. (2009), Key issues on the post-Mesozoic Southern Caribbean Plate boundary, *Geol. Soc. Lond. Spec. Publ.*, *328*(1), 569–586, doi:10.1144/SP328.23.

Audemard, F. (2011), Multiple-trench investigations across the newly ruptured segment of the El Pilar fault in northeastern Venezuela after the 1997 Cariaco earthquake, *Geol. Soc. Am. Spec. Pap.*, *479*, 133–157, doi:10.1130/2011.2479(06).

Audemard, F. A. (1999), El sismo de Cariaco del 09 de julio de 1997, edo. Sucre, Venezuela: Nucleación y progresión de la ruptura a partir de observaciones geológicas, *Mem VI Cong Venez Sismol. E Ing. Sísmica*.

Audemard, F. E., and F. Audemard (2002), Structure of Merida Andes, Venezuela: Relations with South America-Caribbean geodynamic interaction, *Tectonophysics*, *345*, 299–327.

Audemard, F., M. N. Machette, J. W. Cox, R. L. Dart, and K. M. Haller (2000), Map and database of Quaternary faults in Venezuela and its offshore regions—Scale 1:2 000 000. Acompañado por noticia explicativa: Map and Database of Quaternary Faults in Venezuela and Offshore regions (USGS Open-File Report 00-18, 78 p). A project of the International Lithosphere Program Task Group II-2: Major active faults of the world (Regional Coord.: Carlos Costa, Univ. San Luis-Argentina, ILP II-2 co-chairman Western Hemisphere: Michael Machette, USGS-Colorado), *USGS Numbered Series*, *2000-18*, 78 p.

Avouac, J.-P. (2015), From geodetic imaging of seismic and aseismic fault slip to dynamic modeling of the seismic cycle, *Annu. Rev. Earth Planet. Sci.*, *43*(1), 233–271, doi:10.1146/annurev-earth-060614-105302.

Barbot, S., P. Agram, and M. De Michele (2013), Change of apparent segmentation of the San Andreas fault around Parkfield from space geodetic observations across multiple periods, *J. Geophys. Res. Solid Earth*, *118*, 6311–6327, doi:10.1002/2013JB010442.

Baumbach, M., H. Grosser, G. R. Torres, J. L. R. Gonzales, M. Sobiesiak, and W. Welle (2004), Aftershock pattern of the July 9, 1997 $M_w = 6.9$ Cariaco earthquake in northeastern Venezuela, *Tectonophysics*, *379*(1–4), 1–23, doi:10.1016/j.tecto.2003.10.018.

Beltran, C. (1993), Neotectonic map of Venezuela, scale 1: 2 000 000, *Venezuelan Found. Seismol. Res. FUNVISIS*.

Beltran, C., A. Singer, and J. A. Rodriguez (1996), The El Pilar Fault active trace (northeastern Venezuela): Neotectonic evidences and paleoseismic data, in *3rd Symposium International sur la Géodynamique Andine, Saint-Malo, France*, pp. 153–156, ORSTOM, Paris.

Blanpied, M. L., D. A. Lockner, and J. D. Byerlee (1991), Fault stability inferred from granite sliding experiments at hydrothermal conditions, *Geophys. Res. Lett.*, *18*(4), 609–612, doi:10.1029/91GL00469.

Çakir, Z., J.-B. de Chabalier, R. Armijo, B. Meyer, A. Barka, and G. Peltzer (2003), Coseismic and early post-seismic slip associated with the 1999 Izmit earthquake (Turkey), from SAR interferometry and tectonic field observations, *Geophys. J. Int.*, *155*(1), 93–110, doi:10.1046/j.1365-246X.2003.02001.x.

Cavalié, O., C. Lasserre, M.-P. Doin, G. Peltzer, J. Sun, X. Xu, and Z.-K. Shen (2008), Measurement of interseismic strain across the Haiyuan fault (Gansu, China), by InSAR, *Earth Planet. Sci. Lett.*, *275*(3–4), 246–257, doi:10.1016/j.epsl.2008.07.057.

Cetin, E., Z. Cakir, M. Meghraoui, S. Ergintav, and A. M. Akoglu (2014), Extent and distribution of aseismic slip on the Ismetpaşa segment of the North Anatolian fault (Turkey) from persistent scatterer InSAR, *Geochem. Geophys. Geosyst.*, *15*, 2883–2894, doi:10.1002/2014GC005307.

Champenois, J., B. Fruneau, E. Pathier, B. Deffontaines, K.-C. Lin, and J.-C. Hu (2012), Monitoring of active tectonic deformations in the Longitudinal Valley (Eastern Taiwan) using persistent scatterer InSAR method with ALOS PALSAR data, *Earth Planet. Sci. Lett.*, *337–338*, 144–155, doi:10.1016/j.epsl.2012.05.025.

Chang, S.-H., J.-P. Avouac, S. Barbot, and J.-C. Lee (2013), Spatially variable fault friction derived from dynamic modeling of aseismic afterslip due to the 2004 Parkfield earthquake, *J. Geophys. Res. Solid Earth*, *118*, 3431–3447, doi:10.1002/jgrb.50231.

Chaussard, E., F. Amelung, H. Abidin, and S.-H. Hong (2013), Sinking cities in Indonesia: ALOS PALSAR detects rapid subsidence due to groundwater and gas extraction, *Remote Sens. Environ.*, *128*, 150–161, doi:10.1016/j.rse.2012.10.015.

Chaussard, E., R. Bürgmann, H. Fattahi, C. W. Johnson, R. Nadeau, T. Taira, and I. Johanson (2015a), Interseismic coupling and refined earthquake potential on the Hayward-Calaveras fault zone, *J. Geophys. Res. Solid Earth*, *120*, 8570–8590, doi:10.1002/2015JB012230.

Chaussard, E., R. Bürgmann, H. Fattahi, R. M. Nadeau, T. Taira, C. W. Johnson, and I. Johanson (2015b), Potential for larger earthquakes in the East San Francisco Bay Area due to the direct connection between the Hayward and Calaveras faults, *Geophys. Res. Lett.*, *42*, 2734–2741, doi:10.1002/2015GL063575.

Clark, S. A., C. A. Zelt, M. B. Magnani, and A. Levander (2008), Characterizing the Caribbean-South American plate boundary at 64°W using wide-angle seismic data, *J. Geophys. Res.*, *113*, B07401, doi:10.1029/2007JB005329.

D'Amore, F., G. Gianelli, and E. Corazza (1994), The geothermal area of El Pilar-Casanay, state of sucre, Venezuela. Geochemical exploration and model, *Geothermics*, *23*(3), 283–304, doi:10.1016/0375-6505(94)90005-1.

de Juana, C. G., J. M. I. de Arozena, and X. P. Cadillat (1980), *Geología de Venezuela y de sus Cuencas Petrolíferas*, Foninves, Venezuela.

DeMets, C., R. G. Gordon, and D. F. Argus (2010), Geologically current plate motions, *Geophys. J. Int.*, *181*(1), 1–80, doi:10.1111/j.1365-246X.2009.04491.x.

Diao, F., X. Xiong, R. Wang, Y. Zheng, and H. Hsu (2010), Slip model of the 2008 M_w 7.9 Wenchuan (China) earthquake derived from co-seismic GPS data, *Earth Planets Space*, *62*, 869–874, doi:10.5047/eps.2009.05.003.

Diao, F., X. Xiong, and R. Wang (2011), Mechanisms of transient postseismic deformation following the 2001 M_w 7.8 Kunlun (China) earthquake, *Pure Appl. Geophys.*, *168*, 767–779, doi:10.1007/s00024-010-0154-5.

Dieterich, J. H. (1979), Modeling of rock friction: 1. Experimental results and constitutive equations, *J. Geophys. Res.*, *84*(B5), 2161–2168, doi:10.1029/JB084iB05p02161.

Doin, M. P., C. Lasserre, G. Peltzer, O. Cavalié, and C. Doubre (2009), Corrections of stratified tropospheric delays in SAR interferometry: Validation with global atmospheric models, *J. Appl. Geophys.*, *69*(1), 35–50, doi:10.1016/j.jappgeo.2009.03.010.

Doin, M. P., F. Lodge, S. Guillaso, R. Jolivet, C. Lasserre, G. Ducret, R. Grandin, E. Pathier, and V. Pinel (2011), Presentation of the small baseline NSBAS processing chain on a case example: The Etna deformation monitoring from 2003 to 2010 using ENVISAT data, in *Proceedings of the Fringe symposium, Frascati, Italy, ESA SP-697*.

Doin, M.-P., C. Twardzik, G. Ducret, C. Lasserre, S. Guillaso, and S. Jianbao (2015), InSAR measurement of the deformation around Siling Co Lake: Inferences on the lower crust viscosity in central Tibet, *J. Geophys. Res. Solid Earth*, *120*, 5290–5310, doi:10.1002/2014JB011768.

Ducret, G., M.-P. Doin, R. Grandin, C. Lasserre, and S. Guillaso (2014), DEM corrections before unwrapping in a small baseline strategy for InSAR time series analysis, *IEEE Geosci. Remote Sens. Lett.*, *11*(3), 696–700, doi:10.1109/LGRS.2013.2276040.

Fajardo, A. (2015), Neotectonic evolution of the Serrania Del Interior range and Monagas fold and thrust belt, Eastern Venezuela: Morphotectonics, seismic profiles analyses and paleomagnetism, PhD thesis, Université de Pau et des Pays de l'Adour, France.

FUNVISIS (1994), Estudio neotectonico y de geologia de fallas activas de la region Nororiental de Venezuela, Proyecto Intevep, Technical report.

FUNVISIS (2010), Reporte de mecanismo focal obtenido con información de polaridad para primera llegad -onda P-, determinada en cada estación sismológica involucrada en el analisis, Technical online report. [Available at http://www.funvisis.gob.ve/mecanismos_focales.php?pag=4.]

Goldstein, R., H. Zebker, and C. Werner (1988), Satellite radar interferometry—Two-dimensional phase unwrapping, *Radio Sci.*, *23*(4), 713–720, doi:10.1029/RS023i004p00713.

Grandin, R., M.-P. Doin, L. Bollinger, B. Pinel-Puysségur, G. Ducret, R. Jolivet, and S. N. Sapkota (2012), Long-term growth of the Himalaya inferred from interseismic InSAR measurement, *Geology*, *40*(12), 1059–1062, doi:10.1130/G33154.1.

Gratier, J.-P. (2011), Fault permeability and strength evolution related to fracturing and healing episodic processes (years to millennia): The role of pressure solution, *Oil Gas Sci. Technol. Rev. D'IFP Energy Nouv.*, *66*(3), 491–506, doi:10.2516/ogst/2010014.

Gratier, J.-P., J. Richard, F. Renard, S. Mittempergher, M.-L. Doan, G. D. Toro, J. Hadizadeh, and A.-M. Boullier (2011), Aseismic sliding of active faults by pressure solution creep: Evidence from the San Andreas fault observatory at depth, *Geology*, *39*(12), 1131–1134, doi:10.1130/G32073.1.

Hackley, P. C., F. Urbani, A. W. Karlsen, and C. P. Garrity (2005), Geologic shaded relief map of Venezuela, U.S. Geological Survey Open File Report, 1038.

Hernandez, G., T. Rossi, J. Stephan, and R. Blanchet (1987), Etude géologique de la Serrania del Interior Oriental (Venezuela) sur le transect Cariaco-Maturin, *Rev. Inst. Fr. Pétrole*, *42*(1), 3–30.

Hussain, E., T. J. Wright, R. J. Walters, D. Bekaert, A. Hooper, and G. A. Houseman (2016), Geodetic observations of postseismic creep in the decade after the 1999 Izmit earthquake, Turkey: Implications for a shallow slip deficit, *J. Geophys. Res. Solid Earth*, *121*, 2980–3001, doi:10.1002/2015JB012737.

International Seismological Centre (2013), *On-line Bulletin*, Int. Seis. Cent, Thatcham, U. K.

Jacome, M., N. Kusznir, and S. Flint (1999), Structural and isostatic modelling of Serranía del Interior thrust belt and Monagas foreland basin: Eastern Venezuela, in *Fourth International Symposium on Andean Geodynamics Göttingen* (*Germany*), *Oct*, pp. 4–6.

Jolivet, R., R. Grandin, C. Lasserre, M.-P. Doin, and G. Peltzer (2011), Systematic InSAR tropospheric phase delay corrections from global meteorological reanalysis data, *Geophys. Res. Lett.*, *38*, L17311, doi:10.1029/2011GL048757.

Jolivet, R., C. Lasserre, M.-P. Doin, S. Guillaso, G. Peltzer, R. Dailu, J. Sun, Z.-K. Shen, and X. Xu (2012), Shallow creep on the Haiyuan fault (Gansu, China) revealed by SAR interferometry, *J. Geophys. Res.*, *117*, B06401, doi:10.1029/2011JB008732.

Jolivet, R., C. Lasserre, M.-P. Doin, G. Peltzer, J.-P. Avouac, J. Sun, and R. Dailu (2013), Spatio-temporal evolution of aseismic slip along the Haiyuan fault, China: Implications for fault frictional properties, *Earth Planet. Sci. Lett.*, *377–378*, 23–33, doi:10.1016/j.epsl.2013.07.020.

Jolivet, R., M. Simons, P. S. Agram, Z. Duputel, and Z.-K. Shen (2015a), Aseismic slip and seismogenic coupling along the central San Andreas fault, *Geophys. Res. Lett.*, *42*, 297–306, doi:10.1002/2014GL062222.

Jolivet, R., T. Candela, C. Lasserre, F. Renard, Y. Klinger, and M.-P. Doin (2015b), The burst-like behavior of aseismic slip on a rough fault: The creeping section of the Haiyuan fault, China, *Bull. Seismol. Soc. Am.*, *105*(1), 480–488, doi:10.1785/0120140237.

Jouanne, F., F. A. Audemard, C. Beck, A. Van Welden, R. Ollarves, and C. Reinoza (2011), Present-day deformation along the El Pilar fault in eastern Venezuela: Evidence of creep along a major transform boundary, *J. Geodyn.*, *51*(5), 398–410, doi:10.1016/j.jog.2010.11.003.

Kaneko, Y., Y. Fialko, D. T. Sandwell, X. Tong, and M. Furuya (2013), Interseismic deformation and creep along the central section of the North Anatolian fault (Turkey): InSAR observations and implications for rate-and-state friction properties, *J. Geophys. Res. Solid Earth*, *118*, 316–331, doi:10.1029/2012JB009661.

Khoshmanesh, M., M. Shirzaei, and R. M. Nadeau (2015), Time-dependent model of aseismic slip on the central San Andreas fault from InSAR time series and repeating earthquakes, *J. Geophys. Res. Solid Earth*, *120*, 6658–6679, doi:10.1002/2015JB012039.

Kim, J.-W., Z. Lu, H. Lee, C. K. Shum, C. M. Swarzenski, T. W. Doyle, and S.-H. Baek (2009), Integrated analysis of PALSAR/Radarsat-1 InSAR and ENVISAT altimeter data for mapping of absolute water level changes in Louisiana wetlands, *Remote Sens. Environ.*, *113*(11), 2356–2365, doi:10.1016/j.rse.2009.06.014.

Larson, K. M., A. R. Lowry, V. Kostoglodov, W. Hutton, O. Sánchez, K. Hudnut, and G. Suárez (2004), Crustal deformation measurements in Guerrero, Mexico, *J. Geophys. Res.*, *109*, B04409, doi:10.1029/2003JB002843.

Leonard, M. (2010), Earthquake fault scaling: Self-consistent relating of rupture length, width, average displacement, and moment release, *Bull. Seismol. Soc. Am.*, *100*(5A), 1971–1988, doi:10.1785/0120090189.

Levenberg, K. (1944), A method for the solution of certain problems in least squares, *Q. Appl. Math.*, *2*, 164–168.

Lienkaemper, J. J., J. S. Galehouse, and R. W. Simpson (1997), Creep response of the Hayward fault to stress changes caused by the Loma Prieta earthquake, *Science*, *276*(5321), 2014–2016, doi:10.1126/science.276.5321.2014.

Lindsey, E. O., Y. Fialko, Y. Bock, D. T. Sandwell, and R. Bilham (2014), Localized and distributed creep along the southern San Andreas fault, *J. Geophys. Res. Solid Earth*, *119*, 7909–7922, doi:10.1002/2014JB011275.

López, L. V. H. (2013), Hidrogeoquímica de aguas termales de las zonas de El Pilar y Los Ipures, Estado Sucre, Venezuela, Thesis de grado de Licencia, Universidad de Oriente Núcleo de Sucre., 31 January.

López-Quiroz, P., M.-P. Doin, F. Tupin, P. Briole, and J.-M. Nicolas (2009), Time series analysis of Mexico City subsidence constrained by radar interferometry, *J. Appl. Geophys.*, *69*(1), 1–15, doi:10.1016/j.jappgeo.2009.02.006.

Marone, C. J., C. H. Scholtz, and R. Bilham (1991), On the mechanics of earthquake afterslip, *J. Geophys. Res.*, *96*(B5), 8441–8452, doi:10.1029/91JB00275.

Marquardt, D. (1963), An algorithm for least-squares estimation of nonlinear parameters, *J. Soc. Ind. Appl. Math.*, *11*(2), 431–441, doi:10.1137/0111030.

Metz, H. L. (1965), Geology of the El Pilar fault zone state of Sucre, Venezuela, in *IV Caribbean Geological Conference*, pp. 293–298, Mobil Oil Company, Trinidad.

Milliner, C. W. D., C. Sammis, A. A. Allam, J. F. Dolan, J. Hollingsworth, S. Leprince, and F. Ayoub (2016), Resolving fine-scale heterogeneity of co-seismic slip and the relation to fault structure, *Sci. Rep.*, *6*, 27201, doi:10.1038/srep27201.

Moore, D. E., and D. A. Lockner (2013), Chemical controls on fault behavior: Weakening of serpentinite sheared against quartz-bearing rocks and its significance for fault creep in the San Andreas system, *J. Geophys. Res. Solid Earth*, *118*, 2558–2570, doi:10.1002/jgrb.50140.

Motagh, M., R. Wang, T. R. Walter, R. Buergmann, E. Fielding, J. Anderssohn, and J. Zschau (2008), Coseismic slip model of the 2007 August Pisco earthquake (Peru) as constrained by wide swath radar observations, *Geophys. J. Int.*, *174*(3), 842–848, doi:10.1111/j.1365-246X.2008.03852.x.

Motagh, M., B. Schurr, J. Anderssohn, B. Cailleau, T. R. Walter, R. Wang, and J.-P. Villotte (2010), Subduction earthquake deformation associated with 14 November 2007, M_w 7.8 Tocopilla earthquake in Chile: Results from InSAR and aftershocks, *Tectonophysics*, *490*(1–2), 60–68, doi:10.1016/j.tecto.2010.04.033.

Murray, J. R., and P. Segall (2005), Spatiotemporal evolution of a transient slip event on the San Andreas fault near Parkfield, California, *J. Geophys. Res.*, *110*, B09407, doi:10.1029/2005JB003651.

Nadeau, R. M., and T. V. McEvilly (2004), Periodic pulsing of characteristic microearthquakes on the San Andreas fault, *Science*, *303*(5655), 220–222.

Noda, H., and N. Lapusta (2013), Stable creeping fault segments can become destructive as a result of dynamic weakening, *Nature*, *493*(7433), 518–521, doi:10.1038/nature11703.

Okada, Y. (1985), Surface deformation due to shear and tensile faults in a half-space, *Bull. Seismol. Soc. Am.*, *75*(4), 1135–1154.

Pérez, O. J. (1998), Seismological report on the M_w = 6.8 strong shock of 9 July 1997 in Cariaco, northeastern Venezuela, *Bull. Seismol. Soc. Am.*, *88*(3), 874–879.

Pérez, O. J., and Y. P. Aggarwal (1981), Present-day tectonics of the southeastern Caribbean and northeastern Venezuela, *J. Geophys. Res.*, *86*(B11), 10,791–10,804, doi:10.1029/JB086iB11p10791.

Pérez, O. J., R. Bilham, R. Bendick, J. R. Velandia, N. Hernández, C. Moncayo, M. Hoyer, and M. Kozuch (2001), Velocity field across the southern Caribbean plate boundary and estimates of Caribbean/South-American plate motion using GPS geodesy 1994–2000, *Geophys. Res. Lett.*, *28*(15), 2987–2990, doi:10.1029/2001GL013183.

Pindell, J., L. Kennan, G. Draper, W. Maresch, and K. Stanek (2006), Foundations of Gulf of Mexico and Caribbean evolution: Eight controversies resolved, *Geol. Acta Int. Earth Sci. J.*, *4*(1), 303–341.

Rabus, B., M. Eineder, A. Roth, and R. Bamler (2003), The Shuttle Radar Topography Mission—A new class of digital elevation models acquired by spaceborne radar, *ISPRS J. Photogramm. Remote Sens.*, *57*(4), 241–262, doi:10.1016/S0924-2716(02)00124-7.

Radiguet, M., H. Perfettini, N. Cotte, A. Gualandi, B. Valette, V. Kostoglodov, T. Lhomme, A. Walpersdorf, E. Cabral Cano, and M. Campillo (2016), Triggering of the 2014 M_w7.3 Papanoa earthquake by a slow slip event in Guerrero, Mexico, *Nat. Geosci.*, doi:10.1038/ngeo2817.

Reinoza, C. E. (2014), Application de la géodésie satellitaire GNSS à haute résolution à la déformation de la marge Sud-Caraïbe. Implication pour l'aléa sismique dans l'Ouest et le Nord-Est du Venezuela., PhD thesis, Université Joseph Fourier/Université de Savoie Mont-Blanc, Chambéry, 15 December.

Reinoza, C. E., F. Jouanne, F. Audemard, M. Schmitz, and C. Beck (2015), Geodetic exploration of strain along the El Pilar fault in northeastern Venezuela, *J. Geophys. Res. Solid Earth*, *120*, 1993–2013, doi:10.1002/2014JB011483.

Richard, J., J.-P. Gratier, M.-L. Doan, A.-M. Boullier, and F. Renard (2014), Rock and mineral transformations in a fault zone leading to permanent creep: Interactions between brittle and viscous mechanisms in the San Andreas fault, *J. Geophys. Res. Solid Earth*, *119*, 8132–8153, doi:10.1002/2014JB011489.

Rosen, P. A., S. Hensley, G. Peltzer, and M. Simons (2004), Updated repeat orbit interferometry package released, *Eos Trans. Am. Geophys. Union*, *85*(5), 47–47, doi:10.1029/2004EO050004.

Rousset, B., R. Jolivet, M. Simons, C. Lasserre, B. Riel, P. Milillo, Z. Çakir, and F. Renard (2016), An aseismic slip transient on the North Anatolian fault, *Geophys. Res. Lett.*, *43*, 3254–3262, doi:10.1002/2016GL068250.

Ruina, A. (1983), Slip instability and state variable friction laws, *J. Geophys. Res.*, *88*(B12), 10,359–10,370, doi:10.1029/JB088iB12p10359.

Ryan, W. B. F., et al. (2009), Global multi-resolution topography synthesis, *Geochem. Geophys. Geosyst.*, *10*, Q03014, doi:10.1029/2008GC002332.

Ryder, I., and R. Bürgmann (2008), Spatial variations in slip deficit on the central San Andreas fault from InSAR, *Geophys. J. Int.*, *175*(3), 837–852, doi:10.1111/j.1365-246X.2008.03938.x.

Schmidt, D. A., R. Bürgmann, R. M. Nadeau, and M. d'Alessio (2005), Distribution of aseismic slip rate on the Hayward fault inferred from seismic and geodetic data, *J. Geophys. Res.*, *110*, B08406, doi:10.1029/2004JB003397.

Scholz, C. H. (1998), Earthquakes and friction laws, *Nature*, *391*(6662), 37–42, doi:10.1038/34097.

Scuderi, M. M., B. M. Carpenter, P. A. Johnson, and C. Marone (2015), Poromechanics of stick-slip frictional sliding and strength recovery on tectonic faults, *J. Geophys. Res. Solid Earth*, *120*, 6895–6912, doi:10.1002/2015JB011983.

Shirzaei, M., and R. Bürgmann (2013), Time-dependent model of creep on the Hayward fault from joint inversion of 18 years of InSAR and surface creep data, *J. Geophys. Res. Solid Earth*, *118*, 1733–1746, doi:10.1002/jgrb.50149.

Shirzaei, M., R. Bürgmann, and T. Taira (2013), Implications of recent asperity failures and aseismic creep for time-dependent earthquake hazard on the Hayward fault, *Earth Planet. Sci. Lett.*, *371–372*, 59–66, doi:10.1016/j.epsl.2013.04.024.

Taira, T., R. Bürgmann, R. M. Nadeau, and D. S. Dreger (2014), Variability of fault slip behavior along the San Andreas fault in the San Juan Bautista Region, *J. Geophys. Res. Solid Earth*, *119*, 8827–8844, doi:10.1002/2014JB011427.

Thatcher, W. (1979), Systematic inversion of geodetic data in central California, *J. Geophys. Res.*, *84*(B5), 2283–2295, doi:10.1029/JB084iB05p02283.

Thomas, M. Y., J.-P. Avouac, J.-P. Gratier, and J.-C. Lee (2014a), Lithological control on the deformation mechanism and the mode of fault slip on the Longitudinal Valley fault, Taiwan, *Tectonophysics*, *632*, 48–63, doi:10.1016/j.tecto.2014.05.038.

Thomas, M. Y., J.-P. Avouac, J. Champenois, J.-C. Lee, and L.-C. Kuo (2014b), Spatio-temporal evolution of seismic and aseismic slip on the Longitudinal Valley fault, Taiwan, *J. Geophys. Res. Solid Earth*, *119*, 5114–5139, doi:10.1002/2013JB010603.

Turner, R. C., M. Shirzaei, R. M. Nadeau, and R. Bürgmann (2015), Slow and Go: Pulsing slip rates on the creeping section of the San Andreas fault, *J. Geophys. Res. Solid Earth*, *120*, 5940–5951, doi:10.1002/2015JB011998.

Urbani, F. (1989), Geothermal reconnaissance of northeastern Venezuela, *Geothermics*, *18*(3), 403–427, doi:10.1016/0375-6505(89)90066-7.

Van Daele, M., et al. (2011), Reconstruction of Late-Quaternary sea- and lake-level changes in a tectonically active marginal basin using seismic stratigraphy: The Gulf of Cariaco, NE Venezuela, *Mar. Geol.*, *279*(1–4), 37–51, doi:10.1016/j.margeo.2010.10.011.

Vierbuchen, R. (1984), The geology of the El-Pilar fault zone and adjacent areas in northeastern Venezuela, *Geol. Soc. Am. Mem.*, *162*, 189–212.

Vignali, M. (1977), Geology between Casanay and El Pilar (El Pilar fault zone), Estado Sucre, Venezuela, in *VIIIth Caribb. Geol. Conf., Curaçao*, pp. 215–216.

Wang, L., R. Wang, F. Roth, B. Enescu, S. Hainzl, and S. Ergintav (2009), Afterslip and viscoelastic relaxation following the 1999 *M* 7.4 İzmit earthquake from GPS measurements, *Geophys. J. Int.*, *178*(3), 1220–1237, doi:10.1111/j.1365-246X.2009.04228.x.

Wang, R., F. Diao, and A. Hoechner (2013a), SDM—A geodetic inversion code incorporating with layered crust structure and curved fault geometry, in *EGU General Assembly Conference Abstracts*, vol. 15, p. EGU2013.

Wang, R., S. Parolai, M. Ge, M. Jin, T. R. Walter, and J. Zschau (2013b), The 2011 M_w 9.0 Tohoku earthquake: Comparison of GPS and strong-motion data, *Bull. Seismol. Soc. Am.*, *103*, 1336–1347, doi:10.1785/0120110264.

Weber, J. C., T. H. Dixon, C. DeMets, W. B. Ambeh, P. Jansma, G. Mattioli, J. Saleh, G. Sella, R. Bilham, and O. Pérez (2001), GPS estimate of relative motion between the Caribbean and South American plates, and geologic implications for Trinidad and Venezuela, *Geology*, *29*(1), 75–78, doi:10.1130/0091-7613(2001)029<0075:GEORMB>2.0.CO;2.

Weber, J. C., H. Geirsson, J. L. Latchman, K. Shaw, P. La Femina, S. Wdowinski, M. Higgins, C. Churches, and E. Norabuena (2015), Tectonic inversion in the Caribbean-South American plate boundary: GPS geodesy, seismology, and tectonics of the M-w 6.7 22 April 1997 Tobago earthquake, *Tectonics*, *34*, 1181–1194, doi:10.1002/2014TC003665.

Wei, M., and D. T. Sandwell (2010), Decorrelation of L-Band and C-Band interferometry over vegetated areas in California, *IEEE Trans. Geosci. Remote Sens.*, *48*(7), 2942–2952, doi:10.1109/TGRS.2010.2043442.

Wei, M., D. Sandwell, and Y. Fialko (2009), A silent M_w 4.7 slip event of October 2006 on the Superstition Hills fault, southern California, *J. Geophys. Res.*, *114*, B07402, doi:10.1029/2008JB006135.

Wei, M., Y. Kaneko, Y. Liu, and J. J. McGuire (2013), Episodic fault creep events in California controlled by shallow frictional heterogeneity, *Nat. Geosci.*, *6*(7), 566–570, doi:10.1038/ngeo1835.

Xu, C., Y. Liu, Y. Wen, and R. Wang (2010), Coseismic slip distribution of the 2008 M_w 7.9 Wenchuan earthquake from joint inversion of GPS and InSAR data, *Bull. Seismol. Soc. Am.*, *100*(5B), 2736–2749, doi:10.1785/0120090253.

Zinke, R., J. Hollingsworth, and J. F. Dolan (2014), Surface slip and off-fault deformation patterns in the 2013 M_w 7.7 Balochistan, Pakistan earthquake: Implications for controls on the distribution of near-surface coseismic slip, *Geochem. Geophys. Geosyst.*, *15*, 5034–5050, doi:10.1002/2014GC005538.

Zweck, C., J. T. Freymueller, and S. C. Cohen (2002), Three-dimensional elastic dislocation modeling of the postseismic response to the 1964 Alaska earthquake, *J. Geophys. Res.*, *107*(B4), 2064, doi:10.1029/2001JB000409.

[pdf-6] Maubant*, Pathier et al. 2020

The following pages reproduce the paper from Maubant et al. (2020)

Independent Component Analysis and Parametric Approach for Source Separation in InSAR Time Series at Regional Scale: Application to the 2017–2018 Slow Slip Event in Guerrero (Mexico).

Maubant, L., Pathier, E., Daout, S., Radiguet, M., Doin, M. -P., Kazachkina, E.,

Kostoglodov, V., Cotte, N., & Walpersdorf, A.

Published in 2020 in Journal of Geophysical Research: Solid Earth, 125(3).

https://doi.org/10.1029/2019JB018187

* Louise Maubant did this work during her PhD at ISTerre, that I'm supervising with Mathilde Radiguet.

JGR Solid Earth

RESEARCH ARTICLE
10.1029/2019JB018187

Key Points:
- Two multitemporal Sentinel-1 time series were constructed over the 2017–2018 SSE in the Guerrero area
- The atmospheric delays were analyzed and compared with weather models and GNSS Zenithal delay
- The SSE signal was separated from atmospheric noise using ICA and parametric approaches

Supporting Information:
- Supporting Information S1

Correspondence to:
L. Maubant,
louise.maubant@univ-grenoble-alpes.fr

Citation:
Maubant, L., Pathier, E., Daout, S., Radiguet, M., Doin, M.-P., Kazachkina, E., et al. (2020). Independent component analysis and parametric approach for source separation in InSAR time series at regional scale: Application to the 2017–2018 slow slip event in Guerrero (Mexico). *Journal of Geophysical Research: Solid Earth*, *125*, e2019JB018187. https://doi.org/10.1029/2019JB018187

Received 12 JUN 2019
Accepted 28 FEB 2020
Accepted article online 3 MAR 2020

Independent Component Analysis and Parametric Approach for Source Separation in InSAR Time Series at Regional Scale: Application to the 2017–2018 Slow Slip Event in Guerrero (Mexico)

L. Maubant[1], E. Pathier[1], S. Daout[2], M. Radiguet[1], M.-P. Doin[1], E. Kazachkina[3], V. Kostoglodov[3], N. Cotte[1], and A. Walpersdorf[1]

[1]Université Grenoble Alpes, Université Savoie Mont Blanc, CNRS, IRD, IFSTTAR, ISTerre, Grenoble, France, [2]COMET, Department of Earth Sciences, University of Oxford, Oxford, UK, Institute of Geophysics,[3]National Autonomous University of Mexico, Mexico City, Mexico

Abstract Separating different sources of signal in Interferometric Synthetic Aperture Radar (InSAR) studies over large areas is challenging, especially between the long-wavelength changes of atmospheric conditions and tectonic deformations, both correlated to elevation. In this study, we focus on the 2017–2018 slow slip event (SSE) in the Guerrero state (Mexico) where (1) the permanent GPS network has a low spatial density (less than 30 stations in an area of 300 × 300 km) with uneven distribution; (2) the tropospheric phase delays can be as high as 20 cm of apparent ground displacements, with a complex temporal evolution; (3) the tested global weather models fail to correct interferograms with enough accuracy (with residual tropospheric signal higher than the tectonic signal); and (4) the surface displacement caused by the seismic cycle shows complex interactions between seismic sequences and aseismic events. To extract the SSE signal from Sentinel-1 InSAR time series, we test two different approaches. The first (parametric method) consists of a least squares linear inversion, imposing a functional form for each deformation or atmospheric component. The second uses independent component analysis of the InSAR time series. We obtain time series maps of surface displacements along the radar line of sight associated with the SSE and validate these results with a comparison to GPS. Combining those two approaches, we propose a method to separate atmospheric delays and tectonic deformation on time series data not corrected from atmospheric delays. From the extracted ground deformation maps, we propose a first-order slip inversion model at the subduction interface during this SSE.

1. Introduction

At regional scale (typically larger than 250 km × 250 km), Interferometric Synthetic Aperture Radar (InSAR) is a powerful tool to get a spatially continuous measurement of the ground deformation through time with a high sensitivity to vertical displacements and without in situ measurements (e.g., Bürgmann, 2000; Simons & Rosen, 2015). It is a good complement to the temporally dense but spatially sparse measurements from regional Global Navigation Satellite Systems (GNSS) networks. These measurements allow the deformation to be observed during all stages of the seismic cycle (e.g., Elliott et al., 2016; Floyd et al., 2016; Mackenzie et al., 2016). In spite of large data set available from recent satellite constellations like the European Sentinel-1 constellation, which provides images with return periods of 6 to 12 days, extracting transient tectonics deformation from InSAR is still challenging at regional scale. Apart from unwrapping issues linked to high surface displacement gradient or phase decorrelation (e.g., Daout et al., 2017; Doin et al., 2015), the atmospheric contribution to InSAR signal is the main source of disturbance for ground deformation measurements (Zebker et al., 1997), especially in a large study area.

The atmospheric phase screen (APS) contained in InSAR data is a combination of ionospheric signal as well as tropospheric signal. The latter can be described as a turbulent component (randomly variable in time or space) and a stratified component correlated with the topography and coherent in time (with temporal

seasonal variations) (Cavalié et al., 2007; Doin et al., 2009; Hanssen, 2001). The tropospheric signal is the result of spatiotemporal variations of atmospheric pressure and water vapor concentration present in the atmosphere, which modify the air refractivity and thus induce a phase delay (Hanssen, 2001). The ionospheric signal depends on the radar wavelength and is less important in C-band than in L-band. However, significant ionospheric perturbations with long-wavelength signals have been identified in Sentinel-1 interferograms (Gomba et al., 2017). The APS can dominate the InSAR signal and mask the tectonic signal (Bekaert et al., 2015a; Daout et al., 2018; Doin et al., 2009; Jolivet et al., 2011).

Therefore, the separation of the tectonic signal from the atmospheric signal contributions in InSAR data is a key challenge, and several correction approaches have been proposed. Atmospheric perturbations can be estimated empirically (Béjar-Pizarro et al., 2017; Bekaert et al., 2015; Cavalié et al., 2008; Doin et al., 2009; Lin et al., 2010; Shirzaei & Bürgmann, 2012) by characterizing the relationship (linear or nonlinear) between the phase and the topography, or from atmospheric meteorological models (Doin et al., 2009; Jolivet et al., 2011, 2014; Yu et al., 2018). However, empirical estimation of tropospheric effects can be biased by deformation signal correlated to the topography, and global atmospheric model have limitations related to their poor spatial resolution and their uncertainties on water vapor content. Other approaches consist in using the estimations of atmospheric parameters from GPS network, like Zenithal Total Delay (ZTD) (Li et al., 2003; Williams et al., 1998) or multispectral satellite data (e.g., Li et al., 2006, 2005; Walters et al., 2013).

In addition to atmospheric delay perturbations, different sources of crustal deformation (coseismic, postseismic, and seasonal loadings) can be mixed in InSAR time series. To separate all these sources, one approach is to perform a parametric least squares regression on InSAR time series (e.g., Daout et al., 2019; Hetland et al., 2012), where the temporal evolution of each source is imposed, and its amplitude is inverted for. One important limitation arises when the temporal evolution of the source is unknown, which can be the case for atmospheric delays, seasonal loadings, or transient deformations. To overcome this problem, blind source separation approaches aim at unmixing signals without a priori information about the signal sources. Independent component analysis (ICA) (Comon, 1994; Hyvarinen & Oja, 1997; Stone, 2004) is a classical method for blind source separation. It has the advantage over the principal component analysis (PCA) to decompose the signal in a set of statistically independent components, which are more likely to represent independent sources. ICA has been used for GPS data analysis (Gualandi & Belardinelli, 2015; Gualandi et al., 2017) to decompose seasonal loading from other transient or earthquake signals. Recent studies have shown that ICA decomposition has been successful to analyze InSAR time series in small areas (Chaussard et al., 2017; Cohen-Waeber et al., 2018).

In this paper, we investigate different approaches to extract slow tectonic rates of surface displacements, including transient deformation, in a large-scale region where atmospheric signals are dominant. We first investigate the accuracy of global atmospheric models to correct InSAR time series. Second, we compare a parametric decomposition with an ICA approach to identify the signal of interest. We focus on the Guerrero area of the Mexican subduction zone, where large slow slip events (SSEs) occur regularly along the plate interface generating transient surface displacements at long-wavelength (hundreds of kilometers) and over several months duration. In section 2, we will present the study area and the SSEs characteristics. We then detail in section 3 the InSAR data used and the processing method to get InSAR time series for this region. In section 4, we present the parametric and ICA approaches for the decomposition of the InSAR time series, with or without correction from a global weather model. Finally, in section 5, we compare the different methods. We validate them by comparison with the GPS signal in the region and perform a first inversion of the SSE slip distribution on the plate interface.

2. Context of the Study of SSEs in the Mexican Subduction Zone Mexico

Continuous geodetic observations, especially GNSS, over the last two decades, have allowed to discover and characterize SSEs, which correspond to transient aseismic slip events of variable magnitudes, durations, and recurrence times. They have been identified in many subduction zones worldwide like Cascadia, New Zealand, and Japan (Beroza & Ide, 2011; Schwartz & Rokosky, 2007). These SSEs correspond to transient shear slip events that occur along the plate interface of subduction zone, generally in regions downdip or adjacent to the so-called locked patches, where large thrust earthquakes occur (e.g., Obara & Hirose, 2006; Rousset et al., 2017; Wallace et al., 2018). Associated with these SSEs activities tremors and low frequencies earthquakes have been detected, as it is the case for the Japan, Cascadia, Mexico, and the New Zealand

subduction zones (Bartlow et al., 2014; Frank et al., 2015; Husker et al., 2019; Obara & Hirose, 2006; Rogers & Dragert, 2003; Villafuerte & Cruz-Atienza, 2017). Precise assessment of the spatial extension of slip at depth during SSEs, as well as understanding the possible interactions between SSEs and seismic rupture is important for a better understanding of the impact of those events on the seismic cycle and remains an important challenge. Due to their sparsity and uneven distribution, GNSS stations are not always sufficient to correctly measure surface deformation associated with SSEs. InSAR measurements represent a complementary tool, which could enhance the spatial coverage of measurements (Bekaert et al., 2016). Since the launches of Sentinel-1 satellites, temporal recurrence of image acquisition (6 to 12 days) has greatly increased, and it thus became possible to investigate the temporal variations of transient signal with InSAR time series (e.g., Rousset et al., 2016).

Along the Mexican subduction zone, in the Guerrero region, long-term SSEs of equivalent magnitude around Mw 7.5, among the largest worldwide, occur with a recurrence time of about 4 years, with durations between 6 to 14 months (Kostoglodov et al., 2003; Radiguet et al., 2012). These SSEs produce surface displacements up to 5 cm on the horizontal (southward) and up to 3 cm on the vertical components (Radiguet et al., 2012) (Figure 1). The first event observed using GPS was in 1998 (Lowry et al., 2001), and since then successive SSEs have occurred in 2001–2002 (Kostoglodov et al., 2003; Larson et al., 2004), 2006 (Larson et al., 2007; Radiguet et al., 2011; Vergnolle et al., 2010), 2009–2010 (Walpersdorf et al., 2011), and 2014 (Gualandi et al., 2017; Radiguet et al., 2016). In this region, two types of interactions between SSE and earthquakes were previously observed. On one hand, the triggering of the 2010 SSE and associated tremors by a large distant earthquake (Maule Mw 8.8) has been suggested (Walpersdorf et al., 2011; Zigone et al., 2012). On the other hand, the spatiotemporal proximity between the 2014 SSE occurrence and the Mw 7.3 Papanoa earthquake hypocenter (UNAM Seismology Group, 2015) suggests the triggering of the thrust event by the ongoing SSE (Radiguet et al., 2016).

The last SSE of the region, which began in May 2017 and ended in June 2018, occurred during the period of intense seismic activity in the region. In September 2017, two large intraslab earthquakes take place, in Chiapas area (Mw 8.1, 07 September 2017) and in Puebla state (Mw 7.2, 19 September 2017) (Figure 1a) (Melgar, Pérez-Campos, et al., 2018; Melgar, Ruiz-Angulo, et al., 2018; Mirwald et al., 2019; Segou & Parsons, 2018; Suárez et al., 2019). In February 2018, an interface thrust earthquake occurred in Oaxaca state (Pinotepa earthquake, Mw 7.1, 16 February 2018). GPS observations in the region (Figure 1b) show a possible impact of the earthquake occurrence on the SSE evolution, as after the September 2017 seismic sequence, some GPS stations, like the TCPN station, show a change in slope corresponding to a deceleration of the SSE (Figure 1b).

In this study, we investigate the spatiotemporal characteristics of the 2017–2018 SSE in Guerrero, using InSAR in order to enhance the spatial coverage in this region where the GPS network is unevenly distributed causing data gaps like in the Tierra Caliente region (Figure 1a). Two previous studies analyzed the 2006 SSE with InSAR (Bekaert et al., 2015; Cavalié et al., 2013), the main difficulty in these studies was the correction of the atmospheric signal, with amplitudes up to 20 cm and partly controlled by two topographic barriers: the southern border of the Mexican Plateau and the Sierra Madre del Sur (Figure 1a). The second issue is that the long-wavelength SSE signal is correlated to the topography. The presence of vegetation is another difficulty, as it reduces the InSAR coherence.

3. InSAR Data and Processing

We use Sentinel-1 (ESA) TOPSAR data in interferometric wide-swath mode (swath width of about 250 km) between January 2016 and August 2018, with acquisitions separated by 6 days to 1.5 months. Two tracks have been processed (Figure 1a) spanning from the coast to the TMVB (Trans-Mexican Volcanic Belt), one 450 km long swath in ascending orbit (A078) and another 330 km long swath in descending orbit (D041). We choose not to process the data acquired before 2016 for two reasons. First, the time span between successive acquisitions was longer (24 days) before 2016 than after (12 days), resulting in poorer InSAR coherence. Second, the Papanoa earthquake (18 April 2014 Mw 7.3; Radiguet et al., 2016; UNAM Seismology Group, 2015) has a long postseismic signal (at least until the end of 2015) that complicates the time series analysis. For the ascending data, acquisitions are missing between 08 August and 25 September 2017, resulting in a data gap during the initial stage of the SSE before the Mw 8.1 and 7.2 earthquakes. We use, respectively, 90 and 67 acquisitions for the descending and ascending tracks to create a short baseline interferometric network

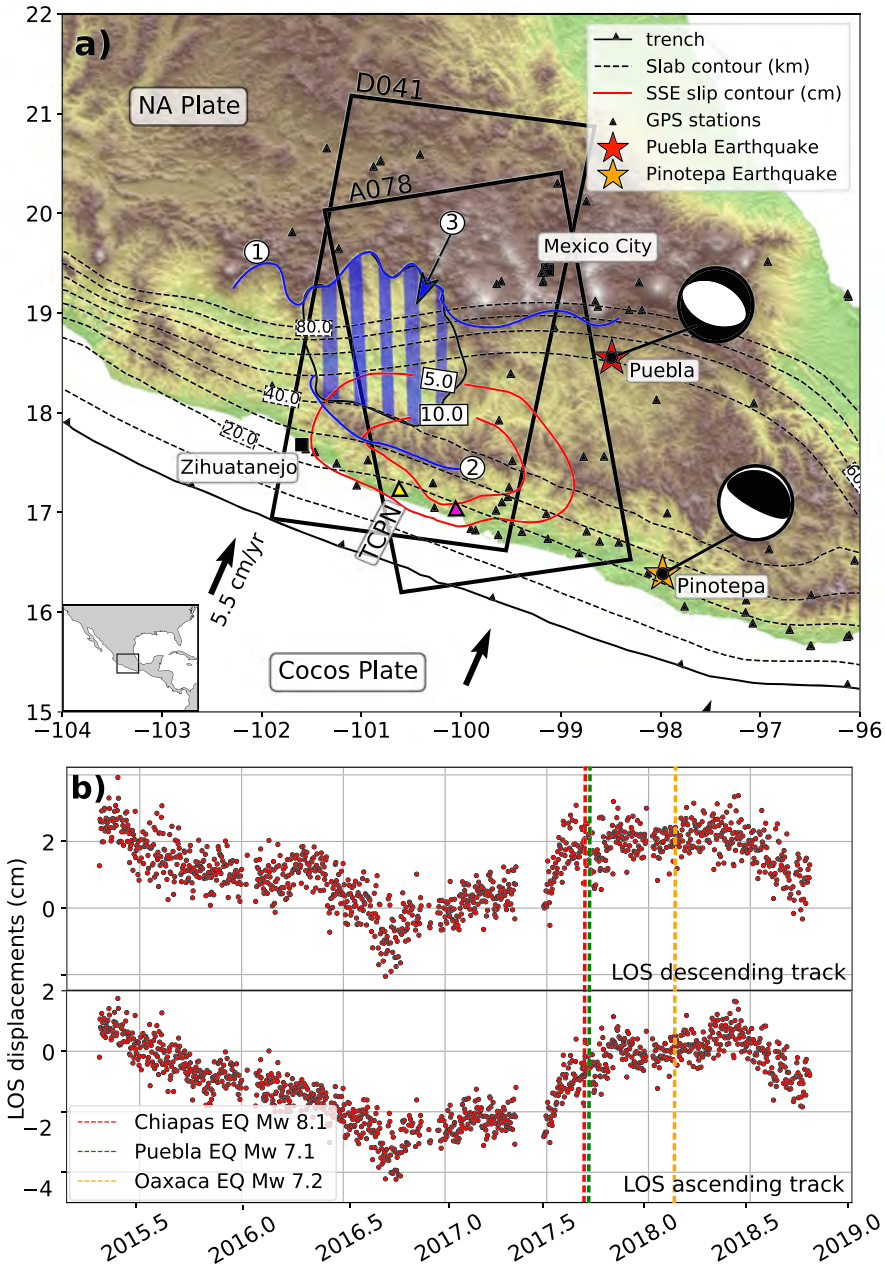

Figure 1. (a) Setting of the Mexican subduction zone around the Guerrero area and location of InSAR and GPS data coverage. The black rectangles represent the coverage of the two InSAR tracks processed in this study. The black arrows indicate the convergence velocities of the Cocos plate with respect to the North America Plate from the PVEL model (DeMets et al., 2010). The black line with triangles represents the Middle American Trench (MAT). Black dashed lines are isodepths (interval of 10 km) of the subduction interface. Red lines are the 5 and 10 cm slip contours of the average of the last three SSEs (2006, 2009–2010, and 2014) occurring on the subduction interface (Radiguet et al., 2012, 2016). The triangles represent the GPS stations (UNAM, IGF, SSN, and TLALOCNet), the yellow and pink filled triangles show the position of TCPN and CAYA GPS stations, respectively. The stars represent the epicenters of Puebla earthquake in red (17 September 2017) and of Pinotepa earthquake in orange (16 February 2018). The blue lines are the topographic barriers (1: Trans-Mexican Volcanic Belt (TMVB), 2: Sierra Madre del Sure (SMdS)). The hatched region (3) represents the Tierra Caliente depression. (b) Example of times series of surface displacements along two different radar lines of sight (top: for descending track D041, bottom for ascending track A078) reconstructed from a time series of TCPN GPS station (yellow triangle on map) between 2015 to October 2018. The timing of the three earthquakes are displaying by dashed vertical lines.

with, respectively, 624 and 431 selected pairs (Figure S1 in the supporting information). We invert those two networks into two independent time series (one for the descending track and one for the ascending), using the New Small Baselines Subset processing chain (Doin et al., 2011; Grandin, 2017), which is based on the ROI_PAC software (Rosen et al., 2004). We provide below some specifications of the data processing strategy.

Once the stack of coregistered interferograms is created (with a spatial resolution reduced by multilooking with two looks in range and eight looks in azimuth) and corrected using an implementation of the enhanced spectral diversity method (Grandin, 2015), the first challenge is to unwrap them. The difficulty arises from the combination of two effects: (1) low coherence in mountains and vegetated areas, especially during summer months and for long interferograms duration, and (2) narrow fringes due to strong atmospheric delays, particularly along steep topography relief. In order to facilitate unwrapping, we use four main procedures: (1) We select in priority the interferograms with better coherence than the average or with limited atmospheric patterns including a few 1 year apart winter-winter pairs (Figure S1), (2) we remove tropospheric delays correlated to the topography (Figure 1a) and spatial ramps before unwrapping, (3) we multilook to 16 looks in azimuth and 4 × 16 in range (620 m pixel spacing) and filter the interferograms (the filter is a weighted average of the gradient of the phase in sliding windows), and (4) we check possible unwrapping errors using network adjustment (López-Quiroz et al., 2009). For step (2) we first tested, for a few dates, the correction from ERA-Interim predictions (Doin et al., 2009; Jolivet et al., 2011). However, we decide to not use this correction because we noticed that for numerous corrected interferograms, the fringe gradient was not significantly decreased and sometimes even increased because of inaccuracy of ERA-Interim model. Instead, we estimate, on each wrapped interferogram, an empirical relation between the wrapped phase and the elevation (e.g., Doin et al., 2015; Grandin et al., 2012). To do that, we begin to search the local linear ratio in subwindows (15 km × 15 km) between the phase and the elevation. These ratios are fitted by the following equation:

$$\phi(z, y) = (a + b * y) * \frac{(z - z_{ref})^2}{2} + (c + d * y) * \frac{(z - z_{ref})^3}{3} \quad (1)$$

where ϕ is the interferometric phase a, b, c, and d are adjusted parameters evaluated by calculating the relation between the phase and the altitude, z is the local altitude, z_{ref} (8,000 m) is the altitude where we assume the convergence of phase delays, and y is the azimuth coordinate. Inconsistencies of parameters (a, b, c, and d) are detected and then reestimated by least squares network adjustment. Then equation (1) is used to correct interferograms with the reestimated parameters. Similarly, in order to flatten the interferogram before unwrapping as much as possible, a linear ramp in range and a quadratic ramp in azimuth are estimated on wrapped interferograms, inverted on the interferograms network, before being used to correct the interferograms.

In the Step 3, the corrected interferograms are multilooked and filtered with a weighting based on colinearity, a modified estimate of coherence, which does not take into account the radar backscatter (Pinel-Puysségur et al., 2012). In natural environment, variations of amplitudes are indeed uncorrelated with the variance of the phase, and it is, therefore, better to not take into account the amplitude as weighting in coherence measurements. We choose to apply a filter with a sliding window of 12 pixels, on which the complex phase is averaged taking into account the local phase gradient. Then the data are filtered and unwrapped as done by Doin et al. (2015). Unwrapping proceeds spatially with a path based on the coherence associated to the filtering step (Grandin et al., 2012). Some remaining unwrapping errors affecting large patches can be identified by visual checking and corrected by imposing the unwrapping path (López-Quiroz et al., 2009). Once unwrapped, we finally reintroduce all previously removed corrections (ramp and atmospheric) to each interferogram to reconstruct the full unwrapped phase signal. The purpose of these corrections was not to separate the source of the signals but to flatten the interferogram to help for unwrapping. Indeed, those corrections estimated on wrapped phase are possibly less accurate than those done on unwrapped phase and may contain some tectonic signals, which is why they are reintroduced. An estimation of the orbital ramps (linear in range and azimuth) is then applied on the less noisy and continuous unwrapped interferograms and adjusted to be consistent within the interferometric network before performing the time series analysis. The phase of the unwrapped interferograms is referenced with respect to a common area where we expect more phase stability, which is the northern part of the track covering the TMVB (see extent in Figure S3). Finally, interferograms are inverted into time series that allows us to detect corresponding remaining unwrapping errors in the interferometric network. If necessary, the processing is then iterated again from the unwrapping step by imposing by hand the right wrapping paths of faulty interferograms.

We construct a phase time series using the New Small Baselines Subset method (Doin et al., 2015; López-Quiroz et al., 2009) relative to the first date.

$$\phi_i = \phi_{def} + APS + \phi_{error} \quad (2)$$

The phase time series ϕ_i is a mix of contributions from surface displacement, ϕ_{def}, and from the atmosphere, APS, and ϕ_{error}, which contain the orbital errors and DEM errors; ϕ_{def} includes at least a linear term and transient term related to SSE. Once the time series is created, we estimate a spatial linear ramp per date as a function of azimuth and range for each acquisition epoch and set to 0 the average phase delay in the nondeforming area, helping to flatten and refer cumulative displacement maps to a common area. All these processes are done in radar geometry, before geocoding. The next challenge consists now in separating the atmospheric signal from tectonic deformation.

4. Signals Decomposition

Once the InSAR time series have been obtained, we intend to extract the tectonic signal despite the fact that the atmospheric contribution is dominant. We are looking for a method that can be applied in most of the active tectonic areas and at regional scale. We first investigate the benefit of using a global weather model to estimate the tropospheric contribution in the InSAR signal by comparing the prediction of existing global weather models to GPS-ZTD (Zenital Total Delay) data. At regional scale, it is rather common in active tectonic areas to have, at least, a few permanent GPS stations available from which time series of ZTD can be estimated. The comparison between global weather models and observed ZTD helps us to validate the model. Then, the objective is to see what is the gain for our source separation approaches of using tropospheric correction of InSAR time series based on global weather model or ZTD measurements. For this purpose, two different data sets are produced: InSAR time series corrected from a global weather model and InSAR time series without any tropospheric correction. On these two data sets we will test two different approaches of source separation: the parametric decomposition and the ICA.

4.1. Tropospheric Correction Using External Data

In a first step, we test the corrections of our time series using two global atmospheric models with different spatial resolutions: the ERA-Interim model (grid with spatial resolution of 0.75° and a time interval of 6 hr) and the HRES-ECMWF model interpolated by GACOS (Yu et al., 2018) with a grid resolution of 0.125 and a time interval of 6 hr). Note that these GACOS data were not including GPS measurements at the time we downloaded them from the GACOS website. The acquisition hour of our SAR data is similar to the calculation hour of the different models (00 hr for the ascending and 12 hr for the descending track). For simplicity, we hereafter refer to these models as ERA-I and GACOS. For each acquisition date, we map the vertical profiles predicted by ERA-I or GACOS along the radar line of sight (LOS) and compute the phase delay at each pixel elevation in radar geometry. In addition, we extract the ZTD obtained from the GPS stations located inside the footprint of the radar images, at the time of each SAR acquisitions. For each station, the values of the ZTD are reprojected in LOS. We will call these data reprojected GPS-TDL_{OS}. ZTD provide a direct estimate of the temporal evolution of the atmospheric effects in the region of interest, and can be compared with the temporal evolution of the two global weather models along the radar LOS.

For the 21 GPS stations considered in the descending track area, all the GPS-TDL_{OS} time series show similar temporal evolutions (Figure 2d). The dispersion depends mainly on the altitude and the latitude of the stations. To compare the temporal evolution of global weather models and of GPS-TDL_{OS}, we perform a PCA on all three data sets to extract the common signal. For GPS-TDL_{OS}, ERA-I, and GACOS models, the first principal component (PC1) accounts for 98%, 89%, and 88% of the data variance, respectively. The PC1 amplitude comparison is displayed in Figures 2a and 2b, whereas the temporal evolutions are shown in Figure 2c. The temporal evolution is coherent between the three PC1 (Figure 2c). The dominant signal in the InSAR time series is the tropospheric signal (Figure 2e). It is relative in time and space, and coherent with the topography, which makes it more difficult to extract and the global weather models seem to underestimate the amplitude of this signal. The amplitude and the sign of the tropospheric delays will therefore depend of the reference point. Concerning the amplitudes of PC1, both models show limitations in reproducing the amplitude of phase delay extracted from GPS-TDL_{OS} (Figures 2a, 2b, and S2c). ERA-Interim shows its main limitation at high altitude (higher than 1,800 m), on the Mexican Plateau, and close to the coast where the

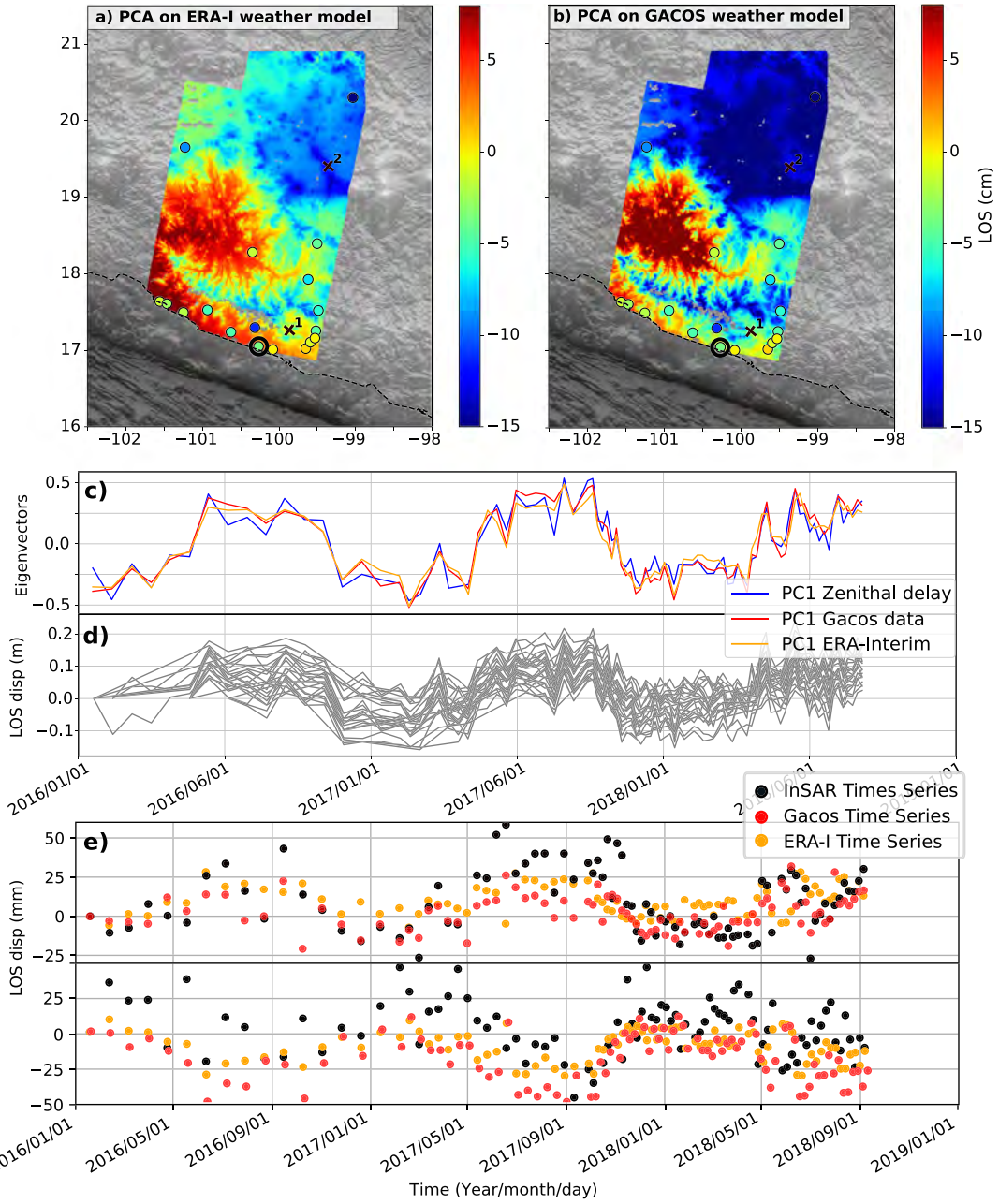

Figure 2. Comparison of LOS phase delay from global weather model and GPS-TDL_{OS} using PCA. (a) Amplitude map of the first component of the principal component decomposition of ERA-I delay maps in centimeters along LOS (referenced relative to the CAYA location, black circle); the colored circles represent the amplitude of the zenithal delay (convert along LOS of the satellite) relative to CAYA station in centimeters. Black crosses give locations of pixel for time series in plot e. (b) Same as (a) but for the GACOS delay maps. (c) The blue line is the temporal evolution of the first component of the TDL_{OS} from GPS data present in the footprint of the track, extracted with a PCA. Red: the first component of GACOS model. Orange: the first component of ERA-Interim. (d) Temporal evolution of GPS-TDL_{OS} for 21 stations located in the footprint of the InSAR tracks, relative to the first date. (e) In black, phase temporal evolution (mm) of two pixels of the InSAR time series (Crosses 1 and 2 in the plot a) referenced to the first date, and the comparison with GACOS (red dots) and ERA-I (orange dots) time series. Up: time series for pixel 1, located in the SSE area. Down: time series or Pixel 2, located in the Mexican Plateau, where the tectonic signal is expected to be smaller.

tectonic signal is expected (Figures 2a and S2a). The GACOS model seems to be able to reproduced better the spatial variability of the tropospheric delay (Figures 2b and S2b). Overall the GACOS model looks better than the ERA-I, in agreement with a previous study from Murray et al. (2019). Consequently, in the following, we will only test corrections of the InSAR time series with the GACOS model.

For the decompositions performed in the following part, we consider two data sets: the first one is the InSAR time series previously computed with equation (2), and corrected from spatial ramps, and the second one is the same time series but with an additional correction from the GACOS weather model.

4.2. Parametric Decomposition

In the Guerrero area, during the period 2016–2018, the surface deformation signal we would like to separate from tropospheric signal in our InSAR time series, mainly consists into an linear trend (called inter-SSE), and a slow-slip event (SSE) signal. To extract the inter-SSE long-wavelength surface displacement rate from our time series and the map of the first-order spatial pattern of the SSE, we perform a parametric decomposition of our time series. The temporal evolution of each component is imposed, and we invert the amplitude of each basis function. We decompose temporally the time series for each pixel, considering two tectonic contributions (inter-SSE and SSE), and an atmospheric signal (for the data set not corrected from GACOS). Based on the signal observed on GPS surface displacement time series (Kazachkina et al., 2018), we model a two phases SSE (one phase before the September 2017 earthquakes and a second after, see Figure 1b and section 2). Each pixel can thus be described as

$$\phi_{(t)} = a * t + b * APS(t) + \frac{C_1}{2}\left(tanh\left(\frac{t-T_1}{\tau_1}\right)+1\right) + \frac{C_2}{2}\left(tanh\left(\frac{t-T_2}{\tau_2}\right)+1\right) + d \quad (3)$$

where t is the time and a, b, C_1, C_2, and d correspond, respectively, to the amplitudes of the linear term, the seasonal tropospheric signal, the first and second phases of the SSE and a constant. To represent the seasonal tropospheric term $APS(t)$, we take the normalized eigenvector of the first principal component estimated from the GPS-TDL_{OS} time series (Figure 2c). This signal contains most of the temporal variations present on the tropospheric signal, as it explains 98% of the GPS-TDL_{OS}. For the data set that is already corrected from GACOS, we suppress the APS term in equation (3). Following Larson et al. (2004), the SSE is modeled with two tangent hyperbolic functions that represent the two phases of the event and allow to model the observe change in slope in the time series (Figure 1c). With this approach, we suppose that the beginning and the end of the SSE are the same for all pixels of the tracks, which means that there is no migration during one phase of the SSE. However, a migration can be taken into account by combining between two phases of the SSE. The temporal scaling (τ_1, τ_2) and median time (T_1, T_2) of the two phases are imposed based on observation of GPS time series in the region (Kazachkina et al., 2018). We determine the 2τ value from which 76% of the surface displacement is produced. We impose T_1 = 2,017.5 (1 July 2017), with τ_1 = 0.25 (3 months): Thus, the first phase began in May 2017 and finished in September 2017. For the second phase, we impose T_2 = 2018.1 and τ_2 = 0.3 (from the end of September 2017 to April 2018).

For each SSE phase, we obtain an amplitude map of the surface displacement (Figures S4 and S7), which we sum up to produce the cumulative map of the SSE amplitude (Figure 3, without GACOS correction, and Figure S3a, with GACOS correction). This amplitude modulates the temporal evolution associated to each function in equation (3), it must not be confused with the radar amplitude. Additionally, we obtain an amplitude map for the inter-SSE trend (Figure 3c) and the atmospheric signals (Figure S6b). We also calculate the residual map between the data and the parametric model (Figures 3b and 3d) using equation (4) to compute the residual for each pixel.

$$RMSE = \sqrt{\frac{\sum_{t=1}^{N}(\phi_{data}(t) - \phi_{model}(t))^2}{N}} \quad (4)$$

where N is the number of acquisition dates and ϕ_{model} is the result of the parametrized decomposition.

Let us first describe the amplitude map of the SSE for the descending track D041. As the horizontal displacements related to SSE in the Guerrero region are almost parallel to the descending track, InSAR measurements for D041 are expected to be mainly sensitive to the vertical displacement of the SSE. The amplitude map of the SSE (Figure 3) shows an uplift pattern well located on the Sierra Madre del Sur (Figure 1a) as well as a subsidence pattern north of this area, as already shown by previous studies (Bekaert et al., 2015; Cavalié et al., 2013). The maximum amplitude for the SSE is 4 cm for the two data sets

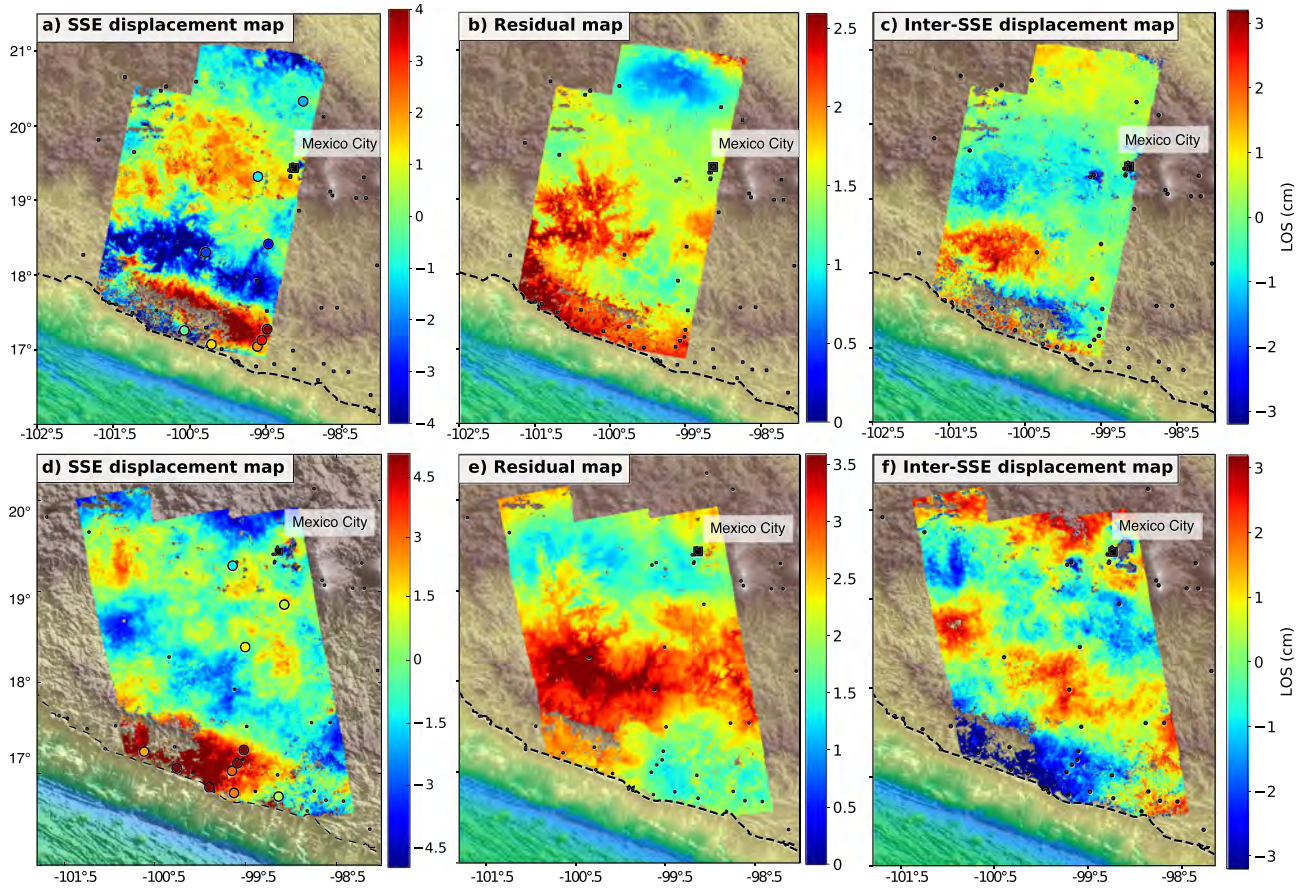

Figure 3. LOS surface displacement of the 2017–2018 SSE estimated from parametric method for descending (top row) and ascending (bottom row) tracks (without prior global weather model corrections). (a and d) Amplitude map of the SSE in centimeters along LOS calculated with the parametric method. Colored dot show the same amplitude but estimated from GPS displacements time series. (b and e) Residual map of the time series. (c and f) Inter-SSE displacement map. The small black points represent the location of GPS stations; the dashed line represents the coast limitation.

(not corrected or corrected with GACOS, Figures 3a and S3a). Regarding the residual maps associated with each data set (Figures 3b and S3b), we observe residuals that are reduced by 20% for the noncorrected data set compared with the data set corrected from GACOS, especially in areas where they are large variation of topography (e.g., bottom of the valleys and volcanoes), like in the Tierra Caliente region. This observation suggests that GACOS weather model is less efficient at capturing the seasonal signal than a parametric estimation of the atmospheric delay based on GPS-TDL_{OS} (APS term in equation (3)). Using GACOS correction and no parametrization of the atmospheric term introduces a larger dispersion of the residual time series induce and therefore a higher error in the estimation of the amplitude of the SSE. We obtain a better fit for the time series data set not corrected from global weather models and decomposed with the GPS-TDL_{OS} vector. We therefore apply this approach based on ZTD measurements for the ascending track, with results shown in Figures 3d and S6 and S7. For this track, we observe a spatial pattern similar to the descending track in the Sierra Madre del Sur (with a displacement toward satellite). In both tracks, the amplitude map of the inter-SSE term (Figures S6 and S8) is opposite to the SSE map. Although this result is expected in the Guerrero region where inter-SSE and SSE with surface displacement of opposite signs alternate (e.g., Cavalié et al., 2013), it is also observed in the northern part of the track, which suggests a trade-off between the SSE and inter-SSE parameters. This trade-off can be due to the fact that in our InSAR time series the main period without SSE is quite short (about 1 year before the SSE) and with less frequent data acquisitions than during the SSE period. We expect this trade-off to be reduced when longer InSAR time series will be processed in the future. The amplitude map of the GPS-TDL_{OS} term is clearly correlated to the topography (Figures S6 and S8). The comparison of the amplitude maps of the two phases of the SSE (Figures S4 and S7) suggests a possible migration toward the east of the event. Reconstruction of the temporal evolution

using these two terms (C_1 and C_2 in equation (3)) also suggests a migration of the event in the eastern part of Guerrero (Figure S5).

To conclude, in the Guerrero area, the parametric decomposition applied here is able to separate the first-order seasonal tropospheric signal from the inter-SSE trend and the SSE signal, with consistent results in ascending and descending tracks. It also provides uncertainties associated with each of these components. However, the main limitation is that this method depends on the imposed parameterization, which requires some a priori knowledge and assumptions. In this particular case, the SSE is parameterized using two subevents of fixed timing and duration. GPS observations suggest that timing and duration of the SSE have some variations depending on the GPS station location due to the SSE migration (Kazachkina et al., 2018), which can bias our parameterization. Moreover, with this approach, we are limited to analyzing transients of already known duration using independent measurements such as GPS. To go further a nonlinear exploration of the SSE timing could be implemented. In the following, we explore an ICA decomposition on the detrended time series of surface displacements.

4.3. ICA Decomposition

4.3.1. Method

The ICA method has the potential to overcome some of the limitations of the previous method, because as it allows the signal to be decomposed without any assumptions. The statistical independence is assumed by considering that each component has a non-Gaussian probability distribution and that the sum of each non-Gaussian component tends toward a Gaussian distribution (Hyvarinen et al., 2004). The InSAR data matrix X is assumed to be described by the following equation:

$$X_{(t*p)} = A_{(t*n)}.S_{(n*p)} \tag{5}$$

where A is the mixing matrix and S is the matrix of independents components, n is the number of independent components considered, p the number of pixels, and t the number of dates. We are performing here a temporal ICA, where we are searching for temporally independent sources as in Gualandi and Belardinelli (2015).

ICA algorithms are more effective on detrended data sets (Gualandi & Belardinelli, 2015). Removing a linear trend in the time series reduces the correlation between the different sources and improves the decomposition of the data. Although the removal of a temporal linear trend may help to separate the SSE signal from other sources, this term corresponds in our case to the inter-SSE signal and implies a prior estimation of it before the decomposition. To be consistent with the parametric approach previously presented, so that the SSE amplitudes obtained using the two methods can be compared, we use the InSAR time series of surface displacements, corrected from the same long-wavelength spatial ramps and the inter-SSE linear trend obtained from the parametric decomposition (Figures S6a and S8a). This step requires an a priori knowledge of the beginning and end of the SSE. However, the trend estimate is not very sensitive to the SSE date estimations in our joint inversion of the parameters. We use the FastICA algorithm (Hyvarinen & Oja, 1997) to determine the independent sources and the corresponding mixing matrices. Note that contrary to PCA, the output components of this algorithm are not ordered and are given in random order. As this algorithm does no support data gap in the times series, we perform a spatial averaging of the data with a mean sliding window on 5×5 pixels, in order to fill the small data gaps in our images and to keep more pixels in our data matrix. Determining the appropriate number of independent components to be considered is one of the main challenges of the ICA method (e.g., Cohen-Waeber et al., 2018; Ebmeier, 2016; Milliner et al., 2018). Selecting too few components may mix different sources together, and selecting too many will result in the splitting of the sources of interest over many components with large errors making their identifications more difficult.

To determine the appropriate number of components, we propose two approaches. First, we use the eigenspectrum derived from a PCA, as previously proposed by Chaussard et al. (2017), and select the number of components that explain at least 80% of data variance (Figure 4). This procedure allows the number of independent components, n, for each track to be selected consistently, based on the data complexity estimated by a PCA. For the Track D041, we select six components, whereas five components are sufficient for the Track A078 to account for the same data variance (Figure 4). In the second approach, we take advantage of the GPS stations present in the area to get some knowledge on the temporal evolution of the signals contained in our InSAR data (displacement and tropospheric). As previously explained, the GPS-TDL_{OS} extracted from GPS

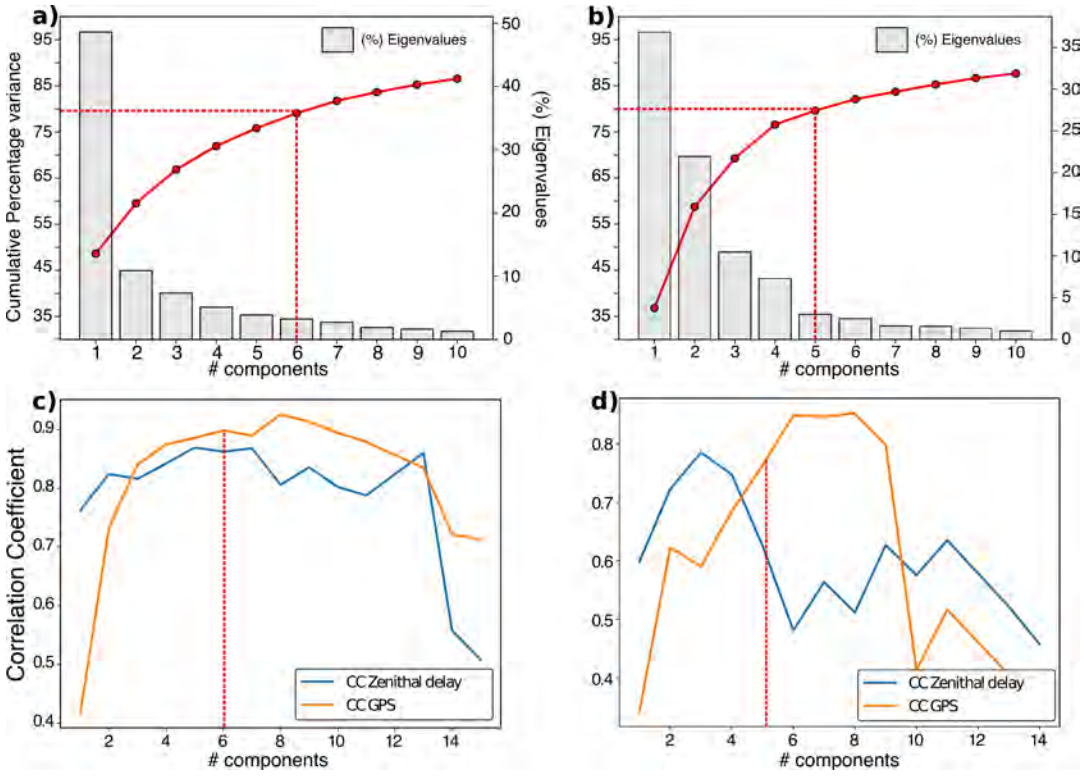

Figure 4. Statistical criteria used to choose the number of components for ICA for both INSAR tracks. (a and c) Track D041. (b and d) Track A078. (top) Percentage of the signal variance explained as a function of the component number with a temporal PCA. Gray histograms are the variance explained by each component, and the red curves are the cumulative variance explained. (bottom) Maximum correlation coefficient for the SSE and the GPS-TDL_{OS} components extracted from the GPS data and their corresponding independent components as a function of the number of components chosen. Vertical red lines indicate the number of components chosen.

(via a PCA, see Figure 2c) gives a good first-order estimate of the tropospheric-related InSAR phase variation with time. We perform an ICA on the detrended GPS data (present in the footprint, 8 stations in descending and 10 in ascending) projected into the radar LOS to extract two independent components, one represents the main features of the tectonic signal in the GPS time series (SSE-ICA), while the second one is a noisy component. We then compare the GPS-TDL_{OS} and SSE-ICA temporal signals with the temporal evolution of the independent components from ICA of the InSAR data time series. To do so, for each imposed number of components in the decomposition, we calculate their correlation coefficient (CC) with GPS-TDL_{OS} and with SSE-ICA. We keep the maximum of these correlation coefficients for GPS-TDL_{OS} and SSE-ICA and plot them as a function of the total number of components used in the decomposition (Figures 4c and 4d). Doing so, we can check the proximity of the extracted InSAR signals to the independent GPS measurements, in order to identify more objectively the InSAR IC that can be representative of the SSE displacement and the one that can be representative of the tropospheric effects. This also allows us to select quantitatively the optimal number of components: We choose the optimal number of components as the one for which the sum of the two CC (CC_{ZTD} and CC_{SSE}) is maximum. The second approach gives results consistent with the first one based on PCA, which reinforces confidence in our final choice of the number of components.

For the descending track, we observe an increase of CC_{SSE} with the number of components between one and four, then a plateau between four and eight components, and a decrease for a larger number of components. The CC_{ZTD} is almost constant (with small variations) up to 12 components and strongly decrease afterward. Our interpretation is that for too few components (less than 4), the SSE signal cannot be separated from the noise, the atmospheric signal, however, has a large amplitude and always appears on a single component. When the number of components is really large (more than 12), the atmospheric signal is then separated in more than one component and becomes more difficult to identify. The sum of both CC is maximal at six components, so we take that value as our optimum number of components. For the ascending track, CC_{ZTD}

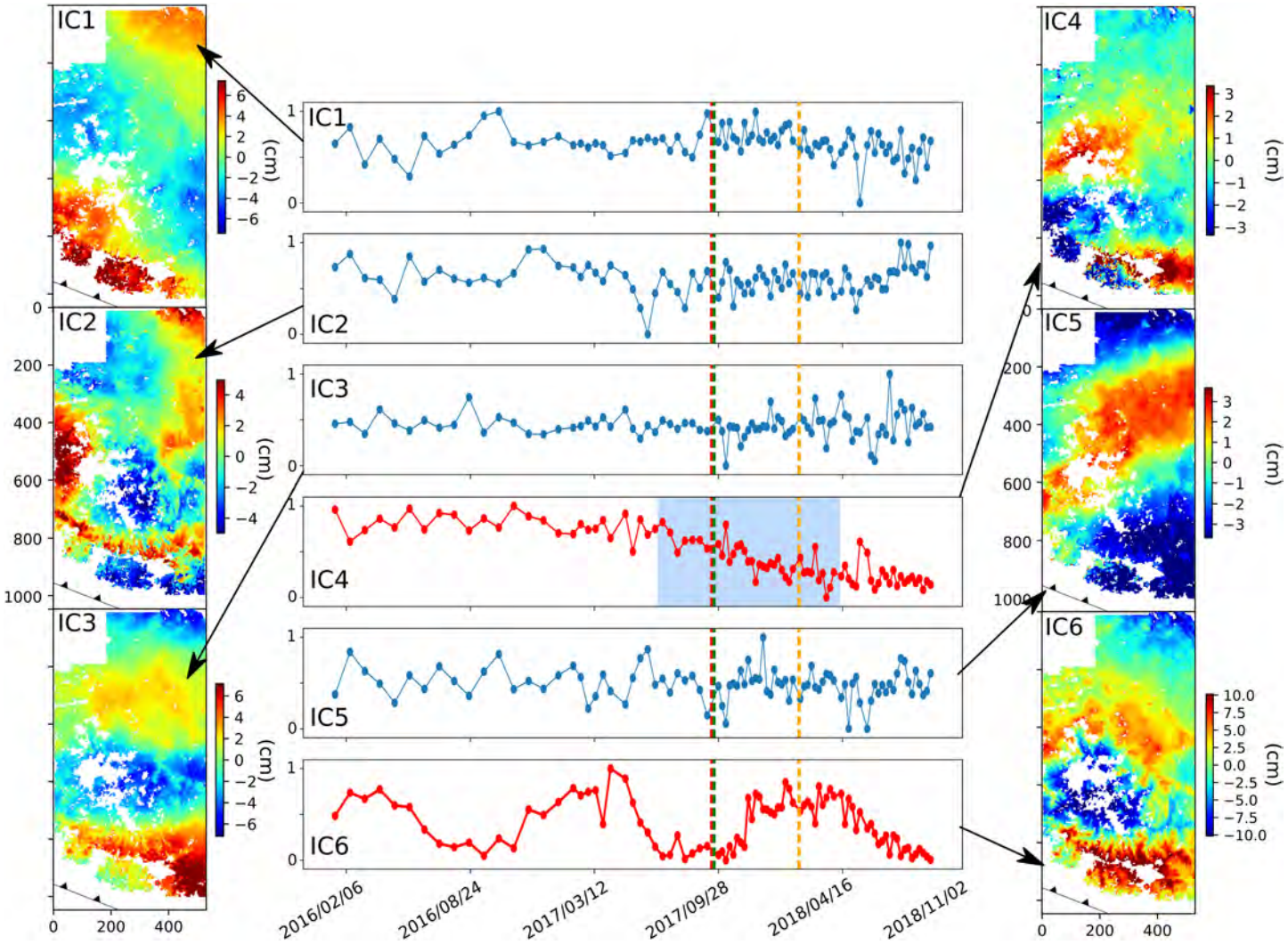

Figure 5. Independent components analysis of InSAR data on descending Track D041 without prior global weather model correction. Middle plot: temporal eigenvectors for the six independent components. The vertical lines show the timing of three major earthquakes that occurred since September 2017. Left and right: maps representing a spatial pattern for each independent component. The IC4 component is consistent with a SSE signal (both phases of the SSE period known from GPS measurements is highlighted in blue). The IC6 component is very consistent with tropospheric temporal variations showing clear seasonal changes. IC1, IC2, IC3, and IC5 are certainly mainly related to the turbulent troposphere, ionosphere or residual orbital error signals, but it is difficult to interpret them individually. All maps are displayed in radar coordinates with an E-W flip to help comparison with other maps.

is larger than 0.6 for three to five components and decreases afterward. CC_{SSE} is maximal for six to eight components (around 0.85). The sum of both CC is maximal for four components; however, this value is very close to the one for five components (1.42 and 1.38). As these values are very close, and because the PCA estimation gives five components, we decide to choose five components as the best compromise.

4.3.2. Results

The results of the ICA applied on InSAR time series without previous atmospheric correction from the global weather model are presented in Figures 5 and 6 for descending and ascending tracks, respectively. Results for data previously corrected from GACOS model are presented in Figure S9. Note that the IC numbers in those results are random and their order has no particular meaning. To identify the signals of interest among the ICs, we analyze their temporal evolution using the previously computed CC_{LTD} and CC_{SSE}, and we also analyze their spatial distribution. For D041, the IC6 (Figure 5) presents a temporal evolution with seasonal oscillations that are very similar to the GPS-TDL_{OS} vector shown in Figure 2 ($CC_{ZTD} = 0.86$), and its amplitude is highly correlated with the topography, as expected for the seasonal variations of the stratified troposphere. We thus interpret IC6 as representing the main contribution of the troposphere. IC4 has a temporal evolution that shows a clear decrease between May 2017 and April 2018, and flatter trend

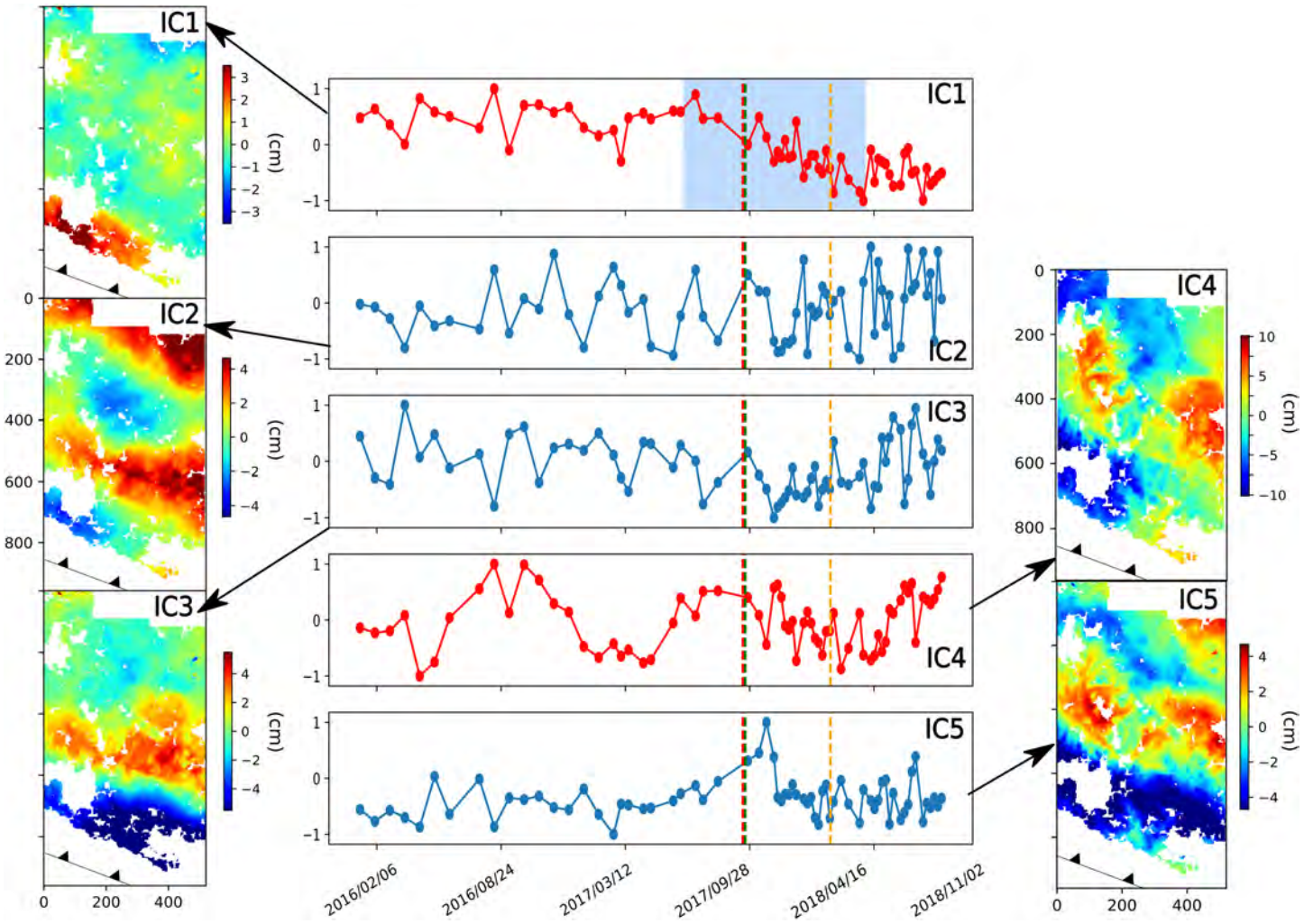

Figure 6. Independent components analysis of InSAR data on ascending Track A078. Same legend as in Figure 5, but here, the SSE pops up in the first component (IC1), and the tropospheric signal in the fourth component (IC4). Maps are in radar geometry with a north-south flip to help comparison with other maps.

segments before and after those dates, as expected for the large SSE transient deformations in the Guerrero area. CC_{SSE} is 0.9 for this component, which indicates a good agreement with the surface displacement signal measured by the GPSs. The spatial pattern is opposite to the inter-SSE signal (Figure S6a) and is similar to its spatial distribution of previous SSE in this region (Bekaert et al., 2015; Cavalié et al., 2013). This component is thus interpreted as the main surface deformation signal from the SSE. The spatial distributions of the amplitude of the first, third, and fifth components (IC1, IC3, and IC5) show long-wavelength signals, and their associated temporal evolutions appear to be varying randomly. Those three components could be related to long-wavelength signals of the turbulent troposphere, ionospheric effects, or residual orbital errors. The second component (IC2) has a spatial distribution showing some correlation with the topography but not everywhere and has a random temporal evolution. This component is more difficult to interpret. However, its amplitude is really small compared to IC6 and explains only 12% of the signal.

The decomposition of the data previously corrected from the GACOS model (Figure S9) has also a component (IC6) with a temporal evolution similar to the GPS-TDL_{OS} vector ($CC_{ZTD} = 0.83$) and a spatial pattern correlated with the topography. However, the amplitudes are smaller than when the data are not previously corrected from GACOS. Thus, the GACOS atmospheric model has only partially corrected the seasonal atmospheric contribution. IC5 (Figure S9) has a spatial pattern close to the one obtained without GACOS correction, except in the northern part of the image where there are larger values. It has a temporal evolution similar to the SSE, but with a lower correlation coefficient with the ICA-GPS compared to the case

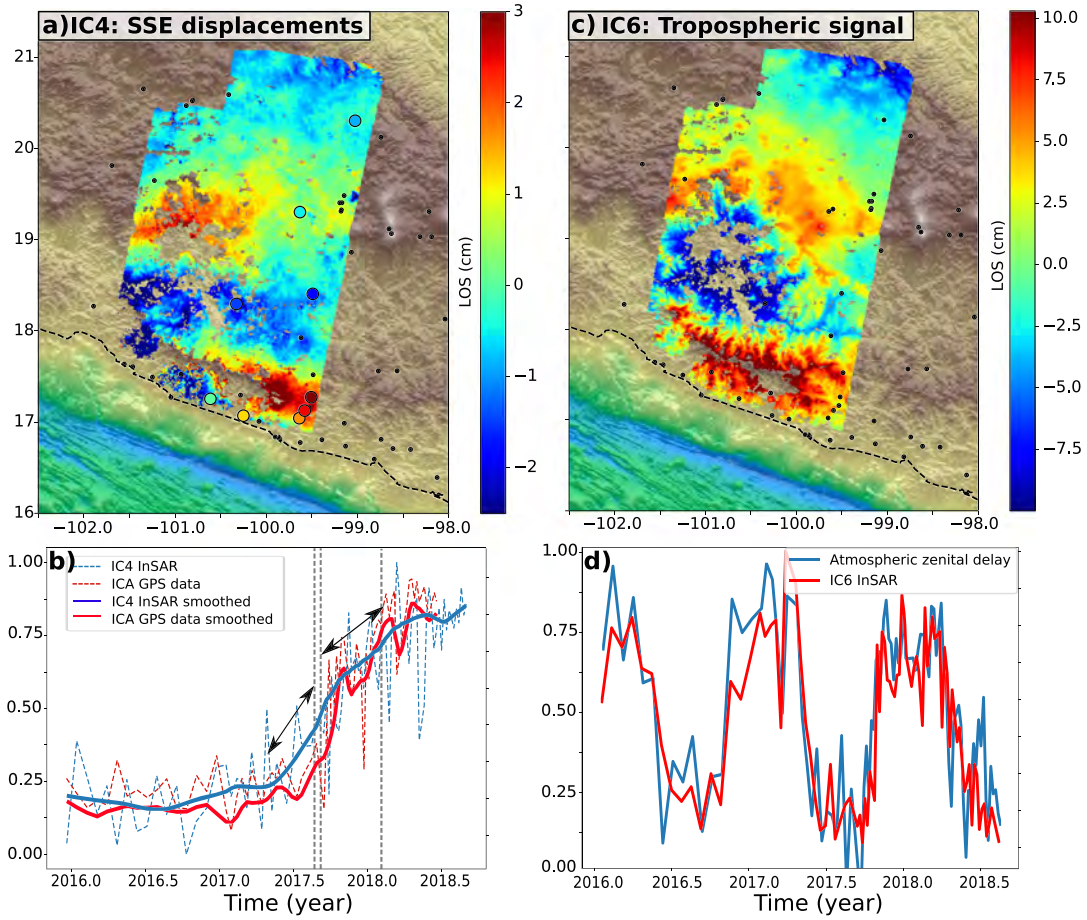

Figure 7. Comparison of ICA components from InSAR (descending Track D041) with respect to ICA components extracted from GPS displacement time series and from GPS-TDL_{OS} time series. (a) Map of amplitude of the SSE (IC4) in centimeters, from InSAR ICA, identified as extracting the SSE surface displacement. Black points show the location of GPS stations. The colored circles represent the SSE displacement extracted from the GPS stations. (b) Temporal evolution. Dashed blue line: SSE-IC4 temporal evolution; dashed red line, ICA-GPS temporal evolution (SSE temporal evolution extracted with ICA from GPS data); solid lines, temporal evolutions smoothed with a mean sliding window. The vertical lines show the timing of the three major earthquakes. The black arrows highlight a change in the slope of the time series that could be associated with earthquakes occurrence. (c) Amplitude map of the tropospheric signal extracted with ICA in centimeters. (d) Red line: tropospheric-ICA vector (IC6) from InSAR; blue line: the GPS-TDL_{OS} from the GPS stations located in the image footprint.

without GACOS correction (CC_{SSE}= 0.78, against 0.9). In the following, we thus decide to consider the case in which the data are not previously corrected from the global weather model.

The ICA for the ascending track A078 (Figure 6) also isolates a component, IC1, with the same temporal and spatial evolution as the expected SSE (with $CC_{SSE} = 0.76$). IC2 and IC3 show spatially long-wavelength pattern (not correlated to the topography) associated with temporal random evolution. IC4 appears spatially correlated to the topography, and temporally correlated to the GPS-TDL_{OS} vector ($CC_{ZTD} = 0.625$). IC5 also displays spatial correlation to the topography but temporally the evolution looks noisy, dominated by a few dates.

These results give good confidence that it is possible to isolate the SSE signal and the main atmospheric contribution from the InSAR time series. To get more confidence in our interpretation of the IC, we compare the IC interpreted as the main SSE and tropospheric signals with respect to GPS derived measurements. The IC corresponding to the tropospheric signal is compared with temporal evolution of the GPS-TDL_{OS} (Figures 7d and 8b), showing a good correlation ($CC_{ZTD} = 0.83$ for descending track and $CC_{ZTD} = 0.625$ for ascending track). The SSE temporal evolution is shown in Figures 7b and 8b. To facilitate the comparison between the IC obtained by InSAR and GPS, we smooth the vectors with a mean sliding window over five InSAR acquisition dates. After smoothing, we observe a change in the slope of the SSE signal, which occurs at the end of September 2017, with a deceleration (velocity 1.5 and 1.8 times smaller for D071 and A048

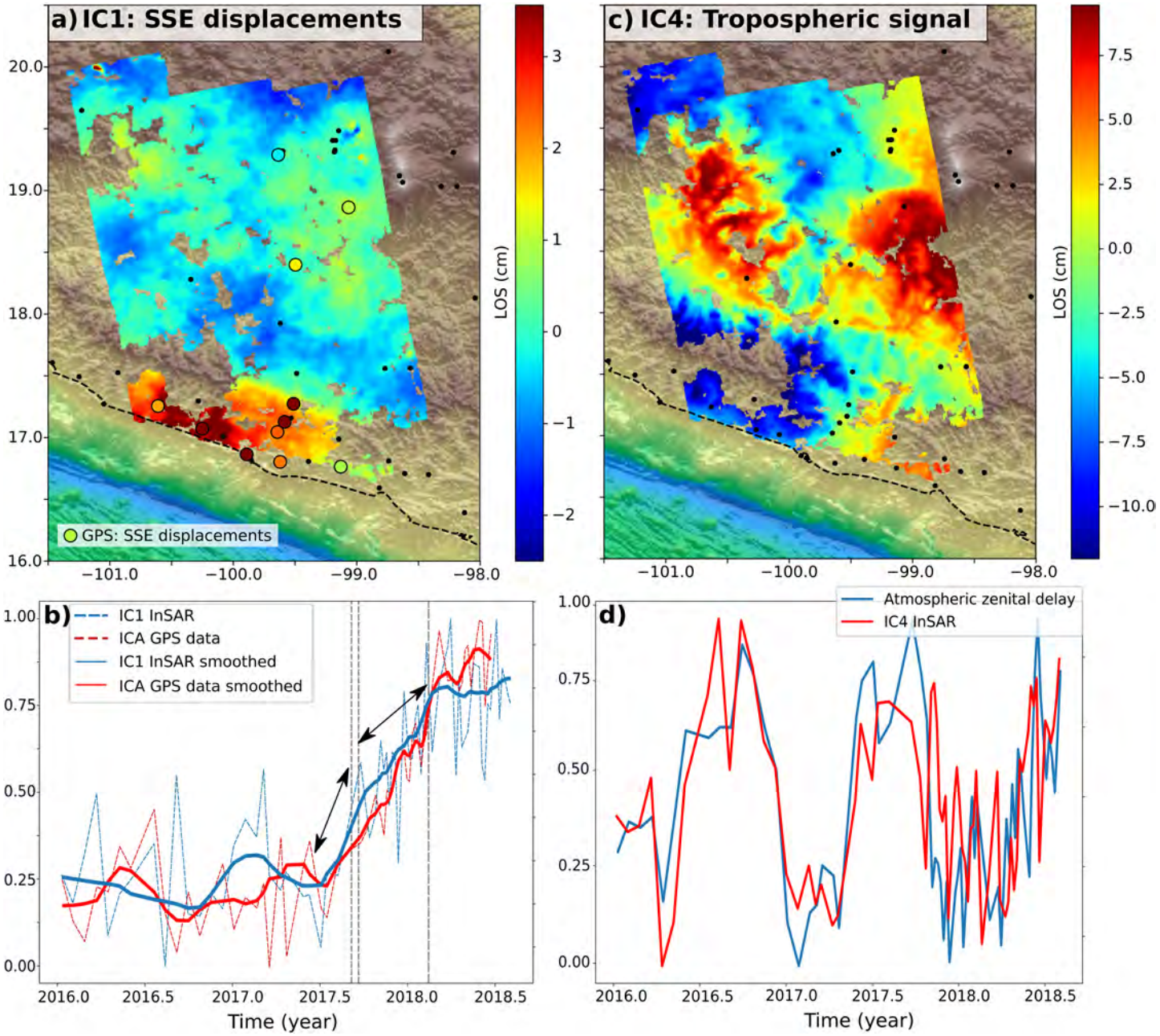

Figure 8. Comparison of ICA components from InSAR (ascending track A078) with respect to ICA components extracted from GPS displacement time series and from GPS-TDL_{OS} time series. Legend as in Figure 7.

respectively). This change of slope occurs just after the September seismic sequence. For both tracks, we were not able to identify in the ICA components that could be clearly related to a possible SSE migration, the latter being likely too small or mixed in several components making its interpretation more difficult.

5. Comparison and Modeling

5.1. Comparison: Parametric Decomposition Versus ICA

Our results show that the two approaches (parametric decomposition and ICA), can isolate a signal which is in agreement with the GPS observations of the 2017–2018 SSE in Guerrero. For both methods, the extracted measurement can be related to slip on the subduction interface, a horizontal displacement toward SSW combined with an uplift around the Sierra Madre del Sur (SMdS, Figure 1a) and a subsidence north of it. In both parametric and ICA results the uplift and subsidence surface displacements are well seen in descending

track, which is mainly sensitive to the vertical displacement, as the horizontal ground deformation is almost orthogonal to the radar LOS (Figures 3a and 7). The maximum is 4 cm for the parametric method and 3 cm for the ICA results, in descending track. In ascending track, both approaches are spatially consistent (Figures 3a and 8). As in descending, the maximum is 4 cm for the parametric method and 3.5 cm for the ICA results. In this case, north of the SMdS, the horizontal displacement causes displacements toward the satellite that is partially compensating the subsidence signal going away from the satellite. There are nevertheless some differences between the results of both methods. For the descending track, in the western part of the track, along the coast, we observe, with the ICA decomposition, a gradient of LOS displacement in agreement with motion away from the satellite (∼−2.5 cm; Figure 7) that is less considerable than in the parametric decomposition (Figure 3a). On the other hand, the parametric decomposition shows in northern most part of the track (latitude >20.5°N), a larger signal (∼2 cm away from satellite), which could be associated with a wrong estimation of the tropospheric temporal pattern by GPS-TDL_{OS} affecting the SSE term estimations. Indeed, this area close to the Gulf of Mexico coast may have different tropospheric temporal pattern than south of it, which could not be well sampled because of the lack of GPS stations here included in the GPS-TDL_{OS} estimation. For the ascending track and for the first phase of the SSE (Figure S7a), we observe in the eastern part of the track a subsidence/uplift bowl pattern close to the epicenter of the Puebla earthquake, which corresponds to the surface displacement of this event. This signal cannot be attributed to the SSE but may be the result of the Puebla earthquake (19 September 17, Mw 7.1). However, the parametric approach cannot separate the SSE from the coseismic signal by adding a Heaviside function (step function) in the parametric decomposition without inducing a trade-off between the functions. This may arise from a lack of data during the initial stage of the SSE and before the earthquake.

Another observation is seen across the Tierra Caliente basin region (see location in Figure 1) from 19.5°N to 18.5°S of latitude. There, the northern part of the basin is moving toward the satellite with respect to the southern part of the basin (Figures 7a and 8a). As the measurements are similar in ascending and descending tracks (but with a lower amplitude in the ascending results), it could be interpreted as a relative uplift. The signal is not well correlated to the topography and is difficult to explain by SSE slip. It may be related to a residual atmospheric signal in that region at the time of the SSE. If the temporal evolution of the atmospheric signal during the SSE is different in that region compared to the rest of the studied area and shows some residual seasonality, there could be a trade-off between the SSE and the atmospheric signal in the decomposition. Alternatively, it may be caused by hydrological or unknown tectonic signal but so far the geophysical interpretation of this pattern remains unclear.

We reconstruct the SSE signal for each method, and we then compare the amplitude for a pixel window (of 5×5) fixed at the location of the CAYA GPS station (close to the coast, Figure 1a), which is one of the stations mostly affected by the SSE. To reconstruct the signal, for the parametric method, we multiply the SSE time vectors (for the two phases) by the amplitudes (C1 and C2) of the pixel at CAYA station coordinates. For the ICA decomposition, we multiply the temporal evolution of the IC corresponding to the SSE by the value of the amplitude map at CAYA location. At this point, the amplitude of the parametric decomposition is 3.9 cm in descending, and 3.1 cm in ascending track. The amplitude of the ICA method is 3.5 cm in descending and 2.9 cm in ascending. We compare these two reconstructions with the displacements observed at the CAYA GPS station, detrended and converted in LOS (Figure 9).

For the descending track, both methods are in agreement with the GPS data revealing a slope change in the SSE displacement curves around the date of the September earthquakes. The dates are similar in both methods, but both methods overestimate the amplitude of the first phase of the SSE compared to the GPS data (Figure 9). However, ICA amplitudes are close to the GPS data considering the complete time series. For the ascending track, the parametric decomposition is not in agreement with the GPS time series for the first phase of the SSE. In this case, the shape of the basis function does not seem appropriate. The second phase of the SSE looks more coherent with the GPS data. The cumulative amplitude is coherent with the GPS data for this station location.

Despite some minor discrepancies, our results show that both approaches are overall coherent in terms of SSE amplitudes and spatial distribution, which gives us confidence in the robustness of the extracted signal. The temporal evolution is more difficult to analyze concerning the parametric decomposition since it is constrained by the initial parameterization, which could be biased. Indeed, ICA has the advantage of not

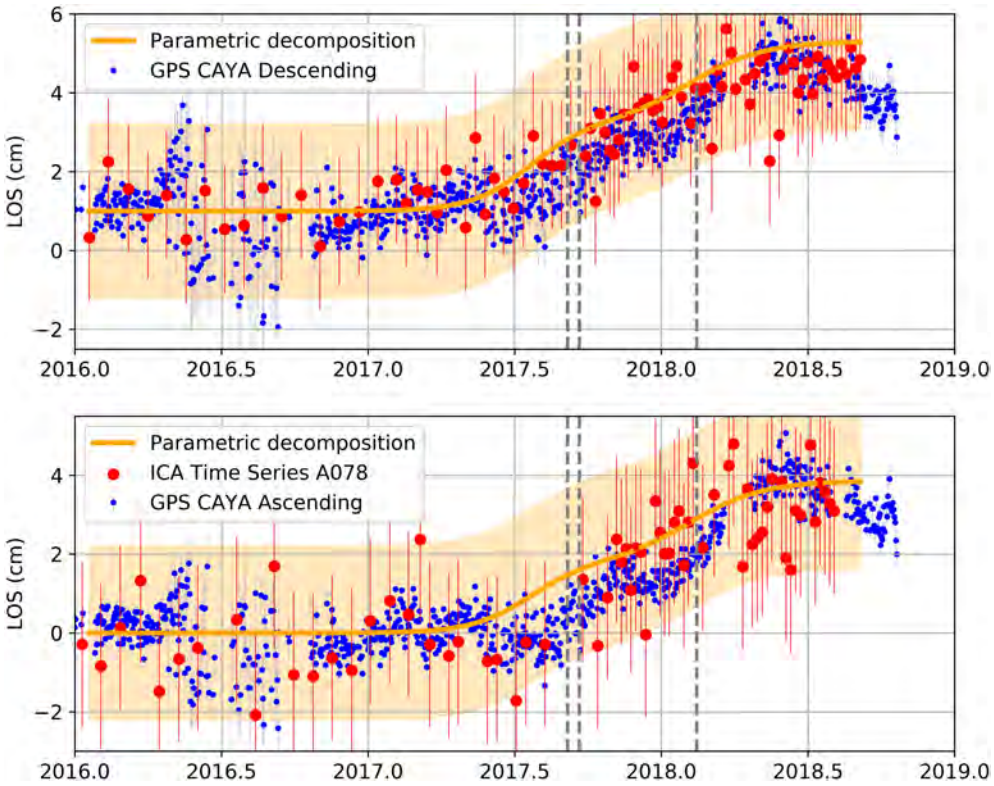

Figure 9. Comparison of the surface LOS displacement of the 2017–2018 SSE, at the location of the CAYA GPS station, estimated from three different approaches. (top) For descending Track D041. (bottom) For ascending Track A078. Blue dots: CAYA GPS time series reprojected along LOS; orange line: parametric reconstruction of the SSE; red dots: displacement reconstructed from the SSE extracted with the ICA method applied to InSAR data (IC4 for descending, and IC1 for ascending) identified as extracted component of the ICA method, applied to InSAR data, identified as representing the SSE surface displacement (IC4 for descending, and IC1 for ascending, see Figures 5 and 6). Some increase of the scatter in GPS data (around 2,016.5) occurred by the sudden change of transmitted data from raw to the Trimble RTX.

requiring a priori information about the form of the transient signal. However, because ICA needs a detrending of the time series prior to the decomposition, we used in our ICA decomposition the data previously detrended from the inter-SSE trend using the parametric approach. This detrending step, which in this case requires an assumption on the SSE dates (because it was done for the inter-SSE period), could also be performed by computing the velocities over the entire time series (detrending from the long-term trend instead of the inter-SSE trend). We tested this approach and observe that it does not change our results significantly. We prefer here to detrend the data from the inter-SSE velocity to be consistent with the parametric approach and with previous studies and models in the regions (Cavalié et al., 2013; Radiguet et al., 2012). Concerning the requirement of having GPS stations in the studied area, with a purely parametric approach, having GPS time series in the region is useful to have an initial guess on the transient time and duration. Regarding the correction from atmospheric delays, ZTD from the GPS data are also used to extract seasonal variations of the atmospheric delays. However, as shown in Figure 2, a temporal evolution extraction with a PCA on the GACOS or ERA-I atmospheric model gives very similar temporal evolutions. With the ICA approach, the GPS data (ZTD and displacements) are used to help choosing the number of components and identifying them. Afterward, only to validate the results of the decomposition in the area where the density of the GPS network is not sufficient to observe with an efficient spatial resolution, the results of the ICA decomposition can be validated with few stations.

5.2. Modeling

In order to make an additional confirmation that the LOS displacement extracted by ICA and parametric approach can be attributed to the SSE, we invert the SSE amplitudes extracted with both methods to estimate the slip distribution of this event on the subduction interface and compare then the estimated slip distribution with previous SSE.

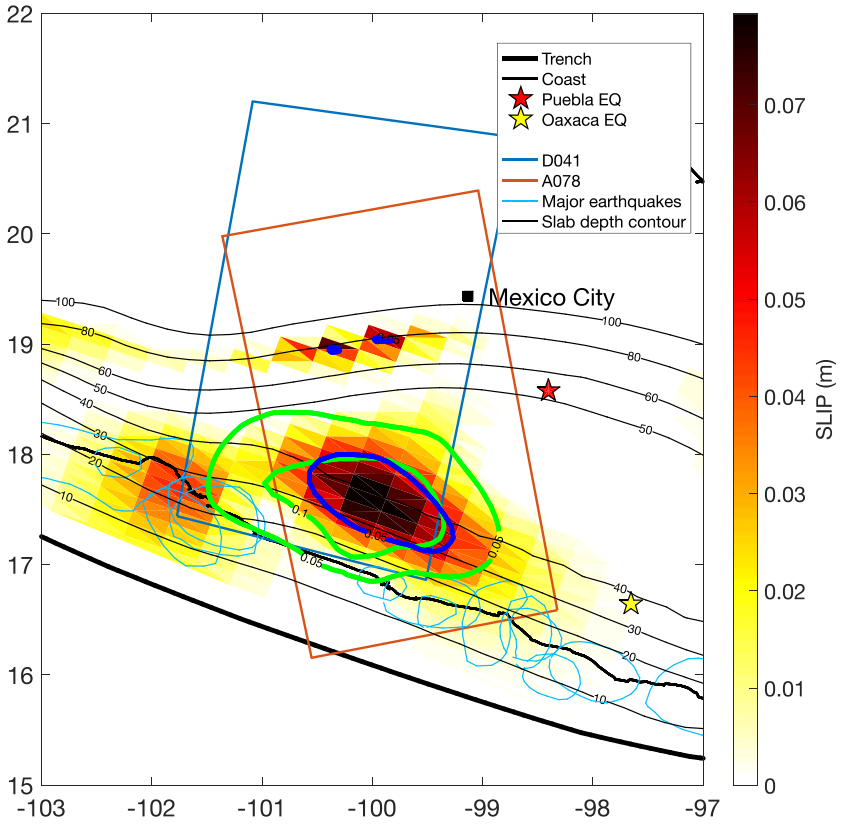

Figure 10. Cumulative slip distribution on the subduction interface for the 2017–2018 SSE inverted from the ICA results. This slip distribution has an equivalent magnitude Mw = 7.2. The green contours represent 5 and 10 cm isocontours of the mean slip distribution of the three past SSEs (2006, 2010, and 2014) (Radiguet et al., 2012, 2016). The thin cyan contours show approximate rupture areas of the major historical earthquakes that occurred on the subduction interface. Stars represent epicenters of the Puebla (MW 7.1, 19 September 2017, in red), and Pinotepa (Mw 7.2, 16 February 2018 in yellow) earthquakes. The orange and dark blue rectangles represent the footprints of the two InSAR tracks. The thin black lines are the isodepth of the plate interface every 10 km, the medium black line the coast, and the bold black line the Middle America Trench.

The SSE surface displacements consist of the two amplitude maps extracted by ICA (IC4 for ascending and IC1 for descending). We perform a static inversion in an elastic medium, using a linear least squares algorithm (Tarantola, 2005) with the regularization scheme of Radiguet et al. (2011). The 3-D slab geometry is similar to Radiguet et al. (2016) and takes into account the flat-slab segment of the plate interface (Pérez-Campos et al., 2008), with a ramp between the trench and 150 km north of the trench, then the slab is flat at 40 km depth. Our forward model (Green's functions) assumes an elastic half-space and is computed using the Okada (1992) dislocation model. For numerical reasons, we reduce the number of pixels for the inversion. We resample the amplitude map from 5.10^5 to 2,770 pixels for the descending track and 2,234 pixels for the ascending one. Because our SSE signal is long-wavelength, we choose a uniform downsampling rather than quadtree algorithms (Jónsson et al., 2002). To associate an uncertainty at each InSAR sampled data sets, we average the residual map of the parametric method in each subsampled zone (Figures S3b and S3d). This measure gives an estimate of the dispersion of our data through the complete time series. These errors provide relative weight between pixels, and allows us to weight each track relatively. Note that we neglect covariance between pixels in our inversion. This gives more weight to the data, and thus tends to produce higher χ_2 (Text S1) and rougher solutions with respect to solutions accounting for covariance.

We test the variability of our model to the smoothing parameters through L curves: We perform an exploration of the damping value (σ_{m0}), and then we choose the best compromise between the χ_2 (Text S1) and small L_2 norm of the solution (Figure S10). We impose to the model a non-negativity constraint, as well as a fixed rake perpendicular to the trench. The data misfit of the selected model is $\chi_2 = 0.23$. We also implement

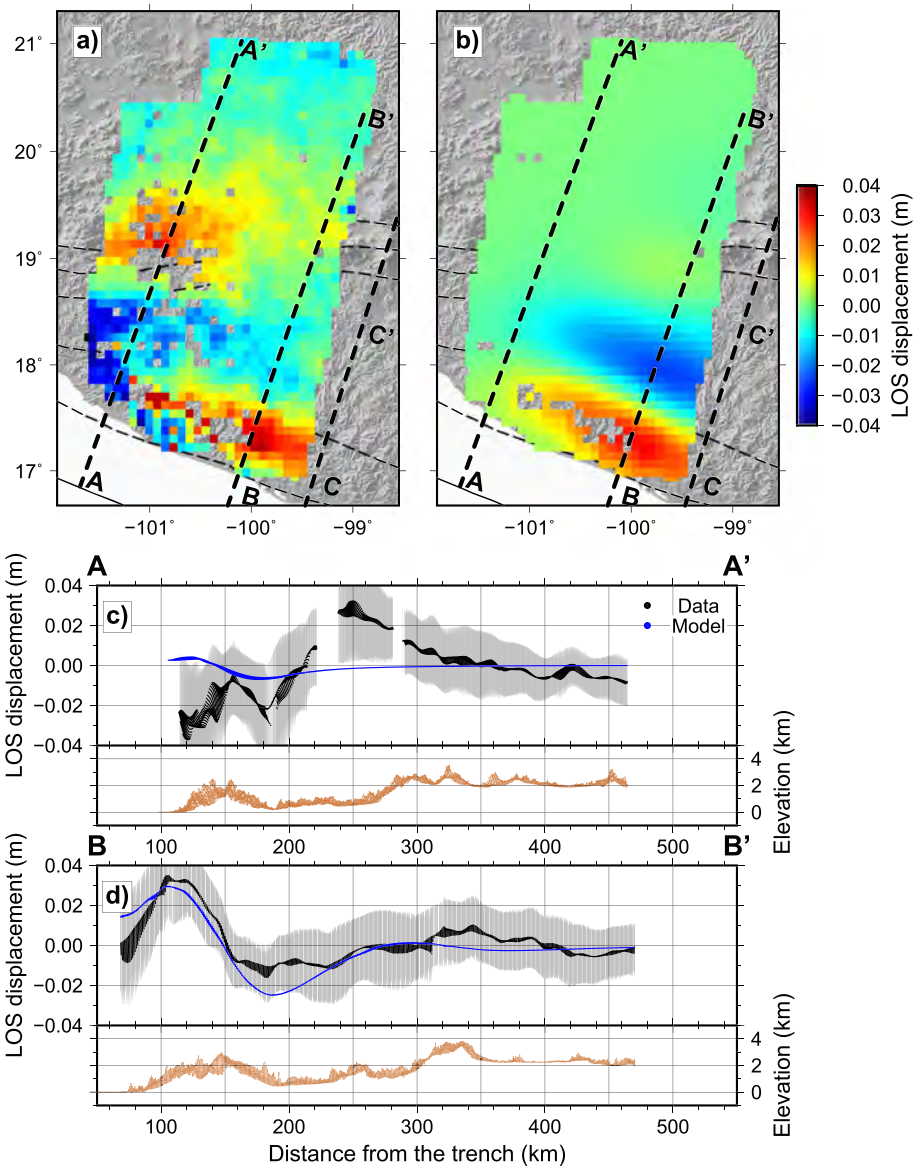

Figure 11. Comparison between observed and inverted surface SSE displacements. (a) The data used for the inversion. (b) Modeled surface displacement. (c) Profile A along the D041 track (width of 5 km). The black dots are the data, the blue dots display the model, and brown dots the topographic profile in this area. (d) Profile B along the D041 track. The annotations are the same as in (c).

a model using the results of the parametric method as input data with the same model parameters than with ICA data and obtain a data misfit of $\chi_2 = 0.85$.

Our inversion results, for both inverted data sets, show a slip pattern along the subduction interface similar to previous SSE models (Figures 10 and S11) (Bekaert et al., 2015; Cavalié et al., 2013; Radiguet et al., 2012). The main SSE slip patch is located in the coastal area, between 20 and 40 km depth, on the deep part of the ramp located above the flat segment of the slab, and extend 250 km along strike.

The equivalent moment magnitude calculated for the 2017–2018 SSE event, using ICA data set, is Mw = 7.2 and slightly lower than the magnitudes of past events (past events have magnitudes between 7.3 and 7.5). This is expected as the surface displacements observed for this event are lower than previous ones. For comparison, the model obtained using the results of the parametric decomposition is shown in Figure S11. The main slip patch is quite similar to a slightly larger magnitude (equivalent Mw 7.4) in this case.

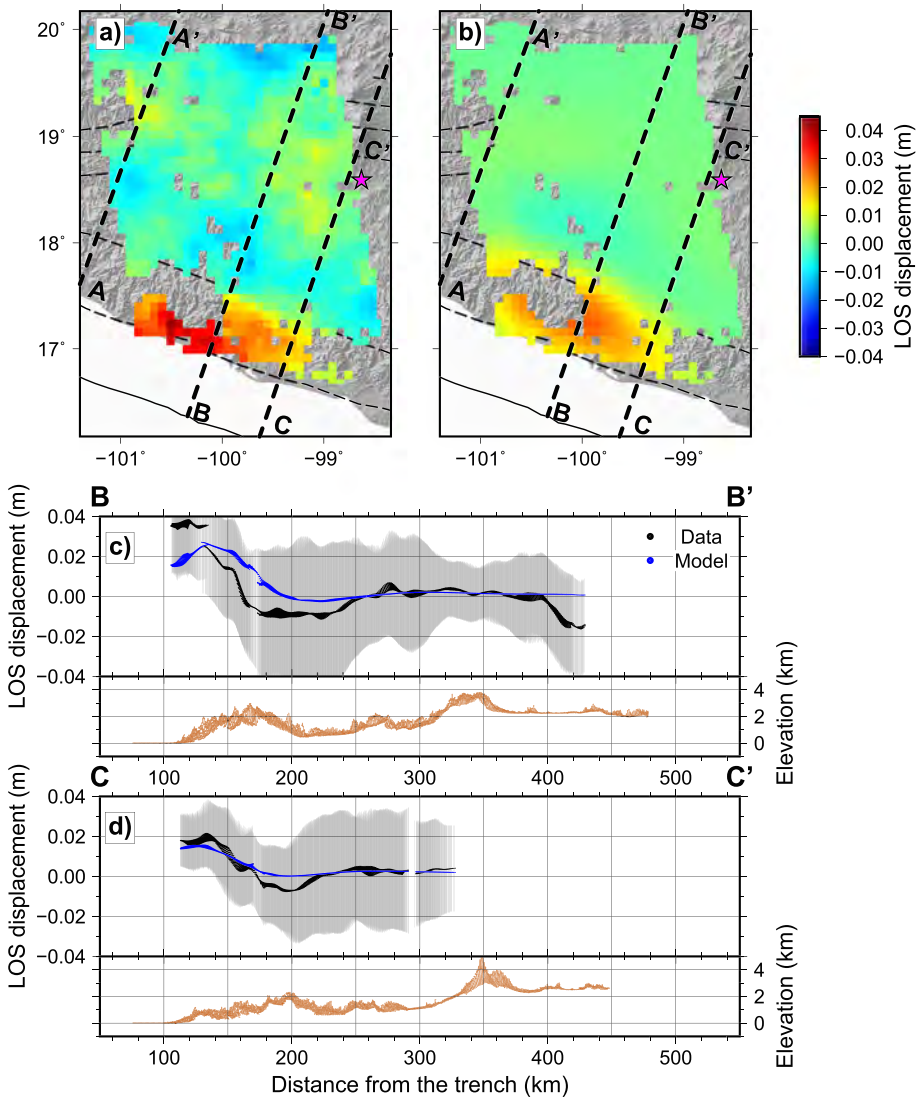

Figure 12. Comparison between observed and modeled SSE displacements for inversions. (a) The data used for the inversion for Track A078. (b) Surface displacement predicted by the model. (c) Profile B perpendicular to the trench with the data as black dots with uncertainties in gray, and the model in blue dots (width of 5 km). The brown dots represent the topography in meters. (d) Profile C along the A078 track with in black dots are the data, in blue dots the model and down the associated topographic profile.

Overall, the model (with both methods) explains well the data, with the same pattern of displacement toward the satellite at the coast and away from the satellite further north. However, the deformation signal in the south of the Tierra Caliente area (see section 5.1) cannot be explained by our model (Figures 11 and 12). As discussed in section 5.1, it is not clear if this signal is a real displacement or due to residual tropospheric signal leaking into the SSE component. In any case, it cannot be modeled by slip on the interface and consequently may be responsible for an artificial deep slip in the northern part of the slip model. We analyze three profiles along the track (a–c in Figures 11 and 12). Profile B is common to both tracks. As previously explained, Profile A shows that the model does not reproduce the Tierra Caliente signal. We observe that the model using ICA results underestimates (~15%) the amplitude of the uplift (at the coast) for the descending track (Figure 11) but overestimates (~45%) the amplitudes in the ascending track (Figure 12). Those variations are also observed in the inversion using parametric results, suggesting that some residual atmospheric signal probably related to the topography of the Sierra Madre del Sur may have leaked into the SSE signal in that region. Nonetheless, the first-order deformation signal extracted with the ICA decomposition is

compatible with the slip on the subduction interface along the convergence direction and with a slip distribution similar to previous SSEs.

6. Conclusion

The temporal densification of the InSAR data with Sentinel-1 makes it possible to generate interferograms of good quality, which can be unwrapped over large regions and results in improved spatial coverage of InSAR measurements. However, separating tectonic deformation from the atmospheric signal remains a challenge, especially in large mountainous areas, as in the Guerrero state of Mexico. In such regions, the atmospheric signal can be larger than the transient deformation and can have complex temporal behavior. It is therefore difficult to extract SSEs deformation signals, like those caused by SSE in subduction zones. Despite these difficulties, we show here that using appropriate InSAR source separation techniques, we can extract from InSAR, at regional-scale, slow aseismic transient signal. To achieve this, we first explore the benefits of correcting the InSAR time series using predictive estimations from global weather models (ERA-I and HRES ECMWF models). We conclude that, for the two methods investigated in our study (parametric and ICA), initial corrections on time series from global weather models does not improve the separation of atmospheric from tectonic signals, mainly because amplitudes of atmospheric delays are not accurately predicted by these models. However, we show that the temporal evolution of atmospheric delays captured by the GPS-TDL_{OS} data, or extracted from global weather models are very similar and can be used as an input to the parametric decomposition to correct the InSAR time series.

The second objective of this study was to compare the benefits and limitations of two methods of signal decompositions (parametric and ICA) to extract the SSE signal in the Guerrero area, Mexico. For the parametric decomposition, the principal limitation is the requirement of some a priori knowledge about the searched signal (SSE time and duration and atmospheric component), which strongly controls the results. However, it has the advantage to be simple, linear, and to provide uncertainties associated with the estimated parameters. Alternatively, the ICA, being a blind approach, does not require any a priori of the signal parameters. Its limitations are the necessity to assess the adequate number of independent components and the subsequent interpretation of these components. We show in this paper that the ICA approach can be powerful to extract the SSE spatial pattern and its temporal evolution. We propose an original approach to validate the component identification by comparison with external GPS data. We also show the possibility with the ICA to extract complex atmospheric delays without a priori information on the evolution of this signal, which can be validated with the GPS-TDL_{OS}. Despite some limitations due to possible trade-off between parameters in the parametric approach or due to the need to detrend the time series for ICA, both methods are complementary and several possibilities can be envisioned depending on the study area. ICA alone appears as a reasonable choice in the case when there is no a priori knowledge on the deformation and no other data are available. In large tectonically active areas like subduction zone, it is likely to have some a priori about expected deformation and also to have data from a few permanent GPS stations. In this case, a hybrid approach can be conducted combining ICA with a parametric model as done in this study. If no GPS-ZTD data are available or if they are not representative of the seasonal atmospheric variations of the studied area, the ZTD time series can be replaced by the temporal evolution of global weather models despite their poor spatial resolution. Obviously, a large number of permanent GPS stations well distributed across the study area and in a large altitude range is more beneficial; however, we have shown that using the PCA combining the ZTD time series of a dozen of stations using the ZTD in the parametric approach is enough to capture the first order of the atmospheric signal. In the best configuration, some GPS stations can capture the tectonic signal of interest. Even if it is not required, it will help to design the parametric approach or to choose and identify the number of components in the ICA approach. For both approaches, it can help to validate their result and provide estimations of their uncertainties. Using a hybrid approach has also proved to be interesting when performing inversion to get the slip distribution model. Comparing the model results inverted from surface displacement provided by each method helps in determining the robust features, which should be common in both models.

Our data show some complexity in the temporal evolution of the SSE, with a change of displacement velocity around September 2017. This reflects a possible interaction between the slow slip and the September 2017 seismic sequence, which deserves further investigations. We provide a preliminary model of slip distribution on the subduction interface and observe that the main slip patch occurs between 20 and 40 km depth at the plate interface. The SSE has an equivalent moment magnitude of Mw 7.2. Its amplitude and spatial

extension are slightly lower but compatible with the previous events (2006, 2009–2010, and 2014). However, several second-order features extracted in the surface displacement (either in the inter-SSE component or in the SSE component) are not consistent with the expected interseismic and SSE signals and remain to be explained. Some of those could be related to residual atmospheric signal present in the displacement signal. One way to estimate better those ambiguities will be to involve more GPS data, and also to use the adjacent Sentinel-1 tracks that are partially overlapping the ones we have just processed, and also to use other InSAR data like ALOS-2 images.

Acknowledgments
We thank Jorge Jara, Roland Bürgmann, Sylvain Michel, Adriano Gualandi, and Susanne Ebmeier for fruitful discussions about this work as well as Franck Thollard. Sentinel-1 data are available online (https://scihub.copernicus.eu), and GPS data were provided by the National Seismological Service of Mexico (SSN) and Department of Seismology, UNAM, whose staff are acknowledged for station maintenance and data acquisition. GPS data, and results are available at https://doi.org/10.5281/zenodo.3666788 website. The FastICA software is available from webpages of the Aalto University (research.ics.aalto./ica/software.shtml) and the University of Helsinki, Finland (www.cs.helsinki.fi/u/ahyvarin/code/isctest/). All the computations presented in this paper were performed using the GRICAD infrastructure (https://gricad.univ-grenoble-alpes.fr), which is partly supported by the EquipMeso project (Reference ANR-10-EQPX-29-01) of the PIA supervised by the French Agence Nationale pour la Recherche. This research was supported by the CNES (L. Maubant PhD funding and Grant APR-CNES for projet SSEMEX), Labex OSUG@2020, and Japan Aerospace Exploration Agency (JAXA) EO-RA2 proposal (ER2A2N021). S. D.'s contribution is supported by the Natural Environment Research Council through the Looking into the Continents from Space (LiCS) large grant (NE/K011006/1) and the Centre for the Observation and modeling of Earthquakes, Volcanoes and Tectonics (COMET). The Editors and the two anonymous reviewers are gratefully acknowledged for their valuable comments.

References

Bürgmann, R. (2000). Synthetic aperture radar interferometry to measure Earth's surface topography and its deformation. *Annual Review of Earth and Planetary Sciences*, *28*, 169–209. https://doi.org/10.1146/annurev.earth.28.1.169

Bartlow, N. M., Wallace, L. M., Beavan, R. J., Bannister, S., & Segall, P. (2014). Time-dependent modeling of slow slip events and associated seismicity and tremor at the Hikurangi subduction zone, New Zealand. *Journal of Geophysical Research: Solid Earth*, *119*, 734–753. https://doi.org/10.1002/2013JB010609

Béjar-Pizarro, M., Notti, D., Mateos, R. M., Ezquerro, P., Centolanza, G., Herrera, G., et al. (2017). Mapping vulnerable urban areas affected by slow-moving landslides using Sentinel-1 InSAR data. *Remote Sensing*, *9*(9), 876. https://doi.org/10.3390/rs9090876

Bekaert, D. P. S., Hooper, A., & Wright, T. J. (2015a). A spatially variable power law tropospheric correction technique for InSAR data. *Journal of Geophysical Research: Solid Earth*, *120*, 1345–1356. https://doi.org/10.1002/2014JB011557.1

Bekaert, D. P. S., Hooper, A., & Wright, T. J. (2015b). Reassessing the 2006 Guerrero slow-slip event, Mexico. *Journal of Geophysical Research: Solid Earth*, *120*, 1357–1375. https://doi.org/10.1002/2014JB011558

Bekaert, D. P. S., Segall, P., Wright, T. J., & Hooper, A. J. (2016). A network inversion filter combining GNSS and InSAR for tectonic slip modeling. *Journal of Geophysical Research: Solid Earth*, *121*, 2069–2086. https://doi.org/10.1002/2015JB012638

Bekaert, D. P. S., Walters, R. J., Wright, T. J., Hooper, A. J., & Parker, D. J. (2015). Statistical comparison of InSAR tropospheric correction techniques. *Remote Sensing of Environment*, *170*(track 255), 40–47. https://doi.org/10.1016/j.rse.2015.08.035

Beroza, G. C., & Ide, S. (2011). Slow earthquakes and nonvolcanic tremor. *Annual Review of Earth and Planetary Sciences*, *39*(1), 271–296. https://doi.org/10.1146/annurev-earth-040809-152531

Cavalié, O., Doin, M.-p., Lasserre, C., & Briole, P. (2007). Ground motion measurement in the Lake Mead area, Nevada, by differential synthetic aperture radar interferometry time series analysis: Probing the lithosphere rheological structure. *Journal of Geophysical Research*, *112*, B03403. https://doi.org/10.1029/2006JB004344

Cavalié, O, Lasserre, C., Doin, M. P., Peltzer, G., Sun, J., Xu, X., & Shen, Z. K. (2008). Measurement of interseismic strain across the Haiyuan fault (Gansu, China), by InSAR. *Earth and Planetary Science Letters*, *275*(3-4), 246–257. https://doi.org/10.1016/j.epsl.2008.07.057

Cavalié, O., Pathier, E., Radiguet, M., Vergnolle, M., Cotte, N., Walpersdorf, A., et al. (2013). Slow slip event in the Mexican subduction zone: Evidence of shallower slip in the Guerrero seismic gap for the 2006 event revealed by the joint inversion of InSAR and GPS data. *Earth and Planetary Science Letters*, *367*, 52–60. https://doi.org/10.1016/j.epsl.2013.02.020

Chaussard, E., Milillo, P., Bürgmann, R., Perissin, D., Fielding, E. J., & Baker, B. (2017). Remote sensing of ground deformation for monitoring groundwater management practices: Application to the Santa Clara Valley During the 2012-2015 California Drought. *Journal of Geophysical Research: Solid Earth*, *122*, 8566–8582. https://doi.org/10.1002/2017JB014676

Cohen-Waeber, J., Bürgmann, R., Chaussard, E., Giannico, C., & Ferretti, A. (2018). Spatiotemporal patterns of precipitation-modulated landslide deformation from independent component analysis of InSAR time series. *Geophysical Research Letters*, *45*, 1878–1887. https://doi.org/10.1002/2017GL075950

Comon, P. (1994). Independent component analysis, A new concept? *Signal Processing*, *36*(3), 287–314. https://doi.org/10.1016/0165-1684(94)90029-9

Daout, S., Doin, M.-p., Peltzer, G., Lasserre, C., Socquet, A., Volat, M., & Sudhaus, H. (2018). Strain partitioning and present-day fault kinematics in NW Tibet from Envisat SAR interferometry. *Journal of Geophysical Research: Solid Earth*, *123*, 2462–2483. https://doi.org/10.1002/2017JB015020

Daout, S., Doin, M.-P., Peltzer, G., Socquet, A., & Lasserre, C. (2017). Large-scale InSAR monitoring of permafrost freeze-thaw cycles on the Tibetan Plateau. *Geophysical Research Letters*, *44*, 901–909. https://doi.org/10.1002/2016GL070781

Daout, S., Sudhaus, H., Kausch, T., Steinberg, A., & Dini, B. (2019). Interseismic and postseismic shallow creep of the North Qaidam thrust faults detected with a multitemporal InSAR analysis. *Journal of Geophysical Research: Solid Earth*, *124*, 7259–7279. https://doi.org/10.1029/2019JB017692

DeMets, C., Gordon, R. G., & Argus, D. F. (2010). Geologically current plate motions. *Geophysical Journal International*, *181*(1), 1–80. https://doi.org/10.1111/j.1365-246X.2009.04491.x

Doin, M.-P., Lasserre, C., Peltzer, G., Cavalié, O, & Doubre, C. (2009). Corrections of stratified tropospheric delays in SAR interferometry: Validation with global atmospheric models. *Journal of Applied Geophysics*, *69*(1), 35–50. https://doi.org/10.1016/j.jappgeo.2009.03.010

Doin, M.-P., Lodge, F., Guillaso, S., Jolivet, R., Lasserre, C., Ducret, G., et al. (2011). Presentation of the small baseline NSBAS processing chain on a case example: The Etna deformation monitoring from 2003 to 2010 using Envisat data. In *Proceedings of the ESA 'Fringe 2011 Workshop', (19–23 September 2011)* (pp. 3434–3437). Frascati, Italy.

Doin, M.-P., Twardzik, C., Ducret, G., Lasserre, C., Guillaso, S., & Jianbao, S. (2015). InSAR measurement of the deformation around Siling Co Lake: Inferences on the lower crust viscosity in central Tibet. *Journal of Geophysical Research: Solid Earth*, *120*, 5290–5310. https://doi.org/10.1002/2014JB011768

Ebmeier, S. K. (2016). Application of independent component analysis to multitemporal InSAR data with volcanic case studies. *Journal of Geophysical Research: Solid Earth*, *121*, 8970–8986. https://doi.org/10.1002/2016JB013765

Elliott, J. R., Walters, R. J., & Wright, T. J. (2016). The role of space-based observation in understanding and responding to active tectonics and earthquakes. *Nature Communications*, *7*(1), 13844. https://doi.org/10.1038/ncomms13844

Floyd, M. A., Walters, R. J., Elliott, J. R., Funning, G. J., Svarc, J. L., Murray, J. R., et al. (2016). Spatial variations in fault friction related to lithology from rupture and afterslip of the 2014 South Napa, California, earthquake. *Geophysical Research Letters*, *43*, 6808–6816. https://doi.org/10.1002/2016GL069428

Frank, W. B., Shapiro, N. M., Husker, A. L., Kostoglodov, V., Bhat, H. S., & Campillo, M. (2015). Along-fault pore-pressure evolution during a slow-slip event in Guerrero, Mexico. *Earth and Planetary Science Letters*, *413*, 135–143. https://doi.org/10.1016/j.epsl.2014.12.051

Gomba, G., Rodriguez Gonzalez, F., & De Zan, F. (2017). Ionospheric phase screen compensation for the Sentinel-1 TOPS and ALOS-2 ScanSAR modes. *IEEE Transactions on Geoscience and Remote Sensing*, *55*(1), 223–235. https://doi.org/10.1109/TGRS.2016.2604461

Grandin, R. (2015). Interferometric processing of SLC Sentinel-1 TOPS data. *Fringe 2015*, *731*, 36. https://doi.org/10.1109/TGRS.2015.2497902

Grandin, R. (2017). Interferometric processing of SLC Sentinel-1 TOPS data. In *FRINGE'15: Advances in the Science and Applications of SAR Interferometry and Sentinel-1 InSAR Workshop, 23-27 March 2015, Mar 2015* Frascati, Italy.

Grandin, R., Doin, M.-p., Bollinger, L., Pinel-puysségur, B., Ducret, G., & Jolivet, R. (2012). Long-term growth of the Himalaya inferred from interseismic InSAR measurement. *Geology*, *40*, 1059–1062. https://doi.org/10.1130/G33154.1

Gualandi, A., Avouac, J. P., Galetzka, J., Genrich, J. F., Blewitt, G., Adhikari, L. B., et al. (2017). Pre- and post-seismic deformation related to the 2015, Mw7.8 Gorkha earthquake, Nepal. *Tectonophysics*, *714-715*, 90–106. https://doi.org/10.1016/j.tecto.2016.06.014

Gualandi, A., & Belardinelli, E. S. M. E. (2015). Blind source separation problem in GPS time series. *Journal of Geodesy*, *90*, 323–341. https://doi.org/10.1007/s00190-015-0875-4

Gualandi, A., Perfettini, H., Radiguet, M., Cotte, N., & Kostoglodov, V. (2017). GPS deformation related to the Mw7.3, 2014, Papanoa earthquake (Mexico) reveals the aseismic behavior of the Guerrero seismic gap. *Geophysical Research Letters*, *44*, 6039–6047. https://doi.org/10.1002/2017GL072913

Hanssen, R. (2001). *Radar interferometry: Data interpretation and error analysis*. Dordrecht; Boston: Kluwer Academic.

Hetland, E. A., Musé, P, Simons, M., Lin, Y. N., Agram, P. S., & Dicaprio, C. J. (2012). Multiscale InSAR Time Series (MInTS) analysis of surface deformation. *Journal of Geophysical Research*, *117*, B02404. https://doi.org/10.1029/2011JB008731

Husker, A., Frank, W. B., Gonzalez, G., Avila, L., Kostoglodov, V., & Kazachkina, E. (2019). Characteristic tectonic tremor activity observed over multiple slow slip cycles in the Mexican subduction zone. *Journal of Geophysical Research: Solid Earth*, *124*, 599–608. https://doi.org/10.1029/2018JB016517

Hyvarinen, A., Karhunen, J., & Oja, E. (2004). *Independent component analysis*. Hoboken: John Wiley. https://doi.org/10.1007/978-3-540-92910-913

Hyvarinen, A., & Oja, E. (1997). A fast fixed-point alogrithm for independent component analysis. *Neural Computation*, *9*, 1483–1492. https://doi.org/10.1162/neco.1997.9.7.1483

Jónsson, S., Zebker, H., Segall, P., & Amelung, F. (2002). Fault slip distribution of the 1999 Mw 7.1 Hector Mine, California, earthquake, estimated from satellite radar and GPS measurements. *Bulletin of the Seismological Society of America*, *92*(4), 1377–1389. https://doi.org/10.1785/0120000922

Jolivet, R., Agram, P. S., Lin, N. Y., Simons, M., Doin, M.-p., Peltzer, G., & Li, Z. (2014). Journal of Geophysical Research: Solid Earth Improving InSAR geodesy using Global Atmospheric Models. *Journal of Geophysical Research: Solid Earth*, *119*, 2324–2341. https://doi.org/10.1002/2013JB010588.Received

Jolivet, R., Grandin, R., Lasserre, C., Doin, M.-p., & Peltzer, G. (2011). Systematic InSAR tropospheric phase delay corrections from global meteorological reanalysis data. *Geophysical Research Letters*, *38*, L17311. https://doi.org/10.1029/2011GL048757

Kazachkina, E., Cotte, N., Jara, J., Kostoglodov, V., Radiguet, M., & Walpersdorf, A. (2018). 2017 SSE in Guerrero interacts with forearc crustal faults, major earthquakes and SSE in Oaxaca, Mexico. American Geophysical Union, Fall Meeting 2018, abstract #T43E-0436.

Kostoglodov, V., Singh, S. K., Santiago, J. A., Franco, S. I., Larson, K. M., Lowry, A. R., & Bilham, R. (2003). A large silent earthquake in the Guerrero seismic gap, Mexico. *Geophysical Research Letters*, *30*(15), 1807. https://doi.org/10.1029/2003GL017219

López-Quiroz, P., Doin, M.-p., Tupin, F., Briole, P., & Nicolas, J. M. (2009). Time series analysis of Mexico City subsidence constrained by radar interferometry. *Journal of Applied Geophysics*, *69*(1), 1–15. https://doi.org/10.1016/j.jappgeo.2009.02.006

Larson, K. M., Kostoglodov, V., Miyazaki, S., & Santiago, J. A. S. (2007). The 2006 aseismic slow slip event in Guerrero, Mexico: New results from GPS. *Geophysical Research Letters*, *34*, L13309. https://doi.org/10.1029/2007GL029912

Larson, K. M., Lowry, A. R., Kostoglodov, V., Hutton, W., Sánchez, O., Hudnut, K., & Suárez, G. (2004). Crustal deformation measurements in Guerrero, Mexico. *Journal of Geophysical Research*, *109*, B04409. https://doi.org/10.1029/2003JB002843

Li, Z., Fielding, E. J., Cross, P., & Muller, J. P. (2006). Interferometric synthetic aperture radar atmospheric correction: GPS topography-dependent turbulence model. *Journal of Geophysical Research*, *111*, B02404. https://doi.org/10.1029/2005JB003711

Li, Z., Muller, J. P., & Cross, P. (2003). Comparison of precipitable water vapor derived from radiosonde, GPS, and Moderate-Resolution Imaging Spectroradiometer measurements. *Journal of Geophysical Research*, *108*(D20), 4651. https://doi.org/10.1029/2003JD003372

Li, Z., Muller, J. P., Cross, P., & Fielding, E. J. (2005). Interferometric synthetic aperture radar (InSAR) atmospheric correction: GPS, Moderate Resolution Imaging Spectroradiometer (MODIS), and InSAR integration. *Journal of Geophysical Research*, *110*, B03410. https://doi.org/10.1029/2004JB003446

Lin, Y. N. N., Simons, M., Hetland, E. A., Muse, P., & Dicaprio, C. (2010). A multiscale approach to estimating topographically correlated propagation delays in radar interferograms. *Geochemistry, Geophysics, Geosystems*, *11*, Q09002. https://doi.org/10.1029/2010GC003228

Lowry, R., Larson, K. M., Kostoglodov, V., & Bilham, R. (2001). Transient fault slip in Guerrero, southern Mexico. *Geophysical Research Letters*, *28*(19), 3753–3756.

Mackenzie, D., Elliott, J. R., Altunel, E., Walker, R. T., Kurban, Y. C., Schwenninger, J. L., & Parsons, B. (2016). Seismotectonics and rupture process of the M W 7.1 2011 Van reverse-faulting earthquake, eastern Turkey, and implications for hazard in regions of distributed shortening. *Geophysical Journal International*, *206*(1), 501–524. https://doi.org/10.1093/gji/ggw158

Melgar, D., Pérez-Campos, X., Ramirez-Guzman, L., Spica, Z., Espíndola, V. H., Hammond, W. C., & Cabral-Cano, E. (2018). Bend faulting at the edge of a flat slab: The 2017 Mw7.1 Puebla-Morelos, Mexico earthquake. *Geophysical Research Letters*, *45*, 2633–2641. https://doi.org/10.1002/2017GL076895

Melgar, D., Ruiz-Angulo, A., Garcia, E. S., Manea, M., Manea, V. C., Xu, X., et al. (2018). Deep embrittlement and complete rupture of the lithosphere during the Mw8.2 Tehuantepec earthquake. *Nature Geoscience*, *11*, 18–25. https://doi.org/10.1038/s41561-018-0229-y

Milliner, C., Materna, K., Bürgmann, R., Fu, Y., Moore, A. W., Bekaert, D., et al. (2018). Tracking the weight of Hurricane Harvey's stormwater using GPS data. *Science Advances*, *4*(9), eaau2477. https://doi.org/10.1126/sciadv.aau2477

Mirwald, A., Cruz-Atienza, V. M., Díaz-Mojica, J., Iglesias, A., Singh, S. K., Villafuerte, C., & Tago, J. (2019). The 19 September 2017 (M w 7.1) intermediate-depth Mexican earthquake: A slow and energetically inefficient deadly shock. *Geophysical Research Letters*, *46*, 2054–2064. https://doi.org/10.1029/2018GL080904

Murray, K. D., Bekaert, D. P., & Lohman, R. B. (2019). Tropospheric corrections for InSAR: Statistical assessments and applications to the Central United States and Mexico. *Remote Sensing of Environment*, *232*, 111326. https://doi.org/10.1016/j.rse.2019.111326

Obara, K., & Hirose, H. (2006). Non-volcanic deep low-frequency tremors accompanying slow slips in the southwest Japan subduction zone. *Tectonophysics*, *417*(1-2), 33–51. https://doi.org/10.1016/j.tecto.2005.04.013

Okada (1992). Internal deformation due to shear and tensile faults in a half space. *Bulletin of the Seismological Society of America*, *82*(2), 1018–1040.

Pérez-Campos, X., Kim, Y. H., Husker, A., Davis, P. M., Clayton, R. W., Iglesias, A., et al. (2008). Horizontal subduction and truncation of the Cocos Plate beneath central Mexico. *Geophysical Research Letters*, *35*, L18303. https://doi.org/10.1029/2008GL035127

Pinel-Puysségur, B., Michel, R., & Avouac, J. P. (2012). Multi-link InSAR time series: Enhancement of a wrapped interferometric database. *IEEE Journal of Selected Topics in Applied Earth Observations and Remote Sensing*, *5*(3), 784–794. https://doi.org/10.1109/JSTARS.2012.2196758

Radiguet, M., Cotton, F., Vergnolle, M., Campillo, M., Valette, B., Kostoglodov, V., & Cotte, N. (2011). Spatial and temporal evolution of a long term slow slip event: The 2006 Guerrero Slow Slip Event. *Geophysical Journal International*, *184*(2), 816–828. https://doi.org/10.1111/j.1365-246X.2010.04866.x

Radiguet, M., Cotton, F., Vergnolle, M., Campillo, M., Walpersdorf, A., & Cotte, N. (2012). Slow slip events and strain accumulation in the Guerrero gap, Mexico. *Journal of Geophysical Research*, *117*, B04305. https://doi.org/10.1029/2011JB008801

Radiguet, M., Cotton, F., Vergnolle, M., Campillo, M., Walpersdorf, A., Cotte, N., & Kostoglodov, V. (2012). Slow slip events and strain accumulation in the Guerrero gap, Mexico. *Journal of Geophysical Research*, *117*, B04305. https://doi.org/10.1029/2011JB008801

Radiguet, M., Perfettini, H., Cotte, N., Gualandi, A., Valette, B., Kostoglodov, V., et al. (2016). Triggering of the 2014 Mw7.3 Papanoa earthquake by a slow slip event in Guerrero, Mexico. *Nature Geoscience*, *9*(11), 829–833. https://doi.org/10.1038/ngeo2817

Rogers, G., & Dragert, H. (2003). Episodic tremor and slip on the Cascadia episodic tremor and slip on the Cascadia Subduction Zone: The. *Science*, *300*(2003), 1942–1943. https://doi.org/10.1126/science.1084783

Rosen, P. A., Hensley, S., Peltzer, G., & Simons, M. (2004). Updated repeat orbit interferometry package released. *Eos*, *85*, 47.

Rousset, B., Campillo, M., Lasserre, C., Frank, W. B., Cotte, N., Walpersdorf, A., et al. (2017). A geodetic matched-filter search for slow slip with application to the Mexico subduction zone. *Journal of Geophysical Research: Solid Earth*, *122*, 10,498–10,514. https://doi.org/10.1002/2017JB014448

Rousset, B., Jolivet, R., Simons, M., Lasserre, C., Riel, B., Milillo, P., et al. (2016). An aseismic slip transient on the North Anatolian Fault. *Geophysical Research Letters*, *43*, 3254–3262. https://doi.org/10.1002/2016GL068250

Schwartz, S. Y., & Rokosky, J. M. (2007). Circum-Pacific subduction zones. *Reviews of Geophysics*, *45*, 1–32. https://doi.org/10.1029/2006RG000208.1

Segou, M., & Parsons, T. (2018). Testing earthquake links in Mexico from 1978 to the 2017 M=8.1 Chiapas and M7.1 Puebla shocks. *Geophysical Research Letters*, *45*, 708–714. https://doi.org/10.1002/2017GL076237

Shirzaei, M., & Bürgmann, R. (2012). Topography correlated atmospheric delay correction in radar interferometry using wavelet transforms. *Geophysical Research Letters*, *39*, L01305. https://doi.org/10.1029/2011GL049971

Simons, M., & Rosen, P. A. (2015). *Interferometric synthetic aperture radar geodesy* (Vol. 3). Oxford: Elsevier B.V. https://doi.org/10.1016/B978-0-444-53802-4.00061-0

Stone, J. V. (2004). Independent component analysis: A tutorial introduction. *Technometrics*, *49*(3), 357–359. https://doi.org/10.1198/004017007000000191

Suárez, G., Santoyo, M. A., Hjorleifsdottir, V., Iglesias, A., Villafuerte, C., & Cruz-Atienza, V. M. (2019). Large scale lithospheric detachment of the downgoing Cocos plate: The 8 September 2017 earthquake (M w 8.2). *Earth and Planetary Science Letters*, *509*, 9–14. https://doi.org/10.1016/j.epsl.2018.12.018

Tarantola, A. (2005). Inverse problem theory and methods for model parameter estimation. Society for Industrial and Applied Mathematics.

UNAM Seismology Group (2015). Papanoa, Mexico earthquake of 18 April 2014 (Mw7.3). *Geofisica Internacional*, *54*, 363–386.

Vergnolle, M., Walpersdorf, A., Kostoglodov, V., Tregoning, P., Santiago, J. A., Cotte, N., & Franco, S. I. (2010). Slow slip events in Mexico revised from the processing of 11 year GPS observations. *Journal of Geophysical Research*, *115*, B08403. https://doi.org/10.1029/2009JB006852

Villafuerte, C., & Cruz-Atienza, V. M. (2017). Insights into the causal relationship between slow slip and tectonic tremor in Guerrero, Mexico. *Journal of Geophysical Research: Solid Earth*, *122*, 6642–6656. https://doi.org/10.1002/2017JB014037

Wallace, L. M., Hreinsdóttir, S., Ellis, S., Hamling, I., D'Anastasio, E., & Denys, P. (2018). Triggered slow slip and afterslip on the Southern Hikurangi Subduction Zone following the Kaikura earthquake. *Geophysical Research Letters*, *45*, 4710–4718. https://doi.org/10.1002/2018GL077385

Walpersdorf, A., Cotte, N., Kostoglodov, V., Vergnolle, M., Radiguet, M., Santiago, J. A., & Campillo, M. (2011). Two successive slow slip events evidenced in 2009–2010 by a dense GPS network in Guerrero, Mexico. *Geophysical Research Letters*, *38*, L15307. https://doi.org/10.1029/2011GL048124

Walters, R. J., Elliott, J. R., Li, Z., & Parsons, B. (2013). Rapid strain accumulation on the Ashkabad fault (Turkmenistan) from atmosphere-corrected InSAR. *Journal of Geophysical Research: Solid Earth*, *118*, 3674–3690. https://doi.org/10.1002/jgrb.50236

Williams, S., Bock, Y., & Fang, P. (1998). Integrated satellite interferometry: Tropospheric noise, GPS estimates and implications for interferometric synthetic aperture radar products. *Journal of Geophysical Research*, *103*(B11), 27,051–27,067. https://doi.org/10.1029/98jb02794

Yu, C., Li, Z., Penna, N. T., & Crippa, P. (2018). Generic atmospheric correction model for interferometric synthetic aperture radar observations. *Journal of Geophysical Research: Solid Earth*, *123*, 9202–9222. https://doi.org/10.1029/2017JB015305

Zebker, H. A., Rosen, P. A., & Hensley, S. (1997). Atmospheric effects in interferometric synthetic aperture radar surface deformation and topographic maps. *Journal of Geophysical Research*, *102*(10), 7547–7563. https://doi.org/10.1029/96JB03804

Zigone, D., Rivet, D., Radiguet, M., Campillo, M., Voisin, C., Cotte, N., et al. (2012). Triggering of tremors and slow slip event in Guerrero, Mexico, by the 2010 Mw 8.8 Maule, Chile, earthquake. *Journal of Geophysical Research*, *117*, B09304. https://doi.org/10.1029/2012JB009160

Appendix 2: CV

Birth date: 08/09/1976, three children.

Present day situation: Assistant professor (Maître de Conférences) at Univ. Grenoble Alpes (French CNU sections: 35/36)

Research Organisations: ISTerre (Institut of Earth Sciences), which belong to the federative research structure **OSUG** related to all aspects of the Universe, the Earth and environmental systems. At ISTerre, member of the research team **Earthquake cycle and transient deformations**

Teaching Departement: teaching at the Univ. Grenoble Alpes, in the department of Physic, Engineering, Earth, Environment and Mecanics (PHITEM)

Address: Maison des Géosciences, BP 53, 38041 Grenoble, Cedex 9, France.

erwan.pathier@univ-grenoble-alpes.fr / 04 76 63 52 09

ORCID: 0000-0002-3662-0784

Positions

• *Since september 2006 :* Assistant Professor at Univ. Grenoble Alpes (formerly Univ. Joseph Fourier)

• *September 2004- august 2006 :* Postdoctoral Research Associate at COMET (Centre for Observation and Modelling of Earthquakes, Volcanoes and Tectonics) at the Department of Earth Sciences of Oxford University, United Kingdom.

• *January 2004 – July 2004 :* Postdoctoral Teaching and Research position at University Paris-Est, Marne-la-Vallée, France.

Formation and diploma

• *November 1999 – December 2003 :* PhD Thesis at University Paris-Est Marne-la-Vallée and at University Paris 6. Contributions to active tectonics of Taiwan from differential SAR interferometry. Supervisors Jacques Angelier, Benoît Deffontaines and Bénédicte Fruneau.

• *September 1998 - August 1999 :* D.E.A. (Equivalent to Master of Sciences) with specialization in GIS at ENSG (national engineering school of geographic sciences), ENST (national engineering schools of telecommunication) and University Paris-Est Marne-la-Vallée, France.

• *September 1996 – June 1998 :* Licence and Maîtrise in geology and geophysics (equivalent to Bachelor of Sciences), University of Nantes, France.

Appendix 3:
Table of study-areas since 2004

Table of the different study areas I have work on since my PhD. The Supervision column indicated when the work was involving a Master student (M), PhD student (PhD) or Post-doc (Post-D).

Area	Short Description	Geodetic techniques (sensor if InSAR)	Supervision	Publications and selected communications
Taiwan	Longitudinal Valley Fault (Creep)	Envisat ALOS-1 GNSS	Champenois J.(PhD) Chararaa R. (Post-D) Peng W. (Post-D)	A11, A19, C37
	SouthWest Taiwan tectonics. Aseismic deformation.	ERS-1/2 Envisat ALOS-1 Sentinel-1 ALOS-2 GNSS Levelling	Champenois J. (PhD) Liao Y.-T. (M) Abraham C. (M) Zhou Y. (Post-D)	A5, A7, A20 C53, C59, C70, C77
	Jiashian EQ, 2010-03-04, Mw 6.4	ALOS-1		C59
	Meinong EQ, 2016-02-05, Mw 6 .4	ALOS-1 Sentinel-1 GNSS		C70
	Global Taiwan deformation map	ALOS-1 Sentinel-1 ALOS-2 GNSS	Fekouani M. (M)	C61, C66
Iran	NE Iran and the South Caspian region	GNSS Envisat	Clouvel G. (M) Mousavi Z. (PhD)	A14
	Interseismic Sharoud Fault	Envisat GNSS	Mousavi Z. (PhD)	A16
	Interseismic Doruneh fault	Envisat GNSS	Mousavi Z. (PhD)	A25
	Teheran Subsidence	Envisat Levelling		O4
Mexico	Guerrero 2006 Slow Slip Event	Envisat GNSS	Cavalié O. (Post-D) Balti H. (M)	A13
	Guerrro 2010 Slow Slip Event	Envisat GNSS	Bacques G. (PhD)	C40, C48
	Petatlan EQ, 2014-04-18, Mw 7.5	Radarsat-2		-
	Guerrero 2017-2018 SSE	Sentinel-1 GNSS	Maubant L. (PhD)	A24
	Chiapias EQ, 2017-09-08, Mw 8.2	ALOS-2, Sentinel-1		-
	Puebla EQ, 2017-09-19, Mw 7.1	Sentinel-1	Maubant L. (PhD)	-
	Oaxaca EQ, 2018-02-16	Sentinel-1	Maubant L. (PhD)	-

	La Venta Fault system	Envisat GNSS	Rojo-Limon G. (M)	C67
	Interseismic, all along the mexican subduction	Envisat (stripmap and ScanSAR) Sentinel-1 ALOS-2 TDX-DEM GNSS	Reverso T. (M) Diomandé A. (M) Maubant L. (PhD)	Article in prep. (Maubant et al.)
Venezuela	El Pillar fault system	ALOS-1, ALOS-2, GNSS	Pousse L. (PhD)	A18
	intersismiqueBocono fault system	ALOS-1 GNSS TDX-DEM	Pousse L. (PhD)	A21
Ecuador	Interseismic Quito fault system	Sentinel-1	Espin P. (M)	C75
Italy	Apennines (interseismic strain and hydrological signal)	Sentinel-1 GNSS	Gaubert-Bastide T. (M)	-
	Norcia EQ (2016 Italy	Sentinel-1 HR Optical imagery	Maubant L. (M)	C82
Turkey	Izmir EQ (2005 Western Turkey), Mw=5.8	Envisat		-
Various Earthquakes studies	2005 Pakistan EQ	Envisat GNSS Aster	Perrin J. (M) Yan Y. (PhD)	A06, A10, A12
	Sichuan EQ (2008, China)	ALOS-1		A08
	Palu EQ (Indonesia 2018)	ALOS-2 Optical Imagery		A23
	Le Teil EQ (2019 France) Mw=5	Sentinel-1		-
Liban	Beyrouth subsidence	Envisat	Roussel C. (M)	-
Grenoble area (France)	Rock-Fall	ERS-1/2	Barnavol J. (M)	-
	City Sudsidence	ERS-1/2 Envisat Levelling	Kniess U. (PhD) Michel S. (M)	C23, C24
	Landslides in Trièves	Lidar, Aerial photo, GNSS, Sentinel-2 Envisat	Kniess U. (PhD)	A09, A17, A22
	Belledonne massif geomorphology	Lidar	Ngouegne-Okouma J. (M)	-
	Buidling seismic vulnerability in city	Lidar, Aerial photo	Matsuka P. (PhD)	P05, A15

Appendix 4:
Research projects listing

Since 2007, I participated to 3 european projects (FP6, FP7, H2020), 5 ANR projects (French National Research Agency), 6 projects from National program, 6 international bilateral projects (Taiwan, Iran), around 20 projects with space agencies (ESA, JAXA, CNES, DLR) and a dozen of project from local calls for project (e.g. from University, OSUG, ISTerre).

European Projets

- FP6 Marie-Curie Research Training Network (2007-2011): “Mountain-Risks”. Involved in working block WB1 “Hazard Analysis”.
- FP7-ENV-2008-1 Projet SHARE (2009-2013): “Seismic Hazard Harmonization in Europe”. Involved in Task 4.4 « Europe-wide proxies to site conditions ».
- H2020-INFRADEV-2014-2015/H2020-INFRADEV-1-2015-1, EPOS IP project (2015-2019, European Plate Observing System, Implementation Phase). Involved in WP12 Satellite Data. implementation of an on demand Service for producing ground deformation product from Satellite data.

ANR Projets (French National Research Agengy):

- EFIDIR (2007-2011): « Extraction et Fusion d’information pour la mesure des déplacements en imagerie radar ». Involved in Work-package 4 “Development of a New Small temporal and spatial baselines (NSBAS) processing chain” and Work-package 5, “Large displacement measurements from multivariate SAR data”.
- GGAP (2008-2012): « Nouvelles perspectives sur le risque sismique associé à la subduction : transitoires, tremors, monitoring passif, tectonique et scénarios ». Involved in Task1 « Geodesy ».
- LIBRIS (2009-2014): « Contribution à l’étude du risque sismique au Liban ». Involved in workpackage 4 «site effects and strong ground motion prediction » in order to use subsidence map from InSAR to infer information about sediment depth and site effects.
- URBASIS (2009-2014): « SISmologie URBAine: évaluation de la vulnérabilité et des dommages sismiques par méthodes innovantes ». Involved in work-package 1 « Analyse à l’échelle de la ville » with the goal to estimate remote-sensing technique capacity to assess building seismic vulnerability at the city scale.
- EQTIME, (2020-2024): « Quantifying the temporal and spatial slip variability in the earthquake cycle spanning months to million years timescales”. Responsible of work-package 2 “Seismic cycle and slip distribution”.

Projects from other national programs

- CNRS-INSU 3F (2007-2008): « Nature et rôle des 'séismes lents' dans le cycle sismique: cas de la lacune de Guerrero, Mexique ». Coordinator of Geodesy-InSAR task.
- CNRS-Post-doc grant (2007-2008): CNRS « séismes lent au Mexique par approche InSAR ». Olivier Cavalié got the position.
- CNRS-INSU PNTS-AO2006, (2007-2011) **(PI)** : « Mesure des déplacements du sol par interférométrie radar satellitaire en bande C et L : optimisation pour les déplacements liés au cycle sismique ».
- CNRS-INSU PNTS_AO2013 (2013 -2016): « Caractérisation de la variabilité spatiale et temporelle du cycle sismique de subduction par la combinaison cGPS et InSAR : un enjeu méthodologique »
- CNRS-AO Mastodons (2013-2017): « Massification du calcul des déformations de surface par imagerie radar multi-temporelle, multi-spectrale et haute résolution ».
- CNRS-MITI 80|Prime (2019) : « DeformVis, Visualisation interactive de séries temporelles et de réseaux d'interférogrammes pour la qualification et l'analyse de données d'interférométrie radar

International Bilateral Projects

- PHC Orchid Projet Hubert Curien France-Taiwan, (2015-2016) **(PI)**, "Active tectonic deformations in Southwestern Taiwan: combined geodetic and seismological approach".
- PRC- CNRS France –Taiwan (2017-2018) **(PI)**, Relationship between slow and fast slip events in southwestern Taiwan
- PHC Gundishapur (2018-2019):"Déformation active et aléa sismique à l'Est de l'Iran"
- INSU-LIA France-Taiwan LIA : involved in LIA-Adept (2007-2014), LIA- D3E (2015-2019)
- INSU-GDRI France-Iran (2017-2020) : TRIGGER, Trans-disciplinary Research on Iranian Geology, Geodynamics, Earthquake and ressources.
- MOST Taiwanese Dragon Gate Program 2018-2020, (Partnership Program for the Connection to the Top Labs in the World) funded by MOST (Ministery of Science and Technology of Taiwan). Collaboration with the research team led by CHEN Hui-Hsuan Kate (NTNU) and Prof. HU Jyr-Ching (NTU)

Projects with space agencies:

Those projects (except the CNES ones) were mainly aiming to get satellite data from Space Agencies, when they are/were not freely available.

- **European Space Agency (ESA) :**
  - # 1041 AO-Cat-1 : « Interferometric study of the tectonic ground displacements of the sismogenic zone of Taiwan »
  - # 5036 AO-Cat-1 **(PI)** "Study of slow earthquakes in Southern Mexico using SAR interferometry",

- # 6124 AO-Cat-1 **(PI)**, "Testing and improving InSAR processing strategies for measuring ground motions: applications to landslide and subsidence in the Grenoble area (French Alps)"
- # 6937 AO-Cat-1 "Present-day fault kinematics in Lebanon and subsidence in Beirut, derived from SAR interferometry : toward a better seismic hazard assessment"
- # 7023 AO-Cat-1 "Slip rate estimation of the Doruneh and Dashte-Bayaz faults (Iran) using InSAR"
- # 21294 ESA Third Party Mission : « Request for Interferometric RADARSAT SAR data to study the 2014 Guerrero (Mexico) Slow Slip Event in relation to the Mw 7.2, 18 April 2014 Petatlan Earthquake. for RADARSAT »

- **Japan Aerospace Exploration Agency (JAXA) :**
  - ALOS-1 1st RA #112: "Active Tectonics and Earthquake Mechanisms in Taiwan From Image Correlation and Insar Techniques".
  - ALOS-1 3rd RA #600: "Land subsidence in Taiwan from L-Band SAR interferometry"
  - ALOS-2 4th RA #1294 **(PI)**: "Monitoring slow-slip events along the Mexican subduction zone by ALOS-2 SAR interferometry"
  - ALOS-2 4th RA #1288 : "Consistent measurements of crustal deformation of the Taiwan Island by ALOS-2 SAR interferometry."
  - ALOS-2 6th RA #3223: "Insights into creep and interseismic deformation along El Pilar and Central Range Fault active strike-slip faults from D-INSAR"
  - ALOS-2 6th RA #3255: "Validation of active deformation along Taiwan collisional orogenic belt by ALOS-2, Sentinel-1 and continuous GPS measurements"
  - ALOS-2 6th RA #3328 **(PI)**: "Validating ability of ALOS-2 InSAR time series analysis to quantify Slow-Slip Events in the Mexican subduction zone.
  - EO-ERA2 #ER2A2N021 **(PI)** : « Source separation in INSAR time-series analysis with application to large-scale ground deformation related to earthquake cycle »

- **French Space Agency / Centre National d'Etude Spatiale (CNES):**
  - CNES-APR (2012-2014): « SAR_ready: outils de mesure des déformations liées aux failles, volcans ou glaciers, par imagerie radar multi-temporelle, multi-spectrale et haute résolution ».
  - CNES-APR (2014-2020) **(PI)**: «"SSEMEX" : study of the slow earthquakes in the Mexican Subduction zone using GPS and satellite SAR interferometry technique.».
  - CNES-APR (2015-2017): "TerrSol Glob-Taiwan" project aiming to produce a global coverage map of ground deformation of Taiwan, using satellite SAR interferometry technique.
  - CNES-APR-(2018-2020) « DeformIran : Caractérisation du comportement des failles actives en Iran de l'Est pour une évaluation réaliste de l'aléa sismique par combinaison de géodésie (GNSS, InSAR), tectonique et modélisation »
  - CNES-APR-(2018-2019) « Temis: Contraindre la variabilité spatiale et temporelle du glissement au cours du cycle sismique de l'échelle du mois à celle du million d'années dans les Apennins Centraux (Italie). »
  - CNES-APR-(2019-2020) « InSAR-VIZ ».

- **German Space Agency (DLR):**
  - TandemX IDEM_GEOL0130 (2014-2016) / DEM_OTHER1338 (2017-2018) **(PI)** : « Study of Slow-slip events along the Mexican subduction zone by SAR interferometry »

- **CEOS seismic risk Pilot (international Committee on Earth Observation Satellite)**
  - 2015-2018, involved in CEOS DRM seismic risk Pilot,.international initiative to enhance the contribution of Earth observation satellites to earthquake risk mitigation. Coordinating role for JAXA data acquisitions http://ceos.org/ourwork/workinggroups/disasters/earthquakes

Projects from local research calls

Since 2017, I have been involved in a dozen of projects in response to local calls for tenders, most of them as a project investigator (**PI**) (IDEX, Labex OSUG@2020, Pôle Grenoblois pour les Risques Naturels, AO Interne ISTerre).

Appendix 5:
Activities as supervisor

In the course of my career I have had the opportunity to supervise several PhD students either as an official PhD co-supervisor (5), or as an unofficial but very involved supervisor of the thesis (2). I have supervised about fifteen Master's or engineering school students. I have also helped to train post-doctoral researchers or engineers on fixed-term contracts. In my publication list, the publications whose first author is related to these supervision are marked with an asterisk (*).

I was thus able to gain experience of different ways of supervising a thesis through the different thesis directors I have worked with, but also experience of different sources of funding that may have implications for the course of a thesis. I have also gained experience on the recruitment phase which is crucial, especially when you need to recruit students you have never worked with before.

List of PhD students that I have co-supervised

- **Louise Maubant** (Oct. 2017- Defense expected in Nov. 2020). «Slow earthquakes and interseismic coupling variability: the mexican subduction as seen from satellite geodesy ». Sources of funding : CNES (50%) and Doctoral School TUE of Univ. Grenoble Alpes (50%). Thesis Director: Erwan Pathier, co-director: Mathilde Radiguet. She already have one published journal article (A24) and another one is in preparation.
- **Zahra Mousavi** (Oct. 2010 – Nov 2013, 37 months). « Characterization of active fault behavior in eastern Iran using a combined geodetic (GPS and InSAR) and tectonic approach; implications on seismic hazard". Source of funding: Doctoral School TUE of Univ. Grenoble Alpes. Thesis Director: Andrea Walpersdorf, co-director : Erwan Pathier. Zahra was an Iranian student I had the opportunity to supervised with A. Walpersdorf for her Master internship. Her PhD work I supervised has been valued in 2 Journal articles (A14, A16). In 2015, Zhara got a Lecturer position at the recognized «Institute for Advanced Studies in Basic Sciences » of Zanjan in Iran (http://www.iasbs.ac.ir). We are still collaborating with her.
- **Panagiota Matsuka** (Oct 2010, abandonned in Dec. 2012). «Seismic risk analysis in urban areas by very high resolution remote sensing and multivariate data analysis". Source of funding: ANR project Urbasis. Thesis Director: Jocelyn Chanussot co-director: Erwan Pathier. Her abondonment at the end of the second year was the result of a growing gap between the expectations of the supervisors and the motivation and above all Panagiota's ability to provide a sustained level of work. The preliminary results were nevertheless the subject of a proceeding (P05) and communication at international congresses and could be taken up and developed in the thesis of Ismaël Riedel resulting in a journal article (A15). I have not heard from Panagiota since she left.
- **Guillaume Bacques** (Feb. 2010 – Nov. 2013, 45 months). «Study of spatio-temporal variations of aseismic landslides along major faults by satellite Differential RADAR interferometry. Sources of funding : CNES (50%), BRGM (50%). Due to the funding, the PhD was on two location ISTerre (first 1.5 year) and then BRGM (Orléan), explaining the large number of supervisors, which retrospectively was not a good solution. Thesis director:

Fabrice Cotton, co-directors : Erwan Pathier, Cécile Lasserre, Daniel Raucoules and Marcello de Michele. His thesis work was valued late by a publication in Nature Scientific Report on the part about the Parkfield fault creep (Bacques et al., 2018). Guillaume found in 2016 a CDD position as a pedagogical engineer at Pierre and Marie Curie University. Between 2017 and 2018, he worked for the company Buzar Drone Solution. Since 2018 he has been working as a CDD engineer at the OPGC with Philippe Labazuy on Virtual Reality for the teaching of Geosciences and at the same time working on radar on board drones.

- **Ulrich Kniess** (May 2007 to Oct 2011, 53 months). « Quantification of the evolution of clay landslides using remote sensing techniques, Application to the Trièves region (Western French Alps) ». Source of funding : Marie-Curie Research Training Network EU project « Mountain Risks ». PhD director: Denis Jongmans, co-director : Erwan Pathier and Stéphane Schwarz. His PhD work has resulted in 3 Journal Articles (A09, A17, A22). Ulrich is now geotechnical engineer est maintenant ingénieur en géotechnique dans la société Ingenieursgesellschaft von Lieberman GmbH.

List of PhD students with active supervsion without being an official PhD director.

- **Léa Pousse** (Oct. 2013 – Dec. 2016, 38 months). « Seismic hazard along major strike slip faults in Venezuela ». Source of funding: Doctoral School of Univ. Savoie Mont-Blanc (USMB). I actively participated by supervising the InSAR work done in her thesis. Thesis Director: François Jouanne, co-director Riccardo Vassalo. Her PhD work I supervised resulted into two Journal articles (A18, A21).After her PhD, Léa has done a first Post-doc at CEREGE (Univ. Aix-Marseille), and she's now post-doc with Ed Nissen at University of Victoria (School of Earth and Ocean Sciences).
- **Johann Champenois** (Oct. 2008 – Dec. 2011, 38 months). «Characterization of interseismic tectonic deformations of Taiwan by radar interferometry ». Source of funding: Doctoral School of Univ. Paris Est Marne-la-Vallée (now Univ. Gustave Eiffel) allocation doctorale de l'université Paris-Est Marne-la-Vallée. I actively participated by supervising the InSAR part and some field work. Thesis Director: Benoit Deffontaines, co-director : Fruneau Benedicte. Her PhD work I supervised resulted into two Journal articles (A11, A19). After his PhD, Johann did a post-doc at Institut de Radioprotection et Sûreté Nucléaire (IRSN) up to 2014, then did a post-doc at the Laboratoire Télédétection et Surveillance de l'Environnement (LTSE, CEA) and then at IPGP, and finally got a permanent position in 2017 as researcher at CEA.

Master students or engineering school students projects I have supervised

- **Corentin Abraham**, Master1 Sciences de la Terre de l'Environnement et des Planètres de l'Univ. Grenoble Alpes (05/2019 - 07/2019). « Etude de déformations de plis en front de chaîne de montagnes à l'aide de modèles cinématiques et de modèles élastiques ». Supervisor at 100%. Pursued in Master 2 STPE at UGA.
- **Pedro Espín Bedón Pedro**, Master 2 Sciences de la Terre de l'Environnement et des Planètres de l'Univ. Grenoble Alpes (02/2019-06/2019). « Surface deformation monitoring from InSAR

Sentinel data in Quito, Ecuador ». Co-Supervisor at 25%. Pursued in PhD thesis at University of Leeds (UK).

- **Thomas Gaubert-Bastide,** Master 2 Sciences de la Terre de l'Environnement et des Planètres de l'Univ. Grenoble Alpes (02/2018-06/2018). "Characterization of interseismic strain rate and hydrological interannual signals in Southern Apennines (Italy) from a combined analysis of GNSS and InSAR time series". Supervisor at 40 %. Pursued in PhD thesis at Université de Pau.
- **Miloud Fekaouni,** Master 2, Ecole Nationale Supérieur de Geographie / Univ Paris Est Marne-la-Vallée (05/2018 - 08/2018). « Cartographie des déformations de surface sur l'île de Taiwan par interférométrie RADAR Sentinel-1 ». Supervisor at 40%. Went back to his position in Algeria after his Master.
- **Arthur Roussel,** summer internship from IUT (06/2017 – 08/2017). « Création d'un plugin QGIS facilitant l'interprétation d'interférogrammes ». Supervisor at 40%.
- **Aïcha Diomandé**, Master 1 Sciences de la Terre de l'Environnement et des Planètres de l'Univ. Grenoble Alpes (29/05/2017-31/08/2017). « Evaluation de la qualité de Modèles Numériques de Terrain (MNT) au Mexique et développement d'une méthode pour réaliser un MNT amélioré pour une application à l'interférométrie radar satellitaire ». Supervisor at 100%.
- **Graciela Rojo Limon**, Master MEEES (Master international Erasmus Mundus en Earthquake Engineering & Engineering Seismology) Univ. Grenoble Alpes (fév. 2016 à juil. 2016). "Intraplate Deformation in the Guerrero Region (Mexico): Testing the Hypothesis of an Activation of the La Venta Fault System". Supervisor at 70%. Pursued in PhD thesis at ETH Zurich.
- **Johanne Ngouegne-Okouma**, Master 1 Sciences de la Terre de l'Environnement de l'Université de Grenoble (01/02/2015-16/06/2015). « Recherche d'indices morphologiques de l'activité de la faille de Belledonne (Isère) à partir d'un Modèle Numérique de Terrain Lidar haute résolution.». Supervisor at 100%. Pursue in Master 2 (specialty Géosciences : Explorations, Risques).
- **Clément Roussel,** Master 2 de l'Université de Bretagne Occidentale (01/04/2014 - 01/09/2014). « Etude de subsidence urbaine au Liban pour l'estimation des effets de sites sismiques ». Encadrement 25%. Pursued in PhD thesis at IFREMER and Victoria University of Wellington (NZ).
- **Yu-Tzu Liao**, Master 1 Sciences de la Terre de l'Environnement de l'Université de Grenoble (01/02/2014 - 12/06/2014). « Identifying active tectonic structures in South-Western Taiwan from geodetic data (GPS – InSAR) ». Supervisor at 100%. She want back to Taiwan finishing her Master of Science at NTU (National Taiwan University).
- **Thomas Reverso**, Master 1 Sciences de la Terre de l'Environnement de l'Université de Grenoble 1(01/02/2011 - 20/05/2011). « L'estimation du potentiel de l'interférométrie radar satellitaire à large fauchée (mode Scansar du satellite Envisat) pour l'étude de séismes lents dans la zone de subduction de Guerrero (Mexique) ». Supervisor at 70%. Pursued in PhD thesis at Univ. Savoie Mont-Blanc.
- **Zahra Mousavi**, Master MEEES (Master international Erasmus Mundus en Earthquake Engineering & Engineering Seismology) de l'Univ. Grenoble 1 (fév. 2010 à juin. 2010). "Interseismic deformation of two major active faults in eastern Iran: contribution of satellite radar interferometry (InSAR)". Supervisor at 50%. Pursued in PhD Thesis at ISTerre with Andrea Walpersdorf and me as supervisors.

- **Jonathan Perrin**, Master 1 Sciences de la Terre de l'Environnement de l'Université de Grenoble 1 (fev. 2010 – mai 2010). « Méthode de télédétection optique du champ de déplacement du séisme au Cachemire en 2005 ». Supervisor at 70%. Pursued in PhD thesis at CINaM (Centre Interdisciplinaire de Nanoscience de Marseille).
- **Grégory Clouvel,** Master 1 SDUEE (spécialité : OACOS) at Univ. Paris 6 (2010). « Extraction des délais troposphériques GPS en Iran de l'Est pour la correction des images InSAR ». Supervision at 20%.
- **Hayethem Balti,** 3rd year of Engineering School, Ecole Supérieure Telecom Tunis, (janv. 2009 – juin 2009). « Correction atmosphérique des images radar en interférométrie différentielle ». Supervision at 40%.
- **Sylvain Michel,** 3rd year of Engineering School, Ecole et Observatoire des Sciences de la Terre de l'Université de Strasbourg (juil. 2009 - dec 2009). «La subsidence peut-elle servir de proxy aux effets de site ? ». Supervision at 30%. After a second master at ENSG, and a geologist position at BM Geological Services Pty. Ltd, He pursued in PhD thesis at Caltech avec J-P Avouac (2014-2018) and he is now post-doc at ENS-Paris.
- **Jérémie Barnavol**, Master 1 STE, Univ. Grenoble 1 (fév. 2008 – mai 2008). « Potentiel de l'imagerie radar satellitaire pour la détection d'éboulement rocheux ». Encadrant principal, coencadrant Didier Hantz. Pursued as geologist-geotechnician engineer at Egis international.

Post-doc and training of Engineers :

- **Yang Zou** (Jan. to Dec. 2020) : 1-year post-doc with research project about « Numerical modelling of aseismic folding deformation in Taiwan using Discrete Element Method ». In collaboration with Frederic Donzé. Source of funding : UGA IDEX-ISP project (PI : Erwan Pathier)**.**
- **Wei Peng** (2019-2020): 20 months post-doc with research projects about « Swarm sequence detection in Taiwan using declustering method » in collaboration with David Marsan and Kate Chen and « Integrating Repeating Eartquake constraints in geodetic inversion of the creep of the Longitudinal Valley fault (Taiwan) in collaboration with Mathilde Radiguet. Source of funding : MOST-Taiwan Dragon Gate project.
- **Ranaa Charara** (2011-2012) : post-doc with research project about « Using cGPS data to mitigate atmospheric perturbations in spaceborne SAR interferometry for ground deformation measurement. Application to the Longitudinal Valley (Taiwan) ». In collaboration with A. Walpersdorf, J. M. Nocquet, J.-C. Hu. Source of funding : ANR project EFIDIR.
- **Olivier Cavalié** (2007-2008): post-doc with research project about «Using InSAR to study the 2006 slow earthquake in the Guerrero gap of the mexican subduction zone». Source of funding : CNRS-InSU. Olivier is now Maître de conférences at Université de Nice.

I also participated in the recruitment and/or training in satellite radar interferometry for three engineers who worked in our research team: Félicity Lodge (2010-2012, CDD, IR), Mathieu Volat (2013-2016, CDD, IR), Franck Thollard (IR-CNRS in the team since September 2016), and Christophe Laurent (2018-2020, CDD IR).

Appendix 6:
Research animation and responsabilites

Responsabilités Au niveau National

- Membre depuis 2019 du groupe de travail Terre Solide du comité TOSCA (Terre solide, Océan, Surfaces Continentales, Atmosphère) du CNES
- Participation à plusieurs projets dans le cadre du pole ForM@Ter de l'Infrastructure de recherche nationale DataTerra (Etalab, EPOS, FlatSIM). Ces projets sont portés par ForM@Ter avec une forte implication du groupe InSAR d'ISTerre.

Responsabilités Au niveau local

- Responsable adjoint de l'Equipe Cycle sismique et déformation transitoire d'ISTerre 2015-2019.
- Membre du Comité de Pilotage du Centre de données de l'OSUG. 2014-2016.

Membre de jurys de thèse

- Examinateur dans le jury de thèse de Johann CHAMPENOIS, dec. 2011 (Université Paris-Est Marne-La-Vallée) sur le sujet « Caractérisation des déformations tectoniques inter-sismiques de l'île de Taiwan par interférométrie radar »
- Examinateur dans le jury de thèse de Romy Schlögel, fev. 2015 (EOST, Université de Strasbourg) sujet « Quantitative landslide hazard assessment with remote sensing observations and statistical modelling »
- Examinateur dans le jury de thèse de Eric Henrion, dec. 2019 (EOST, Université de Strasbourg) sujet « Suivi géodésique des réservoirs souterrains»

Membre de jury de recrutement de Maître de conférences

- Membre de 5 comités de sélection à des postes de Maîtres de conférences depuis 2010 :

  Univ Paris 7 (poste n°1508) 2010, INPG-Gipsalab (poste n°600) 2011, Univ Grenoble 1 (poste n°1416) 2011, INPG-Gipsalab (poste n°600) 2012, Univ. Joseph Fourier (poste n°1111), 2015,

Membre de comités scientifique et de comités d'organisation de conferences ou workshop

- Comité d'organisation du Colloque 2007 du Groupement de Recherche G2 (geodesie Geophysique), Grenoble, 21-23 novembre
- Comité d'organisation du Workshop MDIS, 17-18 Octobre 2013, Autrans,
- Comité scientifique colloque SAGEO 2014
- Comité d'organisation du Workshop MDIS, 7-8-9 octobre 2015, Autrans,

Comité scientifique colloque WEGENER 2018, https://wegener2018.sciencesconf.org/

Membre de comités de suivi de thèse

Lin Kuan-Chan (2011), Gohkan Aslan (2016-2018), Anta-Clarisse Sarr (depuis 2016-2017) , Lea Pousse (2016), Hugo Sanchez (2016-2018).

Autres responsabilités

- Responsable scientifique du Service commun Système d'information Géographique (SIG) de l'OSUG, 2013-2018 (participation au groupe de travail depuis 2007).
- Membre de la commission informatique de l'Observatoire des Sciences de l'Univers de Grenoble (OSUG) 2014-2015.
- Membre suppléant élu au conseil de laboratoire d'ISTerre depuis janvier 2016
- Correspondant Informatique de l'Equipe Cycle sismique dans la Commission des Utilisateurs Informatique d'ISTerre, depuis 2011 (inclus la gestion de la liste de diffusion de l'équipe et la gestion du projet NSBAS sur le mesocentre de calcul de l'UGA.)

Appendix 7:
Teaching activities

En tant que Maître de Conférences, j'effectue un service d'environ 192h/an d'enseignement, à l'exception de l'année 2012-2013 où j'étais à temps partiel à 90% pour des raisons familiales et de l'année 2014-2015 où je n'ai fait qu'un demi-service en raison d'un semestre de CRCT. Depuis 2006, j'ai acquis une large expérience d'enseignement avec des publics très variés (Licence 1 et 2, Licence Pro (en alternance), Master1 et 2 STE, Master en Géographie, Ecole d'Ingénieur Polytech, Master international, Ecole Doctorale). J'ai participé à la création de nouvelles unités d'enseignement, avec notamment le souci d'introduction les outils numériques notamment en TP. J'ai aussi expérimenté de nouvelles méthodes pédagogiques (ateliers tutorés, utilisation de boitier de votes …).

Responsabilités liées à l'enseignement

• Responsable de la 1ère année de licence du parcours géosciences (Mention Sciences de la Terre et de l'Environnement) de 2008 à 2014. Rôle d'accueil, de suivi et d'orientation, impliquant notamment la participation à la commission pédagogique de DLST la participation à la commission d'enseignement de l'OSUG ainsi que la participation à l'élaboration des contrats quinquennaux (2011-2015 et 2016-2020 en cours).

• Responsabilité d'Unité d'Enseignement (UE) :

- Master 1 STPE : UE « Télédétection et SIG pour la Terre Solide » (depuis 2013).
- Master Erasmus Mundus « Earthquake Engineering and Engineering Seismology » : UE « Active Faults and Remote Sensing » (2011-2016).
- Licence Professionnelle « Protection et Prospection des Ressources Naturelles » : UE PPSTE304 : Géologie structurale, géométrie, cartographie 3D (depuis 2011).
- 1ere année de Licence Science et Technique : UE STE204 « Système Terre, Dynamique de la Terre (depuis 2016)
- 2eme année de Licence Science et Technique : UE STE401, « geothermie, gravimetrie, geodesie ». Co-responsable de l'UE (2016-2018) avec M. Radiguet.
- 1ere année d'école d'ingénieur Polytech (Geotechnique/Genie Civil) : UE KAGG6M19, « introduction aux SIG (depuis 2015)

Autres activités liées à l'enseignement

- *Participation aux actions d'orientation des Lycéens et Etudiant*: Journée des Lycéens (depuis 2009), Journée Forum des Masters.
- *Entretiens pédagogique lors de l'inscription des étudiants en première année de licence.*
- *Portage de projet pédagogique* pour améliorer les conditions d'enseignements (DLST, UFR PHITEM, Labex OSUG@2020 AO Formation.

- *Tuteur de moniteurs (LABEL RES) :* 2008-2011 Charlotte Fillon, 2009-2011 Romain Jolivet, 2010-2012 Ainhoa Lincot, depuis 2011-2013 Marie Macquet, 2012-2014 Gabrielle Helio, 2015-2016 Simon Daout, 2014-2017 Yacine Benjelloum et 2015-2018 Laura Airaghi et Olivier Passalacqua.
- *Tuteur de sportif de haut niveau en licence* (2008-2009 Leila Simonet, 2009-2010, Matthieu Ringot et Amandine Monterrat, 2011-2013, Thibaut Rey, 2013 Sylvain Franco)
- *Suivi d'étudiant handicapé* en collaboration avec le service Accueil Handicap de l'université de Grenoble (2009-2013)
- *Fête de la science* oct/nov 2015 : participation au Village de Sciences (Commune de Pont de claix) sur le thème « Observer la Terre & l'Univers avec la complicité de la lumière ! »

Activités d'Enseignements lors de workshop.

- Ecole de printemps, Les Houches, 1-6 mai, 2011, http://efidir.poleterresolide.fr/index.php/efidir-seminars/spring-school-2011. Practical Work on NSBAS processing chain.
- Ecole d'automne MDIS 2017 à Clermont-Ferrand Clermont https://mdis2017.sciencesconf.org/resource/page/id/1 Chaine de traitements interferométriques de la plateforme Form@Ter
- Ecole d'Automne MDIS 2019 à Strasbourg https://mdis-2019.sciencesconf.org/resource/page/id/2 On-demand NSBAS processing chain for S1 data
- Course on InSAR Processing, 3rd France-iran Trigger Conference, 8-10 Octobre 2019, Zanjan, Iran https://iasbs.ac.ir/~trigger/pages/work-shop.html

Récapitulatif des enseignements effectués depuis 2006

Le tableau ci-dessous récapitule les différents enseignements que j'ai effectués depuis mon recrutement en 2006 (la signification des abréviations est donnée ci-après).

Niveau	Intitulé	Description	Type et volume horaire annuel	Années exercées
L1 (divers parcours)	TUE110, STE110	Introduction au Sciences de la Terre	TP intégrés : 38h	2006-2013
L1 SVT	TUE121, STE121/203	Tectonique et sédimentation	Terrain 12h à 24h suivant les années	2007-2018
L1 PCMM	STE204	Syteme Terre, Dynamique de la Terre	9h à 15h de CM 20 à 30h de TP	2016-2020
L2 GSC	STE244	Applications sur le terrain : (Auvergne)	Terrain 30h	2008
L2 GSC/PGM/PHY	STE232	Physique de la Terre	CM 4.5h TD 3h à 9h TP 6h, terrain 4.5h	2010-2016
L2 STE/PM	STE401	Geothermie Gravimétrie Geodesie	CM 4.5h TP 8h, terrain 12h	2016-2020
IUT-1 Mesure Physique	JE2MPH	Géophysique de Terrain	TP 12h	2012
L3Pro PPRS	TUE302	Capteurs, Mesures sur le Terrain, Données	Terrain 3h TP 3h	2009, 2010
L3Pro PPRS	TUE304 STE304	Géologie Structurale, SIG, et Carto 3D	CTD 3h TP 12h	2009-2015
L3Pro PPRS	PARSCUAD	Valorisation et représentation des données en géosciences	CTD 4h TP 26h	2015-2020
Master 1, STE	TUE42R	Séismes et Risques Sismiques	CM 3h	2010
Master 1, STE	TUE402, TUE 416 STE4123 PAX8STAB	Télédétection et Système d'information Géographiques Remote Sensing and GIS (en 2019 passage en anglais)	CM 18 à 21h TP 18h à 39h suivant les années En 2018 passage de 12 h de TP en mode mini-projet	2006-2020
Master 1 STE	TUE407	Exploration du Globe : Gravimétrie	CM 9h TD 6h	2006, 2007

Master 1 STE	TUT410	Ateliers Tutorés Sur les SIG	12h	2009, 2010
M2P GER	TUE521, TUE53P1 STE53G1	Positioning : GIS and Geodesy with Field work	TP 12h à 24h suivant années	2006-2013
MEEES	TUE531	Positioning and GIS	Terrain 9h	2006-2008
MEEES/M2R TS	STE535E STE536c	Active Faults and Remote sensing	CM 7 à 12h TP 3h à 9h	2010-2019
1ere année école d'ingénieur Polytech	KAGG6M19	Introduction au SIG	CM 3h, TP 24h	2014-2020
Ecole Doctorale Terre Univ. Env.	PCED	Introduction au SIG	CM 3h TP 9h	2011, 2013

Abréviations :

GSC/PHY/PGM : parcours de Licence : Géosciences / Physique / Physique Géosciences et Mécanique

L3pro PPRS: Licence Pro en alternance "Prospection et Protection des Ressources Naturelles"

MEEES: Master Erasmus Mondus Earthquake Engineering et Earthquake Seismology

M2P GER: Master 2 Professionnel Géosciences Exploration et Risques

M2R TS: Master 2 Recherche STE Terre-Solide

PCMM : Physique, Chimie, Mécanique, Mathématiques

SIG : Système d'Information Géographique

STE : Sciences de la Terre et de l'Environnement

TUE : Terre Univers Environnement

DLST : Département de la licence Siences et Technologie